

Revealing the secrets  
of symbioses p. 788

Growing monkey embryos for  
20 days in vitro pp. 798, 836, & 837

Cross-linking aliphatic  
polymers pp. 800 & 875

# Science

\$15  
15 NOVEMBER 2019  
**SPECIAL ISSUE**  
sciencemag.org

AAAS







792

## NEWS

### IN BRIEF

**778** News at a glance

### IN DEPTH

**782** A new form of pure carbon dazzles and attracts

Reflective, conductive, and magnetic, U-carbon could have many practical uses—if it's real *By W. Wayt Gibbs*

**783** 'Secret science' plan is back, and critics say it's worse

EPA proposal would allow regulators to ignore many health studies *By D. Malakoff*

**784** Bacterial toxin linked to severe alcoholic liver disease

In mice, viruses known as phages reduced alcohol-related liver problems by eliminating a gut microbe *By E. Frederick*

**785** Drones reveal earthquake hazards hidden in the abyss

Low-cost approach enables United States to double scrutiny of seafloor creep in quake zones *By P. Voosen*

**786** A mysterious disease is striking American beech trees

Researchers debate whether a tiny worm is to blame *By G. Popkin*

**787** Top Democrat wants big AI push

Senator Charles Schumer calls for 5-year, \$100 billion plan *By J. Mervis*

### FEATURES

**788** Life partners

Nancy Moran's passion for insects and their indwelling microbes helped the field of symbiosis come into its own *By E. Pennisi*

**792** Arctic intruder

The *Polarstern* is enabling scientists to spend 1 year frozen in ice. Now, they must make sure the ship doesn't wreck their studies *By S. Hall*

PODCAST

## INSIGHTS

### POLICY FORUM

**794** China's key role in scaling low-carbon energy technologies

Meeting the Paris goals will require collaboration with China *By J. Helveston and J. Nahm*

### PERSPECTIVES

**797** Translating translation in Down syndrome

Protein quality control mechanisms may hold the key to treatment of cognitive disability *By M. Halliday and G. R. Mallucci*

QUALITY CONTROL IN THE CELL p. 816;  
RESEARCH ARTICLE p. 843

**798** Modeling the early development of a primate embryo

Post-implantation embryos from cynomolgus monkeys are cultured for extended periods *By P. P. L. Tam*

RESEARCH ARTICLES pp. 836 & 837

**800** Cross-linking polyethylene through carbenes

A carbene-forming molecule can glue various polymers, even ones lacking functional groups *By F. J. de Zwart et al.*

REPORT p. 875

**801** Piling on the pressures to ecosystems

Identifying dangerous combinations of assaults could prevent ecosystem collapse *By P. Manning*

REPORT p. 886

**802** Cellular survival over genomic perfection

DNA repair pathways permit some damage, leading to mutagenesis but not always cancer *By S. Nik-Zainal and B. A. Hall*

QUALITY CONTROL IN THE CELL p. 816

**804** Overcoming glass brittleness

Thin films of flawless amorphous alumina are ductile at room temperature *By L. Wondraczek*

REPORT p. 864

**805** Reuniting biogeochemistry with ecology and evolution

Mining of biological and geochemical data pinpoints a key trait of freshwater plants *By R. Marcé and B. Obrador*

REPORT p. 878

**806** Microbes and genes in heart failure

Human genetic variants and gut microbiota trigger cardiac inflammation *By S. Epelman*

REPORT p. 881

### BOOKS ET AL.

**809** Returning the fallen

An anthropologist offers compelling context for ongoing efforts to repatriate service members killed in Vietnam *By M. McFate*



## 810 The deadly diffusion of lethal technologies

From 3D-printed guns to weaponized hobby drones, open technologies pose sinister threats *By G. Lucas*

### LETTERS

#### 813 Seabirds: Sentinels beyond the oceans

*By M. Thibault et al.*

#### 813 Save horseshoe crabs and coastal ecosystems

*By H. Yang et al.*

#### 814 Consider Humboldt's map as intended

*By C. U. Ulloa*

#### 814 Technical Comment abstracts

## RESEARCH

### IN BRIEF

**833** From *Science* and other journals

### RESEARCH ARTICLES

#### Developmental biology

**836** In vitro culture of cynomolgus monkey embryos beyond early gastrulation  
*H. Ma et al.*

RESEARCH ARTICLE SUMMARY; FOR FULL TEXT: [DX.DOI.ORG/10.1126/SCIENCE.AAX7890](https://doi.org/10.1126/SCIENCE.AAX7890)

**837** Dissecting primate early post-implantation development using long-term in vitro embryo culture  
*Y. Niu et al.*

RESEARCH ARTICLE SUMMARY; FOR FULL TEXT: [DX.DOI.ORG/10.1126/SCIENCE.AAW5754](https://doi.org/10.1126/SCIENCE.AAW5754)

PERSPECTIVE p. 798

#### 838 Structural biology

Structure of the RSC complex bound to the nucleosome *Y. Ye et al.*

#### 843 Biomedicine

Activation of the ISR mediates the behavioral and neurophysiological abnormalities in Down syndrome *P. J. Zhu et al.*

QUALITY CONTROL IN THE CELL p. 816;  
PERSPECTIVE p. 797

#### 850 Electrochemistry

Engineering bunched Pt-Ni alloy nanocages for efficient oxygen reduction in practical fuel cells *X. Tian et al.*

### SPECIAL SECTION

## Quality control in the cell

### INTRODUCTION

**816** Quality control in cell biology

### REVIEWS

**818** Cellular quality control by the ubiquitin-proteasome system and autophagy *C. Pohl and I. Dikic*

**822** Cellular RNA surveillance in health and disease *S. L. Wolin and L. E. Maquat*

**827** Mitochondrial communication: Shaping health and disease  
*A. Mottis et al.*

PERSPECTIVES pp. 797 & 802  
RESEARCH ARTICLE p. 843

### ON THE COVER



Stylized view of the cell to illustrate that the nucleus exports RNA messages that are translated into proteins (blue) by ribosomes. Proteasomes and lysosomes degrade and recycle internalized, aberrant, or excess

proteins. The endoplasmic reticulum and Golgi complex package and sort cargoes for transport to other organelles or for export from the cell. Mitochondria provide power to the rest of the cell. For more on cellular quality control, see page 816. *Illustration: Nigel Sussman*

### REPORTS

#### 856 Laser physics

Widely tunable compact terahertz gas lasers *P. Chevalier et al.*

#### 860 Optoelectronics

Nano-opto-electro-mechanical switches operated at CMOS-level voltages  
*C. Haffner et al.*

#### 864 Glasses

Highly ductile amorphous oxide at room temperature and high strain rate *E. J. Frankberg et al.*

PERSPECTIVE p. 804

#### 870 2D materials

Electrical control of interlayer exciton dynamics in atomically thin heterostructures  
*L. A. Jauregui et al.*

#### 875 Polymer chemistry

A broadly applicable cross-linker for aliphatic polymers containing C-H bonds *M. L. Lepage et al.*

PERSPECTIVE p. 800

#### 878 Freshwater ecology

Catchment properties and the photosynthetic trait composition of freshwater plant communities  
*L. L. Iversen et al.*

PERSPECTIVE p. 805

#### 881 Immunology

Microbiota-derived peptide mimics drive lethal inflammatory cardiomyopathy  
*C. Gil-Cruz et al.*

PERSPECTIVE p. 806

#### 886 Soil ecology

The role of multiple global change factors in driving soil functions and microbial biodiversity *M. C. Rillig et al.*

PERSPECTIVE p. 801

#### 890 Solar physics

Generation of solar spicules and subsequent atmospheric heating *T. Samanta et al.*

PODCAST

#### 894 Quantum optics

Thermally condensing photons into a coherently split state of light  
*C. Kurtscheid et al.*

### DEPARTMENTS

#### 777 Editorial

CRISPR's unwanted anniversary  
*By Jennifer Doudna*

#### 918 Working Life

An escape into fiction  
*By Jeff Clark*

Science Staff .....	776
New Products .....	898
Science Careers .....	902

SCIENCE (ISSN 0036-8075) is published weekly on Friday, except last week in December, by the American Association for the Advancement of Science, 1200 New York Avenue, NW, Washington, DC 20005. Periodicals mail postage (publication No. 484460) paid at Washington, DC, and additional mailing offices. Copyright © 2019 by the American Association for the Advancement of Science. The title SCIENCE is a registered trademark of the AAAS. Domestic individual membership, including subscription (12 months): \$165 (\$74 allocated to subscription). Domestic institutional subscription (51 issues): \$1971; Foreign postage extra: Mexico, Caribbean (surface mail) \$55; other countries (air assist delivery): \$98. First class, airmail, student, and emeritus rates on request. Canadian rates with GST available upon request. GST #R123456789. Publications Mail Agreement Number 1069624. Printed in the U.S.A. Change of address: Allow 4 weeks, giving old and new addresses and 8-digit account number. Postmaster: Send change of address to AAAS, P.O. Box 96178, Washington, DC 20090-6178. Single-copy sales: \$15 each plus shipping and handling; bulk rate on request. Authorization to reproduce material for internal or personal use under circumstances not falling within the fair use provisions of the Copyright Act can be obtained through the Copyright Clearance Center (CCC), [www.copyright.com](http://www.copyright.com). The identification code for Science is 0036-8075. Science is indexed in the Reader's Guide to Periodical Literature and in several specialized indexes.



Editor-in-Chief Holden Thorp, hthorp@aaas.org

Executive Editor Monica M. Bradford

Editors, Research Valda Vinson, Jake S. Yeston Editor, Insights Lisa D. Chong

**DEPUTY EDITORS** Julia Fahrenkamp-Uppenbrink (UK), Stella M. Hurlley (UK), Phillip D. Szurromi, Sacha Vignieri **SR. EDITORIAL FELLOW** Andrew M. Sugden (UK) **SR. EDITORS** Gemma Alderton (UK), Caroline Ash (UK), Brent Grocholski, Pamela J. Hines, Paula A. Kiberstis, Marc S. Lavine (Canada), Steve Mao, Ian S. Osborne (UK), Beverly A. Purnell, L. Bryan Ray, H. Jesse Smith, Jelena Stajic, Peter Stern (UK), Valerie B. Thompson, Brad Wible, Laura M. Zahn **ASSOCIATE EDITORS** Michael A. Funk, Priscilla N. Kelly, Tage S. Rai, Seth Thomas Scanlon (UK), Keith T. Smith (UK), Yury V. Suleymanov **LETTERS EDITOR** Jennifer Sills **LEAD CONTENT PRODUCTION EDITORS** Harry Jach, Lauren Kmec **CONTENT PRODUCTION EDITORS** Amelia Beyna, Jeffrey E. Cook, Chris Filatreau, Julia Katris, Nida Masiulis, Suzanne M. White **SR. EDITORIAL COORDINATORS** Carolyn Kyle, Beverly Shields **EDITORIAL COORDINATORS** Aneera Dobbins, Joi S. Granger, Jeffrey Hearn, Lisa Johnson, Maryrose Madrid, Ope Martins, Shannon McMahon, Jerry Richardson, Alana Warnke, Alice Whaley (UK), Anita Wynn **PUBLICATIONS ASSISTANTS** Jeremy Dow, Alexander Kief, Ronnel Navas, Hilary Stewart (UK), Brian White **EXECUTIVE ASSISTANT** Jessica Slater **ASI DIRECTOR, OPERATIONS** Janet Clements (UK) **ASI SR. OFFICE ADMINISTRATOR** Jessica Waldoock (UK)

News Editor Tim Appenzeller

**NEWS MANAGING EDITOR** John Travis **INTERNATIONAL EDITOR** Martin Enserink **DEPUTY NEWS EDITORS** Elizabeth Culotta, Lila Guterman, David Grimm, Eric Hand (Europe), David Malakoff **SR. CORRESPONDENTS** Daniel Clerly (UK), Jon Cohen, Jeffrey Mervis, Elizabeth Pennisi **ASSOCIATE EDITORS** Jeffrey Brinard, Catherine Maticic **NEWS REPORTERS** Adrian Cho, Jennifer Couzin-Frankel, Jocelyn Kaiser, Kelly Servick, Robert F. Service, Erik Stokstad (Cambridge, UK), Paul Voosen, Meredith Wadman **INTERMEDIATE FOX CONTRIBUTING CORRESPONDENTS** Warren Cornwall, Ann Gibbons, Mara Hvistendahl, Sam Kean, Eli Kintisch, Kai Kupferschmidt (Berlin), Andrew Lawler, Mitch Leslie, Eliot Marshall, Virginia Morell, Dennis Normile (Shanghai), Elisabeth Pain (Careers), Charles Piller, Michael Price, Tania Rabesandratana (Barcelona), Emily Underwood, Gretchen Vogel (Berlin), Lizzie Wade (Mexico City) **CAREERS** Donisha Adams, Rachel Bernstein (Editor), Katie Langin **COPY EDITORS** Julia Cole (Senior Copy Editor), Cyra Master (Copy Chief) **ADMINISTRATIVE SUPPORT** Meagan Weiland

Creative Director Beth Rakouskas

**DESIGN MANAGING EDITOR** Marcy Atard **GRAPHICS MANAGING EDITOR** Alberto Cuadra **PHOTOGRAPHY MANAGING EDITOR** William Douthitt **WEB CONTENT STRATEGY MANAGER** Kara Estelle-Powers **SENIOR DESIGNER** Chrystal Smith **DESIGNER** Christina Aycock **GRAPHICS EDITOR** Nirja Desai **INTERACTIVE GRAPHICS EDITOR** Xing Liu **SENIOR SCIENTIFIC ILLUSTRATORS** Valerie Altounian, Chris Bickel **SCIENTIFIC ILLUSTRATOR** Alice Kitterman **SENIOR GRAPHICS SPECIALISTS** Holly Bishop, Nathalie Cary **SENIOR PHOTO EDITOR** Emily Petersen

## Interim Chief Executive Officer and Executive Publisher Alan Leshner

Publisher, Science Family of Journals Bill Moran

**DIRECTOR, BUSINESS SYSTEMS AND FINANCIAL ANALYSIS** Randy Yi **DIRECTOR, BUSINESS OPERATIONS & ANALYSIS** Eric Knott **DIRECTOR OF ANALYTICS** Enrique Gonzales **MANAGER, BUSINESS OPERATIONS** Jessica Tierney **SENIOR BUSINESS ANALYST** Cory Lipman, Meron Kebede **FINANCIAL ANALYST** Alexander Lee **ADVERTISING SYSTEM ADMINISTRATOR** Tina Burks **SENIOR SALES COORDINATOR** Shirley Young **DIGITAL/PRINT STRATEGY MANAGER** Jason Hillman **QUALITY TECHNICAL MANAGER** Marcus Spiegler **ASSISTANT MANAGER DIGITAL/PRINT** Rebecca Doshi **SENIOR CONTENT SPECIALISTS** Steve Forrester, Jacob Hedrick, Antoinette Hodal, Lori Murphy **DIGITAL PRODUCTION MANAGER** Lisa Stanford **CONTENT SPECIALIST** Kimberley Oster **ADVERTISING PRODUCTION OPERATIONS MANAGER** Deborah Tompkins **DESIGNER, CUSTOM PUBLISHING** Jeremy Huntsinger **SR. TRAFFIC ASSOCIATE** Christine Hall **SPECIAL PROJECTS ASSOCIATE** Sarah Dhere **ASSOCIATE DIRECTOR, BUSINESS DEVELOPMENT** Justin Sawyers **GLOBAL MARKETING MANAGER** Allison Pritchard **DIGITAL MARKETING MANAGER** Aimee Aponte **MARKETING MANAGER** Shawana Arnold **MARKETING ASSOCIATES** Tori Velasquez, Mike Romano, Ashley Hylton **DIGITAL MARKETING SPECIALIST** Asleigh Rojanavongse **SENIOR DESIGNER** Kim Huynh **TRADE SHOW AND MEETINGS ASSOCIATE** Andrew Clamp

**DIRECTOR AND SENIOR EDITOR, CUSTOM PUBLISHING** Sean Sanders **ASSISTANT EDITOR, CUSTOM PUBLISHING** Jackie Oberst

**DIRECTOR, PRODUCT & PUBLISHING DEVELOPMENT** Chris Reid **DIRECTOR, BUSINESS STRATEGY AND PORTFOLIO MANAGEMENT** Sarah Whalen **ASSOCIATE DIRECTOR, PRODUCT MANAGEMENT** Kris Bishop **ASSOCIATE DIRECTOR, PRODUCT DEVELOPMENT AND SPJ** Hannah Heckner **SR. PRODUCT ASSOCIATE** Robert Koepke **DIGITAL PRODUCT STRATEGIST** Michael Hardesty **SPJ ASSOCIATE** Samantha Bruno Fuller

**DIRECTOR, INSTITUTIONAL LICENSING** Iquo Edim **ASSOCIATE DIRECTOR, RESEARCH & DEVELOPMENT** Elisabeth Leonard **MARKETING MANAGER** Kess Knight **SENIOR INSTITUTIONAL LICENSING MANAGER** Ryan Rexroth **INSTITUTIONAL LICENSING MANAGER** Marco Castellani **MANAGER, SYSTEMS AND OPERATIONS** Brian Holiahn **MANAGER, AGENT RELATIONS & CUSTOMER SUCCESS** Judy Lillibridge **SENIOR OPERATIONS ANALYST** Lana Guo **FULFILLMENT COORDINATOR** Melody Stringer

**DIRECTOR, GLOBAL SALES** Tracy Holmes **US EAST COAST AND MID WEST SALES** Stephanie O'Connor, Glen Cox **US WEST COAST SALES** Lynne Stickrod **US SALES MANAGER, SCIENCE CAREERS** Claudia Paulsen-Young **US SALES REP, SCIENCE CAREERS** Tracy Anderson **ASSOCIATE DIRECTOR, ROW** Roger Gonçalves **SALES REP, ROW** Sarah Lelarge **SALES ADMIN ASSISTANT, ROW** Bryony Cousins **DIRECTOR OF GLOBAL COLLABORATION AND ACADEMIC PUBLISHING RELATIONS**, ASIA Xiaoying Chu **ASSOCIATE DIRECTOR, INTERNATIONAL COLLABORATION** Grace Yao **SALES MANAGER** Danny Zhao **PROJECT MANAGER** Kilo Lan **ASCA CORPORATION, JAPAN** Kaoru Sasaki (Tokyo), Miyuki Tani (Osaka) **COLLABORATION/CUSTOM PUBLICATIONS/JAPAN** Adarsh Sandhu

**DIRECTOR, COPYRIGHT, LICENSING AND SPECIAL PROJECTS** Emilie David **RIGHTS AND LICENSING COORDINATOR** Jessica Adams **RIGHTS AND PERMISSIONS ASSOCIATE** Elizabeth Sandler **CONTRACTS AND LICENSING ASSOCIATE** Lili Catlett

### MAIN HEADQUARTERS

Science/AAAS  
1200 New York Ave. NW  
Washington, DC 20005

### SCIENCE INTERNATIONAL

Clarendon House  
Clarendon Road  
Cambridge, CB2 8FH, UK

### SCIENCE CHINA

Room 1004, Culture Square  
No. 59 Zhongguancun St.  
Haidian District, Beijing, 100872

### SCIENCE JAPAN

ASCA Corporation  
Sibaura TY Bldg. 4F, 1-14-5  
Shibaura Minato-ku  
Tokyo, 108-0073 Japan

### EDITORIAL

science\_editors@aaas.org

### NEWS

science\_news@aaas.org

### INFORMATION FOR AUTHORS

sciencemag.org/authors/  
science-information-authors

### REPRINTS AND PERMISSIONS

sciencemag.org/help/  
reprints-and-permissions

### MEDIA CONTACTS

scipak@aaas.org

### MULTIMEDIA CONTACTS

SciencePodcast@aaas.org  
ScienceVideo@aaas.org

### INSTITUTIONAL SALES

AND SITE LICENSES  
sciencemag.org/librarian

### PRODUCT ADVERTISING

& CUSTOM PUBLISHING  
advertising.sciencemag.org/  
products-services  
science\_advertising@aaas.org

### CLASSIFIED ADVERTISING

advertising.sciencemag.org/  
science-careers  
advertise@sciencecareers.org

### JOB POSTING CUSTOMER SERVICE

employers.sciencecareers.org  
support@sciencecareers.org

### MEMBERSHIP AND INDIVIDUAL

SUBSCRIPTIONS  
sciencemag.org/subscriptions

### MEMBER BENEFITS

aaas.org/membercentral

### AAAS BOARD OF DIRECTORS

**CHAIR** Margaret A. Hamburg  
**PRESIDENT** Steven Chu  
**PRESIDENT-ELECT** Claire M. Fraser  
**TREASURER** Carolyn N. Ainslie  
**INTERIM CHIEF EXECUTIVE OFFICER**  
Alan Leshner  
**BOARD** Cynthia M. Beall  
May R. Berenbaum  
Rosina M. Bierbaum  
Ann Bostrom  
Stephen P.A. Fodor  
S. James Gates, Jr.  
Laura H. Greene  
Kaye Husbands Fealing  
Maria Klawe  
Robert B. Millard  
William D. Provine

### BOARD OF REVIEWING EDITORS (Statistics board members indicated with \$)

Adriano Aguzzi, U. Hospital Zürich  
Takuzo Aida, U. of Tokyo  
Leslie Aiello, Wenner-Gren Foundation  
Judith Allen, U. of Manchester  
Sebastian Amigorena, Institut Curie  
James Analytis, U. of California, Berkeley  
Paola Ariotti, Harvard U.  
Johan Auwerx, EPFL  
David Awschalom, U. of Chicago  
Clare Baker, U. of Cambridge  
Nenad Ban, ETH Zürich  
Franz Bauer, Pontificia Universidad Católica de Chile  
Ray H. Baughman, U. of Texas at Dallas  
Peter Bearman, Columbia U.  
Carlo Beenakker, Leiden U.  
Yasmine Belkaid, NIAID, NIH  
Philip Benfey, Duke U.  
Gabriele Bergers, VIB  
Bradley Bernstein, Mass. General Hospital  
Alessandra Biffi, Harvard Med. School  
Peer Bork, EMBL  
Chris Bowler, Ecole Normale Supérieure  
Ian Boyd, U. of St. Andrews  
Emily Brodsky, U. of California, Santa Cruz  
Ron Brookmeyer, U. of California, Los Angeles (\$) **\$**  
Christian Büchel, UKE Hamburg  
Dennis Burton, Scripps Research  
Carter Tribble Butts, U. of California, Irvine  
György Buzsáki, New York U. School of Med.  
Blanche Capel, Duke U.  
Annmarnie Carlton, U. of California, Irvine  
Lars-Erik Cederman, ETH Zürich  
Nick Chater, U. of Warwick  
Zhijian Chen, UT Southwestern Med. Ctr.  
Ib Chorkendorff, Denmark TU  
James J. Collins, MIT  
Robert Cook-Deegan, Arizona State U.  
Alan Cowman, Walter & Eliza Hall Inst.  
Carolyn Coyne, U. of Pittsburgh  
Roberta Croce, VU Amsterdam  
Jeff L. Dangel, U. of North Carolina  
Tom Daniel, U. of Washington  
Chiara Darai, Caltech  
Nicolas Dauphas, U. of Chicago  
Frans de Waal, Emory U.  
Claude Desplan, New York U.  
Sandra Diaz, Universidad Nacional de Córdoba  
Hong Ding, Inst. of Physics, CAS  
Jennifer Dionne, Stanford U.  
Dennis Discher, U. of Penn.  
Jennifer A. Doudna, U. of California, Berkeley  
Bruce Dunn, U. of California, Los Angeles  
William Dunphy, Caltech  
Christopher Dye, U. of Oxford  
Todd Ehlers, U. of Tübingen  
Jennifer Elisseeff, Johns Hopkins U.  
Tim Elston, U. of North Carolina  
Andrea Encalada, U. San Francisco de Quito  
Nader Engheta, U. of Penn.  
Karen Ersche, U. of Cambridge  
Barry Everitt, U. of Cambridge  
Vanessa Ezenwa, U. of Georgia  
Michael Feuer, The George Washington U.  
Toren Finkel, U. of Pittsburgh Med. Ctr.  
Gwen Flowers, Simon Fraser U.  
Peter Fratzl, Max Planck Inst. Potsdam  
Elaine Fuchs, Rockefeller U.  
Eileen Furlong, EMBL  
Jay Gallagher, U. of Wisconsin  
Susan Gelman, U. of Michigan  
Daniel Geschwind, U. of California, Los Angeles  
Karl-Heinz Glassmeier, TU Braunschweig  
Ramon Gonzalez, U. of South Florida  
Elizabeth Grove, U. of Chicago  
Nicolas Gruber, ETH Zürich  
Kip Guy, U. of Kentucky College of Pharmacy  
Taekjip Ha, Johns Hopkins U.  
Christian Haas, Ludwig Maximilians U.  
Sharon Hammes-Schiffer, Yale U.  
Wolf-Dietrich Hardt, ETH Zürich  
Louise Harra, U. College London  
Jian He, Clemson U.  
Carl-Philipp Heisenberg, IST Austria  
Ykä Helariutta, U. of Cambridge  
Janet G. Hering, Eawag  
Hans Hilgenkamp, U. of Twente  
Kai-Uwe Hinrichs, U. of Bremen  
David Hodell, U. of Cambridge  
Lora Hooper, UT Southwestern Med. Ctr.  
Fred Hughson, Princeton U.  
Randall Hulet, Rice U.  
Auke Ijspeert, EPFL  
Akiko Iwasaki, Yale U.  
Stephen Jackson, USGS and U. of Arizona  
Kai Johnson, EPFL  
Peter Jonas, IST Austria  
Matt Kaerberlein, U. of Washington  
William Kaelin Jr., Dana-Farber Cancer Inst.  
Daniel Kammen, U. of California, Berkeley  
V. Naray Kim, Seoul Nat. U.  
Robert Kingston, Harvard Med. School  
Nancy Knowlton, Smithsonian Institution  
Etienne Koechlin, Ecole Normale Supérieure  
Alexander Kolodkin, Johns Hopkins U.

Thomas Langer, U. of Cologne  
Mitchell A. Lazar, U. of Penn.  
Ottoline Leyser, U. of Cambridge  
Wendell Lim, U. of California, San Francisco  
Marcia C. Linn, U. of California, Berkeley  
Jianguo Liu, Michigan State U.  
Luis Liz-Marzán, CIC bioGUNE  
Jonathan Losos, Washington U. in St. Louis  
Ke Lu, Chinese Acad. of Sciences  
Christian Lüscher, U. of Geneva  
Fabienne Mackay, U. of Melbourne  
Anne Magurran, U. of St. Andrews  
Oscar Marin, King's College London  
Charles Marshall, U. of California, Berkeley  
Christopher Marx, U. of Idaho  
Geraldine Masson, CNRS  
C. Robertson McClung, Dartmouth College  
Rodrigo Medellín, U. of Mexico  
Graham Medley, London School of Hygiene & Tropical Med.  
Jane Memmott, U. of Bristol  
Edward Mielke, U. of California, Berkeley  
Tom Misteli, NCI, NIH  
Yasushi Miyashita, U. of Tokyo  
Alison Motsinger-Reif, NC State U. (\$) **\$**  
Daniel Nettle, Newcastle U.  
Daniel Neumark, U. of California, Berkeley  
Beatriz Noheda, U. of Groningen  
Helga Nowotny, Austrian Council  
Rachel O'Reilly, U. of Warwick  
Harry Orr, U. of Minnesota  
Pilar Ossorio, U. of Wisconsin  
Andrew Oswald, U. of Warwick  
Isabella Pagano, Istituto Nazionale di Astrofisica  
Margaret Palmer, U. of Maryland  
Elizabeth Levy Paluck, Princeton U.  
Jane Parker, Max Planck Inst. Cologne  
Giovanni Parmigiani, Dana-Farber Cancer Inst. (\$) **\$**  
Samuel Pfaff, Salk Inst. for Biological Studies  
Julie Pfeiffer, UT Southwestern Med. Ctr.  
Matthieu Piel, Institut Curie  
Kathrin Plath, U. of California, Los Angeles  
Martin Plenio, Ulm U.  
Elvira Poloczanska, Alfred-Wegener-Inst.  
Julia Pongratz, Ludwig Maximilians U.  
Philippe Poulin, CNRS  
Jonathan Pritchard, Stanford U.  
David Randall, Colorado State U.  
Félix A. Rey, Institut Pasteur  
Trevor Robbins, U. of Cambridge  
Amy Rosenzweig, Northwestern U.  
Mike Ryan, U. of Texas at Austin  
Mitunori Saitou, Kyoto U.  
Shimon Sakaguchi, Osaka U.  
Miquel Salmeron, Lawrence Berkeley Nat. Lab  
Nitin Samarth, Penn. State U.  
Jürgen Sandkühner, U. of Vienna  
Alexander Schier, Harvard U.  
Wolfram Schlenker, Columbia U.  
Susannah Scott, U. of California, Santa Barbara  
Rebecca Sear, London School of Hygiene & Tropical Med.  
Vladimir Shaleev, Purdue U.  
Jie Shan, Cornell U.  
Beth Shapiro, U. of California, Santa Cruz  
Jay Shendure, U. of Washington  
Brian Shiochet, U. of California, San Francisco  
Robert Siliciano, Johns Hopkins U. School of Med.  
Lucia Sivilotti, U. College London  
Alison Smith, John Innes Centre  
Richard Smith, U. of North Carolina (\$) **\$**  
Mark Smyth, QIMR Berghofer  
Pam Solts, U. of Florida  
John Speakman, U. of Aberdeen  
Tara Spire-Jones, U. of Edinburgh  
Allan C. Spradling, Carnegie Institution for Science  
V. S. Subrahmanian, U. of Maryland  
Ira Tabas, Columbia U.  
Sarah Teichmann, U. of Cambridge  
Rocio Titiunik, Princeton U.  
Shubha Tole, Tata Inst. of Fundamental Research  
Wim van der Putten, Netherlands Inst. of Ecology  
Reinhold Veugelen, KU Leuven  
Bert Vogelstein, Johns Hopkins U.  
Kathleen Vohs, U. of Minnesota  
David Wallach, Weizmann Inst. of Science  
Jane-Ling Wang, U. of California, Davis (\$) **\$**  
David Waxman, Fudan U.  
Jonathan Weissman, U. of California, San Francisco  
Chris Winkle, U. of Missouri (\$) **\$**  
Terrie Williams, U. of California, Santa Cruz  
Ian A. Wilson, Scripps Research (\$) **\$**  
Yu Xie, Princeton U.  
Jan Zaenen, Leiden U.  
Kenneth Zaret, U. of Penn. School of Med.  
Jonathan Zehr, U. of California, Santa Cruz  
Maria Zuber, MIT



# CRISPR's unwanted anniversary

**T**here are key moments in the history of every disruptive technology that can make or break its public perception and acceptance. For CRISPR-based genome editing, such a moment occurred 1 year ago—an unsettling push into an era that will test how society decides to use this revolutionary technology.

In November 2018, at the Second International Summit on Human Genome Editing in Hong Kong, scientist He Jiankui announced that he had broken the basic medical mantra of “do no harm” by using CRISPR-Cas9 to edit the genomes of two human embryos in the hope of protecting the twin girls from HIV. His risky and medically unnecessary work stunned the world and defied prior calls by my colleagues and me, and by the U.S. National Academies of Sciences and of Medicine, for an effective moratorium on human germline editing. It was a shocking reminder of the scientific and ethical challenges raised by this powerful technology. Once the details of He's work were revealed, it became clear that although human embryo editing is relatively easy to achieve, it is difficult to do well and with responsibility for lifelong health outcomes.

It is encouraging that scientists around the globe responded by opening a deeper public conversation about how to establish stronger safeguards and build a viable path toward transparency and responsible use of CRISPR technology. In the year since He's announcement, some scientists have called for a global but temporary moratorium on heritable human genome editing. However, I believe that moratoria are no longer strong enough countermeasures and instead, stakeholders must engage in thoughtfully crafting regulations of the technology without stifling it. In this vein, the World Health Organization (WHO) is pushing government regulators to engage, lead, and act. In July, WHO issued a statement requesting that regulatory agencies in all countries disallow any human germline editing experiments in the clinic and in August, announced the first steps in establishing a registry for future such studies. These directives from a global health authority now make it difficult for anyone to

claim that they did not know or were somehow operating within published guidelines. On the heels of WHO, an International Commission on the Clinical Use of Human Germline Genome Editing convened its first meeting to identify the scientific, medical, and ethical requirements to consider when assessing potential clinical applications of human germline genome editing. The U.S. National Academy of Medicine, the U.S. National Academy of Sciences, and the Royal Society of the United Kingdom lead this commission, with the participation of science and medical academies from around the world. Already this week, the commission held a follow-up meeting, reflecting the urgent nature of their mission.

Where is CRISPR technology headed? Since 2012, it has transformed basic research, drug development, diagnostics, agriculture, and synthetic biology. Future CRISPR-based discoveries will depend on increased knowledge of genomes and safe and effective methods of CRISPR delivery into cells. There needs to be more discussion about prioritizing where the technology will have the most impact as well as equitable, affordable access to its products. As for medical breakthroughs, clinical trials using CRISPR are already underway for

patients with cancer, sickle cell disease, and eye diseases. These and many other future uses of genome editing will involve somatic changes in individuals, not heritable changes that are transmissible. But the rapidly advancing genome editing toolbox will soon make it possible to introduce virtually any change to any genome with precision, and the temptation to tinker with the human germ line is not going away.

The “CRISPR babies” saga should motivate active discussion and debate about human germline editing. With a new such study under consideration in Russia, appropriate regulation is urgently needed. Consequences for defying established restrictions should include, at a minimum, loss of funding and publication privileges. Ensuring responsible use of genome editing will enable CRISPR technology to improve the well-being of millions of people and fulfill its revolutionary potential.

—Jennifer Doudna\*



**Jennifer Doudna** is the executive director of the Innovative Genomics Institute, a Howard Hughes Medical Institute investigator, and holds the Li Ka Shing Chancellor's Chair in Biomedical and Health Sciences at the University of California at Berkeley, California, USA. She is also a senior investigator at the Gladstone Institutes, San Francisco, California, USA. [doudna@berkeley.edu](mailto:doudna@berkeley.edu)

**“...the temptation to tinker with the human germ line is not going away.”**

\*J.D. is a cofounder of Caribou Biosciences, Editas Medicine, Scribe Therapeutics, and Mammoth Biosciences; scientific advisory board member of Caribou Biosciences, Intellia Therapeutics, eFFECTOR Therapeutics, Scribe Therapeutics, Mammoth Biosciences, Synthego, and Inari; and director at Johnson & Johnson. Her lab has research projects sponsored by Biogen and Pfizer.



# NEWS

## IN BRIEF

Edited by Jeffrey Brainard



A worker harvests sugarcane in southeastern Brazil, where most of the country's crop is grown

## CONSERVATION

### Brazil supports sugarcane growing in Amazon

**B**razil has reopened the door to expanding sugarcane plantations in the Amazon, even though it is difficult to grow the crop there. Scientists worry the move will increase deforestation and harm biodiversity and carbon sequestration in the jungle. President Jair Bolsonaro, who has pushed for more economic development in the Amazon, on 5 November revoked a 2009 agricultural zoning plan that prohibited public funding for sugarcane production within the Amazon region, where low yields increase risk for private investors. But Bolsonaro's administration says the ban is unnecessary because other laws require that the cultivation

be environmentally sustainable. Brazil is already the world's largest producer of sugarcane, with approximately 10 million hectares of cane fields—only 1.5% of which are now in the Amazon. The region's extremely humid weather and poor soils are not ideal for popular cane varieties, and studies indicate that Brazil has plenty of room to expand sugarcane production elsewhere without competing with other types of food production or conservation. Japan and European countries import Brazilian ethanol, a fuel produced from sugarcane, on the condition that the cane is grown in an environmentally sustainable way.

### Top Russian institute raided

**STATE SECURITY** | A premier Russian research center has become ensnared in an escalating crackdown on scientific contacts with the West. On 30 October, personnel with Russia's Federal Security Service (FSB), wearing masks and toting machine guns, descended on the P. N. Lebedev Physical Institute in Moscow, seizing documents and interrogating its director, Nikolai Kolachevsky, for 6 hours. Security agents also raided his home and extracted a written pledge from him to not leave Moscow. FSB's apparent target was a small optics company that leases office space from the institute and had

allegedly exported "military grade" glass to Germany. The 85-year-old institute, a crown jewel of the Russian Academy of Sciences, counts among its alumni famed nuclear physicist and human rights activist Andrei Sakharov and Vitaly Ginzburg, who won the Nobel Prize in Physics in 2003 for his theoretical work on superconductivity.

### NIH to broaden data policy

**FUNDING** | The U.S. National Institutes of Health (NIH) proposed last week requiring all research grantees to make their data sets available to colleagues, broadening a policy it adopted in 2003. Grant applicants

would need to submit a detailed plan for sharing data, including steps to protect research subjects' privacy. NIH program officers would review data sharing plans before awards were made and would follow up; investigators who didn't comply might be denied future funding. Under the 2003 policy, such rules apply only to NIH grantees receiving more than \$500,000 in direct costs annually. The agency will collect comments on the proposed policy through 10 January 2020 before finalizing it.

### Repairs for space detector

**ASTROPHYSICS** | Astronauts plan to begin spacewalks this week to repair the most



"I don't think he should be held with such honor."

**Yusef Anthony**, a former prison inmate, in *The Chronicle of Higher Education*, about Albert Kligman, who conducted experiments on Anthony and others from the 1950s to 1970s. Kligman, a dermatologist at the University of Pennsylvania (UPenn), developed Retin-A antiwrinkle cream and other treatments by testing them on prisoners, many of whom blamed the experiments for burns and life-long physical ailments. UPenn, which reaped large royalties from Kligman's work, named two endowed professorships for him. The university told *The Chronicle* that Kligman "was involved in research over 40 years ago that would not be acceptable by today's standards." Anthony and author Allen Hornblum, who wrote two books about Kligman, are campaigning for UPenn to publicly apologize and make amends.

expensive cosmic ray detector ever built. Fixed to the International Space Station since 2011, the \$2 billion Alpha Magnetic Spectrometer (AMS) tracks charged particles from space using an array of silicon wafers somewhat like light-sensitive chips in a digital camera. Three of four pumps that keep the wafers cool with liquid carbon dioxide have failed. Astronauts will replace all four during a series of four spacewalks. The brainchild of Nobel Prize-winning particle physicist Samuel Ting, the AMS has recorded anomalies in the flux of antiprotons and positrons that could point to particles of mysterious dark matter annihilating one another. Some researchers doubt the AMS can settle the issue, though.

## Iran's civil nuke work continues

**NONPROLIFERATION** | International projects to develop civilian uses of Iran's nuclear facilities are expected to continue despite the government's announcement last week that it will resume enriching uranium at its underground Fordow site. Iran's move is a further blow to the multilateral agreement reached in 2015 to deter it from pursuing nuclear weapons. On 6 November, Iran said it will use 696 centrifuges at Fordow to enrich uranium hexafluoride gas, producing material with a level of the fissile isotope uranium-235 suitable for commercial power reactors. (Weapons require a higher level of enrichment.) So far, the U.S. Department of State is standing by its 31 October decision to renew waivers to sanctions on Iran that allow key nonproliferation projects in the 2015 deal to go forward: a China-led effort to reconfigure Iran's Arak heavy water reactor to sharply reduce plutonium accumulation in its spent fuel, and Russia's work at Fordow to convert 348 centrifuges to make medical isotopes. But the waivers are only good for 90 days, and some prominent U.S. legislators are pressing to end them.

## United States sues over HIV drug

**PUBLIC HEALTH** | The U.S. Department of Justice last week filed an unusual lawsuit against the drugmaker Gilead Sciences for not paying the government royalties on the sale of an anti-HIV drug produced by the company. The drug, Truvada, has proved highly effective at preventing HIV infection, a strategy called pre-exposure prophylaxis (PrEP). In influential studies of monkeys, researchers at the U.S. Centers for Disease Control and Prevention (CDC) showed in 2006 that Truvada worked in PrEP, for which the

agency received four patents. Hoping to bring down the price of Truvada, which lists at \$21,388 a year per patient, critics have led a drive to push the U.S. government to enforce those patents, although Gilead challenged their validity in August. The company, based in Foster City, California, contends that CDC didn't invent anything and simply built on earlier studies by many others that showed PrEP's promise. Fewer than 200,000 people in the United States take Truvada for PrEP, and usage could increase if the company dropped the price, Gilead's critics contend.

## UC scientist union gets contract

**LABOR** | Thousands of staff scientists employed by the University of California (UC) system, who in 2018 formed the world's first union representing non-tenure-track researchers, voted overwhelmingly on 8 November to ratify their first contract. Members of Academic Researchers United (ARU) approved the



### EVOLUTION

## Earliest flower-pollinating insect found in amber

**A** beetle captured in amber nearly 100 million years ago is the earliest direct evidence of insects pollinating flowering plants, researchers report this week in the *Proceedings of the National Academy of Sciences*. The specimen—a new species named *Angimordella burmitina*—pushes back the dating of this pollination by about 50 million years. Scientists have long thought that insect pollination was key to the rapid spread of flowers during the Cretaceous period, about 145 million to 66 million years ago. The beetle was encased in an amber fragment (above) dug up in northern Myanmar and obtained by scientists in 2012. It sat on a shelf until 2017, when a paleontologist polished the amber and noticed the beetle was special. It had a curved body and head for reaching inside flowers to feed, and golden pollen covered its thorax, abdomen, and legs.



## PUBLIC HEALTH

## A culprit in vaping injuries?

**A** “potential chemical of concern” has been detected in the lungs of some of the hundreds of people afflicted this year by vaping-related lung injuries, the U.S. Centers for Disease Control and Prevention (CDC) announced last week. The discovery is a step in solving the monthslong mystery, but CDC officials and outside scientists stress that more work is needed to definitively blame lung damage on the chemical, vitamin E acetate, a synthetic form of vitamin E oil added to many e-cigarette liquids as a thickener. CDC says it hunted for chemicals in the lung fluid of 29 patients with lung injuries; it found vitamin E acetate in all of them. Although the oil is common in foods and cosmetics, researchers believe that when heated and inhaled, it may be harmful; past research has suggested it can hurt the lungs. Since March, vaping-related lung injuries have struck more than 2000 people in the United States and killed at least 39.

3-year deal 2450 to 53. It gives salary increases of up to 24% and ensures retirement benefits, expanded sick leave, and travel reimbursement, as well as parking and transit services on par with what UC's tenure-track faculty members receive. The contract also commits ARU and the university to working together to establish a bridge funding program for principal investigators covered by the contract; such a program would help support the salaries of researchers between rounds of grant funding.

## Texas cancer agency rides on

**FUNDING** | Texas voters last week approved by a nearly two-to-one margin a ballot measure that extends the life of its pioneering state cancer research funding agency. The state can now sell another \$3 billion in bonds to support the agency. Modeled after California's stem cell research agency and first approved by voters in 2007, the Cancer Prevention

& Research Institute of Texas has so far recruited 181 researchers to the state and awarded \$2.4 billion for research, cancer prevention, and commercialization.

## Scientists honored for bravery

**AWARDS** | An Indonesian forestry expert and a Canadian pharmacist have each received the 2019 John Maddox Prize for Standing up for Science, the London-based charity Sense About Science announced this week. Bambang Hero Saharjo of IPB University in Bogor, Indonesia, has testified in hundreds of court cases about destructive peatland fires in Indonesia, often started illegally by companies such as palm oil producers attempting to clear land quickly. He persisted even after a palm oil company, Jatim Jaya Perkasa, sued him for \$33.5 million in 2018 after it lost a court case in which he testified. (It later withdrew the suit.) The other honoree, Canadian pharmacist Olivier Bernard, publicly criticized health companies that

were lobbying the Quebec government to provide vitamin C injections as an alternative treatment for cancer—a treatment with no clinical basis—despite harassment and smear campaigns against him. Named for a renowned editor of *Nature*, John Maddox, the prize carries an award of £3000.

## China funds many joint papers

**PUBLISHING** | China and the United States are financially supporting joint scientific projects, but China is supporting a greater number, according to a study published last week in *Higher Education*. John Haupt and Jenny Lee of the University of Arizona in Tucson analyzed 175,665 journal articles published from 2014 to 2018 with co-authors in China and the United States; 25% included a third country co-author. Many papers credited both Chinese and U.S. funding sources; of the 10 funders sponsoring the most articles, Chinese funders, most often the National Natural Science Foundation of China, were listed on 114,268 and U.S. funders on 32,730. Amid increasing U.S. efforts to curb research engagement with China, “this study shows the benefits of U.S. collaboration with China for both the U.S. ... and global science,” the authors write.

## Conflicts don't rile reviewers

**PEER REVIEW** | Even when authors of journal articles disclose financial conflicts of interest, reviewers rarely lower the papers' quality scores or offer comments in response, researchers reported last week in *The BMJ*. The researchers say the results raise questions about whether disclosure helps reviewers and whether they are adequately trained to weigh such conflicts. The experiment used 1480 manuscripts submitted to the *Annals of Emergency Medicine*, of which a co-author of the *BMJ* study is editor-in-chief. One group of reviewers received information about authors' disclosures. Each paper was also evaluated by another reviewer who wasn't informed of conflicts—allowing the research team to compare reviewers' quality scores. Differences were insignificant; even so, reviewers said in subsequent surveys that they believed they could correct for biasing influences of conflicts when disclosed. Journals and funders typically require disclosure because studies have found that financial ties tend to produce results favoring the sponsors.

**S** **SCIENCEMAG.ORG/NEWS**  
Read more news from *Science* online.



IN DEPTH

## CHEMISTRY

# A new form of pure carbon dazzles and attracts

Reflective, conductive, and magnetic, U-carbon could have many practical uses—if it's real

By **W. Wayt Gibbs**, in Richmond

A “happy accident” has yielded a new, stable form of pure carbon made from cheap feedstocks, researchers say. Like diamond and graphene, two other guises of carbon, the material seems to have extraordinary physical properties. It is harder than stainless steel, about as conductive, and as reflective as a polished aluminum mirror. Perhaps most surprising, the substance appears to be ferromagnetic, behaving like a permanent magnet at temperatures up to 125°C. The discovery, announced by physicist Joel Therrien of the University of Massachusetts in Lowell on 4 November here at the International Symposium on Clusters and Nanomaterials, could lead to lightweight coatings, medical products, and novel electronic devices.

Therrien's talk elicited both excitement and caution among the dozens of researchers attending the meeting. “Once it is published and the work has been replicated by others, it will generate a lot of interest for sure,” says Qian Wang, an applied physicist at Peking University in Beijing. She notes that carbon is much lighter than other ferromagnetic elements such as manganese, nickel, and iron. Moreover, carbon is nontoxic in the body, she says. “If it can be magnetic, it could be very useful for making biosensors or drug-delivery carriers” that could be magnetically interrogated or directed to diseased tissues.

Robert Whetten, a materials scientist at Northern Arizona University in Tucson, says he's “actually persuaded they have something.” He recalls that in the mid-1980s, when scientists first created “buckyball” spheres made of 60 carbon atoms, “there was the same degree of skepticism, despite all the evidence.” But he also points out that past claims of magnetism in pure carbon, such as one published in *Nature* in 2001, have fallen apart when contamination was later found in the samples.

The researchers have only made thin films of the material, which they have studied with electron microscopes and x-ray spectrometers. “Much more characterization needs to be done,” says Pulickel Ajayan of Rice University in Houston, Texas. “We are trying to be extremely careful.” He and the other researchers say they have so far seen no signs of impurities that could account for the properties of the material. Based on both theoretical models and the analytical data, they believe it consists of corrugated layers of linked carbon atoms stacked like washboards, with additional bonds between the layers.

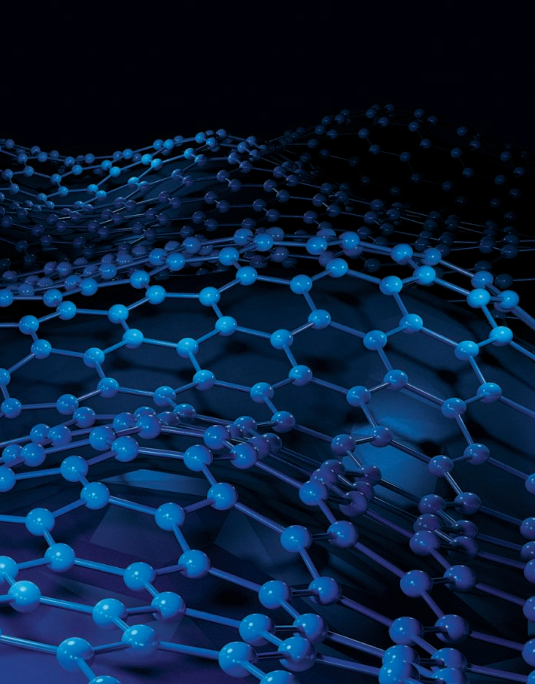
Sumio Iijima, a nanomaterials expert at Meijo University in Nagoya, Japan, renowned for his 1991 discovery of carbon nanotubes, another carbon “allotrope,” says the limited data presented are “not good enough” to convince him the group has found a new allotrope. He wants the team to perform x-ray crystallography, a gold

standard technique to determine structure, on larger samples.

Therrien says the discovery came in a failed attempt to synthesize pentagraphene, a sheet of carbon atoms bound in pentagonal rings that has been predicted but never created. His idea was to exploit a technique known as “geometrical frustration.” He placed a catalyst, a sheet of copper foil, on a pedestal in the center of a chemical vapor deposition (CVD) oven and heated it to about 800°C. But rather than pumping in a feed gas of the usual small hydrocarbons, such as methane, he injected a more complex precursor: 2,2 dimethylbutane, a cheap petrochemical that is available by the ton. As a branched hexane, the chemical has six carbon atoms arranged along a bent backbone.

The high temperatures of CVD normally break down complex hydrocarbons at the catalyst surface into atoms or simple molecules, which then self-organize into graphene sheets or crystals such as diamond. But previous experiments led Therrien to believe the hexane's crooked backbone would persist, creating a geometric constraint that would force the “frustrated” carbon groups to link up into the pentagonal cells of pentagraphene.

They did not—but the atoms settled into a different structure. Therrien says that on 13 November 2017, after teaching an evening class, he returned to his lab to check on his oven and noticed the smell of tar. The in-



Researchers believe films of U-carbon consist of stacks of undulating layers, tiled with six- or 12-atom rings and bound together by covalent bonds.

side of the furnace was caked in black pitch. But the copper foil was covered in something that looked like polished silver. “I just stopped dead,” he says. “I literally spent half an hour just staring at this, trying to figure out what on Earth had happened.”

After 2 years of further experimentation with other branched hexanes, the team was able to reliably create the substance again and again, in films up to 1 micron thick and several centimeters across. Puru Jena, a collaborator at Virginia Commonwealth University in Richmond, says models of molecular dynamics predict that the carbon atoms form corrugated layers tiled with six- or 12-atom rings and linked together by covalent bonds. Graphite, in contrast, consists of flat carbon layers that freely slide across each other.

Ajayan says the x-ray and electron-microscope data support the predicted structure. He says those data have also confirmed another prediction of Jena’s: that the bonds in the material are formed by shared electrons in a mix of particular orbital shells—what chemists call  $sp^2$  and  $sp^3$  bonds. The  $sp^2$  bonds leave electrons “not involved in any bond and kind of dangling,” which makes it easier for their spins to align, Jena says. “That gives you the ferromagnetism.”

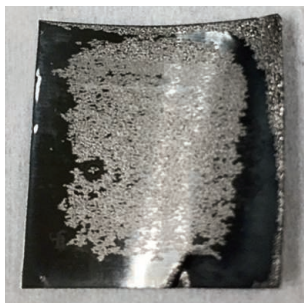
At the meeting, Therrien dramatized the magnetism by showing a video of millimeter-size flakes of the substance suspended in a

water droplet. As he slowly waved a small bar magnet over the water, the flakes followed it back and forth. More tantalizing still is his claim that the material remains magnetic even at the elevated temperatures at which motors and computers typically operate.

The magnetism adds to a suite of properties never before seen together in a form of pure carbon. They include tremendous hardness that presumably results from the bonds joining adjacent layers: “We’ve tried scratching it with steel wool, and it comes off clean,” Therrien says. “The only thing we can say verifiably scratches it is a diamond scribe.” Though the group has yet to measure the tensile strength of the material, the fact that vanishingly thin flakes hold together at millimeter size suggest it may be as strong as some metals, he says.

Then there is the mirrorlike appearance, seen in photos Therrien showed at the meeting. The team’s measurements indicate that the film, even when just 50 nanometers thick, reflects more than 90% of incoming light at wavelengths ranging from the far-ultraviolet to the midinfrared. That attribute could make it a useful reflective coating, more durable than the standard aluminum, for mirrors in cameras and telescopes.

Its electrical conductivity turned out to be just shy of that of stainless steel. But it can also display other electronic properties. Annealing the material by slowly heating it to 1000°C dims its shine and turns it into a semiconductor with a band gap—the energy required to liberate an electron—similar to that of amorphous silicon, which can turn light into electricity. That makes it a candidate material for photovoltaic cells, Therrien suggests.



Shiny films of a new material, up to 1 micron thick, formed in chemical vapor deposition ovens.

Therrien is bullish about the long-term potential of geometrical frustration to synthesize novel allotropes of carbon and other elements. “Even if it works only for carbon, the very fact that

there are probably hundreds of different allotropes that you might be able to make using this approach is going to really open things wide up.”

The group has not yet settled on a name for the mystery material. Jena calls it U-carbon—U for unusual. But Therrien, inspired by medieval alchemists who sought in vain for “adamant,” an unbreakable lodestone, is calling it adamantia. ■

W. Wayt Gibbs is a journalist in Seattle, Washington, and editorial director at Intellectual Ventures.

## U.S. POLICY

# ‘Secret science’ plan is back, and critics say it’s worse

## EPA proposal would allow regulators to ignore many health studies

By David Malakoff

Critics are blasting a revised Trump administration plan to give the U.S. Environmental Protection Agency (EPA) broad power to ignore research results when setting public health rules if officials decide the underlying data are not adequately accessible to the public.

The draft document, a version of which was leaked to *The New York Times* this week, supplements a 2018 data transparency proposal from EPA that was harshly criticized by scientific, environmental, and patient groups (*Science*, 4 May 2018, p. 472), prompting the agency to say it would issue a revision. Although EPA said in a 12 November statement that the leaked document is not the final version it sent earlier this month to the White House for review, the agency did not dispute its core substance.

The proposed supplement “is even worse than we thought it would be,” says Gretchen Goldman of the Union of Concerned Scientists in Washington, D.C. “We didn’t think [the transparency proposal] could get any worse, but we were wrong.”

One issue, critics say, is that EPA wants to greatly broaden the policy’s scope, applying it to all studies and data used by the agency and not just the “dose response” studies mentioned in the initial version. The draft also asks the public to comment on whether, in some cases, the transparency rule should be applied retroactively to past studies used to support regulation, potentially opening the door to challenges of existing rules.

EPA officials have argued that the data transparency policy is needed to ensure that the agency uses only the best “pivotal regulatory science” that can be “independently validated” when crafting “significant” rules that are expected to impose major economic costs. The leaked proposal says EPA regulators should have “the right



to place less weight” on certain studies, “to the point of entirely disregarding them,” if the underlying data are “not made available in full to EPA.”

Critics say that language is primarily designed to weaken regulation by preventing EPA from considering epidemiological and other studies in which researchers have promised to protect the privacy of human subjects. Such confidential health information, which is typically not released to the public, has played a major role in shaping stricter EPA limits on air pollutants. For example, the iconic 1993 Six Cities Study, which linked particulate air pollution to human death and disease, helped spur new EPA soot controls. But some industry groups have long objected to EPA’s use of such “secret science.”

EPA already has ways to assess the quality of studies and decide which it should consider when writing new rules, notes Chris Frey, a former scientific adviser to the agency and an air quality researcher at North Carolina State University in Raleigh. “But what those methods don’t do is say: ‘Just because there isn’t full public disclosure of the data, we’re going to wipe out and ignore that study, regardless of its quality.’ Doing that would prevent you from considering the full weight of the scientific evidence.”

The draft acknowledges that full disclosure may not be possible for some studies involving health or proprietary business information; it would empower political appointees at EPA to exempt certain studies from transparency requirements. It also asks for comment on whether EPA should adopt methods, such as those used by the U.S. Centers for Disease Control and Prevention, for only sharing sensitive data with approved researchers.

But the proposal doesn’t discuss how much such vetting might cost, or how the rule might affect efforts to protect public health, critics note. “There’s no real analysis of what this rule would do, or the costs and benefits ... it’s a solution in search of a problem,” Frey says.

One prominent advocate of the transparency rule, however, welcomes the new draft. “I’m elated. ... We’re making progress,” says Steve Milloy of JunkScience.com in Potomac, Maryland, who served on the Trump administration’s transition team at EPA. “But it’s not the end game by far,” he adds, noting the proposal must still be opened to public comment, and that any final policy will likely face a court challenge. Milloy also notes that even if EPA adopts the rule, agency officials will have leeway in interpreting it. “Words have never really mattered,” he says. “What matters is how the people in charge implement them.” ■

## BIOMEDICINE

# Bacterial toxin linked to severe alcoholic liver disease

In mice, viruses known as phages reduced alcohol-related liver problems by eliminating a gut microbe

By **Eva Frederick**

**F**or a heavy drinker whose liver has been destroyed by alcohol, an organ transplant is often the only realistic option. But because of donor liver shortages and rules that withhold them from people who have not shed their alcohol addiction, many go without. Tens of thousands die from alcoholic liver disease each year in the United States—and some go downhill much faster than others. Now, scientists have found a reason for this disparity: a toxin produced by some strains of a common gut bacterium. Working in mice, they have also tested a potential therapy, based on bacteria-destroying viruses found lurking in the sewer.

Why some drinkers with liver disease fare much worse than others “has always been a conundrum,” says Jasmohan Bajaj, a gastroenterologist and liver specialist at Virginia Commonwealth University in Richmond. The bacterium *Enterococcus faecalis* offers an explanation, Bernd Schnabl, a gastroenterologist at the University of California, San Diego (UCSD), School of Medicine, and colleagues report this week in *Nature*. In fecal samples from patients with alcoholic liver disease, levels of it were 2700 times higher than in nondrinkers, although the mere quantity didn’t correlate with a person’s outcome. Instead, the researchers identified a cell-destroying toxin called cytolysin produced by select strains of *E. faecalis* as the likely reason that some patients with alcoholic liver disease had severe symptoms.

Fewer than 5% of healthy people carry the toxinmaking strains, but the group found them in 30% of the people hospitalized with alcoholic liver disease whom they tested. And those patients had a much higher mortality rate within 180 days of admission—89% of the cytolysin-positive patients died compared with only 3.8% of the other patients. “Cytolysin is a factor that really drives mortality and liver disease severity,” Schnabl says.

He and colleagues don’t know why the strains flourish in people with alcoholic liver disease. But the team confirmed their deadly influence by colonizing some mice with the toxin-producing bacteria and others with nontoxic strains, then dosing the animals with alcohol to damage their livers. Mice with the toxin-producing bacteria fared much worse than those without.

Next, the team sought a way to precisely remove the toxic *E. faecalis* to see whether the animals’ symptoms improved. Traditional antibiotics kill broadly, so the group enlisted UCSD colleagues who study therapeutic uses of bacteriophages, or phages.

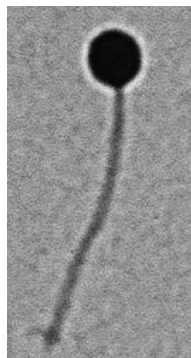
These viruses kill specific bacteria, and researchers—many in Russia and Eastern Europe—have used them for decades to treat conditions such as dysentery and gangrene.

In the university’s sewage plant—a ready-made buffet for organisms that live off fecal bacteria—the team found phages that targeted cytolytic *E. faecalis*. When mice that harbored the deadly bacteria were treated with the phages, they had less liver injury, less inflammation, and less cytolysin in their livers than animals treated with control phages. “We can reduce the

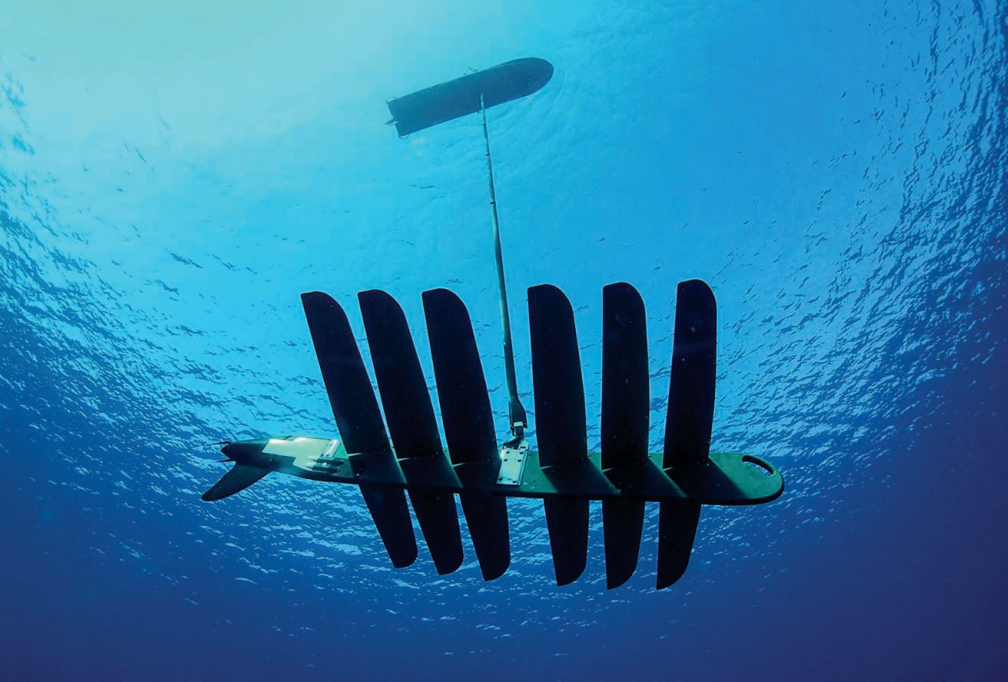
disease but we could not completely get the mice with alcoholic liver disease back to a baseline,” Schnabl says.

Bajaj calls the mouse studies “exquisitely done,” adding that although the phage therapy is far from ready for use clinically, this work pushes research on alcoholic liver disease in “an encouraging direction.”

The UCSD team is now working to create a library of phages isolated from different liver disease patients that are effective against cytolysin-positive *E. faecalis* strains. They plan to evaluate the phages for safety and then consider testing them in people with severe cases of the disease. Andrzej Górski, a phage expert at the Polish Academy of Sciences in Wrocław, applauds the plan. “Now is a good time for performing clinical trials” with phages, he says. ■



This phage can target a toxinmaking gut bacterium.



A submerged “glider” captures wave energy to tow a craft that can collect data from seafloor beacons.

## EARTH SCIENCE

# Drones reveal earthquake hazards hidden in the abyss

Low-cost approach enables United States to double scrutiny of seafloor creep in quake zones

By **Paul Voosen**

**T**here is no force on Earth quite like a subduction zone. Slips along these faults, found where plates of dense ocean crust dive beneath continents, cause the world’s most destructive earthquakes and tsunamis: 1964 in Alaska; 2004 in Indonesia; 2011 in Japan. But much remains unknown about how those faults slip and stick between catastrophes.

The radio signals of GPS, so powerful for tracking crustal movements on land, can’t penetrate the abyss. To gauge motions underwater, scientists rely on a daisy chain in which a ship tracks acoustic beacons on the sea floor—and the ship in turn fixes its position with GPS. Now, a team led by David Chadwell, a geophysicist at the Scripps Institution of Oceanography in San Diego, California, has found a way to cut costs by replacing the expensive ships with ocean-going drones.

“It’s going to make a huge difference,” says Laura Wallace, a geodetic scientist at GNS Science in Lower Hutt, New Zealand. Last month, the U.S. National Science Foundation (NSF) endorsed the approach by announcing a \$5.5 million grant to Chadwell’s team to buy beacons for 16 seafloor sites and three drones to monitor them—more than doubling the ability of U.S. scientists

to track movements of the ocean floor.

Earth scientists use GPS to measure the strain that builds up quietly between quakes. At the Cascadia subduction zone off the Pacific Northwest, for example, GPS stations on land suggest that enough strain has accumulated to drive a magnitude-9 earthquake when the fault finally ruptures. But the land-based measurements also hint that strain along the fault’s midsection, off the coast of Oregon, is being relieved by a type of harmless slip called creep. That suggests the fault could rupture in pieces, in a series of independent, smaller quakes. But without offshore measurements, scientists only see half the picture, says Harold Tobin, a geophysicist at the University of Washington in Seattle.

Acoustic GPS—tracking seafloor beacons by ship—is a pricey way to get these data. Japan has spent more than \$3 billion on acoustic GPS over the past 10 years to monitor its dangerous offshore faults. By 2020, Japan’s acoustic GPS network will include 27 stations, each consisting of multiple beacons.

The few sites that were operating at the time of the 2011 Tohoku earthquake found that the fault slipped more than 30 meters in its shallow sections, driving the devastating tsunami. Frequent monitoring since, with ship visits now every 2 months, has shown how strain accumulates irregularly across

the fault. “They can tell exactly where the patches are that would rupture in the next earthquake,” says Noel Bartlow, a geophysicist at the University of California, Berkeley, who is part of the new NSF grant.

Even more tantalizing is evidence, seen prior to the 2011 earthquake in Tohoku and elsewhere, of fault ruptures that occurred over the course of weeks rather than minutes. Perhaps such “slow slip” regularly precedes earthquakes along subduction zones and could be used as a warning, says Paul Segall, a geophysicist at Stanford University in Palo Alto, California. That, he says, “would have enormous societal implications.”

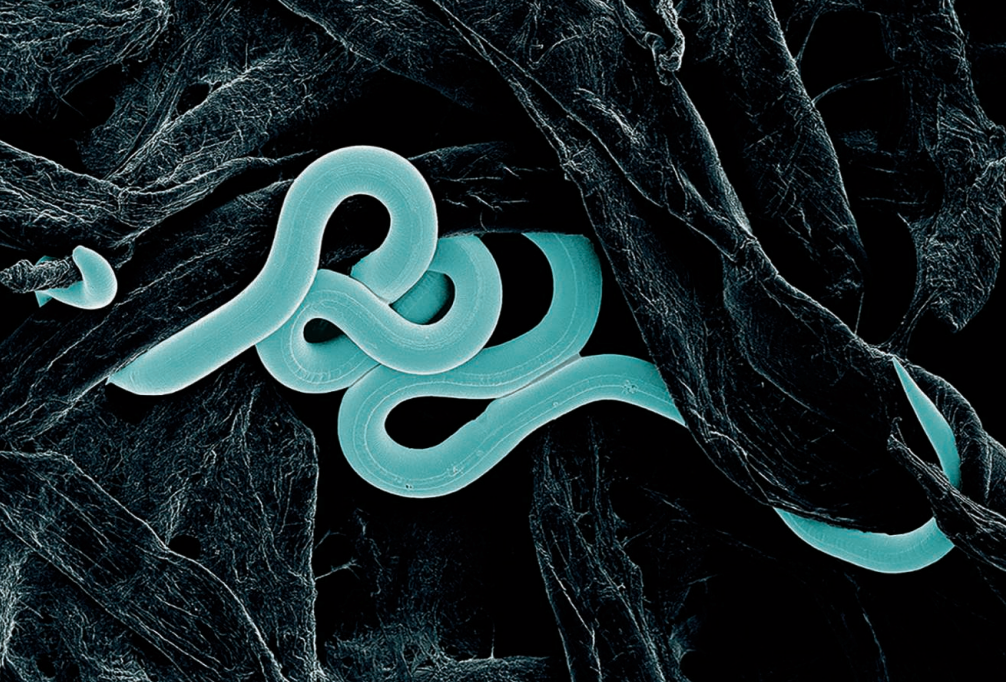
But tracking the acoustic beacons requires research ships with GPS-guided thrusters that cost up to \$50,000 a day to operate. And the measurements are by nature intermittent, depending on ships’ visits.

In 2012, Chadwell began to explore whether the Wave Glider, a drone developed by Liquid Robotics in Sunnyvale, California, could replace ships. The drone is a 3-meter-long surface craft tethered to a tube, 8 meters down, lined with oscillating fins, which harvest energy from ocean waves. Costing just \$500 a day to run, the drone could carry a GPS unit and linger for weeks in a tight circle above the seafloor beacons. In a 2016 test at Cascadia, a glider lasted 40 days and traveled nearly 500 kilometers; its near silence interfered far less with the acoustic signal than a ship’s engine. Since then, Chadwell’s team has used the drones each summer at six acoustic GPS sites at Cascadia, along with others in Alaska and New Zealand.

NSF hasn’t decided where to deploy the new instruments it is funding, but the equipment is enough to cover one subduction zone in detail—and perhaps several. Modeling studies indicate each new seafloor site will add as much knowledge as up to 30 GPS stations on land. And their use isn’t limited to subduction zones, Chadwell says. They could be placed at the seams where tectonic plates spread apart, which are almost all found underwater. Or they could be installed on the flanks of undersea volcanoes, which inflate before eruption.

Many hope the NSF grant will be a down payment for a much larger project, formerly known as the Subduction Zone Observatory and now called SZ4D, that would cost hundreds of millions of dollars and would intensively monitor subduction zones—perhaps even catching a magnitude-9 earthquake in action (*Science*, 23 September 2016, p. 1347). Tobin, who leads planning for SZ4D, says, “Virtually everyone sees this as the first building block for that infrastructure.” ■





## FOREST SCIENCE

# A mysterious disease is striking American beech trees

Researchers debate whether a tiny worm is to blame

By **Gabriel Popkin**

**A** mysterious disease is starting to kill American beeches, one of eastern North America's most important trees, and has spread rapidly from the Great Lakes to New England. But scientists disagree about what is causing the ailment, dubbed beech leaf disease. Some have recently blamed a tiny leaf-eating worm introduced from Asia, but others are skeptical that's the whole story.

Regardless of their views, researchers say the outbreak deserves attention. "We're dealing with something really unusual," says Lynn Carta, a plant disease specialist with the U.S. Department of Agriculture (USDA) in Beltsville, Maryland.

American beech (*Fagus grandifolia*), whose smooth gray trunks can resemble giant elephant legs, can grow to almost 40 meters tall. It is the fifth most common tree species in southern New England and in New York state—and the single most common tree in Washington, D.C. Its annual nut crop provides food for birds, squirrels, and deer.

Beeches in the United States were already struggling with a bark-infesting fungus when, in 2012, biologist John Pogacnik of Lake Metroparks, which manages natural areas in Ohio's Lake County, spotted trees with leaves that were shriveled and had black stripes. By 2018, foresters had documented beeches with

similar symptoms in 24 counties in eastern Ohio, western Pennsylvania and New York, and Canada's Ontario province. Small trees with shriveled leaves were starting to die; on larger beeches, the symptoms crept up the tree toward leaves in the canopy. Worried foresters began to pry loose research funding from USDA and other agencies, and organized a meeting to discuss the disease in May 2018 in Parma, Ohio.

There, plant pathologist David McCann, of the Ohio Department of Agriculture in Reynoldsburg, said he had found thousands of wriggling worms streaming from infected beech leaves. He sent Carta samples of the worms, which can be up to 2 millimeters long. Carta identified the worm as a subspecies of *Litylenchus crenatae*, a nematode that is found in beech trees in Asia but doesn't kill them. The find was eye-opening, Carta says, because no leaf-eating nematode is known to infect a large forest tree in North America.

Next, Carta, together with biologist David Burke of the Holden Arboretum in Kirtland, Ohio, and others, sought to verify Koch's postulates—pathology's gold standard for verifying a putative cause of a disease. The researchers took nematodes from diseased trees, pipetted them onto the buds of young, healthy trees in a greenhouse, then waited for symptoms to appear and reisolated the nematode from the affected leaves. The results of the experiment, which Carta presented at a

Some researchers believe a nematode native to Asia is causing a deadly disease in American beech trees.

conference in July and which have been accepted for publication in the journal *Forest Pathology*, indicate that "nematodes are causing beech leaf disease," Burke says. "We feel like we've closed Koch's postulates."

Enrico Bonello, a plant pathologist at Ohio State University in Columbus, is skeptical. He and a graduate student, Carrie Ewing, have ground up leaves from diseased and healthy looking beeches and then extracted fragments of DNA and RNA. They found nematode DNA in both healthy seeming and diseased trees. In diseased beeches, they also found evidence of three bacteria and three fungi not found in healthy looking trees. They don't know whether any of the microbes sicken trees. But Bonello says the finding, which he plans to present at an upcoming conference, "raises questions" about the role of nematodes. Perhaps, he says, the worms are simply transmitting a microbial pathogen that is the disease's true cause.

Carta's team, however, considers that scenario "highly unlikely." She contends nematode feeding alone could sicken trees.

Whatever its cause, beech leaf disease is getting around. Connecticut officials last month announced detections in Greenwich, Stamford, and New Canaan, on New York City's doorstep. Diseased trees have also been found on Long Island in New York state, some 800 kilometers from the malady's ground zero. Carta and others are investigating whether the nematode is being moved across the landscape by mites found on infected beech trees, or by birds.

USDA's Animal and Plant Health Inspection Service, the agency responsible for dealing with invasive tree killers, is helping study the disease. But it has held off on taking action to limit the disease until it knows more about the cause and how it spreads.

The beech's plight has dismayed forest experts, who are already reeling from an onslaught of introduced tree killers such as the emerald ash borer beetle that has eliminated millions of trees. "I think we should be alarmed," says Robert Marra, a forest pathologist with the Connecticut Agricultural Experiment Station in New Haven. "What's going to be left in forests?"

The beech may face additional threats. Earlier this year, U.S. Forest Service researchers announced they had found an undescribed beetle on stressed European beech trees in a New York City cemetery. The scientists are now studying whether the insect also has a taste for American beech. ■

Gabriel Popkin is a journalist in Mount Rainier, Maryland.





# LIFE PARTNERS

Nancy Moran's passion for insects and their indwelling microbes helped the field of symbiosis come into its own *By Elizabeth Pennisi; Photography by Julia Robinson*

**N**ancy Moran has found clues to evolution in some unlikely places. Some 20 years ago, living in Arizona, she would frequent a Mexican restaurant in Tucson for more than its food. She regularly climbed the fire escape behind it to visit the upper branches of a hackberry tree—along with all the insects lurking there. One night, she reached into the foliage and scooped up a nondescript bug that helped change the way she and other biologists think about the evolution of complex life.

The sesame seed-size bug she nabbed—a psyllid, which causes the plant stems or leaves it feeds on to form hard nodules called

galls around the insect—harbored symbiotic bacteria that appear to capture a key stage in the evolution of the cell. Their genomes are so shrunken, Moran found when she returned to her lab and analyzed the bug's microbial cargo, that they seem to be losing their ability to live on their own. They may be on their way to turning into organelles, like mitochondria and chloroplasts, which originated as symbiotic microbes early in the history of life but ultimately became dependent wards of the cell.

Moran, an evolutionary biologist now at the University of Texas (UT) in Austin, has built a career from groundbreaking findings made in plant-dwelling insects. Her work on psyllids, aphids, and other sap-sucking

insects has uncovered intricate, intertwined relationships with internal bacteria, which help them survive on a meager diet of plant juices. Moran is “one of the people who pioneered symbiosis as a field and did so with rigorous work and creativity,” says John McCutcheon, a former postdoc and now an evolutionary biologist at the University of Montana in Missoula.

Today, such symbioses are widely recognized for creating life as we know it. Energy-producing mitochondria power all complex cells; chloroplasts, where photosynthesis takes place, make plant life possible. The cementing of other host-microbial alliances enabled animals to expand what they could eat, diversify into new species, and conquer



almost all parts of the planet. We humans are increasingly aware that communities of microbes in our guts, on our skin, and elsewhere—our microbiome—shape our physical and perhaps even mental well-being.

Moran, who received a MacArthur “genius grant” early in her career and was elected to the National Academy of Sciences in 2004, has developed her own vital partnership. She has teamed up with Howard Ochman, another UT biologist, for more than 20 years, both personally—they married in 1998—and professionally. She has dedicated her career to symbiosis; he has ranged more widely but has contributed fundamental principles about how microbes evolve. “This is quite the power couple,” says biotechnologist Andrew Ellington, a UT colleague.

After decades uncovering the evolutionary roots of symbiosis, Moran now looks to microbial communities for ways to address today’s challenges. She’s studying the gut bacteria in bees, which depend on microbial guests to thrive. That new system, she hopes, will suggest ways to stop the decline of the bees and other pollinators and perhaps yield a simple model for exploring the roles of gut microbes in people.

**WHILE PLAYING OUTSIDE** with her seven siblings or hanging out at the Dallas, Texas, drive-in theater her father ran, the young Moran would collect bugs, leaves, and flowers wherever she could. “I was known as the kid who liked plants and insects,” she recalls. Her favorites were the tarantulas. (Yes, the entomology Ph.D. knows they are spiders, not insects.) She kept them in jars and fed them crickets. Her family accepted her hobbies, fretting only when, at age 9, she convinced a friend they should test whether the poison ivy next to the school playground really could cause a rash. “That was a horrible disaster,” Moran recalls.

Yet she was slow to realize that she could make a career of biology. At UT, she majored first in art and then in philosophy. But an introductory biology class, a university requirement, had an enduring impact. “Once I learned about evolution and natural selection, I decided this was the most interesting thing to spend time on,” Moran says.

As a graduate student at the University of Michigan in Ann Arbor, Moran trained with the famous 20th century theoretical evolutionary biologist W. D. Hamilton, and they became close friends. “We talked about everything ... big ideas and what kinds of science make a difference in understanding the evolution of life,” Moran says. Entomology

remained her first love, however. Every free moment she wriggled into bushes, looked under leaves, and peered into flowers to see what new insect species she could find.

After she took a faculty job at the University of Arizona in Tucson in 1986, a phone call from Paul Baumann, a microbiologist at the University of California (UC), Davis, helped her link her two scientific passions. Baumann was studying *Buchnera*, a once free-living bacterium now found solely inside aphids. In the 1960s, a German biologist named Paul Buchner had cataloged these



Nancy Moran (above and opposite page) keeps honey bees on a university building rooftop so she can study their microbiomes.

endosymbionts and written a tome with intricate illustrations of where they lived in the aphids, as well as in lice, beetles, and other insects. Buchner suggested those symbioses were essential, life-long relationships that had existed for millions of years.

If so, the microbes and the insects must have evolved together—and their DNA should tell the tale. To test the idea, Baumann needed Moran’s aphid expertise. By sequencing the genomes of various aphid species and their *Buchnera*, Baumann and Moran built family trees for both organisms, and found that the microbes had diversified in step with the insects. Using various aphid fossils to date the trees, they found that the partnership began some 200 million years ago. Since then, *Buchnera* has passed from one aphid generation to the next, coevolving with its host.

For the next 15 years, Baumann, Moran, and their colleagues used similar DNA analyses to document equally long-term relationships between bacteria and white flies, spittlebugs, cicadas, leafhoppers, and psyllids. Some partnerships dated as far back as 270 million years, they concluded. The work “established that symbiosis is a

central part of evolution that goes way back,” Moran says. She and other biologists propose the microbes helped the insects exploit new food sources and habitats, resulting in a rapid diversification that paralleled the diversification of flowering plants.

“Having her as an organismal biologist and him as a microbiologist was really helpful for the field,” McCutcheon says.

The sequencing also suggested why such partnerships have persisted for so long. *Buchnera*, for example, has genes that enable it to make amino acids not available from sap or from the aphid’s own metabolism, compensating for the insect’s poor diet. Meanwhile, living in the protected environment of the aphid’s specialized bacteria-carrying cells, *Buchnera* has lost essential genes, so it has to rely on the aphid to make up for those losses. In the late 1990s, this interdependence seemed remarkable, and it helped reshape how symbiosis was viewed.

Moran’s genomic approaches to symbiosis have since inspired many researchers, says Angela Douglas, who studies insect-microbe interactions at Cornell University. Twenty-five years ago, “We were the crazy people” for thinking symbiosis was so important, she recalls. Today, such close connections have proved to be the rule for many host-microbe partnerships.

Moran’s later work in insects confirmed the power of symbiosis. She, McCutcheon, and others found that some insects can’t survive without multiple symbionts. In the glassy-winged sharpshooter and the cicada—both also sap-sucking insects—one symbiont supplies eight of the 10 essential amino acids missing in their diet, and another symbiont supplies the other two. In other sap-sucking insects, symbionts serve additional functions, Moran and her colleagues discovered. In aphids, a symbiont makes the insect less susceptible to parasitic wasps by carrying a virus that’s toxic to the wasp’s young. Other symbionts improve the aphid host’s tolerance for high temperatures, enabling it to thrive in new environments. That work illustrated the complexity of microbial partnerships and hinted at the spectrum of advantages that microbial guests confer, a theme increasingly evident in studies of the human microbiome.

Moran also unexpectedly discovered that deleterious mutations are often common in the hosted microbes, suggesting symbiosis isn’t always a win-win for both partners. The microbial genomes were naturally decaying through time for two reasons: The bacteria lacked a sexual phase of reproduction, which

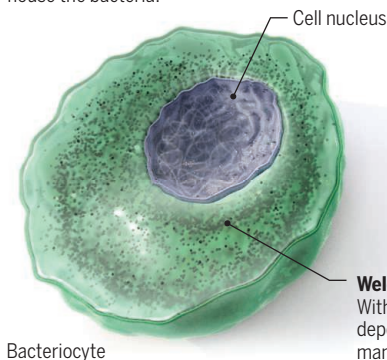
## Can't live without you

Aphids dine on sap they suck from a plant's phloem, or circulatory system, but that diet lacks key nutrients. The insects rely on internal bacteria called *Buchnera* to convert amino acids in sap, such as glutamate, into ones they are missing. The bacteria, in turn, benefit from other nutrients and shelter provided by the aphid.

During embryonic development, aphid offspring pick up *Buchnera* symbionts.

### Luxury suite

So complete is the partnership between the aphid and *Buchnera* that the insect has evolved specialized cells called bacteriocytes that house the bacteria.



### Welcome guests

With tiny genomes, *Buchnera* depend on the aphid to supply many required molecules.

*Buchnera* within bacteriocyte

Reproductive organ

Early-stage embryo

Pea aphid

Bacteriocytes

Gut

Reproductive organ

Bacteriocyte membrane

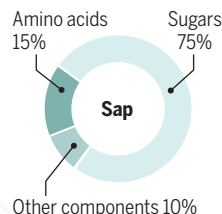
Aphid stylet

Plant phloem

Plant tissue

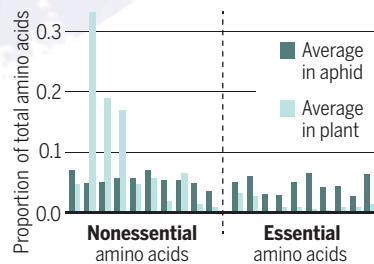
### Poor diet

Sap is mostly sugar water with free amino acids and minor components including organic acids.



### Earning its keep

Sap provides 10 amino acids, none of which is required for animals to make proteins. But *Buchnera* converts them into essential amino acids, albeit in low concentrations.



### Microbial inheritance

During reproduction, a few bacteria escape their bacteriocyte and enter the developing embryo, ensuring their transmission to the next generation.

could recombine DNA and replace bad genes, and only a few of the bacteria trapped inside an aphid pass along to the next generation, a winnowing that further restricts recombination between microbes. The buildup of mutations steadily erodes the number of working genes in the bacteria—*Buchnera* has just 600 genes compared with the 5000 or so powering *Escherichia coli*—and make those that remain less functional. “The insect is basically relying on a symbiont that’s falling apart,” Moran says.

She and Japanese colleagues later identi-

fied one way aphid endosymbionts cope with the decay: by making a lot of heat shock proteins, which can help stabilize faulty proteins produced from the mutated genes. Another bulwark against decay, Moran suggests, is what’s known as horizontal gene transfer, in which essential genes from the partner microbe or outside microbes migrate to the host genome—as genes from mitochondria did. That way they can benefit from the host’s sexual reproduction, which enables intact copies to replace mutated ones.

Moran’s groundbreaking paper on gene

decay came out in 1996. Her lab in Arizona was thriving, but her associate professor’s salary barely covered her bills. “I was broke,” she recalls, and nearly overwhelmed being a single mom. Divorced for the second time in early 1997, with a 5-year-old daughter and a 14-year-old stepdaughter, she struggled to balance work and family life. “If you have kids, you are not allowed to fall apart,” she says. Yet she couldn’t travel to scientific meetings—key to any young professor’s career.

The MacArthur grant she received in 1997, which paid more than \$50,000 annually for



the next 5 years, lifted those burdens. She immediately hired a housekeeper and reduced her teaching load.

At the time, Ochman was studying bacterial genomes. Curious to meet this newcomer to microbial evolution, he prodded organizers of one of the exclusive Gordon Research Conferences to invite Moran. So few women were present that Ochman knew exactly who she was. With characteristic directness, he walked up and asked what she was doing with the MacArthur money. Moran, who tends to be reserved, was charmed. They married 14 months later, and he followed her to the University of Arizona. In 2010, Yale University recruited them to set up a center on microbial diversity. In 2013, the couple moved back to Moran's home state.

She says their shared passion for evolutionary biology and Ochman's encyclopedic knowledge of the field have aided her immeasurably. He "has had a huge positive impact on my science."

Early on, Ochman had been puzzling over two microbial mysteries: why genomes of *E. coli* strains can vary in size by as much as 50%, and how other bacteria abruptly change from benign to pathogenic. By scrutinizing the microbes' genomes, he found that they readily gain and lose genes by swapping them with other bacteria or with their hosts. Such horizontal gene transfer could help explain the genome size variation, how bacteria pick up genes for toxins or other weapons—and also how a symbiont such as the ones Moran studies might shift essential genes to its host.

Moran and Ochman have offices less than 100 meters from each other. He often pops in on her, whether to discuss a possible grant proposal, go over the latest data, or just have lunch. "We spend 18 hours a day together," Ochman says. Yet their personalities are a world apart. Boisterous and impulsive, Ochman jumps quickly into new topics (ape microbiomes recently). Steadfastly loyal, Moran picks a question—or a partnership—and works on it thoroughly. "She is more logical and takes a more long-term view," Ochman says.

Moran's continued insect collecting led her to examples of bacterial symbionts with such tiny genomes that they are inextricably tied to host cells. One was *Carsonella ruddii*, from that psyllid from the Mexican restaurant, which proved to have just 160,000 bases compared with *E. coli*'s 5 million bases and *Buchnera*'s 640,000. Other genomes were even smaller. The findings have convinced her that no clear dividing line separates organelles and endosymbionts. "My view is that these words are just labels," she says.

Honey bees have become one of Moran's enduring interests, prompted by her hy-

pothesis that gut bacteria might play a role in the well-documented decline in the bee population. Her team's early work showed the honey bee gut contains eight species of bacteria—a manageable number compared with the hundreds typical of the mammalian gut—and that every honey bee around the world has the same set. A student in her lab at Yale figured out how to grow each of the eight kinds in the lab; in contrast, *Buchnera* continues to be unculturable.

By isolating pupae before they emerge, Moran's team can keep worker bees from in-

Sanders of UC San Diego, who studies human microbiomes. He expects the honey bee studies will yield insights into how gut microbial communities in general function.

The bee work led to other payoffs after Moran started to work with the Defense Advanced Research Projects Agency (DARPA), which sought proposals to harness microbial systems. At first she hesitated: "The purpose was to engineer something, rather than simply to understand something, as had been true for all my work up until then," she ex-



A room full of plants teeming with aphids keeps Nancy Moran and her team well-supplied for experiments.

oculating the young bees with the bacteria. The resulting "microbiome-free" bees, the group found, vividly demonstrate the importance of these microbial guests. Lacking their usual microbiomes, the bees gain less weight, are more susceptible to pathogens, and die sooner. Hives decline.

Recently, Moran's graduate student Erick Motta showed that bees with an intact microbiome become more susceptible to pathogens when exposed to glyphosate, the herbicide marketed as Roundup. Glyphosate has been considered harmless to insects and other animals because it affects an enzyme that only plants and microbes use. But through its effects on microbial guests, the compound may harm insects as well, the work suggested. (When this work was published last year, Roundup's maker issued a statement saying: "No large-scale study has ever found a link between glyphosate and honey bee health issues.")

To Moran, the honey bee microbiome is complex enough to stand in for the human microbiome but simple enough to be dissected in a way the human counterpart cannot be. Moran's work on bees "has been some of the most reliable, clearly articulated work" on gut microbes, says Jon

plains. But she, UT bioengineer Jeffrey Barrick, and Ellington got DARPA funding to devise methods to alter the bee microbiome in ways that would change the insect's traits. Such tinkering might make bees more resistant to stresses, for example, which could help preserve the vital pollinators. To show a proof of principle, UT graduate student Sean Leonard recently engineered a bacterium from the bee gut to produce RNA that increases production of dopamine, a key neurotransmitter. Preliminary results suggest those bees are better learners as a result.

Colleagues are curious to see what Moran learns next from honey bees or any of the insects whose inner lives she probes. "She's not just a one-hit wonder," says Ute Hentschel, a marine biologist at GEOMAR-Helmholtz Centre for Ocean Research Kiel in Germany who studies sponge-microbe symbioses. "She has an amazing capacity to focus things so that [new insights] precipitate out."

Moran believes that, like most complex partnerships, the unions between insects and microbes will take a lifetime to unravel. "The host and the symbiont communicate in ways we don't understand," she says. "We're working to figure that out." ■





# ARCTIC INTRUDER

The *Polarstern* is enabling scientists to spend 1 year frozen in ice. Now, they must make sure the ship doesn't wreck their studies

Text and photography by **Shannon Hall**, aboard the *Polarstern* in the Arctic Ocean

**T**he flare cut through the sky like a firework, sending the polar bears into a panic. They sprinted across the snow, the mom checking to make sure her cub kept pace. Nearby, two polar bear guards—one who had fired the flare and the other armed with a rifle—stood on snowmobiles, making sure the bears posed no threat to the scientists and crew onboard this German icebreaker, which is spending 1 year here in the Arctic, frozen into the sea ice.

The bears are an occasional threat to this unusual expedition, known as the Multi-disciplinary Drifting Observatory for the Study of Arctic Climate (MOSAiC). But the scientists are also contending with another, much larger intruder: their own ship. The 118-meter-long *Polarstern* is a sophisticated

floating lab that allows MOSAiC scientists to study the atmosphere, sea ice, ocean, and life. But the vessel and the equipment it carries also produce noise, light, heat, and other forms of pollution that can ruin measurements in this pristine environment.

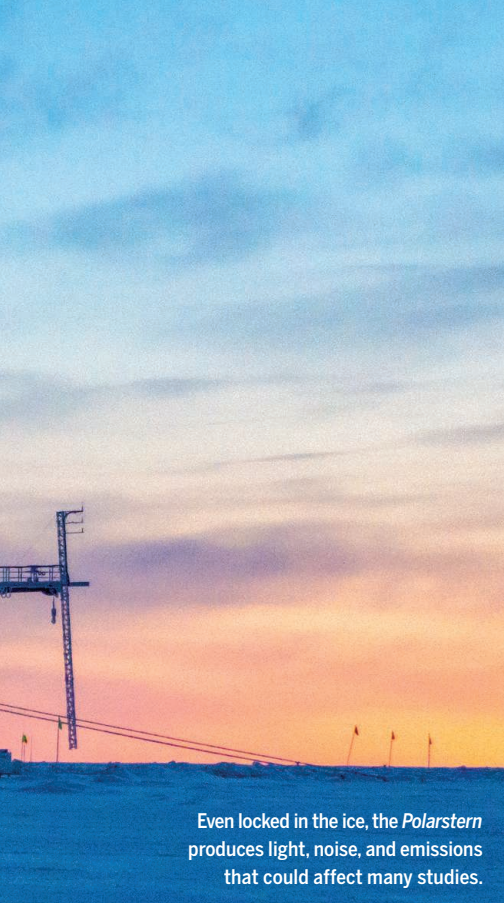
The *Polarstern*'s generators, for instance, spew a steady plume of black smoke, complicating efforts to collect air samples. "We are going to be by far the biggest source of aerosol particles in the neighborhood, and that's a problem," says atmospheric scientist Matthew Shupe of the National Oceanic and Atmospheric Administration and the University of Colorado (CU) in Boulder. But, he adds, "It's also an opportunity" to understand how the arrival of more ships might affect the Arctic in the future.

Our encounter with the polar bears occurred just 6 days after the *Polarstern* locked

itself in the ice near 85° north latitude on 4 October. The ship had left Tromsø, Norway, in September, then steamed north in search of an ice floe thick enough to support the scientists and their equipment for the next 12 months, as they drifted past the North Pole before returning to open water between Greenland and Norway's Svalbard archipelago in the fall of 2020. By then, the some 300 scientists involved in the \$150 million MOSAiC project, led by the Alfred Wegener Institute (AWI) Helmholtz Centre for Polar and Marine Research in Bremerhaven, Germany, hope to have collected a wealth of data that will help reveal how climate change is affecting the Arctic (*Science*, 23 August, p. 728).

Once the *Polarstern*'s propellers had slowed to a stop, causing the ship to grow still and quiet, the dozens of researchers aboard the first leg of the journey wasted





Even locked in the ice, the *Polarstern* produces light, noise, and emissions that could affect many studies.

little time in setting up research sites—with names such as “Balloon Town” and “Ocean City”—on the surrounding ice. They graded tracks for roads, raised instrument towers, and strung power lines. (The cables would later become chew toys for the polar bears.) And they used the ship’s crane and helicopter to haul heavy equipment onto the icy seascape, including a robotic submarine that the researchers will drop into a hole carved through the 60-centimeter-thick ice.

In some areas, however, they were careful to leave vast fields of untouched snow, where instruments monitor the floe from above and below. Expedition members—including the guards responsible for scaring away bears—were warned not to walk or drive snowmobiles across these sites. It is but one example of the ways MOSAiC scientists are working to minimize the so-called observer effect, in which the very presence of a scientist—or their vessel—can skew their observations.

The *Polarstern* can’t be shut down completely, because it must serve as the expedition’s power plant, command center, and hotel—which some might call a five-star. There is a dining room that serves mouth-watering cakes every afternoon at tea time, a sauna, a swimming pool, a gym, a bar, and even small shops where you can buy sweets, tobacco, and alcohol. Although the ship is passively drifting with the ice, it will guzzle 15 tons of diesel fuel per day.

Some of that fuel powers the ship’s many lights. When I learned that I would be aboard the *Polarstern* at MOSAiC’s start, I looked forward to experiencing the onset of polar night and seeing the North Star—which dangles just 40° above the horizon where I live in Colorado—twinkle close to the top of the sky. But the ship floods the ice with light to enable the researchers to work safely and efficiently, creating a powerful glow that blots out the sky. I did not see a single star during my 2 weeks aboard.

For AWI biologist Allison Fong, the glow is a problem. She wants to better understand how microbial plant life survives in the Arctic winter, when there is no sunlight for months on end, but she can’t study samples that have been exposed to artificial light. So, once a week she plans to drive a snowmobile to what she calls the “dark zone” hidden behind a fortress of small ridges of snow and ice some 500 meters from the ship. There, researchers will don red headlamps (red light doesn’t affect most organisms) and collect ice cores that they will analyze back at the ship.

Oceanographers, meanwhile, are dealing with the heat, turbulence, and wastewater produced by the *Polarstern*. “At the main site [around the ship], there’s sort of a dead zone” for collecting data, says Tim Stanton, an oceanographer at the Naval Postgraduate School in Monterey, California. To avoid the issue, he and others have deployed a handful of autonomous instruments, which sit on the ice or float in holes, far from the ship.

The expedition’s own noises, meanwhile, have forced atmospheric scientists to build special defenses. At a site called “Met City” a half-kilometer from the ship, a barrier nearly as tall as a person shelters an instrument that uses pulses of sound to measure the density of air, and thus gain insight into the structure of the atmosphere. The barrier is designed to deaden any artificial noise that might rumble across the seascape, such as blasts of the ship’s horn and the whine of snowmobiles and nearby electronics.

Then there is the *Polarstern*’s sooty exhaust—a huge problem for the many MOSAiC scientists studying the Arctic’s unusually clean air. The researchers want to better understand the sources and fates of aerosols—tiny particles suspended in the atmosphere—that contribute to the formation of small ice crystals within clouds. The number of crystals can determine whether a cloud acts as a blanket to warm Earth or an umbrella to shield it from solar radiation. But scientists aren’t sure exactly where Arctic aerosols originate: Are they swept north from land, or are they formed by ocean organisms and sent skyward by breaking waves?

To gain some insight, Lauriane Quéléver, a chemist at the University of Helsinki, and

her colleagues will spend the next year pulling air samples through tubes mounted on a refashioned shipping container that serves as her lab. Instruments will parse the samples, analyzing and counting particles. Quéléver was astonished to find that the number of particles soared to 28,000 per cubic centimeter—a few thousand times greater than the typical Arctic level—when a second icebreaker arrived to swap instruments, personnel, and fuel. “I really hope that I’m going to get some very natural and pristine data,” she says. “Otherwise I can just go home.”

A snowstorm or strong wind could help her and other scientists by clearing the air, but that rarely happened during my stay. When I visited CU atmospheric scientist Byron Blomquist, he was trying to collect air samples at a tower hanging off the ship’s bow. But his instruments weren’t sampling anything; they had automatically shut down after an alarm signaled that exhaust from the stern of the ship was enveloping the tower. Inside his container, pumps roared like vacuum cleaners as they pushed clean air out through his instruments, to prevent contamination by the smog.

Yet the *Polarstern*’s soot presents an opportunity for some researchers. As the Arctic warms and sea ice melts, shipping in the region is expected to increase dramatically. Those vessels will likely release black carbon, an aerosol formed by diesel engines. When black carbon settles on snow or ice, it can hasten melting by reflecting less solar radiation and absorbing more heat, a process MOSAiC researchers hope to study in detail by sampling ice close to the ship and a planned aircraft runway.

Less than 24 hours after the *Polarstern* settled in, the ship’s emissions were smudging the ice. I noticed a black flake as large as my fingernail within the icy floe, removed a mitten and picked it up, rubbing the flake between my fingers. It turned to an oily smear.

It wasn’t the only preview of what lies ahead. Earlier, I stood on the deck of the *Akademik Fedorov*, a Russian research vessel that participated in MOSAiC’s first few weeks, with Jessie Creamean, an aerosol researcher at Colorado State University in Fort Collins. We watched as the *Polarstern* slowly approached, gliding across a sea of ice. The sky was gray, with a thin stripe of blue at the horizon in every direction—except at the spot where the *Polarstern* had just spent the night. There hung a thick yellow and brown cloud. “Just think,” Creamean said, “if we open the Arctic to shipping it’s all going to look like that.” ■

Shannon Hall is a science journalist in Boulder, Colorado.



# INSIGHTS

## POLICY FORUM

### CLIMATE AND ENERGY

## China's key role in scaling low-carbon energy technologies

Meeting the Paris goals will require collaboration with China

By John Helveston<sup>1</sup> and Jonas Nahm<sup>2</sup>

**M**eeting the goals of the Paris Agreement will require net zero greenhouse emissions by 2050 and substantial reductions before then. It will also require collaboration with China, which has emerged as the global leader in the mass production of low-carbon energy technologies (LCETs). In part because of China's investments in manufacturing, the LCETs required to meet climate targets have become increasingly cost-competitive with fossil fuel sources (1). But some attribute China's rapid rise in LCET sectors to unfair industrial policies—such

as forced technology transfer requirements, massive subsidies, and outright intellectual property (IP) theft—aimed at strategically dominating the next generation of energy technologies (2). Trade relations between China and the world are currently unsettled, especially with the United States, a leading producer of both LCET research and development (R&D) and greenhouse gas (GHG) emissions. Against this backdrop, we outline why engaging with China is the more promising path to accelerate the global deployment of LCETs and to rapidly bring new technologies to mass production.

Chinese contributions to LCETs highlight key distinctions between invention and the complementary assets required to commercialize a product at scale, such as financial investment and competitive manufacturing capabilities (3). Since joining the World Trade Organization in 2001, China has gone

from producing 1% to producing 66% of the world's solar panels (4), and Chinese wind turbine manufacturers now represent roughly one-third of global supply. China is also the largest supplier of (and market for) electric vehicles (5), and according to Bloomberg New Energy Finance, Chinese firms are set to increase their control of the world's supply of lithium-ion batteries from 69% to 76% in the near future. Plans are also under way to nearly double China's nuclear reactor fleet from 45 to 88 plants in the coming decade.

We suggest that it is unrealistic to expect that another nation will be able to rival China's capabilities in LCET scale-up in the time frame needed to limit climate change to below 2°C. The question is not whether to engage, but how, acknowledging that China has applied protectionist policies and has used government procurement directives to discriminate against foreign companies in domestic markets, including in LCET industries. Although it may be improbable that one nation can control all aspects of the innovation process—from invention to mass commercialization—in the global economy, it is just as unreasonable to ignore the importance of upholding IP rights and following international trade rules. Given the common goal of combating climate change, LCET in-

<sup>1</sup>Engineering Management and Systems Engineering, George Washington University, Washington, DC, USA.

<sup>2</sup>Energy, Resources, and Environment, School of Advanced International Studies, Johns Hopkins University, Washington, DC, USA. Email: jph@gwu.edu



A worker inspects a solar panel at a factory in Lianyungang in China's eastern Jiangsu province. China's capabilities in mass manufacturing low-carbon energy technologies are critical to combating global carbon emissions.

dustries are a promising place to start negotiating better rules of engagement while increasing global collaboration to achieve rapid emission reductions.

## MANUFACTURING INNOVATION

China's capabilities in commercialization and mass manufacturing of LCET technologies are unmatched in the world today. These capabilities did not emerge overnight. They relied on unique institutional features of China's domestic economy that supported investments in both innovation and manufacturing at a massive scale and over multiple decades. No other economy has been willing and able to pour even a remotely equivalent level of resources into manufacturing expansion and R&D in recent history. It is therefore highly unlikely that another nation will be able to replicate China's skills in the time frame needed to avoid the worst consequences of climate change.

In China, more than 30 years of institutional support from both national and local governments enabled entrepreneurial manufacturers to thrive in LCET sectors. Beginning in the 1980s, the central government used financial incentives to encourage domestic R&D, including applied research in manufacturing. Government R&D support expanded in 2006 when the central government began encouraging "indigenous innovation" (自主创新) to reduce dependence on foreign technologies through increased domestic R&D efforts. Such efforts further accelerated under President Xi's "Made in China 2025" initiative, which has also designated the development of domestic LCET sectors as a strategic national priority.

Central government support for R&D capabilities was augmented by provincial and municipal governments, which, dependent on tax revenue from the local manufacturing economy, set aside indigenous innovation goals in favor of mass production. They brokered bank loans and provided land, facilities, and tax incentives to manufacturers, including in LCET sectors that were unable to attract large-scale financing in other parts of the world. State investment in domestic clean energy markets further supported local manufacturers by boosting domestic demand for their products (see the figure, upper panel).

In this environment, our research shows that Chinese manufacturers centered their R&D efforts on production improvements rather than new product R&D. Whereas "New Energy" (新能源) technologies could

be licensed, bought, or contracted, capabilities in innovative manufacturing—including the ability to rapidly re-engineer a complex product for "cost-out" mass manufacturing—were difficult to obtain. Chinese manufacturers continued to rely on partnerships with foreign firms to access new technologies while gradually developing their own knowledge-intensive capabilities. As Chinese manufacturers in LCET sectors focused on commercialization, scale-up, and cost reduction, their innovative manufacturing capabilities (rather than basic factor cost advantages) emerged as their source of competitive advantage (6, 7). Even with China's highly supportive domestic institutions, it took decades of growing at a breakneck pace for Chinese firms to establish the capabilities in commercialization and scale-up that the world now needs to bring new energy technologies to market.

## COLLABORATIVE COMMERCIALIZATION

If the world has any hope of deploying the LCET portfolio in the time frame needed, collaboration with China will be essential for firms from around the world. The United States in particular needs to forge closer relationships with China on climate.

The United States and China account for 40% of the world's annual energy consumption, putting these two nations at the center of global efforts to mitigate GHG emissions. They are also uniquely equipped to jointly address this challenge. Historically, the U.S. government has been the largest investor in LCET R&D (see the figure, lower panel), which has led to major advances in key technologies such as solar photovoltaic cells. Since the 1980s, however, the U.S. innovation ecosystem has followed a trend away from large, vertically integrated firms that were able to invent and produce new technologies, and toward smaller, entrepreneurial firms focused on the generation of new ideas. Manufacturing was increasingly outsourced and offshored (8). In many sectors, the United States now lacks China's strengths in commercialization and scale-up. Many U.S. LCET firms, and startups in particular, stand to benefit from collaborating with foreign partners to access the capital and specialized manufacturing capabilities needed to turn their innovations into mass-produced, commercially viable products.

Such collaboration is not without precedent. Access to financial capital and the innovations of Chinese manufacturers in product scale-up and cost reduction have increasingly led firms from a variety of countries to commercialize technologies in China. In LCET sectors, collaborations between Chinese manufacturers and non-Chinese innovators have enabled new technologies to

be commercialized in larger quantities and at increasingly competitive prices.

Germany, for instance, has benefited from China's rapidly growing wind and solar industries through the sale of components, production equipment, and industrial robots. As China's manufacturers became early adopters for a variety of mass production technologies, relationships with Chinese customers became important sources of learning and innovation for German firms (7). In the United States, Innovalight, a Silicon Valley startup, was able to commercialize its core technology, a silicon ink, only after a Chinese solar manufacturer invested a year into jointly testing the technology under mass production conditions that were only available in China (6). In some sectors, such as nuclear energy, multinationals are seeking Chinese partners as part of a survival strategy. With Western nuclear energy markets disappearing, these firms are moving away from engineering design and toward operational and system integration services for Chinese facilities in a bid to gain access to the capital, customers, and competitive component manufacturing available in China.

Successful collaborations with Chinese manufacturers have led to multidirectional learning: Chinese manufacturers gain technological know-how from advanced foreign incumbents, and the foreign partners feed the manufacturing and scale-up solutions their Chinese partners identify back into upstream R&D activities (6, 7). Multinationals absorbing production improvements from their Chinese manufacturing partners has been a long-observed phenomenon in many industries (9). If any reshoring of manufacturing is going to occur in the U.S. economy, partnering with and learning from Chinese manufacturers may be a fruitful strategy.

## RISKS AND CHALLENGES

Entering into collaborations with Chinese firms has not been without risk. China has historically set an uneven playing field in its domestic market in favor of Chinese firms; in some sectors, such as wind energy, foreign firms have been systematically pushed out of China's market through discriminatory government procurement policies. In other industries, such as the auto sector, foreign firms have been forced to share IP and profits with Chinese partners in order to gain market access. Although research has shown that forced partnerships have often failed to produce serious Chinese competitors (5, 10), these policies do not create an inviting environment for collaboration. Allowing foreign firms fair access to its domestic market is one step China could (and should) take to encourage increased collaboration with foreign firms.

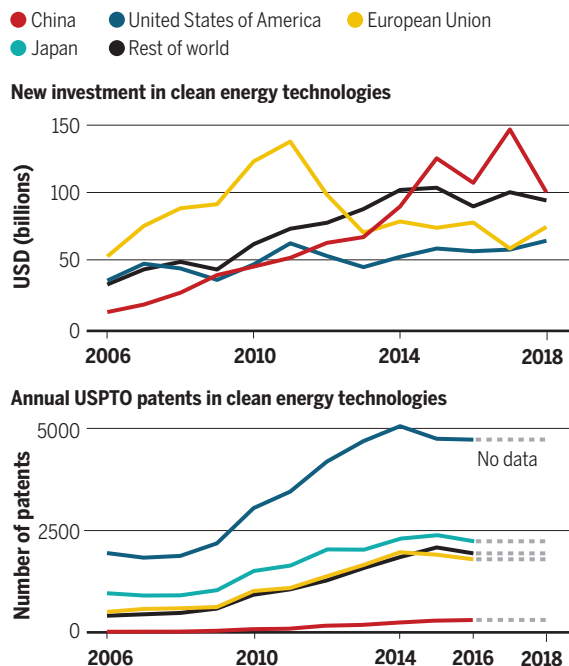
In some areas, the situation is improving. In 2018, the central government announced that it would remove the joint venture requirement for electric vehicle manufacturers so that foreign firms can wholly own their enterprises in China, and this ruling will extend to all auto manufacturers in 2020. China's IP institutions are also strengthening, even though IP theft remains a serious problem. In 2014, China established the first dedicated IP courts in Beijing, Shanghai, and Guangzhou, with additional courts added in 2017. Researchers estimate that the vast majority of cases in the Beijing and Shanghai courts have ruled in favor of foreign plaintiffs against Chinese infringers, with payments of damages to foreign plaintiffs exceeding those to Chinese victims of IP theft by as much as a factor of 3 (11). And it's not just foreign litigators; in 2015, 88.5% of the 11,607 patent cases in these courts involved a Chinese plaintiff and Chinese defendant (12).

Governments in China, the United States, and elsewhere have an important role to play in mitigating concerns over IP and fostering global ties. They can level the playing field and reduce risks for firms to work with one another, and they can help to build and support networks of innovators across national borders. One example is the U.S.-China Clean Energy Research Center (CERC). Spearheaded by former U.S. energy secretary Steven Chu in 2009, CERC established a \$150 million joint pledge by the U.S. and Chinese governments to increase innovation in clean energy technologies. Perhaps most important, CERC established a Technology Management Plan that governed and helped mitigate IP concerns. Although little of the IP produced by the initiative was jointly created, CERC built trust among participants, enabling them to develop new technologies, establish new business ventures in both markets, and gain additional support for technology demonstration projects, all with limited IP conflicts (13).

Beyond IP, concentrating investments in scaling current technologies can also threaten progress in leading-edge innovation (14). In sectors with more constrained markets, such as optoelectronics, shifting manufacturing to East Asia prevented innovation in more advanced technologies in the United States (15). Nonetheless, in the case of LCET sectors, the speed of technology deployment is a more pressing matter. Despite the remarkable growth in renewable energy in recent years, the world is already well be-

## U.S. innovation, Chinese investment

The United States is a leader in low-carbon energy technology (LCET) innovation, and China is the largest investor in LCET, with innovative capabilities in manufacturing and scale-up.



Top: data from Bloomberg New Energy Finance; bottom: U.S. Patent and Trademark Office (USPTO) data from U.S. National Science Foundation Science and Engineering Indicators. Code and data to produce the charts are available at <https://github.com/jhelvy/charts/tree/master/scienceCommentary2019>.

hind schedule on deploying the necessary 300 GW of renewable energy capacity every year from 2018 to 2030 to meet the goals of the Paris Agreement. The world simply does not have time to wait for the next generation of LCETs, irrespective of where they are developed. Greater quantities of current LCETs can be immediately deployed with the existing capabilities of Chinese firms in mass manufacturing, which will set in motion the critical learning processes required to effectively integrate these technologies into future energy systems.

### NOT FIXED OR INEVITABLE

Climate change is a global problem of unparalleled dimensions that requires a global response, including in the invention, commercialization, and production of technologies that can forge deep decarbonization. Collaboration was central to the emergence of contemporary renewable energy technologies (7), and collaboration will be equally important in rapid decarbonization through deployment of LCETs. Governments around the world should work to foster such collaboration, and establishing initiatives like CERC is one promising path toward this goal.

Addressing grand challenges such as climate change will also require fundamental advances in technology. In the United States,

this means continuing to support the core strengths of U.S. firms and universities—the invention of new technologies—through increased investments in basic and applied research. But the technologies that emerge from these efforts must eventually be scaled and deployed. Working with Chinese manufacturers can accelerate this process.

The division of labor between Western inventors and Chinese manufacturers is not fixed or inevitable. Other nations can (and should) continue investing in domestic manufacturing capabilities as part of continued technological innovation. But in a global marketplace such as energy technology, it is unlikely that the entire value chain for a complex, manufactured product would lie entirely within national boundaries. As unsettled trade relations between China and the world threaten to undercut efforts to strengthen global ties in LCET sectors, we cannot lose sight of the climate challenge or risk missing the narrow remaining window to reduce global emissions. Building on the advanced mass manufacturing capabilities of Chinese LCET firms is the most promising path toward rapid global decarbonization. ■

### REFERENCES AND NOTES

1. N. M. Haegel *et al.*, *Science* **364**, 836 (2019).
2. R. D. Atkinson, C. Foote, "Is China Catching Up to the United States in Innovation?" (Information Technology and Innovation Foundation, 2019); <https://itif.org/publications/2019/04/08/china-catching-united-states-innovation>.
3. D. J. Teece, *Res. Policy* **15**, 285 (1986).
4. A. Jäger-Waldau, *Energies* **12**, 769 (2019).
5. J. P. Helveston, Y. Wang, V. J. Karplus, E. R. H. Fuchs, *Res. Policy* **48**, 206 (2019).
6. J. Nahm, E. S. Steinfeld, *World Dev.* **54**, 288 (2014).
7. J. Nahm, *Bus. Polit.* **19**, 68 (2017).
8. R. K. Lester, D. M. Hart, *Unlocking Energy Innovation: How America Can Build a Low-Cost, Low-Carbon Energy System* (MIT Press, 2012).
9. D. Puga, D. Trefler, *J. Dev. Econ.* **91**, 64 (2010).
10. S. T. Howell, *Res. Policy* **47**, 1448 (2018).
11. R. Bian, *SSRN Electron. J.* 10.2139/ssrn.3063566 (2017).
12. H. Wang, "Highest Damages Ever Awarded by Beijing IP Court and Stronger Patent Protection in China," *Patent Lawyer Mag.* (January/February 2017).
13. J. I. Lewis, *Energy Policy* **69**, 546 (2014).
14. V. Sivaram, J. O. Dabiri, D. M. Hart, *Joule* **2**, 1639 (2018).
15. E. R. H. Fuchs, *Science* **345**, 519 (2014).

### ACKNOWLEDGMENTS

We thank D. Hart and the Information Technology and Innovation Foundation, which inspired this commentary by hosting the Energy Innovation Boot Camp for Early Career Scholars. **Author contributions:** Conceptualization, methodology, validation, formal analysis, investigation, resources, writing (review and editing), funding acquisition: J.H. and J.N.; software, data curation, writing (original draft), visualization, supervision, project administration: J.H.

10.1126/science.aaz1014



# Translating translation in Down syndrome

Protein quality control mechanisms may hold the key to treatment of cognitive disability

By Mark Halliday and Giovanna R. Mallucci

**A**cross the spectrum of neurological disorders, from the developmental to the degenerative, clinical features and progression are influenced not only by disease-specific genetic effects but also by more generic mechanisms. Dysregulated stress responses are emerging as common targets for therapeutic intervention independently of causal genes, offering the tantalizing prospect of new treatments for a swathe of diseases irrespective of specific etiology. The integrated stress response (ISR) is a key player in the control of proteostasis—the balance between protein synthesis and degradation that is essential for cellular health. Dysregulated proteostasis is a common feature of the neuropathological landscape, from fragile X syndrome (1) to the neurodegenerative disorders Alzheimer's and Parkinson's diseases (2). On page 843 of this issue, Zhu *et al.* (3) provide compelling evidence that Down syndrome (DS), the most common genetic cause of intellectual disability, joins the pantheon of neurological disorders in which dysregulated ISR signaling plays a key role.

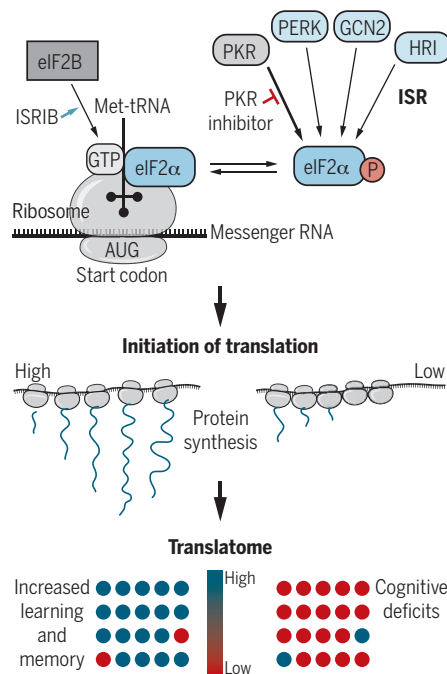
DS is caused by trisomy of human chromosome 21 (HSA21) and classically features cognitive disabilities, neonatal hypotonia (decreased muscle tone), and craniofacial changes. Cardiac defects and susceptibility to leukemias are less common features of DS. Research on DS etiology has largely focused on determining the functional effects of the extra gene dosage arising from the additional chromosome. A plethora of mouse models of DS have revealed a number of dosage-sensitive genes and genomic regions that contribute to cognitive phenotypes that have formed the basis for candidate therapeutic approaches (4).

The ISR controls the rate of protein synthesis initiation (see the figure). A ternary complex, composed of eukaryotic initiation factor 2 (eIF2, comprising  $\alpha$ ,  $\beta$ , and  $\gamma$  subunits), guanosine triphosphate (GTP, sup-

plied by eIF2B), and a methionine transfer RNA (tRNA), is loaded onto a ribosome for translation to begin at the start codon, AUG, on messenger RNA (mRNA) (5). During numerous cellular stresses, it is beneficial to temporarily suspend translation while the stress is resolved to avoid protein misfolding, which is often cytotoxic. This is achieved by phosphorylation of eIF2 $\alpha$ , which inhibits the ability of eIF2B to produce the GTP that is essential for ternary complex formation, thereby blocking translation. Four kinases phosphorylate eIF2 $\alpha$  and make up the ISR:

## Overactivated stress response in Down syndrome

Trisomy of human chromosome 21 leads to ISR activation through PKR, which phosphorylates eIF2 $\alpha$ , reduces global translation rates, and changes the translome. Approaches that inhibit PKR signaling improve learning and memory deficits in a mouse model of Down syndrome, opening potential new treatments for cognitive disability.



eIF2 $\alpha$ , eukaryotic initiation factor 2 $\alpha$ ; GCN2, general control nonderepressible 2; GTP, guanosine triphosphate; HRI, heme-regulated inhibitor; ISR, integrated stress response; ISRIB, ISR inhibitor; Met-tRNA, methionine transfer RNA; P, phosphorylation; PERK, PKR-like endoplasmic reticulum kinase; PKR, protein kinase RNA-activated.

PKR (protein kinase RNA-activated), a sensor of viral double-stranded RNA and interferon; PERK (PKR-like endoplasmic reticulum kinase), which responds to misfolded proteins in the endoplasmic reticulum and links the ISR to the related unfolded protein response (UPR) (6); GCN2 (general control nonderepressible 2), activated by amino acid starvation and HRI (heme-regulated inhibitor), which detects heme deficiency (7).

There is mounting evidence that prolonged ISR activation has detrimental effects on cognitive function and neuronal health. Learning and the encoding of long-term memories are dependent on protein synthesis at the synapse, which is controlled by the amount of phosphorylated eIF2 $\alpha$ . Inhibiting the ISR either genetically (8) or with the ISR inhibitor ISRIB (9), or through similarly acting compounds (10), improves memory in both wild-type mice and memory-impaired mice. There is also extensive evidence for deregulated ISR in neurodegenerative diseases. Overactive ISR signaling is observed in neurons of patients with Alzheimer's disease, Parkinson's disease, and related disorders, as well as in neurons of mouse models of neurodegeneration (2). Reducing eIF2 $\alpha$  phosphorylation, either via ISR or UPR modulation, is profoundly neuroprotective in these mice, independent of disease-specific etiology (2, 11).

Zhu *et al.* found reduced translation rates and high amounts of phosphorylated eIF2 $\alpha$ , consistent with ISR activation, in the brain tissue of a DS mouse model, in human HSA21 trisomic induced pluripotent stem (iPS) cells, and in postmortem brains from individuals with DS. Intriguingly, they find that it is the PKR axis of the ISR that drives the phosphorylation of eIF2 $\alpha$  in DS mice, whereas PERK overactivation is tightly associated with most neurodegenerative disorders (11). The DS mice show several behavioral traits thought to be consistent with core cognitive deficits in DS, including reduced ability to learn in several memory tests (12). The authors corrected these behaviors by genetic or pharmacological inhibition of ISR signaling, by targeting PKR or the interaction between eIF2 $\alpha$  and eIF2B.

How can the reversal of core DS features through ISR modulation be reconciled with

UK Dementia Research Institute at the University of Cambridge, Department of Clinical Neurosciences, Cambridge Biomedical Campus, Cambridge, UK. Email: gm522@cam.ac.uk

evidence from genetic studies that targeting specific pathways and dosage-sensitive genes also rescue some or all of these features? The answer may lie in the transcriptome of the DS mice that Zhu *et al.* examined. They compared genome-wide transcriptional changes, determined by RNA sequencing, with translational changes, determined by sequencing of polysome-associated (actively translating) mRNA in the brains of mice, and found that numerous genes were transcriptionally and/or translationally dysregulated in DS mice. The translation of more than 80% of down-regulated RNAs that were being actively translated was rescued by ablation of the *Pkr* gene in the DS mice, including key proteins involved in learning, synaptic plasticity, and memory storage, which are crucial for cognitive function. Thus, cognitive dysfunction in individuals with DS likely arises, at least in part, from global transcriptome changes that can be corrected by ISR inhibition.

In the future, a detailed analysis of the altered transcriptome may contribute to the genetic understanding of DS. Extending transcriptome analysis to other mouse models of DS and iPS cells from individuals with DS may bring further insights that are also relevant for other features of the syndrome, such as cardiac deficits and susceptibility to leukemias. Why the PKR branch of the ISR, specifically, is activated in DS individuals and mice is unknown and worth exploring. The field of DS research is evolving on many fronts, with drugs targeting specific genes on HSA21 in clinical trials (13). It is likely that treatment of DS will ultimately include both generic and specific therapies. The development of ISR inhibitors is a major focus for the treatment of neurodegenerative diseases, including Alzheimer's disease (2). The work of Zhu *et al.* raises the possibility that DS may also be amenable to this therapeutic approach, with the prospect of reducing cognitive burden in affected individuals. ■

#### REFERENCES AND NOTES

1. M. E. Klein *et al.*, *Neural Plast.* **2016**, 3857934 (2016).
2. C. Hetz, S. Saxena, *Nat. Rev. Neurol.* **13**, 477 (2017).
3. P. J. Zhu *et al.*, *Science* **366**, 843 (2019).
4. Y. Herauld *et al.*, *Dis. Model. Mech.* **10**, 1165 (2017).
5. R. J. Jackson *et al.*, *Nat. Rev. Mol. Cell Biol.* **11**, 113 (2010).
6. P. Walter, D. Ron, *Science* **334**, 1081 (2011).
7. K. Pakos-Zebrucka *et al.*, *EMBO Rep.* **17**, 1374 (2016).
8. M. Costa-Mattoli *et al.*, *Cell* **129**, 195 (2007).
9. C. Sidrauski *et al.*, *eLife* **2**, e00498 (2013).
10. M. Halliday *et al.*, *Brain* **140**, 1768 (2017).
11. M. Halliday *et al.*, *J. Neurochem.* **142**, 812 (2017).
12. R. H. Reeves *et al.*, *Nat. Genet.* **11**, 177 (1995).
13. R. De la Torre *et al.*, *Mol. Nutr. Food Res.* **58**, 278 (2014).

#### ACKNOWLEDGMENTS

G.R.M. is funded by the UK Dementia Research Institute (UKDRI-2001) and European Research Council Consolidator Award UPR Neuro (647479).

10.1126/science.aaz7128

#### DEVELOPMENT

# Modeling the early development of a primate embryo

Post-implantation embryos from cynomolgus monkeys are cultured for extended periods

By Patrick P. L. Tam

**B**ecause mammalian embryos develop inside the uterus after implantation, they are practically inaccessible for direct observation and experimental analysis of the developmental process.

To visualize and study the development of post-implantation embryos, it is necessary to develop a technology that maintains the viability and growth of embryos *ex vivo* in a controlled environment. This is especially the case for nonhuman primate embryos, which are likely to be adopted for modeling early human development. On pages 836 and 837 of this issue, Ma *et al.* (1) and Niu *et al.* (2), respectively, report *in vitro* culture methods for cynomolgus monkey embryos and demonstrate their utility for gaining insights into early primate embryo development.

The laboratory mouse is a road-tested animal model for mammalian development, and its use for investigating the development of pre- to early post-implantation embryos has been substantially enhanced by the ability to conduct experiments on embryos that are grown *in vitro* for various durations between fertilization and early organogenesis (2–5). However, in view of the disparity of species-specific developmental features between mice and humans, there are reservations about the relevance of translating knowledge from mouse models of embryo development to primates (including humans). The use of human embryos for investigating early post-implantation development is limited by the ethical prerogative of the procurement of and experimentation on human embryos, as well as the technical barrier to sustaining normal growth and development beyond a few days. The ability to grow nonhuman primate embryos to post-implantation development provides a new model of early primate de-

velopment. The similarity of genomic, anatomical, and physiological attributes between cynomolgus monkeys and humans posits this nonhuman primate embryo as an appropriate animal model for studying human development.

Pre-implantation cynomolgus embryos have been cultured *in vitro* from the fertilized oocyte, generated by *in vitro* fertilization (IVF), to the blastocyst at 7 days post-fertilization (dpf) (1, 2, 6). The availability of cultured IVF blastocysts removes the constraint of sourcing the scarce experimental material (blastocysts or post-implantation embryos) from pregnant animals for further culture and study. However, there has been little success in using present culture methods to sup-

port further development of the blastocyst.

The three-dimensional *in vitro* culture protocols reported by Ma *et al.* and Niu *et al.* have now extended the development of the blastocyst to the equivalent of 19 to 20 dpf (see the figure). By then, the cultured embryos display morphological signs

of gastrulation: formation of the primitive streak (where cells move to the new germ layers), emergence of diverse cell types, and acquisition of anterior-posterior polarity. Gastrulation marks a critical developmental milestone of the mammalian embryo, occurring at ~15 dpf in the cynomolgus embryo (6), when a diverse range of cell types of the embryonic and extraembryonic tissues are specified and are allocated to the primary germ layers.

Tracking the time course of embryo development in culture, as assessed by morphological landmarks and the appearance of constituent cell types, showed that these embryos have attained the morphogenetic milestones of their *in vivo* counterparts (1, 2). Overall, the embryos in culture recapitulated the *in vivo* development of the cynomolgus embryo up to the stage of early gastrulation. However, only a fraction (10 to 22%) of embryos developed normally past the initiation of gastrulation to 20

**“Information generated from the *in vitro* cynomolgus embryo model will enhance understanding of... early embryogenesis...”**

Embryology Unit, Children's Medical Research Institute, University of Sydney and School of Medical Sciences, Faculty of Medicine and Health, University of Sydney, Westmead, NSW 2145, Australia. Email: ptam@cmri.org.au



dpf. Experience in mouse embryo culture indicates that supporting development beyond gastrulation requires the provision of enriched culture media and unconstrained physical settings that can support extensive embryonic growth and the establishment of a functional fetal-maternal (placental) interface (5). Thus, there is a need to further optimize the present culture methods to enable extended post-gastrulation development.

A wealth of knowledge about the delineation of embryonic and extraembryonic cell types, the specification of the germ line, and the transition of epiblast cells (which give rise to the germ cell layers) from pluripotency to lineage specification has been gleaned from single-cell transcriptome (gene expression) analysis of cynomolgus embryos in vivo (6, 7). The analysis of in vitro embryos by Niu *et al.* and Ma *et al.* demonstrates that the cells of the various embryonic and extraembryonic lineages found in the embryo in vivo were present in the cultured embryos. However, there is some discordance in the clustering of cell types according to transcriptomes between cultured and in vivo embryos, the spectrum of cell types may not be represented completely in vitro, and not all cells of the cultured embryos could be matched to known in vivo cell types. With the availability of multiple datasets (1, 2, 6, 7), it may be informative to reanalyze a merged dataset for collating the multitude of cell types in the in vitro embryo. This may reveal whether cells in an intermediate state in a known lineage, or cells of previously undescribed or transitory lineage, have been captured in the developing embryos in vitro.

A key outcome of gastrulation is the establishment of a blueprint of development according to a body plan that determines the composition and spatial assembly of progenitor cells (the building blocks of tissues and organs) and the form-shaping process of the body parts. The

analysis of marker expression by Ma *et al.* and Niu *et al.* shows that the key cell types were detected at the appropriate developmental stage and location in the cynomolgus embryos in vitro. The regionalization of progenitor cells of different lineages or their descendants in the germ layers and extraembryonic tissues suggests that a body plan may have been established after gastrulation.

The in vitro model also offers the opportunity to perform an analysis of the spatiotemporal (by developmental stage) transcriptome of cell populations at defined positions in the cynomolgus monkey embryo. This may reveal the regionalization of molecular cell fates (8). One way to elucidate the cellular architecture of the body plan would be to map single cells to their inferred positions in the embryo by computational analysis of the transcriptome (9, 10) and integrate the results with data about the spatial distribution of cells of interest (11). Such a method could reveal the spatiotemporal genealogy that is embedded in the body plan. This information would add to the lineage trajectories of embryonic cells identified by Niu *et al.* and Ma *et al.* in cultured embryos. Analysis of the transcriptome and chromatin accessibility by Niu *et al.* has further uncovered the transcriptional, signaling, epigenomic, and molecular activity underpinning the specification and differentiation of cell lineages. Additional multi-omics analysis of genomic function and molecular activity (12, 13) may generate a multidimensional body plan that could serve as the reference of cynomolgus development. These findings would engender testable hypotheses about the role of molecular drivers of lineage differentiation, tissue patterning, and morphogenesis.

Information generated from the in vitro cynomolgus embryo model will enhance understanding of the mechanisms and functional

drivers of early embryogenesis and may outline a universal blueprint of primate development. Translating the knowledge of lineage specification and differentiation of the nonhuman primate embryo to stem cell research will guide efforts in directed differentiation of stem cells to produce clinically useful cell types and the generation of organoids for disease modeling and stem cell medicine. Thus, in vitro culture of cynomolgus post-implantation embryos is a valuable experimental tool for primate embryo research and stem cell biology.

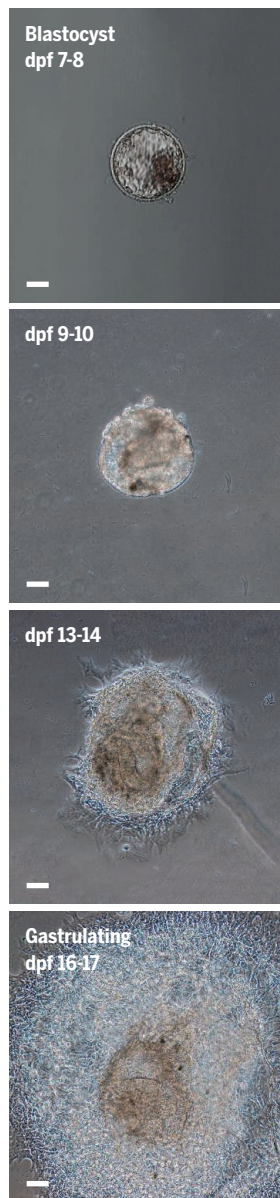
The embryological findings of this model could provide information about errors of development in primate embryos. Blastocysts may be derived from in vitro fertilization of gametes that carry naturally occurring or engineered genetic changes or from genetically modified pre-implantation embryos. Modeling the phenotype and the causal mechanism of genetic diseases may inform how errors of development affect implantation, embryo viability, morphogenesis, and bodily function in ways that may lead to early pregnancy loss and birth defects. Such information could enable the development of preventive and therapeutic treatments and may improve the efficacy of assisted reproductive technologies.

The study of nonhuman primate embryos will offer a valuable cross-species reference of the developmental milestones of human embryos. It could also be informative about the “organismal potential” of synthetic embryos (i.e., whether they can develop like embryos in vivo) that are generated from stem cells—for example, embryoids from embryo-derived stem cells or induced pluripotent stem cells (14, 15). Although animal embryos grown for research may not raise the ethical concerns related to human embryo research and genome editing, it is imperative that the application of this primate embryo model adheres to the ethical principles of animal research and welfare. ■

## REFERENCES AND NOTES

1. H. Ma *et al.*, *Science* **366**, eaax7890 (2019).
2. Y. Niu *et al.*, *Science* **366**, eaaw5754 (2019).
3. S. Zhang *et al.*, *Nat. Commun.* **10**, 496 (2019).
4. B. Sozen *et al.*, *Nat. Cell Biol.* **20**, 979 (2018).
5. J. A. Rivera-Pérez, V. Jones, P. P. L. Tam, *Methods Enzymol.* **476**, 185 (2010).
6. T. Nakamura *et al.*, *Nature* **537**, 57 (2016).
7. K. Sasaki *et al.*, *Dev. Cell* **39**, 169 (2016).
8. G. Peng *et al.*, *Nature* **572**, 528 (2019).
9. G. Peng *et al.*, *Dev. Cell* **36**, 681 (2016).
10. T. Mori, H. Takaoka, J. Yamane, C. Alev, W. Fujibuchi, *Sci. Rep.* **9**, 12597 (2019).
11. K. McDole *et al.*, *Cell* **175**, 859 (2018).
12. P. Yang *et al.*, *Cell Syst.* **8**, 427 (2019).
13. HuBMAP Consortium, *Nature* **574**, 187 (2019).
14. M. N. Shahbazi, E. D. Siggia, M. Zernicka-Goetz, *Science* **364**, 948 (2019).
15. R. Li *et al.*, *Cell* **179**, 687 (2019).

10.1126/science.aaz6976



Over ~10 days of culture in vitro, the cynomolgus monkey blastocyst develops to a gastrulating embryo, which forms three germ layers and is surrounded by trophoblasts (which form the placenta) that allow it to adhere to the gel substrate to mimic implantation. Scale bar = 60  $\mu$ m.

## POLYMER CHEMISTRY

# Cross-linking polyethylene through carbenes

A carbene-forming molecule can glue various polymers, even ones lacking functional groups

By **Felix J. de Zwart, Johan Bootsma, Bas de Bruin**

**T**he development of universal methods for surface modification and cross-linking of polymeric materials is highly desirable. Mechanical properties of natural and synthetic materials rely on the ability of the polymeric chains to form a three-dimensional (3D) network, for example, through cross-linking (1, 2). On page 875 of this issue, Lepage *et al.* (3) show that a rationally designed *bis*-diazirine inspired by the well-known 3-aryl-3-(trifluoromethyl)-3H-diazirine motif can be used for the cross-linking of nonfunctionalized saturated hydrocarbon polymers.

In natural macromolecules such as chitin and synthetic materials such as Kevlar, hydrogen-bond formation between amide groups form noncovalent cross-links. Many oil-based polymer coatings used in paintings and to protect wooden structures derive their 3D structure and strength from covalent cross-links formed in radical-based processes. Other examples of covalent cross-linking, such as vulcanization of rubber and the drying of glues, rely on reactive functional groups already present in the polymer.

Polymers such as polyethylene (PE) and polypropylene (PP) lack reactive cross-linkable groups, but cross-linking can be essential to tune mechanical properties. Copolymerization of ethylene or propylene with functionalized olefins can introduce reactive groups, but the scope of suitable comonomers is limited, and important material properties such as microstructure and molecular weight can become difficult to control (4, 5). It is especially challenging to synthesize high-molecular weight copolymers with tunable amounts of functional groups (5). Mildly efficient cross-linking strategies that break carbon-hydrogen (C–H) bonds by using high-energy radiation or peroxides exist for PE, but these

methods degrade PP (6). High-energy reactants tend to react through hydrogen-atom abstraction (HAA) and related radical-type pathways that damage the polymer.

Free (singlet) carbenes and transition-metal carbene complexes can undergo direct C–H insertion instead of HAA to form covalent carbon-carbon bonds even from unactivated C–H bonds. Carbenes are used for polymer postfunctionalization, as polymerization catalysts and as polymer backbone

amount of cross-linker added, corroborating successful cross-linking of the substrate. The *bis*-diazirine also cross-linked several other polymers, such as polyvinylalcohol (PVA). For PVA, whether carbene insertion occurred through C–H or O–H bonds was not investigated, but the latter seems most likely (9). This cross-linking methodology could find applications in upgrading biopolymers in which O–H bonds are ubiquitous.

The authors also explored application of the cross-linker as an adhesive for high-density PE (HDPE). Adhesion to this low-surface-energy material is difficult—it failed for a control sample with a commercial adhesive (Super Glue). However, the *bis*-diazirine cross-linker showed high performance in adhesion tests, and analysis of ripped samples revealed a cohesive failure mechanism indicative of cross-linking to the HDPE surface. The cross-linker was also an effective synthetic fabric strengthener.

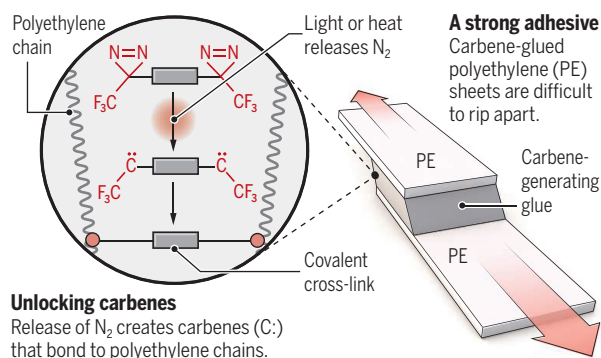
Lepage *et al.* assume that in their reactions, singlet carbenes are generated that insert in a concerted manner into C–H bonds, which makes sense given the relatively controlled reactivity toward cyclohexane. But formation of triplet carbenes that react through radical processes cannot be fully excluded (10). Radical-type pathways could damage polymer integrity, so examining the electronic structure of the formed carbenes is needed. This could also aid in developing carbenes that can be generated at lower temperatures, possibly through transition-metal catalysis (4).

The cross-linker developed by Lepage *et al.* not only has potential applications as an adhesive, but similar reagents could be used in paints and coatings. Prospective bio-based bind-

ers such as cellulose and lignin lack readily cross-linkable groups such as isocyanates, ketones, or alkenes. The cross-linking method of Lepage *et al.* may help turn biomass-based macromolecules into functional materials. ■

## Getting a grip on polyethylene

Lepage *et al.* designed a molecule that generates highly reactive carbenes that can cross-link unreactive alkyl polymers.



(4, 5, 7). Tri- and tetravalent photoactivatable azides and diazirines can cross-link polyethylene glycol, but efficient generic cross-linkers for the strengthening of unfunctionalized polyolefins have not been developed (8).

Lepage *et al.* now report a carbene cross-linker containing two diazirine motifs. Free carbenes can be generated upon photochemically or thermally induced nitrogen ( $N_2$ ) loss (see the figure). A drawback of molecules containing  $N_2$  expelling motifs (such as diazirines) is explosion risk, and the authors abandoned known *bis*-diazirine compounds because of their volatile and explosive nature. They rationally designed a *bis*-diazirine cross-linker that finely balances risk and reactivity and generates two free carbenes that insert into C–H bonds of the polymer. The tethered structure forms cross-links between different polymer chains, even those of PE and PP. The molecular weight of PP increased with the

## REFERENCES AND NOTES

1. D. Wang, T. P. Russell, *Macromolecules* **51**, 3 (2018).
2. A. Nojoomi *et al.*, *Nat. Commun.* **9**, 3705 (2018).
3. M. L. Lepage *et al.*, *Science* **366**, 875 (2019).
4. M. M. Díaz-Requejo *et al.*, *Macromolecules* **38**, 4966 (2005).
5. N. M. G. Franssen *et al.*, *Chem. Soc. Rev.* **42**, 5809 (2013).
6. K. S. Whitely *et al.*, *Polyolefins: Ullman's Encyclopedia of Industrial Chemistry* (Wiley-VCH, 2000).
7. C. W. Bielawski, R. H. Grubbs, *Prog. Polym. Sci.* **32**, 1 (2007).
8. A. Welle *et al.*, *Synthesis* **44**, 2249 (2012).
9. J. Brunner *et al.*, *J. Biol. Chem.* **255**, 3313 (1980).
10. J. Wang, R. S. Sheridan, *Org. Lett.* **9**, 3177 (2007).

## ACKNOWLEDGMENTS

We thank the ARC-CBBC (projects 2016.001.UvA and 2018.015.C) for financial support.

Van 't Hoff Institute for Molecular Sciences (HIMS), University of Amsterdam (UvA), Science Park 904, 1098 XH Amsterdam, Netherlands. Email: b.debruin@uva.nl



# Piling on the pressures to ecosystems

Identifying dangerous combinations of assaults could prevent ecosystem collapse

By **Peter Manning**

A multitude of anthropogenic pressures and perturbations now assault the world's ecosystems. The air is enriched with carbon dioxide (CO<sub>2</sub>), temperature extremes and droughts happen with increasing frequency, and a wide range of pollutants accumulate in the soil and water, including pesticides, microplastics, and excess fertilizer. What is the overall impact of these changes—so-called global environmental change drivers (or factors)—on ecosystems and their functioning? Although a broad scope of scientific approaches is used, including observational studies and modeling, experiments remain key. On page 886 of this issue Rillig *et al.* (1) present an exciting new methodological approach to investigate how these multiple pressures affect ecosystems.

Historically, the dominant approach in global change driver experiments is that of the full factorial design (hereafter factorial), in which drivers are applied to replicate experimental units (typically plots of ground), while others (the controls) remain unmanipulated. With this design, the effect of each driver can be estimated and, if there are multiple drivers, their interaction. However, the nature of this design means that as the number of drivers increases, the experiment gets exponentially larger. As a result, multifactor experiments are very rare because they are simply too expensive, time-consuming, and logistically complex to be performed. Rillig *et al.* surveyed soil-based global change driver experiments and reveal that >98% of these experiments manipulated just one or two drivers, with a tiny number (<2%) involving three or four drivers. Accordingly, when it comes to global change, a fair bit is known regarding the effect of certain individual drivers (for example, warming, nitrogen deposition, and CO<sub>2</sub> enrichment), but very little is known about the combined impact of many drivers.

The lack of multifactor global change driver experiments is problematic because, as in nature, such drivers often occur in concert. For example, an intensive agricultural ecosystem near human habitation and industry may be subject to a cocktail of herbicides,

fungicides, insecticides, high concentrations of fertilizer, warming, drought, atmospheric CO<sub>2</sub> enrichment, microplastic pollution, soil salinization, and heavy-metal contamination. A recent meta-analysis of global change driver experiments reported that multiple drivers affect terrestrial plant communities more strongly than single factors (2), whereas in freshwater ecosystems, the opposite is observed (3). However, what happens beyond a few well-studied drivers is completely unknown. Do the cumulative pressures of multiple drivers push ecosystems out of safe operating space and toward their limits? Could a pollutant leave organisms



Human perturbations bombard agricultural ecosystems, but their combined impact is unknown.

susceptible to drought stress and the negative impacts of other pollutants? For such questions, both theory and data are absent.

The limits of factorial design are cleverly circumvented by Rillig *et al.* to investigate what happens to soil microbial communities and their functioning when multiple drivers hit an ecosystem simultaneously. The authors applied an experimental approach developed in biodiversity-ecosystem functioning research. Such experiments emerged more than 25 years ago to investigate how the functioning of ecosystems responds to species extinctions. Initially, these experiments had a simple design, with high, intermediate, and low amounts of biodiversity (4). However, it soon became clear that it was impossible to distinguish the effects of biodiversity from those of certain combinations of species, because diverse communities could contain species that were not present in any of the

low-diversity communities. Because large numbers of species cannot be combined in a factorial design, a new experimental design was developed. In this, species are drawn randomly from a pool to form communities of varying diversity (5). This allows both the effects of individual species and the overall effect of species richness to be quantified.

In the multifactor experiment of Rillig *et al.*, global change drivers, rather than species, are drawn randomly. In parallel to diversity experiments, the effects of individual drivers can be estimated, as can the effect of adding as many as 10 simultaneous drivers. The findings support the idea that the effect of many drivers is unpredictable from single- and two-factor studies. Some ecosystem properties responded unpredictably to multiple drivers, and more strongly than would be expected from their responses to individual drivers. Although the experimental approach was applied to small microcosms that lack the complexity of real ecosystems, the study's design is generally applicable to any ecosystem facing multiple pressures. Furthermore, thanks to its relatively small size (140 replicates), the use of this approach in real-world ecosystems is also realistic.

The factorial design has provided great insights into how ecosystems respond to specific drivers, and the use of such standard designs has allowed for meta-level studies that provide global generalizations (2, 3). Nevertheless, there is growing recognition that the factorial design has often been applied indiscriminately. Alternative experimental designs are needed to expand and strengthen our understanding of ecosystem responses to global change (1, 6). For example, future studies may merge the multifactor design with the factorial by strategically adding certain driver combinations to the multifactor design to measure interactions between important or likely drivers. ■

## REFERENCES AND NOTES

1. M. C. Rillig *et al.*, *Science* **366**, 886 (2019).
2. K. J. Komatsu *et al.*, *Proc. Natl. Acad. Sci. U.S.A.* **116**, 17867 (2019).
3. M. C. Jackson, C. J. G. Loewen, R. D. Vinebrooke, C. T. Chimimba, *Glob. Chang. Biol.* **22**, 180 (2015).
4. S. Naeem, L. J. Thompson, S. P. Lawler, J. H. Lawton, R. M. Woodfin, *Nature* **368**, 734 (1994).
5. D. Tilman, D. Wedin, J. Knops, *Nature* **379**, 718 (1996).
6. J. Kreyling *et al.*, *Ecol. Lett.* **21**, 1629 (2018).

## ACKNOWLEDGMENTS

E. Allan and M. Neyret provided comments on the text.

10.1126/science.aaz9000

Senckenberg Biodiversity and Climate Research Centre, Frankfurt am Main, Germany.  
Email: peter.manning@senckenberg.de

## HYPOTHESIS

# Cellular survival over genomic perfection

DNA repair pathways permit some damage, leading to mutagenesis but not always cancer

By **Serena Nik-Zainal**<sup>1,2</sup> and **Benjamin A. Hall**<sup>1</sup>

**D**amage to DNA occurs continuously. DNA quality control mechanisms, such as DNA repair and replicative pathways, mitigate that damage and preserve the DNA sequence. Mutations are believed to arise when DNA lesions are not repaired appropriately, and they are thought to be an indicator of ineffectual DNA quality control. Yet, DNA sequencing of normal tissues reveals that considerable somatic mutagenesis is common. Mutagenesis appears to be the inevitable outcome of cellular wear and tear and is not necessarily cancer associated. Perhaps mutagenesis is not due to failings of DNA quality control mechanisms. Rather, such pathways may be naturally limited in activity, resulting in permissiveness to mutagenesis. We suggest that this is a prioritization of survival over genomic perfection, given that most DNA damage is inconsequential and thus, affordable.

Water and oxygen are highly mutagenic to DNA, but essential for life (1). Hydrolysis and oxidation continuously cause DNA modifications that could become permanently embedded in the genome, as mutation (1). In addition to endogenous sources of DNA damage, DNA is regularly exposed to environmental genotoxins such as ultraviolet (UV) radiation or tobacco smoke. DNA damage is thus inevitable. DNA quality control pathways survey and fix the genome to mitigate damage (2, 3). DNA damage, such as double-strand breaks, are poorly tolerated and if unfixed, can induce cell death (2, 3). Moreover, DNA damage checkpoints, which pause cell division to allow time for DNA repair, highlight that maintaining DNA integrity prior to cell division is vital for cell survival (4). Comprehensive DNA quality control pathways are therefore considered crucial to preserving genomic health.

The biologist Theodor Boveri hypothesized that aggregations of heritable material, later called chromosomes, were associated with cancer. His work lay the foundations for the somatic mutation theory of carcinogenesis,

in which stepwise acquisition of mutations are believed to be central to the development of cancer (5). Through statistical analyses of inherited versus sporadic retinoblastoma, Alfred Knudson hypothesized that two “hits” to DNA (driver mutations) were necessary to cause cancer. This explained early, childhood onset of heritable retinoblastoma, because the first mutation was inherited. A raft of “driver” mutation discoveries soon followed. Cancers carry only a handful (less than 10 per tumor) of causally implicated driver mutations that occur in “cancer genes,” so-called because these genes are recurrently mutated across many tumors. This buttressed the somatic mutation theory and was instrumental to the development of targeted therapeutics.

Cancer cells also carry thousands of “passenger” mutations believed to be bystander events devoid of biological effects. Passenger mutations are thought to arise because of incompetencies of DNA quality control pathways to adequately fix DNA damage (6). Indeed, an early step in tumorigenesis has been proposed to be the induction of a “mutator phenotype” (6). Large-scale cancer genome sequencing efforts have revealed the extraordinary extent of mutagenesis such that extensive genetic changes are considered pathognomonic of cancer.

Recently, somatic mutations, including driver mutations and high numbers of passenger mutations, were found to occur in normal tissue with no sign of cancer, implying that mutagenesis could be extensive in normal cells, prior to malignant transformation (7). Notably, samples of redundant eyelid skin removed at blepharectomy were used for ultra-deep sequencing of 74 cancer genes, and characteristic mutations associated with skin cancer (e.g., melanoma) were found in these nonmalignant tissues. Qualitative mutational signatures of UV radiation-induced damage were also appreciable, and the quantitative burden of mutagenesis in normal skin was comparable to that of skin cancers (8). Moreover, ultra-deep targeted sequencing of normal esophageal epithelium discerned hundreds of mutated clonal cell populations per square centimeter. The cancer gene *NOTCH1* was one of the most commonly mutated genes in normal esophageal epithelium, with a frequency exceeding that observed in esophageal cancers (9, 10). In

a comprehensive analysis of RNA sequencing data from >6000 samples of 29 healthy tissue types (11), cancer-associated mutations were found across tissues, levels of mutagenesis were associated with exposure to exogenous mutagens and tissue-specific proliferation rates, and macroscopic clonal expansions were also demonstrable. Hence, driver mutations, widespread mutagenesis, and even a mélange of competitive clones are all compatible with normal tissue and are not necessarily associated with cancer (see the figure).

The high number of passenger mutations, equivalent to 1000 to 10,000 per genome, in normal cells (8, 12) raises questions regarding why DNA quality control mechanisms have failed to limit mutagenesis. Perhaps a somewhat counterintuitive perspective (13) can be considered: If DNA quality control pathways monitor and preserve DNA integrity too strictly, it could be detrimental to cellular survival. The repair of DNA lesions has a cost: It requires time and cellular resources. If every DNA lesion in a cell were repaired, avoiding mutations altogether, the cellular cost associated with performing that repair would have to increase in direct proportion to the amount of damage. In conditions of high DNA damage—through exposure to environmental mutagens, for example—DNA repair could be too costly for cellular survival. Instead, if restrictions or thresholds were placed on DNA quality control to perform some repair but not necessarily of all lesions, then DNA-repair-limited cells are more likely to survive than cells caught in comprehensive repair, which can lead to cell death (apoptosis). This implies that DNA quality control pathways are fully functional but naturally permissive of mutagenesis, even in normal cells.

Evidence to support this hypothesis comes from experiments in which induced pluripotent stem cells (iPSCs) were treated with an array of environmental genotoxins (12). These normal stem cells accumulated extensive passenger mutations showing distinct mutational signatures. Some mutational signatures showed transcriptional strand bias—whereby the non-transcribed DNA strand is more heavily mutated than the transcribed strand (12), the mark of transcription-coupled repair (TCR) activity. TCR fixes DNA damage on both strands, but preferentially on the

<sup>1</sup>MRC Cancer Unit, University of Cambridge, Hutchison-MRC Research Centre, Cambridge Biomedical Campus, Cambridge, UK. <sup>2</sup>Academic Laboratory of Medical Genetics, Addenbrooke's Treatment Centre, Addenbrooke's Hospital, Cambridge, UK. Email: snz@mrc-cu.cam.ac.uk



transcribed strand, and its activity in normal cells was comparable to that in cancer cells. Accordingly, in iPSCs and cancer cells, the presence of strand bias indicates that TCR is competent and operative, but unable to mitigate all DNA damage, and is thus tolerant of mutagenesis.

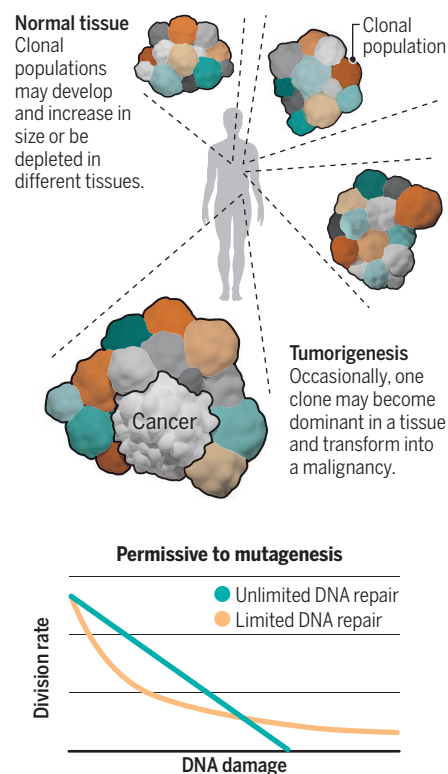
Limited DNA quality control during circumstances of high damage has been suggested through mathematical modeling (13). The model shows that in a situation where individual DNA damaging events are rarely deleterious (that is, when most mutations are passengers) during periods of high damage, DNA-repair-unlimited cells incur high repair costs and become depleted owing to cell death. By contrast, DNA-repair-limited cells may continue with cell division and survive (see supplementary movies S1 and S2). This model could be a useful starting point to explore permissiveness to mutagenesis. Given that most (~98%) of the genome is intronic and intergenic and the majority of mutations that arise as a result of DNA damage are unlikely to affect protein function, the model might explain why normal, healthy cells show considerable amounts of mutagenesis: survival through tolerance of mutation, rather than compromised DNA quality control processes.

The tolerance of mutagenesis in normal cells can, however, lead to the occurrence of new drivers, but not necessarily cancer. For example, in the testes of older men, acquired mutations in genes encoding components of receptor tyrosine kinase–RAS–mitogen-activated protein kinase (MAPK) and fibroblast growth factor receptor (FGFR) signaling pathways, which are commonly associated with cancer, result in increased cellular proliferation rates but seldom cause cancer. Clonal populations of seminiferous tubules generate spermatozoa with these mutations. This explains the high spontaneous birth prevalence and strong paternal age-effect of disorders such as achondroplasia, Apert, and Costello syndromes—all associated with activating mutations in MAPK and FGFR signaling genes. A study of 276 testicular biopsies obtained from five older men (median age of 83) identified additional cancer gene variants, all known to activate RAS-MAPK signaling (14). The aging male germ line therefore accumulates deleterious cancer driver mutations that rarely (if ever) switch to malignancy.

Another example is segmental overgrowth syndromes caused by somatic mutations of the cancer gene, *PIK3CA* (phosphatidylinositol-4,5-bisphosphate 3-kinase catalytic subunit  $\alpha$ ). Although these syndromes are benign in terms of oncology, they can produce debilitating clinical phenotypes with unrelenting tissue growth (15). Referred to

## Mutagenesis in normal tissue

DNA repair pathways permit some damage, resulting in mutagenesis but not necessarily cancer. Most normal tissues are likely to have many clonal populations defined by the distinct set of mutations that they harbor.



Limited DNA repair could promote survival and the emergence of clones.

as *PIK3CA*-related overgrowth syndromes (PROS), affected people are mosaics, wherein discrete clonal populations exhibit mutations. The most frequent *PIK3CA* mutations in PROS (Glu<sup>542</sup>Lys, Glu<sup>545</sup>Lys, and His<sup>1047</sup>Arg) are identical to hotspot cancer driver mutations although other, non-cancer-associated *PIK3CA* mutations also occur in PROS. Notably, surrounding cells in affected tissues that are not *PIK3CA*-mutated are also overgrown (15). It has consequently been suggested that *PIK3CA*-mutated cells do not simply possess cell-autonomous characteristics, they may exert proliferation-enhancing properties on neighboring, non-*PIK3CA*-mutated cells.

Therefore, driver mutations alone are not sufficient to initiate cancer, although they can be disease-causing. Considering that an adult human has ~30 trillion cells, and only one cell develops into a cancer, human cells are remarkably robust at preventing cancer. Because the burden of mutagenesis and the frequencies of driver mutations can be high in normal tissues, mutations alone are possibly not sufficient to initiate cancer.

Additional extrinsic factors, including cellular interactions and the microenvironment, seem to be required to create a selective environment that triggers a cell to become a dominant cancer clone. It is likely that the mutated genome of a cell contributes to the potential for malignant transformation, but it is not deterministic of it. This concept is not unfamiliar: Inherited mutations in DNA repair genes, such as *BRCA1*, *BRCA2*, and *MLH1* (mutL homolog 1), cause familial cancer predisposition. They confer an increased lifetime risk of cancer, but cancer does not always arise. Additional factors seem to be required to tip the balance toward cancer development.

Mutagenesis remains important to explore. Identifying clinically relevant drivers and mutational signatures should provide meaningful directions for patient stratification and prognostication. The use of specific driver mutations is a favored method for patient stratification in clinical studies. However, a cancer gene could play disparate roles in tumors affecting different organs, and its functionality could evolve over the patient's lifetime. Given the mutagenesis observed in normal tissues, perhaps it is time to reflect on whether this is the best approach for stratification. Similarly, although many mutational signatures have been identified, only a subset are clinically instructive—some may occur normally and not be causative of cancer. Others may be biomarkers of DNA repair deficiencies, which are potentially informative for therapy selection. It is imperative to identify mutations that are truly clinically meaningful, to improve cancer management. ■

## REFERENCES AND NOTES

1. T. Lindahl, *Nature* **362**, 709 (1993).
2. T. Rich et al., *Nature* **407**, 777 (2000).
3. J. H. Hoeijmakers, *N. Engl. J. Med.* **361**, 1475 (2009).
4. M. B. Kastan, J. Bartek, *Nature* **432**, 316 (2004).
5. B. Vogelstein et al., *N. Engl. J. Med.* **319**, 525 (1988).
6. L. A. Loebe, *Cancer Res.* **51**, 3075 (1991).
7. C. Tomasetti et al., *Proc. Natl. Acad. Sci. U.S.A.* **110**, 1999 (2013).
8. I. Martincorena et al., *Science* **348**, 880 (2015).
9. I. Martincorena et al., *Science* **362**, 911 (2018).
10. A. Yokoyama et al., *Nature* **565**, 312 (2019).
11. K. Yizhak et al., *Science* **364**, eaaw0726 (2019).
12. J. E. Kucab et al., *Cell* **177**, 821 (2019).
13. J. Breivik, G. Gaudernack, *FEBS Lett.* **563**, 7 (2004).
14. G. J. Maher et al., *Genome Res.* **28**, 1779 (2018).
15. R. R. Madsen et al., *Trends Mol. Med.* **24**, 856 (2018).

## ACKNOWLEDGMENTS

Thanks to M. Hall for valuable discussions. B.A.H. is supported by the Royal Society (grant no. UF130039). S.N.-Z. is supported by a Cancer Research UK (CRUK) Advanced Clinician Scientist Award (C60100/A23916) and the Josef Steiner Foundation. Both authors are supported by a Medical Research Council (MRC) Grant-in-Aid to the MRC Cancer unit.

## SUPPLEMENTARY MATERIALS

[science.sciencemag.org/content/366/6466/802/suppl/DC1](http://science.sciencemag.org/content/366/6466/802/suppl/DC1)

10.1126/science.aax8046

## GLASSES

# Overcoming glass brittleness

Thin films of flawless amorphous alumina are ductile at room temperature

By **Lothar Wondraczek**

**T**he mechanical reliability of modern glass products underlies their diverse uses, which include touch panels and ultrathin flexible displays, lightweight containers, and energy-efficient windows. Most of these applications rely on chemically or thermally strengthened silicate glasses that are strong despite being brittle, but some, such as optical telecommunication fibers, take further advantage of the flexibility of thin materials. A new paradigm of glass materials could be envisioned if brittleness could be overcome by making glasses ductile. On page 864 of this issue, Frankberg *et al.* (1), using in situ transmission electron microscopy and molecular dynamics simulations, report conditions under which thin films of amorphous alumina ( $\alpha\text{-Al}_2\text{O}_3$ ) become ductile at room temperature. These results address the major challenge for creating “indestructible” glasses: initiating unconfined plasticity (irreversible deformation without fracture) that can dissipate mechanical stress within an otherwise rigid, disordered network of covalent bonds.

Improving the strength of glass products has been a long-standing challenge for glass engineers because of the great promise that lies in their intrinsic properties. Considerations based on the atomic interactions in conventional oxide glasses predict values of theoretical strength that approach or even exceed those of the strongest engineered materials. The technological opportunities that would emerge when these theoretical limits could be exploited for practical use are legendary. Indeed, Pliny the Elder wrote about a glass maker who, after presenting a flexible (and probably unbreakable) glass to Roman emperor Tiberius (14 to 37 CE), had his workshop destroyed so as not to spread the knowledge, otherwise materials such as copper, silver, and gold would become worthless (2).

Today's glass products reach only a fraction of the predicted intrinsic strength because of their brittleness. If the mechanical energy imparted to the glass by mechanical loading is not dissipated by elastic (revers-

ible) or plastic (irreversible) deformation, it accumulates in the vicinity of microscopic flaws and defects. This process leads to local stress concentration, which increases with the sharpness of the tip of the flaw (see the figure); thus, the locally acting stress can be much higher than the externally applied one, and the material fails even when supporting only a low load.

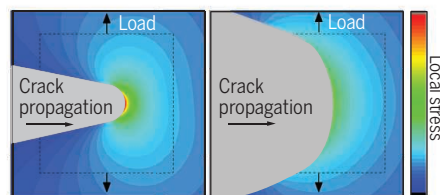
Plastic deformation may cause blunting or rounding of sharp crack tips, which reduces the extent of stress amplification and enhances the material's defect resistance to obtain much higher levels of practical strength (3). However, it is usually assumed that brittle glasses do not undergo plastic deformation in unconfined

## From brittle fracture to viscous creep

Frankberg *et al.* demonstrate how the specific atomic arrangement in amorphous alumina can facilitate macroscopic ductility.

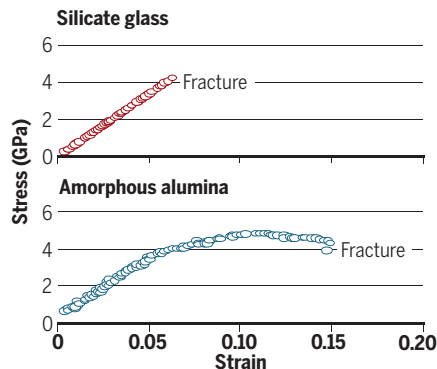
### Brittle fracture

In brittle materials such as silica glass, microscopic flaws cause local stress accumulation (region in red).



### Glass ductility

Plastic deformation by viscous creep may reduce the level of stress amplification through tip blunting, making the material damage-tolerant. In amorphous alumina, pronounced plastic contributions under tensile loading lead to higher strain before failure.



loading conditions. Instead of elongating or permanently bending, they simply break under load. This situation is unlike that in metals, where bonding is less localized and atomic-scale shear has lower energetic barriers relative to materials with primarily covalent bonding. Fracture occurs before the stress level is sufficiently high to initiate plastic flow. In other words, for plastic flow to occur, the acting stress needs to reach a threshold at which bond-switching reactions are initiated that enable atomic rearrangement. At the same time, permanent bond rupture and processes that facilitate cracking (structural cavitation and cavity coalescence) must be averted.

A brittle material must be completely flawless if local stress amplification is to be prevented. Only then can it accommodate macroscopic stress levels approaching the predicted intrinsic strength. For example, when glass scientists sought to prevent even the slightest occurrence of surface defects, values of tensile strength exceeding 10 GPa were achieved for vitreous silica nanowires (4). This value compares to ~1 GPa bending strength for state-of-the-art mobile phone covers that are made of glasses that have a compressive surface layer for strengthening. In the previous understanding, such stress levels would always result in irreversible bond rupture and catastrophic failure rather than initiating viscous creep.

One of the difficulties with glassy materials lies in the fundamental nature of disorder. When a given property (such as the response to mechanical load) ultimately depends on the strength of interatomic interactions and bonding, property predictions require accurate knowledge of the spatial distribution of bond energy. In the absence of such insight, fundamental studies must draw from simplified model systems that approximate certain structural motifs—in particular, packing density, bond directionality, and structural dimensionality (5).

One such model is  $\alpha\text{-Al}_2\text{O}_3$ . Molten alumina is a fragile liquid; at its melting point of 2327 K, its viscosity is only ~30 mPa·s (6), compared to  $10^6$  Pa·s for an archetypical glass-former such as  $\text{SiO}_2$ . Freezing the highly mobile molecular arrangement of liquid  $\text{Al}_2\text{O}_3$  into a glassy solid would require cooling at a rate of several thousand kelvin per second. Hence,  $\text{Al}_2\text{O}_3$  does not typically form a glass but forms crystals such as sapphire or ruby, both of which belong to the trigonal phase of corundum.  $\alpha\text{-Al}_2\text{O}_3$  forms as a combustion product of aluminum-containing solid propellants and may be a component of circumstellar dust (7), but vapor deposition methods are needed to synthesize it for use as an engineering material. Thin layers of  $\alpha\text{-Al}_2\text{O}_3$  combine a high

Otto Schott Institute of Materials Research, University of Jena, Jena, Germany. Email: lothar.wondraczek@uni-jena.de



dielectric constant with a high band-gap energy (8), making it relevant for gate electronics, insulators, or tunneling barriers in microelectronic circuits but also for protective layers.

Whereas everyday silicate glasses are composed of  $\text{SiO}_4$  tetrahedra that assemble through corner-sharing rings to form a three-dimensional network,  $\alpha\text{-Al}_2\text{O}_3$  is composed of groups of four- and five-fold-coordinated Al atoms. Modeling studies suggest that packing creates a distorted pentagonal-bipyramidal lattice that has a substantially higher packing density than that of silica (9, 10). Frankberg *et al.* argue that it is exactly this structural arrangement that is responsible for room-temperature creep. The relatively open network of conventional silicate glasses facilitates cavitation, cavity coalescence, and fracture; by contrast, reactions in which an Al-O bond breaks and a new one forms, leading to mechanical relaxation, are much more likely in  $\alpha\text{-Al}_2\text{O}_3$  (by a factor of  $\leq 25$ ) than similar bond-switching reactions in  $\text{SiO}_2$ . Such reactions generate localized strain events that accumulate into macroscopic flow and render the glass ductile. However, the material must be free of flaws that would trigger local stress amplification and prevent the generation of a sufficiently high homogeneous stress field.

By demonstrating the requisite conditions for generating plasticity in the model of  $\alpha\text{-Al}_2\text{O}_3$ , Frankberg *et al.* provide an important guideline for materials scientists hoping to derive generalized strategies for chemical tailoring of the mechanical properties of oxide glasses. It will not be easy to put these findings to use in the design of commodity glass products just now. To this end, process engineering toward glasses with further reduced flaw propensity and new glass formulations that combine desirable macroscopic properties with microscopic ductility must be explored, making use of the specific structural features of  $\alpha\text{-Al}_2\text{O}_3$ . ■

#### REFERENCES AND NOTES

1. E. J. Frankberg *et al.*, *Science* **366**, 864 (2019).
2. Pliny the Elder, *The Natural History* (J. Bostock, Trans.) (Taylor and Francis, 1855), Book 36, Chapter 66; [www.perseus.tufts.edu/hopper/text?doc=Perseus:text:1999.02.0137](http://www.perseus.tufts.edu/hopper/text?doc=Perseus:text:1999.02.0137).
3. L. Wondraczek *et al.*, *Adv. Mater.* **23**, 4578 (2011).
4. G. Brambilla, D. N. Payne, *Nano Lett.* **9**, 831 (2009).
5. G. N. Greaves, A. L. Greer, R. S. Lakes, T. Rouxel, *Nat. Mater.* **10**, 823 (2011).
6. P.-F. Paradis, T. Ishikawa, *Jpn. J. Appl. Phys.* **44**, 5082 (2005).
7. B. Begemann *et al.*, *Astrophys. J.* **476**, 199 (1997).
8. J. Robertson, B. Falabretti, *J. Appl. Phys.* **100**, 014111 (2006).
9. S. K. Lee, S. B. Lee, S. Y. Park, Y. S. Yi, C. W. Ahn, *Phys. Rev. Lett.* **103**, 095501 (2009).
10. K. Nishio, T. Miyazaki, H. Nakamura, *Phys. Rev. Lett.* **111**, 155502 (2013).

10.1126/science.aaz2127



Bicarbonate concentrations in fresh water can alter the composition of aquatic plant communities, such as those in the Armaris Lagoon at the Menorca Biosphere Reserve in Spain.

#### BIOGEOGRAPHY

## Reuniting biogeochemistry with ecology and evolution

Mining of biological and geochemical data pinpoints a key trait of freshwater plants

By Rafael Marcé<sup>1,2</sup> and Biel Obrador<sup>3</sup>

**B**iodiversity conservation strategies that adapt to ongoing environmental changes require the ability to predict global biogeographical patterns (1). Research on macroecology—the study of relationships between organisms and their environment at large spatial scales—reports a pressing need for new information on freshwater species, which show exceptionally high declines and extinction rates worldwide (2, 3). The anticipation of changes in the distribution and community composition of freshwater organisms has forced scientists to grapple with a complex puzzle of interwoven ecological and evolutionary processes, including the ability of autotrophic organisms to convert different

sources of inorganic carbon to organic compounds (carbon fixation). On page 878 of this issue, Iversen *et al.* (4) report on a pioneering global analysis of a key functional trait in freshwater plants—the ability to use bicarbonate for photosynthesis—as a function of geochemical properties of water catchments.

Classical aquatic ecology studies show that algae and macrophytes use various forms of dissolved inorganic carbon such as carbon dioxide ( $\text{CO}_2$ ) and bicarbonate ( $\text{HCO}_3^-$ ) during photosynthesis. The use of bicarbonate is a physiological adaptation to low concentrations of  $\text{CO}_2$  present in many autotrophs, which influences species sorting and thus has implications for species distribution and community assembly (5). Since the days when data were “so few that no pattern of bicarbonate utilization” had yet emerged (6), new research has substantially increased our understanding of bicarbonate use by freshwater plants. Still lacking, however, was evidence of the global prevalence of this trait and its predictability at varying spatial scales. Now, Iversen *et al.* fill this gap by showing that the

<sup>1</sup>Catalan Institute for Water Research (ICRA), Emili Grahit 101, 17003 Girona, Spain. <sup>2</sup>Universitat de Girona, Girona, Spain. <sup>3</sup>Department of Evolutionary Biology, Ecology and Environmental Sciences, Biodiversity Research Institute (IRBio), University of Barcelona, 08028 Barcelona, Spain. Email: rmarce@icra.cat

global distribution of this trait in freshwater plant communities depends on the concentration of bicarbonate and CO<sub>2</sub> in water.

The work by Iversen *et al.* constitutes a breakthrough for at least three reasons. It paves the way for future studies of the impacts of global change on freshwater biodiversity and ecosystem functioning. It highlights the need to develop models for the dynamics of dissolved inorganic carbon in fresh waters that go beyond the mainstream focus on CO<sub>2</sub> emissions to the atmosphere. And it constitutes a powerful example of integrative ecology across spatial and temporal scales and knowledge domains.

Aquatic ecology developments since the 1980s have established that the competitive advantage of using bicarbonate for photosynthesis vanishes when the preferred carbon source, CO<sub>2</sub>, is present at high concentrations (5). Iversen *et al.* show that the prevalence of this trait differs in lake and river communities because of contrasting CO<sub>2</sub> concentrations in water. Thus, the concentration of CO<sub>2</sub> acts as a biogeochemical switch for the effect of this functional trait on species sorting. This switch is in turn modulated by both ecosystem functioning and geochemical properties of catchments (such as the weathering of minerals, ecosystem metabolism, air-water gas exchange, and hydrology and geomorphology of river networks).

In terrestrial ecology, different carbon-concentrating mechanisms for plant photosynthesis offer a convenient predictive framework for studying the impacts of climate change on biodiversity and function of terrestrial vegetation (7). By analogy, the dependence of bicarbonate use on a switch that is sensitive to global environmental changes might offer the same opportunity for freshwater research. For instance, in rivers, the biogeochemical CO<sub>2</sub> switch might change from off (high CO<sub>2</sub>) to on (low CO<sub>2</sub>) depending on the response of ecosystem metabolism to global changes in temperature and nutrient levels. In turn, metabolic controls of CO<sub>2</sub> concentrations in lakes might interact with ongoing changes of bicarbonate concentrations in catchments (8).

The new study also makes a strong appeal for developing better biogeochemical models of river networks that account for the full complexity of sources and dynamics of dissolved inorganic carbon. The numerous studies published in the past decade on organic carbon fate and CO<sub>2</sub> emissions to the atmosphere have fueled scientists' understanding of the role of inland waters in the global carbon cycle (9). However, these previous studies often lack a comprehensive depiction of inorganic carbon dynamics. Iversen *et al.* show that studies that explicitly account for other components affecting the

inorganic carbon cycle (such as alkalinity, bicarbonate concentration, calcite precipitation, and weathering) (10) are instrumental for deciphering additional ecological and evolutionary processes in fresh waters. Although it is challenging to integrate complex geochemical and biological interactions at large scales (11), such models paint a more precise picture of the freshwater carbon cycle and better inform multidisciplinary research on biodiversity conservation and Earth-system modeling.

The biogeochemical switch in Iversen *et al.*'s study became apparent through the adoption of a multiscale approach (from physiological processes to global patterns) that combined multidisciplinary sources of information (macroecology, physiology, biogeochemistry) and pursued synthesis between community ecology, evolution, and biogeochemistry. This kind of integrative ecological study reveals nature's secrets by bridging gaps at the interfaces between sub-disciplines (12). Other recent contributions highlight the usefulness of this integrative perspective for topics as diverse as niche definition (13), evolution of symbiotic interactions (14), and prokaryotic biogeography of the deep ocean (15). These varied multidisciplinary advancements do not in any way diminish the rapid and invaluable progress in biogeochemistry, community ecology, and evolution that has resulted from research within single knowledge domains. However, the findings of Iversen *et al.* suggest that research that takes a broad view of ecological science has the potential to reveal multifaceted mechanisms that can help scientists to predict global changes that inform biodiversity conservation strategies. ■

#### REFERENCES AND NOTES

1. C. Hof *et al.*, *Front. Biogeogr.* **7**, 155 (2015).
2. A. J. Reid *et al.*, *Biol. Rev. Camb. Philos. Soc.* **94**, 849 (2019).
3. S. A. Blowes *et al.*, *Science* **366**, 339 (2019).
4. L. L. Iversen *et al.*, *Science* **366**, 878 (2019).
5. S. C. Maberly, B. Gontero, *J. Exp. Bot.* **68**, 3797 (2017).
6. B. Moss, *J. Ecol.* **61**, 157 (1973).
7. P. B. Reich, S. E. Hobbie, T. D. Lee, M. A. Pastore, *Science* **360**, 317 (2018).
8. T. W. Drake *et al.*, *Environ. Sci. Technol.* **52**, 8302 (2018).
9. P. Regnier *et al.*, *Nat. Geosci.* **6**, 597 (2013).
10. E. G. Stets *et al.*, *Global Biogeochem. Cycles* **31**, 663 (2017).
11. E. H. Stanley, P. A. del Giorgio, *Limnol. Oceanogr. Lett.* **3**, 39 (2018).
12. S. Pickett *et al.*, *Ecological Understanding: The Nature of Theory and the Theory of Nature* (Academic Press, Amsterdam, 2007).
13. J. Peñuelas *et al.*, *Ecology* **100**, e02652 (2019).
14. M. Lu, L. O. Hedin, *Nat. Ecol. Evol.* **3**, 239 (2019).
15. M. Mestre *et al.*, *Proc. Natl. Acad. Sci. U.S.A.* **115**, E6799 (2018).

#### ACKNOWLEDGMENTS

We thank N. Bonada and A. G. Bravo for insightful comments. Supported by project C-HydroChange (Spanish AEI references CGL2017-86788-C3-2-P and CGL2017-86788-C3-3-P).

10.1126/science.aaz9096

#### IMMUNOLOGY

## Microbes and genes in heart failure

### Human genetic variants and gut microbiota trigger cardiac inflammation

By Slava Epelman

Inflammation of the heart (myocarditis) is a life-threatening condition that remains a poorly understood clinical entity. A variety of etiologies have been proposed; however, defining how risk factors and environmental exposures intersect has remained elusive. The multifactorial nature of host vulnerability highlights the need for a personalized medicine approach to make progress. On page 881 of this issue, Gil-Cruz *et al.* (1) demonstrate how a confluence of factors—including genetic predisposition, production of a commensal gut microbial autoantigen, and systemic inflammation—together trigger the generation of autoreactive CD4<sup>+</sup> T cells that cause autoimmune myocarditis and cardiac dysfunction in animals and patients. This study highlights the parallel investigative streams required to make progress in complex diseases.

Patients with cardiac dysfunction in the absence of coronary artery disease (called nonischemic cardiomyopathy) can generally be divided into two categories. The first is straightforward and composed of those with known or suspected mutations in cardiac contractile proteins. The second is called idiopathic cardiomyopathy, and thus a cause is not known, although this group is thought to include patients with prior myocarditis. Myocarditis is most commonly triggered by cardiac infection, particularly viral infections in the Northern Hemisphere and protozoan infections in the Southern Hemisphere (2). When tracking patients with biopsy-proven myocarditis, ~47% of patients have ongoing cardiac contractile dysfunction, which is a marker of morbidity and mortality (3). Beyond infections, a variety of other risk factors can also cause myocarditis, including rare inflammatory cardiomyopathies and chemotherapeutic agents, which can be directly

Department of Immunology, University of Toronto, Heart & Stroke/Richard Lewar Centre of Excellence, Toronto, Ontario, Canada. Email: slava.epelman@uhn.ca



cardiotoxic or immunomodulatory (3, 4). It is unclear if myocardial inflammation is driven by a true autoimmune process or nonspecific tissue injury in response to cardiac stress.

Animal studies have modeled autoimmune myocarditis; however, the data are in part discrepant with the clinical features of disease in humans. In animals, autoimmune myocarditis is triggered by immunization with cardiac antigens (cardiac myosin) together with immune adjuvants (5); by infusion of dendritic cells loaded with cardiac antigens (6); and can be potentially observed after experimental myocardial infarction (heart attack) (7). These approaches initiate acute onset of myocardial inflammation that can be modulated by targeting inflammatory

nizes cardiac myosin heavy chain 6 (MYH6) peptides presented by major histocompatibility complex class II (MHC II) molecules on the surface of antigen-presenting cells, which develop spontaneous myocarditis (9). They found that *Bacteroides thetaiotaomicron* (*B. theta*), a gut commensal microbe, is required to initiate autoimmune myocarditis. *B. theta* produces  $\beta$ -galactosidase ( $\beta$ -gal), a microbial protein with sequence homology to MYH6. Production of  $\beta$ -gal leads to MYH6-specific CD4<sup>+</sup> T cell proliferation and polarization to interleukin-17 (IL-17)-secreting cells, called T helper 17 (T<sub>H</sub>17) cells. IL-17 is a cytokine involved in inflammatory and autoimmune responses (10). MYH6-specific T<sub>H</sub>17 cells expanded locally, near the

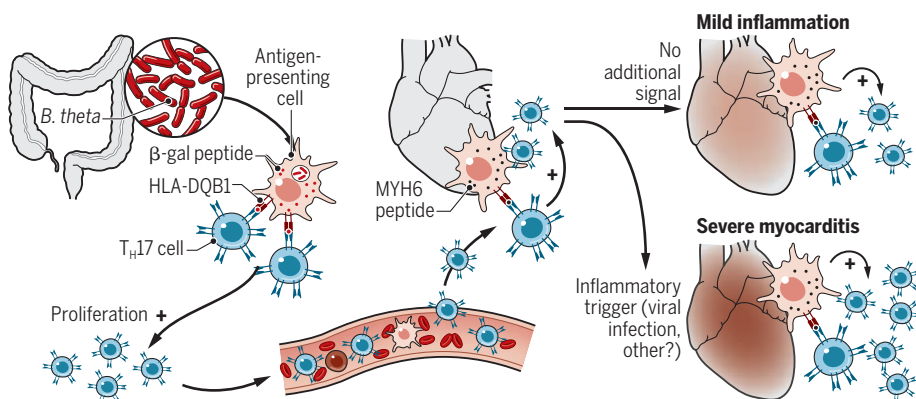
specific antibody titers correlated with progression and severity. Fecal microbiota transplantation of only *B. theta*-containing stool from patients with myocarditis triggered accumulation of cardiac MYH6-specific CD4<sup>+</sup> T cells in mice. These data link myocarditis to the growing body of evidence that the human microbiota is a critical modulator of inflammatory diseases.

Variants in genes encoding antigen-presentation molecules, such as the human leukocyte antigen (HLA)-DQB1, a human MHC II ortholog, as well as the nature of the initial inflammatory trigger (viral, bacterial, or drug) have also been linked to myocarditis patient variability (12). Gil-Cruz *et al.* observed that both individual peptides from  $\beta$ -gal and MYH6 could bind HLA-DQB1 molecules, and activated CD4<sup>+</sup> T cells were found only in patients with HLA-DQB1\*03 variants that recognize both MYH6 and  $\beta$ -gal. Together, these data suggest immunological tolerance to self-tissue is dysfunctional in a subset of patients with myocarditis if the correct peptide and HLA variant are present. So, what triggers myocarditis in patients? It seems unlikely that expansion of gut *B. theta* alone (or  $\beta$ -gal production) is sufficient. Inflammation may be required to initiate the response. In animals, viral myocarditis leads to the infiltration of large numbers of inflammatory monocytes and antigen-specific CD8<sup>+</sup> T cells without substantial cardiac injury, suggesting otherwise innocuous viruses could be potential triggers of myocarditis in the correct patient population (13).

The human microbiota also generates thousands of small proteins with unidentified functions that are likely to further modulate inflammatory responses (14). By incorporating the analysis of gut microbiota composition and individual HLA variations into clinical trials, understanding patient-specific risk profiles for many acute and chronic conditions that are modulated by the immune system are likely to be further refined. ■

## Multifactorial initiation of myocarditis

*Bacteroides thetaiotaomicron* (*B. theta*) colonization of the gut and production of  $\beta$ -galactosidase ( $\beta$ -gal) leads to presentation on human leukocyte antigen (HLA)-DQB1 by antigen-presenting cells and local CD4<sup>+</sup> T cell activation and differentiation into T helper 17 (T<sub>H</sub>17) cells.  $\beta$ -gal-specific T<sub>H</sub>17 cells enter the myocardium and, in the setting of an unknown inflammatory trigger, myosin heavy chain 6 (MYH6) is recognized by  $\beta$ -gal-specific T<sub>H</sub>17 cells and autoimmune myocarditis is triggered.



pathways and immune cells and is similar to well-characterized human autoimmune diseases (such as rheumatoid arthritis). Unfortunately, early clinical trials that used immunosuppressive therapies for myocarditis had poor responses (8). With clinical myocarditis, rarely do clinicians observe the steroid-responsive, relapsing and remitting inflammatory roller coaster characterized by chronic autoimmune diseases. Rather, most clinical myocarditis cases exhibit finite and non-self-sustaining inflammation. Recent data suggest there may be a more apparent role for immunosuppression than previously appreciated; however, the number of patients studied is quite small (3). These data also suggest that once inflammation has resolved after viral clearance, a subset of patients may develop myocarditis that is autoinflammatory and are susceptible to immunosuppression with steroid treatment, for example.

Gil-Cruz *et al.* used transgenic mice with an engineered T cell receptor (TCR) that recog-

nitizes cardiac myosin heavy chain 6 (MYH6) peptides presented by major histocompatibility complex class II (MHC II) molecules on the surface of antigen-presenting cells, which develop spontaneous myocarditis (9). They found that *Bacteroides thetaiotaomicron* (*B. theta*), a gut commensal microbe, is required to initiate autoimmune myocarditis. *B. theta* produces  $\beta$ -galactosidase ( $\beta$ -gal), a microbial protein with sequence homology to MYH6. Production of  $\beta$ -gal leads to MYH6-specific CD4<sup>+</sup> T cell proliferation and polarization to interleukin-17 (IL-17)-secreting cells, called T helper 17 (T<sub>H</sub>17) cells. IL-17 is a cytokine involved in inflammatory and autoimmune responses (10). MYH6-specific T<sub>H</sub>17 cells expanded locally, near the

gut within the colonic mucosa, and subsequently infiltrated the myocardium, driving profound cardiac tissue damage and death in mice colonized with *B. theta* strains that produce  $\beta$ -gal (see the figure). The gut microbiota can influence the outcome of both immune- and nonimmune-based diseases, and thus, this is a variable that must be considered when explaining fluctuating responses to therapy. For example, immune checkpoint blockade (ICB) has revolutionized cancer immunotherapy by targeting immune-suppressive co-receptors and thereby promotes robust antitumor CD8<sup>+</sup> T cell responses. The presence of certain fecal bacterial species tracked with response to ICB, and fecal microbiota samples from mice that responded to ICB that were transplanted into nonresponders induced an antitumor immune response (11). Gil-Cruz *et al.* found that patients with biopsy-proven myocarditis had higher amounts of *B. theta* in their stool and that *B. theta*-

## REFERENCES AND NOTES

1. C. Gil-Cruz *et al.*, *Science* **366**, 881 (2019).
2. C. Elamm, D. Fairweather, L. T. Cooper, *Heart* **98**, 835 (2012).
3. C. Tschöpe, L. T. Cooper, G. Torre-Amione, S. Van Linthout, *Circ. Res.* **124**, 1568 (2019).
4. D. B. Johnson *et al.*, *N. Engl. J. Med.* **375**, 1749 (2016).
5. A. Anzai *et al.*, *J. Exp. Med.* **216**, 369 (2019).
6. U. Eriksson *et al.*, *Nat. Med.* **9**, 1484 (2003).
7. K. Van der Borgh *et al.*, *Cell Rep.* **18**, 3005 (2017).
8. H. S. Chen, W. Wang, S. N. Wu, J. P. Liu, *Syst. Rev.* **10**, CD004471 (2013).
9. V. Nindl *et al.*, *Eur. J. Immunol.* **42**, 2311 (2012).
10. D. D. Patel, V. K. Kuchroo, *Immunity* **43**, 1040 (2015).
11. C. Jobin, *Science* **359**, 32 (2018).
12. I. Portig, A. Sandmoeller, S. Kreilinger, B. Maisch, *Autoimmunity* **42**, 33 (2009).
13. X. Clemente-Casares *et al.*, *Immunity* **47**, 974 (2017).
14. H. Sberro *et al.*, *Cell* **178**, 1245 (2019).

10.1126/science.aaz4400

BOOKS *et al.*

## FORENSIC SCIENCE

# Returning the fallen

An anthropologist offers compelling context for ongoing efforts to repatriate service members killed in Vietnam

By **Montgomery McFate**

Since the U.S. military engagement in Iraq and Afghanistan began in the early 2000s, there have been no unidentified war dead. The number of missing-in-action and unrecovered killed-in-action U.S. service members from the recent conflicts in the Middle East is also incredibly low—only three defense contractors captured in Iraq have not been recovered. Yet the idea of the “unknown soldier” continues to resonate strongly and is a perennial subject of Hollywood movies and popular history.

Every year, the U.S. Defense Prisoner of War/Missing in Action (POW/MIA) Accounting Agency spends \$130 million, nearly 70% of which is allocated to operations in Southeast Asia. Why does the United States spend considerable amounts of money and effort to

identify and repatriate the remains of service members killed in action during overseas wars? Sarah Wagner's book *What Remains* offers a compelling and thoughtful answer.

Wagner is an anthropologist who previously studied the forensic scientific efforts to identify the victims of the Srebrenica genocide in Bosnia and Herzegovina. In *What Remains*, she provides an ethnographic window into the many facets of MIA recovery in Vietnam, including the experiences of American families who have had their loved ones repatriated, the work of forensic scientists who recover and identify human remains, and the bureaucratic wrangles of U.S. military personnel in the Defense POW/MIA Accounting Agency.

Unlike many other previous books on MIA accounting that have focused on the political history of the issue during the Reagan era or that have chronicled a single individual's efforts to recover a family member in Vietnam, Wagner seeks to understand the social context and meaning of MIA forensic accounting. In her view, forensic science is not merely em-

pirical and objective, it also reflects social values: “The scientific pursuit of locating and naming the unaccounted for reveals the values the United States as a nation holds most dear—a moral commitment to reunite the individual and the homeland,” and a faith in the precision of science.

Because she is an anthropologist, Wagner immerses herself in her object of study. For this book, she visited the Defense POW/MIA Accounting Agency, interviewed MIA families in their hometowns, and took part in a recovery mission in Vietnam, which required trekking “into the chaotic mess of vines and branches, slippery rocks and wet leaves.” During the mission, she watched as the forensic investigators and their local Vietnamese counterparts dug and sifted through the earth, uncovering a variety of unexploded munitions and eventually finding a human tooth. “On the surface,” Wagner notes, “teeth are not something we typically associate with someone's individual identity, at least not in an era in which DNA, our genetic ‘fingerprint,’ dominates understandings of unique biological markers.” Yet in this particular recovery mission, a tooth eventually led to the identification of a soldier who had died 40 years earlier in a helicopter crash.

At every turn, Wagner's book is thoughtful and objective, and it seeks to understand the deeper context in which forensic science takes place. In chapter 3, for example, she explores the recent public criticism of the U.S. military's MIA accounting effort, which centered on poor leadership, outdated science, and the paucity of results. News reports painted a grim portrait of the forensic lab's outdated scientific methods and its resistance to forensic genetics. The director was forced to step down, and in 2014, congressional and public pressure to increase the number of MIA identifications led to the restructuring of the military's MIA accounting mission.

As Wagner points out, however, critics of the mission not only lacked any real understanding of forensic science but also represented just the most recent iteration of the long-held “skepticism regarding the federal government's commitment to fulfill its obligation to missing war dead.” Criticism of the forensic scientific component of MIA accounting reflects 21st-century ideals about the U.S. military. An era of agile and precise warfare should be matched, many believe, by cutting-edge forensic science. However, as Wagner notes, “a militarism championing precision and efficacy left little room for the messy reality of war's destruction.” ■



**What Remains:  
Bringing America's  
Missing Home  
from the Vietnam War**  
Sarah E. Wagner  
Harvard University Press,  
2019. 304 pp.

The reviewer is at the Center for Naval Warfare Studies, Naval War College, Newport, RI 02841, USA, and is the author of *Military Anthropology* (Oxford University Press, 2018). Email: montgomery.mcfate@usnwc.edu

10.1126/science.aaz5197



## WEAPONS TECHNOLOGY

# The deadly diffusion of lethal technologies

From 3D-printed guns to weaponized hobby drones, open technologies pose sinister threats

By George Lucas

At first glance, *Power to the People* by Audrey Kurth Cronin might be just another entry in a long line of works devoted to technological fearmongering and dire threat inflation (1, 2). Cronin's warning about technological diffusion and its likely impact on terrorism, however, should not be classified alongside those earlier contributions. Rather than broadly faulting emergent lethal technologies, she makes a very focused and compelling case for attending to the threats posed by open-source "off-the-shelf" technologies that are affordable and easily operated, and are easily weaponized (3D-printed guns and the arming of inexpensive hobby drones are two relevant examples).

Cronin invites readers to consider specific case studies in which similar emergence, diffusion, and affordability of lethal technology fomented and enabled unanticipated terrorist activity. Her underlying framework is a theory of technological development and innovation—referred to as lethal empowerment theory—that is double-edged. New weapons (or weaponizable) technology, she argues, often enables greater force projection in the exercise of political power by militaries of conventional nation-states, but they simultaneously offer new avenues for violent political disruption by nonstate actors and organizations. The latter groups often outstrip military bureaucracies in terms of ingenuity and speed of innovation.

The first of Cronin's two principal historical examples is Alfred Nobel's invention of dynamite. Dynamite was designed for use in deep-shaft mining and building transportation infrastructure. Accordingly, it was easily obtained, and its sale and distribution were lightly regulated (if at all) in most countries other than Great Britain until after World War I.

Despite the known dangers associated with transporting and using dynamite, it was in huge demand worldwide during the height of the Industrial Revolution. By the end of the 19th century, clever anarchists in Russia and France and members of the Irish Republican Army began using it to great effect, creating small, transportable explosive devices that could be remotely detonated in public places.

The second example Cronin considers is the AK-47 assault rifle, invented by Soviet army sergeant Mikhail Kalashnikov at the dawn of the Cold War. Ridiculed by technological purists for its clunky inaccuracy, the

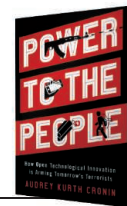


Crowds gather after an anarchist bombing on Wall Street on 16 September 1920.

AK-47 nonetheless proved inexpensive, lightweight, easy for untrained troops to operate, and—perhaps most important—extremely durable in the field. As a result, it became the weapon of choice for ragtag armies intent on overthrowing established authorities or ushering in new regimes throughout the hotly contested developing nations of the postcolonial world.

In both of these historical cases (and in many other smaller examples for which Cronin provides less comprehensive accounts), the violent, disruptive innovation by anarchists, terrorists, and revolutionaries took place against a backdrop of keen interest by ordinary citizens in the prospects of applied scientific advances. This helped foster widespread open access to the latest le-

**Power to the People:  
How Open Technological  
Innovation Is Arming  
Tomorrow's Terrorists**  
Audrey Kurth Cronin  
Oxford University Press,  
2019. 440 pp.



thal technologies that were easily adaptable to the purposes of violent dissidents.

Against this grim backdrop, Cronin turns to her book's central objective of examining the variety of sinister threats posed by increasingly open access to emerging lethal or potentially lethal technologies. She explores the perverse and malevolent uses of smartphones, robotics, social media, and viral "fake news"; of genetic engineering; and especially of the built-in vulnerabilities afforded by the Internet of Things.

Cronin gives serious consideration to the chilling potential misuse of artificial intelligence (AI), envisioning, for example, the hacking of a state-owned, AI-driven unmanned aerial vehicle for the purpose of shooting down a commercial aircraft (a scenario initially put forward by Elon Musk and the late Stephen Hawking). Dissidents might also seek to disrupt autonomous passenger vehicles in large cities, easily causing chaos and casualties.


In a fitting confirmation of her thesis, shortly after Cronin's book went to press, Kyle Mizokami reported in *Popular Mechanics* on the release of the KUB-BLA, a small, affordable suicide drone created by the Russian-based Kalashnikov company that can be armed with up to three pounds of explosives (3). I fear we may be in for a most unpleasant ride. ■

## REFERENCES AND NOTES

1. R. Sparrow, *J. Appl. Philos.* **24**, 62 (2007).
2. R. A. Clarke, R. K. Knake, *Cyber War: The Next Threat to National Security and What to Do About It* (HarperCollins, 2010).
3. K. Mizokami, "Kalashnikov is getting into the business of self-destructing drones," *Popular Mechanics*, 20 February 2019.

The reviewer is professor emeritus at the U.S. Naval Academy, Annapolis, MD 21402, USA. Email: george.r.lucas.jr@gmail.com

10.1126/science.aaz4545



Seabirds offer insight into the health of both marine and terrestrial ecosystems.

Edited by Jennifer Sills

## Seabirds: Sentinels beyond the oceans

In their Perspective “Seabird clues to ecosystem health” (12 July, p. 116), E. Velarde *et al.* rightly point out that seabirds provide crucial information about the state of marine ecosystems. However, they do not mention the role of seabirds on land and shorelines. Seabirds that forage at sea and breed on land play an essential role in cross-ecosystem transport of energy and nutrients, shaping terrestrial (1) as well as marine (2) ecosystems. Seabird colonies can provide insight into coastal and island environments worldwide (3).

In terrestrial (4) and adjacent reef ecosystems, nutrients from seabird guano (such as nitrogen and phosphorus) have been shown to enhance productivity, growth rate, and functioning of coral reef communities (5–9). In addition, because seabirds are highly sensitive to invasive species, visitor disturbance, noise, and light (3), they rely on the tranquility and seclusion of breeding sites to reproduce. Their distribution and the demography are therefore valuable and integrative proxies of anthropogenic pressures at shore (10, 11). In an era of profound and worrying changes that affect both marine and terrestrial environments, seabird populations are barometers of the health of a large variety of oceanic, coastal, and insular ecosystems. Up to 47% of all seabird species are currently declining, with 37% already threatened (12), which will undoubtedly

reduce the monitoring opportunities offered by these sentinel organisms.

M. Thibault<sup>1\*</sup>, F. Houlbrèque<sup>1</sup>, A. Lorrain<sup>2</sup>, E. Vidal<sup>1</sup>

<sup>1</sup>Laboratoire d'Excellence Labex-CORAIL, Institut de Recherche pour le Développement (IRD), UMR ENTROPIE (IRD-Université de La Réunion-CNRS), BP A5, Nouméa Cedex 98848, New Caledonia, France. <sup>2</sup>University of Brest, CNRS, IRD, Ifremer, LEMAR, F-29280 Plouzané, France.  
\*Corresponding author.  
Email: martin.thibault@ird.fr

### REFERENCES AND NOTES

1. D. A. Croll, J. L. Maron, J. A. Estes, E. M. Danner, G. V. Byrd, *Science*, **307**, 1959 (2005).
2. O. Shatova, S. R. Wing, M. Gault-Ringold, L. Wing, L. J. Hoffmann, *J. Exp. Mar. Biol. Ecol.*, **483**, 74 (2016).
3. M. P. Dias *et al.*, *Biol. Conserv.*, **237**, 525 (2019).
4. S. Caut, *PLOS One*, **7**, e39125 (2012).
5. A. Lorrain *et al.*, *Sci. Rep.*, **7**, 3721 (2017).
6. N. A. Graham *et al.*, *Nature*, **559**, 250 (2018).
7. K. Gagnon, E. Rothäusler, A. Syrjänen, M. Yli-Renko, V. Jormalainen, *PLOS One*, **8**, e61284 (2013).
8. C. E. Benkwitt, S. K. Wilson, N. A. Graham, *Glob. Change Biol.*, **25**, 2619 (2019).
9. C. Savage, *Sci. Rep.*, **9**, 4284 (2019).
10. E. Vidal, M. Thibault, K. Bourgeois, *Nature*, **560**, 167 (2018).
11. United Nations, *The First Global Integrated Marine Assessment: World Ocean Assessment I* (Cambridge University Press, Cambridge, UK, 2017).
12. BirdLife International, *State of the World's Birds: Taking the Pulse of the Planet* (BirdLife International, Cambridge, UK, 2018).

10.1126/science.aaz7665

## Save horseshoe crabs and coastal ecosystems

The Chinese horseshoe crab (*Tachypleus tridentatus*) is one of the oldest marine living fossils. Horseshoe crabs have existed for more than 445 million years (1), but populations of the Chinese species have plummeted in recent decades as a result of increasing biomedical demands, harvesting for human

consumption, and habitat loss (2). Urgent action is needed to reverse population declines and protect coastal ecosystems.

Chinese horseshoe crabs play key roles in coastal ecosystems as benthic predators, prey, bioturbators, and hosts for epibionts (3). Their eggs are a major protein source for migratory shorebirds (4). However, discovery and commercialization of the *Limulus* amoebocyte lysate (LAL) test for bacterial endotoxin, which uses blood from horseshoe crabs, has driven population declines (5). More than 610,000 horseshoe crabs were harvested and nearly 80,000 killed for LAL production in 2012 alone (6). Adult horseshoe crabs are also a prized dish in many seafood restaurants. A survey in south China found that 132 of 155 restaurants offered horseshoe crabs (7). Climate change and associated ocean acidification, urbanization, land reclamation, and water pollution are exacerbating habitat loss, affecting horseshoe crabs' spawning activities and juvenile nurseries (8). Breeding pairs in Guangxi Province, the species' Chinese stronghold, declined from between 600,000 and 700,000 in the 1990s to 40,000 20 years later (9). Declining horseshoe crab populations have implications for entire coastal ecosystems, especially shorebirds (4).

In March 2019, the International Union for Conservation of Nature (IUCN) listed the species as endangered (10). Urgent measures are needed to save horseshoe crabs. Research into animal-free LAL production is a priority (6). Management action should focus on protecting spawning and nursery habitats. Relatively few Chinese people are aware of the horseshoe crabs' plight. Public education is therefore needed, especially



# AAAS Travels

Members and friends of AAAS are invited to join AAAS Travels on fascinating trips to all 7 continents!



## Arizona Skies & New Discoveries April 19-26, 2020

From Tucson to Flagstaff, explore the natural and astronomical wonders of Arizona's desert paradise led by a popular archaeoastronomer. Visit the Caris Telescope Mirror Lab, Biosphere 2, and the optical telescopes at Kitt Peak. Also visit the famous Meteor Crater and Lowell Observatory.

\$3,295 pp twin share + air

## The Archaeological Wonders of Cyprus & Rhodes May 4-17, 2020



Join us and discover the archaeological sites, museums, and fascinating ancient cities of the Mediterranean Islands of Cyprus and Rhodes, as well as Bodrum on the Aegean Coast of Turkey, and the Greek Isle of Kos, with leadership by Dr. Blanche Menadier.

\$4,295 pp twin share + air

For a detailed brochure, please call (800) 252-4910  
All prices are per person twin share + air



BETCHART EXPEDITIONS Inc.  
17050 Montebello Rd  
Cupertino, California 95014  
Email: AAASInfo@betchartexpeditions.com  
www.betchartexpeditions.com

for younger generations (11). China's Belt and Road Initiative, including the new Maritime Silk Road, could further increase illegal cross-border animal trade, including horseshoe crab smuggling (12). More international collaboration will be indispensable for protecting this species.

Hong Yang<sup>1,2\*</sup>, Julian R. Thompson<sup>3</sup>, Roger J. Flower<sup>3</sup>

<sup>1</sup>Chongqing Engineering Research Center for Remote Sensing Big Data Application, School of Geographical Sciences, Southwest University, Chongqing 400715, China. <sup>2</sup>Department of Geography and Environmental Science, University of Reading, Reading RG6 6AB, UK. <sup>3</sup>Department of Geography, University College London, London, WC1E 6BT, UK.

\*Corresponding author.

Email: hongyanghy@gmail.com

### REFERENCES AND NOTES

1. D. Rudkin, G. Young, in *Biology and Conservation of Horseshoe Crabs*, J. Tancredi, M. Botton, D. Smith, Eds. (Springer, New York, 2009), pp. 25–44.
2. Y. Li, X. Xie, K. Y. Kwan, *Wetland Sci.* **16**, 690 (2018) [in Chinese].
3. B. K. Kwan, H. K. Chan, S. G. Cheung, *Aquat. Conserv.* **28**, 124 (2018).
4. C. P. McGowan et al., *Ecosphere* **2**, 1 (2011).
5. J. Levin, H. D. Hochstein, T. J. Novitsky, in *The American Horseshoe Crab*, C. Shuster Jr, R. Barlow, H. Brockmann, Eds. (Harvard University Press, Cambridge, MA, 2003), pp. 310–340.
6. G. Gauvry, in *Changing Global Perspectives on Horseshoe Crab Biology, Conservation and Management*, R. Carmichael, M. Botton, P. Shin, S. Cheung, Eds. (Springer International Publishing, Switzerland, 2015), pp. 475–482.
7. Z. Weng et al., *Chin. J. Zool.* **47**, 40 (2012) [in Chinese].
8. Q. Li, *J. Biol.* **27**, 71 (2010) [in Chinese].
9. Q. Li, M. Hu, *Mar. Environ. Sci.* **30**, 131 (2011) [in Chinese].
10. K. Laurie et al., "Tri-spine horseshoe crab: *Tachypleus tridentatus*," *The IUCN Red List of Threatened Species* (2019); [www.iucnredlist.org/species/21309/149768986](http://www.iucnredlist.org/species/21309/149768986).
11. G. Kreamer, S. W. Kreamer, in *Changing Global Perspectives on Horseshoe Crab Biology, Conservation and Management*, R. Carmichael, M. Botton, P. Shin, S. Cheung, Eds. (Springer International Publishing, Switzerland, 2015), pp. 557–574.
12. A. M. Lechner, F. K. S. Chan, A. Campos-Arceiz, *Nat. Ecol. Evol.* **2**, 408 (2018).

10.1126/science.aaz8654

## Consider Humboldt's map as intended

In his News story "Global warming has made iconic Andean peak unrecognizable" (11 September, <https://scim.ag/Chimborazo>), T. Appenzeller describes current scientific work based on Alexander von Humboldt's 1807 illustrated map of plant species found on Ecuador's Mount Chimborazo. Some of this work has pointed out inaccuracies in the map, but it is important to remember that Humboldt was well aware of these imperfections [(1), p. 44].

The recent scrutiny that the *Tableau* has received is puzzling. The illustration's legend clearly reads that it is a summary of all of the observations by Humboldt and fellow botanist Aimé Bonpland in the Andes and neighboring countries [(1), p. 156]. It seems a stretch to draw too fine

conclusions from an illustration that aimed to synthesize observations over a distance of 20° latitude (approximately 2200 km) and a vertical extent of about 6.3 km (the top of Chimborazo is 6268 m) flattened into a two-dimensional drawing (the central panel of the illustration is 40 by 50 cm with a vertical scale of 18 mm for each 500 m) [(1), p. 156].

The legacy of the *Tableau* from a botanical point of view is the amazing number of new plant species amassed during the 5-year voyage and the contribution to our knowledge through publications. Two hundred years later, we are still using and updating names of the species Humboldt observed. His timeless *Tableau* should be considered as originally intended by the author: an innovative depiction and a clever summary of the colossal information his team gathered during their exploration of South America's equatorial regions.

Carmen Ulloa Ulloa

Science and Conservation Division, Missouri Botanical Garden, St. Louis, MO 63110, USA.  
Email: carmen.ulloa@mobot.org

### REFERENCES AND NOTES

1. A. von Humboldt, A. Bonpland, *Essai sur la géographie des plantes; accompagné d'un tableau physique des régions équinoxiales* (Chez Levrault, Schoell et Compagnie, Libraires, Paris, 1805 [1807]); [www.biodiversitylibrary.org/bibliography/9309#/summary](http://www.biodiversitylibrary.org/bibliography/9309#/summary) [in French].

10.1126/science.aaz5068

### TECHNICAL COMMENT ABSTRACTS

#### Comment on "Eocene Fagaceae from Patagonia and Gondwanan legacy in Asian rainforests"

Thomas Denk, Robert S. Hill, Marco C. Simeone, Chuck Cannon, Mary E. Dettmann, Paul S. Manos Wilf et al. (Research Articles, 7 June 2019, eaaw5139) claim that *Castanopsis* evolved in the Southern Hemisphere from where it spread to its modern distribution in Southeast Asia. However, extensive paleobotanical records of Antarctica and Australia lack evidence of any Fagaceae, and molecular patterns indicate shared biogeographic histories of *Castanopsis*, *Castanea*, *Lithocarpus*, and *Quercus* subgenus *Cerris*, making the southern route unlikely.

Full text: [dx.doi.org/10.1126/science.aaz2189](https://doi.org/10.1126/science.aaz2189)

#### Response to Comment on "Eocene Fagaceae from Patagonia and Gondwanan legacy in Asian rainforests"

Peter Wilf, Kevin C. Nixon, María A. Gandolfo, N. Rubén Cúneo

Denk et al. agree that we reported the first fossil Fagaceae from the Southern Hemisphere. We appreciate their general enthusiasm for our findings, but we reject their critiques, which we find misleading and biased. The new fossils unequivocally belong to *Castanopsis*, and substantial evidence supports our Southern Route to Asia hypothesis.

Full text: [dx.doi.org/10.1126/science.aaz2297](https://doi.org/10.1126/science.aaz2297)

Cite as: T. Denk *et al.*, *Science*  
10.1126/science.aaz2189 (2019).

# Comment on “Eocene Fagaceae from Patagonia and Gondwanan legacy in Asian rainforests”

Thomas Denk<sup>1\*</sup>, Robert S. Hill<sup>2</sup>, Marco C. Simeone<sup>3</sup>, Chuck Cannon<sup>4</sup>, Mary E. Dettmann<sup>5</sup>, Paul S. Manos<sup>6</sup>

<sup>1</sup>Swedish Museum of Natural History, Stockholm, Sweden. <sup>2</sup>Environment Institute, University of Adelaide, Australia. <sup>3</sup>Università degli Studi della Tuscia, Viterbo, Italy. <sup>4</sup>Center for Tree Science, Morton Arboretum, Lisle, IL, USA. <sup>5</sup>Queensland Museum, Hendra, Queensland, Australia. <sup>6</sup>Department of Biology, Duke University, Durham, NC, USA.

\*Corresponding author. Email: thomas.denk@nrm.se

Wilf *et al.* (Research Articles, 7 June 2019, eaaw5139) claim that *Castanopsis* evolved in the Southern Hemisphere from where it spread to its modern distribution in Southeast Asia. However, extensive paleobotanical records of Antarctica and Australia lack evidence of any Fagaceae, and molecular patterns indicate shared biogeographic histories of *Castanopsis*, *Castanea*, *Lithocarpus*, and *Quercus* subgenus *Cerris*, making the southern route unlikely.

In a recent paper (1), Wilf *et al.* described fossils belonging to the north hemispheric family Fagaceae (oak family) from sediments of Patagonia dated to 52.2 million years (Ma) ago, the early Eocene. The fossils comprise one immature (pistillate) infructescence and four mature fruits attached to an axis and are assigned to the extant genus *Castanopsis* on the basis of a DNA-scaffold analysis using seven scored morphological traits. Wilf *et al.* state that “the new fossils represent ... the oldest record, by ~8 million years, of the genus *Castanopsis*” and conclude that “*Castanopsis* evolved in the Southern Hemisphere” and, moving along a “southern route,” provided the stock for the modern survivors of *Castanopsis*, ~120 to 130 tree species ranging from northwestern India to New Guinea and Japan. They speculate that this ancestral *Castanopsis* represents one of several paleo-Antarctic plant genera that are today in Southeast Asian rainforests. Consequently, numerous younger fossils from North America and Eurasia previously assigned to *Castanopsis* must represent “more distant relatives of the extant genus” than the Patagonian fossils.

We acknowledge the importance of the fossil that geographically extends the record of Fagaceae but suggest an alternative evolutionary and biogeographic interpretation that takes into account genetic differentiation patterns of modern genera.

We (i) show that the character suite that links the Patagonian fossil to modern *Castanopsis* is plesiomorphic, making its generic assignment ambiguous. We (ii) use the extensive pollen and macrofossil record (Australia, Antarctica) to demonstrate that a southern route of Fagaceae to Southeast Asia currently lacks any fossil evidence. Finally, (iii) molecular data reject geographically isolated early evo-

lutionary histories of the castaneoid genera *Castanea*, *Castanopsis*, and *Lithocarpus* and link them to the Eurasian *Quercus* subgenus *Cerris*.

Regarding (i), we note that slightly younger infructescences from Tennessee described as *Castanopsoidea* (2) share features with the fossil from Patagonia but differ by three-flower cupules, a condition also present in modern *Castanopsis*; *Castanopsis rothwellii* from Patagonia shows a character suite that is distinctly primitive within the paraphyletic Castaneoideae [Fig. 1 and Table 1; character 7, inflorescence sexuality, was coded as unisexual for extant *Castanopsis* and *Lithocarpus*; this should be unisexual and mixed instead (3)]. On the basis of the available data, it is impossible to decide whether *Castanopsoidea* and *Castanopsis rothwellii* represent stem Castaneoideae/Fagaceae, are extinct sister lineages of *Castanea*-*Castanopsis*, or belong to the modern genus.

Regarding (ii), the southern route of *Castanopsis* to Asia, we note that evidence for such a pathway is currently missing. First, the genus was present in North America in the late early Eocene (4) less than 4 Ma after *C. rothwellii*. The revised age of the Nut Beds flora in Oregon is 48.32 Ma (5). In addition, the genus was present in Europe during the Eocene. Second, despite extensive paleopalynological and macrofossil work in Antarctica and Australia/Tasmania, dispersed pollen, leaves, or reproductive structures of Castaneoideae or any other Fagaceae, common in the Northern Hemisphere during the Paleogene, have never been recovered from Late Cretaceous to Oligocene strata across Gondwana. Instead, these regions were inhabited by temperate rainforests dominated by podocarps, Araucariaceae, Nothofagaceae, Proteaceae, and tree ferns (6, 7), which occupied



niches potentially suitable for Fagaceae since the Late Cretaceous. Hence, the southern route hypothesis would require that generations of palynologists had overlooked the characteristic pollen of Castaneoideae in Gondwanan records. Third, Wilf *et al.* argue that the Patagonian fossil plant assemblages are similar to modern assemblages with “substantial Gondwanic history.” We note that a large part of modern *Castanopsis* distribution occurs outside living plant communities with substantial Gondwanan history. Modern plant communities with *Castanopsis* differ considerably in New Guinea, the Himalayas, and Japan (8).

Regarding (iii), molecular data reject the notion that “North American and European fossils assigned to *Castanopsis* [are] more distant relatives of the extant genus than are the new Argentine fossils” and are at odds with the southern route hypothesis. Nuclear data (9) show a sister relationship of *Castanopsis* with *Castanea*. *Castanea-Castanopsis* are close relatives of oaks, genus *Quercus*. *Quercus* was evolved and started to radiate by the early Eocene (10). *Castanea-Castanopsis* were already diverged when the North and South American *Castanopsis*-like fossils were deposited. Isolated biogeographic history inevitably would have left imprints in plastome signatures of *Castanopsis*; for instance, South American Nothofagaceae (subgenus *Nothofagus*) have different plastid signatures than their New Guinean–New Caledonian sister (subgenus *Brassospora*) despite potential long-distance dispersal (11). Within *Nothofagus*, three divergent, old plastid lineages indicate chloroplast capture and a larger distribution area in the past (12). Nuclear-plastid incongruence and strong geographic signal in the plastids is also found in core Fagaceae, which include all Castaneoideae and *Quercus*. If the Patagonian fossil represented the already diverged genus *Castanopsis* and if it were a precursor of modern-day Asian *Castanopsis*, one should find a divergent and genus-diagnostic plastid signature in at least some *Castanopsis*, with closer affinity to New World than to Old World Fagaceae. Shared plastid histories and near-identical plastid plant barcodes (*matK*, *rbcl*, *atpB-rbcL*, *trnH-psbA*) reflect shared biogeographic histories in the eastern hemispheric *Quercus* subgenus *Cerris*, *Lithocarpus*, *Castanea*, and *Castanopsis* (13–15) and set them apart from the western hemispheric *Quercus* subgenus *Quercus*, *Notholithocarpus*, and *Chrysolepis*. On the basis of all available genetic data, modern *Castanopsis* evolved near *Castanea*, *Lithocarpus*, and the mainly subtropical Eurasian oaks (subgenus *Cerris*), all of which lack a fossil record outside Eurasia but existed during the Paleogene of Eurasia. Therefore, the range expansion into South America was a dead end in the biogeographic history of the Fagaceae.

In sum, we are excited by the finding of Wilf and colleagues, but without fossil (Antarctic Castaneoideae) and molecular (distinct plastid signature of *Castanopsis*) evi-

dence, we do not see any evidence for the southern route as proposed by them.

## REFERENCES

1. P. Wilf, K. C. Nixon, M. A. Gandolfo, N. R. Cúneo, Eocene Fagaceae from Patagonia and Gondwanan legacy in Asian rainforests. *Science* **364**, eaaw5139 (2019). doi:10.1126/science.aaw5139
2. W. L. Crepet, K. C. Nixon, Earliest megafossil evidence of Fagaceae: Phylogenetic and biogeographic implications. *Am. J. Bot.* **76**, 842–855 (1989). doi:10.1002/j.1537-2197.1989.tb15062.x
3. R. B. Kaul, E. C. Abbe, Inflorescence architecture and evolution in the Fagaceae. *J. Arnold Arb.* **65**, 375–401 (1984). www.jstor.org/stable/43782573
4. S. R. Manchester, Fruits and seeds of the middle Eocene Nut Beds Flora, Clarno Formation, Oregon. *Palaeontogr. Am.* **58**, 1–205 (1994).
5. S. R. Manchester, Fruits of Ticodendraceae (Fagales) from the Eocene of Europe and North America. *Int. J. Plant Sci.* **172**, 1179–1187 (2011). doi:10.1086/662135
6. M. E. Dettmann, in *Origins and Evolution of the Antarctic Biota*, J. A. Crame, Ed. (Geological Society Special Publication 47, 1989), pp. 89–105.
7. J. Pross, L. Contreras, P. K. Bijl, D. R. Greenwood, S. M. Bohaty, S. Schouten, J. A. Bendle, U. Röhl, L. Tauxe, J. I. Raine, C. E. Huck, T. van de Flierdt, S. S. R. Jamieson, C. E. Stickley, B. van de Schootbrugge, C. Escutia, H. Brinkhuis, Integrated Ocean Drilling Program Expedition 318 Scientists, Persistent near-tropical warmth on the Antarctic continent during the early Eocene epoch. *Nature* **488**, 73–77 (2012). doi:10.1038/nature11300 Medline
8. L. Y. Menitsky, *Oaks of Asia* (Science Publishers, 2005).
9. S.-H. Oh, P. S. Manos, Molecular phylogenetics and cupule evolution in Fagaceae as inferred from nuclear CRABS CLAW sequences. *Taxon* **57**, 434–451 (2008).
10. A. L. Hipp, P. S. Manos, M. Hahn, M. Avishai, C. Bodénès, J. Cavender-Bares, A. A. Crowl, M. Deng, T. Denk, S. Fitz-Gibbon, O. Gailing, M. S. González-Elizondo, A. González-Rodríguez, G. W. Grimm, X. L. Jiang, A. Kremer, I. Lesur, J. D. McVay, C. Plomion, H. Rodríguez-Correa, E. D. Schulze, M. C. Simeone, V. L. Sork, S. Valencia-Avalos, Genomic landscape of the global oak phylogeny. *New Phytol.* **nph.16162** (2019). doi:10.1111/nph.16162 Medline
11. M. Knapp, K. Stöckler, D. Havell, F. Delsuc, F. Sebastiani, P. J. Lockhart, Relaxed molecular clock provides evidence for long-distance dispersal of *Nothofagus* (southern beech). *PLOS Biol.* **3**, e14 (2005). doi:10.1371/journal.pbio.0030014 Medline
12. A. C. Premoli, P. Mathiasen, M. C. Acosta, V. A. Ramos, Phylogeographically concordant chloroplast DNA divergence in sympatric *Nothofagus* s.s. How deep can it be? *New Phytol.* **193**, 261–275 (2012). doi:10.1111/j.1469-8137.2011.03861.x Medline
13. C. H. Cannon, P. S. Manos, Phylogeography of the Southeast Asian stone oaks (*Lithocarpus*). *J. Biogeogr.* **30**, 211–226 (2003). doi:10.1046/j.1365-2699.2003.00829.x
14. P. S. Manos, C. H. Cannon, S.-H. Oh, Phylogenetic relationships and taxonomic status of the paleoendemic Fagaceae of Western North America: Recognition of a new genus. *Notholithocarpus*. *Madrono* **55**, 181–190 (2008). doi:10.3120/0024-9637-55.3.181
15. M. C. Simeone, G. W. Grimm, A. Papini, F. Vessella, S. Cardoni, E. Tordoni, R. Piredda, A. Franc, T. Denk, Plastome data reveal multiple geographic origins of *Quercus* Group *Ilex*. *PeerJ* **4**, e1897 (2016). doi:10.7717/peerj.1897 Medline

## ACKNOWLEDGMENTS

**Funding:** Supported by a grant of the Swedish Research Council (VR; project no. 2015-03986) to T.D. **Author contributions:** T.D. wrote the first draft. All authors discussed and wrote the final manuscript. **Competing interests:** The authors declare that they have no competing interests. **Data and materials availability:** All data needed to evaluate the conclusions in the paper are present in the paper. For

further information regarding the fossil record of Castaneoideae, please contact the corresponding author.

21 August 2019; accepted 8 October 2019  
Published online 15 November 2019  
10.1126/science.aaz2189

**Table 1.** Emended and corrected seven-character matrix. Boldface entries are corrected from the Wilf *et al.* matrix.

	Style number	Cupule appendages	Cupule dehiscence	Female flowers per node	Flowers per cupule	Valve dehiscence	Inflorescence sexuality
<i>"Castanopsis" rothwellii</i>	Three	Scaly	Valvate	Solitary	One	Partial	Unisexual*
<i>Castanopsoidea</i> UCPC B627a	Three	Scaly	Valvate	Solitary?	Three	Partial?	Unisexual*
<i>Castanopsoidea</i> UCPC B849	Three	Spinose	Valvate	Solitary?	Three	Partial?	Unisexual*
<i>Fagus</i>	Three	Scaly	Valvate	—	<b>Two</b>	Complete	Unisexual
<i>Castanea</i> chestnut group	Six	Spinose	Valvate	Solitary/clustered	Three	Complete	Unisexual/mixed
<i>Castanea</i> pumila group	Six	Spinose	Valvate	Clustered	One	Complete	Unisexual/mixed
<i>Castanopsis</i> fissa group	Three	Scaly	Valvate/hemispheric indehiscent	Solitary	One	Partial/none	<b>Unisexual/mixed</b>
<i>Castanopsis</i> group	Three	Spinose	Valvate/hemispheric indehiscent	Solitary	One/three	Complete/partial/none	<b>Unisexual/mixed</b>
<i>Chrysolepis</i>	Three	Spinose	Valvate	Clustered	More than three	Complete	Unisexual/mixed
<i>Lithocarpus</i> A	Three	Scaly	Hemispheric indehiscent	Solitary/clustered	One	None	<b>Unisexual/mixed</b>
<i>Lithocarpus</i> B	Three	Scaly	Hemispheric indehiscent	Clustered	One	None	<b>Unisexual/mixed</b>
<i>Notholithocarpus</i>	Three	Scaly	Hemispheric indehiscent	Clustered	One	None	Unisexual/mixed
<i>Quercus</i>	Three	Scaly	Hemispheric indehiscent	Solitary	One	None	Unisexual
<i>Colombobalanus</i>	Three	Scaly	Valvate	Solitary	One to many	Complete	Unisexual
<i>Formanodendron</i>	Three	Scaly	Valvate	Solitary	One to many	Complete	Unisexual/mixed
<i>Trigonobalanus</i>	Three	Scaly	Valvate	Clustered	One to many	Complete	Unisexual/mixed

\*Difficult to assess on the basis of limited material.



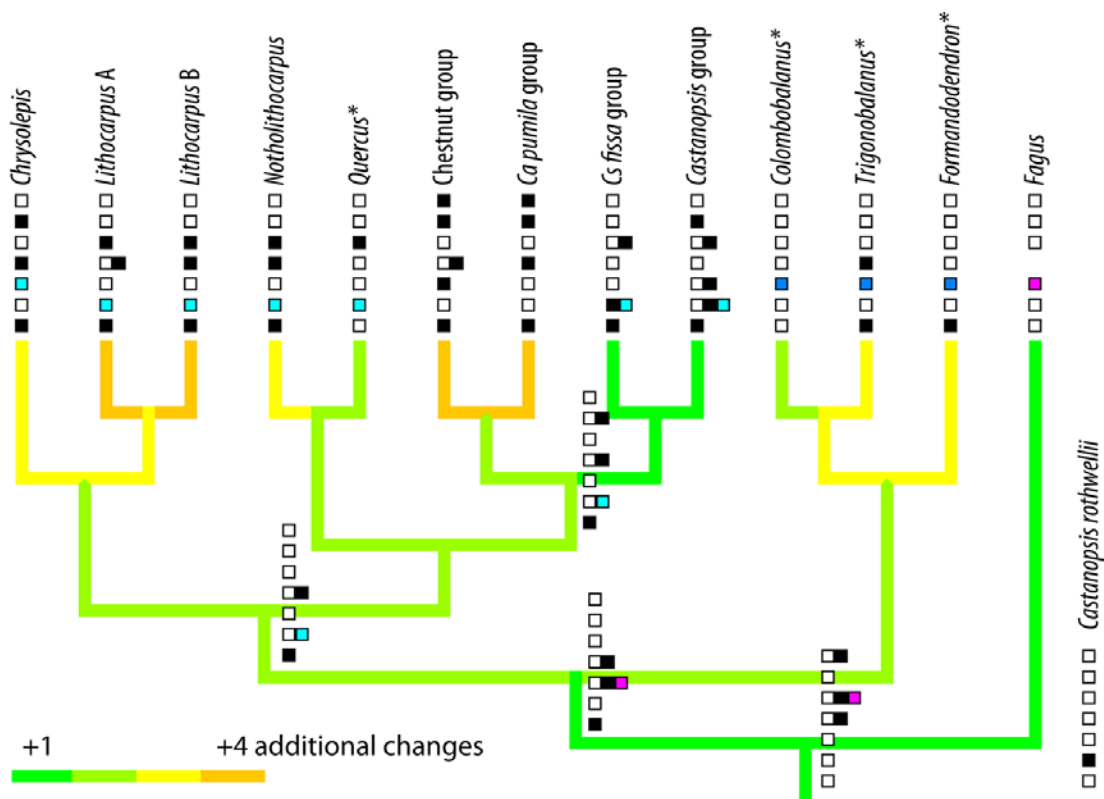


**Fig. 1. Phylogenetic information content of the seven-character matrix used by Wilf *et al.* when using parsimony.** Phylogenetic framework is from Oh and Manos (9) with a paraphyletic Castaneoideae. Character 7 was incorrectly coded in Wilf *et al.* for *Castanopsis* and *Lithocarpus*; character 5 was incorrectly coded for *Fagus*. Character states for characters 1 to 7 are indicated by open or solid squares (top to bottom) for terminal taxa; reconstructed character suites (using the standard parsimony model implemented in Mesquite version 3.6) are shown for selected hypothetical common ancestors. Tree length is 20. Colors of branches indicate numbers of additional steps (evolutionary changes) required by placing the fossil(s) on the corresponding branch. Note that the number of steps does not change whether *C. rothwellii* is placed as sister to all Fagaceae, sister to *Fagus*, sister to trigonobalanoids and quercoids, or as part of *Castanopsis*. Asterisks indicate genera not included in Wilf *et al.*'s analysis.

Cite as: P. Wilf *et al.*, *Science*  
10.1126/science.aaz2297 (2019).

# Response to Comment on “Eocene Fagaceae from Patagonia and Gondwanan legacy in Asian rainforests”

Peter Wilf<sup>1\*</sup>, Kevin C. Nixon<sup>2</sup>, María A. Gandolfo<sup>2</sup>, N. Rubén Cúneo<sup>3</sup>

<sup>1</sup>Department of Geosciences, Pennsylvania State University, University Park, PA 16802, USA. <sup>2</sup>Liberty Hyde Bailey Hortorium, Plant Biology Section, School of Integrative Plant Science, Cornell University, Ithaca, NY 14853, USA. <sup>3</sup>CONICET, Museo Paleontológico Egidio Feruglio, 9100 Trelew, Chubut, Argentina.

\*Corresponding author. Email: pwilf@psu.edu

Denk *et al.* agree that we reported the first fossil Fagaceae from the Southern Hemisphere. We appreciate their general enthusiasm for our findings, but we reject their critiques, which we find misleading and biased. The new fossils unequivocally belong to *Castanopsis*, and substantial evidence supports our Southern Route to Asia hypothesis.

We recently (1) reported two *Castanopsis rothwellii* fossil infructescences from the early Eocene [52 million years (Ma) ago] of Argentine Patagonia. These are (we maintain) the oldest fossils assigned to the genus by ~8 Ma (2, 3), and they co-occur with hundreds of fagaceous leaves indistinguishable from those of living *Castanopsis*. The same fossil beds contain numerous taxa whose close living relatives characteristically associate with *Castanopsis* in New Guinea and elsewhere, including *Papuacedrus*, *Agathis*, *Araucaria* Sect. *Eutacta*, *Dacrycarpus*, a *Phyllocladus* relative (4), *Podocarpus*, *Retrophyllum*, *Ripogonum*, *Eucalyptus*, *Ceratopetalum*, *Gymnostoma*, engelhardioid Juglandaceae, and *Todea*, as cited (1). Nearly all these lineages are well-known examples of the Southern Route to Asia confirmed by fossil evidence from one or more of Antarctica, Australasia, and Asia (5–7), and we concluded that *Castanopsis* most likely had similar biogeographic history. *Castanopsis* thrives on the Australian plate today in New Guinea, and its southern range is only a short distance over shallow water from Australia, with which New Guinea had frequent past land connections and biotic interchanges (8).

In short, we presented a suite of positive evidence for our Southern Route hypothesis that led us to favor the idea. Most notably, we reported the first remains of Fagaceae trees that grew on Gondwana, clearly identifiable as *Castanopsis* and found in a fossilized New Guinea-type association. However, Denk *et al.* (9) assert that “evidence for such a pathway is currently missing.”

First, we reject Denk *et al.*’s appeal-to-authority argument: “...the southern route hypothesis would require that generations of palynologists had overlooked the characteristic pollen of Castaneoideae in Gondwanan records.” This statement appears biased regarding both South America, an

integral part of Gondwana 52 Ma ago (10), and those who work there. The current “generation” has found fossil Castaneoideae in Gondwana (1), even though previous highly skilled colleagues had not.

Second, Denk *et al.* invoke a moving-the-goalposts argument. Even though we just reported Fagaceae fossils several thousand kilometers south of any previous occurrences (1), Denk *et al.* hold that the family did not range any farther south (their South American “dead end”). Theirs is a perilous position because there was no oceanic separation of South America and Antarctica 52 Ma ago, and thus no “end” to South America (10); instead, abundant austral biotic interchange took place at that time (11). The South American “dead end” would also require that *Castanopsis* went extinct in the Southern Hemisphere, then rejoined the same New Guinea-type lineages at a much later date via an entirely different Holarctic path after crossing several climate zones. This scenario seems far less likely than the Southern Route, which is supported by our finding the oldest *Castanopsis* already in a perhumid New Guinea-type rainforest association 52 Ma ago in West Gondwana (1). It is irrelevant that *Castanopsis* occurs in other plant associations in its living range (9), as we discussed (1).

Third, Denk *et al.* wrongly assert that molecular data from living Fagaceae can be used to reject a hypothesis about the affinities of specific early Cenozoic fossils determined from paleobotany (“molecular data reject the notion that...”). In so doing, Denk *et al.* also mistakenly state that *Castanea* “lacks a fossil record outside Eurasia.” The oldest fossil *Castanea*, as we cited (1), is from the middle Eocene of Tennessee, not Eurasia. Thus, shared sequences from the sister genera *Castanea* and *Castanopsis* in all likelihood reflect their common ancestry in the ancient New World, not



the Old World as Denk *et al.* argue.

Fourth, Denk *et al.* erroneously contend that *Castanopsis rothwellii*, a fossil with so many diagnostic characters preserved that it could only be assigned to *Castanopsis* if “found alive” today (1), has plesiomorphic features and cannot be placed confidently in the extant genus. Their idea rests on a misleading phylogenetic argument (see below), and it is unacceptable at face value because it ignores basic botany and our detailed taxonomic treatment (1). The diagnostic characters of *Castanopsis* in the fossils are in no way generalized for all Fagaceae, including the spike-like infructescence axes of numerous solitary, asymmetrical, valved, and sutured lateral cupules that entirely enclose the single nut, which retains three short, linear, “castaneoid” styles with unexpanded stigmas. These features match *Castanopsis* precisely and definitely exclude the fossils from placement with *Quercus*, *Fagus*, and the trigonobalanoids. Within the remaining castaneoid genera, *C. rothwellii* only matches *Castanopsis*, and thus there is no basis whatsoever for separating this fossil from *Castanopsis*. Denk *et al.* also pose an invalid syllogism by arguing that because *Castanopsoidea* and *C. rothwellii* have some similar features, and the former is an extinct genus, then our fossils do not belong in an extant genus.

Denk *et al.*’s phylogenetic conclusions from their emended tree and matrix are misleading, in that any morphological matrix includes characters that are relevant only for the taxa included in the analysis. Because the fossils are castaneoid in all features, we did not include all Fagaceae in our original analysis (1) and likewise did not include all characters relevant to non-castaneoid fagaceous taxa. Denk *et al.* added several genera to their analysis without adding any morphological characters to resolve these additional taxa, then used their uninformative result to criticize our phylogenetic interpretation as uninformative. In their framework, even a living *Castanopsis* would not resolve in *Castanopsis*! By adding just three relevant characters to the Denk *et al.* scaffold to accommodate the genera they added (Table 1), the fossil *Castanopsis rothwellii* is placed only with *Castanopsis* in the single most parsimonious tree (Fig. 1). We note that even when the same morphological data are used alone, without any scaffold, the fossil resolves with the *Castanopsis fissa* group. We acknowledge our miscoding of *Fagus* for flower number, a typographic error that does not affect the outcome of any of our analyses. The other character re-codings by Denk *et al.* only make the morphological data less precise.

We expected vigorous debate regarding the biogeographic implications of our Gondwanan *Castanopsis* fossils, which hold importance for understanding and conserving the imperiled southern-sourced associations that survive in Asian rainforests (1, 6). Unfortunately, Denk *et al.* do not

advance the discussion. Only time and many more fossils, not negative evidence and misleading assertions (9), will tell where else the Fagaceae occurred.

## REFERENCES

1. P. Wilf, K. C. Nixon, M. A. Gandolfo, N. R. Cúneo, Eocene Fagaceae from Patagonia and Gondwana legacy in Asian rainforests. *Science* **364**, eaaw5139 (2019). doi:10.1126/science.aaw5139
2. S. R. Manchester, Fruits and seeds of the middle Eocene Nut Beds flora, Clarno Formation, Oregon. *Palaeontogr. Am.* **58**, 1–205 (1994).
3. M. C. Muhlbachler, J. X. Samuels, A small-bodied species of Brontotheriidae from the middle Eocene Nut Beds of the Clarno Formation, John Day Basin, Oregon. *J. Paleontol.* **90**, 1233–1244 (2016). doi:10.1017/jpa.2016.61
4. A. Andrichow-Colombo, P. Wilf, I. H. Escapa, A South American fossil relative of *Phyllocladus*: *Huncocladus laubenfelsii* gen. et sp. nov. (Podocarpaceae), from the early Eocene of Laguna del Hunco, Patagonia, Argentina. *Aust. Syst. Bot.* **32**, 290–309 (2019).
5. R. S. Hill, in *History of the Australian Vegetation: Cretaceous to Recent*, R. S. Hill, Ed. (Cambridge Univ. Press, 1994), pp. 390–419.
6. R. M. Kooyman, P. Wilf, V. D. Barreda, R. J. Carpenter, G. J. Jordan, J. M. K. Sniderman, A. Allen, T. J. Brodribb, D. Crayn, T. S. Feild, S. W. Laffan, C. H. Lusk, M. Rossetto, P. H. Weston, Paleo-Antarctic rainforest into the modern Old World tropics: The rich past and threatened future of the “southern wet forest survivors”. *Am. J. Bot.* **101**, 2121–2135 (2014). doi:10.3732/ajb.1400340 Medline
7. X.-K. Wu, N. E. Zavalova, T. M. Kodrul, X.-Y. Liu, N. V. Gordenko, N. P. Maslova, C. Quan, J.-H. Jin, Northern Hemisphere megafossil of *Dacrycarpus* (Podocarpaceae) from Miocene of South China and its evolutionary and palaeoecological implication. *J. Syst. Evol.* jse.12534 (2019). doi:10.1111/jse.12534
8. D. M. J. S. Bowman, G. K. Brown, M. F. Braby, J. R. Brown, L. G. Cook, M. D. Crisp, F. Ford, S. Haberle, J. Hughes, Y. Isagi, L. Joseph, J. McBride, G. Nelson, P. Y. Ladiges, Biogeography of the Australian monsoon tropics. *J. Biogeogr.* **37**, 201–216 (2010). doi:10.1111/j.1365-2699.2009.02210.x
9. T. Denk, R. S. Hill, M. C. Simeone, C. Cannon, M. E. Dettmann, P. S. Manos, Comment on “Eocene Fagaceae from Patagonia and Gondwanan legacy in Asian rainforests”. *Science* **365**, eaaz2189 (2019).
10. L. A. Lawver, L. M. Gahagan, I. W. D. Dalziel, in *Tectonic, Climatic, and Cryospheric Evolution of the Antarctic Peninsula*, J. B. Anderson, J. S. Wellner, Eds. (American Geophysical Union, 2011), pp. 5–33.
11. P. Wilf, N. R. Cúneo, I. H. Escapa, D. Pol, M. O. Woodburne, Splendid and seldom isolated: The paleobiogeography of Patagonia. *Annu. Rev. Earth Planet. Sci.* **41**, 561–603 (2013). doi:10.1146/annurev-earth-050212-124217

## ACKNOWLEDGMENTS

**Funding:** Supported by NSF grants DEB-1556666, DEB-1556136, EAR-1925755, and EAR-1925552 (P.W. and M.A.G.). **Author contributions:** All authors contributed to researching and writing this response.

10 September 2019; accepted 8 October 2019  
Published online 15 November 2019  
10.1126/science.aaz2297

**Table 1. Additional character scores for phylogenetic analysis.** Scores are shown in the following order (left to right). Stigma: expanded = 0; unexpanded = 1. Nut in cross section: triangular/flattened = 0; generally rounded = 1. Cupule symmetry: symmetrical = 0; asymmetrical = 1.

Taxon	Score
<i>Castanopsis rothwellii</i> fossils	111
<i>Fagus</i>	000
<i>Castanea</i> chestnut group	110
<i>Castanea pumila</i> group	110
<i>Castanopsis fissa</i> group	111
<i>Castanopsis</i> group	11[0,1]
<i>Chrysolepis</i>	100
<i>Lithocarpus</i> A	110
<i>Lithocarpus</i> B	110
<i>Notholithocarpus</i>	110
<i>Colombobalanus</i>	000
<i>Formanodendron</i>	00[0,1]
<i>Trigonobalanus</i>	000
<i>Quercus</i>	010

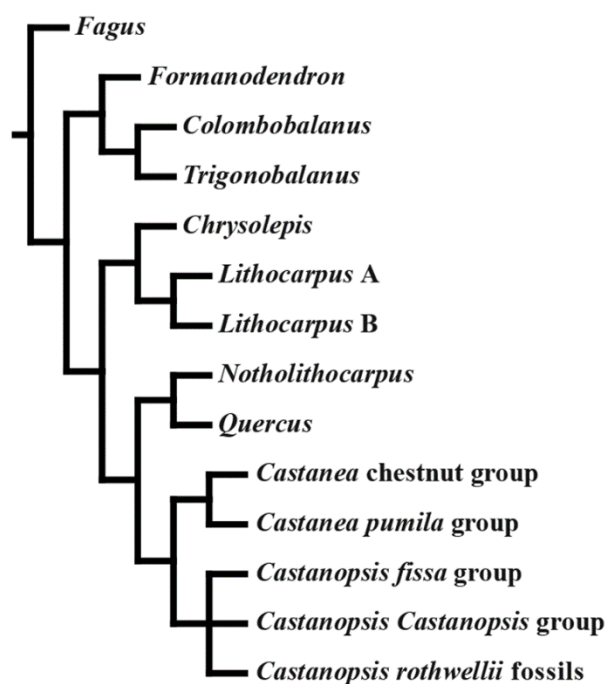


**Fig. 1. Phylogenetic analysis.** Consensus of the two most parsimonious trees, based on the Denk *et al.* (9) scaffold and emended morphological matrix with the addition of the three characters listed in Table 1, generated using the same analytical methods described previously (1). See text for discussion.



# QUALITY CONTROL IN CELL BIOLOGY

By *Stella Hurtley and Gemma Alderton*

## REVIEWS

Cellular quality control by the ubiquitin-proteasome system and autophagy p. 818

Cellular RNA surveillance in health and disease p. 822

Mitochondrial communication: Shaping health and disease p. 827

## RELATED ITEMS

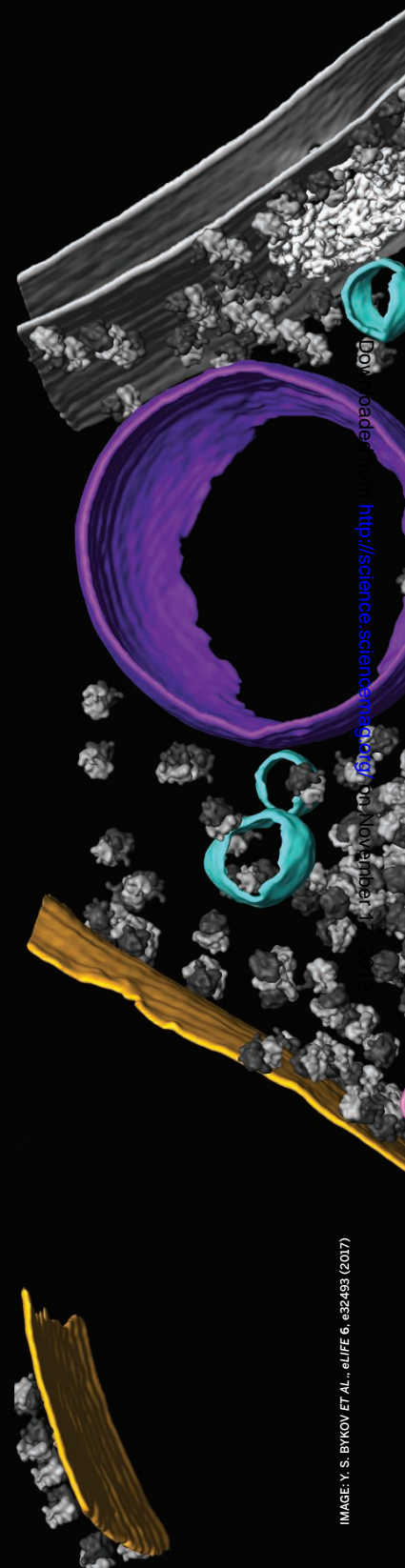
PERSPECTIVES pp. 797 & 802 RESEARCH ARTICLE p. 843

**O**ur cells are in a constant state of flux—growing, dividing, and continually responding to their environment. To maintain optimal performance of these processes, a range of quality control mechanisms is required.

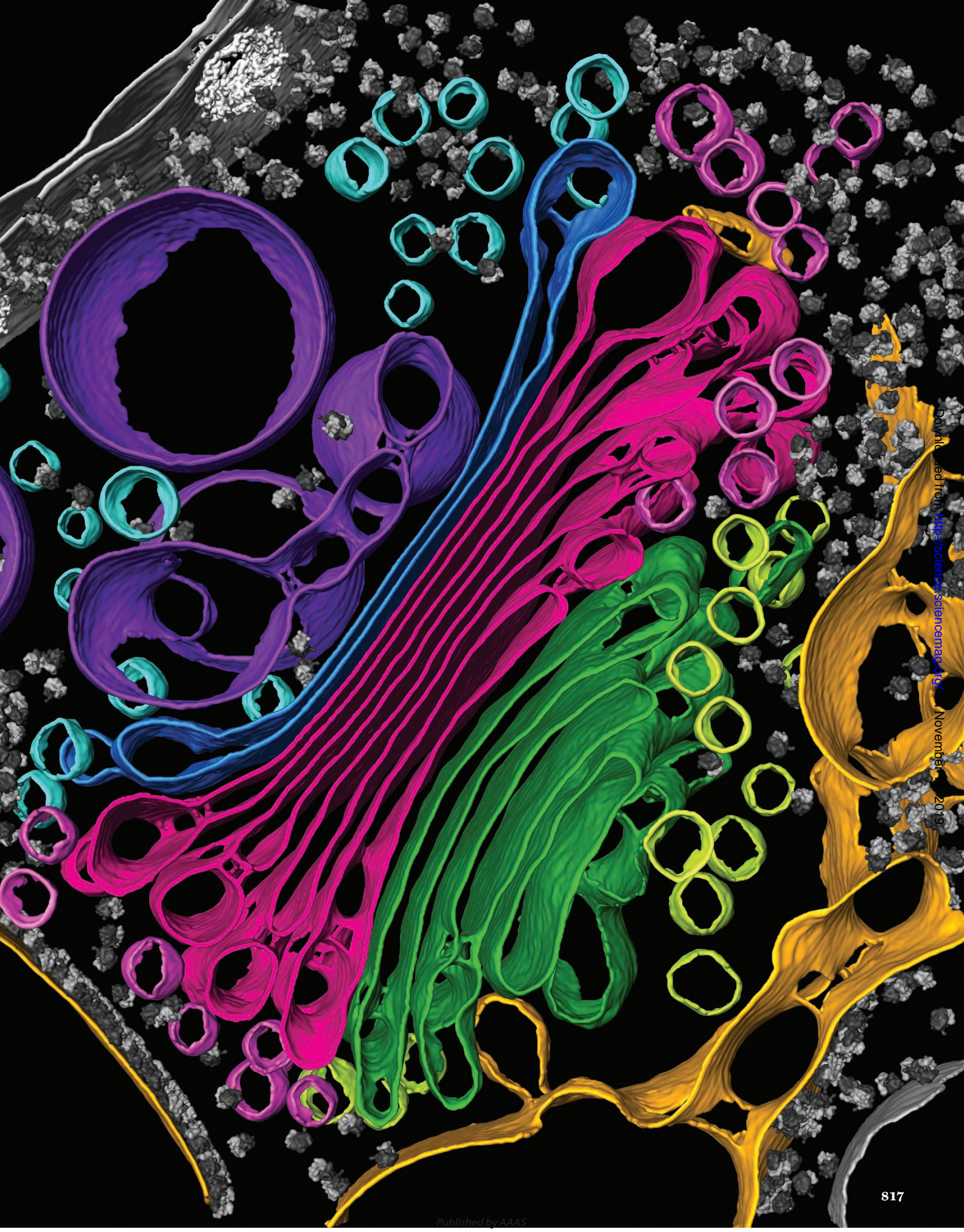
Quality control within cells involves a variety of self-regulating activities, one of which keeps protein synthesis in balance with the breakdown of dysfunctional proteins. Similarly, the components from which molecules are built must be recycled and redistributed to ensure that cellular systems can continue running. Other pathways are important to guarantee that RNA is created faithfully and shuttled through the cell to make the right proteins at the right time. Moreover, DNA quality control pathways maintain the genetic code while enabling cellular survival and proliferation. Our cells contain a variety of organelles that must cooperate during growth and cell regulation. A case in point is the need for mitochondria, which have their own limited genome, to coordinate their metabolism and growth with that of the cell as a whole. A sophisticated set of feedback controls is required to keep the nucleus and the mitochondria in sync.

Failures in cellular quality control are linked to cancer, neurodegeneration, and other developmental diseases and diseases of aging. Deciphering the mechanistic underpinnings of these quality control processes, whether they have limits, and how they are regulated as disease develops should help us understand, prevent, and even treat a wide range of conditions.

Morphology of intracellular membranes revealed by in situ cryo-electron tomography. This 3D segmentation of a cellular tomogram contains a representative Golgi stack: cis cisternae (green), cis vesicles (light green), medial cisternae (magenta), medial vesicles (light pink), the trans cisterna (blue), trans vesicles (light blue), and the trans Golgi network (purple). The endoplasmic reticulum is highlighted in yellow. Other membranes, the nuclear envelope, nuclear pore complexes, and ribosomes are shown in gray.









## REVIEW

# Cellular quality control by the ubiquitin-proteasome system and autophagy

Christian Pohl<sup>1,2\*</sup> and Ivan Dikic<sup>1,2,3\*</sup>

To achieve homeostasis, cells evolved dynamic and self-regulating quality control processes to adapt to new environmental conditions and to prevent prolonged damage. We discuss the importance of two major quality control systems responsible for degradation of proteins and organelles in eukaryotic cells: the ubiquitin-proteasome system (UPS) and autophagy. The UPS and autophagy form an interconnected quality control network where decision-making is self-organized on the basis of biophysical parameters (binding affinities, local concentrations, and avidity) and compartmentalization (through membranes, liquid-liquid phase separation, or the formation of aggregates). We highlight cellular quality control factors that delineate their differential deployment toward macromolecular complexes, liquid-liquid phase-separated subcellular structures, or membrane-bound organelles. Finally, we emphasize the need for continuous promotion of quantitative and mechanistic research into the roles of the UPS and autophagy in human pathophysiology.

The widely adopted anthropomorphic view of cellular quality control often considers quality control to be a decision-making process that discriminates between normal and malfunctioning proteins or subcellular structures. Its purpose, similar to industrial quality control, is to “achieve and maintain the fitness for use of its products or services” (1). Indeed, mechanisms analogous to those of industrial quality control are found in cellular systems, such as surveillance, feedback control, and adaptation to altered conditions. However, cells do not operate on management systems that choose between quality control measures. Instead, the main cellular quality control systems for proteins and organelles, the ubiquitin-proteasome system (UPS) and autophagy, are controlled by biophysical properties and coordinated at multiple layers securing cellular well-being and appropriate responses to stress and damage.

## Features of the UPS

The UPS and autophagy were both initially thought to act as unspecific bulk recycling routes. It is now recognized that they exhibit a high degree of specificity involving selective enzymatic reactions and discriminatory receptors, with modular domain structures that deliver substrates either to proteasomes or to lysosomes, respectively (Fig. 1). Substrate size critically influences pathway choice: The UPS mostly degrades single, unfolded polypeptides able to enter into the narrow channel of the proteasome, whereas autophagy primarily deals with larger, cytosolic structures such as protein

complexes, cellular aggregates, organelles, or pathogens (2).

The UPS is predominantly driven by ubiquitin (Ub) as a degradation tag, which is controlled by multilayered, reversible enzymatic reactions. These reactions show specific kinetics for each substrate, resulting in protein half-lives ranging from seconds to hours. Ub conjugation is carried out by a hierarchically acting enzymatic cascade. First, adenosine triphosphate-

## “Despite their distinct degradation mechanisms, the UPS and autophagy share molecular determinants...”

dependent Ub activation has to occur (E1s,  $n \geq 2$  in humans), followed by transfer of a Ub thioester to a Ub-conjugating enzyme (E2s,  $n > 50$ ) and formation of an isopeptide bond catalyzed by Ub ligases (E3s,  $n > 500$  in humans). These latter enzymes are endowed with substrate specificity (2, 3). When substrates are progressively modified with Ub, either at the N terminus (Met<sup>1</sup>) or at a lysine side chain of Ub (Lys<sup>6</sup>, Lys<sup>11</sup>, Lys<sup>27</sup>, Lys<sup>29</sup>, Lys<sup>33</sup>, Lys<sup>48</sup>, Lys<sup>63</sup>), various linear or branched Ub chains are built. Thus, Ub tags can be diverse in structure and will dictate the outcome of protein modification, because they can recruit accessory factors or receptors harboring Ub-binding domains (UBDs), including shuttle factors that deliver substrates to the proteasome. Poly-Ub Lys<sup>48</sup>-linked and branched Lys<sup>48</sup>-Lys<sup>11</sup> chains serve as the most potent signals for degradation by the proteasome. Monoubiquitination can alter protein localization and protein complex stoichiometries; however,

recent systematic analyses have revealed that monoubiquitination can also target up to 40% of proteins for degradation by the proteasome (4), particularly proteins of 20 to 150 residues. Ub conjugation is readily reversible owing to the existence of numerous deubiquitinating enzymes (3).

## Macroautophagy and its link to ubiquitin

The flux of substrates through the autophagy pathway is a multistep process that relies on protein-protein- and protein-lipid-driven interactions. The best-characterized form of autophagy is macroautophagy (hereafter called autophagy), which is characterized by the engulfment of cellular material by a double-membrane structure, the autophagosome. Autophagy is the major response to cellular stress, maintains metabolic building blocks during periods of nutrient deprivation, and eliminates unwanted cellular contents such as toxic protein aggregates, damaged organelles, or intracellular pathogens (2). Autophagy is initiated by the activation of the ULK1 kinase complex, which gives rise to a spatiotemporally highly restricted enzymatic cascade that promotes the local assembly of multiprotein complexes. These complexes promote the conjugation of members of the ATG8 protein family [in higher eukaryotes, LC3s (microtubule-associated protein 1 light chain 3) and GABARAPs ( $\gamma$ -aminobutyric acid receptor-associated protein)] to phosphatidylethanolamine or phosphatidylserine, thereby anchoring them into membranes.

ATG8s exposed on growing autophagic membranes can also sequester substrates delivered by selective autophagic receptors that contain LC3-interacting regions or GABARAP-interacting motifs (LIRs or GIMs, respectively). Very often, these receptors, such as p62/SQSTM1, NBR1, NDP52, OPTN, and TAX1BP1, are also equipped with UBDs, bridging ubiquitinated proteins and autophagic membranes (5). It is estimated that more than half of all selective autophagic substrates rely on Ub as an “eat me” signal, whereas other substrates are recognized in a Ub-independent manner (6).

## Ubiquitin and p62 at the crossroads of the UPS and autophagy

Despite their distinct degradation mechanisms, the UPS and autophagy share molecular determinants and substrates. Accumulating evidence indicates a dynamic cross-talk between the two pathways, with Ub playing a role in most of the multiple layers of communication.

First, both systems use Ub as a degradation signal for substrates; thus, cellular Ub concentration as well as accessibility of Ub receptors both appear crucial. The most studied Ub receptor is p62/SQSTM1, which binds to ubiquitinated substrates via its Ub-associated (UBA) domain, to the proteasome via its Phox and

<sup>1</sup>Institute of Biochemistry II, Faculty of Medicine, Goethe University, 60590 Frankfurt am Main, Germany. <sup>2</sup>Buchmann Institute for Molecular Life Sciences, Goethe University, 60438 Frankfurt am Main, Germany. <sup>3</sup>Max Planck Institute of Biophysics, 60438 Frankfurt am Main, Germany.

\*Corresponding author. Email: dikic@biochem2.uni-frankfurt.de (I.D.); pohl@em.uni-frankfurt.de (C.P.)

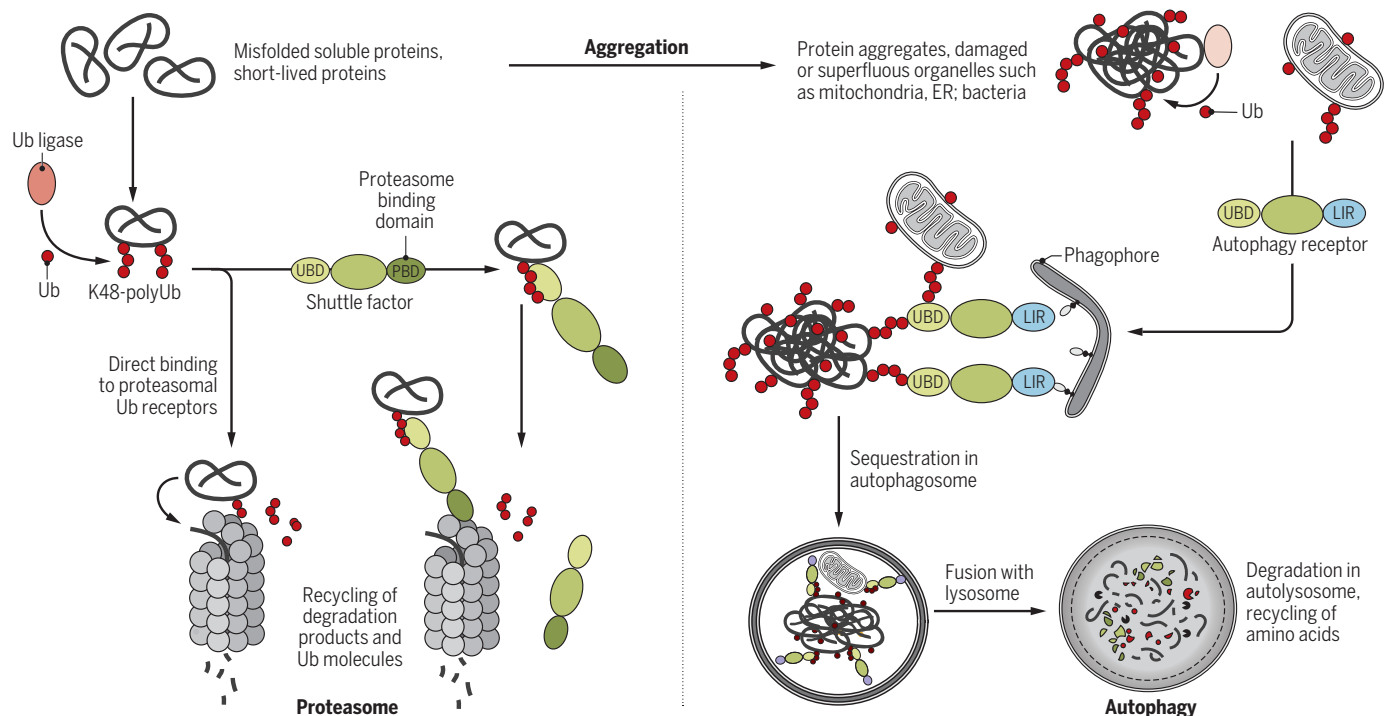


**Fig. 1. Overview and comparison of UPS and autophagy.** Left: The UPS is characterized by the strong dependence on Ub as a degradation signal and on the size limit of substrates. Soluble single proteins are polyubiquitinated in an inducible and reversible manner. Lys<sup>48</sup> (K48)-linked polyUb attached by the substrate-specific Ub E3 ligase is recognized either by intrinsic Ub receptors of the proteasome (e.g., Rpn10 or Rpn13) or shuttle factors that are equipped with both a Ub-binding domain and a domain that binds to the proteasome (e.g., Ubl, PB1). Before degradation in the inside of the barrel-shaped proteasome, substrates are deubiquitinated and unfolded. Right: Selective

autophagy is able to degrade large and heterogeneous cytosolic material, including aggregated proteins, organelles, bacteria, and molecular machines. Substrate labels recognized by the autophagic machinery are more diverse and include Ub, lipid-based signals (e.g., galectins), or organelle-intrinsic autophagy receptors that become exposed to the cytosol. A growing phagophore engulfs autophagic cargo that is connected to the ATG8/LC3-decorated membrane via LIR motif-containing autophagy receptors. Eventually, the phagophore closes around the cargo to give rise to the autophagosome that finally fuses with the lysosome.

Bem1p domain (PB1), and to autophagic membranes via its LIR domain (5). Hence, p62 can escort ubiquitinated substrates to the proteasome and can also act as an autophagy receptor recruiting Ub-conjugated substrates to autophagosomes (Fig. 2). Recent studies have revealed that competition between proteasomal and lysosomal degradation is governed by avidity determinants of a complex, rather than by individual affinity of receptors for Ub (7). Thus, bona fide UPS-dedicated receptors can be transformed into autophagy-dedicated receptors upon formation of oligomers. A switch of these receptors between the dimeric and oligomeric or filamentous state determines which pathway is used by p62-delivered substrates (8). This switch can also be controlled by Ub itself: Under conditions of Ub stress (e.g., at high concentrations of free Ub as observed upon heat shock or prolonged proteasome inhibition), ubiquitination can block UBA domain-dependent dimerization of p62. This favors oligomerization and substrate channeling to autophagy (9).

Second, the proteasome itself can both be regulated by and targeted for autophagic deg-

radation by ubiquitination. Depending on the trigger and the type of ubiquitination, ubiquitination can lead to autoinhibition of proteasomes (10) or autophagic degradation of proteasomes, also called proteaphagy (11). Proteaphagy is observed under chronic amino acid starvation and, at lower capacity, under basal metabolic conditions. This suggests that proteaphagy may act as a key mechanism for proteasome turnover (11). Proteaphagy was first described in plants and yeast, and it can be further regulated by compartmentalization upon specific stresses. Upon nitrogen starvation in yeast, proteasomes can be degraded by autophagy, whereas during carbon starvation, proteasomes are sequestered in proteasome storage granules where specific factors (including the HEAT-repeat protein Bln10 and the deubiquitinating enzymes Rpn11 and Ubp3/Bre5) seem to protect them from autophagy (12).

Third, the UPS and autophagy are also linked by various properties of p62 and Ub. For example, p62 can recognize proteins that expose positively charged or bulky N-terminal residues, so-called degradation signals (degrons) for the N-end rule pathway, which usually trig-

ger proteasomal degradation (13). This binding triggers p62 aggregation through formation of disulfide bonds between p62 molecules, ultimately leading to autophagic degradation of the N-end rule substrate. This corroborates the notion that receptor oligomerization can determine pathway choice.

The interaction between the UPS and autophagy is exemplified well when studying nutrient shortage or upon inhibition of one of the two systems. Acute nutrient stress will lead to replenishment of the cellular amino acid pool via the proteasomal route before autophagy is activated (14), and cells will up-regulate proteasomal activity at both transcriptional and posttranslational levels (15). The critical importance of this fast response becomes evident upon proteasome inhibition, which eventually leads to cell death caused by amino acid deprivation (16). In fact, amino acid scarcity has been shown to be the critical signal that blocks amino acid consumption by protein synthesis and activates autophagy through an mTOR (mechanistic target of rapamycin)-dependent pathway. This results in the bulk degradation of cytosolic material in an attempt



to rescue the amino acid pool (16). Furthermore, proteasome inhibition causes rapid, Nrf1-dependent induction of proteasomal subunits (15) as well as expression of p62 and GABARAPs, which help to sequester ubiquitinated proteins into inclusions (17). Similarly, mTOR signaling regulates autophagic gene transcription, mainly through phosphorylation and cytoplasmic retention of the MiT/TFE-type transcription factors TFEB, TFE3, and MITF. Upon nutrient stress, dephosphorylation of MiT/TFE transcription factors leads to their nuclear translocation and promotes the transcription of autophagy genes, Ub receptors (including p62), and lysosomal genes (18), also through Nrf1, which is a direct TFEB target gene itself (19).

Thus, Ub can act on several regulatory layers to affect substrate channeling, specifically at the level of Ub receptors and more generally at the level of proteasome activity. This latter type of regulation leads to a transcriptional feedback, which is still not well understood under physiological conditions. Moreover, autophagy is directly affected by adaptations in the UPS and is subject to an apparently more complex feedback regulation. For instance, the autophagy-initiating kinase ULK1 is targeted for proteasomal degradation during autophagy

progression (20). Similarly, Beclin1, a component of the lipid kinase complex immediately downstream of ULK1, requires the activity of deubiquitinating enzymes for its maintenance at steady-state levels (21). Although these two examples require (de)ubiquitination, Ub-independent degradation of autophagy pathway components that mediate autophagosome-lysosome fusion has also been reported (22). Further study of the cross-talk and feedback between the UPS and autophagy will most likely reveal an even greater level of mutual control.

### Quality control of cytosolic membraneless structures

As discussed above, substrate processing through the UPS or autophagy critically depends on the biophysical state of the substrate. Although the focus has long been on the two states of soluble versus aggregated, more recently it has become clear that many proteinaceous, membraneless subcellular structures are better described by a third biophysical state, a phase-separated condensate assembled by liquid-liquid phase separation (LLPS). Such structures include the centrosome, the nucleolus, Cajal bodies, P-bodies, and stress granules. During LLPS, a

stimulus-responsive condensation drives the spontaneous separation of fluid- or gel-like phases when one phase is composed of molecules that harbor intrinsic, associative properties. Such molecules must be multivalent, either harboring multiple adhesive domains or linear motifs or harboring polyvalent, intrinsically disordered regions (23). LLPS can have outcomes that are hard to predict, and molecules showing LLPS need to be evaluated systematically to uncover the stimulus or regulatory mechanisms that lead to condensation.

Recently, such systematic studies have unraveled the importance of LLPS for the UPS and autophagy. For example, the ability to oligomerize influences the recruitment of a Cul3 Ub ligase complex to liquid-like nuclear speckles. Self-association of the ligase is induced by binding of its substrate adaptor SPOP to substrates, which affects localization of the ligase and its activity (24). In stress granule formation, autophagy pathway components can co-partition with stress granules. LC3s/GABARAPs, in particular, show a high degree of direct interactions with other granule components (25). In addition, dynamic aspects and a cross-talk between the UPS and autophagy have been documented for LLPS. The ability

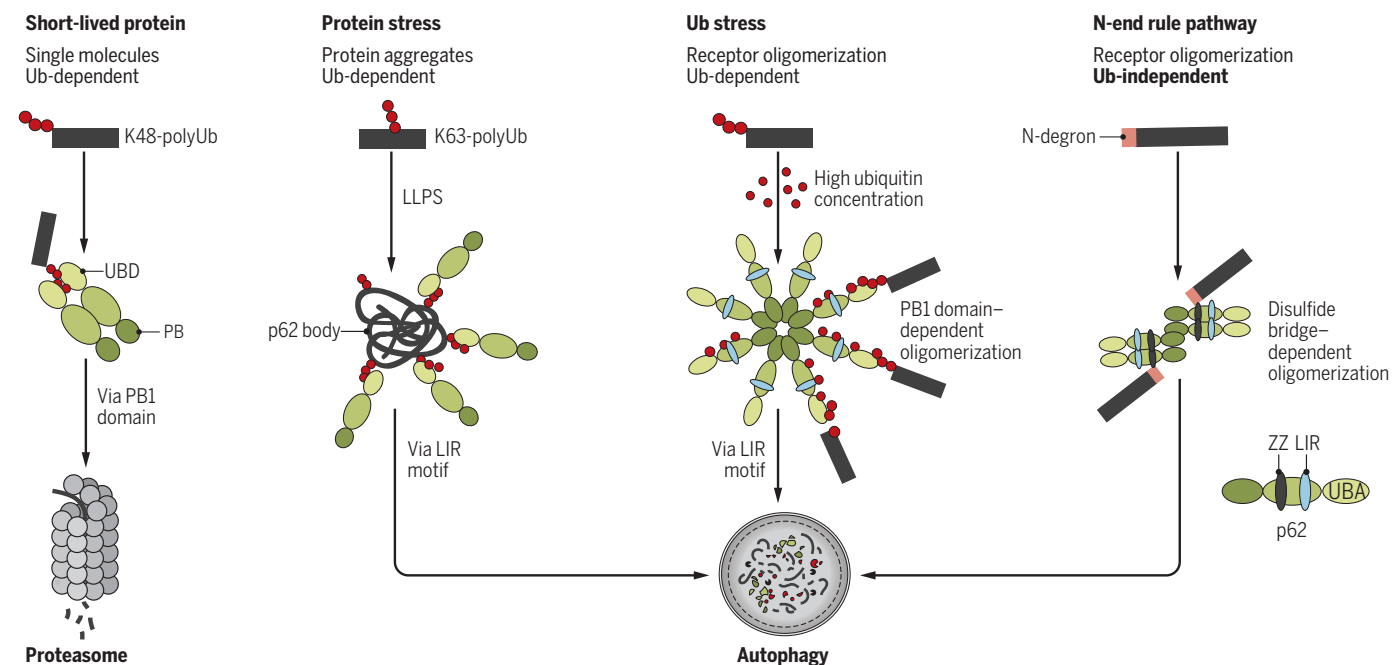


**Fig. 2. Ub and p62 at the crossroads of UPS and autophagy.** The p62 protein can serve both as a selective autophagy receptor (via its LIR domain) and as a proteasomal shuttle factor (via its PB domain) for ubiquitinated substrates. The pathway choice depends on the oligomeric state of p62. Left: The p62 dimer recognizes single protein molecules labeled with K48-linked polyUb via its UBA domain and shuttles them to the proteasome via interaction of its PB domain. Middle left: Binding to K63-linked polyUb chains induces oligomerization of p62 via its PB domain and liquid-liquid phase separation, resulting in the formation of p62 bodies that subsequently

recruit autophagic membranes via the LIR domain. Middle right: A high concentration of cellular Ub can lead to oligomerization of p62. The process involves ubiquitination of p62 at multiple lysines, resulting in destabilization of UBA dimerization and PB1-mediated oligomerization, which favors LIR-mediated autophagic targeting of polyubiquitinated cargo. Right: Oligomerization can also be induced independently of Ub: N-degrons bound by the ZZ domain of p62 promote formation of p62 oligomers stabilized by disulfide bridges between PB1 domains. Again, oligomeric p62 favors the autophagic route via LIR-mediated interactions.

of p62 to oligomerize and the multivalence of poly-Ub chains recognized by it can drive both phase separation and segregation of the substrates into autophagic degradation (26). In contrast, for proteasomal Ub receptors such as ubiquilins, partitioning through LLPS is inhibited by binding to mono-Ub or Ub chains, which block multivalent interactions between ubiquitin moieties (27). Ubiquilins can affect autophagy in more indirect ways (most likely not requiring LLPS) by regulating lysosomal acidification (28). Hence, to evaluate dynamic changes and steady states of proteasomal versus autophagy-dependent degradation of stimulus-responsive condensates, a proper characterization of their biophysical properties will be crucial. In most of these systems, the physiological relevance of LLPS in vivo still needs to be addressed.

Quality control of organelles

Quality control of damaged or superfluous organelles is largely driven by selective autophagy (also called organellophagy) (Fig. 3). This is a critical step in cellular surveillance because multiple cellular functions depend on proper functioning of organelles. Exhausted or damaged organelles are recognized by dedicated autophagy receptors that are localized in organelle membranes or are recruited from the cytosol. These receptors harbor LIR or GIM motifs that facilitate incorporation into nascent autophagosomes. Autophagy-mediated turnover of mitochondria (mitophagy) is a particularly well-studied example. Mitophagy occurs during different physiological situations that rely on different types of autophagy receptors: The family of NIX/BNIP3 mitochondrial autophagy receptors promote mitophagy during development or erythrocyte maturation independently of Ub signals (29). In contrast, mitophagy of damaged or depolarized mitochondria relies on ubiquitination of several proteins of the outer mitochondrial membrane driven by the PINK1-parkin pathway (30). UBD-containing autophagy receptors, including OPTN, NDP52, p62, NBR1, and TAXBP1, link ubiquitinated mitochondria with autophagic membranes (31, 32). In addition, OPTN and NDP52 can also recruit ULK1 directly to ubiquitinated mitochondria to initiate autophagosome formation locally (31). Such spatiotemporal control of ULK1 activation is dependent on the TBK1 kinase, but not on AMPK (adenosine monophosphate-activated protein kinase) or mTOR activities or the presence of ATG8/LC3, and is common for multiple selective autophagy

processes, including, for example, bacterial clearance (xenophagy) (33). Another recently characterized example of organellar quality control is the autophagic degradation of topologically distinct domains of the endoplasmic reticulum (ER), or ER-phagy.

Deficiencies in ER-phagy have been linked to several human diseases, including neuropathies (34). Several ER-phagy receptors have been identified that mediate the delivery of ER tubules (RTN3, ATL3), ER tubular junctions (TEX264), ER-luminal components (CCPG1), and ER sheets (FAM134B) to autophagic membranes (34). ER-phagy is also indirectly linked with UPS functions because it degrades substrates of the ER-associated degradation (ERAD) pathway. FAM134B,




through the cooperation with the ER chaperone calnexin, mediates the quality control-dependent turnover of ER luminal proteins that are refractory to ERAD, such as misfolded procollagen (35) or  $\alpha$ 1-antitrypsin Z (ATZ) (36). A recent study has revealed the requirement for some components of the COPII secretory pathway for ER-phagy of procollagen (37) and ATZ in the lysosome (38). Thus, multiple ER-phagy pathways may deliver protein aggregates within the ER to the lysosome. Interestingly, growing ER-phagy vesicles at ER exit sites (ERESs) (containing procollagen, Ub, and COPII elements) may be directly bridged to the lysosome (37).

Accumulating evidence suggests that some forms of selective autophagy can be mediated by noncanonical autophagy pathways. A crucial indication of the existence of such pathways came somewhat unexpectedly from the

reexamination of drugs claimed to block canonical autophagosome formation (including ionophores, such as CCCP, or basic lipophiles, such as chloroquine). However, these chemicals do not block flux in the canonical pathway, as previously thought, but rather induce lysosomal LC3/GABARAP lipidation at single membranes and do so independently of ATG9, ATG13, or PI3P generation (39). Direct lipidation of LC3s/GABARAPs on single membranes in the form of LC3-associated phagocytosis (LAP) functions also in a wide range of physiological processes, such as the vision cycle, neurodegenerative disease, tumor cell immunotolerance, and bacterial infection (40). Further analysis of the functions of organellophagy in normal physiology might thus allow us to modify key hypotheses in the field, especially concerning the existence of physiologically relevant noncanonical pathways that act in parallel to or instead of the canonical autophagy pathway.

Implications for pathophysiology

Although often found in the context of the same pathophysiologic conditions, the UPS and autophagy are mostly examined as discrete entities. Indeed, the simultaneous investigation of the two pathways in any given pathology entails a huge experimental effort. Nonetheless, there is accumulating evidence that autophagy and the UPS are simultaneously affected and may mutually affect each other in a variety of diseases (41). This has been particularly evident in disorders of the central nervous system that involve inflammatory or immune alteration, such as Parkinson's, Alzheimer's, and Huntington's diseases (42). Also, in several types of cancer, molecular links between the UPS and autophagy have been discovered (2), but general concepts have not yet been demonstrated in clinical settings. A main reason for this is that the cell-autonomous and -nonautonomous roles

	Ub-dependent	Ub-independent	Contribution of proteasome
<b>Mitophagy</b> 	<b>PINK1/Parkin</b> pathway upon mitochondrial damage/depolarization involving Ub-binding autophagy receptors: <b>OPTN, TAX1BP1, NBR1, NDP52, p62</b>	<b>NIX/BNIP3:</b> erythrocyte maturation <b>FUNDCl:</b> hypoxia-induced mitophagy	Control of mitochondrial PINK1 levels, degradation of several Parkin-substrates
<b>ER-phagy</b> 	Unknown	ER-resident ER-phagy receptors: <b>FAM134B, CCPG1, RTN3, ATL3, TEX264</b>	Unknown
<b>Proteophagy</b> 	Starvation-induced polyubiquitination recruits <b>p62</b>	Unknown	...

**Fig. 3. Summary of Ub dependency of organellophagy.** Depending on the type of organelle, selective autophagic degradation of exhausted or damaged organelles may involve both Ub-dependent and -independent autophagy receptors and may also involve proteasomal activity.



of autophagy are not yet fully understood, not only with respect to metabolic adaptations within the tumor tissue itself but also in regulating host tissue adaptation (43). Moreover, immune responses to tumors seem also to rely on noncanonical forms of autophagy (40). Thus, understanding the cross-talk of the two systems is highly relevant for therapeutic approaches involving the inhibition or activation of either one. For example, the proteasome inhibitor bortezomib has been used successfully in the treatment of cancers such as multiple myeloma (41). However, as discussed above, prolonged inhibition of the proteasome will eventually lead to activation of autophagy, which can in turn be exploited as a prosurvival mechanism by cancer cells. Several reports have also indicated the highly contextual role of autophagy, suggestive of a highly dynamic and complex influence of autophagy in different types of cells as well as at distinct stages of cancer development (42).

## Conclusion

The UPS and autophagy act as an integrated quality control network embedded in the general cellular stress response. However, the UPS and autophagy are still primarily investigated from a unicellular perspective that neglects the complexities arising in multicellular contexts. Thus, in the physiological context, many aspects regarding the mechanisms of selectivity and cross-talk remain elusive. Specifically, unraveling the kinetics, feedback controls, and membrane dynamics will require the development of methods to locally determine protein quantities and stoichiometries for the UPS and autophagy machineries in vivo. Also, it will be crucial to better understand the interplay among LLPS, ubiquitin, and autophagy, eventually allowing researchers and physicians to target the UPS and autophagy in patho-

physiological processes that are associated with defective LLPS, like those observed in neurodegeneration. For the latter to be successful, a combination of biophysical experiments and modeling should help us to identify the constraints of autophagic membrane formation around phase-separated subcellular structures and how this is modulated by Ub-dependent mechanisms. Finally, the recent discoveries on organellophagy and the growing list of physiological processes depending on noncanonical autophagy pathways necessitate a reexamination of quality control in vivo. This will require the adaptation of quantitative, molecular tools from cellular to animal and organoid models, as well as engineering tools for the administration of chronic and low-dose stress in vivo to better mimic human pathophysiology in cancer, chronic infection, diabetes, and neurodegeneration. Ultimately, these approaches will provide much deeper insights into physiological and medical aspects of integrated cellular quality control pathways.

## REFERENCES AND NOTES

1. A. B. Bishop, *AlIE Trans.* **6**, 275–283 (1974).
2. I. Dikic, *Annu. Rev. Biochem.* **86**, 193–224 (2017).
3. E. Oh, D. Akopian, M. Rape, *Annu. Rev. Cell Dev. Biol.* **34**, 137–162 (2018).
4. O. Braten et al., *Proc. Natl. Acad. Sci. U.S.A.* **113**, E4639–E4647 (2016).
5. V. Rogov, V. Dötsch, T. Johansen, V. Kirkin, *Mol. Cell* **53**, 167–178 (2014).
6. A. Khaminets, C. Behl, I. Dikic, *Trends Cell Biol.* **26**, 6–16 (2016).
7. K. Lu, F. den Brave, S. Jentsch, *Nat. Cell Biol.* **19**, 732–739 (2017).
8. B. Wurzer et al., *eLife* **4**, e08941 (2015).
9. H. Peng et al., *Cell Res.* **27**, 657–674 (2017).
10. H. C. Besche et al., *EMBO J.* **33**, 1159–1176 (2014).
11. V. Cohen-Kaplan et al., *Proc. Natl. Acad. Sci. U.S.A.* **113**, E7490–E7499 (2016).
12. R. S. Marshall, R. D. Vierstra, *eLife* **7**, e34532 (2018).
13. H. Cha-Molstad et al., *Nat. Commun.* **8**, 102 (2017).
14. R. M. Vabulas, F. U. Hartl, *Science* **310**, 1960–1963 (2005).

15. S. K. Radhakrishnan et al., *Mol. Cell* **38**, 17–28 (2010).
16. A. Suraweera, C. Münch, A. Hanssum, A. Bertolotti, *Mol. Cell* **48**, 242–253 (2012).
17. Z. Sha, H. M. Schnell, K. Ruoff, A. Goldberg, *J. Cell Biol.* **217**, 1757–1776 (2018).
18. C. Di Malta, L. Cinque, C. Settembre, *Front. Cell Dev. Biol.* **7**, 114 (2019).
19. G. Mansueto et al., *Cell Metab.* **25**, 182–196 (2017).
20. F. Nazio et al., *J. Cell Biol.* **215**, 841–856 (2016).
21. J. Liu et al., *Cell* **147**, 223–234 (2011).
22. E. Njomen, J. J. Tepe, *Cell Chem. Biol.* **26**, 1283–1294.e5 (2019).
23. S. Boeynaems et al., *Trends Cell Biol.* **28**, 420–435 (2018).
24. J. J. Bouchard et al., *Mol. Cell* **72**, 19–36.e8 (2018).
25. S. Markmiller et al., *Cell* **172**, 590–604.e13 (2018).
26. D. Sun, R. Wu, J. Zheng, P. Li, L. Yu, *Cell Res.* **28**, 405–415 (2018).
27. T. P. Dao et al., *Mol. Cell* **69**, 965–978.e6 (2018).
28. M. Şentürk et al., *Nat. Cell Biol.* **21**, 384–396 (2019).
29. I. Novak et al., *EMBO Rep.* **11**, 45–51 (2010).
30. J. M. Heo, A. Ordureau, J. A. Paulo, J. Rinehart, J. W. Harper, *Mol. Cell* **60**, 7–20 (2015).
31. M. Lazarou et al., *Nature* **524**, 309–314 (2015).
32. J. N. S. Vargas et al., *Mol. Cell* **74**, 347–362.e6 (2019).
33. B. J. Ravenhill et al., *Mol. Cell* **74**, 320–329.e6 (2019).
34. P. Grumati, I. Dikic, A. Stolz, *J. Cell Sci.* **131**, jcs217364 (2018).
35. A. Forrester et al., *EMBO J.* **38**, e99847 (2019).
36. I. Fregno et al., *EMBO J.* **37**, e99259 (2018).
37. S. Omari et al., *Proc. Natl. Acad. Sci. U.S.A.* **115**, E10099–E10108 (2018).
38. Y. Cui et al., *Science* **365**, 53–60 (2019).
39. E. Jacquin et al., *Autophagy* **13**, 854–867 (2017).
40. L. Galluzzi, D. R. Green, *Cell* **177**, 1682–1699 (2019).
41. D. Popovic, D. Vucic, I. Dikic, *Nat. Med.* **20**, 1242–1253 (2014).
42. J. Blasiak, E. Pawlowska, J. Szczepanska, K. Kaarniranta, *Int. J. Mol. Sci.* **20**, E210 (2019).
43. L. Poillet-Perez, E. White, *Genes Dev.* **33**, 610–619 (2019).

## ACKNOWLEDGMENTS

We thank D. Hoeller, K. Koch, A. Gubas, L. Alves, and P. Grumati for critical comments on the manuscript and D. Hoeller for help with preparation of figures. **Author contributions:** C.P. and I.D. designed the structure for the review, wrote the manuscript, and prepared the figures. **Funding:** Supported by the DFG-funded Collaborative Research Centre on Selective Autophagy (SFB 1177) (I.D. and C.P.) and by the European Research Council (ERC) under the European Union's Horizon 2020 research and innovation program (grant agreement 742720) (I.D.). **Competing interests:** Authors declare no competing interests.

10.1126/science.aax3769

## REVIEW

## Cellular RNA surveillance in health and disease

Sandra L. Wolin<sup>1\*</sup> and Lynne E. Maquat<sup>2,3\*</sup>

The numerous quality control pathways that target defective ribonucleic acids (RNAs) for degradation play key roles in shaping mammalian transcriptomes and preventing disease. These pathways monitor most steps in the biogenesis of both noncoding RNAs (ncRNAs) and protein-coding messenger RNAs (mRNAs), degrading ncRNAs that fail to form functional complexes with one or more proteins and eliminating mRNAs that encode abnormal, potentially toxic proteins. Mutations in components of diverse RNA surveillance pathways manifest as disease. Some mutations are characterized by increased interferon production, suggesting that a major role of these pathways is to prevent aberrant cellular RNAs from being recognized as “non-self.” Other mutations are common in cancer, or result in developmental defects, revealing the importance of RNA surveillance to cell and organismal function.

RNA surveillance pathways sculpt cellular transcriptomes by degrading aberrant, potentially harmful RNAs. Most, if not all, RNAs are subject to surveillance. The most abundant RNAs are long-studied “classical” noncoding RNAs (ncRNAs) such as the ribosomal RNAs (rRNAs) and transfer RNAs (tRNAs) that function in protein synthesis and the small nuclear RNAs (snRNAs) that carry out pre-mRNA splicing. These and many other ncRNAs, including the more recently described microRNAs (miRNAs), are synthesized as precursors that fold into intricate three-dimensional structures, assemble with proteins, and undergo one or more processing events to achieve their functional forms. As ncRNA precursors can misfold, fail to assemble into larger complexes, or be incorrectly processed, cells must distinguish correct ncRNAs from RNAs that should be degraded. All cells also contain many less abundant ncRNAs, some of which derive from bidirectional transcription at the promoters of protein-coding genes. Many of these ncRNAs are surveillance targets, as they increase in amount when specific ribonucleases are inactivated. Failure to degrade some of these ncRNAs can alter transcription of adjacent protein-coding genes and can result in formation of RNA–DNA hybrids (R-loops) that render cells prone to DNA damage and chromosomal rearrangements (1). Although mRNAs constitute only a small fraction of cellular RNA, incompletely processed mRNAs can form RNA–DNA hybrids with their DNA templates, and mutation-containing mRNAs can encode abnormal (e.g., truncated) and toxic proteins (2). Thus, all cells contain extensive surveillance

pathways that recognize and target aberrant ncRNAs and mRNAs for degradation.

A feature of surveillance pathways for both ncRNAs and protein-coding RNAs is that they target newly synthesized RNAs in competition with their normal processing pathways. For ncRNAs, surveillance occurs in kinetic competition with (i) assembly of nascent ncRNAs with their core proteins to form ribonucleoproteins (RNPs), (ii) enzymes that trim or modify

nascent ncRNA 5′ or 3′ ends, and (iii) binding of proteins required for nuclear export of the assembled and matured RNPs (1). Consistent with competition, ncRNAs that fail to undergo RNP assembly and correct maturation are primarily targeted for degradation. Similarly, for mRNAs and long noncoding RNAs (lncRNAs), which resemble mRNAs in that they are synthesized by RNA polymerase II but are computationally defined as not encoding protein), transcription elongation, capping of the newly synthesized 5′ end, splicing, 3′ end formation, and nuclear export compete with targeting for decay. Because surveillance takes place at multiple steps in RNA biogenesis, aberrant RNAs that escape one surveillance pathway are often subsequently targeted by another.

## Surveillance of aberrant ncRNAs

Although the ribonucleases that degrade defective RNAs are the major effectors of RNA surveillance pathways, they do not operate in isolation. Instead, most ribonucleases rely on protein cofactors, or adaptors, that recognize defective RNAs and recruit the nucleases. For example, a critical ncRNA surveillance pathway in eukaryotic nuclei involves a multiprotein nuclease complex called the RNA exosome,

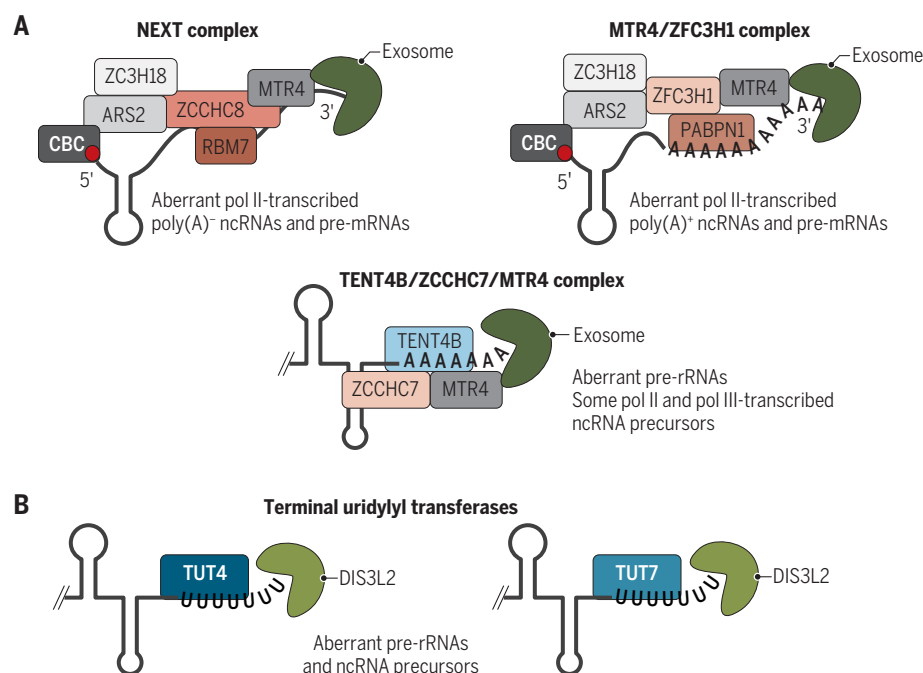


**Fig. 1. Protein adaptors target aberrant RNAs for degradation.** (A) In the nucleus, NEXT (top left) targets newly synthesized RNA polymerase II-transcribed poly(A)<sup>-</sup> ncRNAs and pre-mRNAs for degradation by the RNA exosome, whereas MTR4-ZFC3H1 (top right) targets nascent RNA polymerase II-transcribed poly(A)<sup>+</sup> ncRNAs and poly(A)<sup>+</sup> pre-mRNAs for exosome degradation. Although not shown, ZFC3H1 may bind RNA. Prematurely terminated pre-rRNA precursors, as well as some RNA polymerase II- and RNA polymerase III-transcribed ncRNA precursors, are adenylated by the TENT4B-ZCCHC7-MTR4 complex (bottom), facilitating degradation by the RNA exosome. (B) In the cytoplasm, TUT4 (left) and TUT7 (right) add a short U tail to defective ncRNA precursors, stimulating degradation by the DIS3L2 exoribonuclease.

<sup>1</sup>RNA Biology Laboratory, Center for Cancer Research, National Cancer Institute, Frederick, MD 21702, USA.

<sup>2</sup>Department of Biochemistry and Biophysics, School of Medicine and Dentistry, University of Rochester, Rochester, NY 14642, USA. <sup>3</sup>Center for RNA Biology, University of Rochester, Rochester, NY 14642, USA.

\*Corresponding author. Email: sandra.wolin@nih.gov (S.L.W.); lynne\_maquat@urmc.rochester.edu (L.E.M.)



which manifests both 3'-to-5' exoribonucleolytic and endoribonucleolytic activities. In all studied eukaryotic species, adaptor complexes containing the RNA helicase MTR4 and one or more RNA-binding proteins recognize defective ncRNAs and recruit the exosome (3). In these complexes, the RNA-binding moieties recognize the defective RNAs, while MTR4 binds a conserved surface on the exosome. Upon association of MTR4 with the exosome, the unwinding activity of MTR4 is enhanced, allowing MTR4 to deliver single-stranded RNA to the exosome for degradation (4). A major adaptor complex in human nuclei, called the nuclear exosome targeting complex (NEXT), is composed of MTR4, the zinc finger protein ZCCHC8, and the RNA-binding protein RBM7 (5) (Fig. 1A). RBM7 binds single-stranded U-rich sequences near the ends of many aberrant nascent RNA polymerase II-transcribed ncRNAs, whereas ZCCHC8 scaffolds the interaction of RBM7 with MTR4 and may also contribute to RNA binding (6). A second complex, consisting of MTR4 and the zinc finger protein ZFC3H1, targets polyadenylated RNA polymerase II transcripts that are prematurely terminated or are generated by bidirectional promoter activity for degradation, most likely through interactions with the nuclear poly(A)-binding protein, PABPN1 (7, 8) (Fig. 1A).

Another major category of ribonuclease adaptors includes or consists of terminal nucleotidyl transferase (TENT) that adds short A or U tails to defective ncRNAs. In human nucleoli, a complex consisting of TENT4B, the RNA-binding protein ZCCHC7, and MTR4 adds a short A tail to the 3' ends of prematurely terminated pre-rRNAs (5) (Fig. 1A). These tails, which are too short to be bound by PABPN1, provide a single-stranded end for MTR4 binding and degradation by exosome exoribonucleases. In the cytoplasm, terminal uridylyl transferases TUT4 and TUT7 (also called TENT3A and TENT3B) add short U tails to the ends of many defective ncRNAs, stimulating degradation by the exoribonuclease DIS3L2 (Fig. 1B) (9, 10).

How are ncRNAs recognized as aberrant? For those adaptors that have been studied, specificity is conferred through some combination of subcellular location, association with the RNA synthesis machinery, affinity for specific RNA sequences, and the presence of an accessible 3' end. For example, the NEXT and MTR4-ZFC3H1 complexes are located in the nucleoplasm (5, 7, 8), whereas TENT4B-ZCCHC7-MTR4 is primarily nucleolar (5). NEXT and MTR4-ZFC3H1 are also in proximity to their targets because they associate, through their respective ZCCHC8 and ZFC3H1 subunits, with the cap-binding complex (CBC, consisting of cap-binding proteins CBP80 and CBP20) that binds the 5' cap of nascent RNA polymerase II-transcribed RNAs (11) (Fig. 1A). Because TENT proteins

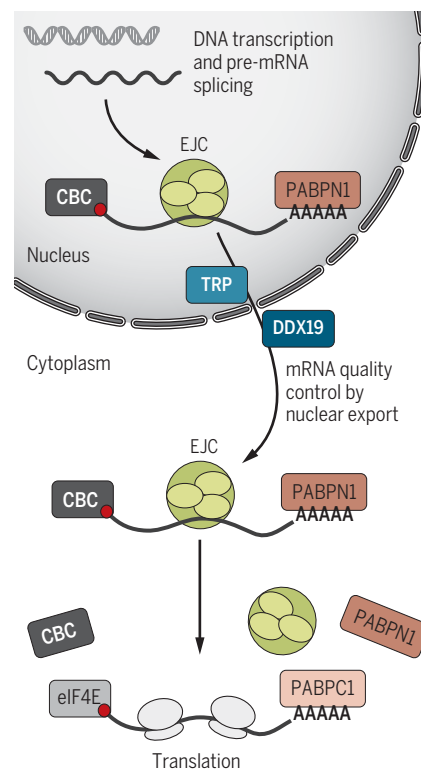


**Fig. 2. Nuclear synthesis and surveillance of protein-coding transcripts.** Following transcription, pre-mRNA splicing, EJC deposition, and 3'-end formation, mRNAs are subject to quality control at the nuclear pore. After passage through the pore and dissociation of nuclear transport factors from the mRNA by the DDX19 helicase, ribosomes engaged in the pioneer round of translation remove EJCs in their path, the CBC is replaced by eIF4E, and PABPN1 is replaced by the cytoplasmic poly(A) binding protein PABPC1.

add nontemplated tails, they recognize RNAs with an accessible single-stranded 3' end.

### Nuclear surveillance of protein-coding RNAs

Many of the mechanisms that surveil aberrant RNA polymerase II-transcribed ncRNAs also recognize and degrade aberrant pre-mRNAs. Pre-mRNA processing, including capping of the newly made 5' end, splicing-mediated removal of introns and formation of the 3' end, usually occurs while the pre-mRNA is being synthesized. Surveillance mechanisms often sense the absence of one or more RNA-binding proteins during a critical window of time, reducing transcript half-life concurrently with or subsequent to the affected processing step.

A critical step for both mRNA biogenesis and mRNA surveillance is binding of the CBC to the capped 5' end. Transcripts that fail to bind the CBC as the 5' end emerges from elongating RNA polymerase II undergo decapping by the decapping and exoribonuclease (DXO) enzyme and degradation by the 5'-to-3'

exoribonuclease XRN2 (12). Capping occurs concomitantly with release of the polymerase from promoter-proximal pausing (13). Those transcripts that prematurely terminate (instead of undergoing productive elongation) are recognized by NEXT and degraded by the exosome. During elongation, the CBC associates with the ARS2 (arsenite-resistance 2) protein, which serves as an interaction hub for the formation of mutually exclusive complexes that either promote pre-mRNA splicing, 3'-end formation, and nuclear export or target incomplete and unprocessed transcripts for degradation by NEXT and MTR4-ZFC3H1 (14). In general, NEXT targets transcripts that lack poly(A) tails, whereas MTR4-ZFC3H1, together with PABPN1, targets unspliced polyadenylated mRNAs for degradation (7, 8) (Fig. 1A).

The exon-junction complex (EJC) is another central player that links mRNA biogenesis to quality control (15). Deposition of this multiprotein complex upstream of a splicing-generated exon-exon junction marks an mRNA as having undergone splicing (Fig. 2). The EJC, by interacting with additional proteins, enhances subsequent steps of mRNA transport to the cytoplasm, protein synthesis and, if appropriate, nonsense-mediated mRNA decay (NMD, discussed below). The human genome also contains a sea of cryptic splice sites that are similar in sequence to the canonical sites, the regulated use of which results in mRNAs encoding functional proteins. The EJC, through association with the splicing factor RNPS1 (RNA-binding protein with serine-rich domain 1), suppresses the inappropriate recognition of nearby cryptic splice sites, thus protecting transcriptome integrity (16).

Termination of transcription and formation of pre-mRNA 3' ends are also subject to surveillance. Pre-mRNAs contain numerous cryptic polyadenylation sites that, if utilized, can result in synthesis of truncated, nonfunctional proteins. Use of these sites is suppressed by binding of the U1 snRNP, a component of the spliceosome, to upstream 5'-splice sites (17). At least some pre-mRNAs that undergo premature termination and polyadenylation are degraded by the exosome, most likely through binding of PABPN1 to the polyadenylated mRNA and recruitment of MTR4-ZFC3H1 (18) (Fig. 1A).

Nuclear export is yet another step at which nonfunctional and incompletely processed mRNAs are subject to quality control. The nuclear RNA export factor NXF1 is preferentially loaded on spliced mRNAs through connections with the CBC, splicing factors, the EJC and the 3'-end formation machinery (19, 20). In addition, the nuclear basket protein translocated promoter region (TPR) is part of a nuclear pore-based surveillance mechanism that prevents export of incompletely spliced mRNAs (21) (Fig. 2). Together, these mechanisms help ensure that only properly spliced

and processed mRNAs are exported. These surveillance mechanisms can be subverted, as some mRNAs with retained introns reach the cytoplasm (22). Some cytoplasmic intron-containing mRNAs are rapidly degraded through surveillance mechanisms described below, particularly NMD, whereas others remain stable.

### Cytoplasmic surveillance of protein-coding RNAs

A distinctive feature of protein-coding RNAs is the ability to use translation to monitor RNA quality. In the best-characterized of these pathways, NMD, mRNAs containing premature termination codons (PTCs; also called nonsense codons) are identified and targeted for decay during the first round of translation, before the CBC is replaced with the cap-binding eukaryotic translation initiation factor 4E (eIF4E). During this pioneer round of translation, which is defined as the translation of CBC-bound mRNA, ribosomes displace EJCs on those mRNAs that have undergone splicing (Fig. 2). In this way, the NMD pathway “inspects” mRNAs for genetic or processing defects that manifest in the premature termination of translation (2). As a rule, if the pioneer round of translation terminates more than ~50 to 55 nucleotides upstream of an EJC-bound exon–exon junction, the terminating ribosome will fail to physically displace that EJC (and any remaining downstream EJCs) and target the mRNA for NMD (Fig. 3A).

A translation-dependent quality control mechanism that depends on a PTC and also feeds back to the nucleus is transcriptional adaptation (23, 24). This occurs when transcription of paralogous genes increases to compensate for a defective gene and explains the observation that inactivating a gene can be less deleterious than depleting the mRNA with small interfering RNAs (siRNAs) or short hairpin RNAs (shRNAs). Two recent studies showed that those mutant genes that result in increased transcription of paralogs produce mRNAs containing PTCs (23, 24). Degradation of the mRNA by the NMD machinery triggers transcriptional adaptation through a mechanism that involves the UPF3 (also called UPF3A) component of the NMD machinery. UPF3 interacts with the COMPASS complex to recruit chromatin modifiers that up-regulate the expression of genes with sequence complementarity to the PTC-containing mRNA (23, 24). How the COMPASS complex is guided to paralogous gene promoters remains unclear but could involve fragments of the degraded mRNAs. Future therapeutic strategies targeting defective genes will undoubtedly take note of those genes that, when engineered to harbor a PTC, would allow one or more paralogs to functionally substitute for the deficiency.

A third translation-dependent pathway is triggered when ribosomes move pathologi-

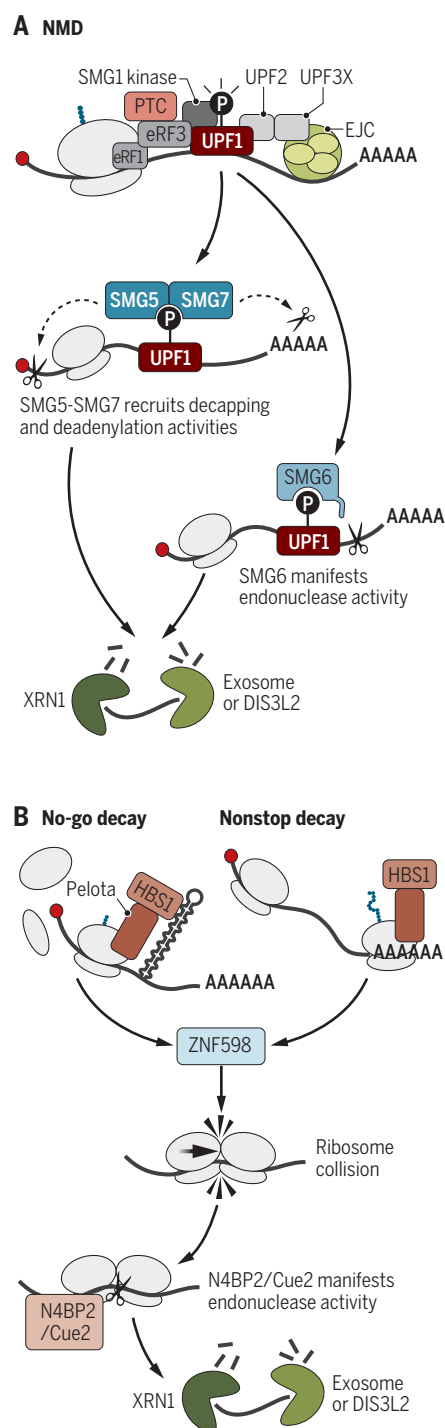


**Fig. 3. Cytoplasmic surveillance of protein-coding transcripts.** (A) If the ribosome terminates before reaching the final EJC, the NMD machinery interacts with the EJC and targets the mRNA for degradation. (B) In no-go and possibly nonstop decay, a ribosome stalls during translation elongation. Consequently, ribosomes collide, providing a surface for ubiquitination by ZNF598. Afterwards, the N4BP2/Cue2 endonuclease cleaves at the 5' side of the stalled ribosome, allowing rescue and recycling by PELO and HBS1.

cally slowly or stall during translation elongation. Causes of so-called “no-go” mRNA decay include difficulties forming peptide bonds between particular amino acids in the growing polypeptide chain; rare or suboptimal codons due to inadequate amounts of the corresponding tRNA(s); and mRNA structures that impede ribosome progression (25). A collided di-ribosome constitutes the decisive indicator that triggers both ribosome and mRNA quality control by forming a surface recognized by the ubiquitin ligase ZNF598, a prerequisite for triggering endonucleolytic cleavage of the mRNA (26, 27) (Fig. 3B). The responsible endonuclease in yeast no-go mRNA decay was identified recently as the Cue2 protein, the putative human ortholog of which is NEDD4 binding protein 2 (N4BP2) (28). Following cleavage, ribosome rescue factors pelota (PELO) and HBS1 bind and initiate ribosome subunit dissociation and recycling for further use. A related pathway, called “nonstop” mRNA decay, occurs when mRNAs lack a stop codon, either because they are truncated or have undergone premature 3'-end cleavage and polyadenylation in the nucleus. In either case, the ribosome stalls after translating to the end of the mRNA. As in no-go decay, removal of the arrested ribosome involves endonucleolytic cleavage of the mRNA and ribosome rescue by PELO and HBS1 (25), and a preliminary report has identified Cue2/N4BP2 as the required endonuclease (29).

There are also examples of mRNA surveillance in which the precipitating event is the failure of the nascent polypeptide to bind a partner as it emerges from the ribosome tunnel. One example involves mRNAs encoding secretory proteins. Although the synthesis of proteins destined for the endoplasmic reticulum (ER) initiates in the cytosol, the translating ribosomes are targeted to the ER through binding of the signal recognition particle (SRP) to the signal peptide as it emerges from the elongating ribosome. Failure of the signal peptide to engage SRP, due to a mutant signal peptide or SRP depletion, results in degradation of the mRNA (30). Although the mechanisms that connect the nascent polypeptide to cotranslational mRNA decay are not understood, this and other examples where coding region sequences are coupled to mRNA decay support the idea of cross-talk between mRNA and protein quality control pathways.

### Diseases linked to defective RNA surveillance

Because the nucleases that degrade defective RNAs have myriad targets and have roles outside surveillance, it is difficult to attribute mutant phenotypes to a specific role in quality control or even to quality control at all. Nonetheless, missense mutations that partly inactivate RNA exosome function cause multiple developmental disorders. Mutations in exosome core subunits EXOSC3 and EXOSC8



cause pontocerebellar hypoplasia (PCH) 1B and 1C, respectively, which are autosomal recessive syndromes presenting early in childhood that are characterized by cerebellar atrophy and spinal motor neuron degeneration (37). Although only one patient with a homozygous mutation in the RBM7 component of NEXT has been described, this patient exhibited spinal motor neuron degeneration similar to that of PCH1 patients, suggesting that PCH1 could be due to altered RNA surveillance (37). Several other PCH subtypes (PCH2 to PCH7 and PCH10) are caused by mutations that specifically disrupt processing of tRNAs or snRNAs (32), suggesting that accumulation of unprocessed and defective ncRNAs could contribute to PCH.

Other mutations in RNA surveillance pathway components are also associated with childhood disease. Mutations in DIS3L2 cause Perlman syndrome, an autosomal recessive overgrowth syndrome associated with increased frequency of Wilms tumor, the most common kidney tumor in children (33). Although the mechanisms by which DIS3L2 mutations cause Perlman syndrome have not been fully elucidated, kidney progenitor cells lacking DIS3L2 up-regulate expression of IGF2 (insulin-like

**“...examples where coding region sequences are coupled to mRNA decay support the idea of cross-talk between mRNA and protein quality control pathways.”**

growth factor 2), which is strongly associated with Wilms tumorigenesis (34). Disease may reflect the toxic accumulation of one or more of the many abnormal RNAs that are routinely eliminated by DIS3L2 (1). Mutations in genes encoding the NMD factors UPF2 or UPF3X (also called UPF3B) are associated with neurodevelopmental disorders, including autism spectrum disorder and schizophrenia (35).

In other cases, failure to degrade aberrant RNAs is clearly linked to disease. For example, failure of translation-based surveillance mechanisms, such as NMD, affect disease through the synthesis of an aberrant, often truncated, and harmful protein that functions in dominant-negative ways. Failure to degrade excess RNAs

results in activation of cytoplasmic innate immune sensors, the normal role of which is to recognize viral RNAs and trigger an antiviral response mediated by signaling molecules called interferons. These sensors, which recognize double-stranded RNA (dsRNA) generated during virus infection, include retinoic acid inducible gene I (RIG-I) and melanoma differentiation-associated protein 5 (MDA5), which activate an antiviral signaling cascade, and protein kinase R (PKR), which phosphorylates the eIF2 $\alpha$  translation initiation factor to inhibit protein synthesis (36). Mutations that inactivate proteins that are important for eliminating cellular dsRNAs, such as the adenosine deaminase acting on RNA 1 (ADAR1), which disrupts dsRNA by deaminating adenosines in double-stranded regions to inosines (37), or polynucleotide phosphorylase (PNPT1), a 3'-to-5' exonuclease that degrades mitochondrial dsRNAs (38), result in neurologic diseases characterized by increased production of interferon (39). Although the full catalog of aberrant cellular RNAs that can activate RIG-I and MDA5 is not known, loss of ADAR1 results in increased amounts of dsRNA formed from members of the *Alu* family of repetitive elements. These dsRNAs, many of which derive from *Alu-Alu* inverted repeats in mRNA untranslated regions, activate MDA5 to trigger interferon production and PKR to shut down translation (40, 41) (Fig. 4A). Mutations in PNPT1 result in accumulation of mitochondrial dsRNAs that enter the cytoplasm and activate MDA5 (38) and PKR (42) (Fig. 4B).

Both the up-regulation and down-regulation of RNA surveillance pathways make critical contributions to cancer pathogenesis. In many tumors, mutations in ADAR1 are associated with increased interferon secretion, growth inhibition, and increased sensitivity to radiotherapy and immunotherapy through pathways mediated by PKR and MDA5 (43). Although these effects are likely due to dsRNA accumulation, ADAR1 up-regulation in chronic myeloid leukemia progenitor cells drives proliferation by editing primary miRNA precursors and mRNA 3'-untranslated regions, reducing the amounts of specific miRNAs and their interactions with key targets (44). Up-regulation and down-regulation of NMD also contribute to cancers, depending on the cell of origin and how the cancer evolved (45). Down-regulation of the RNA exosome likely contributes to some cancers, because mutations in the DIS3 catalytic subunit are common in some hematologic malignancies, particularly multiple myeloma. Although the mechanism(s) by which DIS3 mutations affect cancer progression are unknown, most mutations impair exonuclease activity, resulting in accumulation of many RNA targets (46).

Neurodegenerative diseases such as amyotrophic lateral sclerosis (ALS) may also be in

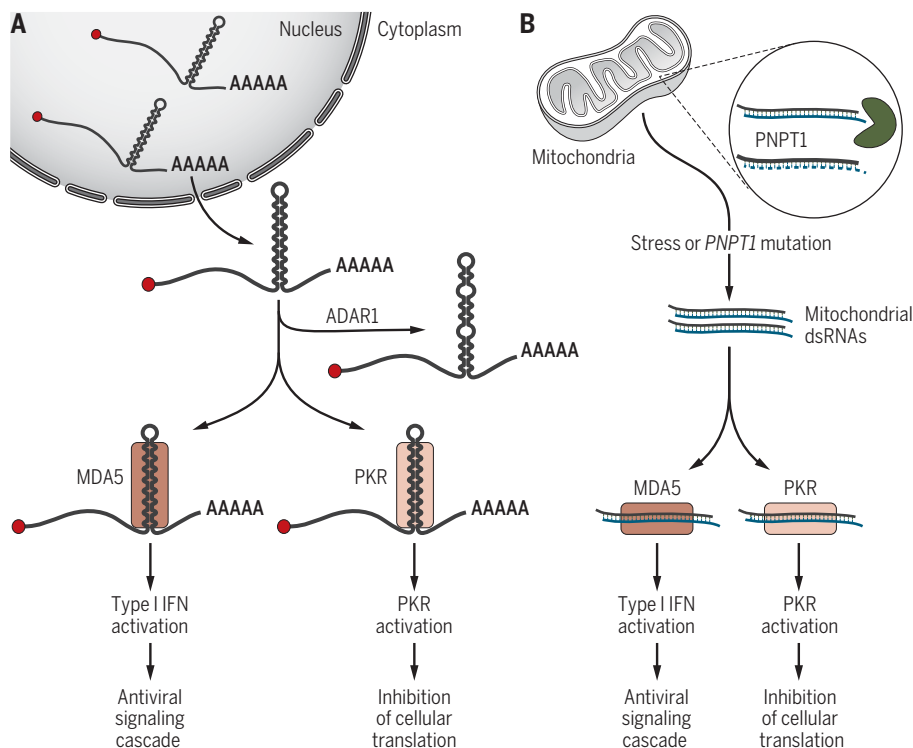


**Fig. 4. Surveillance of dsRNA. (A)** In the cytoplasm, ADAR1 deaminates adenines in dsRNA to inosine, disrupting base pairing. RNAs that fail to undergo editing can activate MDA5 and PKR. **(B)** Formation of mitochondrial dsRNA is normally prevented by PNPT1, which degrades the antisense RNA. Under stress, or when PNPT1 is mutated, mitochondrial dsRNAs can enter the cytosol and activate MDA5 and PKR. Although not shown, MDA5 forms oligomers upon dsRNA binding, whereas PKR forms dimers.

CREDIT: KELLIE HOLOSKI/SCIENCE

part due to the failure of RNA quality control. Notably, in animal models of ALS, toxicity caused by expressing mutant versions of the splicing factors FUS or TDP43 in neurons or nervous tissue can be partially suppressed by overexpressing the key NMD factor called up-frameshift 1 (UPF1) (35). The toxicity associated with the most common mutation in familial ALS and the related frontotemporal dementia, a repeat expansion in the *C9orf72* gene, can similarly be suppressed by overexpressing UPF1 (47). Cell toxicity may derive from an increase in splicing mistakes caused by the mutant proteins, overwhelming the ability of NMD to degrade the ~10% of physiologic mRNAs that are natural NMD targets, the ~33% of newly synthesized mRNAs that normally contain pre-mRNA splicing errors (2), and an additional load of aberrant mRNAs caused by the mutant protein (35). In addition to misprocessed mRNAs, repeat element transcripts and dsRNAs are also increased in the brains of patients with the *C9orf72* lesion and in mouse models of disease (48), hinting at a failure of multiple RNA surveillance pathways.

### Perspectives

The examples discussed above illustrate only some of the ways in which surveillance systems monitor cellular RNA quality. Numerous other mechanisms monitor mRNAs and ncRNAs for correct processing, RNP assembly, nuclear export, and function. Also not discussed is the role of RNA modifications, which stabilize tRNA structure and have an emerging role in mRNA stabilization and surveillance (49). Nonetheless, it is clear that gene expression can be viewed as a tightly orchestrated homeostatic continuum of RNA checks and balances—of spatially and temporally connected RNA processing steps that begin in the nucleus, continue in the

cytoplasm and, in specialized instances, feed back to the nucleus. Most if not all steps rely on the success of the previous step within a defined period of time, or the process will be stopped, usually through RNA destruction, to minimize the ensuing cellular damage. This seemingly straightforward concept behind transcriptomic quality control is complicated by the susceptibility of many steps to genetic or environmental changes and the multitasking abilities of many of the proteins that mediate each step. It follows that disease would result from defects in both the mediators and the sensors of such homeostasis-maintaining systems. Awareness of what defines a transcript that passes quality control is key to the burgeoning use of RNAs as therapeutic targets and tools (50).

### REFERENCES AND NOTES

- C. Belair, S. Sim, S. L. Wolin, *Chem. Rev.* **118**, 4422–4447 (2018).
- T. Kurosaki, M. W. Popp, L. E. Maquat, *Nat. Rev. Mol. Cell Biol.* **20**, 406–420 (2019).
- J. C. Zinder, C. D. Lima, *Genes Dev.* **31**, 88–100 (2017).
- E. M. Weick et al., *Cell* **173**, 1663–1677.e21 (2018).
- M. Lubas et al., *Mol. Cell* **43**, 624–637 (2011).
- M. R. Puno, C. D. Lima, *Proc. Natl. Acad. Sci. U.S.A.* **115**, E5506–E5515 (2018).
- K. Ogami et al., *Genes Dev.* **31**, 1257–1271 (2017).
- N. Meola et al., *Mol. Cell* **64**, 520–533 (2016).
- M. J. Eckwahl, S. Sim, D. Smith, A. Telesnitsky, S. L. Wolin, *Genes Dev.* **29**, 646–657 (2015).
- M. Pirouz, P. Du, M. Munafò, R. I. Gregory, *Cell Rep.* **16**, 1861–1873 (2016).
- P. R. Andersen et al., *Nat. Struct. Mol. Biol.* **20**, 1367–1376 (2013).
- X. Jiao, J. H. Chang, T. Kilic, L. Tong, M. Kiledjian, *Mol. Cell* **50**, 104–115 (2013).
- F. X. Chen, E. R. Smith, A. Shilatfard, *Nat. Rev. Mol. Cell Biol.* **19**, 464–478 (2018).
- W. M. Schulze, F. Stein, M. Rettel, M. Nanao, S. Cusack, *Nat. Commun.* **9**, 1701 (2018).
- H. Le Hir, J. Saulière, Z. Wang, *Nat. Rev. Mol. Cell Biol.* **17**, 41–54 (2016).
- V. Boehm et al., *Mol. Cell* **72**, 482–495.e7 (2018).
- C. C. Venters, J. M. Oh, C. Di, B. R. So, G. Dreyfuss, *Cold Spring Harb. Perspect. Biol.* **11**, a032235 (2019).
- A. C. Chiu et al., *Mol. Cell* **69**, 648–663.e7 (2018).
- M. Stewart, *J. Biol. Chem.* **294**, 2977–2987 (2019).
- S. Chen et al., *Mol. Cell* **74**, 118–131.e7 (2019).
- A. F. Palazzo, E. S. Lee, *Front. Genet.* **9**, 440 (2018).
- D. Rekosh, M. L. Hammarskjöld, *Wiley Interdiscip. Rev. RNA* **9**, e1470 (2018).
- M. A. El-Brolosy et al., *Nature* **568**, 193–197 (2019).
- Z. Ma et al., *Nature* **568**, 259–263 (2019).
- A. P. Schuller, R. Green, *Nat. Rev. Mol. Cell Biol.* **19**, 526–541 (2018).
- S. Juszkiewicz et al., *Mol. Cell* **72**, 469–481.e7 (2018).
- K. Ikeuchi et al., *EMBO J.* **38**, e100276 (2019).
- K. N. D'Orazio et al., *eLife* **8**, e49117 (2019).
- M. L. Glover et al., *bioRxiv* **674358** (2019); <https://doi.org/10.1101/674358>.
- A. L. Karamyshev et al., *Cell* **156**, 146–157 (2014).
- D. J. Morton et al., *RNA* **24**, 127–142 (2018).
- T. van Dijk, F. Baas, P. G. Barth, B. T. Poll-The, *Orphanet J. Rare Dis.* **13**, 92 (2018).
- D. Astuti et al., *Nat. Genet.* **44**, 277–284 (2012).
- R. W. Hunter et al., *Genes Dev.* **32**, 903–908 (2018).
- S. R. Jaffrey, M. F. Wilkinson, *Nat. Rev. Neurosci.* **19**, 715–728 (2018).
- S. Hur, *Annu. Rev. Immunol.* **37**, 349–375 (2019).
- D. P. Reich, B. L. Bass, *Cold Spring Harb. Perspect. Biol.* **11**, a035352 (2019).
- A. Dhir et al., *Nature* **560**, 238–242 (2018).
- C. Uggenti, A. Lepelley, Y. J. Crow, *Annu. Rev. Immunol.* **37**, 247–267 (2019).
- S. Ahmad et al., *Cell* **172**, 797–810.e13 (2018).
- H. Chung et al., *Cell* **172**, 811–824.e14 (2018).
- Y. Kim et al., *Mol. Cell* **71**, 1051–1063.e6 (2018).
- A. Bhate, T. Sun, J. B. Li, *Mol. Cell* **73**, 866–868 (2019).
- Q. Jiang et al., *Cancer Cell* **35**, 81–94.e7 (2019).
- M. W. Popp, L. E. Maquat, *Curr. Opin. Genet. Dev.* **48**, 44–50 (2018).
- R. Tomecki et al., *Nucleic Acids Res.* **42**, 1270–1290 (2014).
- W. Xu et al., *Brain* **142**, 1349–1364 (2019).
- Y. J. Zhang et al., *Science* **363**, eaav2606 (2019).
- N. Jonkhout et al., *RNA* **23**, 1754–1769 (2017).
- F. Pastor et al., *Nat. Rev. Drug Discov.* **17**, 751–767 (2018).

### ACKNOWLEDGMENTS

We apologize to our many colleagues whose work we omitted because of space constraints. We thank T. Kurosaki (University of Rochester) and A. Kane (National Cancer Institute) for help with figures. **Funding:** Research in the Wolin lab is supported by the Intramural Research Program of the National Institutes of Health, National Cancer Institute, Center for Cancer Research. Research in the Maquat lab is supported by National Institutes of Health grants R37 GM074593 and R01 GM059614 to L.E.M. **Competing interests:** The authors declare no competing interests.

10.1126/science.aax2957



## REVIEW

# Mitochondrial communication: Shaping health and disease

Adrienne Mottis\*, Sébastien Herzig\*, Johan Auwerx†

Throughout the animal kingdom, mitochondria are the only organelles that retain their own genome and the transcription and translation machineries that are all essential for energy harvesting. Mitochondria have developed a complex communication network, allowing them to stay in tune with cellular needs and nuclear transcriptional programs and to alleviate mitochondrial dysfunction. Here, we review recent findings on the wide array of mechanisms that contribute to these mitocellular communication networks, spanning from well-studied messenger molecules to mitonuclear genetic interactions. Based on these observations and developments, we advocate a broad and inclusive view on mitocellular interactions, which can have profound impacts on physiological, pathological, and evolutionary processes.

Mitochondria are essential components of eukaryotic cells. They are not, however, isolated organelles; mitochondria exchange molecules—from ions and small metabolites to proteins and lipids—with the rest of the cell and the organism. Mitochondria originate from the endosymbiotic interaction between an  $\alpha$ -proteobacterium and its host cell >1 billion years ago. During evolution, most genes encoded in the mitochondrial genome were transferred to the nucleus, leaving only a few protein-coding genes in the vestigial circular mitochondrial DNA (mtDNA); therefore, mitochondria and nucleus need to communicate to ensure optimal cellular function. Moreover, mitochondria actively influence other cellular components such as the lysosomes, the endoplasmic reticulum (ER), and cytosolic pathways, creating a mitocellular communication network that is based on a variety of signals and cues, akin to different languages (Fig. 1A).

Mitochondria can use such signals to adapt to various stresses, leading to a beneficial outcome in a phenomenon termed mitohormesis. In other cases, deleterious consequences for the cell or the organism ensue. Understanding the differences between adaptive and maladaptive responses to stress is key to leveraging mitochondrial communication to maintain health at the cellular or organismal level. The cellular response to mitochondrial dysfunction ranges from up-regulation of chaperones and proteases to improve proteostasis to the degradation of mitochondria by mitophagy. During aging, mitochondria lose function and mitocellular communication pathways break down; strategies to maintain and invigorate mitochondrial function therefore increase the health span and life span.

Laboratory of Integrative Systems Physiology, Ecole Polytechnique Fédérale de Lausanne (EPFL), CH-1015 Lausanne, Switzerland.

\*These authors contributed equally to this work.

†Corresponding author. Email: admin.auwerx@epfl.ch

## Small molecules as mitochondrial messengers

As the focal point of cellular metabolism, it comes as no surprise that metabolites play a prime role in signaling changes in mitochondrial activity to other cellular compartments (1) (Fig. 1B).

### AMP

Because mitochondria are the major site of adenosine 5'-triphosphate (ATP) generation, ATP levels are a sensitive signal of mitochondrial health. In the wake of decreases in ATP production, ongoing energy utilization leads to an increase in the cellular adenosine 5'-monophosphate (AMP)/ATP ratio, which activates a specialized signaling pathway, the AMP-activated protein kinase (AMPK) pathway. Active AMPK phosphorylates key enzymes and regulatory nodes involved in various metabolic pathways, such as lipid and glucose metabolism, mitochondrial dynamics, autophagy, and protein synthesis, to restore energy balance (2). In addition, AMPK also leads to transcriptional adaptations to energy stress, allowing cells to further match their metabolism to mitochondrial signals, such as decreased ATP levels. Exploiting these mitohormetic energetic stress-signaling pathways through activation of AMPK holds promise for the management of several diseases.

### NAD<sup>+</sup>

The nicotinamide adenine dinucleotide (NAD<sup>+</sup>)/NADH ratio is another indicator of the metabolic status of the mitochondria. NAD<sup>+</sup> is a cofactor for numerous metabolic reactions, but it also serves as a cosubstrate for enzymes such as CD38, poly-ADP-ribose polymerases, and the sirtuins, a family of seven protein deacetylases and deacylases localized in the nucleus (SIRT1, SIRT6, and SIRT7), cytosol (SIRT2), and mitochondria (SIRT3 to SIRT5). Changes in the abundance of NAD<sup>+</sup> directly affect the activity of the sirtuins in multiple cellular compartments, allowing the fine tuning of metabolism through the deacetylation of multiple

metabolic regulators often linked to mitochondrial homeostasis (3). NAD<sup>+</sup> levels not only vary with metabolic activity, e.g., caloric restriction and high-fat diets, but also decrease during aging (4) and increase during exercise and upon pharmacological or nutraceutical interventions that increase NAD<sup>+</sup> levels. Elevated NAD<sup>+</sup> levels are linked to improved health span and life span in multiple model organisms (5). Therefore, NAD<sup>+</sup> levels and their commanding function on the activity of the sirtuins are key contributors to sensing and communicating the mitochondrial metabolic status to other cellular compartments.

### Oxygen

Mitochondria require oxygen for ATP generation, so low oxygen levels, or hypoxia, influence mitochondrial function. In return, mitochondria consume oxygen and thus potentially reduce local oxygen concentration. Cells are capable of sensing low oxygen through prolyl hydroxylase domain proteins (PHDs) that stabilize hypoxia-inducible factor (HIF)-1/2 $\alpha$ . HIF-1 $\alpha$  stabilization mediates some of the deleterious effects of decreased NAD<sup>+</sup> levels and sirtuin activity on mitochondrial function in aged mice, a process that is reversed by boosting NAD<sup>+</sup> levels or by caloric restriction (6). Stabilization of HIF-1 $\alpha$  in vivo by knocking out the VHL (Von Hippel-Lindau) gene in zebrafish or by chronic hypoxia in mice improves the viability of mitochondrial disease models (7). This sounds counterintuitive at first, as restricting oxygen availability may further impair mitochondrial function. However, the fact that hypoxia and HIF signaling allow cells to adapt to lower mitochondrial function and thus decrease the strain imposed on dysfunctional mitochondria explains this apparent conundrum.

### ROS

Mitochondrial dysfunction can also generate toxic by-products such as reactive oxygen species (ROS). Under physiological conditions, ROS act as signaling molecules to control hypoxic responses, immunity, and stem cell function (8). Several lines of evidence also point to ROS as a mediator of longevity downstream of mitochondrial modulation. ROS produced by mitochondria stabilizes HIF-1 $\alpha$  (9), which is important for life-span extension induced by mitochondrial inhibition in *Caenorhabditis elegans* and replicative life span of mammalian cells (10). Thus, mitochondrial ROS and modulation of HIF signaling participate in the mitohormetic response.

### Metabolites

Metabolites that are produced and used inside mitochondria, most notoriously tricarboxylic acid (TCA) cycle components, also signal mitochondrial health. For example, acetyl-coenzyme

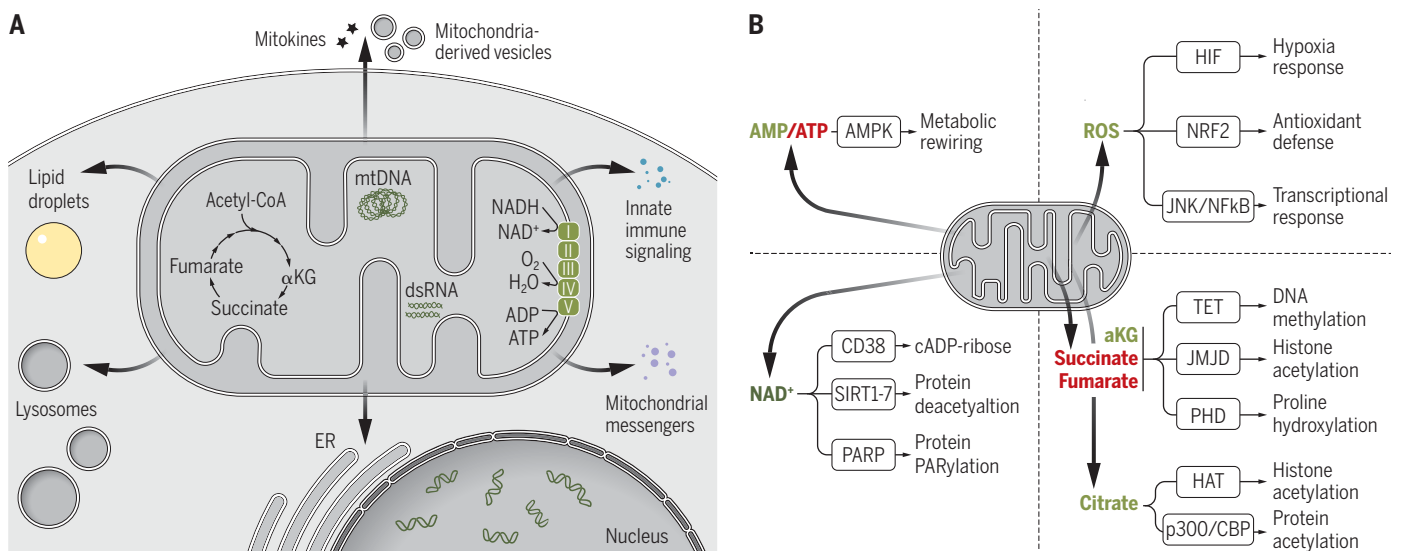


**Fig. 1. Overview of mitocellular interactions. (A)** Mitochondria interact with the cellular environment through physical contacts, signaling molecules, and extracellular signals. **(B)** Mitochondrial metabolic languages. Various mitochondrial metabolites are sent by the mitochondria and translated by cellular signaling pathways into an appropriate response. Green indicates metabolites that activate the pathway and red indicates inhibitory signals.

A (acetyl-CoA), which is produced from various sources inside mitochondria—e.g., pyruvate, amino acids, and fatty acids—enters the TCA cycle to generate citrate. Citrate can either continue within the TCA cycle or exit mitochondria and produce acetyl-CoA, which is an essential cosubstrate for the acetyl transferases to fuel histone and protein acetylation (11). Variations in acetyl-CoA are thus mitochondrial signals that can modulate broad gene expression programs.  $\alpha$ -Ketoglutarate ( $\alpha$ KG), succinate, and fumarate also act as signaling molecules.  $\alpha$ KG serves as a cofactor for dioxygenase enzymes such as the Jumonji C domain-containing histone demethylases (JMJDs), TET (Ten-Eleven Translocation) DNA demethylases, and PHDs; conversely, succinate and fumarate inhibit these  $\alpha$ KG-dependent enzymes (12). Dioxygenases can also be inhibited by 2-hydroxyglutarate (2-HG), a metabolite similar in structure to  $\alpha$ KG. Whereas D2-HG is produced by isocitrate dehydrogenase (IDH)-1/2 mutant cancer cells, mitochondria produce L2-HG during hypoxia (13) or respiratory chain inhibition (14) and regulate metabolism through epigenetic modifications.

#### Proteotoxic stress: Transcriptional and epigenetic regulation

The mitochondrial stress response (MSR) orchestrates the remodeling of gene expression programs after mitochondrial proteotoxic stress. The mitochondrial unfolded protein response (UPR<sup>mt</sup>), an arm of the MSR that signals proteotoxic stress to induce an adaptive response aimed at resolving protein-folding stress, has been particularly well studied in *C. elegans* (15), although recent work suggests its conservation in vertebrates (16–18). The

MSR is induced by toxins or mitochondrial dysfunctions typified by a stoichiometric mismatch between nuclear DNA (nDNA)- and mtDNA-encoded oxidative phosphorylation complex (OXPHOS) subunits, resulting in the accumulation of orphan, unassembled OXPHOS subunits in the mitochondria. Most UPR<sup>mt</sup>-triggering insults are accompanied by a drop in mitochondrial protein import capacity. The localization of ATFS-1 (activating transcription factor associated with stress-1), the master transcriptional regulator of the *C. elegans* UPR<sup>mt</sup>, is also controlled by mitochondrial protein import. Whereas ATFS-1 is normally imported in healthy mitochondria, mitochondrial stress blocks its import, favoring its nuclear localization (19). ATFS-1 induces UPR<sup>mt</sup> genes, including chaperones, proteases, detoxification enzymes, and mediators of metabolic reprogramming. Worm UPR<sup>mt</sup> involves active epigenetic reprogramming; chromatin decompaction and induction of UPR<sup>mt</sup> genes is mediated by the H3K27 demethylases JMJD-3.1 and JMJD-1.2, and a global chromatin compaction is achieved by the histone lysine transferase MET-2, assisted by LIN-65, to avoid transcription of nonessential genes in stressful conditions (20, 21) (Fig. 2A). Epigenetic remodeling caused by mitochondrial stress extends the life span (20) and is transmitted over four generations through histone H3K4 methylation (22). JMJD expression also correlates with life span and UPR<sup>mt</sup> genes in the BXD mouse genetic reference population, indicating that this link between epigenetic remodeling and life extension may be conserved in mammals (20).

In mammalian cells, several mitochondrial insults, including proteotoxic stress and ROS,

signal through the integrated stress response (ISR) (23, 24). The activated GCN2 kinase is one of the kinases known to phosphorylate the translation initiation factor eIF2 $\alpha$  (25). eIF2 $\alpha$  phosphorylation generally leads to a global slowdown of cytosolic, cap-dependent translation, transitioning to stress-induced alternative translation, a mechanism used by various stressors (24). This favors the translation of stress transcripts containing upstream open reading frames, including the *Atf4*, *Atf5*, and *Chop* transcription factors that coordinate a gene expression program considered the mammalian equivalent of UPR<sup>mt</sup> (Fig. 2A). It also suggests that signaling of the mammalian UPR<sup>mt</sup> is directly connected to and partially dependent on the same actors that govern cytosolic proteostasis, a functional link supported by the mitochondria-to-cytosol stress response in *C. elegans* (24). Another mediator of the mammalian MSR was recently shown to adopt a mechanism recalling ATFS-1 signaling in *C. elegans*. After mitochondrial membrane depolarization, G-Protein Pathway Suppressor 2 (GPS2) translocates from mitochondria to the nucleus, where it binds to target promoters and induces H3K9 demethylation, enabling transcription of mitochondrial- and stress-responsive genes, which partially overlap with ATF4 targets (26).

Mitochondrial stress signaling in both invertebrates and vertebrates, albeit different, shares similarities: in both cases, it is dependent on the ATF transcription factor family and involves the modulation of H3 methylation and the mitonuclear translocation of transcription factors. Together with the antioxidant response, the MSR is one of the major mitochondrial pathways mediating mitohormesis.



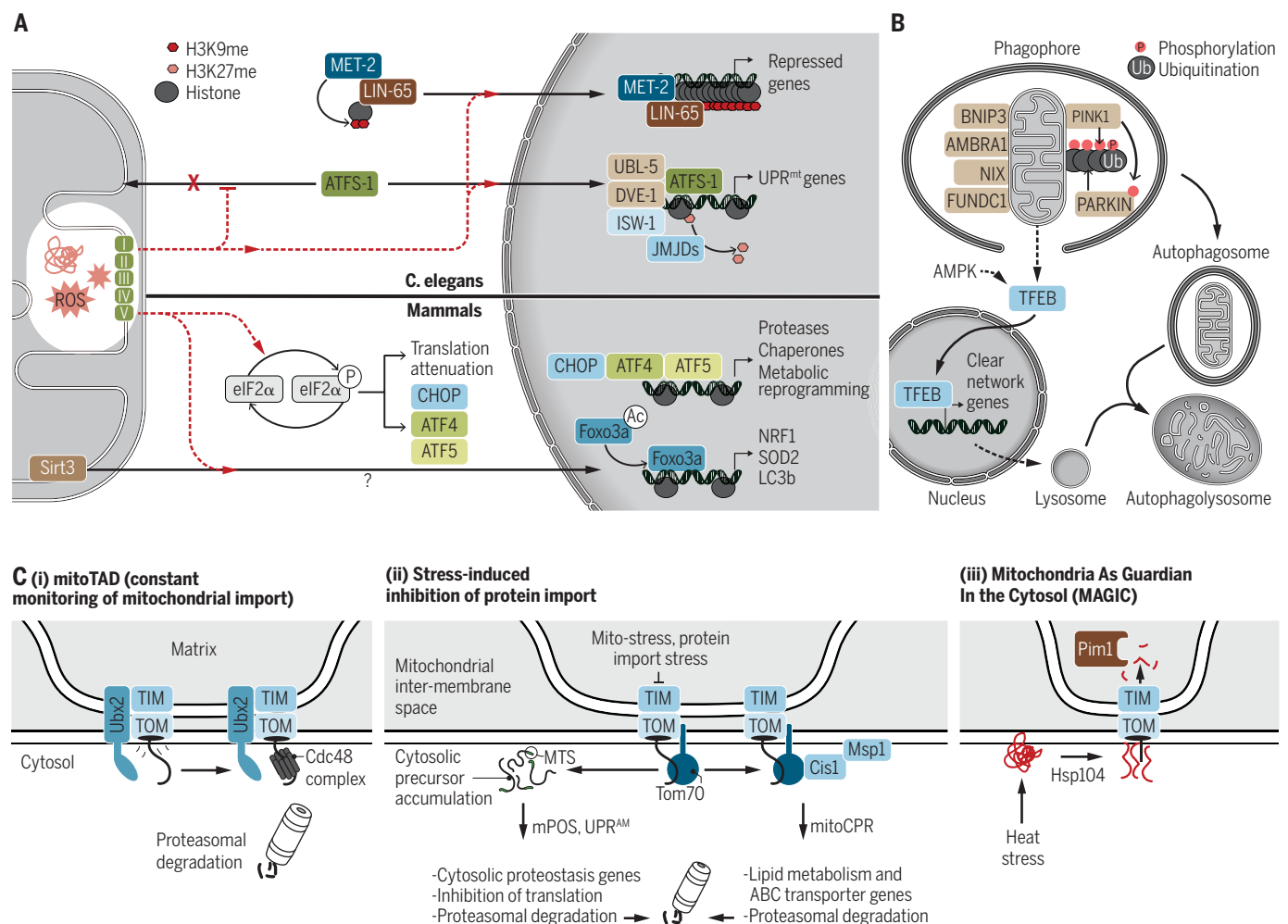


**Fig. 2. Main mechanisms of translational control of the MSR in *C. elegans* and mammals.**

(A) A variety of mitochondrial stressors (unfolded proteins, electron transport chain loss-of-function, ROS) can induce nuclear translocation of transcription factors and changes in chromatin conformation and gene expression. The top part of the panel summarizes MSR signaling in *C. elegans*, and the bottom part focuses on mammalian cells. (B) Overview of the mitophagy pathway mediating the removal of mitochondria. Cross-talk between mitochondria and lysosomes through regulation of lysosomal genes is essential for efficient execution of MSR pathways such as mitophagy. (C) Quality control pathways involving the mitochondrial protein import machinery. (i) In yeast, mitochondrial protein translocation-associated degradation (mitoTAD) is mediated by Ubx2, which recruits the AAA-ATPase

Cdc48 to prevent clogging of the TOM complex with mitochondrial precursor proteins. (ii) Mitochondrial stress slows down mitochondrial protein import and leads to the accumulation of precursors in the cytosol. This “mitochondrial precursor overaccumulation stress” (mPOS) and the UPR activated by mistargeting of proteins (UPR<sup>AM</sup>) triggers programs to restore cytosolic proteostasis, inhibit translation, and activate the proteasome. Protein import stress activates the mitochondrial-compromised protein import response (mitoCPR). It induces gene expression and recruits the AAA-ATPase Msp1 through Tom70 and Cis1 to degrade precursor stalled in the TOM complex. (iii) Protein aggregates that form at mitochondrial surface upon heat shock are disaggregated by the chaperone Hsp104, imported by the TOM complex, and degraded by the LON protease Pim1.

As mentioned before, such adaptations are not always beneficial; the persistent induction of mitohormetic signature genes (e.g., antioxidant and mitophagy genes) by the SIRT3 arm of the UPR<sup>mt</sup> contributes to breast cancer invasiveness (17). The remodeling of mitochondrial signaling therefore appears to be a key step in malignancy, because mitohormesis allows tumor cells to resist oxidative stress and favors their survival.

### Lysosomes, ER, and cytosol

Mitocellular communication also encompasses how mitochondria affect other organelles’

function through direct contact and indirect signaling. Mitochondria physically interact with many other organelles to ensure proper cellular function (27). For example, mitochondria-associated ER membranes (MAMS) are sites of physical proximity of the ER and the mitochondrial outer membranes, allowing lipid and calcium exchanges and dictating how mtDNA is replicated and segregated, as well as when and where mitochondria divide (28).

Mitochondria also physically interact with lysosomes (29). They affect the regulation of lysosomal function, which is essential for au-

tophagy and mitophagy, a process by which damaged mitochondria are removed (Fig. 2B) (30). Lysosomal function is regulated in part by the TFEB (transcription factor EB) family of transcription factors through induction of the CLEAR (Coordinated Lysosomal Expression and Regulation) network, a gene set involved in lysosome biogenesis and function. TFEB activity is modulated downstream of mitochondrial dysfunction by AMPK (31, 32) and through an AMPK-independent, PINK1- and Parkin-dependent pathway that also requires the autophagy gene ATG5 (33). Thus, mitochondrial dysfunction signals to increase lysosomal

function, which in turn ensures proper removal of damaged mitochondria. Lysosomal storage disorders are accompanied by mitochondrial dysfunction and, conversely, mitochondrial diseases are associated with impairments in lysosomal function (34).

This reciprocal regulation of mitochondrial quality by lysosomes and lysosomal function by mitochondrial quality plays a key role in neurodegeneration. Mutations in PINK1 and Parkin and impaired mitophagy are associated with familial forms of Parkinson's disease (PD). Mitochondrial deficiency also occurs in patients with  $\beta$ -amyloid diseases such as Alzheimer's disease (AD). An MSR gene signature typifies patients with AD and cognitive impairment, and activating two components of the MSR, UPR<sup>mt</sup> and mitophagy, in AD models delays protein aggregation and disease progression (35). From a therapeutic perspective, it is interesting that boosting mitophagy by administration of urolithin A improves mitochondrial and muscle function in *C. elegans*, mouse, rat (36), and humans (37); has beneficial effects in animal models of AD (38); and extends life span in *C. elegans* (36). Consistent with these observations, activation of lysosomal function reestablishes youthful proteostasis in old *C. elegans* oocytes immediately before fertilization, a phenomenon accompanied by improvement of mitochondrial parameters (39).

Proteostasis in the mitochondria is also intimately connected to cytosolic proteostasis (24). Despite uncoordinated transcription of nDNA- and mtDNA-encoded OXPHOS mRNAs, OXPHOS stoichiometry is maintained through coordinated protein synthesis (40). During mitochondrial stress in mammals, activation of cap-independent cytosolic translation and activation of the ISR is part of the defense system (23, 24). In yeast, mitochondrial protein translocation-associated degradation (mitoTAD) constitutively monitors mitochondrial protein import to prevent obstruction of the TOM (translocase of the outer membrane) import channel with mitochondrial protein precursors (41) [Fig. 2C(i)]. During mitochondrial stress, the impairment of protein import causes precursor proteins to accumulate in the cytosol, referred to as "mitochondrial precursor over-accumulation stress" (mPOS), leading to the induction of cytosolic genes promoting alternative cytosolic translation mechanisms and protein folding and degradation (24) [Fig. 2C(ii)]. Cytosolic proteostasis is also restored by the UPR activated by mistargeting of proteins (UPR<sup>AM</sup>), which inhibits protein synthesis and activates the proteasome (24), and by the mitochondrial-compromised protein import response (mitoCPR), which removes stalled precursors accumulated on the mitochondrial surface (42) [Fig. 2C(ii)]. Conversely, mitochondria buffer cytosolic protein aggregate load by importing and degrading aggregation-

prone proteins in normal physiological and heat-stress conditions in yeast (43) [Fig. 2C(iii)].

Mitochondria maintain a degree of specialization across tissues and even within the same cell, leading to the coexistence of several mitochondrial subpopulations (44, 45). In brown adipose tissue, peridroplet mitochondria are specialized and dedicated to lipid synthesis and droplet expansion; mediators of mitochondrial dynamics are pivotal in segregating these mitochondria pools (45). In mammalian breast tissue, stemness of daughter cells is conserved by asymmetric sorting of young mitochondria; Parkin and mitochondrial fission are necessary to confine old mitochondria to the perinuclear region of mother cells (46). Likewise, mitochondrial dynamics (fusion) determines the asymmetric distribution of mitochondria and the fate of mammary stem cells in the epithelial-mesenchymal transition (47).

#### **Nucleic acids: Linking mitochondria and inflammation**

Cells depend on pattern-recognition receptors and innate immune pathways to detect and contend with viral and bacterial components in the cytosol. Accommodating an endosymbiotic guest such as the mitochondria implies

### **"...reciprocal regulation of mitochondrial quality by lysosomes and lysosomal function by mitochondrial quality plays a key role in neurodegeneration."**

a possible reactivity toward the components inherited from its bacterial ancestry. Accordingly, immunostimulation can ensue from the release of N-formylated peptides or mtDNA, as well as of several nucleic acid species generated by mitochondria, such as double-stranded RNA (dsRNA) or DNA-RNA hybrids (48). A wide range of mitochondrial insults can lead to the presence of mtDNA in the cytosol or even in the circulation, which upon detection by Toll-like receptors (TLRs), NOD-like receptors (NLRs), or interferon (IFN)-stimulatory DNA receptors, triggers proinflammatory and type I IFN responses (48) involving the cGAS-STING pathway. This pathway is responsible for the inflammation observed in *Pink1*<sup>-/-</sup> and *Prkn*<sup>-/-</sup> mice upon an exercise challenge and for the loss of dopaminergic neurons and motor defects in aged *Prkn*<sup>-/-</sup>; *mutator* mice, which accumulate mtDNA mutations (49). Therefore, mitophagy is key in preventing mitochondrial leakage and the resulting immunostimulation, which seems crucial in the pathogenesis of PD.

Cells also conserved immunity against highly unstable mitochondrial dsRNA, highlighting the pivotal role of the polynucleotide phosphorylase (PNPase), which limits dsRNA accumulation in the mitochondrial matrix and intermembrane space (50). Moreover, mtDNA synthesis is instrumental in activating the NLRP3 inflammasome: various NLRP3 activators induce the release of mtDNA, which amplifies initial NLRP3 priming (51). Together, these findings reinforce the contribution of mitochondria and mitochondrial quality control in immune regulation and warrant the study of mitochondrial contributions to pervasive inflammatory processes that are common in many age-related diseases. Mitochondria can, however, regulate innate and adaptive immunity through multiple mechanisms (52). As an example, disrupted mitophagy and the resulting presentation of mitochondrial antigens are responsible for autoimmunity and PD-like symptoms upon bacterial infection in the intestine of *Pink1*<sup>-/-</sup> mice (53).

#### **Mitokines: Mitochondrial hormones**

Mitochondria not only signal within the cell, but also communicate with distant tissues in a non-cell-autonomous manner through circulating molecules. Mitokines are nuclear-encoded signaling molecules secreted by cells experiencing mitochondrial stress. They are thought to mediate metabolic adaptation of distant tissues by enhancing oxidative metabolism, lipolysis, and ketogenesis as a logical reaction to the energy crisis produced by mitochondrial dysfunction. In mammals, circulating levels of FGF21 (25) and GDF15 (54) are increased in mouse models with mitochondrial dysfunction in an ATF4- and CHOP-dependent manner, respectively, as well as in patients with mitochondrial diseases (15). In *C. elegans*, the Wnt/EGL-20 ligand is the best characterized neuronal mitokine and is dependent on serotonin secretion to transduce an MSR to distant tissues (55). Mitochondrial-derived peptides, which are encoded within alternative reading frames in the mitochondrial genome, can also act as signaling factors to achieve systemic cytoprotective effects and stress resistance by improving insulin sensitivity and adiposity (56).

Finally, one can speculate about mitochondria communicating with distant tissues through mitochondria-derived vesicles containing mtDNA or mitochondrial components (57, 58) or even through intercellular transfer of mitochondria (59). These processes can be triggered upon acute neuronal or cardiac stress (60, 61), leading to positive feedback and cytoprotection of the recipient cells. Worm and mouse neuronal cells can also transfer mitochondria to outsource their degradation to other cells (62, 63). Although the signaling role of these mechanisms has not yet been



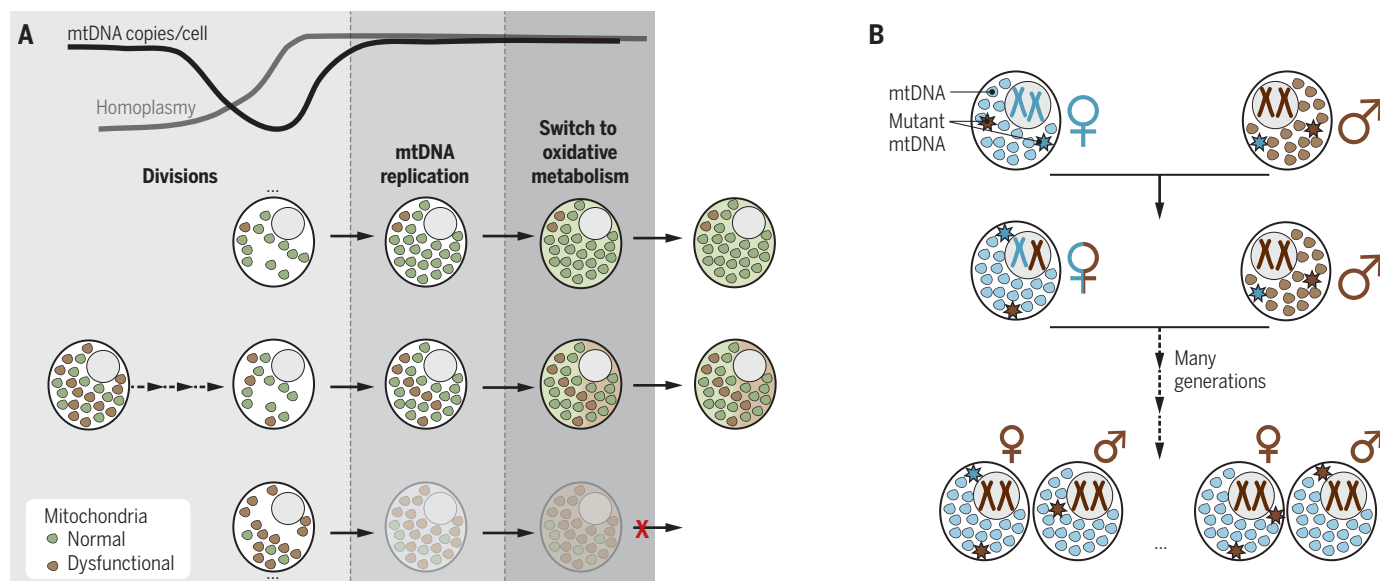


**Fig. 3. Mitonuclear genomic interactions.** (A) Simplified representation of the mitochondrial germline bottleneck. (B) When mtDNA and nDNA ancestries diverge, new haplotype-specific polymorphisms tend to match the nuclear ancestry rather than the mitochondrial haplotype in which they arose. [Figure adapted from Wei *et al.* (70)]

established, it is tempting to speculate that the molecular content of these different vesicles could trigger adaptive responses in recipient cells.

### Interactions between mitochondrial and nuclear genomes

Because both the mitochondrial and nuclear genomes encode mitochondrial proteins, they have evolved functional and genetic interactions as another form of mitonuclear communication that determines mtDNA maintenance, expression, and transmission (64).

mtDNA encodes 13 subunits that play key roles in the proper function of the OXPHOS complexes (65). Despite the importance of these proteins, mtDNA has a high mutation rate that is resolved at both the organism and population levels (65). At the organism level, mechanisms exist in female germline cells to prevent transmission of deleterious mtDNA mutations to the next generation, underpinning mitochondrial germline bottleneck effects (66, 67) (Fig. 3A). Early primordial germ cells (PGCs) experience a profound decrease in mtDNA copy number, reducing the number of mtDNA variants in each cell. This is followed by a phase of mtDNA replication, resulting in increased level of homoplasmy in each PGC (67). The subsequent shift from glycolytic to oxidative metabolism in the PGCs acts as a soliciting test allowing expression and selection of mtDNA variants that do not impair mitochondrial function.

Because four out of five OXPHOS complexes combine subunits from mixed origins, bioenergetics are crucially affected by the compatibility of mitochondrial and nuclear OXPHOS

subunits and by extension by the compatibility of the two genomes (65). Nuclear and mitochondrial genomes coevolved in populations of the same species, ultimately leading to the complementarity of mtDNA haplogroups and their nuclear background (65). This mitonuclear compatibility at the population level reflects the fact that mitonuclear genetic interactions profoundly affect mitochondrial function and whole-body physiology. In the mouse C57BL/6 strain, replacing mtDNA with that of the NZB/OlaHsd strain triggers a limited level of stress and induces proteostasis, UPR<sup>mt</sup>, and ROS signaling, ultimately remodeling mitochondrial dynamics and improving metabolism and aging (68). In humans, discordance of ancestry between nuclear and mitochondrial genomes leads to incompatibility that affects crucial markers of mitochondrial fitness such as mtDNA copy number (69). Analyzing ~13,000 human whole-genome sequences demonstrated that selection of mtDNA variants is influenced by the nuclear genetic background: new polymorphisms more likely converge to match the nuclear rather than the mitochondrial genetic ancestry (Fig. 3B) (70). In other words, the nuclear genome has a selective power over mtDNA polymorphisms.

mtDNA can thus be seen as an uncontrollable guest evolving in a selfish manner and eventually causing mitonuclear conflicts (71); therefore, mitonuclear genetic interactions were shaped into mechanisms guiding the fate of mtDNA, such as the germline bottleneck at the organism scale and the nucleus-imposed selection on mtDNA at the population level. A detailed understanding of mitonuclear genomic

compatibility and its consequences must be sought to master the promise of mitochondrial replacement therapy (72) and to improve the genotype-specific efficacy of some treatments. Genome-wide association studies often ignore mtDNA variants (73) and mitonuclear genetic interactions, advocating for systematic investigation of mitonuclear genotypic predisposition to diseases.

### Conclusions and perspectives

Mitochondria have a versatile and complex nature; they can take the appearance of a unified network or of individual units depending on the context, continuously communicating and interacting with the cellular milieu and thus challenging our vision and working models. As an example, mtDNA haplogroups are known to directly affect physiology and to be associated with diseases such as degenerative or autoimmune disorders, although the exact mechanisms remain unclear (65). The intricate links between multiple aspects of mammalian physiology and the gut microbiome are well established. The results of this review suggest that we also consider the importance of our so-called mitobiome, which is 10-fold larger than our microbiome and more complex (given that there are multiple differences in subcellular and cellular pools of mitochondria). Mitochondria should thus be thought of as small, “semiautonomous” (bacterial-like) entities that have their own genome and are occasionally shaped into populations that are able to communicate with each other, with other organelles, and even with distant tissues through a multitude of

languages. If these mitochondrial languages are fully understood, then this will certainly unveil their central impact on homeostasis in a deeper and more integrated dimension than ever thought and would allow the development of mitochondrial medicines to treat diverse pathologies (74, 75).

## REFERENCES AND NOTES

1. N. S. Chandel, *Cell Metab.* **22**, 204–206 (2015).
2. S. Herzig, R. J. Shaw, *Nat. Rev. Mol. Cell Biol.* **19**, 121–135 (2018).
3. E. Verdin, *Science* **350**, 1208–1213 (2015).
4. L. Mouchiroud *et al.*, *Cell* **154**, 430–441 (2013).
5. E. Katsyuba, J. Auwerx, *EMBO J.* **36**, 2670–2683 (2017).
6. A. P. Gomes *et al.*, *Cell* **155**, 1624–1638 (2013).
7. I. H. Jain *et al.*, *Science* **352**, 54–61 (2016).
8. L. Diebold, N. S. Chandel, *Free Radic. Biol. Med.* **100**, 86–93 (2016).
9. N. S. Chandel *et al.*, *Proc. Natl. Acad. Sci. U.S.A.* **95**, 11715–11720 (1998).
10. M. Schieber, N. S. Chandel, *Curr. Biol.* **24**, R453–R462 (2014).
11. S. L. Campbell, K. E. Wellen, *Mol. Cell* **71**, 398–408 (2018).
12. S. Nowicki, E. Gottlieb, *FEBS J.* **282**, 2796–2805 (2015).
13. W. M. Oldham, C. B. Clish, Y. Yang, J. Loscalzo, *Cell Metab.* **22**, 291–303 (2015).
14. S. E. Weinberg *et al.*, *Nature* **565**, 495–499 (2019).
15. T. Shpilka, C. M. Haynes, *Nat. Rev. Mol. Cell Biol.* **19**, 109–120 (2018).
16. R. H. Houtkooper *et al.*, *Nature* **497**, 451–457 (2013).
17. T. C. Kenny, A. J. Craig, A. Villanueva, D. Germain, *Cell Rep.* **27**, 2292–2303.e6 (2019).
18. Y. Wu *et al.*, *Cell* **158**, 1415–1430 (2014).
19. A. M. Nargund, M. W. Pellegrino, C. J. Fiorese, B. M. Baker, C. M. Haynes, *Science* **337**, 587–590 (2012).
20. C. Merkwirth *et al.*, *Cell* **165**, 1209–1223 (2016).
21. Y. Tian *et al.*, *Cell* **165**, 1197–1208 (2016).
22. C. Ma *et al.*, *Nat. Cell Biol.* **21**, 319–327 (2019).
23. K. Pakos-Zebrucka *et al.*, *EMBO Rep.* **17**, 1374–1395 (2016).
24. D. D'Amico, V. Sorrentino, J. Auwerx, *Trends Biochem. Sci.* **42**, 712–725 (2017).
25. P. M. Quirós, A. Mottis, J. Auwerx, *Nat. Rev. Mol. Cell Biol.* **17**, 213–226 (2016).
26. M. D. Cardamone *et al.*, *Mol. Cell* **69**, 757–772.e7 (2018).
27. I. Gordaliza-Alaguero, C. Cantó, A. Zorzano, *EMBO Rep.* **20**, e47928 (2019).
28. H. Wu, P. Carvalho, G. K. Voeltz, *Science* **361**, ean5835 (2018).
29. Y. C. Wong, S. Kim, W. Peng, D. Krainc, *Trends Cell Biol.* **29**, 500–513 (2019).
30. S. Pickles, P. Vigié, R. J. Youle, *Curr. Biol.* **28**, R170–R185 (2018).
31. L. J. Eichner *et al.*, *Cell Metab.* **29**, 285–302.e7 (2019).
32. L. Fernández-Mosquera *et al.*, *Sci. Rep.* **7**, 45076 (2017).
33. C. L. Nezhich, C. Wang, A. I. Fogel, R. J. Youle, *J. Cell Biol.* **210**, 435–450 (2015).
34. N. Plotegher, M. R. Duchén, *Trends Mol. Med.* **23**, 116–134 (2017).
35. V. Sorrentino *et al.*, *Nature* **552**, 187–193 (2017).
36. D. Ryu *et al.*, *Nat. Med.* **22**, 879–888 (2016).
37. P. A. Andreux *et al.*, *Nat. Metab.* **1**, 595–603 (2019).
38. E. F. Fang *et al.*, *Nat. Neurosci.* **22**, 401–412 (2019).
39. K. A. Bohnert, C. Kenyon, *Nature* **551**, 629–633 (2017).
40. M. T. Couvillion, I. C. Soto, G. Shipkovenska, L. S. Churchman, *Nature* **533**, 499–503 (2016).
41. C. U. Mårtensson *et al.*, *Nature* **569**, 679–683 (2019).
42. H. Weidberg, A. Amon, *Science* **360**, ean4146 (2018).
43. L. Ruan *et al.*, *Nature* **543**, 443–446 (2017).
44. L. L. Lackner, *Trends Cell Biol.* **29**, 580–590 (2019).
45. I. Y. Benador *et al.*, *Cell Metab.* **27**, 869–885.e6 (2018).
46. P. Katajisto *et al.*, *Science* **348**, 340–343 (2015).
47. M.-J. Wu *et al.*, *Cell Metab.* **29**, 993–1002.e6 (2019).
48. A. P. West, G. S. Shadel, *Nat. Rev. Immunol.* **17**, 363–375 (2017).
49. D. A. Sliter *et al.*, *Nature* **561**, 258–262 (2018).
50. A. Dhir *et al.*, *Nature* **560**, 238–242 (2018).
51. Z. Zhong *et al.*, *Nature* **560**, 198–203 (2018).
52. E. L. Mills, B. Kelly, L. A. J. O'Neill, *Nat. Immunol.* **18**, 488–498 (2017).
53. D. Matheoud *et al.*, *Nature* **571**, 565–569 (2019).
54. H. K. Chung *et al.*, *J. Cell Biol.* **216**, 149–165 (2017).
55. Q. Zhang *et al.*, *Cell* **174**, 870–883.e17 (2018).
56. S.-J. Kim, J. Xiao, J. Wan, P. Cohen, K. Yen, *J. Physiol.* **595**, 6613–6621 (2017).
57. A. Sugiura, G. L. McLelland, E. A. Fon, H. M. McBride, *EMBO J.* **33**, 2142–2156 (2014).
58. D. Torralba *et al.*, *Nat. Commun.* **9**, 2658 (2018).
59. D. Torralba, F. Baixauli, F. Sánchez-Madrid, *Front. Cell Dev. Biol.* **4**, 107 (2016).
60. V. J. J. Cadete *et al.*, *J. Physiol.* **594**, 5343–5362 (2016).
61. K. Hayakawa *et al.*, *Nature* **535**, 551–555 (2016).
62. C. H. Davis *et al.*, *Proc. Natl. Acad. Sci. U.S.A.* **111**, 9633–9638 (2014).
63. I. Melentijevic *et al.*, *Nature* **542**, 367–371 (2017).
64. D. B. Sloan *et al.*, *Nat. Rev. Genet.* **19**, 635–648 (2018).
65. D. C. Wallace, *Cell* **163**, 33–38 (2015).
66. V. I. Floros *et al.*, *Nat. Cell Biol.* **20**, 144–151 (2018).
67. J. B. Stewart, P. F. Chinnery, *Nat. Rev. Genet.* **16**, 530–542 (2015).
68. A. Latorre-Pellicer *et al.*, *Nature* **535**, 561–565 (2016).
69. A. A. Zaidi, K. D. Makova, *Nat. Ecol. Evol.* **3**, 213–222 (2019).
70. W. Wei *et al.*, *Science* **364**, eaau6520 (2019).
71. J. C. Havird *et al.*, *Curr. Biol.* **29**, R496–R511 (2019).
72. D. C. Wallace, *Nat. Genet.* **50**, 1642–1649 (2018).
73. G. Pesole *et al.*, *EMBO Rep.* **13**, 473–474 (2012).
74. P. A. Andreux, R. H. Houtkooper, J. Auwerx, *Nat. Rev. Drug Discov.* **12**, 465–483 (2013).
75. M. P. Murphy, R. C. Hartley, *Nat. Rev. Drug Discov.* **17**, 865–886 (2018).

## ACKNOWLEDGMENTS

We thank members of the Auwerx lab, in particular A. Bachmann, as well as N. Chandel and J. A. Enríquez, for their helpful comments on the manuscript. We apologize for the omission of many relevant studies due to space constraints. **Funding:** The work in the laboratory of the authors is supported by the EPFL, the European Research Council (ERC-AdG-787702), and the Swiss National Science Foundation (31003A-179435). **Competing interests:** J.A. is a founder of Mitobridge, which develops mitochondrial therapeutics.

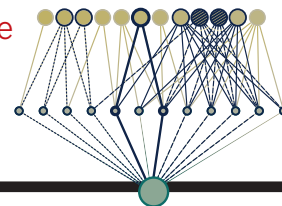
10.1126/science.aax3768



# RESEARCH

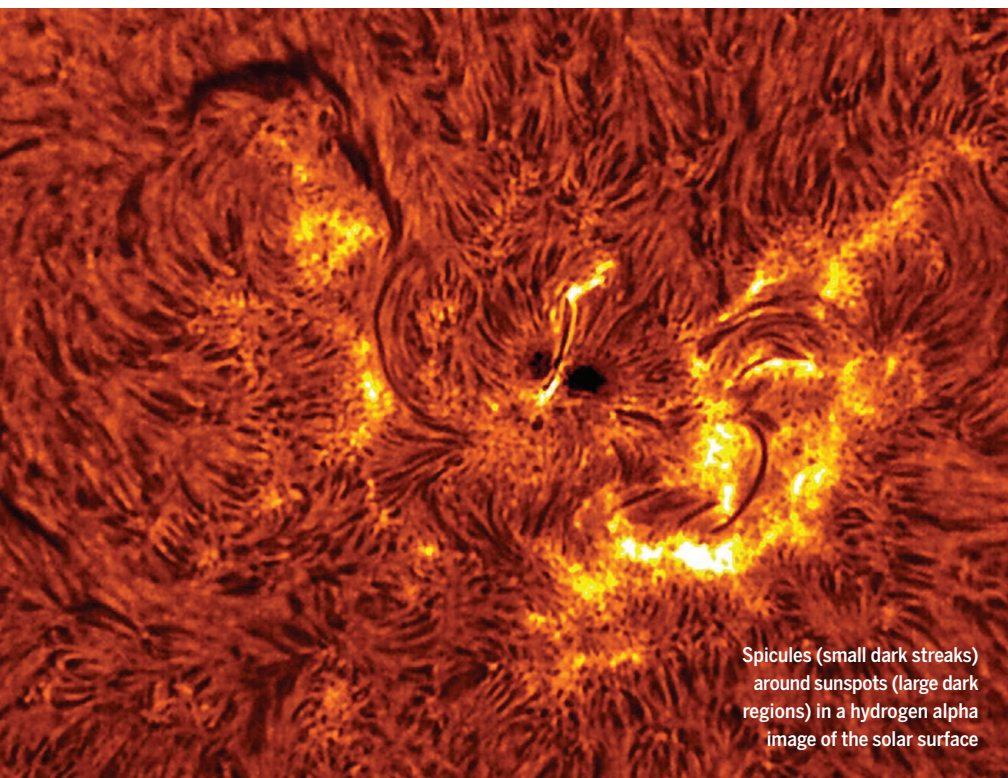
Many factors drive  
change in soils

Rillig *et al.*, p. 886



IN SCIENCE JOURNALS

Edited by Michael Funk



Spicules (small dark streaks)  
around sunspots (large dark  
regions) in a hydrogen alpha  
image of the solar surface

## SOLAR PHYSICS

### Magnetic fields can generate spicules

**S**picules are small jets of plasma from the surface of the Sun that last a few minutes. Around a million are occurring at any moment, even during periods of low solar activity. The mechanism responsible for launching spicules remains unknown, as is their contribution to heating the solar corona. Samanta *et al.* observed emerging spicules and the magnetic fields in the adjacent solar surface. They found that many spicules appear a few minutes after a patch of reverse-polarity magnetic field and that the overlying corona is heated shortly afterward. This result provides evidence that magnetic reconnection can generate spicules, which then transfer energy to the corona. —KTS

*Science*, this issue p. 890

## BIOMEDICINE

### Tuning stress protects cognition

Down syndrome (DS) is a chromosomal disorder that occurs when a person has an extra copy of chromosome 21. DS causes intellectual disabilities, among other health issues, but little is known about the mechanisms underlying the memory deficits in DS. Zhu *et al.* used a multidisciplinary approach to show that a defect in integrated stress response, a conserved pathway that controls protein homeostasis, can explain the cognitive and neuronal deficits in a mouse model of DS (see the Perspective by Halliday and

Mallucci). These insights into the biological basis underlying DS could potentially help in the design of treatments for this condition. —SMH

*Science*, this issue p. 843;  
see also p. 797

## STRUCTURAL BIOLOGY

### The architecture of the RSC complex

RSC is a Snf2-family chromatin remodeler complex that controls the promoter architecture of most of the genes in yeast. Using single-particle cryo-electron microscopy, Ye *et al.* determined the structure of RSC bound to the nucleosome. The structure

reveals the modular architecture of RSC, shows how RSC engages the nucleosome, and explains the remodeling directionality. RSC shows strong similarities to homologous human complexes that are frequently mutated in cancers, and this structure provides valuable information for understanding these systems. —SYM

*Science*, this issue p. 838

## QUANTUM OPTICS

### Irreversible splitting of light

Prisms and dielectric beam splitters tend to be unitary and reversible optical elements,

with the quantum properties of the photons largely irrelevant. Kurtscheid *et al.* introduce a method of irreversibly, but coherently, populating a split state with photons by thermalizing the photons into a low-energy ground state by repeated absorption-emission interaction with a fluorescent dye within a double-dimple optical cavity. Generation of such a coherent split state could be used as a precursor step to the quasi-continuous creation of many-body entangled states of light, which could be useful in applications in quantum communication, computing, and simulation. —ISO

*Science*, this issue p. 894

CREDITS (FROM TOP): RILLIG *ET AL.*; GREG PIEPOL/SCIENCE SOURCE

## IMMUNOLOGY

## Peptide mimicry breaks the heart

Myocarditis, a prolonged chronic inflammation of heart muscle, can eventually progress to inflammatory cardiomyopathy, a serious condition associated with heart failure. Activated T helper ( $T_H$ ) cells that recognize myosin heavy chain 6–derived peptides are thought to play a central role in this pathogenesis. Using a mouse model of myocarditis, Gil-Cruz *et al.* found that cardiac myosin–reactive  $T_H$  cells are initially primed by myosin-peptide mimics derived from commensal *Bacteroides* species in the gut (see the Perspective by Epelman). Unlike healthy controls, human myocarditis patients also showed detectable immune reactivity to both *Bacteroides* and cardiac myosin antigens. Treatment with antibiotics dampened inflammatory responses and prevented lethal heart disease. —STS

*Science*, this issue p. 881;  
see also p. 806

## NUTRIENT DELIVERY

## Mitigating micronutrient deficiency

Micronutrient deficiencies that impair growth and contribute to disease remain leading public health concerns, particularly within the developing world. Although fortification of food can help treat deficiencies, heat used during cooking and other conditions can degrade vitamins, preventing adequate absorption. Anselmo *et al.* developed a polymer coating to encapsulate micronutrients, 11 of which showed improved stability against oxidation, heat, and other conditions. Micronutrients were absorbed by the intestine when microparticles were administered to rodents. The researchers used data from two clinical trials and experiments using human intestinal tissue to optimize microparticle formulations, enhance iron loading, improve

bioavailability, retain stability during cooking, and allow for scale-up. This microparticle platform could help improve oral delivery of micronutrients. —CC

*Sci. Transl. Med.* **11**, eaaw3680 (2019).

## ANTHROPOLOGY

## Change in climate withered an empire

From roughly 912 to 609 BCE, the Neo-Assyrian Empire rose as one of the most powerful superpowers of its time, dominating much of the Near East. Sinha *et al.* propose that megadroughts played an important role in the rapid decline in the empire's power, from its height around 670 BCE to its collapse only six decades later. Precisely dated cave deposits from northern Iraq preserved a record of precipitation and effective moisture over a 4000-year period that includes the span of the Neo-Assyrian Empire. This record demonstrates that the rise of the empire occurred during a roughly 200-year interval of abundant rainfall. Subsequently, severe megadroughts characterized the climate across the empire, likely contributing to the empire's rapid decline. —KVH

*Sci. Adv.* 10.1126/sciadv.aax6656 (2019).

## ELECTROCHEMISTRY

## Nanocage-chain fuel cell catalysts

The expense and scarcity of platinum has driven efforts to improve oxygen-reduction catalysts in proton-exchange membrane fuel cells. Tian *et al.* synthesized chains of platinum-nickel alloy nanospheres connected by necking regions. These structures can be etched to form nanocages with platinum-rich surfaces that are highly active for oxygen reduction. In fuel cells running on air and hydrogen, these catalysts operated for at least 180 hours. —PDS

*Science*, this issue p. 850

## IN OTHER JOURNALS

Edited by **Caroline Ash**  
and **Jesse Smith**



## ORGANIC CHEMISTRY

## Anti-Markovnikov hydroamination

Catalytic hydroamination is an efficient and waste-free way to form amines, enamines, and imines, which are important synthetic intermediates in many organic syntheses of bioactive compounds and often have essential physiological and biological activity themselves. The development of these types of hydroamination reactions is a persistent research topic in organic and pharmaceutical chemistry. Miller *et al.* report a synthetic protocol for the intermolecular anti-Markovnikov hydroamination of unactivated alkenes with primary alkylamines to generate secondary amine products in the presence of an iridium photocatalyst and a thiol cocatalyst. This protocol addresses a long-standing synthetic challenge of monoalkylation of primary amines and demonstrates high selectivity for secondary amines over tertiary amine products, though further work is required to understand its underlying mechanism. —YS

*J. Am. Chem. Soc.* **141**, 16590 (2019).

## POLLINATION

## Nectar—but not for parasites

Bumble bees are vulnerable to parasitism by a flagellated trypanosome (some species of which are important human pathogens). The parasite *Crithidia bombi*, in combination with environmental stresses, can promote declines in bumble bee populations by reducing foraging and reproductive success. Koch *et al.* developed a chromatographic pipeline to efficiently search for natural products in single-species honey that might protect pollinators. Of the four most bioactive species the authors found, nectar from *Calluna vulgaris*, an iconic moorland plant in the United Kingdom, contains a compound called callunene, which promotes flagella shedding by the parasite, eliminating its ability to attach to the bumble bees' gut epithelial cells and cause infection. If bees ingest *C. vulgaris* nectar in high amounts, they are protected from infection, but if they are already infected, there is no curative effect. —CA

*Curr. Biol.* **29**, 3494 (2019).

PHOTO: RDW AERIAL IMAGING/ALAMY STOCK PHOTO





## FOREST CONSERVATION

### Corridors for biodiversity among oil palms

**C**onnections between areas of natural habitat are key to conservation in landscapes fragmented by human activity. Scriven *et al.* modeled the effectiveness of set-aside conservation patches in oil palm plantation landscapes in Borneo for connectivity among forest organisms with different levels of dispersal ability. They found that the connectivity benefits of the set-aside patches, if they are fully reforested, would be greatest for relatively poorly dispersing organisms, such as smaller winged insects. These findings provide guidance for the effective management of the patches of habitat and biodiversity that remain in these highly impacted landscapes. —AMS *J. Appl. Ecol.* **56**, 2274 (2019).

Forest corridors in oil palm plantations help the dispersal of smaller organisms.

## NANOMATERIALS

### Watching metal nanoparticle exsolution

Metal nanoparticles (NPs) grown from complex oxides through exsolution can be better anchored to their support in “sockets” than ones deposited on the surface. Neagu *et al.* followed the formation of nickel NPs from two perovskites,  $\text{La}_{0.43}\text{Ca}_{0.37}\text{Ni}_{0.06}\text{Ti}_{0.94}\text{O}_3$  and  $\text{La}_{0.8}\text{Ce}_{0.1}\text{Ni}_{0.4}\text{Ti}_{0.6}\text{O}_3$ . An environmental transmission electron microscope enabled kinetics and structural studies of powder

samples exposed to reducing gases [hydrogen ( $\text{H}_2$ ) and carbon monoxide ( $\text{CO}$ )] at high temperatures (650° to 1000°C). Different atmospheric conditions changed NP shape—exposure to  $\text{H}_2$  formed rounder NPs, NPs formed in vacuum were more faceted, and exposure to  $\text{CO}$  formed cubic NPs. NP growth was not monotonic but occurred in a stepwise manner, alternating between growth spurts and periods of quiescence. —PDS

*ACS Nano* **10**, 1021/acs.nano.9b05652 (2019).

3D model of a nickel nanoparticle grown under vacuum on perovskite

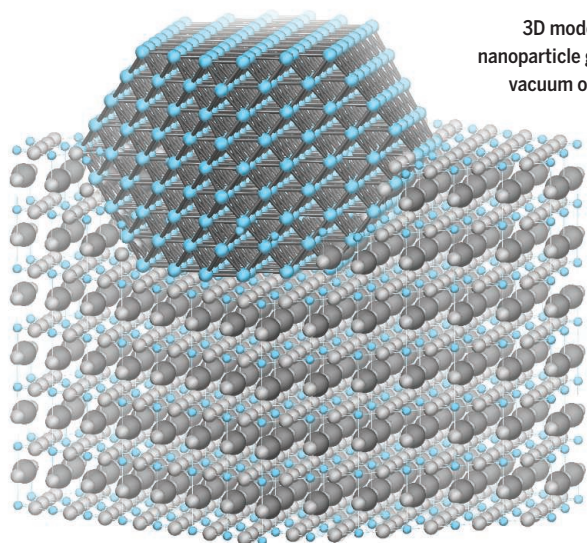


IMAGE: NEAGU ET AL., ACS NANO 10, 1021/ACS.NANO.9B05652 (2019)

## REPRODUCTION

### Organelle fusion in fertility

The fertility of organisms as diverse as male fruit flies and mice requires a mitochondrial fusion gene. But what for? Mitochondria cluster and fuse during early sperm development with the help of guanosine triphosphatases called mitofusins. When mitochondrial fusion fails, oxidative phosphorylation decreases, and mitochondrial transport and degradation are also affected. Varuzhanyan *et al.* tested how reliant the success of male germ cell development in mice is on mitofusins. Mitofusins are needed to trigger a metabolic shift during meiosis. When mitofusins are eliminated, germ cells display damage to the cristae ultrastructure, increased apoptosis, reduced oxidative phosphorylation, and a loss of mitochondrial ribosomes. Thus, mitofusins are vital for maintaining translation of respiratory chain and mitochondrial proteins to enable male fertility. —BAP

*eLife* **8**, e51601 (2019).

## T CELLS

### VISTA is a pH-selective checkpoint

The V-domain immunoglobulin suppressor of T cell activation (VISTA) is a negative checkpoint regulator that restrains T cell antitumor activity. VISTA modulates innate and adaptive immune responses using mechanisms unlike those of other immune checkpoint molecules. Johnston *et al.* report that under acidic pH conditions, such as those found within the tumor microenvironment, VISTA suppresses T cell activity. The researchers further show that VISTA deactivates immune responses because it is a ligand for the adhesion and coinhibitory receptor P-selectin glycoprotein ligand-1 (PSGL-1), which it engages through a histidine-rich interface. Disruption of VISTA–T cell interactions using acidic pH-selective antibodies could reverse T cell suppression. Modulation of VISTA may therefore provide a therapeutic means to enhance antitumor immunity. —PNK

*Nature* **574**, 565 (2019).

## SOCIAL SCIENCE

### Predicting future terror attacks

Future attacks by terrorist organizations are difficult to predict because their organizational capabilities and resources are hidden. Yang *et al.* developed a modeling approach for estimating these parameters to predict future terror attacks. By testing their model against the Global Terrorism Database, they could explain about 60% of the variance in a terrorist group's future lethality using only its first 10 to 20 attacks, outperforming previous models. The model also captures the dynamics by which terror organizations shift from random, low-fatality attacks to nonrandom, high-fatality attacks. These results have implications for efforts to combat terrorism worldwide. —TSR

*Proc. Natl. Acad. Sci. U.S.A.* **116**, 21463 (2019).

ALSO IN *SCIENCE* JOURNALS

Edited by Michael Funk

**DEVELOPMENTAL BIOLOGY**  
**In vitro development of monkey embryos**

Owing to technical and ethical limitations, the molecular and cellular mechanisms underlying primate gastrulation are far from clear (see the Perspective by Tam). Two independent studies used an in vitro culture system to study cynomolgus monkey embryo postimplantation development up to and beyond gastrulation (day 9 to day 20). Niu *et al.* observed in vivo morphogenetic events and used single-cell RNA sequencing and single-cell chromatin accessibility to study the distinct cell lineages in developing embryos. Ma *et al.* also observed that key events of in vivo early development were recapitulated in their system, and single-cell RNA sequencing analysis revealed molecular signatures of post-implantation cell types. These systems will help elucidate the dynamics and regulation of gastrulation in primates, including possible relevance to human development. —BAP

*Science*, this issue p. 837, p. 836;  
see also p. 798

**LASER PHYSICS**  
**Filling the terahertz gap**

Compared with other wavelengths, coherent sources of electromagnetic radiation in the terahertz regime are relatively scarce. Despite a number of applications in security imaging, spectroscopy, and chemical analysis, it has been experimentally challenging to produce such light. Chevalier *et al.* demonstrate an approach involving the excitation of a molecular gas with a quantum cascade laser. They show that they can tune into a broad range of desired wavelengths by carefully selecting the required molecular transition. A compact platform—the size of a shoe box—and widely tunable source of coherent terahertz radiation

should find immediate application across a number of fields. —ISO

*Science*, this issue p. 856

**GLASSES****A glass that won't break**

Oxide glasses are important for applications ranging from smartphone screens to window panes. One familiar feature of glass is that it fractures and shatters when rapidly deformed, limiting the number of potential uses. However, Frankberg *et al.* found that they could deform thin films of glassy alumina ( $\text{Al}_2\text{O}_3$ ) with high strain rates at room temperature (see the Perspective by Wondraczek). This surprising observation is supported by simulations of the material that show that dense and flawless glassy alumina samples can deform this way. The discovery provides important insight into designing new glasses that might be more fracture resistant. —BG

*Science*, this issue p. 864;  
see also p. 804

**OPTOELECTRONICS****Switching light on-chip**

The development of practical, reconfigurable photonics requires a platform that can be scaled to large circuits and driven by low-voltage complementary metal-oxide semiconductor (CMOS) electronics. Such a platform requires that switching devices possess a compact footprint, low driving voltages, fast switching, low optical losses, and low power consumption. Haffner *et al.* demonstrate that the combination of opto-electro-mechanical effects with plasmonic devices can provide a platform that meets all the above criteria. The results are promising for developing on-chip integrated optical networks that can be switched by CMOS-level voltages. —ISO

*Science*, this issue p. 860

**POLYMER CHEMISTRY**  
**Cross-linking a range of alkyl polymers**

Some alkyl polymers, such as polyethylene, can be cross-linked by using peroxides or high-energy radiation or through the addition of a radical forming agent. Others, like polypropylene, are likely to undergo chain scission, and this process tends to be uncontrolled in the distribution of the cross-links. Lepage *et al.* developed a widely applicable approach using *bis*-diazirine molecules as cross-linking agents (see the Perspective by de Zwart *et al.*). These molecules can be thermally or photochemically activated to form carbenes that readily insert into the polymer carbon-hydrogen bonds, thus leading to cross-linking. The *bis*-diazirine is nonexplosive, nonvolatile, and easily activated at relatively mild temperatures and thus could be used to fine-tune the properties of existing polymers through small chemical modifications. —MSL

*Science*, this issue p. 875;  
see also p. 800

**FRESHWATER ECOLOGY**  
**Change in plants as bicarbonate rises**

Freshwater plants can be broadly divided into two major categories according to their photosynthetic traits: Some use carbon dioxide as their carbon source, whereas others use bicarbonate. Iversen *et al.* found that the relative concentrations of these two inorganic carbon forms in water determine the functional composition of plant communities across freshwater ecosystems (see the Perspective by Marcé and Obrador). They created global maps revealing that community composition is structured by catchment geology and not climate (in contrast to the terrestrial realm, where the trait composition is structured by temperature and

rainfall). Anthropogenic influences from land-use change are causing large-scale increases in bicarbonate concentrations in freshwater catchments and are thus leading to wholesale changes in the composition of their aquatic plant communities. —AMS

*Science*, this issue p. 878;  
see also p. 805

**SOIL ECOLOGY****Many factors influence global change**

Global environmental change is driven by multiple natural and anthropogenic factors. With a focus on global change as it affects soils, Rillig *et al.* point out that nearly all published studies consider just one or two factors at a time (see the Perspective by Manning). In a laboratory experiment, they tested 10 drivers of global change both individually and in combination, at levels ranging from 2 to 10 factors. They found that soil properties, processes, and microbial communities could not be predicted from single-effect responses and that multiple factors in combination produced unsuspected responses. They concluded that single-factor studies remain important for uncovering mechanisms but that global change biology needs to embrace more fully the multitude of drivers impinging on ecosystems. —AMS

*Science*, this issue p. 886;  
see also p. 801

**ASTHMA****Neutrophils keep the peace**

Allergic airway inflammation is a complex disease, and multiple immune and nonimmune factors contribute to its development and progression. Using a house dust mite-induced mouse model of allergic inflammation, Patel *et al.* found that depletion



of neutrophils worsens airway inflammation and enhances myelopoiesis—the proliferation of bone marrow cells—driven by granulocyte colony-stimulating factor (G-CSF). Experiments demonstrate a previously unsuspected link between this hormone and type 2 innate lymphoid cells (ILC2s). G-CSF acts directly on both human and mouse ILC2s to promote production of the cytokines interleukin-5 and -13. —AB

*Sci. Immunol.* **4**, eaax7006 (2019).

## 2D MATERIALS

### Taking electrical control

Excitons—bound pairs of electrons and holes in a solid—can, in principle, be used as information carriers. However, their lifetime is limited because the electrons and holes tend to quickly recombine. One way to extend this lifetime is to physically separate electrons and holes—for example, by having them reside in different layers of a van der Waals heterostructure. Jauregui *et al.* used this strategy to form long-lived interlayer excitons in a heterostructure made out of monolayers of molybdenum diselenide (MoSe<sub>2</sub>) and tungsten diselenide (WSe<sub>2</sub>). Through electrical control of the layers in the heterostructure, the researchers further increased exciton lifetime and formed and manipulated charged excitons. —JS

*Science*, this issue p. 870

## RESEARCH ARTICLE SUMMARY

## DEVELOPMENTAL BIOLOGY

# In vitro culture of cynomolgus monkey embryos beyond early gastrulation

Huaxiao Ma\*, Jinglei Zhai\*, Haifeng Wan\*, Xiangxiang Jiang\*, Xiaoxiao Wang, Lin Wang, Yunlong Xiang, Xiechao He, Zhen-Ao Zhao, Bo Zhao, Ping Zheng†, Lei Li†, Hongmei Wang†

**INTRODUCTION:** Gastrulation is a landmark event in development that involves a complex series of molecular, physical, and energetic remodeling transitions in early embryogenesis. Processes vary among species, leading to the diversity of animal forms on Earth. A dearth of primate embryo samples at the gastrulation stage has limited our understanding of this critical event in primates. Recently, human embryos were grown in culture for 12 to 13 days. Many governments and international organizations have recommended that human embryos should not be allowed to grow beyond 14 days in vitro. Therefore, it is expected that analysis of nonhuman primate embryo model systems will elucidate mechanisms underlying gastrulation and hopefully

shed light on human development and the processes associated with defects and disease that arise during early development.

**RATIONALE:** Monkeys have long been considered a reliable animal model with which to study human physiological and pathological events because of their high degree of similarity to humans in both genomic and morphological characteristics. Therefore, we developed a system that supports the growth of cynomolgus monkey embryos in vitro for up to 20 days postfertilization (d.p.f.). Histological and immunofluorescent staining, combined with single-cell RNA-sequencing (RNA-seq) analysis, demonstrated that these in vitro-cultured (IVC) monkey embryos de-

veloped beyond early gastrulation and recapitulated key events of early primate in vivo postimplantation development.

**RESULTS:** We cultured cynomolgus monkey blastocysts with a mature blastocoel (d.p.f. 7 to 8) using the IVC system. At d.p.f. 13 to 14, a bilaminar disc-like structure appeared in  $\sim 27.7 \pm 3.2\%$  of the IVC embryos ( $n = 167$ , 26 experiments). At d.p.f. 15 to 16, the disc-like structure was clearly observable under the optical microscope. Some of the embryos successfully developed to d.p.f.

## ON OUR WEBSITE

Read the full article at <http://dx.doi.org/10.1126/science.aax7890>

20 in vitro. Hematoxylin and eosin (H&E) and immunofluorescent staining confirmed that the IVC embryos recapitulated the major hallmarks of in vivo

early postimplantation development: segregation of the epiblast ( $OCT4^+$ ,  $NANOG^+$ ) and hypoblast ( $GATA6^+$ ) lineages; formation of the amniotic and yolk sac cavities; appearance of the presumptive primordial germ cells ( $SOX17^+$ ,  $TFAP2C^+$ ,  $BLIMP1^+$ ); establishment of the anterior-posterior axis (asymmetric localization of  $OTX2^+$  cells); and gastrulation itself (gastrulating cells:  $T^+/OCT4^+$ ,  $VIMENTIN^+/T^+/OCT4^+$ ). Furthermore, single-cell RNA-seq analysis showed that the monkey IVC embryos were similar to their in vivo counterparts in gene expression profiles and cell types, including presumptive parietal trophoblasts, extraembryonic mesenchyme cells, postimplantation early and late epiblasts (E-EPI and L-EPI, respectively), visceral and yolk sac endoderm, early primordial germ cells (E-PGC), early gastrulating cells (E-Gast), late gastrulating cells 1 and 2 (L-Gast1 and L-Gast2, respectively), early amnion cells (E-AM), and late amnion cells 1 and 2 (L-AM1 and L-AM2, respectively).

**CONCLUSION:** We have established an IVC system that can support the development of cynomolgus monkey embryos beyond early gastrulation in vitro. The IVC embryos recapitulate numerous key events of in vivo early postimplantation development of primate embryos. Single-cell RNA-seq analysis reveals the molecular signatures of several cell types of primate early postimplantation embryos, including amnion cells. The monkey IVC system provides a platform for future studies of molecular signatures and mechanisms of early embryogenesis that are specific to primates with potential relevance to human diseases that arise during early development. ■

The list of author affiliations is available in the full article online.

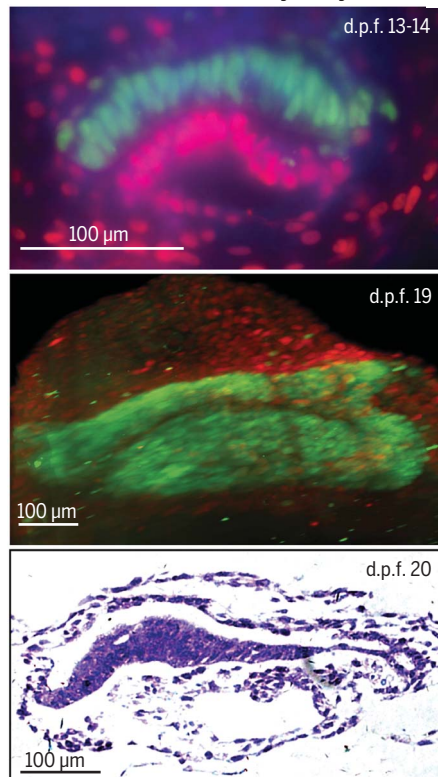
\*These authors contributed equally to this work.

†Corresponding author. Email: [li@ioz.ac.cn](mailto:li@ioz.ac.cn) (L.L.);

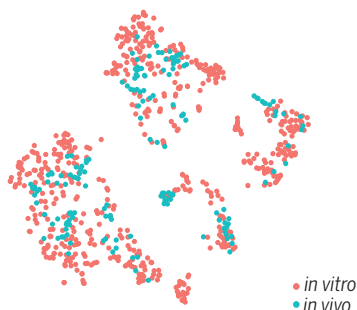
[zhengp@mail.kiz.ac.cn](mailto:zhengp@mail.kiz.ac.cn) (P.Z.); [wanghm@ioz.ac.cn](mailto:wanghm@ioz.ac.cn) (H.W.)

Cite this article as H. Ma et al., *Science* 366, eaax7890 (2019). DOI: 10.1126/science.aax7890

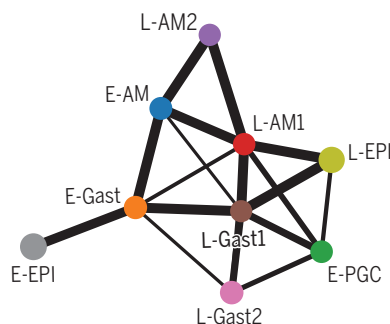
## In vitro culture of monkey embryos



## Single-cell analysis



## Developmental trajectory



**Monkey embryos grow in vitro beyond early gastrulation.** IVC embryos were stained with antibodies for OCT4 (green) and GATA6 (red) (d.p.f. 13 to 14 or 19) or H&E (d.p.f. 20). Single-cell transcriptome analysis revealed the similarities among cell types in the in vitro and in vivo monkey early embryos and the developmental trajectory of epiblast derivatives. Scale bars, 100  $\mu$ m.



## RESEARCH ARTICLE

## DEVELOPMENTAL BIOLOGY

# In vitro culture of cynomolgus monkey embryos beyond early gastrulation

Huaxiao Ma<sup>1,2,3\*</sup>, Jinglei Zhai<sup>1,3,4\*</sup>, Haifeng Wan<sup>1,3\*</sup>, Xiangxiang Jiang<sup>1,3\*</sup>, Xiaoxiao Wang<sup>1,3,4</sup>, Lin Wang<sup>2</sup>, Yunlong Xiang<sup>1</sup>, Xiechao He<sup>5</sup>, Zhen-Ao Zhao<sup>1</sup>, Bo Zhao<sup>2</sup>, Ping Zheng<sup>2,5,6†</sup>, Lei Li<sup>1,3,4†</sup>, Hongmei Wang<sup>1,3,4†</sup>

Gastrulation is a key event in embryonic development when the germ layers are specified and the basic animal body plan is established. The complexities of primate gastrulation remain a mystery because of the difficulties in accessing primate embryos at this stage. Here, we report the establishment of an in vitro culture (IVC) system that supports the continuous development of cynomolgus monkey blastocysts beyond early gastrulation up to 20 days after fertilization. The IVC embryos highly recapitulated the key events of in vivo early postimplantation development, including segregation of the epiblast and hypoblast, formation of the amniotic and yolk sac cavities, appearance of the primordial germ cells, and establishment of the anterior-posterior axis. Single-cell RNA-sequencing analyses of the IVC embryos provide information about lineage specification during primate early postimplantation development. This system provides a platform with which to explore the characteristics and mechanisms of early postimplantation embryogenesis in primates with possible conservation of cell movements and lineages in human embryogenesis.

The mammalian zygote develops to the blastocyst stage through several cleavage divisions in the oviduct before the blastocyst implants into the maternal uterus for further development (1). After implantation, gastrulation occurs, which is defined by the formation of the primitive streak (PS); the activation of a set of molecular markers, including *T/Brachyury* and *Otx2* (2, 3); and a succession of morphogenetic rearrangements, resulting in the formation of the primary germ layers and a fundamental body plan (4, 5). Gastrulation has been very difficult to observe and analyze because it happens within the uterus. Therefore, in vitro culture (IVC) systems serve as a powerful tool to solve this problem. Mouse blastocysts have been cultivated in vitro up to the egg cylinder stage (6–10). In fact, by combining an IVC system with live imaging, anterior-posterior (A-P) axis formation and egg cylinder morphogenesis

have been characterized in mouse embryos cultured in vitro (11, 12).

Despite the advances made with mouse embryo IVC systems, murine development events do not fully reflect primate embryogenesis because the morphogenesis of early postimplantation primate embryos is very different from that in rodent embryos (13, 14). Instead of forming a cuplike egg cylinder as in the mouse embryo, epiblast (EPI) cells in the primate embryo are flattened to form a bilaminar disc. Human embryos have been cultured in vitro for 12 to 13 days to initiate the formation of the EPI cells, amnion, and yolk sac (15, 16), and this system has been used to investigate the exit of EPI cells from the naïve pluripotent state in human embryos (17). Because of ethical regulations worldwide, culture of human embryos has to be stopped before 14 days postfertilization (d.p.f.), so human gastrulation-related events have not been explored in vitro (14, 18). Monkeys have been considered a reliable animal model with which to study human physiology and pathology because of their evolutionary, genomic, and physiological similarities to humans (13). The establishment of an IVC system for monkey postimplantation development would substantially improve our understanding of primate and human early embryonic development and related diseases. In particular, the blastocysts of the marmoset, a New World primate species, have been previously cultured for the study of postimplantation primate embryonic development. However, the resultant embryoids were not correctly organized (19). In the present study, we have established a system that allows cyn-

omolgus monkey blastocysts to grow in vitro up to d.p.f. 20. Our IVC monkey embryos largely recapitulate critical events of in vivo early postimplantation development at the structural, cellular, and molecular levels and develop beyond early gastrulation.

## In vitro culture of monkey embryos until d.p.f. 20

Cynomolgus monkey (*Macaca fascicularis*) blastocysts were obtained from an in vitro fertilization (IVF) procedure as previously reported (Fig. 1A and fig. S1, A and B) (20). Blastocysts at d.p.f. 7 to 8 with a mature blastocoel (>75% volume of the embryo) were selected for further culture (Fig. 1B and fig. S1, A and B). After removing the zona pellucida, the monkey blastocysts ( $n = 167$ ) were cultured in conventional Matrigel-coated petri dishes containing media adapted from mouse blastocyst culture media (Fig. 1, fig. S2, and tables S1 and S2) (7, 10). After 2 days of culture, at d.p.f. 9 to 10,  $\sim 67.3 \pm 3.5\%$  of embryos started to attach onto the dish, whereas the remainder attached onto the dish at d.p.f. 11 to 12 (table S3). The culture medium was changed daily after the embryos attached onto the dish (table S2). At d.p.f. 9 to 10, the embryos gradually enlarged, whereas the trophoblastic cells adjacent to the inner cell mass (ICM) firmly attached onto the Matrigel. At d.p.f. 11 to 12, the trophoblastic cells migrated onto the Matrigel surface and rapidly proliferated to form a flat and roughly circular sheet of outgrowth cells. By contrast, the ICM remained as a spherical and dense cell mass in the center of the outgrowth. At d.p.f. 13 to 14, a disclike structure appeared in  $\sim 27.7 \pm 3.2\%$  of the IVC embryos ( $n = 167$ , 26 experiments; Fig. 1B, fig. S3, and table S3). At d.p.f. 15 to 16, the disclike structure was clearly observable under the optical microscope (Fig. 1B). Embryos that attached onto the dish at d.p.f. 8 to 9 had a higher chance of successfully forming disclike structures than those that attached onto the dish at d.p.f. 10 to 11 ( $35.4 \pm 3.9\%$ ,  $n = 115$ , versus  $5.9 \pm 2.8\%$ ,  $n = 52$ ;  $p < 0.01$ ), suggesting that successful implantation during a critical time window might be important for further embryonic development. Although many IVC embryos started to show worsening morphology after d.p.f. 15, a portion of embryos with the bilaminar disc-like structure survived and developed to d.p.f. 16 to 17 ( $n = 14$ ), and some even up to d.p.f. 19 to 20 ( $n = 4$ ) (fig. S3).

IVC embryos with the disclike structures were fixed and analyzed by hematoxylin and eosin (H&E) staining for study of their overall morphology. The d.p.f. 15 IVC embryos contained tightly packed, columnar EPI-like cells (EPILCs) and epithelial amnion-like cells (AMLCs), together forming the amnion sac-like cavity (AMSLC) (Fig. 1C). Adjacent to EPILCs, we also observed a secondary yolk sac-like cavity (SYSCL), which was surrounded

<sup>1</sup>State Key Laboratory of Stem Cell and Reproductive Biology, Institute of Zoology, Chinese Academy of Sciences, Beijing 100101, China. <sup>2</sup>State Key Laboratory of Genetic Resources and Evolution, Kunming Institute of Zoology, Chinese Academy of Sciences, Kunming 650223, China.

<sup>3</sup>Innovation Academy for Stem Cell and Regeneration, Chinese Academy of Sciences, Beijing 100101, China.

<sup>4</sup>Institute of Zoology, University of Chinese Academy of Sciences, Chinese Academy of Sciences, Beijing 100049, China. <sup>5</sup>Primate Research Center, Yunnan Key Laboratory of Animal Reproduction, Kunming Institute of Zoology, Chinese Academy of Sciences, Kunming 650223, China. <sup>6</sup>Center for Excellence in Animal Evolution and Genetics, Chinese Academy of Sciences, Kunming 650223, China.

\*These authors equally contributed to this work.

†Corresponding author. Email: lil@ioz.ac.cn (L.L.); zhengp@mail.kiz.ac.cn (P.Z.); wanghm@ioz.ac.cn (H.W.)

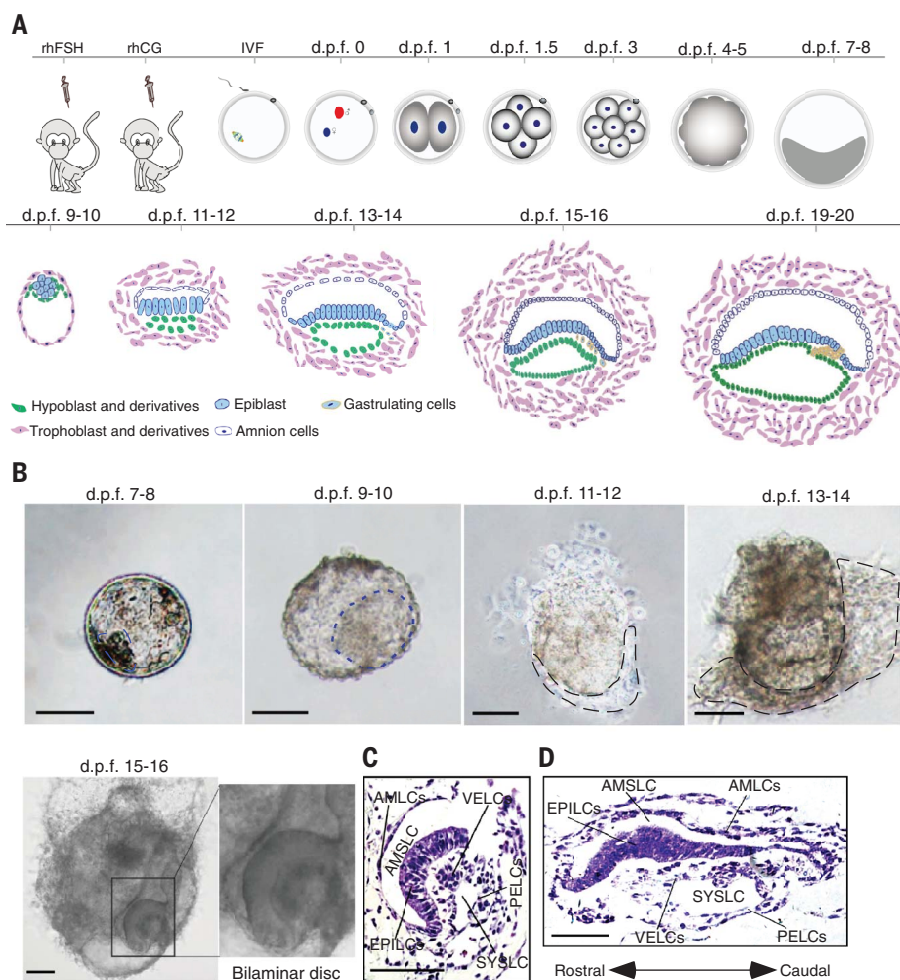


**Fig. 1. Establishment of the IVC system for monkey embryos.** (A) Time scheme of superovulation, IVF, and one-cell to gastrulation transition in the IVC system. rhFSH, recombinant human follicle-stimulating hormone; rhCG, recombinant human chorionic gonadotrophin. (B) Representative bright-field images of cynomolgus monkey embryos growing at the indicated stages of development. Blue dashed line indicates the ICM in d.p.f. 7 to 10 IVC embryos. Black dashed line indicates a portion of the expanded trophoblast cells in d.p.f. 11 to 14 IVC embryos. Scale bars, 100 μm. (C and D) H&E staining of the sections of IVC embryos with optically visible disclike structure at d.p.f. 15 [ $n = 1$  (C)] and d.p.f. 20 [ $n = 1$  (D)]. Scale bars, 100 μm.

by irregular visceral endoderm-like cells (VELCs) and squamous parietal endoderm-like cells (PELCs) (Fig. 1C). These structures in the IVC embryos continued growing between d.p.f. 15 and 20, with the rostral end of the discs appearing thicker than the caudal end at d.p.f. 20 (Fig. 1D). Notably, the diameter of the embryonic discs increased nearly three times from  $\sim 0.166 \pm 0.017$  mm at d.p.f. 15 to  $\sim 0.469 \pm 0.019$  mm at d.p.f. 19 to 20, resembling the size changes of in vivo monkey embryos at similar stages (21, 22). These histological results suggest that the IVC embryos were similar to those of monkey embryos in vivo (22).

#### IVC monkey embryos recapitulate the key events of early postimplantation development

To determine whether the key cellular events of monkey early embryogenesis also occur in

the IVC embryos, we performed immunofluorescent staining on IVC embryos at different time points using the following lineage markers: OCT4 and NANOG for EPI cells; GATA6 for hypoblast cells; and SOX17, TFAP2C, and BLIMP1 for primordial germ cells (PGCs) (23, 24). In d.p.f. 7 to 8 IVC embryos, the segregation of EPI cells and hypoblast progenitor cells was observable, and OCT4<sup>+</sup>/NANOG<sup>+</sup> EPI cells formed a spherical cluster (Fig. 2A and fig. S4A). In d.p.f. 9 to 10 IVC embryos, OCT4<sup>+</sup>/NANOG<sup>+</sup> EPI cells started to surround a proamniotic cavity-like lumen, whereas GATA6<sup>+</sup> hypoblast cells clustered to one side of the EPI cells (Fig. 2A and fig. S4B). In d.p.f. 11 to 12 IVC embryos, the amniotic cavity-like lumen expanded while GATA6<sup>+</sup> hypoblast cells were clustered to one side, marking the preparative step for yolk sac formation (Fig. 2A and fig. S4C). SOX17<sup>+</sup>/

TFAP2C<sup>+</sup> cells were detected at the amnion adjacent to the trophoblasts, beneath the EPI cells, or within the visceral endoderm (VE) (Fig. 2B and fig. S5). In d.p.f. 13 to 14 IVC embryos, EPI cells maintained robust OCT4 and NANOG expression, whereas amniotic cells expressed a relatively low level of OCT4 and NANOG. Simultaneously, the amniotic cavity further expanded, and the GATA6<sup>+</sup> hypoblast cells formed the yolk sac cavity (Fig. 2A and fig. S4D). The amniotic cavity and the yolk sac cavity delineated a disc structure (Fig. 2A and figs. S4D, S5, and S7, A and B). At d.p.f. 14 to 16, SOX17<sup>+</sup>/TFAP2C<sup>+</sup> and TFAP2C<sup>+</sup>/BLIMP1<sup>+</sup> cells appeared beneath the posterior EPI cells or within the VE (Fig. 2, B and C, and figs. S5 and S6). Therefore, these IVC embryos are similar to monkey embryos in vivo (24). The mRNA expression of the lineage markers was further validated in d.p.f. 15 IVC embryos by reverse transcription polymerase chain reaction (RT-PCR) (Fig. 2D and table S4). Moreover, these d.p.f. 15 IVC embryos expressed other important ontogenic genes, such as SOX2, GATA4, and the mesodermal transcription factor and gastrulation regulator *T/Brachyury* (25) (Fig. 2D). Together, these data suggest that IVC embryos develop beyond the bilaminar disc stage and recapitulate the major hallmarks of monkey in vivo early postimplantation development: segregation of the EPI cells and hypoblasts, formation of the amniotic and yolk sac cavities, the appearance of presumptive PGCs, and probably the initiation of gastrulation.

#### Gastrulation is initiated in monkey IVC embryos

In mammals, gastrulation starts with PS formation and is marked by the migration of gastrulating cells (4). When we examined a representative d.p.f. 14 IVC embryo stained with OCT4 and GATA6, we observed that some OCT4<sup>+</sup> cells appeared between the EPI cells and hypoblasts, especially at the presumptive caudal end of the disc, suggesting that these cells were gastrulating cells (Fig. 3, A and B; fig. S7, A and B; and movie S1). We reconstructed the images of this embryo at 90° orientation and found a putative PS at the caudal end of the embryo disc (Fig. 3, C and D, and fig. S7C). To further confirm the gastrulating cells, we performed coimmunostaining on the IVC embryos with antibodies against OCT4, GATA6, and T, the marker of gastrulating cells (23). At d.p.f. 11 to 12, T<sup>+</sup>/OCT4<sup>+</sup> cells were detected at the amnion (Fig. 3E and fig. S8A). In d.p.f. 13 to 14 IVC embryos, the majority of T<sup>+</sup>/OCT4<sup>+</sup> cells were still detected at the dorsal amnion, but a few began to appear between the EPI cells and the VE (Fig. 3E and fig. S8B). In d.p.f. 15 to 16 IVC embryos, only a few T<sup>+</sup>/OCT4<sup>+</sup> cells were still located at the amnion; most were detected between the EPI cells and the VE (Fig. 3E, fig. S8C, and movie S2). At d.p.f. 19,



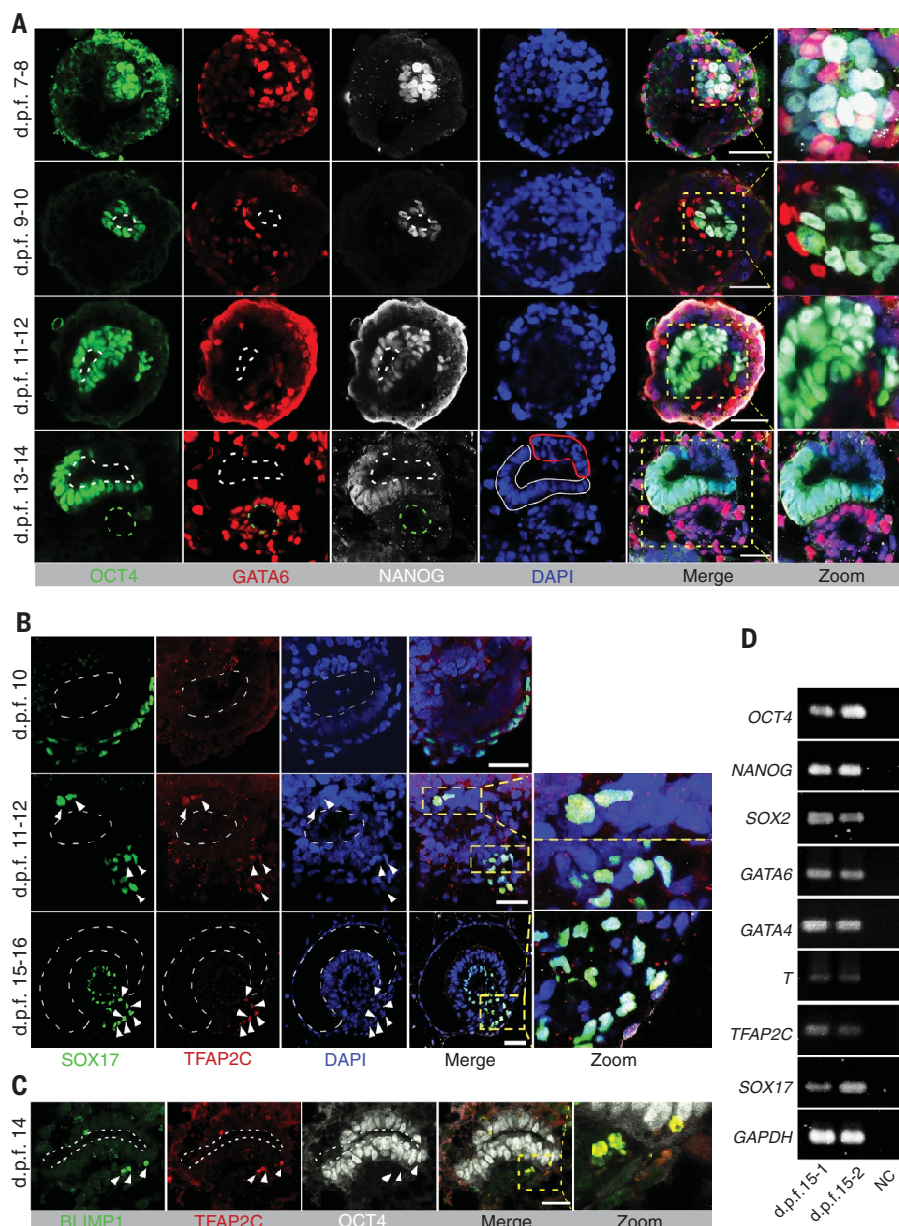


**Fig. 2. Recapitulation of monkey early postimplantation development in IVC embryos.** (A) Monkey blastocysts were cultured until d.p.f. 7 to 8 ( $n = 2$ ), d.p.f. 9 to 10 ( $n = 2$ ), d.p.f. 11 to 12 ( $n = 3$ ), and d.p.f. 13 to 14 ( $n = 5$ ) and fixed for whole-mount staining with antibodies for OCT4 (green), GATA6 (red), and NANOG (white). Shown are representative images reconstructed with the representative confocal z-images (d.p.f. 7 to 8, plane nos. 11 to 29; d.p.f. 9 to 10, plane nos. 12 to 39; d.p.f. 11 to 12, plane nos. 10 to 37; and d.p.f. 13 to 14, plane nos. 13 to 42). White dashed line and green dashed line indicate the proamniotic (d.p.f. 9 to 12) and amniotic (after d.p.f. 13) cavity and the yolk sac cavity, respectively. White line and red line indicate the EPI cells and amniotic cells in the d.p.f. 13 to 14 embryo, respectively. Scale bars, 50  $\mu\text{m}$ . (B) Monkey blastocysts were cultured until d.p.f. 10 ( $n = 1$ ), d.p.f. 11 to 12 ( $n = 3$ ), and d.p.f. 15 to 16 ( $n = 4$ ) and then fixed for whole-mount staining with antibodies for SOX17 (green) and TFAP2C (red). The images were reconstructed with the representative confocal z-images (d.p.f. 10, plane nos. 13 to 38; d.p.f. 11 to 12, plane nos. 18 to 44; and d.p.f. 15 to 16, plane nos. 12 to 45). White arrowheads indicate SOX17<sup>+</sup> and TFAP2C<sup>+</sup> cells. White dashed line indicates the proamniotic and amniotic cavities at the indicated stages. Scale bars, 50  $\mu\text{m}$ . (C) Monkey blastocysts were cultured until d.p.f. 14 ( $n = 1$ ) and fixed for whole-mount staining with antibodies for BLIMP1 (green), TFAP2C (red), and OCT4 (white). Shown are representative images reconstructed with the representative confocal z-images (plane nos. 29 to 46). White arrowheads indicate BLIMP1<sup>+</sup> and TFAP2C<sup>+</sup> cells. White dashed line indicates the amnion cavity. Scale bar, 50  $\mu\text{m}$ . (D) Monkey embryos ( $n = 2$ ) were cultured until d.p.f. 15 and the discs in the embryos were harvested for RT-PCR of the indicated genes. PCR without template cDNAs was included as the negative control (NC).

the number of T<sup>+</sup> cells increased considerably (Fig. 3E, fig. S8D, and movie S3). These observations suggest that the T<sup>+</sup>/OCT4<sup>+</sup> cells might be gastrulating cells and could be a mixture of nascent gastrulating cells that originated from the EPI or cells that might have migrated from the dorsal amnion, consistent with previous reports (23, 24).

Gastrulation is also characterized by the epithelial-mesenchymal transition (EMT) of gastrulating cells and the establishment of an A-P axis (4). We costained the IVC embryos with antibodies for T, OCT4, and VIMENTIN, a marker for EMT (26). The results showed that some T<sup>+</sup>/OCT4<sup>+</sup> cells expressed VIMENTIN in d.p.f. 13 to 14 and d.p.f. 16 IVC embryos (Fig. 4A and fig. S9). We also stained the IVC embryos with antibodies for OTX2 and EOMES,

two important transcription factors for mouse germ layer specification (27, 28). The protein expression of OTX2 and EOMES was observed in the visceral endoderm of d.p.f. 13 IVC embryos (Fig. 4, B and C, and fig. S10, A to C). Notably, OTX2 was expressed strongly at the anterior region but weakly at the posterior region in the visceral endoderm of d.p.f. 15 to 16 IVC embryos (Fig. 4B and fig. S10B). This asymmetrical distribution of OTX2 cells in d.p.f. 15 to 16 IVC embryos indicates the establishment of an A-P axis. We also observed neural crest-like, forebrain-like, and neural groove-like structures in d.p.f. 19 IVC embryos (Fig. 4D; fig. S11, A and B; and movies S3 and S4) (29), similar to human embryos at embryonic days 17 (E17) to E19 [Carnegie stage 8 (29, 30)]. Taken together, these lines of evi-

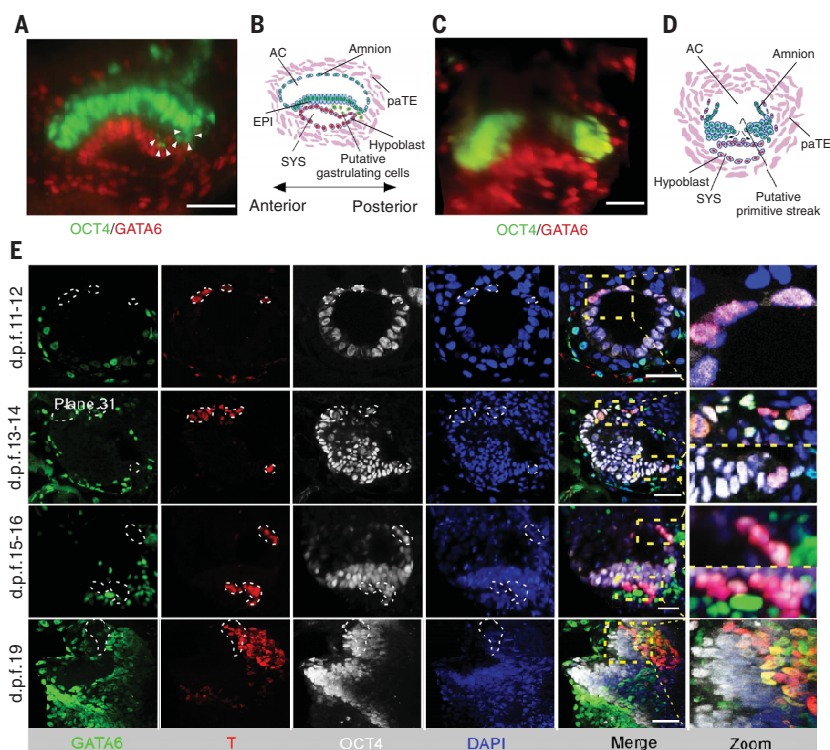
dence suggest that the IVC monkey embryos have developed beyond early gastrulation.

### IVC monkey embryos' molecular signatures are similar to in vivo counterparts

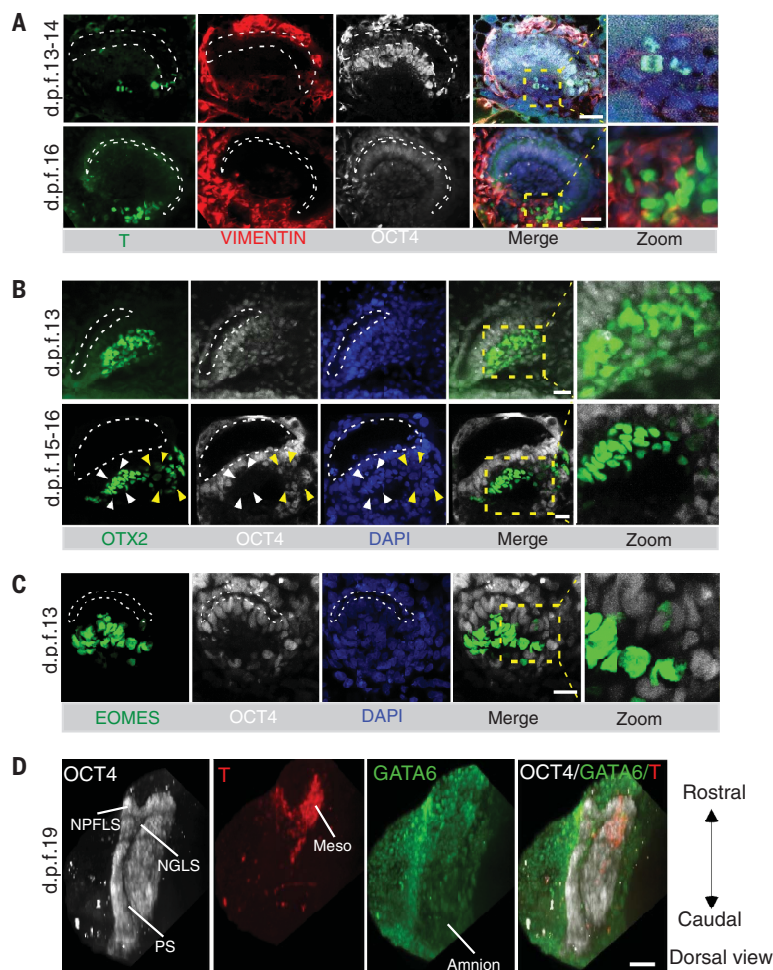
Previous studies using single-cell RNA-sequencing (RNA-seq) analysis delineated the cells of the monkey early postimplantation embryos as postimplantation early or late EPI (postE-EPI or postL-EPI, respectively); gastrulating cells 1, 2a, and 2b (Gast1, 2a and 2b); visceral/yolk sac endoderm (VE/YE); extraembryonic mesenchyme (EXMC); postimplantation parietal trophoblast (paTE); and early PGC (E-PGC) (23, 24). To identify the various cell types of the IVC monkey embryos and to understand their gene expression dynamics, we collected 2016 single cells from nine IVC

**Fig. 3. Gastrulation in monkey IVC embryos.**

(A) One representative d.p.f. 14 IVC embryo stained with antibodies for OCT4 (green) and GATA6 (red). Shown is an image reconstructed with the representative confocal z-images (plane nos. 206 to 220). Arrowheads indicate presumptive gastrulating cells. Scale bar, 60  $\mu$ m. (B) Diagram based on the image in (A). AC, amniotic cavity. (C) The image in (A) was reconstructed at a 90° pitch. Scale bar, 60  $\mu$ m. (D) Diagram based on the image in (C). (E) Monkey blastocysts were cultured until d.p.f. 11 to 12 ( $n = 2$ ), d.p.f. 13 to 14 ( $n = 2$ ), d.p.f. 15 to 16 ( $n = 2$ ), and d.p.f. 19 ( $n = 1$ ) and fixed for whole-mount staining with antibodies for GATA6 (green), T (red), and OCT4 (white). Shown are images reconstructed with representative confocal z-images (d.p.f. 11 to 12, plane nos. 24 to 48; d.p.f. 15 to 16, plane nos. 34 to 55; and d.p.f. 19, plane nos. 18 to 43). T<sup>+</sup>/OCT4<sup>+</sup> cells are indicated with a white dashed line at the indicated stages. Scale bars, 50  $\mu$ m.

**Fig. 4. EMT and the establishment of the A-P axis in IVC embryos.**

(A) Monkey d.p.f. 13 to 14 ( $n = 2$ ) and d.p.f. 16 ( $n = 1$ ) IVC embryos with the disc were stained with antibodies for T (green), VIMENTIN (red), and OCT4 (white). Shown are images reconstructed with representative confocal z-images (d.p.f. 13 to 14, plane nos. 19 to 27; d.p.f. 16, plane nos. 206 to 223). White dashed line indicates the amniotic cavity at the indicated stages. Scale bars, 50  $\mu$ m. (B) Monkey blastocysts were cultured until d.p.f. 13 ( $n = 1$ ) and d.p.f. 15 to 16 ( $n = 2$ ) and fixed for whole-mount staining with antibodies for OTX2 (green) and OCT4 (white). White and yellow arrowheads indicate the anterior and posterior region in VE, respectively. Shown are images reconstructed with representative confocal z-images (d.p.f. 13, plane nos. 34 to 45; d.p.f. 15 to 16, plane nos. 58 to 68). White dashed line indicates the amniotic cavity at the indicated stages. Scale bars, 50  $\mu$ m. (C) Monkey blastocyst was cultured until d.p.f. 13 ( $n = 1$ ) and fixed for whole-mount staining with antibodies for EOMES (green) and OCT4 (white). Shown are images reconstructed with representative confocal z-images (plane nos. 28 to 45). White dashed line indicates the amniotic cavity at the indicated stages. Scale bar, 50  $\mu$ m. (D) Images from Fig. 3E at d.p.f. 19 reconstructed by Imaris 9.0.2 with representative whole z-stack images. The 3D image was rotated 90° around the y-axis and then clockwise rotated at 45° orientation around the z-axis (movie S4). NPFLS, neural plate of forebrain-like structure; NGLS, neural groove-like structure; Meso, mesoderm. Scale bar, 100  $\mu$ m.





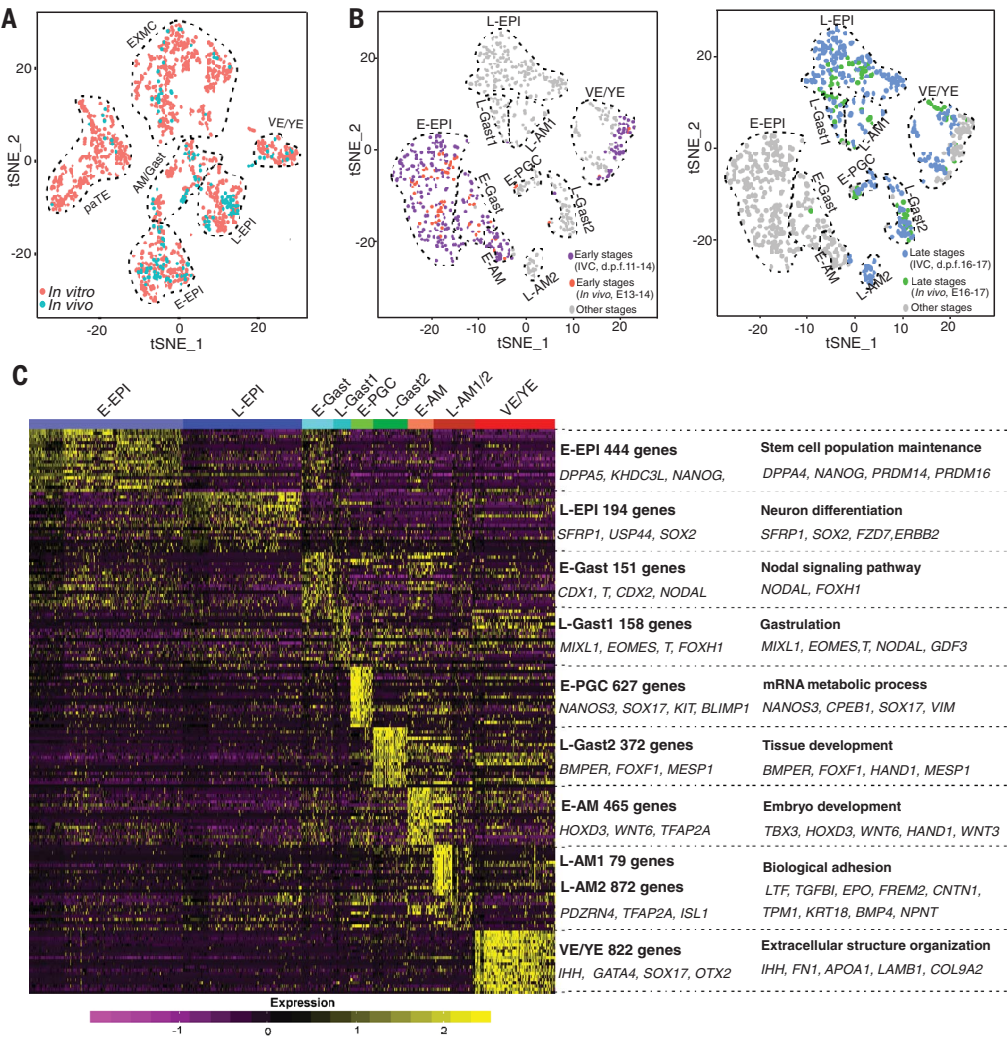


**Fig. 5. Classification of key cell types in the IVC embryos by single-cell RNA-seq analysis.** (A) Visualization of major classes of cells from the IVC embryos (d.p.f. 11, 12, 13, 14, 16, and 17; red,  $n = 1453$ ) and the archived in vivo embryos [E13, E14, E16, and E17; cyan,  $n = 211$ ; (23)] by t-SNE analysis. AM/Gast, amnion/gastrulating cells. (B) Key cell types identified from IVC and in vivo embryos at the indicated developmental stages by t-SNE analysis. After excluding paTE and EXMC, 10 clusters were identified and marked with different colors at specific stages [in vitro,  $n = 588$ ; in vivo,  $n = 167$ ; (23)]. (C) Heat map of DEGs in the 10 clusters of the post-implantation embryos. The colors from magenta to yellow indicate relative expression levels from low to high. Right, representative genes and key gene ontology (GO) enrichment analysis results (table S7).

embryos at six developmental stages (d.p.f. 11,  $n = 1$ ; d.p.f. 12,  $n = 2$ ; d.p.f. 13,  $n = 2$ ; d.p.f. 14,  $n = 2$ ; d.p.f. 16,  $n = 1$ ; and d.p.f. 17,  $n = 1$ ) and performed single-cell RNA-seq using a modified Smart-seq2 technique (fig. S12, A and B) (37). Among these 2016 cells, 1453 single cells with expression of >2000 genes were selected for further analyses (fig. S12C and table S5). We compared these single cells with those from their in vivo counterparts (23). t-Distributed stochastic neighbor embedding (t-SNE) analysis revealed that cells from IVC and in vivo embryos were clustered into six cell types as described previously (23), including postE-EPI, postL-EPI, VE/YE, Gast, EXMC, and paTE (Fig. 5A and fig. S13, A and B). After excluding the paTE and EXMC cells, the 755 cells [IVC,  $n = 588$ ; in vivo,  $n = 167$  (23)] were reclassified into 10 clusters, including the previously annotated postE-EPI, postL-EPI, VE/YE, E-PGC, and Gast (23, 24). We annotated gastrulating cells into three distinct clusters, the early gastrulating cells (E-Gast) and late gastrulating cells 1 and 2 (L-Gast1 and L-Gast2). We also annotated early amnion cells (E-AM) and

late amnion cells 1 and 2 (L-AM1 and L-AM2) (Fig. 5B, fig. S14, and tables S5 to S7). The cell clusters that appeared in d.p.f. 11 to 14 IVC embryos were similar to those in the E13 to E14 embryos in vivo, whereas the clusters in d.p.f. 16 to 17 IVC embryos were similar to those in E16 to E17 embryos in vivo (Fig. 5B). We annotated these cell clusters on the basis of their differentially expressed genes (DEGs) and the timing of their appearance during development (early stages: in vivo E13 to E14/ in vitro d.p.f. 11 to 14; late stages: in vivo E16 to E17/ in vitro d.p.f. 16 to 17; Fig. 5, B and C). The postE-EPI, postL-EPI, VE/YE, and E-PGC highly expressed genes that were enriched in numerous developmental pathways, such as stem cell population maintenance in postE-EPI, neuron differentiation in postL-EPI, extracellular structure organization in VE/YE, and mRNA metabolic processes in E-PGC (Figs. 5C and 6A and figs. S15 and S16). The representative genes that were validated by our immunostaining experiments in these cell clusters included *NANOG* and *OCT4* in postE-EPI, *OTX2* in VE/YE, *BLIMP1* and *TFAP2C* in

E-PGC, and *SOX17* in VE/YE and E-PGC (Figs. 2, A and B, and 4B and fig. S5). We also observed high or low levels of marker gene expression (*OTX2*, *GATA6*, and *IHH*) in the VE/YE cluster, suggesting early or later VE/YE cell identities (Fig. 6A and fig. S16B). Our platform and the number of cells involved in this study allowed us to reannotate the gastrulating cells as E-Gast, L-Gast1, and L-Gast2. E-Gast cells were mostly from d.p.f. 11 to 14 IVC embryos, whereas L-Gast1 and L-Gast2 were mainly from d.p.f. 16 to 17 IVC embryos (Fig. 5B and fig. S14, A and B). E-Gast cells expressed *CDX1/2* and *T* and were enriched with genes in the Nodal signaling pathway, such as *NODAL* and *FOXH1* (Figs. 5C and 6B and fig. S17A). L-Gast1 cells were enriched for genes in the gastrulation signatures, such as *T*, *MIXL1*, and *EOMES* (Figs. 5C and 6C and fig. S17B). L-Gast2 cells strongly expressed mesodermal development-related transcription factors such as *FOXF1*, *HAND1*, and *MESP1* (Figs. 5C and 6D and fig. S17C) (32, 33). The expression levels of gastrulating cell markers (*T*, *EOMES*, *NODAL*, *LEF1*, and

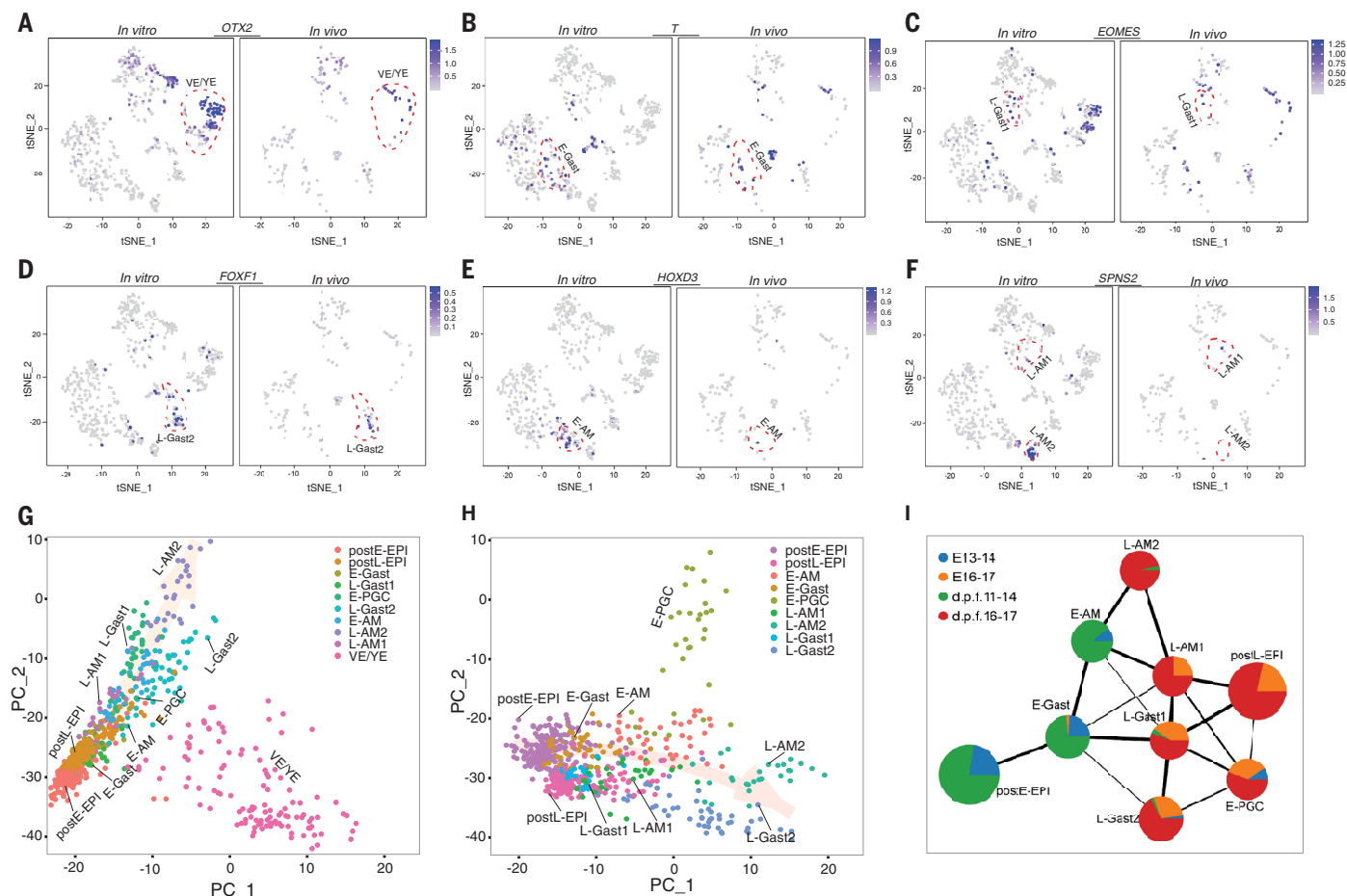


**Fig. 6. Gene expression analysis of single cells from the postimplantation embryos.** (A to F) t-SNE plots showing the expression patterns of ontogenic markers in VE/YE (A), E-Gast (B), L-Gast1 (C), L-Gast2 (D), E-AM (E), and L-AM (F) cells (red dashed lines) from the IVC and in vivo embryos. (G) PCA on the single cells of postimplantation embryos [IVC, 588 cells; in vivo, 167 cells (23)]. (H) PCA on the single cells of postimplantation embryos after excluding VE/YE [IVC, 487 cells; in vivo, 149 cells (23)]. (I) PAGA analysis on 636 single cells from IVC and in vivo embryos. The boldness of the line indicates the degree of the relationship between clusters.

*MIXL1*) were different in these clusters of cells (Fig. 6, A to C, and fig. S17, A and B). In addition, both in vitro and in vivo postE-EPI, postL-EPI, E-Gast, L-Gast, and VE/YE cells expressed representative genes in the Wnt signaling pathway in heterogeneous patterns, probably reflecting the shared importance of Wnt signaling in many subsets of cells during gastrulation (fig. S18) (4). The heterogeneous expression patterns of the gastrulation markers and key regulators of important developmental pathways in these clusters further suggest the progressive establishment of an A-P axis in the IVC embryos (2, 11).

We also observed three clusters of cells exhibiting *OCT4<sup>+</sup>/BMP4<sup>+</sup>/SOX2<sup>low/-</sup>* (fig. S19), representing potential monkey amnion cells (24). We annotated these three clusters as E-AM cells, which primarily appeared in d.p.f. 11 to 14 IVC embryos and E13 to E14 embryos in vivo, and late amnion cells 1 and 2 (L-AM1 or L-AM2), which were primarily present in d.p.f. 16 to 17 IVC embryos and E16 to E17

embryos in vivo (Fig. 5B and fig. S14) (24). The E-AM cells highly expressed embryonic genes such as *HOXD3*, *WNT6*, and *TFAP2A* (Figs. 5C and 6E and fig. S20), whereas the L-AM1 and L-AM2 cells highly expressed genes involved in biological adhesion, such as *SPNS2*, *PDZRN4*, and *NGF* (Figs. 5C and 6F and fig. S20).

We next examined the transitions between cell lineages. Principal component analysis (PCA) indicated a unidirectional progression in the EPI developmental trajectory, suggesting an orderly and progressive specification of EPI derivatives (Fig. 6G). By contrast, PCA indicated a scattered distribution of VE/YE cells (Fig. 6G), suggesting complex and heterogeneous origins of VE/YE cells. To clarify our understanding of the EPI developmental trajectory of EPI derivatives, we excluded the VE/YE cells and performed PCA and partition-based graph abstraction (PAGA) analyses. These analyses revealed a close relationship between E-Gast and postE-EPI or E-AM cells, as well as a close similarity between L-Gast1

and postL-EPI or L-AM1 cells, supporting the idea that gastrulating cells originate from EPI and/or amnion cells (Fig. 6, H and I). These relationships were well insolated with force-directed graph-drawing analysis (fig. S21). Single-cell analysis of genome-wide gene expression profiles suggests that the IVC embryos have cell types with gene signatures that are very similar to their in vivo counterparts, further supporting our morphological and cellular observations that our IVC monkey embryos could develop beyond early gastrulation.

### Concluding remarks

In this study, we developed an IVC system that supports the growth and development of cynomolgus monkey embryos for up to d.p.f. 20 without maternal contribution. We provide several lines of evidence to demonstrate that these IVC embryos recapitulate most of the key events of early postimplantation development as seen in their in vivo counterparts: (i) formation of a clear, bilaminar,



dislike structure delineated by the amniotic cavity and yolk sac cavity; (ii) timely occurrence of several hallmark events, including segregation of the EPI and hypoblast, formation of the amniotic and yolk sac cavities, specification of the presumptive PGCs, and the establishment of the A-P axis; (iii) initiation of gastrulation, as demonstrated by the formation of the PS, the appearance of gastrulating cells, and the EMT process of gastrulating cells; and (iv) similarities in cell types and gene expression profiles between IVC embryos and their *in vivo* counterparts at the single-cell and genome-wide levels.

We analyzed the IVC embryos by single-cell RNA-seq and obtained insights into primate early embryogenesis. We identified primate amnion cells and characterized their molecular signatures at different developmental stages. We also reannotated primate gastrulating cells as E-Gast, L-Gast1, and L-Gast2 cells to represent the shifting identities of these dynamic cells during primate early embryogenesis.

This study provides a platform technology and a data resource with which to further investigate the characteristics and key regulators of early postimplantation embryogenesis in primates. In combination with CRISPR-Cas9-mediated gene editing and cell lineage tracing, the monkey IVC system could help to elucidate the mysterious dynamics of early embryonic development in primates, with possible relevance to human development.

### Summary of materials and methods

The experiments on the cynomolgus monkey and the mouse were performed according to the guidance of the ethics committees of the Institute of Zoology and Kunming Institute of Zoology, Chinese Academy of Sciences (CAS). An *in vitro* culture system for monkey blastocysts based on the culture system for mouse postimplantation embryos was established. H&E staining, RT-PCR, and whole-mount embryo immunostaining were used to examine the histology, key cellular events, and cell lineages of early postimplantation development in the IVC monkey embryos. To investigate the profiles of gene expression and cell types, single cells were isolated from the IVC monkey embryos. The libraries of single-cell transcriptomes were constructed using the Smart-seq2 method and sequenced with the Hiseq4000 system. The single-cell data were analyzed by the Seurat version 3.0 R package and the Scanpy version 1.4.4 Python package. Details of the materials and methods are available in the supplementary materials.

### REFERENCES AND NOTES

- H. Wang, S. K. Dey, Roadmap to embryo implantation: Clues from mouse models. *Nat. Rev. Genet.* **7**, 185–199 (2006). doi: [10.1038/nrg1808](https://doi.org/10.1038/nrg1808); pmid: [16485018](https://pubmed.ncbi.nlm.nih.gov/16485018/)
- S. J. Arnold, E. J. Robertson, Making a commitment: Cell lineage allocation and axis patterning in the early mouse embryo. *Nat. Rev. Mol. Cell Biol.* **10**, 91–103 (2009). doi: [10.1038/nrm2618](https://doi.org/10.1038/nrm2618); pmid: [19129791](https://pubmed.ncbi.nlm.nih.gov/19129791/)
- G. Peng *et al.*, Molecular architecture of lineage allocation and tissue organization in early mouse embryo. *Nature* **572**, 528–532 (2019). doi: [10.1038/s41586-019-1469-8](https://doi.org/10.1038/s41586-019-1469-8); pmid: [31391582](https://pubmed.ncbi.nlm.nih.gov/31391582/)
- P. P. L. Tam, D. A. F. Loebel, Gene function in mouse embryogenesis: Get set for gastrulation. *Nat. Rev. Genet.* **8**, 368–381 (2007). doi: [10.1038/nrg2084](https://doi.org/10.1038/nrg2084); pmid: [17387317](https://pubmed.ncbi.nlm.nih.gov/17387317/)
- J. A. Rivera-Pérez, A. K. Hadjantonakis, The dynamics of morphogenesis in the early mouse embryo. *Cold Spring Harb. Perspect. Biol.* **7**, a025867 (2014). pmid: [24968703](https://pubmed.ncbi.nlm.nih.gov/24968703/)
- E. J. Jenkinson, I. B. Wilson, *In vitro* support system for the study of blastocyst differentiation in the mouse. *Nature* **228**, 776–778 (1970). doi: [10.1038/228776a0](https://doi.org/10.1038/228776a0); pmid: [5472970](https://pubmed.ncbi.nlm.nih.gov/5472970/)
- Y. C. Hsu, Post-blastocyst differentiation *in vitro*. *Nature* **231**, 100–102 (1971). doi: [10.1038/231100a0](https://doi.org/10.1038/231100a0); pmid: [4930085](https://pubmed.ncbi.nlm.nih.gov/4930085/)
- D. Solter, W. Biczysko, M. Pienkowski, H. Koprowski, Ultrastructure of mouse egg cylinders developed *in vitro*. *Anat. Rec.* **180**, 263–279 (1974). doi: [10.1002/ar.1091800202](https://doi.org/10.1002/ar.1091800202); pmid: [4417946](https://pubmed.ncbi.nlm.nih.gov/4417946/)
- A. J. Copp, The mechanism of mouse egg-cylinder morphogenesis *in vitro*. *J. Embryol. Exp. Morphol.* **61**, 277–287 (1981). pmid: [7264546](https://pubmed.ncbi.nlm.nih.gov/7264546/)
- I. Bedzhov, C. Y. Leung, M. Bialecka, M. Zernicka-Goetz, *In vitro* culture of mouse blastocysts beyond the implantation stages. *Nat. Protoc.* **9**, 2732–2739 (2014). doi: [10.1038/nprot.2014.186](https://doi.org/10.1038/nprot.2014.186); pmid: [25356584](https://pubmed.ncbi.nlm.nih.gov/25356584/)
- S. A. Morris *et al.*, Dynamics of anterior-posterior axis formation in the developing mouse embryo. *Nat. Commun.* **3**, 673 (2012). doi: [10.1038/ncomms1671](https://doi.org/10.1038/ncomms1671); pmid: [22334076](https://pubmed.ncbi.nlm.nih.gov/22334076/)
- I. Bedzhov, M. Zernicka-Goetz, Self-organizing properties of mouse pluripotent cells initiate morphogenesis upon implantation. *Cell* **156**, 1032–1044 (2014). doi: [10.1016/j.cell.2014.01.023](https://doi.org/10.1016/j.cell.2014.01.023); pmid: [24529478](https://pubmed.ncbi.nlm.nih.gov/24529478/)
- G. Yan *et al.*, Genome sequencing and comparison of two nonhuman primate animal models, the cynomolgus and Chinese rhesus macaques. *Nat. Biotechnol.* **29**, 1019–1023 (2011). doi: [10.1038/nbt1992](https://doi.org/10.1038/nbt1992); pmid: [22002653](https://pubmed.ncbi.nlm.nih.gov/22002653/)
- J. Rossant, P. P. L. Tam, Exploring early human embryo development. *Science* **360**, 1075–1076 (2018). doi: [10.1126/science.aas9302](https://doi.org/10.1126/science.aas9302); pmid: [29880675](https://pubmed.ncbi.nlm.nih.gov/29880675/)
- A. Deglincerti *et al.*, Self-organization of the *in vitro* attached human embryo. *Nature* **533**, 251–254 (2016). doi: [10.1038/nature17948](https://doi.org/10.1038/nature17948); pmid: [27144363](https://pubmed.ncbi.nlm.nih.gov/27144363/)
- M. N. Shahbazi *et al.*, Self-organization of the human embryo in the absence of maternal tissues. *Nat. Cell Biol.* **18**, 700–708 (2016). doi: [10.1038/ncb33347](https://doi.org/10.1038/ncb33347); pmid: [27144686](https://pubmed.ncbi.nlm.nih.gov/27144686/)
- M. N. Shahbazi *et al.*, Pluripotent state transitions coordinate morphogenesis in mouse and human embryos. *Nature* **552**, 239–243 (2017). doi: [10.1038/nature24675](https://doi.org/10.1038/nature24675); pmid: [29186120](https://pubmed.ncbi.nlm.nih.gov/29186120/)
- J. B. Hurlbut *et al.*, Revisiting the Warnock rule. *Nat. Biotechnol.* **35**, 1029–1042 (2017). doi: [10.1038/nbt.4015](https://doi.org/10.1038/nbt.4015); pmid: [29121021](https://pubmed.ncbi.nlm.nih.gov/29121021/)
- A. Lopata, D. J. Kohlman, L. G. Bowes, W. B. Watkins, Culture of marmoset blastocysts on matrigel: A model of differentiation during the implantation period. *Anat. Rec.* **241**, 469–486 (1995). doi: [10.1002/ar.1092410405](https://doi.org/10.1002/ar.1092410405); pmid: [7604962](https://pubmed.ncbi.nlm.nih.gov/7604962/)
- X. Wang *et al.*, Transcriptome analyses of rhesus monkey preimplantation embryos reveal a reduced capacity for DNA double-strand break repair in primate oocytes and early embryos. *Genome Res.* **27**, 567–579 (2017). doi: [10.1101/gr.198044.115](https://doi.org/10.1101/gr.198044.115); pmid: [28223401](https://pubmed.ncbi.nlm.nih.gov/28223401/)
- W. P. Luckett, Origin and differentiation of the yolk sac and extraembryonic mesoderm in presomite human and rhesus monkey embryos. *Am. J. Anat.* **152**, 59–97 (1978). doi: [10.1002/aja.1001520106](https://doi.org/10.1002/aja.1001520106); pmid: [98035](https://pubmed.ncbi.nlm.nih.gov/98035/)
- A. C. Enders, S. Schlafke, A. G. Hendrickx, Differentiation of the embryonic disc, amnion, and yolk sac in the rhesus monkey. *Am. J. Anat.* **177**, 161–185 (1986). doi: [10.1002/aja.1001770205](https://doi.org/10.1002/aja.1001770205); pmid: [3788819](https://pubmed.ncbi.nlm.nih.gov/3788819/)
- T. Nakamura *et al.*, A developmental coordinate of pluripotency among mice, monkeys and humans. *Nature* **537**, 57–62 (2016). doi: [10.1038/nature19096](https://doi.org/10.1038/nature19096); pmid: [27556940](https://pubmed.ncbi.nlm.nih.gov/27556940/)
- K. Sasaki *et al.*, The Germ Cell Fate of Cynomolgus Monkeys Is Specified in the Nascent Amnion. *Dev. Cell* **39**, 169–185 (2016). doi: [10.1016/j.devcel.2016.09.007](https://doi.org/10.1016/j.devcel.2016.09.007); pmid: [27720607](https://pubmed.ncbi.nlm.nih.gov/27720607/)
- R. S. P. Beddington, P. Rashbass, V. Wilson, Brachyury—A gene affecting mouse gastrulation and early organogenesis. *Dev. Suppl.* **116**, 157–165 (1992). pmid: [1299362](https://pubmed.ncbi.nlm.nih.gov/1299362/)
- M. G. Mendez, S. Kojima, R. D. Goldman, Vimentin induces changes in cell shape, motility, and adhesion during the epithelial to mesenchymal transition. *FASEB J.* **24**, 1838–1851 (2010). doi: [10.1096/fj.09-151639](https://doi.org/10.1096/fj.09-151639); pmid: [20097873](https://pubmed.ncbi.nlm.nih.gov/20097873/)
- A. Simeone *et al.*, A vertebrate gene related to the orthodenticle contains a homeodomain of the bicoid class and demarcates anterior neuroectoderm in the gastrulating mouse embryo. *EMBO J.* **12**, 2735–2747 (1993). doi: [10.1002/j.1460-2075.1993.tb05935.x](https://doi.org/10.1002/j.1460-2075.1993.tb05935.x); pmid: [8101484](https://pubmed.ncbi.nlm.nih.gov/8101484/)
- B. G. Ciruna, J. Rossant, Expression of the T-box gene Eomesodermin during early mouse development. *Mech. Dev.* **81**, 199–203 (1999). doi: [10.1016/S0925-4773\(98\)00243-3](https://doi.org/10.1016/S0925-4773(98)00243-3); pmid: [10330500](https://pubmed.ncbi.nlm.nih.gov/10330500/)
- R. O'Rahilly, F. Müller, The first appearance of the human nervous system at stage 8. *Anat. Embryol.* **163**, 1–13 (1981). doi: [10.1007/BF00315766](https://doi.org/10.1007/BF00315766); pmid: [7316219](https://pubmed.ncbi.nlm.nih.gov/7316219/)
- M. A. Hill, *Embryology: Carnegie Stage 8* (2019); [https://embryology.med.unsw.edu.au/embryology/index.php/Carnegie-stage\\_8](https://embryology.med.unsw.edu.au/embryology/index.php/Carnegie-stage_8)
- S. Picelli *et al.*, Full-length RNA-seq from single cells using Smart-seq2. *Nat. Protoc.* **9**, 171–181 (2014). doi: [10.1038/nprot.2014.006](https://doi.org/10.1038/nprot.2014.006); pmid: [24385147](https://pubmed.ncbi.nlm.nih.gov/24385147/)
- M. Mahlapuu, M. Ormestad, S. Enerbäck, P. Carlsson, The forkhead transcription factor Foxf1 is required for differentiation of extra-embryonic and lateral plate mesoderm. *Development* **128**, 155–166 (2001). pmid: [11124112](https://pubmed.ncbi.nlm.nih.gov/11124112/)
- Y. Saga *et al.*, MesP1: A novel basic helix-loop-helix protein expressed in the nascent mesodermal cells during mouse gastrulation. *Development* **122**, 2769–2778 (1996). pmid: [8787751](https://pubmed.ncbi.nlm.nih.gov/8787751/)

### ACKNOWLEDGMENTS

We are grateful to Q. Zhou, W. Li, F. Gao, and N. Jing at the CAS, and N. Plachta at A\*STAR in Singapore, for helpful discussions; F. Tang and X. Fan at Peking University for helping to establish the single-cell RNA-seq platform; S. Ng (CAS) for critical reading of the manuscript; and S. Li and X. Zhu of the imaging platform of CAS for their outstanding support. **Funding:** This work was supported by the Strategic Priority Research Program of the CAS (XDA16020700), the National Key R&D Program of China (2018YFC1004500, 2017YFC1001400), the National Natural Science Foundation of China (31571533, 31590832), and the exchange program of State Key Laboratory of Genetic Resources and Evolution, Kunming Institute of Zoology, CAS (GREK17-10). **Author contributions:** H.M. designed and developed the monkey embryo culture system, drafted the manuscript, and performed data analyses. J.Z. and H.W. performed embryo culture experiments, whole-mount staining of IVC monkey embryos, imaging, and analyses. X.J. performed single-cell experiments and analyzed data. Y.X., L.W., and Z.-A.Z. optimized the culture system for mouse blastocysts. L.W., X.H., and B.Z. contributed to monkey maintenance. L.L., P.Z., and H.W. initiated and supervised the study, analyzed data, and wrote the manuscript. All authors commented on the manuscript. **Competing interests:** The authors declare no competing interests. **Data and materials availability:** All data are available in the main text or the supplementary materials or from the corresponding authors upon request.

### SUPPLEMENTARY MATERIALS

[science.sciencemag.org/content/366/6467/eaax7890/suppl/DC1](https://science.sciencemag.org/content/366/6467/eaax7890/suppl/DC1)  
Materials and Methods  
Figs. S1 to S21  
Tables S1 to S7  
References (34–43)  
Movies S1 to S4

[View/request a protocol for this paper from Bio-protocol.](#)

24 May 2019; accepted 16 October 2019  
10.1126/science.aax7890

## RESEARCH ARTICLE SUMMARY

## DEVELOPMENTAL BIOLOGY

## Dissecting primate early post-implantation development using long-term in vitro embryo culture

Yuyu Niu<sup>\*†</sup>, Nianqin Sun<sup>†</sup>, Chang Li<sup>†</sup>, Ying Lei<sup>†</sup>, Zhihao Huang, Jun Wu, Chenyang Si, Xi Dai, Chuanyu Liu, Jingkuan Wei, Longqi Liu, Su Feng, Yu Kang, Wei Si, Hong Wang, E. Zhang, Lu Zhao, Ziwei Li, Xi Luo, Guizhong Cui, Guangdun Peng, Juan Carlos Izpisua Belmonte<sup>\*</sup>, Weizhi Ji<sup>\*</sup>, Tao Tan<sup>\*</sup>

**INTRODUCTION:** The period from peri-implantation to gastrulation is critical for mammalian embryogenesis. During this time, connections between embryonic and maternal tissues are set up, and the primary germ layers and body plan are established. There is a substantial gap in our knowledge of early human postimplantation development because of technological limitations and ethical considerations. To extend the study of human embryogenesis to the postimplantation period, an in vitro culture system has been established that extends human blastocyst development to the pregastrulation stage (up to 12 days) after fertilization, and the molecular and cellular events are revealed.

**RATIONALE:** With the general prohibition of growing human embryos beyond 14 days, closely related surrogate species can be examined. In addition, improvements are needed for primate embryo culture to support extended growth periods. The establishment of an in vitro culture system that enables the development of primate embryos beyond the implantation period provides an accessible way to study molecular and cellular mechanisms that un-

derlie postimplantation development, including gastrulation.

**RESULTS:** In this study, we have modified a human embryo in vitro culture protocol that enables the development of cynomolgus monkey (long-tailed macaque) embryos to develop up to 20 days after fertilization. The cultured cynomolgus embryos recapitulated key primate in vivo morphogenetic events, including amniotic and yolk sac cavitation, embryonic and extraembryonic lineage specification, specification of primordial germ-like cells (PGCLCs), and primitive streak cells. We demonstrated that the amniotic lumenogenesis is accompanied by the polarization of the epiblast (EPI); however, the polarization of PE was not observed during yolk sac cavitation. We used single-cell RNA-sequencing to delineate the developmental trajectories of EPI, trophoblast, and primitive endoderm (PE) lineages. We observed that accompanying the transition from the naïve to primer state, the metabolic mode of oxidative phosphorylation is no longer used in the EPI cells. Furthermore, the trophoblast differentiates in a stepwise manner, and ex-

pression of the trophoectoderm marker CDX2 decreases rapidly after day 11 in the trophoblast but maintains in the amniotic epithelium cells. In addition, we identified two types of PE lineage. Coordinated interactions were observed among EPI, trophoblast, PE, and extraembryonic mesenchyme cells during

## ON OUR WEBSITE

Read the full article at <http://dx.doi.org/10.1126/science.aaw5754>

the postimplantation period. Furthermore, we showed that PGCLCs specified in vitro are similar to early-stage PGCs in vivo. Using the single-cell assay for transposase-accessible chromatin followed by sequencing (scATAC-seq), we also identified EPI, trophoblast, PE, and EXMC lineages. Last, scATAC-seq revealed that distal regions of chromatin in the EPI lineage exhibited higher accessibility than in other cell types.

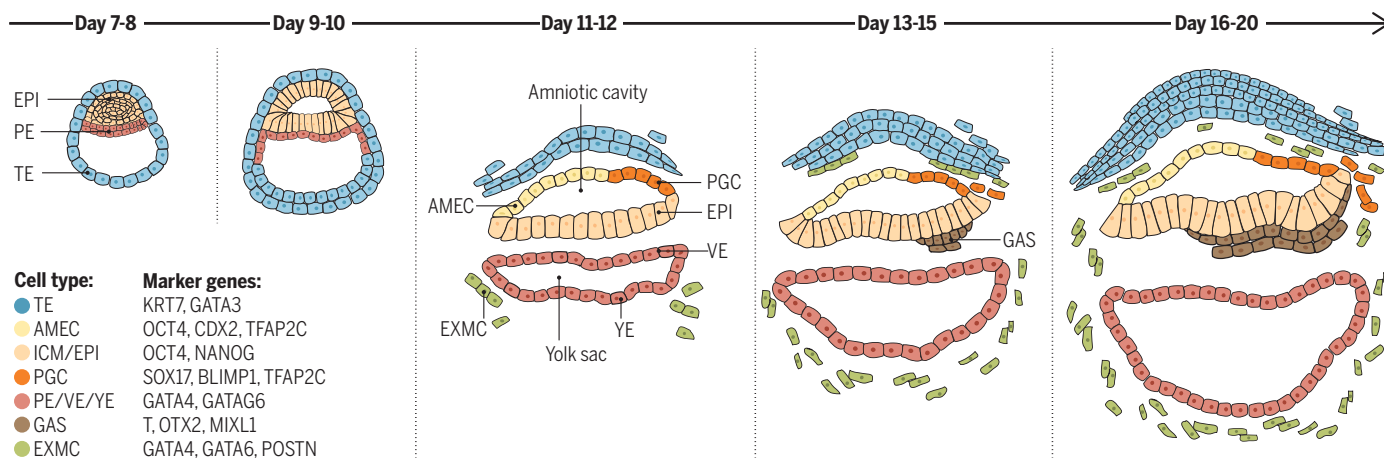
**CONCLUSION:** In this study, we show that monkey embryos show robust development beyond 14 days after fertilization, surviving until day 20 without support from maternal tissue. We also provide insights into the transcriptional programs and chromatin dynamics that underlie monkey post-implantation development. Our system provides a platform to analyze molecular and cellular dynamics during primate early development. Last, our data may help guide the development of improved differentiation protocols for primate pluripotent stem cells. ■

The full list of author affiliations is available online.

<sup>\*</sup>Corresponding author. Email: [tant@lpbr.cn](mailto:tant@lpbr.cn) (T.T.); [niuyy@lpbr.cn](mailto:niuyy@lpbr.cn) (Y.N.); [wji@lpbr.cn](mailto:wji@lpbr.cn) (W.J.); [belmonte@salk.edu](mailto:belmonte@salk.edu) (J.C.I.B.)

<sup>†</sup>These authors contributed equally to this work.

Cite this article as: Niu et al., *Science* 366, eaaw5754 (2019). DOI: 10.1126/science.aaw5754



**Monkey embryos cultured in vitro recapitulate primate postimplantation embryogenesis in vivo.** Scheme of monkey postimplantation embryogenesis cultured in vitro. ICM, inner cell mass; EPI, epiblast; PE, primitive endoderm; TE, trophoectoderm; AMEC, amniotic epithelium cell; PGC, primordial germ cell; VE, visceral endoderm; YE, yolk-sac endoderm; EXMC, extra-embryonic mesenchyme cell; and GAS, gastrulating cell.



## RESEARCH ARTICLE

## DEVELOPMENTAL BIOLOGY

# Dissecting primate early post-implantation development using long-term in vitro embryo culture

Yuyu Niu<sup>1\*</sup>, Nianqin Sun<sup>1†</sup>, Chang Li<sup>1†</sup>, Ying Lei<sup>2,3†</sup>, Zhihao Huang<sup>2,3</sup>, Jun Wu<sup>4,5,6</sup>, Chenyang Si<sup>1</sup>, Xi Dai<sup>2,3</sup>, Chuanyu Liu<sup>2,3</sup>, Jingkuan Wei<sup>1</sup>, Longqi Liu<sup>2,3</sup>, Su Feng<sup>7</sup>, Yu Kang<sup>1</sup>, Wei Si<sup>1</sup>, Hong Wang<sup>1</sup>, E. Zhang<sup>1</sup>, Lu Zhao<sup>1</sup>, Ziwei Li<sup>1</sup>, Xi Luo<sup>8</sup>, Guizhong Cui<sup>9</sup>, Guangdun Peng<sup>8,9</sup>, Juan Carlos Izpisua Belmonte<sup>6\*</sup>, Weizhi Ji<sup>1,10\*</sup>, Tao Tan<sup>1\*</sup>

The transition from peri-implantation to gastrulation in mammals entails the specification and organization of the lineage progenitors into a body plan. Technical and ethical challenges have limited understanding of the cellular and molecular mechanisms that underlie this transition. We established a culture system that enabled the development of cynomolgus monkey embryos in vitro for up to 20 days. Cultured embryos underwent key primate developmental stages, including lineage segregation, bilaminar disc formation, amniotic and yolk sac cavitation, and primordial germ cell-like cell (PGCLC) differentiation. Single-cell RNA-sequencing analysis revealed development trajectories of primitive endoderm, trophoblast, epiblast lineages, and PGCLCs. Analysis of single-cell chromatin accessibility identified transcription factors specifying each cell type. Our results reveal critical developmental events and complex molecular mechanisms underlying nonhuman primate embryogenesis in the early postimplantation period, with possible relevance to human development.

From peri-implantation, when the blastocyst attaches to the uterine endometrium, to gastrulation when the primary germ layers and body plan are established, mammalian embryos undergo numerous cellular and molecular transitions (1). Mouse studies have revealed the molecular mechanisms that control gastrulation (2–7). However, there are considerable anatomical, physiological, and developmental differences between mice and humans, limiting the insights derived from mice that are applicable to human embryogenesis (8–10). Although our knowledge of early human development is improving, owing to the derivation of embryonic

stem cells (ESCs) from human blastocysts, our understanding of the molecular and cellular events during early human postimplantation development remains limited.

Recently, an in vitro culture system that allows human embryos to develop beyond the blastocyst stage has facilitated study of the postimplantation period. Epiblast (EPI) expansion, lineage segregation, and amnion and yolk sac formation have been observed in vitro (11, 12), but embryos become disorganized by day 12. Beyond that point, improved culture conditions are needed. However, there are ethical considerations in generating human embryos, such as the 14-day rule. It is expected that examination of closely related species would reveal mechanisms conserved among different primates, including human. Among nonhuman primates, the monkey is our closest kin and represents an excellent surrogate species. In vivo derived cynomolgus monkey embryos have been used to analyze several primate postimplantation events, including amnion formation and germ cell specification. For example, single-cell RNA-sequencing (scRNA-seq) analysis has helped delineate the pluripotency program in EPI cells (13, 14). However, critical questions remain, including whether primate embryos can be cultured beyond the gastrulation stage in vitro and what the molecular determinants are of embryonic and extraembryonic lineage specification.

To address these questions, we used the human embryo culture protocol (11, 12) to culture cynomolgus embryos beyond gastrulation (~14 days) and up to 20 days in vitro. The cultured cynomolgus embryos underwent peri- and postimplantation events typical of higher

primate species (9, 10, 15), including embryonic and extraembryonic lineage segregation, bilaminar disc generation, amniotic and yolk sac cavitation, and primordial germ cell-like cell (PGCLC) specification. scRNA-seq and single-cell assay for transposase-accessible chromatin using sequencing (scATAC-seq) were used to analyze transcriptional and accessible chromatin profiles of cynomolgus post-implantation embryos at single-cell resolution, delineating the developmental trajectories of EPI, primitive endoderm (PE), trophoblast (TE), and PGCs and characterizing transcription factor (TF) regulatory networks and signaling pathway interactions. Our results reveal the molecular details of early cynomolgus development and will help gain mechanistic insights into primate embryogenesis.

## Results

### In vitro culture of cynomolgus embryos

To determine whether primate embryos could be cultured in vitro beyond gastrulation (~14 days), we used the human embryo culture protocol (11, 12) with several modifications: Advanced Dulbecco's Modified Eagle Medium/Ham's F-12 (Advanced DMEM/F12) was replaced with DMEM/F12, which was more suitable for monkey embryos culture, and 8  $\mu$ M Rho-associated, coiled-coil containing protein kinase (ROCK) inhibitor, Y-27632, was included in culture media to prevent apoptosis (Materials and methods). Fertilized embryos were cultured to the blastocyst stage, the zona pellucida was removed, and denuded blastocysts were plated; 99.4% ( $n = 104$  embryos) were attached to the cell-culture dishes by way of the polar TE, similar to the human embryos (11, 12). Mouse blastocysts implant by way of the mural TE in vivo and in vitro (16, 17), suggesting species-specific differences in the establishment of the embryo-endometrial epithelial interface. Most (92.31%,  $n = 104$  embryos) cynomolgus embryos attached at day 10, and after attachment, the monkey blastocyst cavity expanded continuously until day 20 (21.74%,  $n = 46$  embryos) (Fig. 1A). Inner cell mass (ICM) cells also continued to proliferate, forming a disc-like structure (Fig. 1B), with diameter increased from 113.75 by 86.28  $\mu$ m (long axis by short axis, respectively) at day 9 to 216.62 by 178.33  $\mu$ m at day 20 (Fig. 1B). We observed trophoblast villi-like structures sprouting from the embryos at day 15 and became evident at day 17 (Fig. 1C). In comparison, the human embryo blastocyst cavity collapsed soon after embryo attachment at day 8, and the disc-like and placenta villi-like structures were not clearly observed (11, 12).

### Lineage specification in cynomolgus embryos

Expression of lineage-specific markers—EPI (OCT4, NANOG), hypoblast (GATA6), and TE (CDX2)—was analyzed by means of

<sup>1</sup>Yunnan Key Laboratory of Primate Biomedical Research, Institute of Primate Translational Medicine, Kunming University of Science and Technology, Kunming, Yunnan 650500, China. <sup>2</sup>BGI-Shenzhen, Shenzhen, Guangdong 518083, China. <sup>3</sup>China National GeneBank, BGI-Shenzhen, Shenzhen, Guangdong 518120, China. <sup>4</sup>Department of Molecular Biology, University of Texas Southwestern Medical Center, Dallas, TX 75390, USA. <sup>5</sup>Hamon Center for Regenerative Science and Medicine, University of Texas Southwestern Medical Center, Dallas, TX 75390, USA. <sup>6</sup>Gene Expression Laboratory, Salk Institute for Biological Studies, La Jolla, CA 92037, USA. <sup>7</sup>State Key Laboratory of Cell Biology, CAS Center for Excellence in Molecular Cell Science, Shanghai Institute of Biochemistry and Cell Biology, Chinese Academy of Sciences (CAS), University of Chinese Academy of Sciences, Shanghai 200032, China. <sup>8</sup>CAS Key Laboratory of Regenerative Biology, Guangdong Provincial Key Laboratory of Stem Cell and Regenerative Medicine, Guangzhou Institutes of Biomedicine and Health, CAS, Guangzhou 510530, China. <sup>9</sup>Center of Cell Lineage and Atlas, Guangzhou Regenerative Medicine and Health Guangdong Laboratory (GRMH-GDL), Guangzhou 510530, China. <sup>10</sup>CAS Center for Excellence in Brain Science and Intelligence Technology, CAS, Shanghai 200032, China.

\*Corresponding author. Email: tant@lpbr.cn (T.T.); niuyy@lpbr.cn (Y.N.); wji@lpbr.cn (W.J.); belmonte@salk.edu (J.C.I.B.)

†These authors contributed equally to this work.

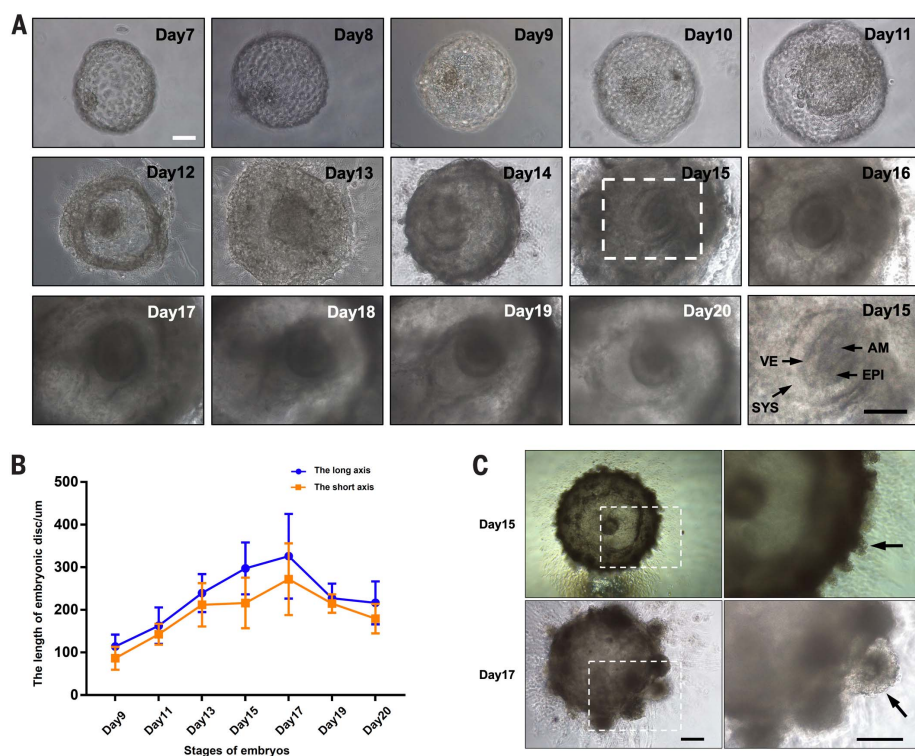


**Fig. 1. An in vitro culture system for monkey embryos.** (A) Representative bright-field images of monkey embryos developing in vitro until day 20 ( $n = 9$  embryos for days 13, 15, and 17 and  $n = 7$  embryos for other stages). Scale bars, 100  $\mu\text{m}$ . Bottom right shows higher magnification of area indicated in dotted box in day 15. (B) Measurements of length of embryonic disc (micrometer by micrometer) (long axis by short axis) ( $n = 9$  embryos of days 13, 15, and 17 and  $n = 7$  embryos of other stages). (C) Representative bright-field images of villous-like structure at days 15 and 17 in cultured embryos ( $n = 9$  embryos of each stage). Scale bars, 200  $\mu\text{m}$ . Arrows indicate villous-like structure. EPI, epiblast; AM, amnion; VE, visceral endoderm; SYS, secondary yolk sac.

immunofluorescence (IF) in in vitro cultured cynomolgus embryos. At day 8, OCT4 was principally expressed in the ICM and weakly expressed in the TE. GATA6 was expressed in all CDX2<sup>+</sup> cells. GATA6<sup>+</sup>/CDX2<sup>+</sup>/OCT4<sup>+</sup> cells were found in the ICM on day 8, suggesting that lineage specification was not complete in these cells (Fig. 2A). GATA6 expression is not detectable in human and mouse TE cells (13), suggesting species-specific differences in TE specification between humans and monkeys. By day 9, a few GATA6<sup>+</sup>/OCT4<sup>+</sup> cells were detected in the ICM, and CDX2<sup>+</sup>/OCT4<sup>+</sup> cells were detected in the TE, suggesting that lineage transitions are still occurring in these cells (Fig. 2B).

After attachment (approximately day 10), few OCT4<sup>+</sup>/GATA6<sup>+</sup> and SOX17<sup>+</sup>/OCT4<sup>+</sup> cells were detected in the ICM. CDX2<sup>+</sup>/GATA6<sup>+</sup> cells were detected mainly in the TE, implying complete lineage segregation of EPI and TE at this stage (Fig. 2C and fig. S1A). On day 11, GATA6<sup>+</sup> cells formed a layer ventral to the EPI cells, indicating ongoing differentiation of the visceral and yolk sac endoderm (VE/YE) (Fig. 2D).

TE marker CDX2 was coexpressed with OCT4 and GATA6 in peri-implantation cynomolgus embryos (days 8 and 9) (Fig. 2, A and B). These markers are not coexpressed in mouse and human embryos (13, 18); CDX2 is expressed in mouse trophoblast stem cells (TSCs) but not in human TSCs (19). To study TE development in cynomolgus embryos, we analyzed CDX2, OCT4, and GATA6 expression. CDX2 was not detected in trophoblast derivatives from day 12 onward, whereas it was expressed in amniotic epithelium cells, which showed low or undetectable GATA6 levels (Fig. 2E and fig. S1B). From day 12 onward, two groups of OCT4<sup>+</sup> cells were present: columnar cells in proximity to the VE/YE and squamous cells close to trophoblast, a sign of the amniotic epithelium differentiation (Fig. 2, F and G). NANOG was expressed at high levels in the EPI and was only weakly expressed or undetectable in the amniotic epithelium, whereas OCT4 was expressed both in the EPI and amniotic epithelium (Fig. 2, F and G, and fig. S1C). By contrast, mouse NANOG expression decreases after embryo implantation (20), representing species-specific difference.

Investigation of the expression of TE markers CDX2, GATA3, and CK7 (21–23) revealed that CDX2 was not expressed in the CK7<sup>+</sup> cells at day 12. CK7/GATA3 expression was maintained in subpopulations of trophoblast cells until day 17 (fig. S1D). These data imply that the putative placenta progenitors persisted at least until day 17, indicating that CDX2 alone is not a suitable marker for cynomolgus TS cells. Thus, cynomolgus embryos cultured in vitro could initiate embryonic and extraembryonic lineage specification in the absence of the maternal environment and maternal tissues.

#### Apical adherent junctions and the amnion

We asked whether in vitro cultured cynomolgus embryos could form amnion and yolk sac cavities. NANOG, FOXA1, and COL6A1 expression were used to delineate the EPI, VE/YE, and extraembryonic mesenchyme cells (EXMCs) (13, 15, 24). At day 11, we found a small lumen surrounded by NANOG<sup>+</sup> cells. VE/YE cells (FOXA1<sup>+</sup>) lined beneath the EPI cells (Fig. 3A). At day 13, primary yolk sac composed of FOXA1<sup>+</sup> cells was visible (Fig. 3B). The EPI continued to proliferate, forming a convex shape relative to the amnion cavity from day 17 onward, and the secondary yolk sac-like cavity was clearly observed beneath the NANOG-expressing EPI (Fig. 3C).

In mice and humans, polarized EPI cells initiate amnion cavity formation (12, 16). We postulated that EPI polarization would trigger amnion cavity formation in cynomolgus embryos. To test this idea, we analyzed E-cadherin (E-CAD) and atypical protein kinase C (aPKC) expression from day 11 to day 17 to trace EPI cell (OCT4<sup>+</sup>) polarization. At day 11, E-CAD and aPKC were apically localized in EPI cells, which formed a rosette-like structure lining a lumen at the center of the EPI (Fig. 3D). After expansion of the amnion cavity, the polarized localization of E-CAD and aPKC persisted in EPI cells from day 12 (Fig. 3E) to day 17 (fig. S1E), suggesting maintenance of polarization of EPI during development.

To investigate whether a similar mechanism underlines yolk sac formation in cynomolgus embryos, we examined E-CAD and aPKC expression in VE/YE cells (FOXA1<sup>+</sup>). E-CAD was not detected, and aPKC was not apically localized in the yolk sac, either at day 11 or day 17 (Fig. 3F). Together, these results suggest that the apical localization of the adherent junctions plays no roles in amnion and yolk sac cavity formation in cultured cynomolgus embryos.

#### WNT signaling during primitive streak induction

Ethical considerations regarding human embryos means primitive streak (PS) induction remains poorly understood. Cynomolgus embryos develop for up to 20 days in culture, suggesting that cynomolgus PS induction may be recapitulated in vitro. To test this idea, we



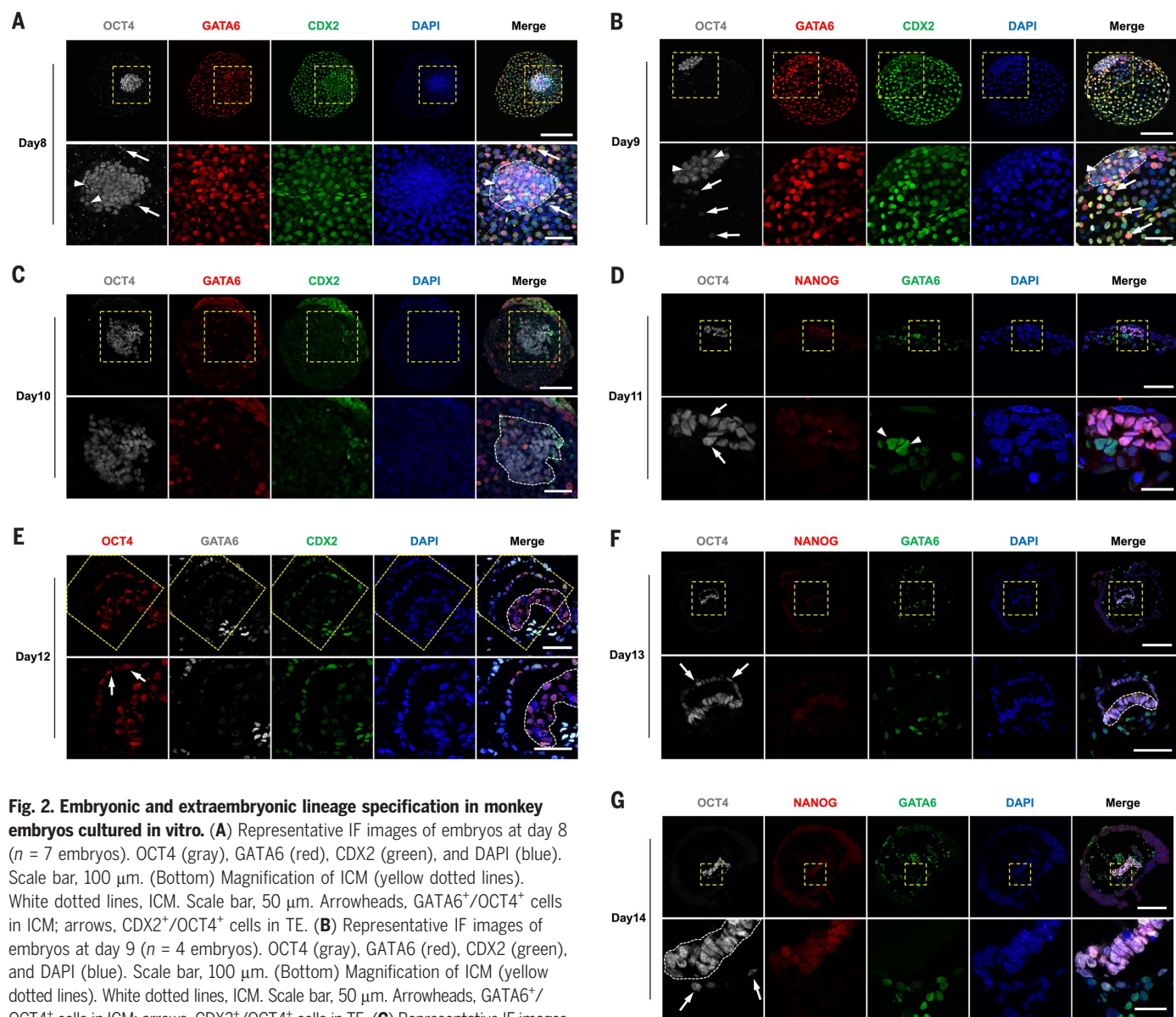


**Fig. 2. Embryonic and extraembryonic lineage specification in monkey embryos cultured in vitro.** (A) Representative IF images of embryos at day 8 ( $n = 7$  embryos). OCT4 (gray), GATA6 (red), CDX2 (green), and DAPI (blue). Scale bar, 100  $\mu\text{m}$ . (Bottom) Magnification of ICM (yellow dotted lines). White dotted lines, ICM. Scale bar, 50  $\mu\text{m}$ . Arrowheads, GATA6<sup>+</sup>/OCT4<sup>+</sup> cells in ICM; arrows, CDX2<sup>+</sup>/OCT4<sup>+</sup> cells in TE. (B) Representative IF images of embryos at day 9 ( $n = 4$  embryos). OCT4 (gray), GATA6 (red), CDX2 (green), and DAPI (blue). Scale bar, 100  $\mu\text{m}$ . (Bottom) Magnification of ICM (yellow dotted lines). White dotted lines, ICM. Scale bar, 50  $\mu\text{m}$ . Arrowheads, GATA6<sup>+</sup>/OCT4<sup>+</sup> cells in ICM; arrows, CDX2<sup>+</sup>/OCT4<sup>+</sup> cells in TE. (C) Representative IF images of embryos at day 10 ( $n = 7$  embryos). OCT4 (gray), GATA6 (red), CDX2 (green), and DAPI (blue). Scale bar, 250  $\mu\text{m}$ . (Bottom) Magnification of inserts (yellow dotted lines) in top panels. White dotted lines, ICM. Scale bar, 100  $\mu\text{m}$ . (D) Representative IF images of embryos at day 11 ( $n = 4$  embryos) staining for OCT4/NANOG/GATA6. Scale bar, 50  $\mu\text{m}$ . (Bottom) Zooms of inserts (yellow dotted lines) in top panels. Scale bar, 25  $\mu\text{m}$ . Arrows, EPI; arrowheads: VE/YE. (E) Representative IF images of embryos at day 12 ( $n = 7$  embryos) staining for OCT4/GATA6/CDX2. Scale bar, 100  $\mu\text{m}$ . (Bottom) Zooms of inserts (yellow dotted lines) in top panels. Arrows, amniotic epithelium cells. White dotted lines, EPI. Scale bar, 50  $\mu\text{m}$ . (F) Representative

IF images of embryos at day 13 ( $n = 6$  embryos) staining for OCT4/NANOG/GATA6. Scale bar, 100  $\mu\text{m}$ . (Bottom) Enlargements of inserts (yellow dotted lines) in top panels. Scale bar, 50  $\mu\text{m}$ . Arrows, amniotic epithelium cells. White dotted lines, EPI. (G) Representative IF images of day 14 embryos ( $n = 7$  embryos) staining for OCT4/NANOG/GATA6. Scale bar, 100  $\mu\text{m}$ . (Bottom) Enlargements of inserts (yellow dotted lines) in top panels. Scale bar, 50  $\mu\text{m}$ . Arrows, the amniotic epithelium cells. White dotted lines, EPI. ICM, inner cell mass; TE, trophectoderm; EPI, epiblast; VE, visceral endoderm; YE, yolk-sac endoderm.

analyzed BRACHYURY (also known as T) expression, a PS marker, from day 11 (24, 25). On day 11, T-expressing cells localized mainly to the dorsal amnion cavity, and OCT4 expression in these cells was weak. Around day 13, some of these cells were found underneath the EPI, and OCT4 expression was further reduced (Fig. 4A). Because T<sup>+</sup>-expressing EPI cells migrated into the space between the EPI and

VE during gastrulation and the orientation of nuclei of migrating cells changed (26, 27), we observed that T<sup>+</sup> cell nuclei outside EPI were progressively oriented parallel rather than perpendicular to the EPI layer [day 15 (Fig. 4B) and day 18 (fig. S2A)]. Approximately 63.83% ( $n = 30$  nuclei) of nuclei of T<sup>+</sup> cells ( $n = 47$  cells), outside the EPI, were parallel to the EPI layer, whereas 79.30% ( $n = 157$  cells) of T<sup>+</sup> cells with-

in the EPI ( $n = 198$  cells) were perpendicular to EPI layer in total identified T<sup>+</sup> cells ( $n = 245$  cells) from day 11 to day 20 (Fig. 4C).

PS induction is characterized by the epithelial-mesenchymal transition (EMT) (1, 26); we therefore analyzed expression of EMT maker genes, such as SNAI2 and MIXL1, in identified gastrulating cells, which were identified by using markers characterized in a previous report (13).

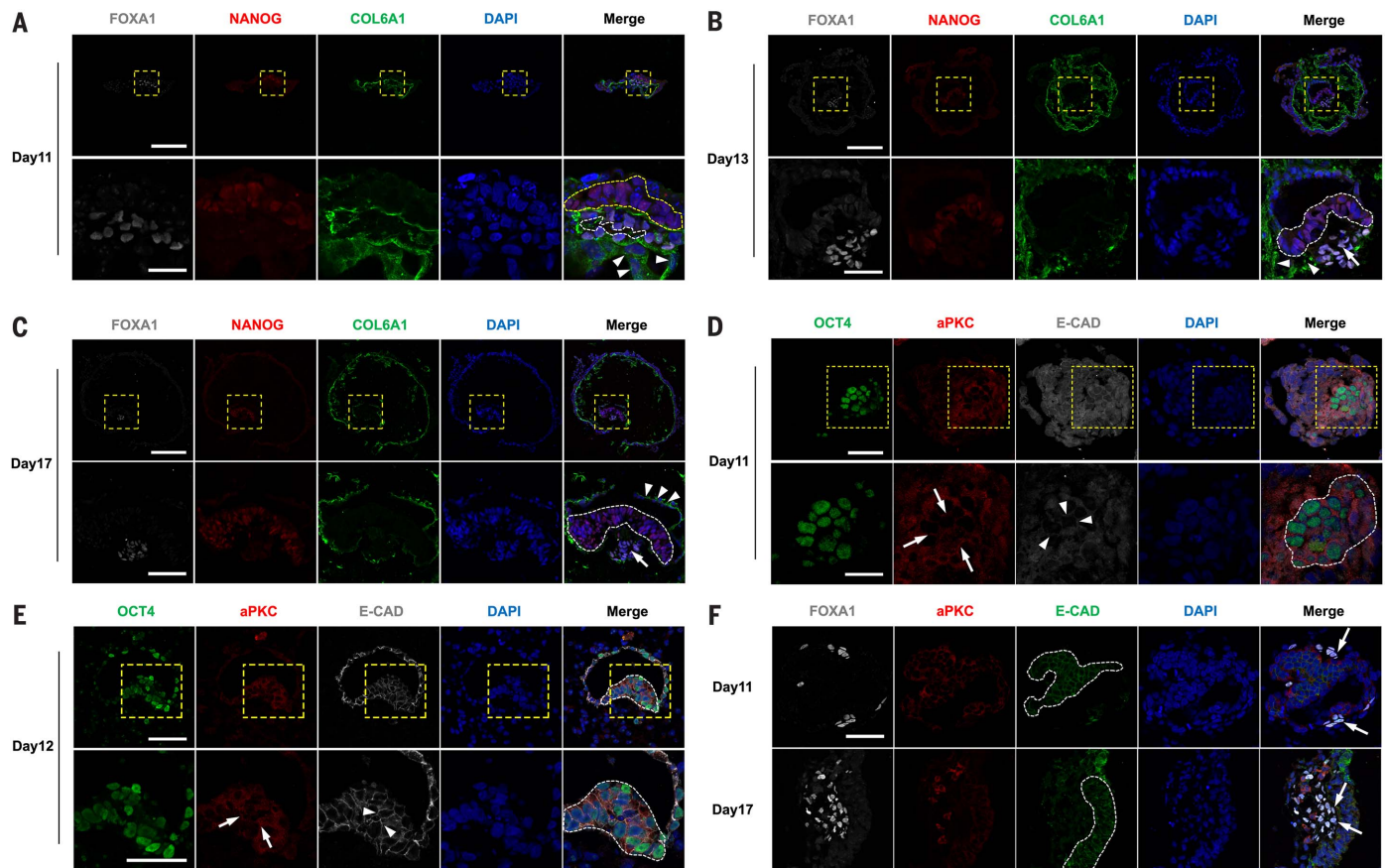


**Fig. 3. Amnion and yolk sac cavity formation.** Embryos at indicated stage were stained with FOXA1 (PE marker), NANOG (EPI marker), and COL6A1 (EXMC marker) to monitor amnion and yolk sac cavity formation. **(A)** Representative IF images of embryos at day 11 ( $n = 4$  embryos) staining for FOXA1/NANOG/COL6A1. Scale bar, 250  $\mu\text{m}$ . (Bottom) Enlargements of inserts (yellow dotted lines) in top panels. Scale bar, 50  $\mu\text{m}$ . Yellow dotted lines, EPI; white dotted lines, yolk sac; arrowheads, EXMC. **(B)** Representative IF images of embryos at day 13 ( $n = 6$  embryos) staining for FOXA1/NANOG/COL6A1. Scale bar, 250  $\mu\text{m}$ . (Bottom) Enlargements of inserts (yellow dotted lines) in top panels. Scale bar, 50  $\mu\text{m}$ . Arrow, primary yolk sac cavity; white dotted lines, EPI; arrowheads, EXMC. **(C)** Representative IF images of embryos at day 17 ( $n = 6$  embryos) staining for FOXA1/NANOG/COL6A1. Scale bar, 250  $\mu\text{m}$ . (Bottom) Enlargements of inserts (yellow dotted lines) in top

panels. Scale bar, 50  $\mu\text{m}$ . Arrow, secondary yolk sac cavity; white dotted lines, EPI; arrowheads, EXMC. **(D)** Representative IF images of embryos at day 11 ( $n = 4$  embryos) staining for OCT4/aPKC/E-CAD. (Bottom) Enlargements of inserts (yellow dotted lines) in top panels. Scale bar, 50  $\mu\text{m}$ . Arrows, apical localization of aPKC; arrowheads, apical localization of E-CAD; white dotted lines, EPI. **(E)** Representative IF images of embryos at day 12 ( $n = 7$  embryos) staining for OCT4/aPKC/E-CAD. (Bottom) Enlargements of inserts (yellow dotted lines) in top panels. Scale bar, 50  $\mu\text{m}$ . Arrows, apical localization of aPKC; arrowheads, E-CAD apical localization; white dotted lines, EPI. **(F)** Representative IF images of embryos at day 11 ( $n = 4$  embryos) and day 17 ( $n = 6$  embryos) staining for FOXA1/aPKC/E-CAD. Scale bar, 50  $\mu\text{m}$ . Arrows, FOXA1<sup>+</sup> VE/YE cells; white dotted lines, EPI. PE, primitive endoderm; EPI, epiblast; EXMC, extra-embryonic mesenchyme cell.

SNAI2 and MIXL1 were significantly elevated in gastrulating cells (Fig. 4D). The PS marker, OTX2 (28–30), was also expressed in gastrulating cells (located under the EPI layer) (Fig. 4, D and E), indicating that PS formation occurs in cultured cynomolgus embryos.

We asked whether the WNT signaling pathway is involved in PS induction because it is in mouse embryos and in human ESCs (29, 31, 32). High WNT3, WNT5A, WNT5B, and WNT8A expression levels (Fig. 4F and fig. S2B) were found in gastrulating cells by use of scRNA-seq, similar to human ESCs (29). WNT pathway repressors, such as the secreted proteins CER1, are required for mouse gastrulation (33) and induction of PS in human ESCs (29).

scRNA-seq revealed that CER1 was highly expressed in gastrulating cells (Fig. 4G). IF staining of cryosections from embryos cultured in vitro at day 13 and day 17 revealed WNT3 and WNT5A expression in EPI and gastrulating cell, which was confirmed with scRNA-seq profiles (Fig. 4H). scATAC-seq analysis revealed open chromatin regions over gene regulatory regions of WNT signaling family members in gastrulating cells (fig. S5E). These results imply a putative role for WNT signaling in PS formation in cultured cynomolgus embryos.

#### Cynomolgus PGCLC specification in vitro

Primate primordial germ cell (PGC) specification occurs during the second or third week

after fertilization (34), within the time frame of our embryo culture. SOX17<sup>+</sup>/CDX2<sup>+</sup> cells were detected in amniotic epithelium at day 13 (Fig. 5B). Because SOX17 is a critical specifier of primate PGC (14, 35), we postulated that PGCLC could emerge in amnion. Expression of two primate-specific PGC markers (SOX17/TFAP2C) was detected from day 13 to day 17. SOX17<sup>+</sup>/TFAP2C<sup>+</sup> cells were detected within the amnion, and SOX17 was expressed in cells within the amnion epithelium and beneath the EPI (gastrulating cells) at day 13 (Fig. 5A). From days 14 to 16, SOX17<sup>+</sup>/TFAP2C<sup>+</sup> cells were detected among amniotic cells and at the junction region between amnion and EPI (Fig. 5A). At day 17, SOX17<sup>+</sup>/BLIMP1<sup>+</sup> PGCLCs



# Fig. 4. Development of PS in cultured embryos.

(A) Representative IF images of embryo cryosections at day 11 ( $n = 4$  embryos) and day 13 ( $n = 6$  embryos) for OCT4 (red) and T (green) merged with DAPI (blue). Scale bar, 100  $\mu\text{m}$ .

(Bottom) Enlargements of inserts (yellow dotted lines) in top panels. Scale bar, 50  $\mu\text{m}$ . Arrows,  $T^{\text{high}}\text{OCT4}^{\text{low}}$  cells outside EPI.

(B) Representative IF images of embryos at day 15 ( $n = 6$  embryos) for E-CAD (gray), NANOG (red), and T (green) with merges with DAPI (blue). Scale bar, 100  $\mu\text{m}$ .

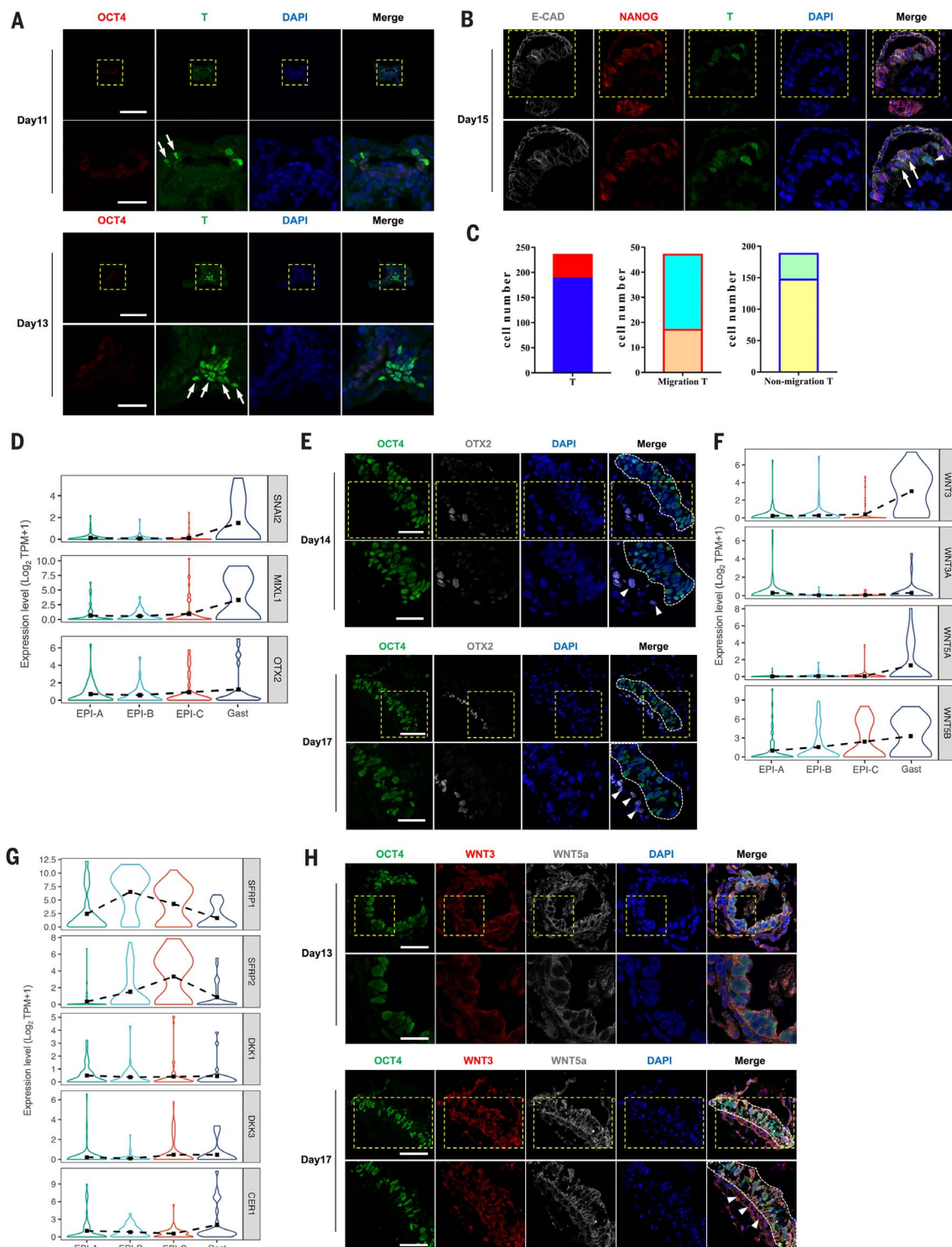
(Bottom) Enlargements of inserts (yellow dotted lines) in top panels. Scale bar, 50  $\mu\text{m}$ .  $T^+$  cells outside EPI (arrowhead) is  $T^+\text{NANO-G}^{\text{low}}$ , and  $T^+$  cells within EPI (arrows) are  $T^{\text{low}}\text{NANOG}^+$ .

$T^+$  cells outside EPI (arrowhead) show nucleus relatively parallel to the EPI layer (layer of NANOG positive cells).

(C) Quantification of cells ( $n = 245$  cells) with nuclei oriented parallel or perpendicular to the EPI layer in  $T^+$  cells outside ( $T^{\text{high}}\text{OCT4}^{\text{low}}$  or  $T^+\text{NANOG}^{\text{low}}$  or  $T^+\text{NANOG}$ ) or within ( $T^{\text{low}}\text{OCT4}^{\text{high}}$  or  $T^{\text{low}}\text{NANOG}^{\text{high}}$ ) EPI.

(Left) Percentage of  $T^+$  cells outside (red bar,  $n = 47$  cells, 19.18%) and within (blue bar,  $n = 198$  cells, 80.82%) EPI. (Middle) Percentage of cells with nuclei oriented parallel (light blue bar,  $n = 30$  cells, 63.83%) or perpendicular (orange bar,  $n = 17$  cells, 36.17%) to the EPI layer in  $T^+$  cells outside

EPI. (Right) Percentage of cells with nuclei oriented parallel (green bar,  $n = 41$  cells, 20.70%) or perpendicular (yellow bar,  $n = 157$  cells, 79.30%) to the EPI layer in  $T^+$  cells within EPI. (D) Violin plot of SNAI2, MIXL1, and OTX2 expression in EPI (EPI-A, EPI-B, and EPI-C) and gastrulating cells (Gast) identified in Fig. 6G. (E) Representative IF images of embryo cryosections at day 14 ( $n = 7$  embryos) and day 17 ( $n = 6$  embryos) for OCT4 (green) and OTX2 (gray) merged with DAPI (blue). Scale bar, 100  $\mu\text{m}$ . (Bottom) Enlargements of inserts (yellow dotted lines) in top panels. Scale bar, 50  $\mu\text{m}$ . White dotted lines, EPI; arrowheads, OTX2 $^+$  gastrulating cell. (F) Violin plot of WNT3, WNT3A, WNT5A, and WNT5B expression in EPI (EPI-A, EPI-B, and EPI-C) and gastrulating cells (Gast) identified in Fig. 6G. (G) Violin plot of WNT inhibitors expression in EPI (EPI-A, EPI-B, and EPI-C) and gastrulating cells (Gast) identified in Fig. 6G. CER1 is highly expressed in Gast ( $P < 0.05$ ). (H) Representative IF images of embryo cryosections at day 13 ( $n = 6$  embryos) and day 17 ( $n = 6$  embryos) for OCT4 (green), WNT3 (red), and WNT5A (gray) merged with DAPI (blue). Scale bar, 100  $\mu\text{m}$ . (Bottom) Enlargements of inserts (yellow dotted lines) in top panels. Scale bar, 50  $\mu\text{m}$ . White dotted lines, EPI; arrowheads, gastrulating cell. EPI, epiblast; Gast, gastrulating cell.



were found underneath the EPI (fig. S3). Expression of EOMES, another transcription factor required for PGCLC specification in humans (36, 37), was not detected in SOX17<sup>+</sup>/TFAP2C<sup>+</sup> cells at day 12 or day 17, whereas EOMES<sup>+</sup>/SOX17<sup>+</sup> cells were detected in gastrulating cells, which may represent precursors of the definitive endoderm (Fig. 5C) and is consistent with the amnion being a PGC source in vivo (14).

T can induce PGCLCs from germ-cell competent human PSCs (35, 38) or were induced when the PGC specified in vivo (14). T<sup>+</sup>/SOX17<sup>+</sup>/TFAP2C<sup>+</sup> cells were found in amnion from day 14 (Fig. 5A). From day 16, T was expressed in SOX17<sup>+</sup>/TFAP2C<sup>+</sup> cells and in the PS (SOX17<sup>-</sup>/TFAP2C<sup>-</sup> cells) (Fig. 5A), which is consistent with data from in vivo derived embryos (14).

We examined the expression of PGC markers using scRNA-seq in putative PGCLCs expressing SOX17, TFAP2C, and PRDM1 but not SOX2 (cells are identified in fig. S8A). The identified PGCLCs expressed PGC markers—including OCT4, NANOS3, SOX17, TFAP2C, and PRDM1 (Fig. 5D)—and also genes associated with the EMT, including VIMENTIN and CDH1 (Fig. 5E), which characterize early-stage PGCs in vivo (14), demonstrating the emergence of PGCLCs in cultured embryos, with a similar spatial location and molecular signatures as their in vivo counterparts.

#### Transcriptional regulation of lineage specification

To study lineage specification in the cultured cynomolgus embryos, scRNA-seq and scATAC-seq were performed on profile embryo transcriptomes at different developmental stages; 1014 and 1198 single cells from pre- and post-implantation embryos at seven time points (days 9, 11, 13, 15, 17, 19, and 20) were analyzed, respectively. After filtering, 600 and 978 cells were used for the final scRNA-seq and scATAC-seq analyses, respectively (table S1). scRNA-seq captured, on average, 4568 genes per cell (fig. S4A). Using t-distributed stochastic neighbor embedding (t-SNE) analysis, we identified four clusters of cells in vitro, the same cell types as identified in vivo (Fig. 6A) (13): EPI cells expressed high levels of pluripotency markers (OCT4 and NANOG); TE cells expressed KRT7 and GATA2; PE cells expressed GATA4, GATA6, and DPPA3; and EXMC cells also expressed GATA4 and GATA6 but not DPPA3 (Fig. 6B). t-SNE analysis showed that EPI, PE, TE, and EXMC of the in vitro cultured embryos were clustered with their in vivo counterparts (fig. S4, B and C) (13). EPI, PE, TE, and EXMC of the in vitro cultured embryos exhibited a close correlation with their in vivo counterparts, as did expression of key genes (fig. S4D). In vivo embryos at days 16, 18, and 20 were collected for low-input RNA-sequencing (Geo-seq) (table S1). t-SNE analysis revealed that EPI, PE, TE,

and EXMC of in vitro cultured embryos clustered with those of their in vivo counterparts (Geo-seq) (fig. S4E). scATAC-seq analysis revealed six cell clusters, including EPI, gastrulating cells (named Gast a and Gast b), PE, EXMC, and TE (fig. S5, A and B), similar to the scRNA-seq analysis. Transcription factor motifs, such as OTX2 in gastrulating cells, were identified (fig. S5C). Furthermore, a clustered heatmap of differential chromatin accessibility in each cluster, at the proximal and distal sites of marker genes, revealed that a majority of distal sites-accessible genes were enriched in EPI and gastrulating cells, and proximal sites-accessible genes were enriched in other cell types (fig. S5D).

We explored TE specification by examining transcriptional changes, revealing a continuous shift in the TE transcriptome from days 9 to 20, suggesting that TE cells differentiate in a stepwise fashion (Fig. 6C). On the basis of pseudotime analysis, TE cells were subdivided into two types accompanying the reduced expression of CDX2 from day 11 (Fig. 6D): Cells expressing high levels of TCEAL4 were likely cytotrophoblasts (CTs), and cells expressing high levels of GCM1 were likely syncytiotrophoblasts (STs) (11, 39). At day 11, yolk sac TE (ysTE) cells (11) were also found in the cultured cynomolgus embryos. These cells are positive for TE markers (such as GATA3) and express low levels of the EPI markers (such as SOX2) and PE markers (such as GATA4) (Fig. 6D).

The transcriptomic profiles delineate the developmental trajectory of the PE cells revealed two clusters of cells. Cluster 1 and cluster 2 expressed high levels of APOA2 and CXCR4, respectively, representing potential VE/YE differentiation (Fig. 6E and table S2). Gene Ontology (GO) term analysis revealed that cluster 1 was enriched for genes involved in lipid metabolism and transport, whereas cluster 2 was enriched for genes mediating transcription and protein synthesis (Fig. 6F). We also identified EXMCs, which are only found in higher primates (15). EXMCs exhibited similar marker gene expression to PE cells, suggesting that EXMCs might originate from the PE (fig. S6A). Furthermore, the GO terms analysis showed that pathways involved in extracellular matrix and EMT were enriched in EXMCs (fig. S6B and table S3). Transforming growth factor- $\beta$  (TGF $\beta$ ) signaling regulates the EMT. We found that TGF $\beta$  family members were highly expressed in EXMCs (fig. S6C), presumably suggesting that PE cells differentiate into EXMCs through the EMT, a process likely regulated by the TGF $\beta$  signaling pathway, which is consistent with their putative biological function in vivo (13, 24).

Amniotic epithelial cells form a thin membrane that contains the amniotic fluid, protecting the developing embryo or fetus (40, 41).

There has been limited characterization of amniotic epithelial cells during postimplantation in primates. Monkey amniotic epithelial cells expressed the markers OCT4, CDX2, and TFAP2C but not NANOG (Figs. 2E and 5A). We therefore analyzed amniotic epithelial cell scRNA-seq profiles on the basis of the expression of these markers and determined the relationship between EPI, EXMC, PE (VE/YE), and amniotic epithelial cells. Amniotic epithelial cells exhibited a profile highly similar to that of EXMC (fig. S7A), suggesting a potential developmental relationship between these two types of cells. We identified differential-expressed genes between these four types of cells but did not detect significant gene expression differences between amniotic epithelium and EPI cells (fig. S7B), probably because of the small numbers ( $n = 12$ ) of scRNA-seq profiles of amniotic epithelial cells and the similarity between amniotic epithelium and EPI cells. GO terms analysis showed that TGF $\beta$  signaling was enriched in amniotic epithelial cells (fig. S7C).

Examination of the pluripotency transition from the naïve to primed state in EPI cells during peri- to postimplantation stage revealed four clusters of EPI cells. Clusters 1 to 3 represented early- to late-stage EPI (EPI-A, EPI-B, and EPI-C, respectively), and cluster 4 represented gastrulating cells (Gast), because t-SNE analysis showed EPI-A and EPI-B were clustered with in vivo early-stage EPI cells, EPI-C was clustered with in vivo late-stage EPIs, and Gast was clustered with in vivo gastrulating cells (Fig. 6G and fig. S4C). We examined the expression of naïve and primed pluripotency-related genes and found that naïve genes (such as *TBX3*, *KLF4*, and *KLF5*) were highly expressed in early-stage EPI cells (EPI-A and EPI-B), whereas primed-specific genes (such as *ID1*, *ZIC2*, and *FGFR1*) gradually increased in later-stage EPI cells (EPI-C and Gast) (fig. S6D). GO term analysis revealed genes enriched in EPI-A were involved in oxidative phosphorylation and mitochondrial respiratory, whereas genes enriched in EPI-B and EPI-C were related to ribosome biogenesis and translation. Genes up-regulated in Gast were involved in embryonic morphogenesis, and mitochondrial oxidative metabolism was no longer enriched in these cells (Fig. 6H and table S4). Thus, naïve-state EPI cells favor the metabolic model of oxidative phosphorylation, as previously shown in PSCs (42, 43).

To explore signaling pathways potentially involved in lineage specification, we examined expression of the canonical signaling pathway. We observed that FGF (FGF2) and WNT ligands (WNT3A and WNT5B) were highly expressed in the EPI, whereas FGF (FGFR1 and FGFR2) and WNT receptors (FZD4 and FZD7) were enriched in PE and TE cells. IHH, a hedgehog pathway ligand, was highly expressed



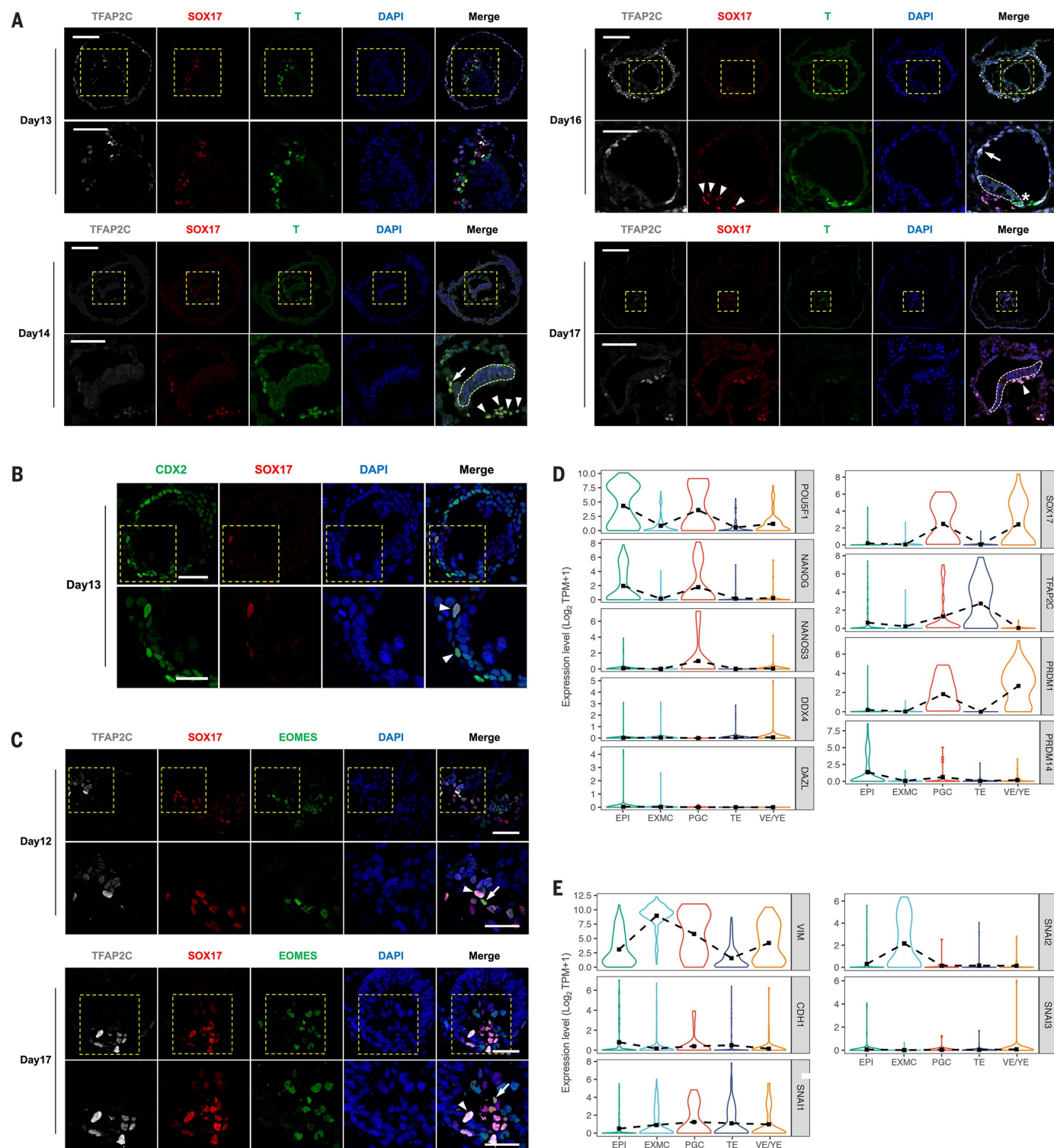


**Fig. 5. PGCLCs originate from amnion.** (A) Representative IF images of embryos at days 13 ( $n = 6$  embryos), 14 ( $n = 7$  embryos), 16 ( $n = 7$  embryos), and 17 ( $n = 6$  embryos) stained for TFAP2C/SOX17/T. Scale bar, 100  $\mu\text{m}$ . (Bottom) Enlargements of inserts (yellow dotted lines) in top panels. Scale bars, 50  $\mu\text{m}$ . Arrows, PGCLCs within amnion; arrowheads, PGCLCs beneath the EPI; asterisk, SOX17<sup>+</sup>/TFAP2C<sup>-</sup> cells. (B) Representative IF images of embryos at day 13 ( $n = 5$  embryos) stained for CDX2/SOX17. (Bottom) Enlargements of inserts (yellow dotted lines) in top panels. Arrowhead, CDX2<sup>+</sup>/SOX17<sup>+</sup> cell. Scale bars,

50  $\mu\text{m}$ . (C) Representative IF images of embryos at days 12 ( $n = 7$  embryos) and 17 ( $n = 6$  embryos) stained for TFAP2C/SOX17/EOMES. Arrows, SOX17<sup>+</sup>EOMES<sup>+</sup> cells; arrowheads, TFAP2C<sup>+</sup>SOX17<sup>+</sup> cells. Scale bar, 100  $\mu\text{m}$ . (Bottom) Enlargements of inserts (yellow dotted lines) in top panels. Scale bars, 50  $\mu\text{m}$ . (D) Violin plot of PGC marker genes expressions in identified PGCLCs. (E) Violin plot of EMT marker genes [VIMENTIN (VIM), CDH1, SNAI1, SNAI2, and SNAI3] expressions in identified PGCLCs. PGCLC, primordial germ cell-like cell; EMT, epithelial-mesenchymal transition.

in PE cells (Fig. 6I). DLL3, a NOTCH pathway ligand, was highly expressed in EPI, and the receptor NOTCH2 was highly expressed in EXMC (Fig. 6I). Because PE (VE/YE), EXMC, and EPI may form a niche coordinating-lineage specification, we determined potential cellular communication interactions among PE (VE/YE), EXMC, EPI, and TE using public ligand-receptor databases (Materials and methods). EXMC and PE (VE/YE) frequently interacted with other cell types through ligand expression, and EPI cells mainly expressed receptors to receive the ligand from PE (VE/YE), EXMC, and TE (fig. S7D). For example, insulinlike growth factor 2 (IFG2) and granulin (GRN) were enriched in EXMC and PE (VE/YE), respectively. TGFBR3 was specifically expressed in EPI (fig. S7D). Overall, our study suggests the specific expression spectrum of ligands and receptors and corresponding interactions within PE (VE/YE), EXMC, EPI, and TE.

#### Transcriptional regulation of PGCLCs specification

To investigate potential transcriptional mechanisms underlying cynomolgus PGCLCs specification, PGCLC candidates (expressing SOX17, TFAP2C, and PRDM1/ BLIMP1 but not SOX2) (fig. S8A) (14) were compared with EPI cells because our data indicate that PGCLCs may originate from the amnion. Pseudotime analysis revealed two types of PGCLCs, one clustered with EPI cells (PGCLC-EPI) and one that did not (PGCLC) (fig. S8B). GO term analysis revealed that genes enriched in PGCLC-EPI cells were involved in ribosome biogenesis, whereas genes enriched in PGCLC cells were related to responses to fibroblast growth factor and cell-cell signaling by WNT (fig. S8C and table S5). These findings suggest heterogeneity in PGCLC population during development in vitro.

Genes differentially expressed between PGCLCs and the EPI included enrichment of the GO terms cell substrate adhesion and extracellular structure organization in PGCLCs (fig. S8D and table S6), implying that migration is a characteristic of PGCs, which is in agreement with expression of EMT-related genes in cynomolgus PGCs in vivo (14). We examined the correlation between PGCLCs and in vivo PGCs (early and late stage) (14). PGCLCs exhibited close correlation with in vivo early-stage PGCs (fig. S8E). Thus, PGCLCs specified in vitro exhibited a transcriptome similar to that of early in vivo PGCs.

#### Discussion

Gastrulation in primates involves extensive remodeling of the embryo's transcriptional landscape to facilitate the formation of the body plan (1, 7). However, information about post-implantation development in primates remains limited because of ethical considerations, tech-

nical limitations, and high research costs. In vitro culture systems have been developed to study early postimplantation development in humans (11, 12). Here, we modified the human embryo culture system for cynomolgus embryos, enabling them to develop in vitro for up to 20 days and recapitulate the specification of embryonic and extraembryonic lineages, the cavitation of amnion and yolk sac, PS formation, and PGC specification. The structure of the embryos, especially amnion and yolk sac cavity, varied among cultured embryos, which was not observed from in vivo derived embryos. This discrepancy can potentially be attributed to different microenvironments, such as mechanical and biochemical cues, between in vivo and in vitro. The structure of cultured embryos eventually collapsed around 20 days, which highlights the need to further improve culture parameters to enable more faithful and extended monkey embryo development in vitro.

Single-cell -omics analyses of the cultured cynomolgus embryos revealed molecular details of how the EPI, PE, TE, and EXMC lineage are specified. We found that cynomolgus PE cells differentiated into putative visceral and yolk sac endoderm and also EXMCs, during which PE cells undergo the EMT, regulated by the TGF $\beta$  signaling pathway. In mice, PE differentiate into parietal and visceral endoderm. Then the latter further differentiates into distal and anterior visceral endoderm (DVE/AVE) (10). Whether monkey PE cells follow a similar developmental path warrants further studies. We saw evidence of the metabolic state transition from early- to late-stage EPI, accompanying the switch from naive to primed pluripotency. This is consistent with the notion that interactions between the metabolome and histone modifications drive the metabolic switch from naive to primed pluripotency in ESCs (44). Our results support the notion that PGCs originate from the amnion in vivo (14). The transcriptional profiles of a small group of the PGCLCs were similar to that of the EPI, suggesting that these PGCLCs may also have been derived from the EPI.

One of the advantages of in vitro monkey embryo culture is that it provides an accessible platform to gain in-depth insights into the dynamic molecular and cellular changes during primate early development on the basis of the improvement of culture conditions that could support more homogenous and extended embryo development. Combining the embryo culture system with live-cell imaging, lineage tracing, signaling pathway perturbation through activators and inhibitors, and single-cell -omics analyses will help determine key factors and pathways underlying the specification and development of different lineages and thereby guiding the development of improved differentiation protocols from primate PSCs, including humans.

We have cultured primate embryos beyond day 14 and provide a comprehensive analysis of the transcriptional features of postimplantation embryos using scRNA-seq and scATAC-seq. This culture system provides a platform with which to dissect the mechanisms underlying primate embryonic development.

#### Materials and methods

##### Embryo in vitro culture

The monkey blastocysts were collected at 6 to 7 days post fertilization. Zona pellucida of blastocyst was removed by exposure to hyaluronidase from bovine testes about 30s. Zona-free blastocysts were seeded on 8-well  $\mu$ -plates (80826, Ibidi) with pre-equilibrated in vitro culture medium 1 (IVC1). After embryos attached to the well, half of the IVC1 was exchanged with in vitro culture medium 2 (IVC2). Thereafter, half of the medium were replaced daily with fresh IVC2, and monkey embryos were harvested at the indicated stage. Embryo culture was performed at 37°C in 5% CO<sub>2</sub>. All chemicals were from Sigma Chemicals unless otherwise stated.

IVC1: DMEM/F12 (11320-033, Thermo Fisher Scientific) supplemented with 20% (vol/vol) heat-inactivated fetal bovine serum (FBS) (35-076-CV, Corning), 2mM L-glutamine (25030; Thermo Fisher Scientific), Penicillin (25 units/ml)/streptomycin (25  $\mu$ g/ml) (15070-063; Thermo Fisher Scientific), 1 $\times$  ITS-X (51500-056; Thermo Fisher Scientific), 8 nM  $\beta$ -estradiol, 200 ng/ml progesterone and 25  $\mu$ M N-acetyl-L-cysteine.

IVC2: 20% (vol/vol) heat-inactivated FBS of IVC1 was replaced with 30% (vol/vol) Knock-Out Serum Replacement (10828010, Thermo Fisher Scientific).

##### Single cell collection and embryo laser capture microdissection

After washing with phosphate buffered saline (PBS) (MA0008, meilunbio), the embryo was digested with 0.1% trypsin (25200-072, Gibco) at 37°C for 5 to 10 min. Then the trypsin was neutralized with 2% FBS (04-002-1A, Biological Industries) and FBS was washed off with cold PBS with 0.1 to 1% bovine serum albumin (BSA). Finally, individual cells were picked into a lysis medium on ice with a mouth pipette. All procedures were performed under stereomicroscope.

The transcriptome of in vivo embryos was obtained according to Geo-seq method (4). Briefly, one monkey embryo at day 16, two at day 18 and two at day 20 were embedded in optimal cutting temperature compound (OCT; 4583, Tissue-Tek OCT, skura). Embryos were cryo-sectioned along the anterior-posterior axis. Populations of approximately 20 cells from putative EPI, TE, EXMC or VE/YE were collected by laser microdissection and processed for low-input RNA sequencing based on Smart-seq2 method.



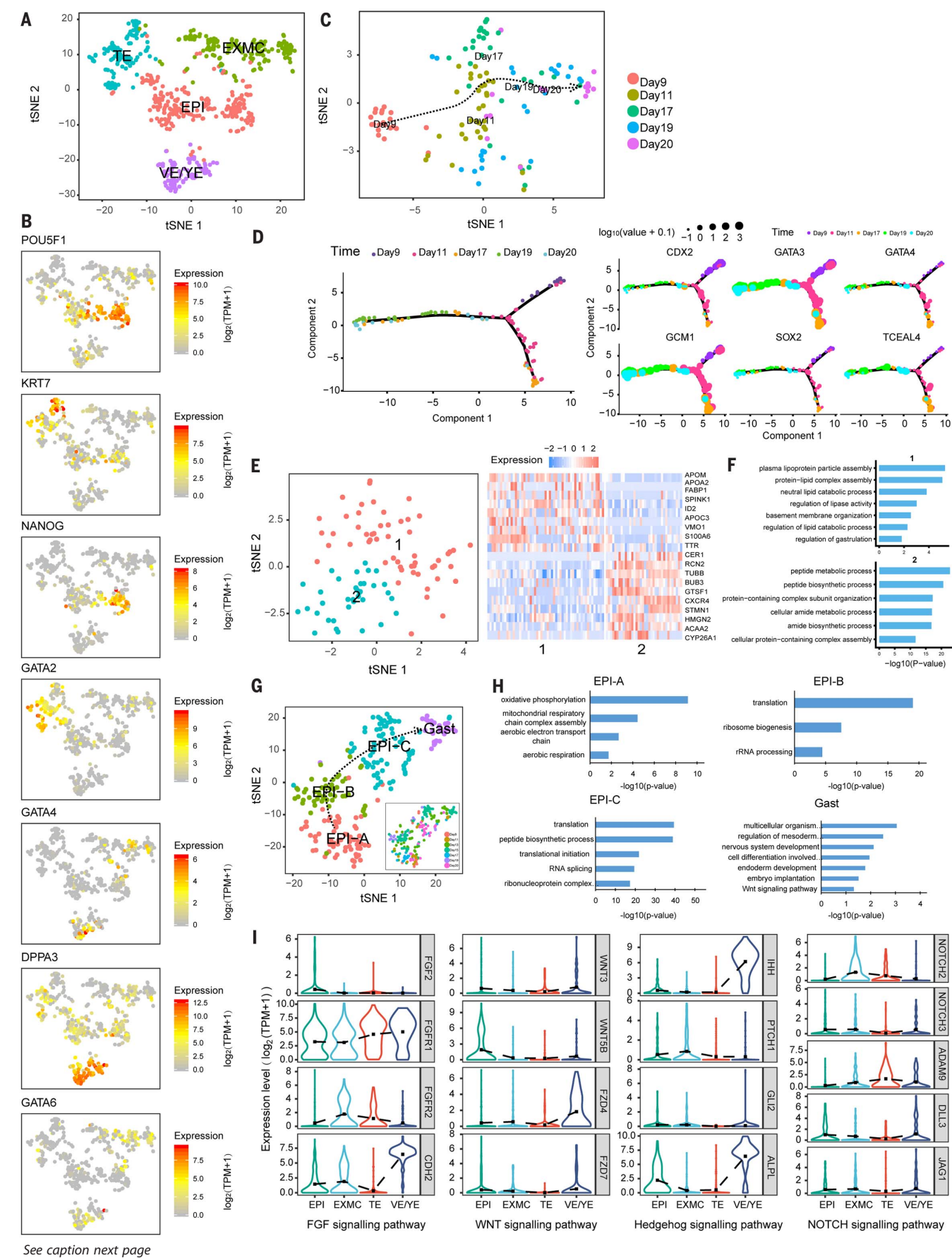


**Fig. 6. Transcription landscape of monkey peri- and postimplantation embryos.** (A) t-distributed stochastic neighbor embedding (t-SNE) plot of cells at representative stages (days 9, 11, 13, 15, 17, 19, and 20). Cells were identified as epiblast (EPI), primitive endoderm (PE), trophectoderm (TE), and extraembryonic mesenchyme (EXMC) cells. (B) Expression of lineage-specific marker genes exhibited on t-SNE plots. A gradient of gray, yellow, and red indicates low to high expression. (C) t-SNE plot of TE cells at seven time points. (D) (Left) Pseudotime construction of single TE cells colored according to embryonic stage. (Right) Expression patterns of CDX2, TCEAL4, GCM1, GATA3, SOX2, and GATA4 exhibited on pseudotime construction. Dot-size gradient indicates low to high expression. (E) (Left) t-SNE plot of PE cells at seven time points, revealing two cell types, with (right) expressions of cell-type specific genes. (F) Gene Ontology (GO) term analysis: Cluster 1, enriched for lipid metabolism and transport; cluster 2, enriched for transcription and protein synthesis. (G) t-SNE plot of EPI cells at seven time points. Cells are designated as EPI-A, EPI-B, EPI-C, and gastrulating cell (Gast). (Inset) Single cells colored according to embryonic stage. (H) GO term analysis of classified EPI cells. (I) Violin plot of FGF/WNT/NOTCH signaling components expression in the various lineages.

### IF analysis

Monkey *in vivo* and *in vitro* postimplantation embryos were harvested and fixed in 4% paraformaldehyde in PBS for 30 min at room temperature. Then embryos were washed with PBS, and then day 9 and day 10 embryos were stained directly. Other stages of embryos were dehydrated in sucrose (57-50-1, meilunbio) solutions each for 6 hours with increasing concentration from 15% to 30% (15%, 20% 30%; (w/vol). Next, embryos were embedded in OCT, frozen and stored at -80°C. Then the samples were prepared as cryosections with 8  $\mu$ m thickness on pre-treated glass slides (1A5105, CITOTEST), and air-dried for 1 hour. After permeabilized in PBST (PBS with 0.3% Triton X-100) (0694, Amresco) for 30 min at room temperature, samples were blocked with 3% (w/v) BSA and 10% (w/vol) FBS (04-001-1ACS, Biological Industries) in PBS for overnight at 4°C. Slides were then incubated with primary antibodies overnight at 4°C. After wash, fluorescence-conjugated secondary antibodies, and 4',6-diamidino-2-phenylindole (DAPI) were incubated with the slides in dark at 25°C for 2 hours. Images were taken using Leica TCS SP8 confocal microscope (Leica). For antibodies used, see table S7.

### scRNA-seq

Plate-based single-cell cDNA synthesis, amplification and library construction were performed as previously described (45, 46). Briefly, single cell was placed into the lysis buffer by mouth pipette. The reverse transcription reactions and pre-amplification were performed using SuperScript II (18064-071, Invitrogen), and KAPA HiFi HotStart ReadyMix (KK2602; KAPA biosystems.), respectively. For library construction, the cDNA was fragmented by Tn5 transposase (BGE005, BGI) mix at 55°C for 15 min. After that, 0.25% SDS was added to each well to stop the fragmentation, followed by polymerase chain reaction (PCR) amplification using KAPA HIFI Hotstart polymerase mix (KK2602, KAPA biosystems) and primer sets with 25 cycles of denaturation. Then the libraries were purified with AMPure XP magnetic beads (A63881, Beckman Coulter), and were circularized by incubating with T4 DNA ligase (EL0011, Fermentas) at 37°C for 1 hour. After removal of linear DNA, the libraries were then purified by PEG32 (MP07123, CG) and sequenced on BGISEQ-500 (BGI).

### scATAC-Seq

Plate-based single-cell transposition reactions were performed with transposase mixture at 37°C for 15 min with agitation at 300 rpm, following with a modified FAST-ATAC method (47). The release buffer was added and the reaction was maintained at 50°C for 15 min. Then plasmid DNA (30 ng) was added as the carrier DNA to the mixture. Afterwards, the DNA was purified with Ampure XP beads. Then the DNA was pre-amplified with NEBNext High-Fidelity 2 $\times$  PCR Master Mix (M0541, New England Biolabs) and transposase adapters. The pre-amplified DNA was purified with Ampure XP beads and used for libraries construction as previously described (48). Briefly, DNA was amplified for 14 cycles using the NEBNext High-Fidelity 2 $\times$  PCR Master Mix and barcode primers. Then the libraries were size-selected with Ampure XP beads for fragments between 150 and 700 base pairs (bp) and sequenced on BGISEQ-500.

### scRNA-seq and scATAC-seq data pre-processing

For RNA-seq data, adapters and low quality reads (*N* rate > 0.2) were removed by Cutadapt (v1.15) (49). Then raw reads were mapped to *Macaca fascicularis* (*Macaca\_fascicularis\_5.0*) genome by STAR (v2.5.3) program (50). We calculated the transcripts per million mapped reads (TPM) as expression level using RSEM v1.3.0 with default parameters (51). The single cells with mapped reads >1 million and more than 2000 genes with TPM value >1 were used to further analysis.

For ATAC-seq data, the inherent sequence of Tn5 for each cell was removed using cutadapt (v1.16) (49) and aligned to the cynomolgus reference genome (*Macaca fascicularis\_5.0*) using bowtie2 (v2.2.5) with the parameter -X 2000 (52). SAMtools (v1.9) (53) was used to filter reads for alignment quality of >Q30 and Picard tools (v2.6.0) (Broad Institute; <http://broadinstitute.github.io/picard>) was used to remove duplicate reads. Cells with usable fragments under 10000 and promoter regions (500 bp around transcriptional start site) with ratio of fragments under 10% were filtered out. The fragments were aggregated and reference peak were called using Sambamba (v0.6.6) (54) and MACS2 (v2.1.2) (55) respectively. Then the number of fragments per reference peak per cell was counted using chromVAR (v1.4.0) (56) to construct the matrix of fragment counts in peaks X.

### Cell clustering and differentially expressed gene analysis

Cell clustering and differential gene expression analysis were performed by Seurat (v2.3.4), a package in R (57). Principal components analysis (PCA) was performed to select principal components for clusters finding based on a jack straw method. Then graph-based clustering approaches were applied to identify cell clusters and t-distributed stochastic neighbor embedding (t-SNE) was used for visualization of distance between cells in the reduced 2D space.

### t-SNE analysis of scATAC-seq data

chromVAR (56) were used to perform t-SNE analysis and Cicero (v1.0.11) (58) were used to define clusters in t-SNE embedding.

### Transcription factor motifs analysis and differentially accessible sites identification

TF motif deviations were obtained from “deviationScores” function in chromVAR (56). To identify differentially accessible sites, we adopt the method in previously report (59). We randomly sampled 20 cells from each of the clusters identified above to generate the reference panel. Then we implement “binomialff” test using Monocle 2 package (60, 61) to get differentially accessible sites at a 1% FDR threshold (Benjamini-Hochberg method). We calculated specificity scores for differentially accessible sites based on Jensen-Shannon divergence using method in previous report (59). We set 0.02 for specificity score threshold to determine cluster specific accessible sites. To investigate chromatin accessibility of WNT signaling family members, we calculated “gene activity scores” to evaluate the chromatin accessibility degree of genes using Cicero (58).

### Functional enrichment analysis

GO analysis of differentially expressed genes (DEGs) was performed using ClueGO (v2.5.2) (62, 63) as previously described (64).

### Single cell pseudotime analysis

For scRNA-seq data, the pseudo-temporal analysis was performed using the R package Monocle2 (60, 61, 65).

### Similarity analysis between *in vivo* and *in vitro* embryos

scRNA-seq dataset of our cultured and previously published *in vivo* embryos were aligned by



using canonical correlation analysis (CCA) of Seurat R package (57). We selected the union of the top 1000 genes of highest variance for our and published dataset and calculated 20 canonical correlates (CCs) with diagonal CCA. The first 10 CCs were used for t-SNE visualization. Then, the correlation analysis was employed to detect the correspondence of cell subtype for in vivo and in vitro cultured embryo cells by using expression matrix of 200 high variable genes that contributed to the first 20 CCs. Also, scRNA-seq data of cultured embryos and Geo-seq data of in vivo embryos were aligned using CCA. To compare PGCLC with published in vivo early and late PGCs, the correlation analysis was performed with expression matrix of in vivo early and late PGCs DEGs.

### Analysis of cross-talk between different cell types

CellphoneDB (v2.0.1) (66) was used to build signaling cross-talks and their directionality between different cell types. The R package Circlize (67) was used for the interaction visualization.

### REFERENCES AND NOTES

1. L. Solnica-Krezel, D. S. Sepich, Gastrulation: Making and shaping germ layers. *Annu. Rev. Cell Dev. Biol.* **28**, 687–717 (2012). doi: [10.1146/annurev-cellbio-092910-154043](https://doi.org/10.1146/annurev-cellbio-092910-154043); pmid: 22804578
2. G. Chen et al., Single-cell analyses of X Chromosome inactivation dynamics and pluripotency during differentiation. *Genome Res.* **26**, 1342–1354 (2016). doi: [10.1101/gr.201954.115](https://doi.org/10.1101/gr.201954.115); pmid: 27486082
3. H. Mohammed et al., Single-cell landscape of transcriptional heterogeneity and cell fate decisions during mouse early gastrulation. *Cell Rep.* **20**, 1215–1228 (2017). doi: [10.1016/j.celrep.2017.07.009](https://doi.org/10.1016/j.celrep.2017.07.009); pmid: 28768204
4. G. Peng et al., Spatial transcriptome for the molecular annotation of lineage fates and cell identity in mid-gastrula mouse embryo. *Dev. Cell* **36**, 681–697 (2016). doi: [10.1016/j.devcel.2016.02.020](https://doi.org/10.1016/j.devcel.2016.02.020); pmid: 27003939
5. A. Scialdone et al., Resolving early mesoderm diversification through single-cell expression profiling. *Nature* **535**, 289–293 (2016). doi: [10.1038/nature18633](https://doi.org/10.1038/nature18633); pmid: 27383781
6. K. Takaoka, H. Hamada, Cell fate decisions and axis determination in the early mouse embryo. *Development* **139**, 3–14 (2012). doi: [10.1242/dev.060095](https://doi.org/10.1242/dev.060095); pmid: 22147950
7. P. P. Tam, D. A. Loebe, Gene function in mouse embryogenesis: Get set for gastrulation. *Nat. Rev. Genet.* **8**, 368–381 (2007). doi: [10.1038/nrg2084](https://doi.org/10.1038/nrg2084); pmid: 17387317
8. J. Rossant, Mouse and human blastocyst-derived stem cells: Vive les differences. *Development* **142**, 9–12 (2015). doi: [10.1242/dev.115451](https://doi.org/10.1242/dev.115451); pmid: 25516964
9. J. Rossant, P. P. L. Tam, New insights into early human development: Lessons for stem cell derivation and differentiation. *Cell Stem Cell* **20**, 18–28 (2017). doi: [10.1016/j.stem.2016.12.004](https://doi.org/10.1016/j.stem.2016.12.004); pmid: 28061351
10. M. N. Shahbazi, M. Zernicka-Goetz, Deconstructing and reconstructing the mouse and human early embryo. *Nat. Cell Biol.* **20**, 878–887 (2018). doi: [10.1038/s41556-018-0144-x](https://doi.org/10.1038/s41556-018-0144-x); pmid: 30038253
11. A. Deglincerti et al., Self-organization of the in vitro attached human embryo. *Nature* **533**, 251–254 (2016). doi: [10.1038/nature17948](https://doi.org/10.1038/nature17948); pmid: 27144363
12. M. N. Shahbazi et al., Self-organization of the human embryo in the absence of maternal tissues. *Nat. Cell Biol.* **18**, 700–708 (2016). doi: [10.1038/ncb3347](https://doi.org/10.1038/ncb3347); pmid: 27144686
13. T. Nakamura et al., A developmental coordinate of pluripotency among mice, monkeys and humans. *Nature* **537**, 57–62 (2016). doi: [10.1038/nature19096](https://doi.org/10.1038/nature19096); pmid: 27556940
14. K. Sasaki et al., The germ cell fate of cynomolgus monkeys is specified in the nascent amnion. *Dev. Cell* **39**, 169–185 (2016). doi: [10.1016/j.devcel.2016.09.007](https://doi.org/10.1016/j.devcel.2016.09.007); pmid: 27720607
15. T. Boroviak, J. Nichols, Primate embryogenesis predicts the hallmarks of human naïve pluripotency. *Development* **144**, 175–186 (2017). doi: [10.1016/j.dev.145177](https://doi.org/10.1016/j.dev.145177); pmid: 28096211
16. I. Bedzhov, M. Zernicka-Goetz, Self-organizing properties of mouse pluripotent cells initiate morphogenesis upon implantation. *Cell* **156**, 1032–1044 (2014). doi: [10.1016/j.cell.2014.01.023](https://doi.org/10.1016/j.cell.2014.01.023); pmid: 24529478
17. H. Wang, S. K. Dey, Roadmap to embryo implantation: Clues from mouse models. *Nat. Rev. Genet.* **7**, 185–199 (2006). doi: [10.1038/nrg1808](https://doi.org/10.1038/nrg1808); pmid: 16485018
18. E. Maltepe, S. J. Fisher, Placenta: The forgotten organ. *Annu. Rev. Cell Dev. Biol.* **31**, 523–552 (2015). doi: [10.1146/annurev-cellbio-100814-125620](https://doi.org/10.1146/annurev-cellbio-100814-125620); pmid: 26443191
19. S. Chari, Self-renewal and lineage transitions. *Cell Stem Cell* **22**, 1–2 (2018). doi: [10.1016/j.stem.2017.12.016](https://doi.org/10.1016/j.stem.2017.12.016); pmid: 29304335
20. D. Acampora, L. G. Di Giovannantonio, A. Simeone, Otx2 is an intrinsic determinant of the embryonic stem cell state and is required for transition to a stable epiblast stem cell condition. *Development* **140**, 43–55 (2013). doi: [10.1242/dev.085290](https://doi.org/10.1242/dev.085290); pmid: 23154415
21. K. K. Nian, K. Eggan, Analysis of human embryos from zygote to blastocyst reveals distinct gene expression patterns relative to the mouse. *Dev. Biol.* **375**, 54–64 (2013). doi: [10.1016/j.ydbio.2012.12.008](https://doi.org/10.1016/j.ydbio.2012.12.008); pmid: 23261930
22. H. Sritanadomchai et al., CDX2 in the formation of the trophectoderm lineage in primate embryos. *Dev. Biol.* **335**, 179–187 (2009). doi: [10.1016/j.ydbio.2009.08.025](https://doi.org/10.1016/j.ydbio.2009.08.025); pmid: 19733166
23. G. C. Douglas, C. A. VandeVoort, P. Kumar, T. C. Chang, T. G. Golos, Trophectoderm stem cells: Models for investigating trophectoderm differentiation and placental development. *Endocr. Rev.* **30**, 228–240 (2009). doi: [10.1210/er.2009-0001](https://doi.org/10.1210/er.2009-0001); pmid: 19299251
24. A. C. Enders, S. Schlafke, A. G. Hendrick, Differentiation of the embryonic disc, amnion, and yolk sac in the rhesus monkey. *Am. J. Anat.* **177**, 161–185 (1986). doi: [10.1002/aja.100170205](https://doi.org/10.1002/aja.100170205); pmid: 3788819
25. W. P. Luckett, Origin and differentiation of the yolk sac and extraembryonic mesoderm in presomite human and rhesus monkey embryos. *Am. J. Anat.* **152**, 59–97 (1978). doi: [10.1002/aja.1001520106](https://doi.org/10.1002/aja.1001520106); pmid: 98035
26. M. Williams, C. Burdsal, A. Periasamy, M. Lewandowski, A. Sutherland, Mouse primitive streak forms in situ by initiation of epithelial to mesenchymal transition without migration of a cell population. *Dev. Dyn.* **241**, 270–283 (2012). doi: [10.1002/dvdy.23711](https://doi.org/10.1002/dvdy.23711); pmid: 22170865
27. B. Sozen et al., Self-assembly of embryonic and two extra-embryonic stem cell types into gastrulating embryo-like structures. *Nat. Cell Biol.* **20**, 979–989 (2018). doi: [10.1038/s41556-018-0147-7](https://doi.org/10.1038/s41556-018-0147-7); pmid: 30038254
28. S. D. Vincent, N. R. Dunn, S. Hayashi, D. P. Norris, E. J. Robertson, Cell fate decisions within the mouse organizer are governed by graded Nodal signals. *Genes Dev.* **17**, 1646–1662 (2003). doi: [10.1101/gad.1100503](https://doi.org/10.1101/gad.1100503); pmid: 12842913
29. I. Martyn, T. Y. Kanno, A. Ruzo, E. D. Siggia, A. H. Brivanlou, Self-organization of a human organizer by combined Wnt and Nodal signalling. *Nature* **558**, 132–135 (2018). doi: [10.1038/s41586-018-0150-y](https://doi.org/10.1038/s41586-018-0150-y); pmid: 29795348
30. A. Simeone, Otx1 and Otx2 in the development and evolution of the mammalian brain. *EMBO J.* **17**, 6790–6798 (1998). doi: [10.1093/emboj/17.23.6790](https://doi.org/10.1093/emboj/17.23.6790); pmid: 9843484
31. O. G. Kelly, K. I. Pinson, W. C. Skarnes, The Wnt co-receptors Lrp5 and Lrp6 are essential for gastrulation in mice. *Development* **131**, 2803–2815 (2004). doi: [10.1242/dev.01137](https://doi.org/10.1242/dev.01137); pmid: 15142971
32. P. Liu et al., Requirement for Wnt3 in vertebrate axis formation. *Nat. Genet.* **22**, 361–365 (1999). doi: [10.1038/11932](https://doi.org/10.1038/11932); pmid: 10431240
33. L. Robb, P. P. Tam, Gastrula organizer and embryonic patterning in the mouse. *Semin. Cell Dev. Biol.* **15**, 543–554 (2004). doi: [10.1016/j.semcdb.2004.04.005](https://doi.org/10.1016/j.semcdb.2004.04.005); pmid: 15271300
34. A. T. Clark et al., Primate Primordial Germ Cells Acquire Transplantation Potential by Carnegie Stage 23. *Stem Cell Reports* **9**, 329–341 (2017). doi: [10.1016/j.stemcr.2017.05.002](https://doi.org/10.1016/j.stemcr.2017.05.002); pmid: 28579394
35. N. Irie et al., SOX17 is a critical specifier of human primordial germ cell fate. *Cell* **160**, 253–268 (2015). doi: [10.1016/j.cell.2014.12.013](https://doi.org/10.1016/j.cell.2014.12.013); pmid: 25543152
36. D. Chen et al., Germline competency of human embryonic stem cells depends on eomesodermin. *Biol. Reprod.* **97**, 850–861 (2017). doi: [10.1093/biolre/iox138](https://doi.org/10.1093/biolre/iox138); pmid: 29091993
37. Y. Kojima et al., Evolutionarily distinctive transcriptional and signaling programs drive human germ cell lineage specification from pluripotent stem cells. *Cell Stem Cell* **21**, 517–532.e5 (2017). doi: [10.1016/j.stem.2017.09.005](https://doi.org/10.1016/j.stem.2017.09.005); pmid: 28985527
38. K. Sasaki et al., Robust in vitro induction of human germ cell fate from pluripotent stem cells. *Cell Stem Cell* **17**, 178–194 (2015). doi: [10.1016/j.stem.2015.06.014](https://doi.org/10.1016/j.stem.2015.06.014); pmid: 26189426
39. Y. Li et al., BMP4-directed trophoblast differentiation of human embryonic stem cells is mediated through a ΔNp63+ cytotrophoblast stem cell state. *Development* **140**, 3965–3976 (2013). doi: [10.1242/dev.092155](https://doi.org/10.1242/dev.092155); pmid: 24004950
40. P. O. Favaron, R. C. Carvalho, J. Borghesi, A. R. Anunciacao, M. A. Miglio, The amniotic membrane: Development and potential applications - A Review. *Reprod. Domest. Anim.* **50**, 881–892 (2015). doi: [10.1111/rda.12633](https://doi.org/10.1111/rda.12633); pmid: 26510939
41. B. F. King, Developmental changes in the fine structure of rhesus monkey amnion. *Am. J. Anat.* **157**, 285–307 (1980). doi: [10.1002/aja.1001570305](https://doi.org/10.1002/aja.1001570305); pmid: 6773409
42. S. Chandrasekaran et al., Comprehensive mapping of pluripotent stem cell metabolism using dynamic genome-scale network modeling. *Cell Rep.* **21**, 2965–2977 (2017). doi: [10.1016/j.celrep.2017.07.048](https://doi.org/10.1016/j.celrep.2017.07.048); pmid: 29212039
43. H. Sperber et al., The metabolome regulates the epigenetic landscape during naïve-to-primed human embryonic stem cell transition. *Nat. Cell Biol.* **17**, 1523–1535 (2015). doi: [10.1038/ncb3264](https://doi.org/10.1038/ncb3264); pmid: 26571212
44. J. Wu, A. Ocampo, J. C. I. Belmonte, Cellular metabolism and induced pluripotency. *Cell* **166**, 1371–1385 (2016). doi: [10.1016/j.cell.2016.08.008](https://doi.org/10.1016/j.cell.2016.08.008); pmid: 27610564

### ACKNOWLEDGMENTS

We thank Y. Hou and S. Liu for discussion of this study and L. Xu and Y. Wang for their technical assistance. We are grateful to K. Chen, X. Lin, and X. Liu for helpful feedback on the manuscript. **Funding:** This work was supported by the National Key Research and Development Program (2016YFA0101401), the National Natural Science Foundation of China (81760271), Major Science and Technology Projects of Yunnan Province (2017ZF028), Key Projects of Basic Research Program in Yunnan Province (2017FA010), and Frontier Research Program of Guangzhou Regenerative Medicine and Health Guangdong Laboratory (2018GZR110105013). **Author contributions:** Y.N., J.C.I.B., T.T., and W.J. designed the study and supervised overall experiments. Y.N., C.S., Y.K., N.S., and H.W. performed samples collection work, including superovulation, micromanipulation, and animal care. N.S., C.Li, C.Liu, J.W., L.L., W.S., E.Z., L.Z., Z.L., S.F., G.C., X.L., and G.P. carried out experiments or contributed critical reagents and protocols. Y.L., Z.H., J.W., X.D., J.C.I.B., and T.T. analyzed the data and performed statistical analyses. Y.N., J.W., J.C.I.B., W.J., and T.T. wrote the manuscript. **Competing interests:** The authors declare no competing financial interests. **Data and materials availability:** All sequencing data were deposited at the National Center for Biotechnology Information Sequence Read Archive under accession no. SRP175059. The data were also deposited at the China National GeneBank (CNCB) Nucleotide Sequence Archive (CNSA); <https://db.cngb.org/cnsa> under accession no. CNP0000231.

### SUPPLEMENTARY MATERIALS

[science.sciencemag.org/content/366/6467/eaaw5754/suppl/DC1](https://science.sciencemag.org/content/366/6467/eaaw5754/suppl/DC1)  
Materials and Methods  
Figs. S1 to S8  
Tables S1 to S7  
References (45–74)

**View/request a protocol for this paper from Bio-protocol.**

7 January 2019; accepted 16 October 2019  
10.1126/science.aaw5754

## RESEARCH ARTICLE

## STRUCTURAL BIOLOGY

## Structure of the RSC complex bound to the nucleosome

Youpi Ye<sup>1,2\*</sup>, Hao Wu<sup>2,3\*</sup>, Kangjing Chen<sup>1,2</sup>, Cedric R. Clapier<sup>4</sup>, Naveen Verma<sup>4</sup>, Wenhao Zhang<sup>2</sup>, Haiteng Deng<sup>2</sup>, Bradley R. Cairns<sup>4†</sup>, Ning Gao<sup>5†</sup>, Zhucheng Chen<sup>1,2,6†</sup>

The RSC complex remodels chromatin structure and regulates gene transcription. We used cryo-electron microscopy to determine the structure of yeast RSC bound to the nucleosome. RSC is delineated into the adenosine triphosphatase motor, the actin-related protein module, and the substrate recruitment module (SRM). RSC binds the nucleosome mainly through the motor, with the auxiliary subunit Sfh1 engaging the H2A-H2B acidic patch to enable nucleosome ejection. SRM is organized into three substrate-binding lobes poised to bind their respective nucleosomal epitopes. The relative orientations of the SRM and the motor on the nucleosome explain the directionality of DNA translocation and promoter nucleosome repositioning by RSC. Our findings shed light on RSC assembly and functionality, and they provide a framework to understand the mammalian homologs BAF/PBAF and the Sfh1 ortholog INI1/BAF47, which are frequently mutated in cancers.

In chromatin, DNA wraps around histone octamers to form nucleosomes. Access to the nucleosomal DNA is facilitated by Snf2-family chromatin remodelers, which are highly conserved from yeast to mammals (1). Snf2 and Sth1, two closely related paralogs, are the catalytic motor subunits of the two similar yeast SWI/SNF and RSC remodeling complexes, respectively. Although the motors remodel nucleosomes in vitro on their own, they function in complexes with multiple auxiliary subunits in vivo to provide regulation and targeting. RSC is enriched at nucleosomes that flank nucleosome-free regions (NFRs) and controls the promoter architecture of most genes in yeast (2). It makes use of DNA translocation to slide or eject the promoter +1 nucleosomes to extend NFRs, possibly to expose transcription start sites and promote transcription.

Low-resolution structures of SWI/SNF, RSC, and the human homolog PBAF complexes have been reported (3, 4). However, it remains unclear how the subunits assemble the complexes and engage nucleosomes. Here, we report the cryo-electron microscopy (cryo-EM) structure of RSC bound to the nucleosome,

providing insights into RSC organization and function.

### Overall structure of RSC bound to the nucleosome

Purified RSC was mixed with nucleosomes and the stable adenosine triphosphate (ATP) analog ADP-BeF<sub>x</sub> and subjected to cryo-EM analysis (fig. S1 and table S1). The RSC-nucleosome complexes were highly flexible, with two prominent classes identified. One class (class A) showed a slightly unwrapped linker DNA, with an overall resolution of 7.1 Å (fig. S2, A and B), whereas the other class (class B) showed EM density for a longer linker DNA, with an overall resolution of 7.6 Å (fig. S2, C to E).

We found that RSC in either class is organized into three modules (Fig. 1A and movie S1): the motor module (motor domain of Sth1), the actin-related protein (ARP) module (the HSA helix of Sth1 bound by an Arp7-Arp9-Rtt102 trimer), and the substrate recruitment module (SRM, including the N-terminal fragment of Sth1 and multiple additional subunits). The three modules, connected through two disordered loops of Sth1, show rigid-body motions relative to each other (fig. S3), explaining the flexibility. Because the biological implications of classes A and B are the same, we mainly focused on the 7.1 Å class A structure.

Focused refinements led to a 3.8 Å map of the motor domain (fig. S2F) and a 3.4 Å map of the SRM, with the rigid core at ~3.0 Å (figs. S1G and S2, G to K). The high-quality map of the SRM allowed us to build atomic models of the N-terminal fragment of Sth1, Rsc2, Rsc3, Rsc4, Rsc6, Rsc7, Rsc9, Rsc30, Rsc58, Htl1, Sfh1, and two molecules of Rsc8 (termed Rsc8a and Rsc8b) (Fig. 1B). The interactions among the subunits were further validated by cross-linking

mass spectrometry (CL-MS) analyses (fig. S4 and data S1).

The nucleosome is mainly bound by the motor domain of Sth1, with limited contacts from other subunits, except Sfh1 (see below). An open space embraced by the SRM and some weak density was found (fig. S2, B and D), which may relate to the hypothetical nucleosome-binding central cavity proposed previously (5). However, no nucleosome was found inside this open space.

The SRM comprises the majority of RSC (Fig. 1A), with the conserved subunits Rsc6, Rsc8, Rsc9, Rsc58, and the N-terminal fragment of Sth1 interweaving into a rigid core. The SRM is further organized into three lobes. Rsc3 and Rsc30, which contain DNA-binding Zn-cluster domains (ZnDs), decorate the conserved core at DNA-binding lobe (DB lobe) (6, 7). Rsc2 and Rsc4, which contain histone tail-binding bromodomains (BDs) and BAH domain (8–10), are located at the histone tail-binding lobe (HB lobe). Sfh1, which contains a nucleosome-binding C-terminal tail (CTT; see below), is located at the nucleosome-binding lobe (NB lobe). As a result of tethering to the SRM through flexible loops, the structures of the substrate-binding motifs (e.g., ZnD, BD, BAH, and CTT) could not be resolved under current conditions. Nonetheless, the SRM clearly positions these elements to colocalize along one side of the nucleosome, with the DB, HB, and NB lobes proximal to their binding epitopes, suggesting mechanisms for coordinated nucleosome recruitment or retention.

### Structure of Sth1 in the context of the RSC complex

Sth1 is composed of five major domains (Figs. 1B and 2A): the N-terminal domain (NTD), the domain preceding the HSA helix (preHSA), HSA, motor, and the C-terminal extension and BD. A polyalanine model was built for the poorly conserved NTD because of the lack of defined features (fig. S5A). The modestly conserved preHSA (~25% identity between Sth1 and HsBRG1) threads through the DB and HB lobes. The HSA helix connects to the preHSA and motor domains through flexible loops. The motor domain interacts with the nucleosome in a manner very similar to the isolated adenosine triphosphatase (ATPase) fragment of Snf2 (fig. S6) (11, 12).

One surface of HSA binds to the ARP proteins, as observed in the structure of HSA<sup>Snf2</sup> (13), and the exposed surface, containing multiple conserved positively charged residues (fig. S5A), is proximal to the nucleosomal DNA (Fig. 2A and fig. S5B). The structure suggests that HSA may function to orient RSC by projecting the ARP proteins away from the nucleosome and by orienting HSA, the preHSA, and the associated SRM toward the exit DNA (Fig. 2A). As a result, we found one preferred

<sup>1</sup>MOE Key Laboratory of Protein Science, Tsinghua University, Beijing 100084, P.R. China. <sup>2</sup>School of Life Science, Tsinghua University, Beijing 100084, P.R. China. <sup>3</sup>Peking University–Tsinghua University–National Institute of Biological Sciences Joint Graduate Program, Beijing 100084, China. <sup>4</sup>Howard Hughes Medical Institute and Department of Oncological Sciences, Huntsman Cancer Institute, University of Utah School of Medicine, Salt Lake City, UT 84112, USA. <sup>5</sup>State Key Laboratory of Membrane Biology, Peking–Tsinghua Joint Center for Life Sciences, School of Life Sciences, Peking University, Beijing 100871, China. <sup>6</sup>Tsinghua–Peking Joint Center for Life Sciences, Beijing Advanced Innovation Center for Structural Biology, Beijing 100084, China.

\*These authors contributed equally to this work.

†Corresponding author. Email: zhucheng\_chen@tsinghua.edu.cn (Z.C.); gaon@pku.edu.cn (N.G.); brad.cairns@hci.utah.edu (B.R.C.)



nucleosome orientation with the linker DNA at the exit side. This contrasted with the isolated motor domain of Snf2, which binds to either of the two nucleosome orientations in the presence of ADP-BeF<sub>x</sub> (11).

The ARP proteins adopt a conformation largely similar to that found in the crystal structure of the HSA<sup>Snf2</sup>-Arp7-Arp9-Rtt102 complex; they make limited direct interaction with the nucleosome or the Sth1 motor domain. The structure suggests that the ARPs may stabilize the helical conformations of HSA and/or affect the conformation of the adjacent post-HSA, which interacts with the motor (14, 15), and hence modulates the structural

integrity of the complex and the remodeling efficiency (16).

The preHSA interacts with several conserved auxiliary subunits (Fig. 2B). Specifically, Arg<sup>292</sup> of Sth1 packs against Rsc9 at the DB lobe (figs. S2I and S5C). Likewise, Arg<sup>258</sup>, Arg<sup>198</sup>, and Arg<sup>202</sup> interact with Rsc8 and Rsc58 at the HB lobe (fig. S5, D and E). These residues are highly conserved (fig. S5A), with mutations of the equivalent residues recurrently found in human cancers (17).

### Structure of the NB lobe and its implications for nucleosome binding

Sfh1 is the major component of the NB lobe (Fig. 3A). It is highly conserved with Snf5 in

budding yeast and INI1/BAF47 in animals (fig. S7A). The conserved domain contains two imperfect repeats, RPT1 and RPT2 (repeat 1 and 2), which interact with the SWIRM domains of Rsc8a and Rsc8b, respectively (Fig. 3B and fig. S2H). This is in line with the crystal structure of the RPT1 domain of INI1 bound to the SWIRM domain of BAF155 (homolog of Rsc8) (18). The INI1-BAF155 interaction is highly similar to that of Sfh1-Rsc8 (fig. S7B), supporting a conserved assembly mechanism.

One prominent feature of the NB lobe is the CTT of Sfh1, which is close to the H2A-H2B dimer and the H4 tail of the nucleosome but is largely disordered in the structure (Fig. 3C).

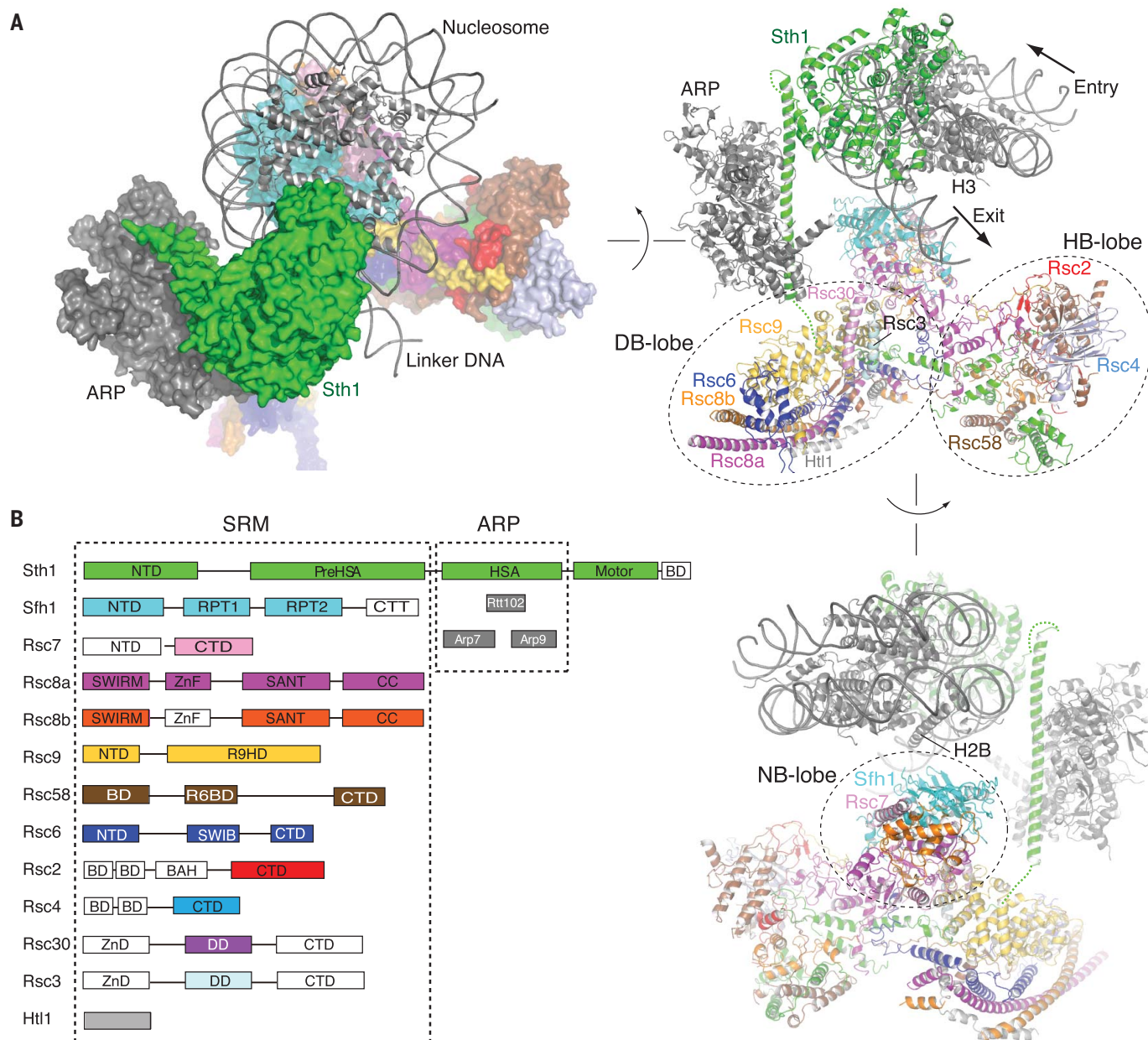


**Fig. 1. Overall structure of the RSC-nucleosome complex.** (A) Three different views of the structure of the complex. Arrows indicate the directionality of DNA translocation. (B) Domain architectures of the RSC subunits. The domains that are not structurally resolved in the current study are colored white.

The CTTs of Sfh1 homologs are enriched in positively charged residues (Fig. 3D), which suggests that these residues may bind to the acidic pocket of H2A-H2B and/or the nearby DNA strands. In line with this idea, we identified

a block of EM density proximal to the CTT above the H2A-H2B surface (fig. S8A). Similar to Snf5 (19, 20), the CTT of Sfh1 forms cross-links with H2A and H2B (fig. S4B), supporting close proximity in space.

Regarding CTT function, whereas a plasmid encoding wild-type *SFH1* fully complemented the lethal phenotype of *sfh1Δ* (21), a plasmid encoding the *sfh1* CTT truncation mutant (amino acids 1 to 384, named Sfh1-ΔCTT) restored viability but displayed multiple strong conditional phenotypes, likely resulting from defects in the transcription of stress response genes (22) (Fig. 3E and fig. S8B). Furthermore, the loss of individual arginine or lysine residues (replacement by alanine) in the CTT did not confer phenotypes, suggesting the functional involvement of multiple positively charged residues. To further explore the function of the CTT, we examined its nucleosome binding in vitro (fig. S8, C and D). The CTT bound the nucleosome, and mutation of the individual conserved positively charged residues Arg<sup>401</sup>, Arg<sup>404</sup>, Lys<sup>403</sup>, or Arg<sup>400</sup> to alanine modestly weakened the binding. Interestingly, mutations of all four residues together largely diminished the binding, which suggests that the CTT may bind to the nucleosome through multivalent interactions.

To determine the role of the Sfh1 CTT in nucleosome remodeling, we purified (fig. S8E)

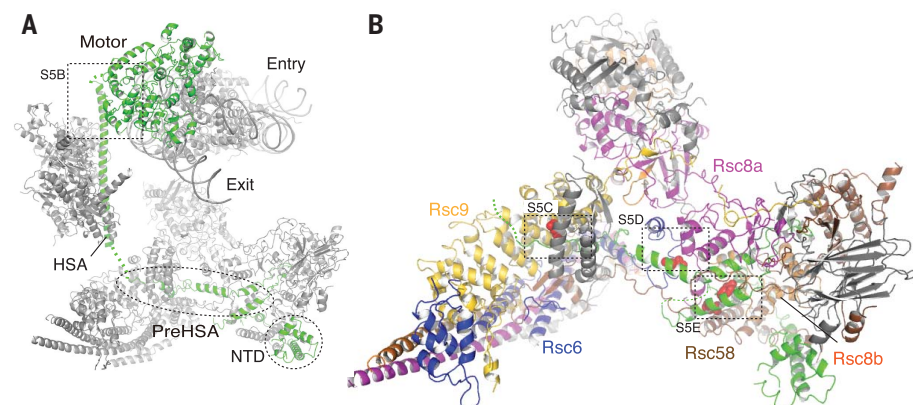


**Fig. 2. Structure of Sth1.** (A) Locations of the different domains of Sth1 within the RSC-nucleosome complex. The boxed region is enlarged in fig. S5B. (B) SRM assembly through preHSA. Residues related to the cancer-associated mutations in the human homologs are shown as red spheres. The boxed regions are enlarged in fig. S5, C to E.

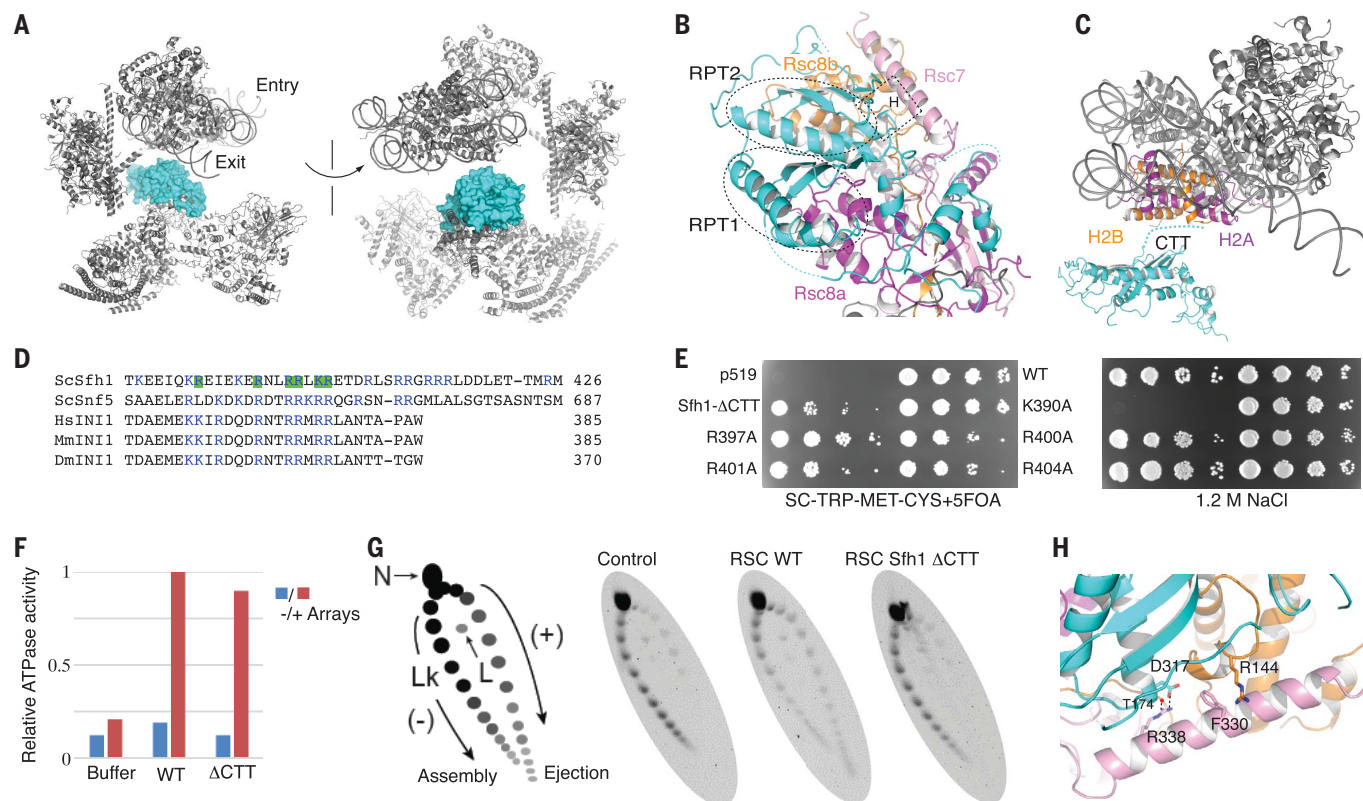


**Fig. 3. Structure of the NB lobe.** (A) Sfh1 (cyan) is proximal to the nucleosome. (B) Structure of the NB lobe. The boxed region is enlarged in (H). The positions of RPT1 and RPT2 of Sfh1 are indicated by ovals. (C) The CTT of Sfh1 is close to the H2A (purple)–H2B (orange) surface. (D) Multiple sequence alignments of the CTTs of Sfh1-like proteins. The residues mutated in this study are highlighted in green. (E) Complementation assays of Sfh1 derivatives on synthetic dropout medium with 5-fluoroorotic acid (5FOA) (left) and at high-salt conditions (right).

p519, control. (F) Relative ATPase activities of the wild-type and Sfh1-ΔCTT RSCs. (G) Comparative nucleosome ejection on plasmid arrays by wild-type and Sfh1-ΔCTT RSCs. Left: Schematic of the ejection assay, with supercoiled plasmid (topoisomer) distribution revealed by a 2D gel. Lk, linking number; N, nicked; L, linear. A representative gel from multiple experiments is shown. (H) Interactions among Rsc7, Rsc8, and Sfh1. Amino acid abbreviations: A, Ala; D, Asp; E, Glu; F, Phe; G, Gly; I, Ile; K, Lys; L, Leu; M, Met; N, Asn; P, Pro; Q, Gln; R, Arg; S, Ser; T, Thr; W, Trp.



and compared the biochemical activity of wild-type RSC to that of mutant RSC lacking the Sfh1 CTT (Sfh1- $\Delta$ CTT). The nucleosome-dependent ATPase activity and the nucleosome sliding activity (on yeast 5S nucleosomes) of the mutant complex were robust and comparable to the wild type (Fig. 3F and fig. S8F). Notably, RSC Sfh1- $\Delta$ CTT was unable to eject yeast nucleosomes residing in closed circular arrays, whereas wild-type RSC was fully capable of ejection (Fig. 3G). These results suggested that the Sfh1 CTT helps RSC bind to the dish face of the nucleosome and stabilize RSC association during DNA translocation, enabling nucleosome ejection (16, 23, 24). Taken together, these results show that the CTT of Sfh1, by homology INI1/BAF47 in human cells, functions to stably anchor RSC on the nucleosome, thereby facilitating nucleosome ejection in vitro and fitness in vivo.

The NB lobe contains one additional component, Rsc7. Whereas the N-terminal region of the Rsc7 is not essential for the RSC assembly, the C-terminal domain (CTD) confers full Rsc7 function (22). Consistent with these studies, we could not detect the NTD in the structure, whereas we could identify the CTD (fig. S9A), which staples Sfh1 and Rsc8b together (Fig. 3H). The Sfh1-Rsc8 binding sequence of Rsc7 is conserved in animal BAF45a ( $\alpha$ 1, fig. S10). In agreement, BAF45a forms cross-links to the Sfh1 homolog in the PBAF complex (25).

### Structure of the DB lobe and its implications for exit DNA binding

We found that the core of the DB lobe comprises Rsc9, Rsc6, the coiled-coil (CC) domain of Rsc8, the C-terminal half of the preHSA, and a middle segment of Rsc58 (Fig. 4A). On the surface of the DB lobe reside the yeast-specific subunits Rsc3, Rsc30, and Htt1 (Fig. 4A).

Rsc9 is composed of armadillo repeats (fig. S11A) (26), referred to as the Rsc9 homology domain (R9HD). The R9HD binds to Rsc6 and the preHSA at the DB lobe, with the less conserved N-terminal tail extending to the HB lobe (fig. S9B). The R9HD shows some conservation to BAF200 in animals, with ~30% sequence similarity to human BAF200 (fig. S11B), which is the characteristic component of the PBAF complex (1).

Rsc8 is a multidomain protein containing SWIRM, zinc finger (ZnF), SANT, and CC domains (Fig. 4B). All these structural elements except the ZnF domain are highly conserved (fig. S12). Consistent with a previous study (27), Rsc8a and Rsc8b dimerize mainly through the CC domains. The Rsc8 dimer connects the three lobes of SRM together, with SWIRM at the NB lobe, ZnF and SANT at the HB lobe, and CC at the DB lobe (Fig. 4C and fig. S9C), suggesting a key role of Rsc8 in RSC assembly. These findings provide the structural basis for earlier studies suggesting the formation of a core complex by BRG1-BAF155-BAF170-INI1

tetramer (28) and the central role of BAF155-BAF170 in BAF/PBAF assembly (25).

Rsc6, which is highly similar to Swp73 in yeast and BAF60s in animals (fig. S13A), bundles to the CC domain of Rsc8 (Fig. 4A and fig. S9D). In support of the conservation, the SWIB domain of Rsc6 adopts a structure homologous to that of mouse BAF60a (fig. S13B). The domain following SWIB does not fold into a rigid conformation but extends out from the DB lobe, contacting the weak EM density that probably results from Rsc3 and Rsc30 (fig. S2, B and D). We speculate that Swp73 and BAF60s may fold into the same structure as Rsc6, with a domain extending to bind to different transcription factors (29, 30); this would support the function of the DB lobe in linker DNA binding.

The middle Rsc6-binding domain (R6BD) of Rsc58 binds to Rsc6 and Rsc8 (fig. S14B). The interacting residues are highly conserved (figs. S11 to S14), which suggests that this structure may serve as a model for the human complexes. In support of this notion, the Rsc58 homolog BRD7 is a unique component of the PBAF complex (25, 31).

Rsc3 and Rsc30 are yeast-specific transcription factors that can heterodimerize and show a binding preference for GC-rich DNA sequences (6, 7, 32). Rsc3 and Rsc30 each contain an N-terminal DNA-binding ZnD, a dimerization domain (DD), and a CTD (Fig. 1B).

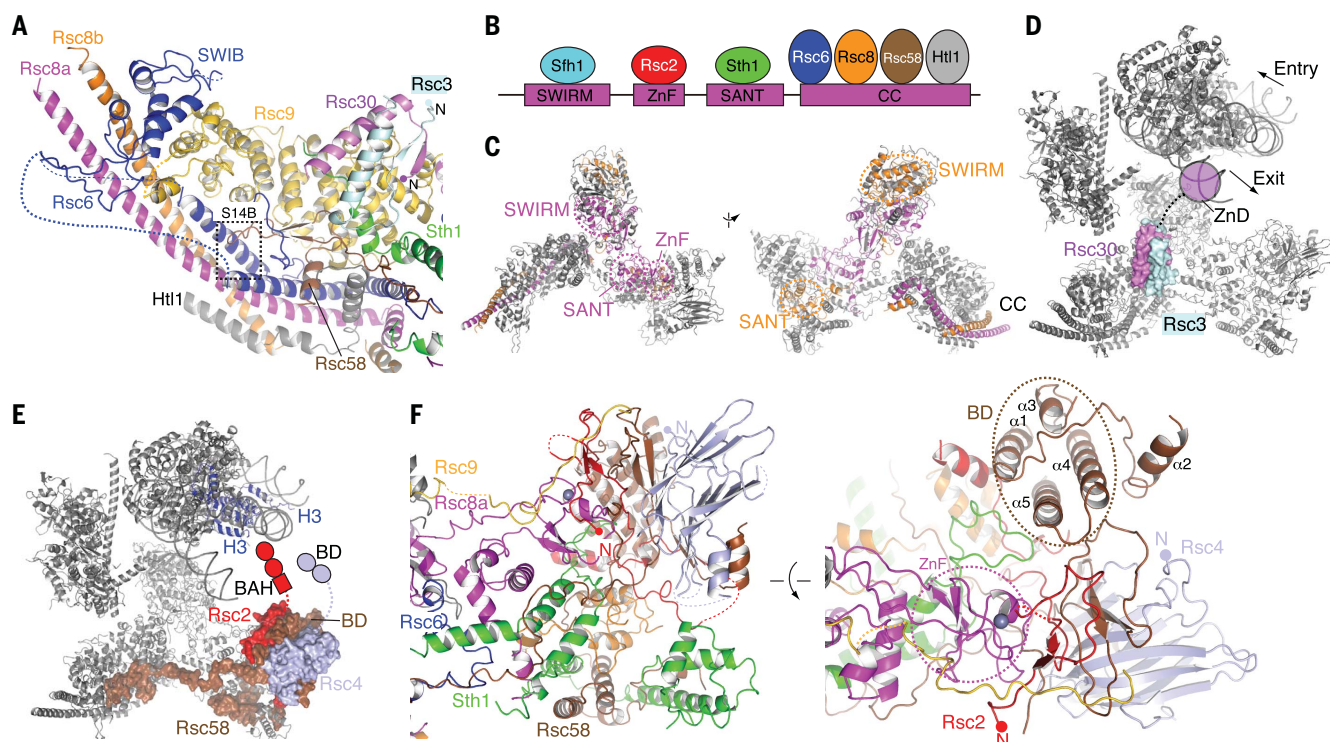
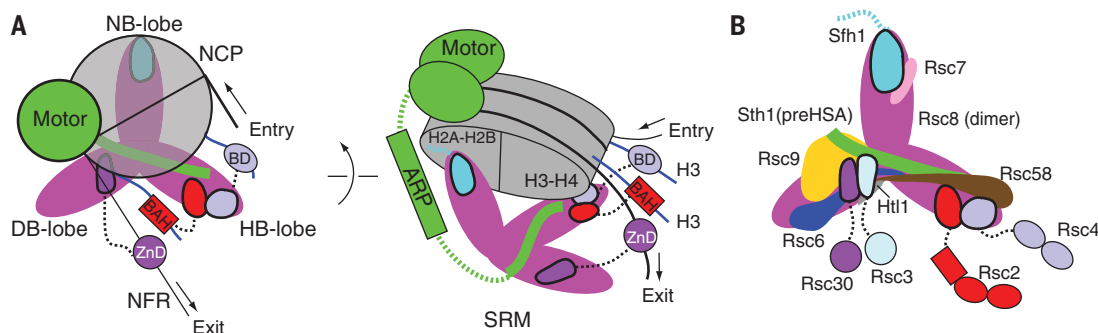


**Fig. 4. Structures of the DB lobe and HB lobe.** (A) Structure of the DB lobe. The boxed region is enlarged for analysis in fig. S14B. (B) Schematic illustration of the interactions of Rsc8 with other subunits of RSC. (C) Two different views of the Rsc8 structure. (D) Positions of Rsc3 and Rsc30. (E) Rsc2, Rsc4, and the BD of Rsc58 are located close to the N-terminal tails of histone H3. (F) Two different views of the structure of the HB lobe.

**Fig. 5. Model of the assembly and action of RSC.** (A) Schematic of the structure of RSC bound to the nucleosome. Only the major structural elements are shown. DNA translocation results in the movement of the nucleosome away from the NFR.

(B) Organization of the SRM.



We identified short  $\beta$  sheets and helices of the DDs, which form a dimer binding to the surface of Rsc9 (Fig. 4A). The interaction between the dimerization helices was also detected by CL-MS analysis (fig. S4B). Weak EM densities near the DDs were found (fig. S2E), which may result from the flexible ZnDs and CTDs of Rsc3 and Rsc30.

The DDs of Rsc3 and Rsc30 are located on the DB lobe at a position distal to the DNA entry side but close to the exit side; thus, they position the N-terminal ZnDs to bind the exit DNA (Fig. 4D). The N termini of DDs are  $\sim 60$  Å away from the exit DNA and are connected to the ZnDs through spacer sequences with a length of  $\sim 100$  residues, which would allow a large degree of flexibility to sample the exit DNA. Htl1, a yeast-specific small subunit of RSC, binds to the CC domain of Rsc8 (Fig. 4A and fig. S9F), in agreement with interactions between Htl1 and the C terminus of Rsc8 (33).

### Structure of the HB lobe and its implications for histone tail binding

RSC and PBAF both contain subunits carrying multiple BDs, such as Rsc2 and Rsc4 in RSC, and their ortholog BAF180 in PBAF, which are partly responsible for recruitment of the complexes through binding to histone tails (8, 10). Interestingly, these histone tail-binding elements cluster at the HB lobe (Fig. 4E), containing one additional histone tail-binding element, the BD of Rsc58 (Fig. 4F).

Whereas the structures of the BDs and BAH of Rsc2 and Rsc4 could not be detected, we were able to identify the CTDs of Rsc2 (residues 741 to 883) and Rsc4 (residues 364 to 625), which map to the tip of the HB lobe (Fig. 4E). This structure is consistent with studies showing that the CTD of Rsc2 is necessary and sufficient for RSC assembly (34). Similarly, the C terminus of Rsc4 mediates RSC assembly (8). The CTDs of Rsc2 and Rsc4 are exposed at the surface and  $\sim 70$  Å away from the H3 tails. They connect to the N-terminal BAH and BDs through long spacer sequences with a length of  $>100$  and 50 residues, respectively, which would poise these histone tail-binding elements to access their substrates, in agree-

ment with the functions of BDs and BAH in histone tail binding (9, 10). The BD of Rsc58 loosely packs at the periphery of the HB lobe (Fig. 4F), with its histone-binding pocket exposed to solvent and  $\sim 60$  Å away from histone H3 (class B complex, fig. S3A), suggesting that Rsc58 might still bind to the histone H3 tails. The spatial proximity of the BDs and BAH domains to the histone tails was also supported by the CL-MS analysis (fig. S4B).

### Discussion

In this work, we determined the structure of RSC bound to the nucleosome. Within RSC, Sth1 functions as a global organizer orchestrating the complex into three modules (Fig. 5A), and Rsc8 works as a local organizer delineating the SRM into three substrate-binding lobes (Fig. 5B).

RSC binds to the nucleosome primarily through the motor domain of Sth1, with the majority of the histone-DNA contacts maintained. This model is different from the previous notion of nucleosome embracement (5), which was proposed to result in extensive rearrangement of histone-DNA contacts to facilitate DNA translocation. Our findings support a unified mechanism of chromatin that involves the action of the motor domain itself (12, 35). This is consistent with DNA translocation by the different remodelers involving 1- to 2-base pair movements of DNA along the octamer surface (11, 24, 36–38).

RSC repositions the promoter +1 nucleosome away from the NFR, whereas ISWI slides the nucleosome toward the open DNA (39, 40). Our structure suggests that Rsc3-Rsc30 binds to the open NFR DNA such that the motor of Sth1 is loaded onto the +1 nucleosome at the side distal to the NFR (Fig. 5A). RSC would then push the +1 nucleosome away from the NFR. In contrast, the HSS domain of ISWI binds to the NFR DNA and positions the motor domain to the nucleosome at the proximal side, and thus slides the nucleosome toward the NFR (39). Therefore, Rsc3-Rsc30 in RSC and HSS in ISWI both recognize the NFR DNA, yet the specific architectures of these remodeling complexes position their motors differently, enabling the enzymes to respond to

the chromatin cues distinctly and conferring specific functions at promoters.

The structure of RSC also sheds light on the assembly of the mammalian homologs PBAF and BAF. In addition to the well-known conserved components (1), our work provides evidence that yeast Rsc2 and Rsc4 together represent the mammalian polybromo protein BAF180, as Rsc2 and Rsc4 are adjacent, and their BAH and BDs combine to largely constitute polybromo. Furthermore, our work shows that BAF45a, BAF200, and BRD7, which are the characteristic subunits of the PBAF (25), are homologous to Rsc7, Rsc9, and Rsc58 in RSC, respectively.

### REFERENCES AND NOTES

- C. R. Clapier, B. R. Cairns, *Annu. Rev. Biochem.* **78**, 273–304 (2009).
- Y. Lorch, R. D. Kornberg, *Q. Rev. Biophys.* **50**, e5 (2017).
- A. E. Leschziner, *Curr. Opin. Struct. Biol.* **21**, 709–718 (2011).
- Z. Zhang et al., *Protein Cell* **9**, 1045–1049 (2018).
- Y. Chaban et al., *Nat. Struct. Mol. Biol.* **15**, 1272–1277 (2008).
- M. L. Angus-Hill et al., *Mol. Cell* **7**, 741–751 (2001).
- G. Badis et al., *Mol. Cell* **32**, 878–887 (2008).
- M. Kastan et al., *EMBO J.* **23**, 1348–1359 (2004).
- A. L. Chambers, L. H. Pearl, A. W. Oliver, J. A. Downs, *Nucleic Acids Res.* **41**, 9168–9182 (2013).
- A. P. VanDemark et al., *Mol. Cell* **27**, 817–828 (2007).
- M. Li et al., *Nature* **567**, 409–413 (2019).
- C. R. Clapier, J. Iwasa, B. R. Cairns, C. L. Peterson, *Nat. Rev. Mol. Cell Biol.* **18**, 407–422 (2017).
- H. L. Schubert et al., *Proc. Natl. Acad. Sci. U.S.A.* **110**, 3345–3350 (2013).
- X. Liu, M. Li, X. Xia, X. Li, Z. Chen, *Nature* **544**, 440–445 (2017).
- X. Xia, X. Liu, T. Li, X. Fang, Z. Chen, *Nat. Struct. Mol. Biol.* **23**, 722–729 (2016).
- C. R. Clapier et al., *Mol. Cell* **62**, 453–461 (2016).
- J. Gao et al., *Sci. Signal.* **6**, pii1 (2013).
- L. Yan, S. Xie, Y. Du, C. Qian, *J. Mol. Biol.* **429**, 1650–1660 (2017).
- M. L. Dechassa et al., *Mol. Cell Biol.* **28**, 6010–6021 (2008).
- P. Sen et al., *Cell Rep.* **18**, 2135–2147 (2017).
- Y. Cao, B. R. Cairns, R. D. Kornberg, B. C. Laurent, *Mol. Cell Biol.* **17**, 3323–3334 (1997).
- B. Wilson, H. Erdjument-Bromage, P. Tempst, B. R. Cairns, *Genetics* **172**, 795–809 (2006).
- M. L. Dechassa et al., *Mol. Cell* **38**, 590–602 (2010).
- G. Sirinakis et al., *EMBO J.* **30**, 2364–2372 (2011).
- N. Mashtalir et al., *Cell* **175**, 1272–1288.e20 (2018).
- C. Reichen et al., *Acta Crystallogr. D* **72**, 168–175 (2016).
- I. Treich, M. Carlson, *Mol. Cell Biol.* **17**, 1768–1775 (1997).
- M. L. Phelan, S. Sif, G. J. Narlikar, R. E. Kingston, *Mol. Cell* **3**, 247–253 (1999).
- R. R. Wang et al., *Protein Cell* **9**, 207–215 (2018).



30. B. R. Cairns, R. S. Levinson, K. R. Yamamoto, R. D. Kornberg, *Genes Dev.* **10**, 2131–2144 (1996).
31. M. D. Kaeser, A. Aslanian, M. Q. Dong, J. R. Yates 3rd, B. M. Emerson, *J. Biol. Chem.* **283**, 32254–32263 (2008).
32. C. Yan, H. Chen, L. Bai, *Mol. Cell* **71**, 294–305.e4 (2018).
33. Y. M. Lu *et al.*, *Mol. Genet. Genomics* **269**, 321–330 (2003).
34. B. R. Cairns *et al.*, *Mol. Cell* **4**, 715–723 (1999).
35. L. Yan, Z. Chen, *Trends Biochem. Sci.* 10.1016/j.tibs.2019.09.002 (2019).
36. B. T. Harada *et al.*, *eLife* **5**, e10051 (2016).
37. A. Sabantsev, R. F. Levendosky, X. Zhuang, G. D. Bowman, S. Deindl, *Nat. Commun.* **10**, 1720 (2019).
38. S. Deindl *et al.*, *Cell* **152**, 442–452 (2013).
39. K. Yen, V. Vinayachandran, K. Batta, R. T. Koerber, B. F. Pugh, *Cell* **149**, 1461–1473 (2012).
40. T. J. Parnell, A. Schlichter, B. G. Wilson, B. R. Cairns, *eLife* **4**, e06073 (2015).

## ACKNOWLEDGMENTS

We thank the Electron Microscopy Laboratory, CryoEM platform, and High-performance Computing Platform of Peking University, and the Bio-Computing Platform at Tsinghua University.

**Funding:** The National Key Research and Development Program (2017YFA0102900 to Z.C., 2016YFA0500700 to N.G., 2019YFA0508900 to Z.C. and N.G.), the National Natural Science Foundation of China (31570731 and 31630046 to Z.C., 31725007 and 31630087 to N.G.), HHMI (B.R.C.), NCI R01 CA 201396 (C.R.C. and N.V.), and NCI CA042014 to Huntsman Cancer Institute for core facilities. **Author contributions:** Y.Y. prepared the samples for EM and MS analyses; W.Z., K.C., and H.D. performed MS analyses; H.W., K.C., N.G., and Z.C. performed EM analysis and model building; C.R.C., N.V., and B.R.C. conducted genetic and biochemical analyses; Z.C. oversaw the project and wrote the manuscript with help from all the authors. **Competing interests:** Authors declare no competing interests. **Data and materials availability:** Density

maps are deposited at the Electron Microscopy Database (accession code EMD-9905, 0777, 0778) and protein coordinates are deposited at the Protein Data Bank (PDB 6K15, 6KW3, and 6KW4) for the SRM, class A complex, and class B complex, respectively.

## SUPPLEMENTARY MATERIALS

[science.sciencemag.org/content/366/6467/838/suppl/DC1](https://science.sciencemag.org/content/366/6467/838/suppl/DC1)

Materials and Methods

Figs. S1 to S14

Table S1

Movie S1

Data S1

References (41–57)

11 May 2019; accepted 20 October 2019

Published online 31 October 2019

10.1126/science.aay0033

## BIOMEDICINE

# Activation of the ISR mediates the behavioral and neurophysiological abnormalities in Down syndrome

Ping Jun Zhu<sup>1,2</sup>, Sanjeev Khatiwada<sup>1,2,3</sup>, Ya Cui<sup>4,5</sup>, Lucas C. Reineke<sup>1,2</sup>, Sean W. Dooling<sup>2,6</sup>, Jean J. Kim<sup>4,7</sup>, Wei Li<sup>4,5</sup>, Peter Walter<sup>8,9,\*</sup>, Mauro Costa-Mattioli<sup>1,2,\*</sup>

Down syndrome (DS) is the most common genetic cause of intellectual disability. Protein homeostasis is essential for normal brain function, but little is known about its role in DS pathophysiology. In this study, we found that the integrated stress response (ISR)—a signaling network that maintains proteostasis—was activated in the brains of DS mice and individuals with DS, reprogramming translation. Genetic and pharmacological suppression of the ISR, by inhibiting the ISR-inducing double-stranded RNA-activated protein kinase or boosting the function of the eukaryotic translation initiation factor eIF2-eIF2B complex, reversed the changes in translation and inhibitory synaptic transmission and rescued the synaptic plasticity and long-term memory deficits in DS mice. Thus, the ISR plays a crucial role in DS, which suggests that tuning of the ISR may provide a promising therapeutic intervention.

Intellectual disability (ID) affects ~2 to 3% of the human population (1). Recent array-based comparative genomic studies have identified a large number of chromosomal aberrations in individuals with ID (2, 3). Down syndrome (DS) is a chromosomal condition and the most common genetic cause of ID. DS is a substantial biomedical and socioeconomic problem (4), for which there is no effective treatment. Thus, the identification of neuronal targets for the development of pharmacotherapies to treat the memory decline associated with DS is an important goal.

DS results from the presence of an extra copy of human chromosome 21 (CH21; also known as *Homo sapiens* autosome 21, HSA21) leading to genetic imbalance. Gene expression studies have shown that the overall genome-wide differences between individuals with DS and euploid controls map not only to CH21 but also to other chromosomes (5, 6). Thus, the DS phenotype could be caused by widespread pleiotropic dysregulation of gene expression (7). Consequently, most of the focus in the field has been to understand how alterations in the expression of specific genes in CH21 trisomic

cells lead to neurodevelopmental dysfunction (8). However, the degree to which defects in protein homeostasis (proteostasis) might contribute to the cognitive deficits associated with DS has remained largely unexplored.

The brain must adapt to stress conditions that occur as a result of numerous environmental and/or genetic factors. The integrated stress response (ISR) is one of the circuits that responds to stress conditions and serves to restore proteostasis by regulating protein synthesis rates (9). The central regulatory hub of the ISR is the eukaryotic translation initiation factor eIF2, the target of four kinases that are activated in response to different stresses. In its guanosine triphosphatase (GTP)-bound state, eIF2 assembles into the eIF2-GTP-Met-tRNA<sub>i</sub> ternary complex (TC) that delivers the methionyl initiator tRNA (Met-tRNA<sub>i</sub>) to the small ribosomal subunit (40S), priming translation initiation (10). After recognition of an AUG codon, GTP is hydrolyzed and the resulting eIF2-GDP leaves the ribosome (GDP, guanosine diphosphate). eIF2-GDP is recycled to the GTP-bound state by eIF2B, which serves as eIF2's dedicated guanine nucleotide exchange factor (GEF).

Translational control by the ISR is exerted by phosphorylation of the  $\alpha$  subunit of eIF2 (eIF2-P) on a single serine (serine 51), which converts eIF2 from a substrate into an inhibitor of eIF2B: eIF2-P binds more tightly to eIF2B and blocks its GEF activity. Thus, reducing TC formation inhibits general translation (10).

## Activation of the ISR in the brains of Ts65Dn mice and individuals with DS

To determine whether protein homeostasis is altered in DS, we first measured protein synthesis rates in the brain of a mouse model of DS (Ts65Dn) that recapitulates the learning and memory deficits of the human syndrome (11, 12). Ts65Dn mice are trisomic for approximately two-thirds of the genes orthologous

to human CH21. We measured translation in the hippocampus of wild-type (WT) euploid mice and Ts65Dn mice by comparing polysome sedimentation in sucrose gradients and then assessing ribosome and mRNA engagement. In this assay, the position of a given mRNA in the sucrose gradient is determined by the number of associated ribosomes. mRNAs that are poorly translated or not translated at all accumulate near the top, whereas translationally active mRNAs are associated with multiple ribosomes (polysomes) and sediment to the bottom of the gradient (Fig. 1A). Compared with WT mice, mRNA translation in the hippocampus of Ts65Dn mice was reduced, as indicated by a  $32 \pm 8\%$  decrease in the polysome/subpolysome ratio (Fig. 1, B and C). An independent translation assay measuring puromycin incorporation into nascent polypeptide chains confirmed that protein synthesis was markedly reduced ( $39 \pm 7\%$ ) in the hippocampus of Ts65Dn mice (Fig. 1, D and E).

To determine the mechanism(s) underlying the reduced translation in Ts65Dn mice, we first asked whether the ISR, a major pathway that regulates translation initiation (9), is activated in the brains of Ts65Dn mice. Consistent with the decrease in overall protein synthesis (Fig. 1, B to E), the ISR was activated in the hippocampus of Ts65Dn mice, as determined by the increased eIF2-P levels (Fig. 1F). To assess whether these changes were also observed in the human condition, we measured eIF2-P levels in postmortem brain samples from human individuals with DS. We found increased eIF2-P levels in brain samples from human individuals with DS compared with non-DS euploid controls (Fig. 1G and table S1). Moreover, when we reprogrammed a fibroblast line derived from an individual with DS (CCL-54<sup>TM</sup> from ATCC) into induced pluripotent stem cells (iPSCs), we identified one clone that was CH21-trisomic (DS) and another clone from the same individual that was fortuitously euploid (control) (fig. S1). Microsatellite and karyotyping analysis demonstrated that the euploid iPSC clone was isogenic (fig. S1 and see supplementary materials and methods), likely because the individual had mosaic DS, or the extra chromosome was lost during cell line propagation. Although extensive serial passaging (>70 passages) of trisomic-21 iPSCs may have caused cells to become euploid (13), we find this unlikely because karyotyping was performed on passage 9 (fig. S1). Regardless of its etiology, the euploid isogenic line offered the rare opportunity of an ideal isogenic control for our studies. Notably, the ISR was activated in the CH21-trisomic iPSCs but not in the isogenic euploid iPSCs, as indicated by increased eIF2-P levels (Fig. 1H). Similarly, the ISR was also activated in a previously reported CH21-trisomic iPSC line (DS1) (14) compared with

<sup>1</sup>Department of Neuroscience, Baylor College of Medicine, Houston, TX, USA. <sup>2</sup>Memory and Brain Research Center, Baylor College of Medicine, Houston, TX, USA. <sup>3</sup>Verna and Marrs McLean Department of Biochemistry and Molecular Biology, Baylor College of Medicine, Houston, TX, USA. <sup>4</sup>Division of Biostatistics, Dan L. Duncan Comprehensive Cancer Center, and Department of Molecular and Cellular Biology, Baylor College of Medicine, Houston, TX, USA. <sup>5</sup>Department of Biological Chemistry, University of California, Irvine, Irvine, CA, USA. <sup>6</sup>Department of Molecular and Human Genetics, Baylor College of Medicine, Houston, TX, USA. <sup>7</sup>Stem Cells and Regenerative Medicine Center, Baylor College of Medicine, Houston, TX, USA. <sup>8</sup>Howard Hughes Medical Institute, University of California at San Francisco, San Francisco, CA, USA. <sup>9</sup>Department of Biochemistry and Biophysics, University of California at San Francisco, San Francisco, CA, USA. \*Corresponding author. Email: costamatt@bcm.edu (M.C.-M.); peter@walterlab.ucsf.edu (P.W.)



its respective isogenic control (DS2U) (fig. S2). As expected from the increased eIF2-P levels (Fig. 1H), protein synthesis was reduced in the DS iPSC line compared with the euploid isogenic control (Fig. 1, I and J). Thus, activation of the ISR in the brains of Ts65Dn mice and human individuals with DS provides a common molecular signature of the condition.

We next examined whether changes in the activity of mTORC1 (mammalian target of rapamycin complex 1), which regulates translation initiation rates by a pathway that is distinct and independent from the ISR (15), could also contribute to the decreased translation in the brain of Ts65Dn mice. mTORC1 regulates translation rates by phosphorylating its downstream targets, the ribosomal protein S6, and the translational repressor cap-binding

protein eIF4E binding protein 1 (4E-BP1) (fig. S3A). In the hippocampus of WT and Ts65Dn mice, the phosphorylation states of these mTORC1 targets, as well as that of the cap-binding protein eIF4E [a key translation initiation factor (10)], were indistinguishable (fig. S3, B to G), underscoring the idea that the translation repression in DS mice was likely exerted by ISR activation.

### The PKR branch of the ISR is activated in the brain of Ts65Dn mice

In the brain, eIF2 is phosphorylated by three kinases: PKR (double-stranded RNA-dependent protein kinase), GCN2 (general control non-repressible 2), and PERK (PKR-like endoplasmic reticulum kinase) (fig. S4A). The fourth ISR kinase, HRI (heme-regulated inhibitor), has

been extensively studied in erythroid cells, but little is known about its function in the brain. To examine which eIF2 kinase was responsible for the increase in eIF2-P in Ts65Dn mice, we measured their degree of autophosphorylation, indicative of their activation (16). Phosphorylation of PKR, but not of GCN2 or PERK, was increased in the hippocampus of Ts65Dn mice (fig. S4, B to G). The unfolded protein response (UPR), which, in addition to PERK, includes the ER stress sensors IRE1 (inositol requiring enzyme 1) and ATF6 (activating transcription factor 6), has recently been implicated in DS (17, 18). We did not observe changes in the activity of IRE1 and ATF6 in the brains of Ts65Dn mice (fig. S5). Taken together with the fact that PERK was not activated in Ts65Dn mice, our data indicate that the ISR (but not the UPR) is

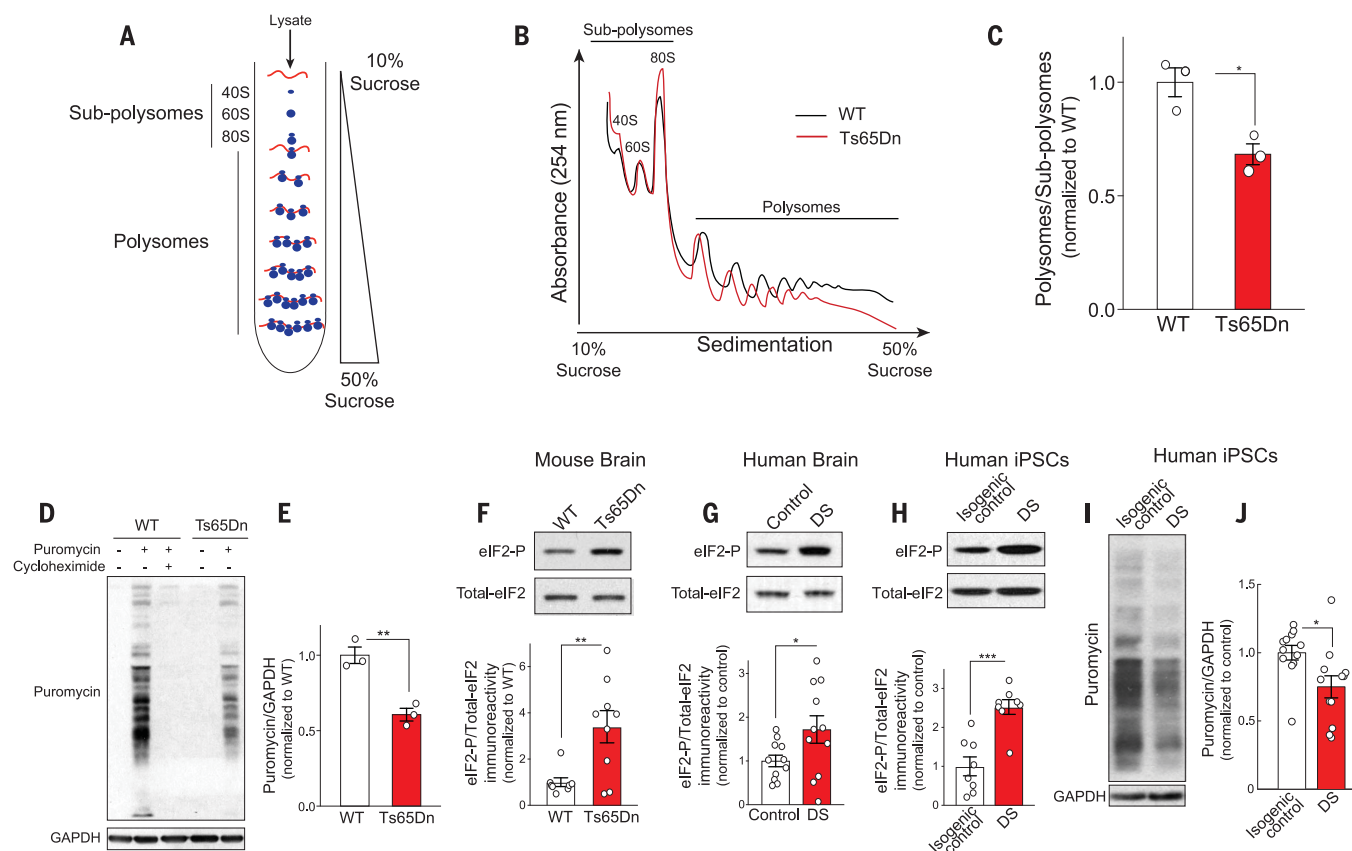


**Fig. 1. The ISR is activated in the brains of DS mice (Ts65Dn) and individuals with DS.** (A) Schematic of polysome profiling sedimentation. After ultracentrifugation, subpolysomes (40S, 60S, and 80S) and polysomes were separated on the basis of size. (B and C) Representative polysome profile traces (B) and quantification (C) of polysome/subpolysome ratio in the hippocampus of WT and Ts65Dn mice ( $n = 3$  per group,  $t_4 = 4.05$ , two-tailed Student's  $t$ -test). (D and E) Incorporation of puromycin into nascent peptides was detected using an anti-puromycin antibody. A representative immunoblot (D) and quantification (E) in hippocampal extract from WT and Ts65Dn mice ( $n = 3$  per group,  $t_4 = 5.69$ ). Treatment with the protein synthesis inhibitor cycloheximide was included as control. GAPDH, glyceraldehyde phosphate dehydrogenase. (F to H) Representative immunoblot and quantification of eIF2-P levels in (F)

hippocampal extracts from WT and Ts65Dn mice ( $n = 8$  or 9 per group,  $t_{15} = 3.14$ ), (G) postmortem human brain extracts from controls and individuals with DS ( $n = 11$  per group,  $t_{20} = 2.10$ ), and (H) human iPSC extracts from an individual with DS (CH21-trisomic,  $n = 8$  per group,  $t_{14} = 4.95$ ) compared with its isogenic control. (I and J) Incorporation of puromycin into nascent peptides in iPSCs was detected using an anti-puromycin antibody. A representative immunoblot (I) and quantification (J) in the DS CH21-trisomic iPSCs compared with the isogenic control line ( $n = 12$  per group,  $t_{22} = 2.51$ ). "Isogenic control" indicates iPSCs that are diploid for CH21, whereas "DS" indicates iPSCs that are CH21-trisomic. Both lines were derived from the same individual with DS, and the experiment was replicated in 8 to 12 wells per genotype. Data are mean  $\pm$  SEM. \* $P < 0.05$ , \*\* $P < 0.01$ , \*\*\* $P < 0.001$ .

selectively activated in the hippocampus of Ts65Dn mice.

It is notable that in the hippocampus (Fig. 2, A and B) and cortex (fig. S6) of Ts65Dn mice lacking PKR (Ts65Dn-*Pkr*<sup>-/-</sup> mice), eIF2-P levels were reduced compared with Ts65Dn mice. Moreover, genetic inhibition of PKR in Ts65Dn mice (Ts65Dn-*Pkr*<sup>-/-</sup> mice) was sufficient to derepress translation in the brains of Ts65Dn mice (Fig. 2, C and D). Thus, the increased levels of eIF2-P and the resulting sustained translational repression in the brain of Ts65Dn mice are mediated, at least in part, by activation of the PKR branch of the ISR.

### Inhibition of the PKR branch of the ISR rescues the deficits in long-term memory and synaptic plasticity in Ts65Dn mice

Individuals with DS exhibit learning and memory deficits, specifically in hippocampus-

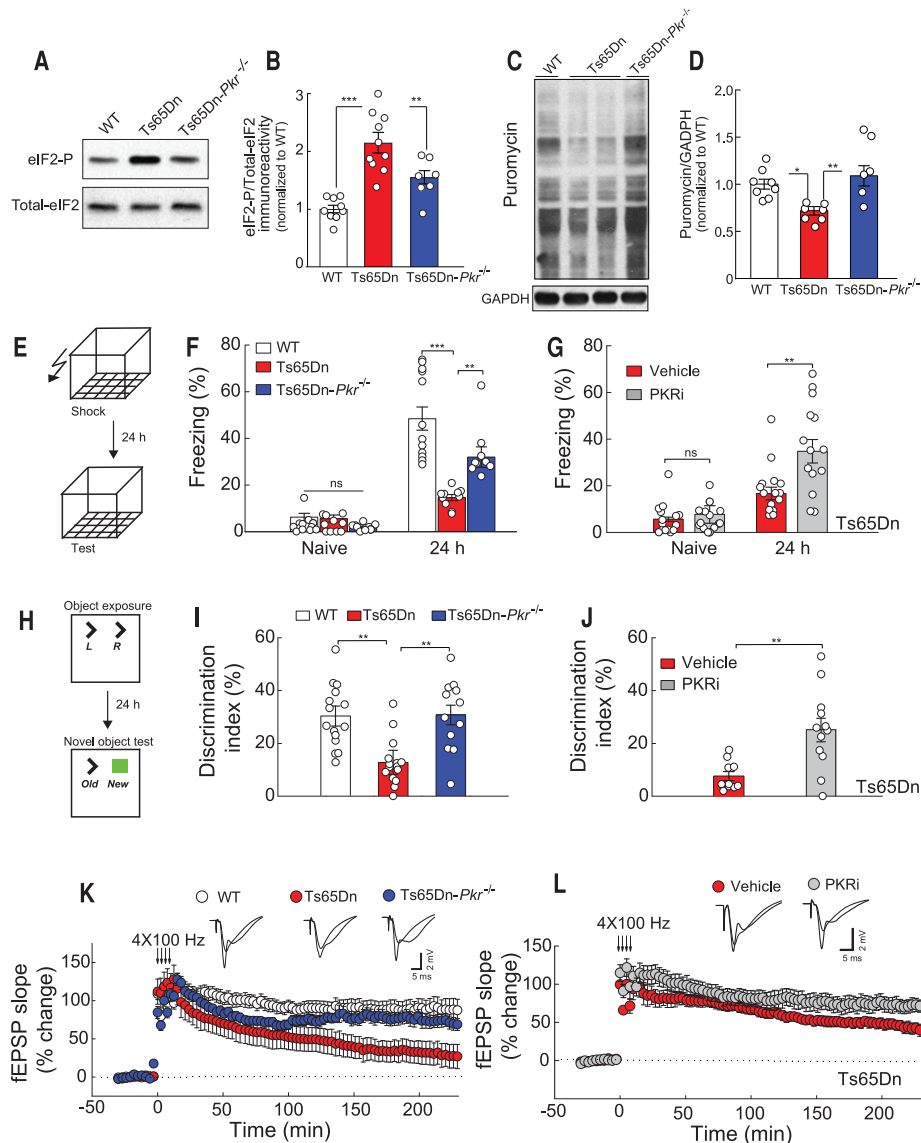
dependent tasks (4, 19). To investigate whether activation of the ISR contributes to long-term memory deficits in DS mice, we first examined hippocampus-dependent contextual fear memory. In this task, we paired a context (conditioned stimulus, CS) with a foot shock (unconditioned stimulus, US). Twenty-four hours after training, we exposed mice to the CS and measured their fear responses (in this case, freezing behavior) as an index of the strength of their long-term memory (Fig. 2E). Although freezing prior to training was similar in Ts65Dn mice and naïve WT mice, Ts65Dn mice exhibited a significant reduction in freezing behavior 24 hours after a normal training paradigm (two foot shocks at 0.7 mA for 2 s), indicating that their long-term contextual fear memory was impaired (Fig. 2F), as expected (20, 21). Genetic ablation of PKR in Ts65Dn mice (Ts65Dn-*Pkr*<sup>-/-</sup> mice) significantly improved their long-term

memory (Fig. 2F). A weak training protocol (one foot shock at 0.35 mA for 1 s) is known to induce a better long-term fear memory in *Pkr*<sup>-/-</sup> mice compared with their WT littermates (22). However, in response to a normal and more conventional training protocol (two foot shocks at 0.7 mA for 2 s), the one we used to reveal that Ts65Dn mice exhibited impaired memory, *Pkr*<sup>-/-</sup> mice and WT littermates showed normal long-term memory (fig. S7A). Thus, genetic deletion of PKR selectively improves long-term memory in Ts65Dn mice. Consistent with these results, treatment with an inhibitor of PKR, PKRi (22), reversed the long-term memory deficits in Ts65Dn mice (Fig. 2G) but had no effect on WT mice (fig. S7B).

To corroborate these findings, we assessed long-term object recognition memory, which is also dependent on the hippocampus (23). In this task, animals need to differentiate between

### Fig. 2. Inhibition of PKR rescues the deficits in long-term memory and synaptic plasticity in Ts65Dn mice.

(A and B) Representative immunoblot (A) and quantification (B) of eIF2-P levels in hippocampal extracts from WT ( $n = 9$ ), Ts65Dn ( $n = 10$ ), and Ts65Dn-*Pkr*<sup>-/-</sup> mice [ $n = 7$ ,  $F_{2,23} = 4.12$ , one-way analysis of variance (ANOVA)]. (C and D) Incorporation of puromycin into nascent peptides was detected using an anti-puromycin antibody. A representative immunoblot (C) and quantification (D) in hippocampal extracts from WT ( $n = 8$ ), Ts65Dn ( $n = 7$ ), and Ts65Dn-*Pkr*<sup>-/-</sup> mice ( $n = 6$ ,  $F_{1,12} = 25.16$ ). (E) Schematic of the fear conditioning paradigm. (F) Genetic inhibition of PKR: freezing behavior before (naïve) and 24 hours after training in WT ( $n = 12$ ), Ts65Dn ( $n = 10$ ), and Ts65Dn-*Pkr*<sup>-/-</sup> mice ( $n = 9$ ,  $H = 22.74$ , one-way ANOVA on ranks). (G) Pharmacological inhibition of PKR: freezing behavior before (naïve) and 24 hours after training in vehicle-treated ( $n = 15$ ) and PKRi-treated Ts65Dn mice ( $n = 14$ ,  $t_{27} = 3.21$ ). (H) Schematic of the object recognition task. (I) Genetic inhibition of PKR: novel object discrimination index 24 hours after training in WT ( $n = 15$ ), Ts65Dn ( $n = 15$ ), and Ts65Dn-*Pkr*<sup>-/-</sup> mice ( $n = 12$ ,  $F_{2,39} = 11.56$ ). (J) Pharmacological inhibition of PKR: novel object discrimination index 24 hours after training in vehicle-treated ( $n = 10$ ) and PKRi-treated Ts65Dn mice ( $n = 12$ ,  $t_{20} = 3.48$ ). (K) Genetic inhibition of PKR: L-LTP induced by four trains of high frequency stimulation (HFS,  $4 \times 100$  Hz) in WT ( $n = 10$ ), Ts65Dn ( $n = 14$ ), and Ts65Dn-*Pkr*<sup>-/-</sup> mice ( $n = 14$ ,  $H = 15.72$ ,  $P < 0.05$ ). fEPSP, field excitatory postsynaptic potential. (L) Pharmacological inhibition of PKR: L-LTP induced by  $4 \times 100$  Hz of HFS in vehicle-treated ( $n = 7$ ) and PKRi-treated Ts65Dn mice ( $n = 13$ ,  $U = 41.00$ ,  $P < 0.05$ , Mann-Whitney  $U$  test). Data are mean  $\pm$  SEM. \* $P < 0.05$ , \*\* $P < 0.01$ , \*\*\* $P < 0.001$ .





a familiar and a novel object. During acquisition, two identical objects are placed in a box, and mice are allowed to explore them (Fig. 2H). Ts65Dn and WT mice spent, on average, an equal amount of time investigating the identical objects (fig. S8, A and B). When one object was replaced by a novel one 24 hours later, WT mice, relying on their memory for the old object, preferentially explored the novel object.

In contrast, Ts65Dn mice showed markedly reduced object discrimination, indicating that their long-term object recognition memory was impaired (Fig. 2I), as expected (19, 24). Again, these deficits in long-term memory were ameliorated by genetic (Fig. 2I) or pharmacological inhibition of PKR in Ts65Dn mice (Fig. 2J and fig. S8). Both genetic and pharmacological inhibition of the PKR restored behavioral flexibility in Ts65Dn mice in a spontaneous alternation T-maze task (fig. S9).

We next investigated whether the inhibition of PKR could improve the long-term deficits in synaptic plasticity in Ts65Dn mice. To this end, we recorded protein synthesis-dependent late long-term potentiation (L-LTP), which is thought to underlie long-term memory (25), in hippocampal slices. As expected, L-LTP was impaired in slices from Ts65Dn mice, and genetic ablation of PKR rescued the impaired L-LTP in Ts65Dn mice (Fig. 2K). Consistent with these data, treatment with PKRi improved L-LTP in slices from Ts65Dn mice (Fig. 2L). Genetic or pharmacological inhibition of PKR does not further enhance L-LTP induced by four tetanic trains in WT slices (22); hence, the effects of these manipulations were specific to Ts65Dn mice. Thus, in Ts65Dn mice, the cognitive impairment at both the behavioral and synaptic levels is caused, at least in part, by activation of the PKR branch of the ISR.

### Inhibition of the ISR rescues the dysregulated translational program in Ts65Dn mice

To decipher the translational landscape in the brain of Ts65Dn mice in an unbiased manner, we next compared genome-wide transcriptional changes by RNA sequencing (RNA-seq) with translational changes, as determined by the sequencing of polysome-associated mRNA in the brain of WT and Ts65Dn mice (Fig. 3A). As expected, in Ts65Dn mice, numerous genes were transcriptionally and/or translationally dysregulated (Fig. 3, B and C). Gene ontology-term enrichment analysis revealed categories of genes involved in mRNA metabolism, and signaling pathways involved in LTP regulation and memory storage (Fig. 3D). To identify the mRNAs whose translation was altered in Ts65Dn mice, we focused on mRNAs that were not significantly altered at the transcriptional level but were translationally increased or decreased (>1.5-fold) in Ts65Dn mice. We found 662 differences in the brains of Ts65Dn mice (Fig. 3E and table S2). Of note, the expression of

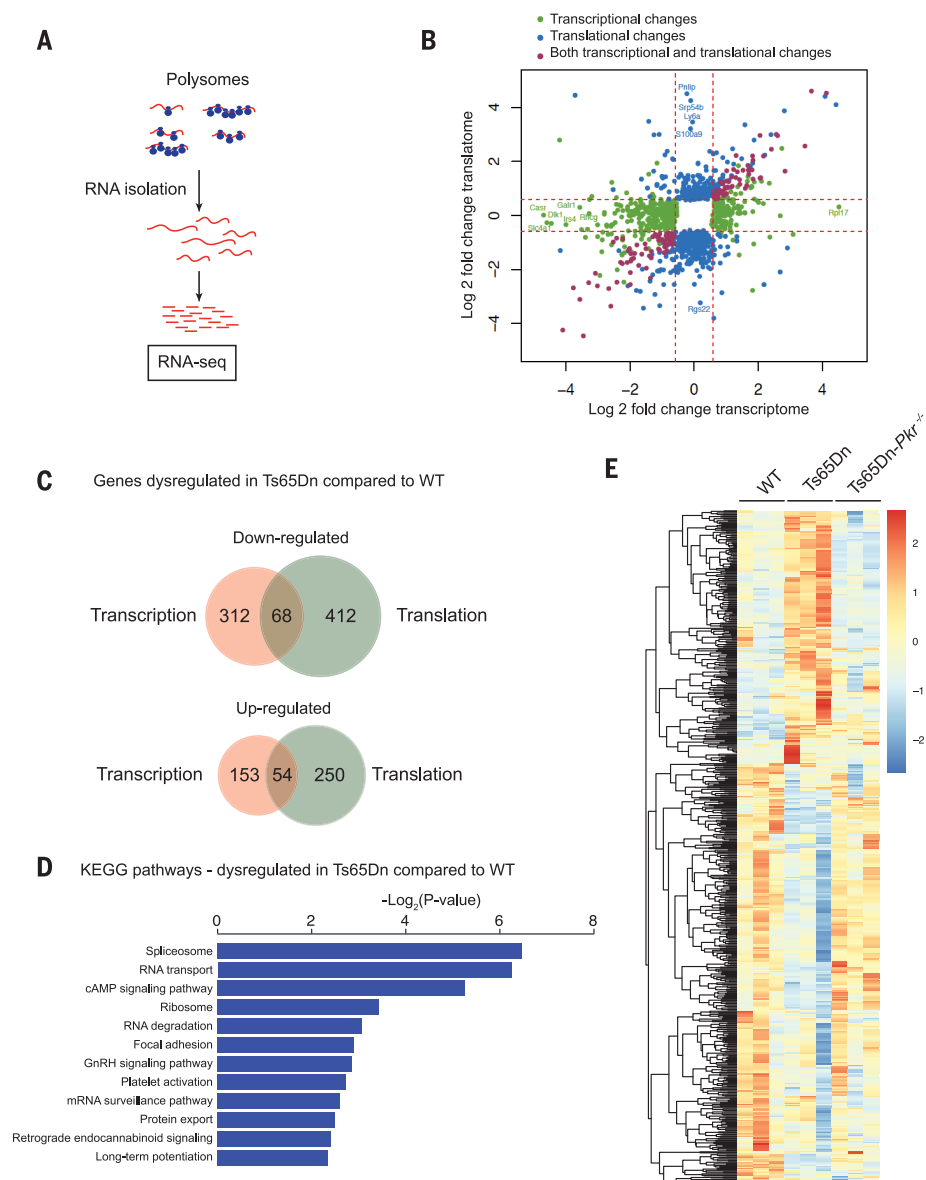


**Fig. 3. Inhibition of the ISR rescues the dysregulated translational program in the brain of Ts65Dn mice.** (A) Schematic of the polysome profiling followed by RNA-seq protocol. (B) Scatterplot showing the genes significantly up- or down-regulated (>1.5 fold) at the transcriptional and/or translational levels in the brain of Ts65Dn mice. mRNAs whose expression was not altered between genotypes were removed from the analysis (white square). (C) Venn diagram depicting transcriptionally and translationally up- or down-regulated genes in Ts65Dn mice. (D) Kyoto Encyclopedia of Genes and Genomes (KEGG) pathway enrichment analysis of the genes down-regulated in Ts65Dn mice compared with WT. cAMP, 3',5'-cyclic adenosine monophosphate; GnRH, gonadotropin-releasing hormone. (E) Heat map showing genes that are significantly up- or down-regulated only at the translational level in Ts65Dn mice and rescued in Ts65Dn-Pkr<sup>-/-</sup> mice (n = 3 per group).

>80% of the mRNAs whose association with ribosomes was reduced in Ts65Dn mice was selectively corrected in Ts65Dn-Pkr<sup>-/-</sup> mice (Fig. 3E, table S2, and fig. S10). Moreover, in an outcome that would be expected of ISR induction, a subset of mRNAs showed increased association with the polysome fraction in Ts65Dn mice but not in Ts65Dn-Pkr<sup>-/-</sup> mice (Fig. 3E and table S2). Thus, inhibition of the PKR branch of the ISR partially cor-

rects the dysregulated translational program in Ts65Dn mice.

### Inhibition of the ISR rescues the deficits in protein synthesis, long-term memory, and synaptic plasticity in Ts65Dn mice

Because (i) eIF2 is the central hub of the ISR and its phosphorylation reduces general protein synthesis rates by inhibiting eIF2B (10), (ii) the ISR is activated in the brains of Ts65Dn

mice, and (iii) protein synthesis is a primary node of proteostatic control, and its regulation is crucial for synaptic plasticity and long-term memory formation (26), we reasoned that either direct inhibition of the ISR by reducing eIF2-P levels or promoting the activity of eIF2B should similarly reverse the cognitive deficits in Ts65Dn mice. To test these predictions, we first crossed Ts65Dn mice with heterozygous *Eif2s1<sup>S/A</sup>* mice, in which in one of the alleles the phosphorylation site at serine 51 of eIF2 $\alpha$  was replaced by nonphosphorylatable alanine. In the brains of Ts65Dn-*Eif2s1<sup>S/A</sup>* mice, eIF2-P levels were reduced compared with Ts65Dn mice (Fig. 4, A and B). As expected, direct reduction of eIF2-P levels in Ts65Dn mice (Ts65Dn-*Eif2s1<sup>S/A</sup>* mice) restored the aberrant translation (Fig. 4, C and D). More importantly, reduction of eIF2-P levels corrected the deficits in long-term memory (Fig. 4E and fig. S11) and L-LTP in Ts65Dn mice (Fig. 4F) but had no effect on WT mice (fig. S12). Thus, direct reduction of eIF2-P levels and correction of the aberrant translation in Ts65Dn mice rescues their deficits in L-LTP and long-term memory.

To further support these findings, we treated Ts65Dn mice with the small-molecule, drug-like ISR inhibitor ISRIB. ISRIB is a potent eIF2B activator that enhances GEF activity by facilitating eIF2B assembly into its decameric holoenzyme, resulting in the reversal of eIF2-P-mediated translational events (27–29). Treatment with ISRIB paralleled the effects of reducing eIF2-P levels genetically: ISRIB rescued the impairment in long-term memory (Fig. 4G) and L-LTP (Fig. 4H) in Ts65Dn mice, although it did not further enhance L-LTP (fig. S13A) or long-term fear memory (fig. S13B) in WT mice. Thus, direct genetic or pharmacological manipulation of the efficacy of the central ISR effector eIF2-P rescues the core deficits in long-term memory and synaptic plasticity in Ts65Dn mice.

#### Inhibition of the ISR reverses the enhanced inhibitory synaptic transmission in Ts65Dn mice

According to previous reports, the deficits in L-LTP and long-term memory in Ts65Dn mice can be attributed to enhanced inhibitory synaptic transmission (24, 30, 31). Thus, we first wondered whether reversal of the PKR-mediated increase in eIF2-P also corrects the abnormally high inhibitory synaptic transmission observed in Ts65Dn mice. As expected, whole-cell recordings showed that inhibitory synaptic transmission was enhanced in Ts65Dn mice (Fig. 5, A and B). Specifically, we observed significant enhancement of the frequency (but not the amplitude) of miniature inhibitory postsynaptic currents (mIPSCs) in hippocampal slices from Ts65Dn mice (Fig. 5, A and B, and fig. S14A). The enhanced synaptic inhibition was reduced

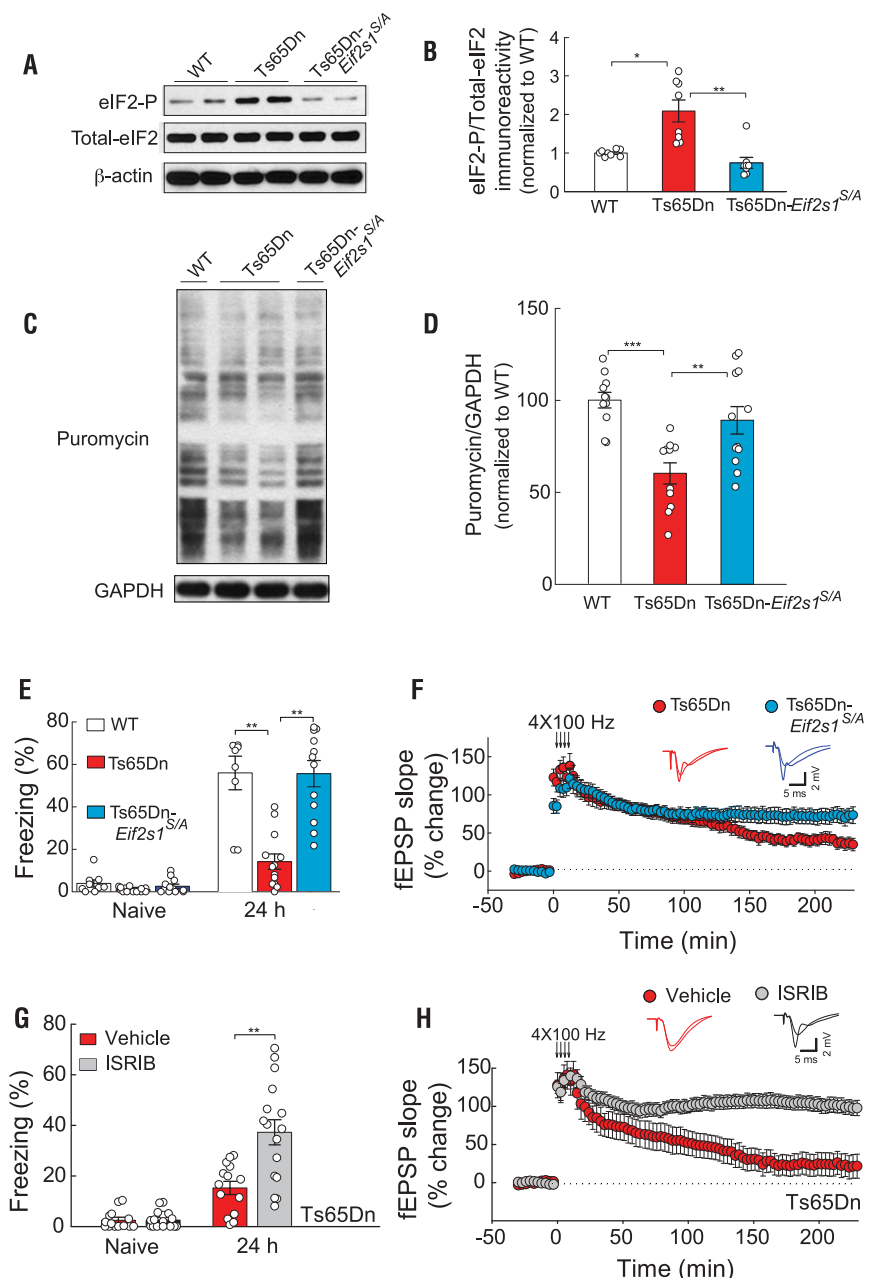


**Fig. 4. Genetic or pharmacological inhibition of the ISR rescues the deficits in memory and synaptic plasticity in Ts65Dn mice.** (A and B) Representative immunoblot (A) and quantification (B) of eIF2-P levels in hippocampal extracts from WT ( $n = 8$ ), Ts65Dn ( $n = 8$ ), and Ts65Dn-*Eif2s1<sup>S/A</sup>* mice ( $n = 8$ ,  $H = 15.92$ ). (C and D) Incorporation of puromycin into nascent peptides was detected using an anti-puromycin antibody. A representative immunoblot (C) and quantification (D) in hippocampal extracts from WT ( $n = 11$ ), Ts65Dn ( $n = 11$ ), and Ts65Dn-*Eif2s1<sup>S/A</sup>* mice ( $n = 12$ ,  $F_{3,12} = 11.23$ ). (E) Genetic inhibition of the ISR: freezing behavior before (naïve) and 24 hours after training in WT ( $n = 9$ ), Ts65Dn ( $n = 13$ ), and Ts65Dn-*Eif2s1<sup>S/A</sup>* mice ( $n = 12$ ,  $F_{2,31} = 20.25$ ). (F) Genetic inhibition of the ISR: L-LTP induced by  $4 \times 100$  Hz of HFS in Ts65Dn ( $n = 10$ ) and Ts65Dn-*Eif2s1<sup>S/A</sup>* mice ( $n = 9$ ,  $t_{17} = 3.1$ ,  $P < 0.01$ ). (G) Pharmacological inhibition of the ISR: freezing behavior before (naïve) and 24 hours after training in vehicle-treated ( $n = 14$ ) and ISRIB-treated ( $n = 16$ ) Ts65Dn mice ( $U = 43.50$ , Mann-Whitney  $U$  test). (H) Pharmacological inhibition of the ISR: L-LTP induced by  $4 \times 100$  Hz of HFS in vehicle-treated ( $n = 8$ ) and ISRIB-treated ( $n = 9$ ) Ts65Dn mice ( $t_{15} = 4.84$ ,  $P < 0.001$ ). Data are mean  $\pm$  SEM. \* $P < 0.05$ , \*\* $P < 0.01$ .



in hippocampal slices from Ts65Dn-*Pkr*<sup>-/-</sup> mice (Fig. 5, A and B), as well as in slices from Ts65Dn mice treated with PKRi (Fig. 5, C and D, and fig. S14B). Excitatory synaptic transmission (determined by measuring miniature excitatory postsynaptic current frequency and amplitude) was not altered in the hippocampus of Ts65Dn mice (fig. S15). Accordingly, genetic reduction of eIF2-P levels (Fig. 5, E and F, and fig. S14C) or promoting the activity of eIF2B with ISRIB (Fig. 5, G and H, and fig. S14D) reduced the enhanced synaptic inhibition in Ts65Dn mice. Thus, inhibition of the ISR at the level of the initiating kinase PKR or at its central eIF2-eIF2B regulatory hub reverses the enhanced synaptic inhibitory tone in Ts65Dn mice.

### The ISR: A molecular switch for long-term memory formation that is turned off in cognitive disorders

It is widely accepted that de novo protein synthesis is required for the formation of long-term memory (32, 33). Research in different species and animal models over the past decade has shown that the ISR is a central proteostasis network causally controlling long-term memory formation. This conclusion is supported by three types of observations. First, genetic or pharmacological suppression of the ISR, by inhibiting the eIF2 kinases or boosting the function of the eIF2-eIF2B complex, facilitates long-term memory formation (26, 34). Second, activation of the ISR by inhibiting the eIF2 phosphatases or activating PKR in the hippocampus impairs long-term memory (26, 34). Finally, mutations in key components that induce the ISR have been associated with ID (35–37), underscoring the importance of the ISR in mnemonic processes.

In this study, we found that activation of the ISR can account, at least in part, for the core behavioral and neurophysiological abnormalities in Ts65Dn mice, a model system of DS. The potential significance of our findings is highlighted by the observation that the activation of the ISR in the brains of Ts65Dn mice is recapitulated in the brains of individuals with DS, as well as in human CH21-trisomic iPSCs derived from individuals with DS. Thus, ISR-mediated maladapted regulation of protein synthesis may emerge as a central molecular mechanism underlying the cognitive decline associated with DS.

Given the heterogeneity of the genetic perturbations in DS, it seems unlikely that aberrant levels of a single protein are the sole cause of the long-term memory deficits associated with DS. Instead of repairing the expression of individual genes, we correct the overall translational program controlled by the ISR by restoring the function of eIF2-eIF2B, where the ISR exerts its central control. Briefly, we find that inhibition of the activated ISR either

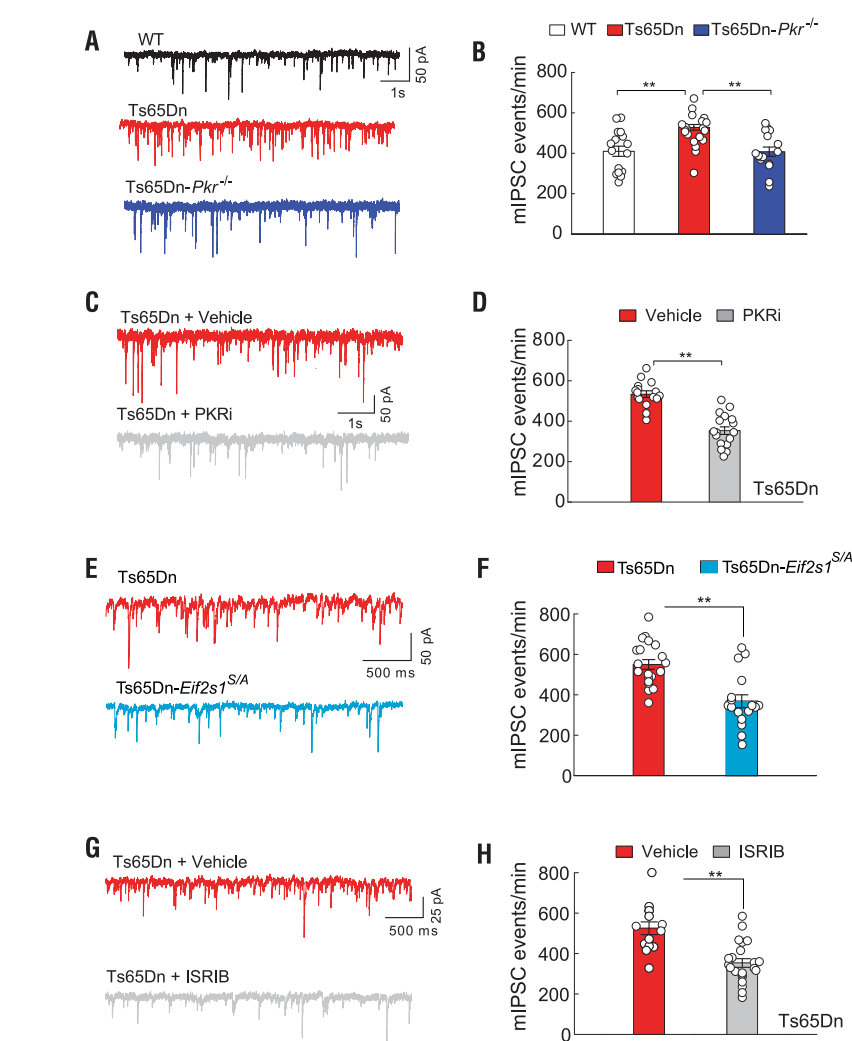


**Fig. 5. Genetic or pharmacological inhibition of the ISR suppresses the increased inhibitory synaptic responses in Ts65Dn mice.** (A and B) Sample traces (A) and summary data (B) show frequency of mIPSCs in CA1 neurons from WT ( $n = 16$ ), Ts65Dn ( $n = 20$ ), and Ts65Dn-*Pkr*<sup>-/-</sup> ( $n = 16$ ) mice ( $F_{2,49} = 7.76$ ). (C and D) Sample traces (C) and summary data (D) show frequency of mIPSCs in CA1 neurons from vehicle-treated ( $n = 16$ ) and PKRi-treated ( $n = 17$ ) Ts65Dn mice ( $t_{31} = 7.09$ ). (E and F) Sample traces (E) and summary data (F) show frequency of mIPSCs in CA1 neurons from Ts65Dn ( $n = 20$ ) and Ts65Dn-*Eif2s1*<sup>S/A</sup> mice ( $n = 17$ ,  $t_{35} = 4.58$ ). (G and H) Sample traces (G) and summary data (H) show frequency of mIPSCs in CA1 neurons from vehicle-treated ( $n = 13$ ) and ISRIB-treated Ts65Dn mice ( $n = 22$ ,  $t_{33} = 6.18$ ). Data are mean  $\pm$  SEM. \*\* $P < 0.01$ .

upstream at the level of the ISR-inducing kinase PKR, or downstream by manipulating the central ISR signaling hub (eIF2-eIF2B), rescues the cognitive deficits and neurophysiological abnormalities in Ts65Dn mice. By correcting the translational program controlled by the ISR, we overcame a central limitation of the field: It is simply not feasible to determine in vivo the causal role of all of the individually dysregulated proteins in long-term memory formation by overexpressing or knocking them down, which would require hundreds of experiments, and given the current technology, it is certainly not possible to test all combinatorial possibilities. Beyond these limi-

tations, it may prove not to be useful to target specific genes if the ultimate cause of the disorder lies in global proteostasis defects that are sensed as a generic stress condition in the brain by the ISR.

Excessive synaptic inhibition is thought to cause the deficits in hippocampal L-LTP and long-term memory in Ts65Dn mice (24, 30, 37). We provide genetic and pharmacological evidence that inhibition of the ISR reverses the excessive synaptic inhibition and, in turn, the deficits in L-LTP and long-term memory that likely result from it. Thus, our findings present a model that links these two axes of dysfunction—increased synaptic inhibition,

and impaired L-LTP and long-term memory formation—through a single proteostasis network, the ISR.

In addition to reducing enhanced synaptic inhibition, other manipulations and pathways [serotonin, sonic hedgehog (Shh), minocycline, lithium, exercise, brain-derived neurotrophic factor (BDNF)] have been shown to improve the memory and/or L-LTP deficits in Ts65Dn mice. It is of interest that these manipulations modulate the ISR: minocycline, which has been reported to improve memory in Ts65Dn mice (38), inhibits the ISR by reducing eIF2-P levels (39). Treatment with fluoxetine, a selective serotonin reuptake inhibitor, improves long-term memory in Ts65Dn mice (40) and has been shown to inhibit the PKR branch of the ISR (41). The synthetic activator of the Shh pathway SAG 1.1 rescues memory in Ts65Dn mice (42). Although it is currently unknown whether SAG 1.1 inhibits the ISR, another pharmacological activator of the Shh blocks the PERK branch of the ISR, resulting in decreased eIF2-P levels (43). Lithium improves LTP and memory in Ts65Dn mice (44) and inhibits the ISR by promoting eIF2B activity (45). Exercise, which has been reported to improve cognitive function in Ts65Dn mice (46), has recently been shown to block the ISR in the hippocampus of an Alzheimer's disease (AD) mouse model (47). Finally, pharmacological induction of BDNF with the recently developed BDNF-mimetic drug 7,8-dihydroxyflavone (DHF) reverses the deficits in LTP and long-term memory in Ts65Dn mice (48), and BDNF inhibits the ISR in neurons by promoting eIF2B activity and reducing eIF2-P levels (49). These observations raise the intriguing possibility that the manipulations reported to reverse the memory deficits in Ts65Dn may do so, either directly or indirectly, by modulating the ISR, which might lie at the crossroad of the different pathways implicated in DS.

Finally, DS is characterized by a high incidence of early onset AD, and activation of the ISR has been implicated in a variety of neurodegenerative disorders, including AD (50), trau-

matic brain injury (51), prion disease (52), and myelination disorders (53, 54). Thus, genetic or pharmacological modulation of the ISR may emerge as a promising avenue to alleviate a wide range of cognitive disorders resulting from a disruption in protein homeostasis.

## REFERENCES AND NOTES

- K. Gardiner *et al.*, *J. Neurosci.* **30**, 14943–14945 (2010).
- C. Rosenberg *et al.*, *J. Med. Genet.* **43**, 180–186 (2006).
- H. van Bokhoven, *Annu. Rev. Genet.* **45**, 81–104 (2011).
- M. Dierssen, *Nat. Rev. Neurosci.* **13**, 844–858 (2012).
- A. Letourneau *et al.*, *Nature* **508**, 345–350 (2014).
- J. L. Olmos-Serrano *et al.*, *Neuron* **89**, 1208–1222 (2016).
- S. E. Antonarakis, *Nat. Rev. Genet.* **18**, 147–163 (2017).
- T. F. Haydar, R. H. Reeves, *Trends Neurosci.* **35**, 81–91 (2012).
- H. P. Harding *et al.*, *Mol. Cell* **11**, 619–633 (2003).
- A. G. Hinnebusch, I. P. Ivanov, N. Sonenberg, *Science* **352**, 1413–1416 (2016).
- R. H. Reeves *et al.*, *Nat. Genet.* **11**, 177–184 (1995).
- I. Das, R. H. Reeves, *Dis. Model. Mech.* **4**, 596–606 (2011).
- M. Inoue *et al.*, *Lab. Invest.* **99**, 885–897 (2019).
- J. P. Weick *et al.*, *Proc. Natl. Acad. Sci. U.S.A.* **110**, 9962–9967 (2013).
- N. Sonenberg, A. G. Hinnebusch, *Cell* **136**, 731–745 (2009).
- H. Lavoie, J. J. Li, N. Thevakumaran, M. Therrien, F. Sighieri, *Trends Biochem. Sci.* **39**, 475–486 (2014).
- C. Lanzillotta *et al.*, *J. Alzheimers Dis.* **62**, 347–359 (2018).
- S. Aivazidis *et al.*, *PLOS ONE* **12**, e0176307 (2017).
- F. Fernandez, C. C. Garner, *Behav. Brain Res.* **188**, 233–237 (2008).
- A. C. Costa, J. J. Scott-McKean, M. R. Skasko, *Neuropsychopharmacology* **33**, 1624–1632 (2008).
- G. Deidda *et al.*, *Nat. Med.* **21**, 318–326 (2015).
- P. J. Zhu *et al.*, *Cell* **147**, 1384–1396 (2011).
- S. D. Vann, M. M. Albasser, *Curr. Opin. Neurobiol.* **21**, 440–445 (2011).
- F. Fernandez *et al.*, *Nat. Neurosci.* **10**, 411–413 (2007).
- G. Neves, S. F. Cooke, T. V. Bliss, *Nat. Rev. Neurosci.* **9**, 65–75 (2008).
- S. A. Buffington, W. Huang, M. Costa-Mattioli, *Annu. Rev. Neurosci.* **37**, 17–38 (2014).
- C. Sidrauski *et al.*, *eLife* **2**, e00498 (2013).
- C. Sidrauski *et al.*, *eLife* **4**, e07314 (2015).
- Y. Sekine *et al.*, *Science* **348**, 1027–1030 (2015).
- A. M. Kleschevnikov *et al.*, *J. Neurosci.* **24**, 8153–8160 (2004).
- A. M. Kleschevnikov *et al.*, *Neurobiol. Dis.* **45**, 683–691 (2012).
- E. R. Kandel, *Science* **294**, 1030–1038 (2001).
- M. Costa-Mattioli, W. S. Sossin, E. Klann, N. Sonenberg, *Neuron* **61**, 10–26 (2009).
- W. S. Sossin, M. Costa-Mattioli, *Cold Spring Harb. Perspect. Biol.* (2018).
- B. Abdulkarim *et al.*, *Diabetes* **64**, 3951–3962 (2015).
- G. Borck *et al.*, *Mol. Cell* **48**, 641–646 (2012).
- K. D. Kernohan *et al.*, *Hum. Mol. Genet.* **24**, 6293–6300 (2015).

- C. L. Hunter, D. Bachman, A. C. Granholm, *Ann. Neurol.* **56**, 675–688 (2004).
- Y. Choi *et al.*, *Neuropsychopharmacology* **32**, 2393–2404 (2007).
- P. Bianchi *et al.*, *J. Neurosci.* **30**, 8769–8779 (2010).
- R. H. Du *et al.*, *Int. J. Neuropsychopharmacol.* **19**, pyw037 (2016).
- I. Das *et al.*, *Sci. Transl. Med.* **5**, 201ra120 (2013).
- M. Jimenez-Sanchez *et al.*, *Nat. Commun.* **3**, 1200 (2012).
- A. Contestabile *et al.*, *J. Clin. Invest.* **123**, 348–361 (2013).
- S. Bertsch, C. H. Lang, T. C. Vary, *Shock* **35**, 266–274 (2011).
- E. Kida, A. Rabe, M. Walus, G. Albertini, A. A. Golabek, *Exp. Neurol.* **240**, 178–189 (2013).
- J. Xia *et al.*, *Neurosci. Lett.* **703**, 125–131 (2019).
- M. Parrini *et al.*, *Sci. Rep.* **7**, 16825 (2017).
- N. Takei, M. Kawamura, K. Hara, K. Yonezawa, H. Nawa, *J. Biol. Chem.* **276**, 42818–42825 (2001).
- T. Ma *et al.*, *Nat. Neurosci.* **16**, 1299–1305 (2013).
- A. Chou *et al.*, *Proc. Natl. Acad. Sci. U.S.A.* **114**, E6420–E6426 (2017).
- J. A. Moreno *et al.*, *Nature* **485**, 507–511 (2012).
- H. J. Kim *et al.*, *Nat. Genet.* **46**, 152–160 (2014).
- S. W. Way, B. Popko, *Lancet Neurol.* **15**, 434–443 (2016).

## ACKNOWLEDGMENTS

We thank M. Grasso and C. Genero for administrative support, H. Zhou for technical support, and A. Placzek and members of the Costa-Mattioli laboratory for comments on the manuscript. We also thank P. Zhang and A. LaGrone of the Human Stem Cell Core at Baylor College of Medicine for their technical support. Human tissue was obtained from the NIH Neurobiobank at University of Maryland, Baltimore, MD. **Funding:** This work was supported by funding from the NIH (R01 NS076708) and the generous support from Sammons Enterprises to M.C.-M. and by funding from the NIH (R01HG007538, R01CA193466, and R01 CA228140) to W.L. P.W. is an investigator of the Howard Hughes Medical Institute. **Author contributions:** Conceptualization and design, P.J.Z., S.K., P.W., and M.C.-M.; Acquisition of data, P.J.Z., S.K., Y.C., L.C.R., S.W.D., J.J.K., and W.L.; Writing – Reviewing & Editing, P.J.Z., S.K., P.W., and M.C.-M. **Competing interests:** P.W. is an inventor on U.S. Patent 9708247 held by the Regents of the University of California that describes ISRIB and its analogs. Rights to the invention have been licensed by UCSF to Calico. W.L. is a consultant for the Chosen Med. The authors declare no other competing interests. **Data and materials availability:** All data needed to evaluate the conclusions in the paper are present in the paper and/or the supplementary materials, and the RNA-seq data have been deposited in public databases. Accession number of the RNA-seq data is NCBI GEO: GSE138371.

## SUPPLEMENTARY MATERIALS

science.sciencemag.org/content/366/6467/843/suppl/DC1  
Materials and Methods  
Figs. S1 to S15  
Tables S1 and S2  
References (55–68)

**View/request a protocol for this paper from Bio-protocol.**

31 December 2018; resubmitted 31 July 2019  
Accepted 8 October 2019  
10.1126/science.aaw5185



## ELECTROCHEMISTRY

## Engineering bunched Pt-Ni alloy nanocages for efficient oxygen reduction in practical fuel cells

Xinlong Tian<sup>1,2\*</sup>, Xiao Zhao<sup>3\*</sup>, Ya-Qiong Su<sup>4\*</sup>, Lijuan Wang<sup>1</sup>, Hongming Wang<sup>5</sup>, Dai Dang<sup>6</sup>, Bin Chi<sup>7</sup>, Hongfang Liu<sup>1</sup>, Emiel J.M. Hensen<sup>4</sup>, Xiong Wen (David) Lou<sup>8†</sup>, Bao Yu Xia<sup>1†</sup>

Development of efficient and robust electrocatalysts is critical for practical fuel cells. We report one-dimensional bunched platinum-nickel (Pt-Ni) alloy nanocages with a Pt-skin structure for the oxygen reduction reaction that display high mass activity (3.52 amperes per milligram platinum) and specific activity (5.16 milliamperes per square centimeter platinum), or nearly 17 and 14 times higher as compared with a commercial platinum on carbon (Pt/C) catalyst. The catalyst exhibits high stability with negligible activity decay after 50,000 cycles. Both the experimental results and theoretical calculations reveal the existence of fewer strongly bonded platinum-oxygen (Pt-O) sites induced by the strain and ligand effects. Moreover, the fuel cell assembled by this catalyst delivers a current density of 1.5 amperes per square centimeter at 0.6 volts and can operate steadily for at least 180 hours.

**P**latinum (Pt) is the most active electrocatalyst for the oxygen reduction reaction (ORR) in fuel cells and metal-air batteries with promising stability (1–3). Nevertheless, the state-of-the-art Pt catalysts still lack activity and stability with respect to the cost and availability for large-scale commercial implementation (4, 5). Engineering the near-surface composition of nanostructured Pt alloys represents one promising approach to enhance the electrocatalytic performance of Pt-based electrocatalysts, in which the exposure of highly active sites with optimum performance can be maximized (6, 7). Adding other transition metals can enhance the catalytic performance via ligand and strain effects through modifying the binding strength of Pt-oxygen intermediates (8–10).

The introduction of open nanostructures, including hollow and porous nanoparticles such as nanocages (NCs) and nanoframes, may help in achieving this goal and also enhance mass transfer (11). Porous metal structures

usually exist as nanoparticles and typically do not display long-term stability because they agglomerate or detach from the (usually carbon) support (12, 13). By contrast, one-dimensional (1D) nanostructures and their assemblies can exhibit enhanced stability because of their inherent anisotropic, higher flexibility and higher conductivity (14). The anisotropy of 1D nanostructures can lead to greater surface contact with the usual carbon support, thus resulting in high stability (15). Recently, 1D Pt-based alloy nanostructures have been explored for their promising ORR activity and stability (16, 17). However, these solid 1D nanostructures contain a substantial proportion of noble metals in the bulk versus at the surface, which limits the noble-metal utilization (18). Moreover, although desirable ORR performance has been established in model studies with, for example, rotating disk electrodes (RDEs), relatively few works have studied nanostructured Pt electrocatalysts in a complete cell configuration (19). The limitations in comparing performance at the RDE level with those at the cell level are known (20). To this end, it follows that optimum ORR catalysts based on Pt should be designed by having a high Pt utilization efficiency (porous nanostructures), a favorable nanoscale chemical environment for ORR (chemical alloying) with an optimized structure in terms of the exposure of active sites, and stability derived from both the nanostructure itself as well as its interface with the support.

We demonstrate Pt-Ni bunched NCs (BNCs) in 1D form that exhibit superior ORR activity and durability compared with conventional Pt electrocatalysts. We first prepared 1D Pt-Ni bunched nanospheres (BNSs) by reducing Pt and Ni precursors with varying ratios in oleylamine by a one-pot solvothermal method. Treatment under acidic conditions selectively removed Ni species to leave 1D Pt-Ni BNCs with ultrathin walls composed of a

Pt skin and a residual Pt-Ni alloy below this skin (Fig. 1A). The nanostructures with a Pt<sub>1.5</sub>Ni starting composition exhibited the highest mass and specific activities of 3.52 A mg<sub>Pt</sub><sup>−1</sup> and 5.16 mA cm<sub>Pt</sub><sup>−2</sup>, respectively. These values are more than one order of magnitude higher than those of a commercial Pt/C catalyst [60 weight % (wt %), Johnson Matthey (JM)] and comparable to those of very recently reported Pt nanostructure catalysts (table S1). The catalyst also exhibited superb durability with a negligible activity decay (less than 1.5%) after 50,000 potential-scanning cycles. In addition, the Pt-Ni BNC electrocatalyst showed improved performance in a fuel cell test compared with commercial Pt/C, both in a hydrogen-air proton exchange membrane fuel cell (PEMFC) and an air-breathing PEMFC setup at room temperature and ambient pressure. In situ x-ray absorption fine structure (XAFS) and theoretical calculations revealed that the Pt-Ni alloy nanostructures had optimal adsorption energies of oxygen intermediates with respect to Pt.

## Bunched nanospheres

The Pt-Ni BNSs were synthesized in nearly 100% yield from platinum(II) acetylacetonate [Pt(acac)<sub>2</sub>], nickel(II) acetylacetonate [Ni(acac)<sub>2</sub>], cetyltrimethylammonium bromide (CTAB), and oleylamine mixtures that were ultrasonicated and then heated at 180°C for several hours (see supplementary materials and fig. S1). Composition studies included Pt<sub>3</sub>Ni, Pt<sub>2</sub>Ni, Pt<sub>1.5</sub>Ni, Pt<sub>1</sub>Ni, and PtNi<sub>2</sub> samples, and the transmission electron microscopy-energy-dispersive spectroscopy (TEM-EDS) profiles, together with inductively coupled plasma optical emission spectrometry (ICP-OES) results, suggest complete reduction of the precursors because the Pt/Ni ratios of the final products were nearly the same as the ratios used in the synthesis mixture (fig. S2). We further studied the effect of the concentration of the various reagents, including CTAB and glucose, and the Pt/Ni ratio in the synthesis solution on the formation of the structures (figs. S3 to S6). The x-ray diffraction (XRD) patterns of Pt-Ni BNSs with varying Pt-Ni composition (Pt<sub>x</sub>Ni<sub>y</sub>-BNSs) confirmed the efficient alloy formation (fig. S5), indicating that the composition can be adjusted by judicious choice of the amount of Pt and Ni precursors (21). Only when no Ni was present during the synthesis were Pt nanowires (NWs) with a smooth surface obtained. The surfaces became rougher with the increasing Ni/Pt feeding ratio (fig. S6). We used TEM-EDS to monitor time-dependent reaction progress, which revealed the formation of Pt NWs before Ni inclusion. This sequence is expected, given the higher redox potential of Pt (figs. S7 and S8). Finally, stable Pt-Ni alloys were formed under solvothermal conditions (22).

<sup>1</sup>Key Laboratory of Material Chemistry for Energy Conversion and Storage (Ministry of Education), Hubei Key Laboratory of Material Chemistry and Service Failure, Wuhan National Laboratory for Optoelectronics, School of Chemistry and Chemical Engineering, Huazhong University of Science and Technology (HUST), 1037 Luoyu Road, Wuhan 430074, PR China. <sup>2</sup>State Key Laboratory of Marine Resource Utilization in South China Sea, Hainan University, Haikou 570228, PR China. <sup>3</sup>Innovation Research Center for Fuel Cells, The University of Electro-Communications, Chofugaoka, Chofu, Tokyo 182-8585, Japan. <sup>4</sup>Laboratory of Inorganic Materials and Catalysis, Department of Chemical Engineering and Chemistry, Eindhoven University of Technology, P.O. Box 513, 5600 MB Eindhoven, Netherlands. <sup>5</sup>Institute for Advanced Study, Nanchang University, 999 Xuefu Road, Nanchang, PR China. <sup>6</sup>School of Chemical Engineering and Light Industry, Guangdong University of Technology, Guangzhou, Guangdong 510006, PR China. <sup>7</sup>The Key Laboratory of Fuel Cell Technology of Guangdong Province, School of Chemistry and Chemical Engineering, South China University of Technology, Guangzhou 510641, PR China. <sup>8</sup>School of Chemical and Biomedical Engineering, Nanyang Technological University, 62 Nanyang Drive, Singapore 637459, Singapore.

\*These authors contributed equally to this work.

†Corresponding author. Email: xwlou@ntu.edu.sg (X.W.L.); byxia@hust.edu.cn (B.Y.X.)

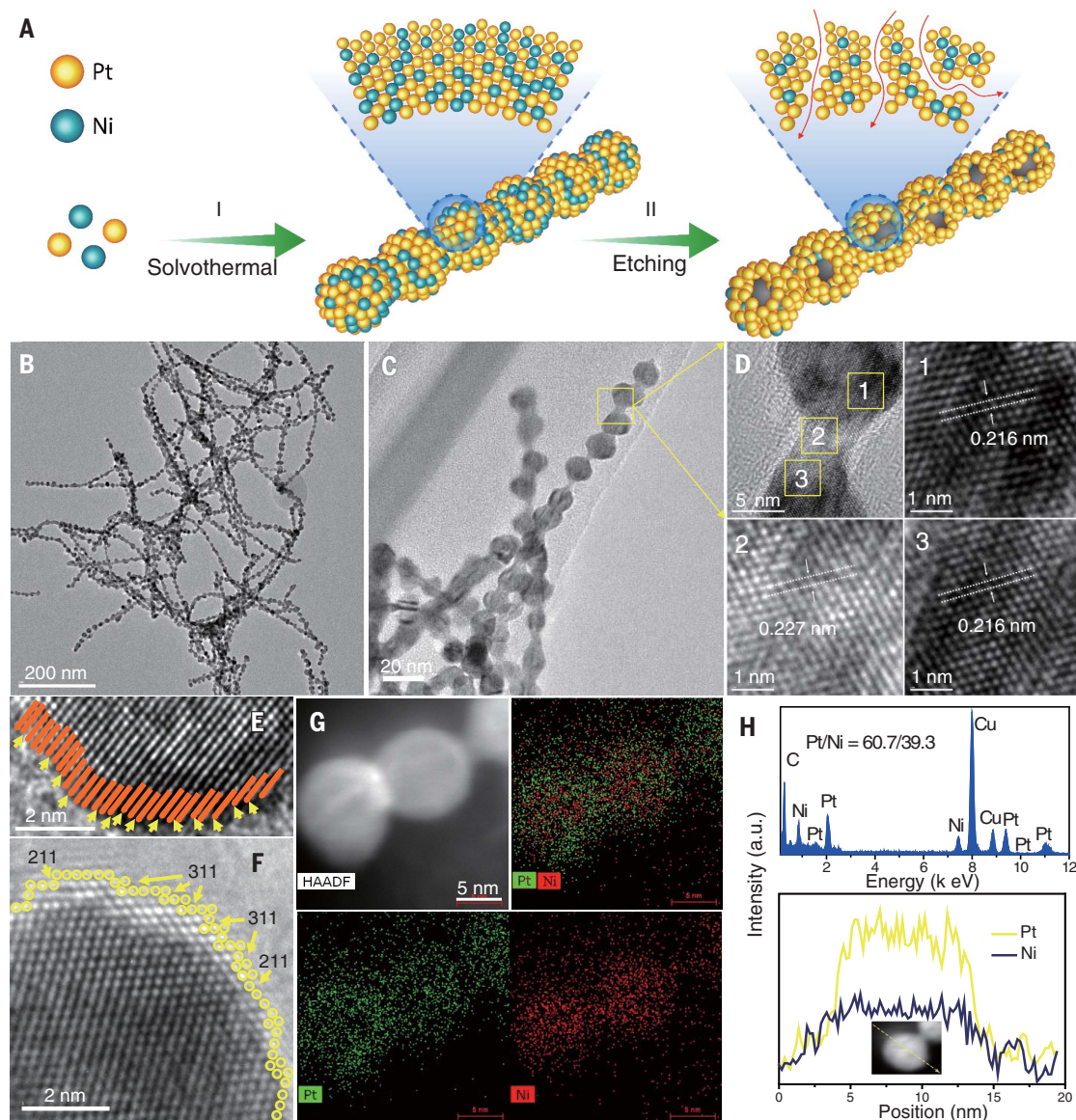


**Fig. 1. Structural and compositional characterizations of Pt<sub>1.5</sub>Ni-BNSs.**

(A) Schematic illustration of the preparation of PtNi-BNSs. (B and C) TEM images of PtNi-BNSs. (D) Enlarged TEM image of the area indicated in (C) and the corresponding HRTEM images of the areas marked by yellow squares. The white dots and arrows indicate the lattice spacing. (E and F) Atomic-resolution HRTEM images. Orange bars indicate the edges of the lattice planes, yellow arrows indicate the surface steps, and yellow circles indicate the outermost atoms. (G) High-angle annular dark-field (HAADF)-STEM image and the corresponding EDS elemental mapping of PtNi-BNSs. (H) EDS profile of PtNi-BNSs (top) and STEM-EDS line-scanning profile (bottom) of a single nanoparticle. The inset shows the studied nanoparticle and the line-scanning analysis along the yellow arrow. a.u., arbitrary units.

Representative scanning electron microscopy (SEM) and TEM images emphasize the uniform 1D morphology of the as-synthesized samples for the Pt<sub>1.5</sub>Ni composition (labeled as PtNi-BNSs, and this one, after etching, leads to the best ORR activity) with a length of hundreds of nanometers consisting of BNSs (Fig. 1, B and C). High-resolution TEM (HRTEM) images reveal lattice fringes of 0.227 nm at the stems and 0.216 nm at the shells (Fig. 1D), corresponding to (111) planes of Pt and Pt-Ni alloys (23), respectively, suggesting that the alloyed Pt-Ni nanospheres would be connected by Pt-rich NWs. Scanning transmission electron microscopy (STEM)-EDS line scanning of the stems of different regions showed the existence of Ni in the stems and an average Pt/Ni ratio of roughly 5/1 (fig. S9). It seems that the nanospheres were Ni-rich compared with the stems, because the scans may not reveal the overall

compositions, whereas Pt-rich alloys can be confirmed at the stems. Atomic-resolution HRTEM images depict the uneven surface of the PtNi-BNSs (i.e., Pt<sub>1.5</sub>Ni composition) and the occurrence of high-index (211) and (311) facets (Fig. 1, E and F). The presence of abundant high-index facets is favorable for ORR, because they exhibit distinct binding energies with oxygen-containing surface intermediates in the ORR mechanism (24). The presence of alloyed features is verified by STEM-EDS elemental mapping analysis, emphasizing the homogeneous distribution of Pt and Ni across the analyzed zone, which contains a Ni-rich core (Fig. 1G). The line-scanning analysis of PtNi-BNSs demonstrates that both Pt and Ni elements are dispersed uniformly across the whole sphere, with an atomic Pt/Ni ratio near 60/40, according to TEM-EDS profile (Fig. 1H). This result is consistent with the bulk elemen-

tal ICP-OES analysis that informed a Pt/Ni ratio of 62/38.

### Bunched nanocages

We obtained Pt-enriched BNCs by selectively removing the more reactive Ni species through a simple acid-etching method. TEM images of the PtNi-BNCs (this sample is from the PtNi-BNSs after the etching) showed that the products were still highly dispersed without structural collapse after the etching treatment (Fig. 2A). The presence of internal voids was deduced from the observation of the darker walls of the NCs (Fig. 2B). The average wall thickness was ~2.2 nm (Fig. 2C), roughly corresponding to 11 atomic Pt layers. The lattice fringe of 0.221 nm was consistent with the (111) plane of a Pt-Ni alloy (23) and was slightly larger than that of PtNi-BNSs because of the decreased Ni content after etching. In addition, the high density of



steps and edges was well preserved during the etching step (Fig. 2D). STEM-EDS elemental mapping analysis indicated that the skin structure of the wall in the Pt-Ni NCs was Pt-rich (Fig. 2E). Figure 2F shows the EDS-line scanning of a single sphere in PtNi-BNCs, further confirming a well-defined Pt-skin structure of the NCs formed after the Ni etching. The

thickness of the outer shell was  $\sim 0.63$  nm, corresponding to roughly two to three atomic Pt layers (25).

On the basis of the above analysis, we propose that the walls of NCs are heterogeneous in composition, with Pt-rich skins on both the outer and inner surfaces and Pt-Ni alloy in the inner region of the wall. The precise Pt/Ni

atomic ratio of PtNi-BNCs was revealed by the TEM-EDS profile as 80.7/19.3 (fig. S10, A and B), consistent with the ICP-OES result (81/19). The increased Pt/Ni ratio was likely caused by selective Ni leaching. The XRD diffraction peaks of PtNi-BNCs showed a small shift to lower angles compared with PtNi-BNSs (fig. S10C), which is consistent with the lower overall Ni

**Fig. 2. Structural and compositional characterizations of PtNi-BNCs derived from etching of Pt<sub>1.5</sub>Ni-BNSs.** (A and B) TEM images of PtNi-BNCs. (C) Enlarged TEM image and the corresponding HRTEM images of the areas marked by yellow squares. (D) Atomic-resolution HRTEM image. Orange dotted lines indicate the atoms along the plane, and yellow arrows indicate the surface steps. (E) HAADF-STEM images. (F) EDS profile of PtNi-BNCs (top) and STEM-EDS line-scanning profile (bottom) of a single NC. The inset shows the studied NC and the line-scanning analysis along the yellow arrow. The red dashed-dotted lines and arrows indicate the thickness of outermost Pt layers.

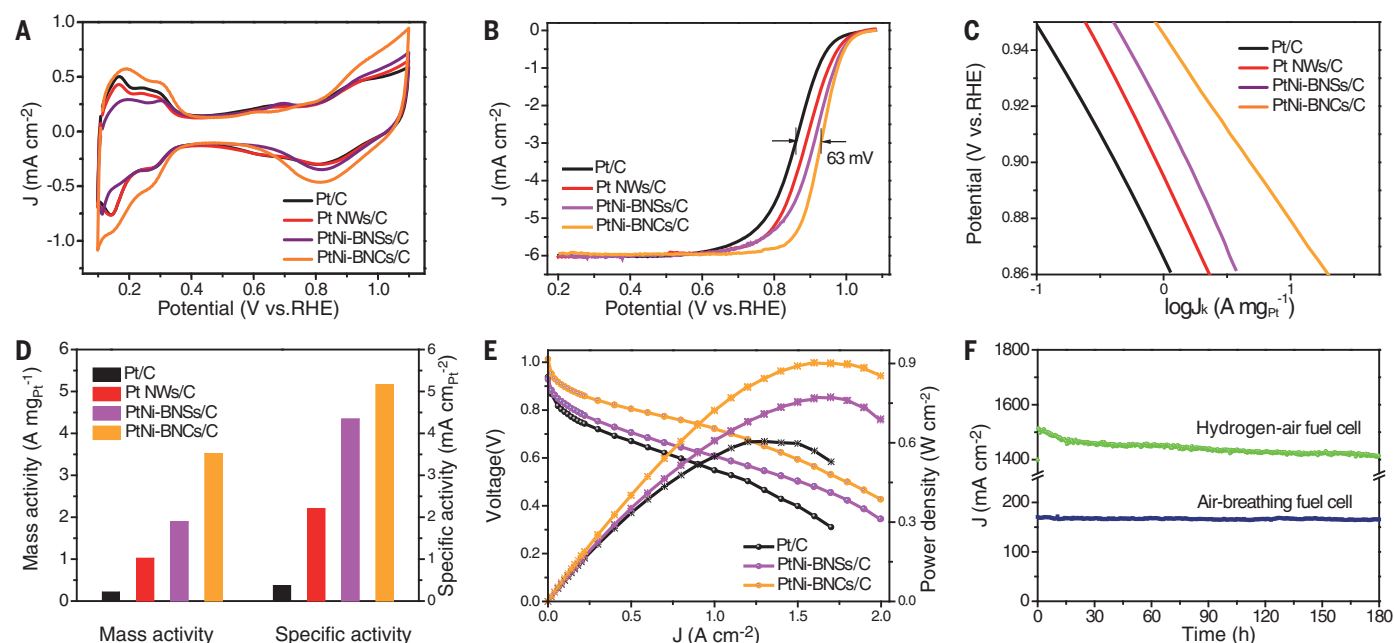
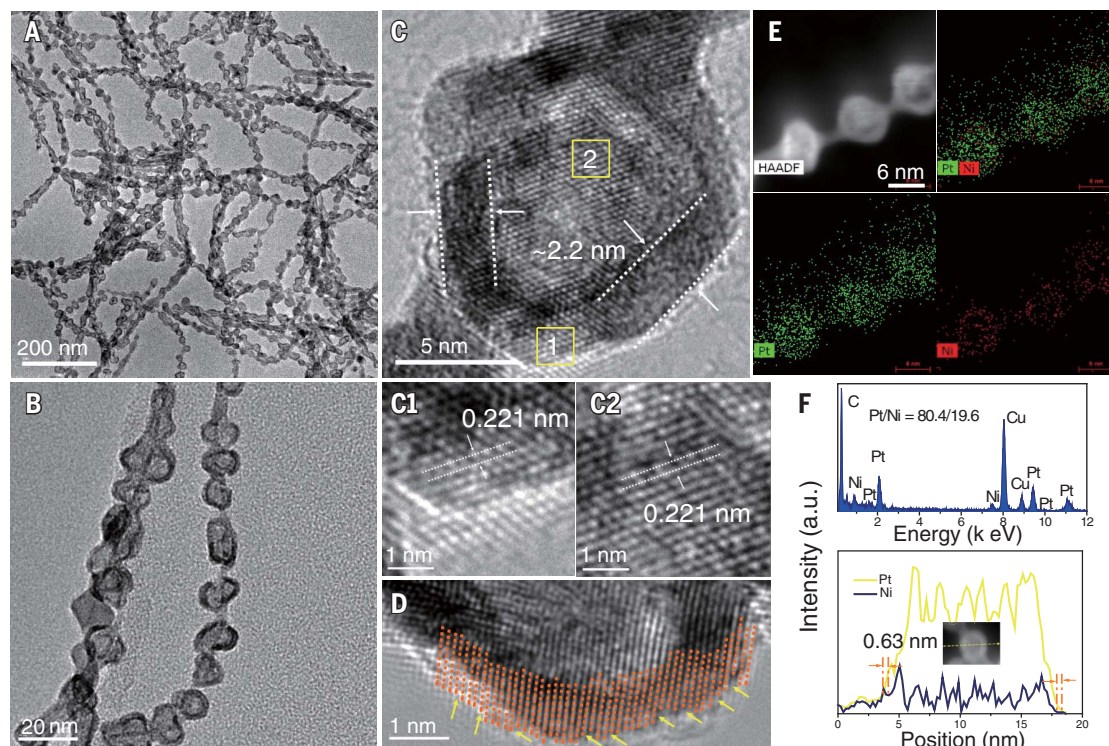


**Fig. 3. Electrochemical and fuel-cell performance of various Pt-based samples.** (A to D) CVs (A), LSVs (B), corresponding Tafel plots (C), and mass and specific activities (D) of Pt/C, Pt NWs/C, PtNi-BNSs/C, and PtNi-BNCs/C at 0.9 V (versus RHE). J, current density. (E) H<sub>2</sub>-air fuel cell polarization plots with Pt/C, PtNi-BNSs/C, and PtNi-BNCs/C as the cathode catalysts. (F) Stability test of H<sub>2</sub>-air and air-breathing fuel cells at 0.6 V.

content of the former. X-ray photoelectron spectroscopy (XPS) of Pt 4f revealed a shift of the Pt core levels to lower binding energies compared with Pt/C, likely because of electron donation from Ni to Pt (fig. S10D). The ligand effect would downshift the Pt d-band center, lowering the binding affinity between Pt and oxygen intermediates and thus enhancing the ORR activity (5).

### Electrocatalytic activity

We evaluated PtNi-BNCs as ORR catalysts, and Fig. 3A presents cyclic voltammetry (CV) results of Pt/C (60 wt %, JM), Pt NWs/C, PtNi-BNSs/C, and PtNi-BNCs/C in a  $N_2$ -saturated 0.1 M  $HClO_4$  solution (fig. S11). The CV curves for carbon-supported PtNi-BNCs were investigated as a function of the Pt/Ni ratio (fig. S12). The electrochemically active surface area (ECSA) measured by hydrogen underpotential deposition ( $H_{UPD}$ ) of PtNi-BNCs/C was  $68.2 \text{ m}^2 \text{ g}_{Pt}^{-1}$ , which is substantially higher than that of PtNi-BNSs/C ( $43.5 \text{ m}^2 \text{ g}_{Pt}^{-1}$ ), confirming the advantage of a hollow structure created by acid leaching. Moreover, the ECSA values for Pt/C, Pt NWs/C, Pt<sub>3</sub>Ni-BNCs/C, Pt<sub>2</sub>Ni-BNCs/C, Pt<sub>1.5</sub>Ni-BNCs/C, Pt<sub>1</sub>Ni-BNCs/C, and PtNi<sub>2</sub>-BNCs/C (for convenience, all  $x$  and  $y$  values in the names of BNCs were labeled the same values as in the starting BNSs) were 56.5, 46.3, 37.4, 59.1, 68.2, 70.7, and  $80.3 \text{ m}^2 \text{ g}_{Pt}^{-1}$ , respectively, demonstrating the enhanced ECSA of Pt-Ni BNCs with increasing Ni content. TEM images of Pt-Ni BNCs with varying Ni contents demonstrate the increased porosity with increasing Ni/Pt ratio (fig. S13), in agreement with the larger ECSA values.

We also measured the ECSA from the electro-oxidation of CO (CO stripping), given the sensitive nature of the Pt-alloyed surface, because the ECSA derived from the  $H_{UPD}$  method would be lower than the real values because of the weakened binding interaction caused by the alloying effects (the ECSA obtained from the CO stripping should be unaffected, fig. S14). The ECSA values of Pt/C and PtNi-BNCs/C obtained from the CO stripping are 56.7 and  $101.5 \text{ m}^2 \text{ g}_{Pt}^{-1}$ , respectively; thus, the  $ECSA_{CO}/ECSA_{HUPD}$  ratio measured for Pt/C was equal to 1 but was 1.49 for PtNi-BNCs/C, verifying the formation of a Pt-skin structure of PtNi-BNCs (4, 26). Figure 3, B and C, shows the linear sweep voltammetry (LSV) curves and Tafel plots, respectively, of Pt NWs/C, PtNi-BNSs/C, PtNi-BNCs/C, and the commercial Pt/C reference. The smaller Tafel slope obtained for PtNi-BNCs/C ( $54 \text{ mV decade}^{-1}$ ) as compared with that of the other samples demonstrates the enhanced kinetics for the ORR. The mass and specific activities of Pt NWs/C ( $1.02 \text{ A mg}_{Pt}^{-1}$  and  $2.20 \text{ mA cm}_{Pt}^{-2}$ ) and PtNi-BNSs/C ( $1.89 \text{ A mg}_{Pt}^{-1}$  and  $4.34 \text{ mA cm}_{Pt}^{-2}$ ) at 0.9 V [versus reversible hydrogen electrode (RHE)] were much higher than those of the Pt/C reference ( $0.21 \text{ A mg}_{Pt}^{-1}$

and  $0.36 \text{ mA cm}_{Pt}^{-2}$ ). Furthermore, PtNi-BNCs/C shows mass and specific activities of  $3.52 \text{ A mg}_{Pt}^{-1}$  and  $5.16 \text{ mA cm}_{Pt}^{-2}$ , which are respectively  $\sim 17$  and  $\sim 14$  times higher than those of the Pt/C reference. In general, the catalytic performance was enhanced with increasing Ni/Pt ratio, which can be ascribed to the higher amount of exposed active sites achieved by Ni leaching (fig. S12). The inferior ORR activities of Pt<sub>3</sub>Ni-BNCs/C and PtNi<sub>2</sub>-BNCs/C were ascribed to the structural collapse upon excessive Ni dissolution (fig. S13).

To further corroborate the ORR performance obtained at the RDE level, practical  $H_2$ -air and air-breathing PEMFC tests were conducted (fig. S15) with fuel cells containing PtNi-BNSs/C and PtNi-BNCs/C at a loading of  $0.15 \text{ mg cm}^{-2}$  as a cathode catalyst material. The  $H_2$ -air fuel cell of PtNi-BNCs/C delivers a current density of  $1.5 \text{ A cm}^{-2}$  at 0.6 V and achieves a peak power density of  $920 \text{ mW cm}^{-2}$  (Fig. 3E), outperforming the PtNi-BNSs/C-based ( $1.0 \text{ A cm}^{-2}$  and  $770 \text{ mW cm}^{-2}$ ) and Pt/C-based ( $0.8 \text{ A cm}^{-2}$  and  $600 \text{ mW cm}^{-2}$ ) systems. Considering comparable Pt loadings, this performance is among

the best reported performance for Pt-based catalysts (table S1). In addition, the air-breathing PEMFC operated at room temperature and ambient pressure exhibited a current density of  $170 \text{ mA cm}^{-2}$  at 0.6 V, compared with  $100 \text{ mA cm}^{-2}$  for Pt/C, resulting in an improvement of 70% (fig. S15E). The  $H_2$ -air and air-breathing PEMFCs were stably operated at a constant working voltage of 0.6 V for at least 180 hours with a negligible decay ( $<3\%$ ) of the output current densities (Fig. 3F).

### Structural changes under electrochemical operation

To evaluate the stability under better defined conditions, Pt/C, PtNi-BNSs/C, and PtNi-BNCs/C were subjected to continuous cycling for 20,000 cycles between 0.6 and 1.1 V in an  $O_2$ -saturated 0.1 M  $HClO_4$  solution. The ORR performance variations recorded every 4000 cycles show that the mass activity and ECSA of Pt/C declined by 61.9 and 59.4%, respectively, and the half-wave potential shifted by 54 mV to more negative values compared with that of the fresh sample (Fig. 4, A and B). By contrast,

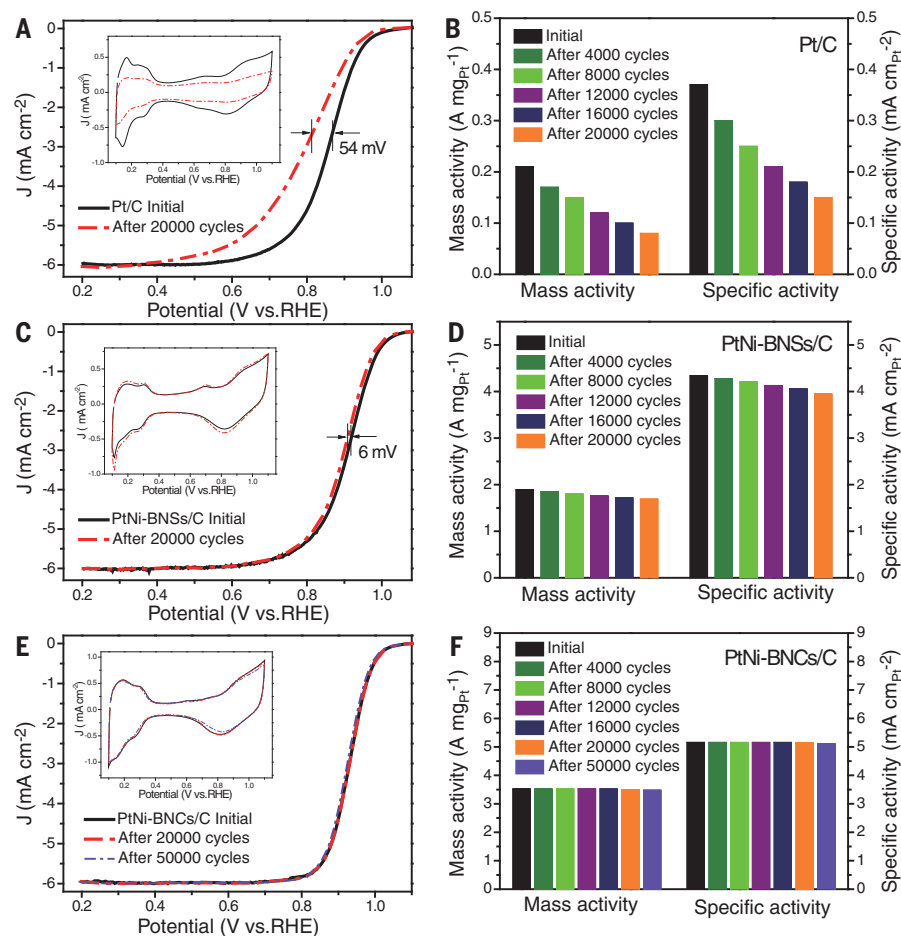


**Fig. 4. Durability performance of various catalysts.** (A, C, and E) LSV evolutions. The insets show the CV variations. (B, D, and F) Mass and specific activity evolutions for Pt/C [(A) and (B)], PtNi-BNCs/C [(C) and (D)], and PtNi-BNCs/C [(E) and (F)] before and after the durability test for various potential-scanning cycles.



the high durability of PtNi-BNSs/C was evidenced by the much smaller loss in mass activity and ECSA by 13.7 and 9.4%, respectively, along with a 6-mV negative-shifted half-wave potential (Fig. 4, C and D). The PtNi-BNSs/C sample became hollow and porous after the stability test through electrochemical leaching (dealloying) (fig. S16, A to C), whereas the bunched architecture was destroyed to some degree compared with PtNi-BNCs/C. These results suggest a strong chemical difference between electrochemical dealloying and chemical etching, because structural collapse and Ni leaching caused substantial performance loss of PtNi-BNSs/C (fig. S16D). Comparatively, the performance loss of PtNi-BNCs/C is negligible, even after the prolonged durability test for 50,000 cycles (Fig. 4, E and F). The mass activity and ECSA only dropped by 1.3 and 1.1%, respectively, after the durability test compared with that of the fresh one, demonstrating the robustness of PtNi-BNCs/C as an ORR electrocatalyst. The composition and structure of the PtNi-BNCs/C catalysts after the durability test were further investigated. The hollow and core-shell (Pt-rich surface) structures of PtNi-BNCs/C were retained during the durability test (fig. S17), and TEM-EDS results revealed that Ni loss was negligible (fig. S18). The Pt-skin structure may have protected the electrocatalysts against further Ni leaching from the inner region of the wall.

We probed the dynamic changes in oxidation state and local coordination environment at ORR-relevant potentials by in situ XAFS. Figure 5A shows the potential-dependent Pt-L<sub>3</sub> edge x-ray absorption near-edge spectra (XANES) of PtNi-BNCs/C, emphasizing the metallic state of Pt at applied potentials of 0.54, 0.7, and 0.9 V (versus RHE). A 5-nm Pt/C (TEC10E50E-HT) reference was used for comparison to reduce the influence of the size effect. For comparison, the Pt-L<sub>3</sub> edge XANES of PtNi-BNSs/C is depicted in fig. S19. The normalized white-line intensities ( $\mu_{\text{norm}}$ ) at the Pt-L<sub>3</sub> edge increased with increasing applied potentials because of the chemisorption of surface oxygenated species (Fig. 5B) (27, 28). The trends in  $\mu_{\text{norm}}$  with potential differed between the catalysts and were used to understand the mechanistic origins of ORR activity (29). At 0.54 V, both PtNi-BNCs/C and PtNi-BNSs/C showed a higher  $\mu_{\text{norm}}$  than Pt/C, probably because of the chemisorption of \*OH and/or \*O species in the double layer region (30). With an increase of the potential to 0.7 V, the increase of  $\mu_{\text{norm}}$  [i.e.,  $\Delta\mu_{\text{norm}}$  (0.7–0.54 V) =  $\mu_{\text{norm}}$  (0.7 V) –  $\mu_{\text{norm}}$  (0.54 V)] was larger for PtNi-BNSs/C and smaller for PtNi-BNCs/C in comparison to the change for Pt/C. When the potential was increased to 0.9 V, a negligible  $\Delta\mu_{\text{norm}}$  (0.9–0.7 V) was seen for PtNi-BNSs/C and PtNi-BNCs/C relative to Pt/C (Fig. 5, B and C). Together, PtNi-BNSs/C showed an initially higher  $\Delta\mu_{\text{norm}}$

from 0.54 to 0.7 V and subsequently an inhibited  $\Delta\mu_{\text{norm}}$  from 0.7 to 0.9 V relative to that of Pt/C, similar with previous reports (28, 30). However, PtNi-BNCs/C only showed a higher  $\mu_{\text{norm}}$  at 0.54 V and subsequently the suppressed  $\Delta\mu_{\text{norm}}$  over the whole range of 0.54 to 0.9 V compared with that of PtNi-BNSs/C and Pt/C. Thus, the in situ XANES characteristic of PtNi-BNCs/C may partly account for its particularly high ORR activity and durability through the inhibition of strongly bonded oxygenated species from 0.54 to 0.9 V relative to Pt/C and PtNi-BNSs/C.

The fitted extended x-ray absorption fine structure (EXAFS) spectra conducted at 0.54 V (Fig. 5D, figs. S19 to S21, and tables S2 to S5), a potential in the double-layer region with the minimum interference from the adsorption of \*OH and/or \*O species, showed bond lengths of Pt-Pt ( $\text{BL}_{\text{Pt-Pt}}$ ) and coordination numbers of Pt-Ni ( $\text{CN}_{\text{Pt-Ni}}$ ) in the PtNi-BNCs/C ( $\text{BL}_{\text{Pt-Pt}}$  = 2.69 Å;  $\text{CN}_{\text{Pt-Ni}}$  = 0.6), PtNi-BNSs/C ( $\text{BL}_{\text{Pt-Pt}}$  = 2.71 Å;  $\text{CN}_{\text{Pt-Ni}}$  = 1.0), and Pt/C ( $\text{BL}_{\text{Pt-Pt}}$  = 2.76 Å). The evidently shorter  $\text{BL}_{\text{Pt-Pt}}$  for both PtNi-BNCs/C and PtNi-BNSs/C than that for Pt/C could be well ascribed to the smaller size of Ni atoms compared with Pt thus inducing the global stress for PtNi-BNCs and PtNi-BNSs. However, compared with PtNi-BNSs/C, PtNi-BNCs/C exhibited a slightly smaller  $\text{CN}_{\text{Pt-Ni}}$  but a slightly shorter  $\text{BL}_{\text{Pt-Pt}}$ , which indicated an additional source of strain, presumably induced by structural defects, as demonstrated in a recent report (7). Additionally, the fitting results of EXAFS at 0.9 V revealed the absence of a definite Pt-O path for both PtNi-BNCs/C and PtNi-BNSs/C (tables S3 and S5), despite a clear electrochemical adsorption of oxygenated species on their surface. This lack of a Pt-O scattering peak in the EXAFS spectra for both PtNi-BNCs/C and PtNi-BNSs/C agrees with their XANES results and may be correlated with the surface disorder produced by the defects (steps and grain boundaries; see TEM analysis) and the corresponding disturbance to interfacial water structures (28, 30).

Interestingly, TEM examinations after the ORR stability test showed a nearly hollow structure but irregular shape for PtNi-BNSs/C, whereas dimensionally uniform hollow structures were observed for PtNi-BNCs/C (figs. S16 and S17). The differences in hollow microstructures between PtNi-BNSs/C and PtNi-BNCs/C were likely caused by the different corrosion methods for the Ni dissolution and the accompanied restructuring, that is, a moderate acid corrosion for PtNi-BNCs/C versus an electrochemical corrosion for PtNi-BNSs/C. Expectedly, these microstructural differences induced the distinct density and distribution of defects and correlated microstrain on the surface of catalysts, causing different electrocatalytic in situ

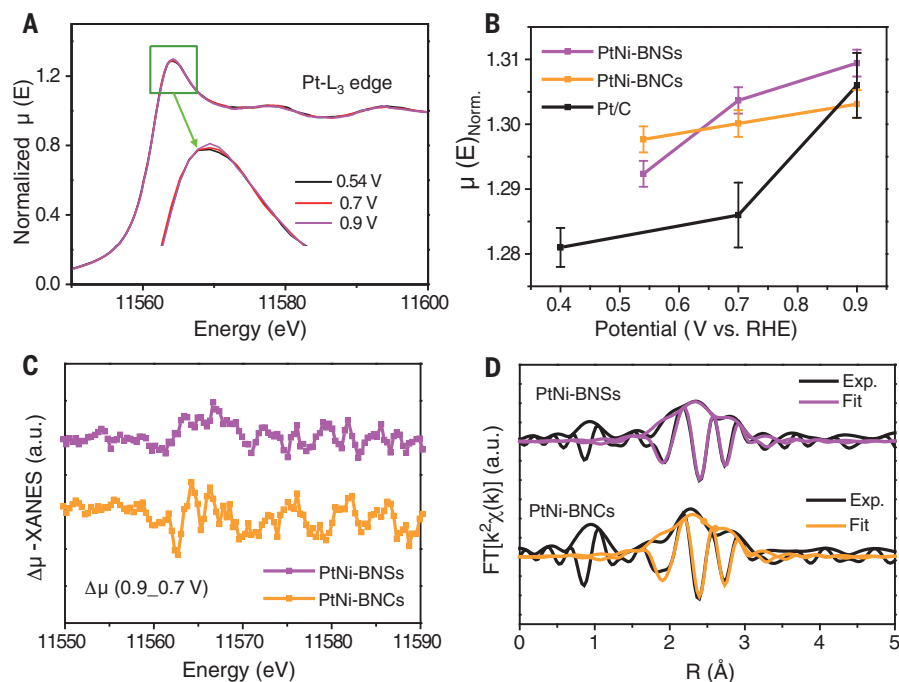


**Fig. 5. In situ XAFS and XANES analysis.** (A) In situ Pt-L<sub>3</sub> edge XANES spectra for PtNi-BNCs, with an enlarged view of the area marked by the green square. (B) In situ potential-dependent normalized white-line peak intensities [ $\mu(E)_{\text{norm}}$ ]. (C)  $\Delta\mu$ -XANES spectra (0.9–0.7 V) of PtNi-BNSs and PtNi-BNCs. (D) First-shell EXAFS fitting in R space for spectral data at 0.54 V.  $\text{FT}[k^2\chi(k)]$ , Fourier-transformed  $k^2$ -weighted EXAFS. Exp., experimental.

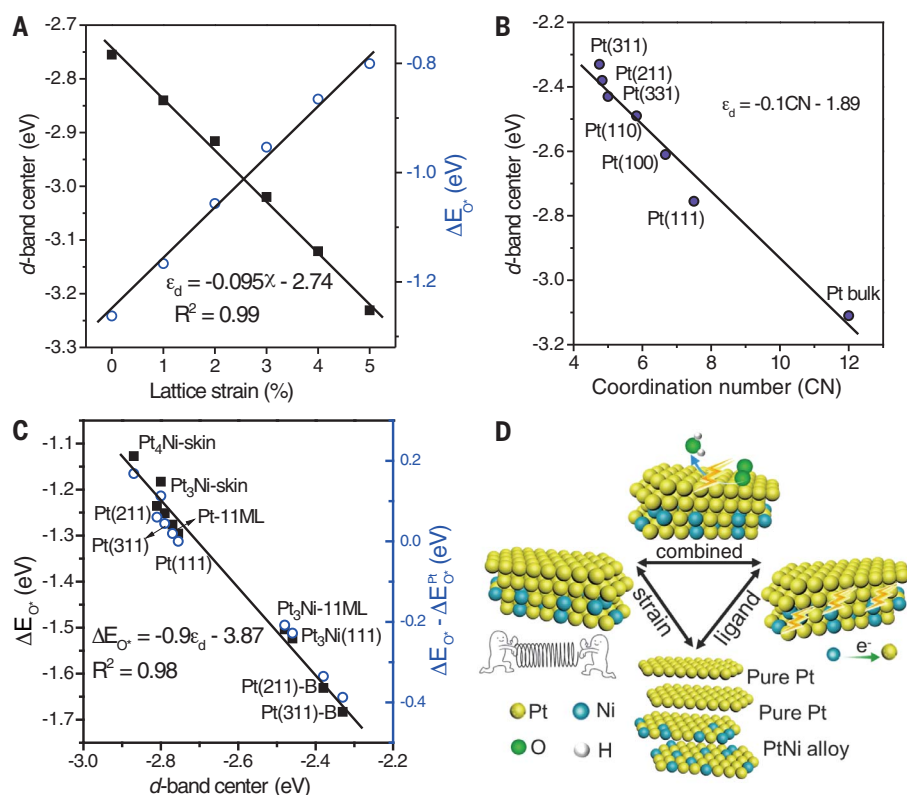


**Fig. 6. Disentangling the correlation of lattice strain and ligand effects on the d-band center, and the atomic O adsorption energy from DFT calculations.** (A) DFT-determined correlation of d-band center and atomic O adsorption energy with the compressive lattice strain of Pt(111) facet.  $R^2$ , coefficient of determination. (B) DFT-determined correlation between the d-band center and the generalized coordination number of surface Pt atoms of various Pt(*hkl*) planes. (C) DFT-determined correlation of atomic O adsorption energy with d-band center of surface sites. Pt(211)-B and Pt(311)-B denote the bridge sites of Pt(211) and Pt(311) planes, respectively. (D) Illustration of the synergistic effects derived from both the lattice strain and ligand effects in the catalysts.

XANES and EXAFS behaviors between PtNi-BNSs/C and PtNi-BNCs/C. Specifically, the irregular hollow structures in PtNi-BNSs/C easily created local overstrained domains that undermined the electrochemical stability of PtNi-BNSs/C to some extent, whereas the dimensionally uniform hollow structures in PtNi-BNCs/C were observed to be stable under the conditions we investigated. Thus, our work suggests that the fine regulation of microstructures by tailored synthesis could produce electrochemically durable hollow-structured ORR catalysts, although discrete hollow particles are generally less stable because of their high free energy.

### Theoretical studies

On the basis of these experimental data, we performed density functional theory (DFT) calculations to understand the high ORR performance of PtNi-BNCs, using Pt<sub>3</sub>Ni-skin and Pt<sub>4</sub>Ni-skin models (Fig. 6). It is generally accepted that the atomic O adsorption energy  $\Delta E_{O^*}$  can be used to evaluate the ORR activity, and the optimal value of  $\Delta E_{O^*}$  is  $\sim 0.2$  eV weaker than the one for Pt(111) (5, 37).  $\Delta E_{O^*}$  is modu-

lated by the d-band center (labeled as  $\epsilon_d$ ) of Pt, whereas the downshift or upshift of  $\epsilon_d$  is tuned by surface lattice strain (noted as  $\chi$ ) and coordination environment (coordination number, noted as CN) (32–34). High-index crystal facets such as Pt(211) and Pt(311) exhibit a compressive lattice strain ( $\chi$ ) relative to Pt(111), which brings a downshift of  $\epsilon_d$  of surface Pt atoms and weakening of  $\Delta E_{O^*}$ . Herein, DFT calculation is focused on investigating the synergistic effect of  $\chi$  and CN on  $\epsilon_d$ , and finally on  $\Delta E_{O^*}$ , and the correlations between them (Fig. 6, A and B). Figure 6C corroborates that the Pt<sub>4</sub>Ni-skin has higher ORR activity than the Pt<sub>3</sub>Ni-skin, but activities of both are substantially improved relative to that of Pt(111).  $\Delta E_{O^*}$  values are 0.17 and 0.11 eV weaker on Pt<sub>4</sub>Ni- and Pt<sub>3</sub>Ni-skin, respectively, than on Pt(111), which are near the optimal  $\Delta E_{O^*}$  value (table S6). Both skins have a 2.5% compressive lattice strain (fig. S22 and table S7). The bridge sites of Pt(211) and Pt(311) have a stronger O binding than those on Pt(111), whereas the hexagonal close-packed sites of them adsorb O slightly less strongly. For the ORR that happened at the electrode surface in aqueous

solution, the bridge sites of high-index crystal planes are preferentially occupied by water molecules, and the other sites account for the observed high ORR activity (figs. S23 to S26). In addition, the determined potential energy profiles demonstrate that Pt<sub>4</sub>Ni-skin has a lower overpotential for ORR than Pt<sub>3</sub>Ni-skin and Pt(111) (fig. S27 and table S8). On the basis of the above analysis, we propose that the synergistic effects of strain and coordination environment, incorporation of Ni, and the appropriate Pt/Ni ratio provide a properly weakened Pt-O binding strength, thus leading to the superior ORR activity of PtNi-BNCs (Fig. 6D). Furthermore, DFT calculations were also conducted to gain insight into the high stability of PtNi-BNCs (fig. S28). The binding energy of the surface Pt atoms in Pt<sub>4</sub>Ni- or Pt<sub>3</sub>Ni-skin models is higher compared with that of other [Pt(111), Pt(211), and Pt(311)] models, indicating higher stability of the Pt-skin structures under the condition of lattice strain and coordination environment. Also, it was found that the required activation energy for the spillover of surface Pt atoms is substantial, indicating that dissolution of surface Pt atoms is kinetically prohibited for Pt-skin structures, even in the presence of oxygen adsorbates (table S9). The above results agreed well with the observed robust structure of our catalyst during the durability test.

### Discussion

We prepared bunched Pt-Ni NCs and demonstrated that they are efficient and durable ORR electrocatalysts for fuel cells. The as-obtained bunched Pt-Ni alloy NCs showed high mass and specific activities of  $3.52 \text{ A mg}_{\text{Pt}}^{-1}$  and  $5.16 \text{ mA cm}_{\text{Pt}}^{-2}$ , respectively, which are 16.8 times and 14.3 times higher than those of a commercial Pt/C catalyst. Our catalyst also exhibited robust stability with negligible activity decay even after 50,000 potential-scanning cycles. The H<sub>2</sub>-air fuel cell assembled by this Pt-Ni catalyst achieves a peak power density of  $920 \text{ mW cm}^{-2}$  and delivers a current density of  $1.5 \text{ A cm}^{-2}$  at a voltage of 0.6 V for at least 180 hours, demonstrating the great potential for practical application. In situ XAFS, theoretical calculation, and experimental results reveal that such excellent performance could be ascribed to the integration of a hollow structure and dimensional architecture in the bunched Pt-Ni alloy NCs. This work provides an effective strategy for the rational design of Pt alloy nanostructures and will help guide the future development of catalysts for their practical applications in energy conversion technologies and beyond.

### REFERENCES AND NOTES

1. Z. W. Seh et al., *Science* **355**, eaad4998 (2017).
2. A. Kulkarni, S. Siahrostami, A. Patel, J. K. Nørskov, *Chem. Rev.* **118**, 2302–2312 (2018).
3. M. K. Debe, *Nature* **486**, 43–51 (2012).



4. C. Chen *et al.*, *Science* **343**, 1339–1343 (2014).
5. J. Greeley *et al.*, *Nat. Chem.* **1**, 552–556 (2009).
6. D. F. van der Vliet *et al.*, *Nat. Mater.* **11**, 1051–1058 (2012).
7. R. Chattot *et al.*, *Nat. Mater.* **17**, 827–833 (2018).
8. P. Strasser *et al.*, *Nat. Chem.* **2**, 454–460 (2010).
9. L. Bu *et al.*, *Science* **354**, 1410–1414 (2016).
10. B. Lim *et al.*, *Science* **324**, 1302–1305 (2009).
11. D. S. He *et al.*, *J. Am. Chem. Soc.* **138**, 1494–1497 (2016).
12. L. Zhang *et al.*, *Science* **349**, 412–416 (2015).
13. L. Wang, Y. Yamauchi, *J. Am. Chem. Soc.* **135**, 16762–16765 (2013).
14. M. Li *et al.*, *Science* **354**, 1414–1419 (2016).
15. C. Koenigsmann, M. E. Scofield, H. Liu, S. S. Wong, *J. Phys. Chem. Lett.* **3**, 3385–3398 (2012).
16. L. Bu *et al.*, *Adv. Mater.* **27**, 7204–7212 (2015).
17. B. Y. Xia *et al.*, *J. Am. Chem. Soc.* **135**, 9480–9485 (2013).
18. V. R. Stamenkovic *et al.*, *Nat. Mater.* **6**, 241–247 (2007).
19. L. Chong *et al.*, *Science* **362**, 1276–1281 (2018).
20. D. Banham, S. Ye, *ACS Energy Lett.* **2**, 629–638 (2017).
21. P. Wang, K. Jiang, G. Wang, J. Yao, X. Huang, *Angew. Chem. Int. Ed.* **55**, 12859–12863 (2016).
22. C. Cui, L. Gan, M. Heggen, S. Rudi, P. Strasser, *Nat. Mater.* **12**, 765–771 (2013).
23. K. Jiang *et al.*, *Adv. Funct. Mater.* **27**, 1700830 (2017).
24. M. Luo *et al.*, *Adv. Mater.* **30**, 1705515 (2018).
25. X. Wang *et al.*, *Nat. Commun.* **6**, 7594 (2015).
26. N. Becknell *et al.*, *J. Am. Chem. Soc.* **137**, 15817–15824 (2015).
27. S. W. Lee *et al.*, *J. Phys. Chem. Lett.* **1**, 1316–1320 (2010).
28. X. Zhao *et al.*, *J. Am. Chem. Soc.* **141**, 8516–8526 (2019).
29. Q. Jia *et al.*, *ACS Nano* **9**, 387–400 (2015).
30. Q. Jia *et al.*, *Nano Lett.* **18**, 798–804 (2018).
31. S. J. Hwang *et al.*, *J. Am. Chem. Soc.* **134**, 19508–19511 (2012).
32. J. Li *et al.*, *J. Am. Chem. Soc.* **140**, 2926–2932 (2018).
33. L. Wang *et al.*, *Science* **363**, 870–874 (2019).
34. Y. Feng *et al.*, *Sci. Adv.* **4**, eaap8817 (2018).

#### ACKNOWLEDGMENTS

We thank S. Liao from South China University of Technology for support with the fuel cell test. We thank X. Guo from Huazhong University of Science and Technology for valuable discussions. We thank Y. Iwasawa for support with XAFS measurements and the New Energy and Industrial Technology Development Organization (NEDO), Ministry of Economy, Trade, and Industry (METI), Japan; XAFS measurements were performed with Spring-8 subject numbers 2018B7800 and 2019A7800. Supercomputing facilities were provided by Netherlands Organisation for Scientific Research (NWO). The authors also acknowledge the support of the Analytical and Testing Center of Huazhong University of Science and Technology for XRD, XPS, ICP-OES, SEM, and TEM measurements. **Funding:** This work is funded by the National Natural Science Foundation of China (21805104 and 21802048), the National 1000 Young Talents Program of China and the Fundamental Research Funds for the Central Universities (2018KFYXJC044, 2018KFYYXJJ121, and 2017KFXXJC002), and the Start-up

Research Foundation of Hainan University [KYQD(ZR)1908]. X.W.L. acknowledges funding support from the National Research Foundation (NRF) of Singapore via the NRF Investigatorship (NRF-NRFI2016-04). **Author contributions:** B.Y.X. and X.W.L. conceived the idea and designed the experiments. X.T. and L.W. carried out the sample synthesis, characterization, and measurements. X.Z. performed the in situ XAFS measurements. Y.-Q.S. and E.J.M.H. provided theoretical calculations. X.T. and D.D. performed the fuel cell measurements. B.C., H.W., and H.L. participated in the discussion of the experimental results. X.T., X.W.L., and B.Y.X. co-wrote and revised the manuscript. All the authors contributed to the overall scientific interpretation and edited the manuscript. X.T., X.Z., and Y.-Q.S. contributed equally to this work. **Competing interests:** The authors declare no competing financial interests. **Data and materials availability:** All data needed to evaluate the conclusions in the paper are present in the paper or the supplementary materials.

#### SUPPLEMENTARY MATERIALS

science.sciencemag.org/content/366/6467/850/suppl/DC1  
Materials and Methods  
Figs. S1 to S28  
Tables S1 to S9  
References (35–54)

21 January 2019; resubmitted 9 August 2019  
Accepted 22 October 2019  
10.1126/science.aaw7493

## REPORT

## LASER PHYSICS

## Widely tunable compact terahertz gas lasers

Paul Chevalier<sup>1</sup>, Arman Amirzhan<sup>1</sup>, Fan Wang<sup>2</sup>, Marco Piccardo<sup>1</sup>, Steven G. Johnson<sup>3,4</sup>, Federico Capasso<sup>1,\*</sup>, Henry O. Everitt<sup>5,6\*</sup>

The terahertz region of the electromagnetic spectrum has been the least utilized owing to inadequacies of available sources. We introduce a compact, widely frequency-tunable, extremely bright source of terahertz radiation: a gas-phase molecular laser based on rotational population inversions optically pumped by a quantum cascade laser. By identifying the essential parameters that determine the suitability of a molecule for a terahertz laser, almost any rotational transition of almost any molecular gas can be made to lase. Nitrous oxide is used to illustrate the broad tunability over 37 lines spanning 0.251 to 0.955 terahertz, each with kilohertz linewidths. Our analysis shows that laser lines spanning more than 1 terahertz with powers greater than 1 milliwatt are possible from many molecular gases pumped by quantum cascade lasers.

The problem of generating terahertz-frequency radiation (0.3 to 3.0 THz)—in the middle of the electromagnetic spectrum between the microwave region and the infrared (IR) region—has challenged researchers for decades. Not only would wireless communications and radar benefit from operating in the terahertz region, because of appealing characteristics such as high bandwidth, high spatial resolution, compact size, and/or adjustable atmospheric propagation (1), but so would applications requiring stable local oscillators, such as spectroscopy and astronomical observations of the interstellar media. Among the many techniques developed to generate terahertz radiation, the most widely used (2) include harmonic multipliers of tunable microwave sources (3), vacuum electronics (backward-wave oscillators, gyrotrons, and carcinotrons) (4), supercontinua generated by ultrafast lasers and photoconductive switches (5), and difference-frequency mixing of tunable continuous-wave lasers (6–8). Commercial versions of each of these terahertz sources are becoming increasingly available and powerful, but none of them produce much power near 1 THz, and their cost and idiosyncrasies have prevented widespread adoption. Terahertz quantum cascade lasers (9) are compact and can span portions

of the region, but they currently have limited fractional tunability (<25%) and operate below room temperature (10, 11).

Often overlooked is one of the earliest sources of terahertz radiation, optically pumped far-infrared (OPFIR) lasers (12). These gas-phase lasers use a discretely line-tunable carbon dioxide (CO<sub>2</sub>) laser to excite a specific rotational-vibrational (ro-vibrational) transition in a specific molecular gas to create a rotational population inversion within a tunable cavity. These lasers generate appreciable power (up to 100 mW) and exhibit a narrow linewidth ( $\Delta\nu < 10$  kHz), a combination of features that is not available with most other terahertz sources. However, OPFIR lasers are inefficient, large (~1 m), and require an equally large CO<sub>2</sub> laser and high-voltage power supply. Moreover, they are poorly tunable, requiring the laser gas and CO<sub>2</sub> laser line to be changed each time a different frequency is needed. Consequently, OPFIR lasers fell from widespread use when other sources became available.

Here, we introduce an OPFIR laser concept characterized by frequency tunability over the entire range of rotational transitions from the molecular gas gain medium. Broad terahertz tunability is made possible by using a continuously tunable mid-IR pump source, the quantum cascade laser (QCL) (13). A tunable QCL can optically pump almost any ro-vibrational transition  $J_L \rightarrow J_U$  of almost any molecule, thereby promoting population from lower level  $J_L$  into a virtually empty excited vibrational level (Fig. 1A). Sufficient pumping of upper level  $J_U$  by the QCL inverts the rotational transition  $J_U \rightarrow J_U - 1$  and induces this “direct” transition to lase at frequency  $\nu \approx 2BJ_U$ , where  $B$  is the rotational constant of the molecule. The rotational quantum number  $J_U$  is selected by the type of ro-vibrational transition excited by the QCL: for P-, Q-, and R-branch transitions,  $J_U = J_L -$

1,  $J_L$ , and  $J_L + 1$ , respectively. With sufficient QCL power, it is also possible to induce the “refilling” transition  $J_L + 1 \rightarrow J_L$  to lase, effectively doubling the number of laser lines for a given molecular gas.

The QCL-pumped molecular laser (QPML) is a universal concept: Almost any rotational transition from any molecule with a permanent dipole moment and a vapor pressure can be made to lase if a QCL can be precisely tuned across one of its IR bands. Terahertz lasing was recently reported on several NH<sub>3</sub> transitions near 1.0 THz (14), but we show theoretically and experimentally that the QPML tuning range can be much broader, a 200% fractional tunability covering the entire span of a molecule’s rotational spectrum, whose frequencies have been tabulated in several catalogs (15–17). The tuning range for several simple molecules (OCS, N<sub>2</sub>O, CH<sub>3</sub>F, HCN, and CO) is illustrated in Fig. 1B. Because  $B$  is inversely proportional to a principal moment of inertia of the molecule (18, 19), a low moment of inertia molecule like CO has sparser spacing, a broader tuning range, and a peak emission intensity at a high frequency, whereas a higher moment of inertia molecule like OCS has a denser spacing, a narrower tuning range, and a peak at a lower frequency. The number of available transitions increases as the molecular symmetry decreases and molecular mass increases.

Our comprehensive, physics-based multilevel model of the dominant collisional processes shows that OPFIR lasers operate most efficiently in compact cavities, with volumes more than 1000-fold smaller than conventional cavities (20–23). Our compact QPML configuration (Fig. 2A) includes aspects of the cavity design previously reported (20, 22): a 5-mm-diameter, 15-cm-long evacuated copper tube into which is inserted a copper rod rear reflector with a curved face that can be longitudinally scanned until the cavity mode overlaps the gain profile. The output coupler is a 1-mm-diameter pinhole in a flat front plate through which both the QCL and QPML beams propagate. The IR beam from the QCL is focused by a 15-cm-focal-length lens through a Brewster-angled ZnSe window to maximize power into the cavity (typically ~85%), while the terahertz beam diffracts through the pinhole and is refocused into a room-temperature power meter, a Schottky-diode detector, or a receiver operating in the frequency band of interest.

For a given QCL pump power, the terahertz power achievable by this room temperature laser depends on several factors. To ascertain the potential of a given molecular gas as a QPML, consider first the very low-pressure regime in which molecular collisions with the chamber walls occur more frequently than any intermolecular collisions, so a simple three-level model captures the salient behavior. Given that the ~1-MHz QCL linewidth (24) is much less

<sup>1</sup>Harvard John A. Paulson School of Engineering and Applied Sciences, Harvard University, Cambridge, MA 02138, USA. <sup>2</sup>Department of Mechanical Engineering, Massachusetts Institute of Technology, Cambridge, MA 02139, USA. <sup>3</sup>Department of Mathematics, Massachusetts Institute of Technology, Cambridge, MA 02139, USA. <sup>4</sup>Department of Physics, Massachusetts Institute of Technology, Cambridge, MA 02139, USA. <sup>5</sup>U.S. Army Combat Capabilities Development Command Aviation and Missile Center, Redstone Arsenal, AL 35898, USA. <sup>6</sup>Department of Physics, Duke University, Durham, NC 27708, USA.

\*Corresponding author. Email: everitt@phy.duke.edu (H.O.E.); capasso@seas.harvard.edu (F.C.)



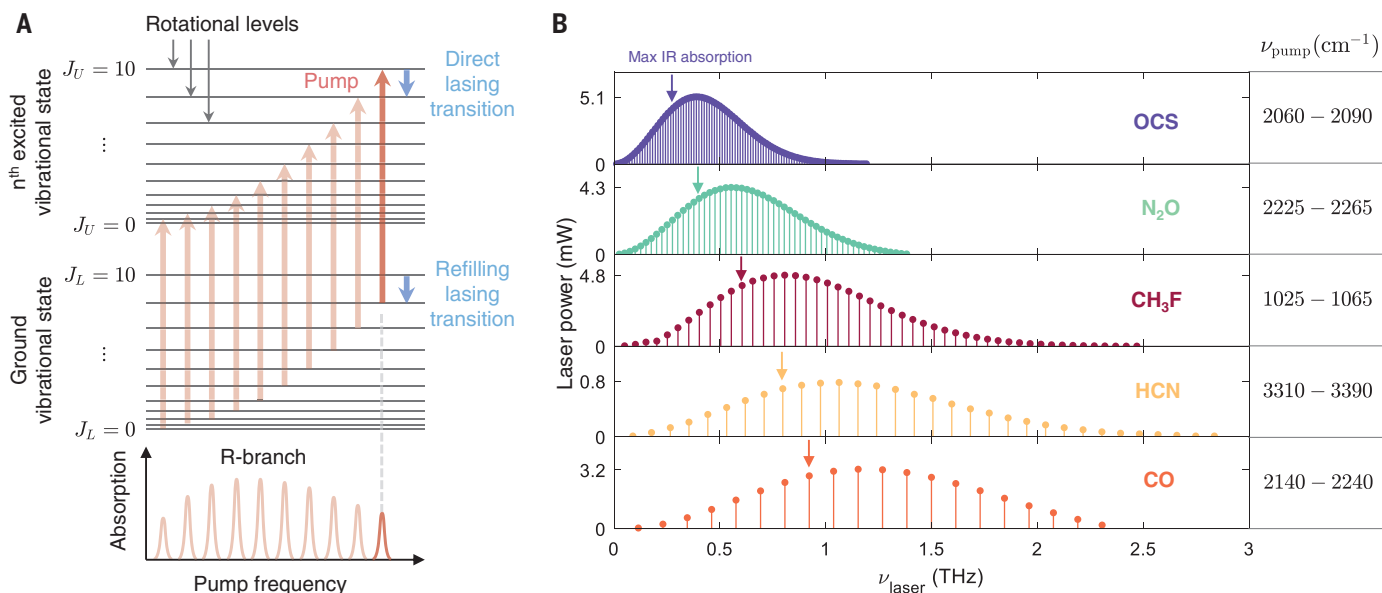


**Fig. 1. Universality of the quantum cascade laser-pumped molecular laser.**

(A) Diagram showing the rotational levels of a molecule for the ground and excited vibrational states. The red arrows illustrate R-branch transitions  $J_L \rightarrow J_U$  responsible for the IR absorption spectrum whose strength depends on the population of each  $J_L$ . The blue arrows indicate lasing transitions at frequencies corresponding to an inversion between two rotational states in the excited ("direct") or ground ("refilling") vibrational level. The frequency of the laser emission increases with increasing  $J_L$ . (B) Plot showing the QCL-pumped

molecular laser tuning range and power predicted by the simple model for direct transitions in 20 mTorr of various molecular gases in a compact cylindrical cavity pumped by a 0.25-W QCL: carbonyl sulfide (OCS), nitrous oxide (N<sub>2</sub>O), methyl fluoride (CH<sub>3</sub>F), hydrogen cyanide (HCN), and carbon monoxide (CO). The arrow indicates the laser transition corresponding to a pump transition from the rotational level with maximum population, illustrating how the Manley-Rowe effect skews the peak power to higher frequency. Also listed is the QCL tuning range required to pump the associated R-branch transitions.

than the ~50- to 150-MHz Doppler width of the IR molecular transition, a simple expression (25) gives the QPML power

$$P_{\text{THz}} = \frac{T}{4} \left( \frac{\nu_{\text{THz}}}{\nu_{\text{IR}}} \right) \left( \frac{\alpha_{\text{IR}}}{\alpha_{\text{cell}}} \right) [P_{\text{QCL}} - P_{\text{th}}] = \eta [P_{\text{QCL}} - P_{\text{th}}] \quad (1)$$

and identifies the essential parameters on which it depends at frequency  $\nu_{\text{THz}}$ . Here,  $\alpha_{\text{IR}}$  is the IR absorption coefficient of the gas molecule at the frequency  $\nu_{\text{IR}}$  to which the QCL is tuned,  $\alpha_{\text{cell}}$  captures the losses of the cavity,  $P_{\text{QCL}}$  is the QCL pumping power, and  $T$  is the front window transmission coefficient for the terahertz output. For our pinhole coupler with  $\nu_{\text{THz}} > c/2r_0$ ,  $T \approx (r_0/R_{\text{cell}})^2$ , where  $R_{\text{cell}}$  is the cavity radius and  $r_0$  is the radius of the output coupler. Combined, the factors before the square bracket in Eq. 1 constitute the power efficiency  $\eta$  of the QPML. The lasing threshold

$$P_{\text{th}} = \frac{h^2 \nu_{\text{IR}}}{4\pi \alpha_{\text{IR}}} (\alpha_{\text{cell}} R_{\text{cell}}) \frac{u^2}{|\langle J_U - 1 | \mu | J_U \rangle|^2} \quad (2)$$

depends on many of the same parameters, as well as the average absolute molecular velocity  $u$  and the transition dipole matrix element of the rotational transition  $\langle J_U - 1 | \mu | J_U \rangle$ . As expected, the threshold increases with increasing cavity loss, but the dependence of  $P_{\text{th}}$  on

cell radius is more subtle because of the strong increase of  $\alpha_{\text{cell}}$  with decreasing  $R_{\text{cell}}$  due to ohmic loss (26) experienced by the modes of the hollow metal cavity. The threshold decreases for increasing dipole moment and decreasing  $\nu_{\text{IR}}$ , indicating that terahertz lasing is favored for strongly polar molecules with low frequency vibrational modes.

Equation 1 shows that the maximum power achievable by the QPML, often known as the Manley-Rowe limit (27), is determined by the ratio of the terahertz laser and IR pump frequencies  $\nu_{\text{THz}}/\nu_{\text{IR}}$ . Any vibrational band may be pumped by the QCL, but this Manley-Rowe limit (27) also recommends low frequency vibrational modes pumped by long-wavelength QCLs. Currently, more powerful QCLs are available at higher frequencies, so the selection of which vibrational mode to excite must be determined by its absorption strength, the Manley-Rowe factor, and the available QCL power.

Moreover, the Manley-Rowe factor indicates that the maximum power of the QPML grows with increasing laser frequency for a given QCL and vibrational band, in great contrast with electronic sources. This Manley-Rowe effect is tempered by the pressure-dependent population  $n_{J_L}$ , manifested in the IR absorption term  $\alpha_{\text{IR}}$ , available for the QCL to excite. One may simply look at the IR spectrum of a molecule to estimate how the power of the corresponding terahertz laser will depend on  $J_L$ . However,

the predicted power (Eq. 1) is proportional to the product of  $\alpha_{\text{IR}}$  and  $\nu_{\text{THz}}/\nu_{\text{IR}}$  and Fig. 1B confirms that the peak power occurs when the QCL pumps a transition with higher  $J_L$  than the peak of the IR band (where  $n_{J_L}$  is maximum) because of this Manley-Rowe effect.

The simple model of Eqs. 1 and 2 captures the molecular and cavity parameters essential for ascertaining how a given molecular gas will perform as a QCL-pumped terahertz laser. Table 1 and Fig. 1B summarize these behaviors for several candidate polar molecules, sorted by threshold pump power. The oblate symmetric top NH<sub>3</sub> has recently been reported as a low threshold QPML near 1 THz (14), and the simple model reveals high power efficiency and large output power from many of these pure inversion transitions (25). However, the other molecules offer much greater tunability, in both range and spacing, and those with large  $\alpha_{\text{IR}}$  (NH<sub>3</sub>, CH<sub>3</sub>F, OCS, N<sub>2</sub>O, and CO) exhibit many lines with powers above 1 mW.

Because the simple, three-level model in Eqs. 1 and 2 is only valid at very low pressures where there is no collisional quenching of the laser inversion,  $P_{\text{THz}}$  is predicted to increase linearly with increasing pressure (through  $\alpha_{\text{IR}}$ ). This best-case approximation fails at higher pressures when intermolecular dipole-dipole, rotational-state randomizing, and velocity-randomizing collisions dominate the laser performance and quench the inversion in a manner that depends

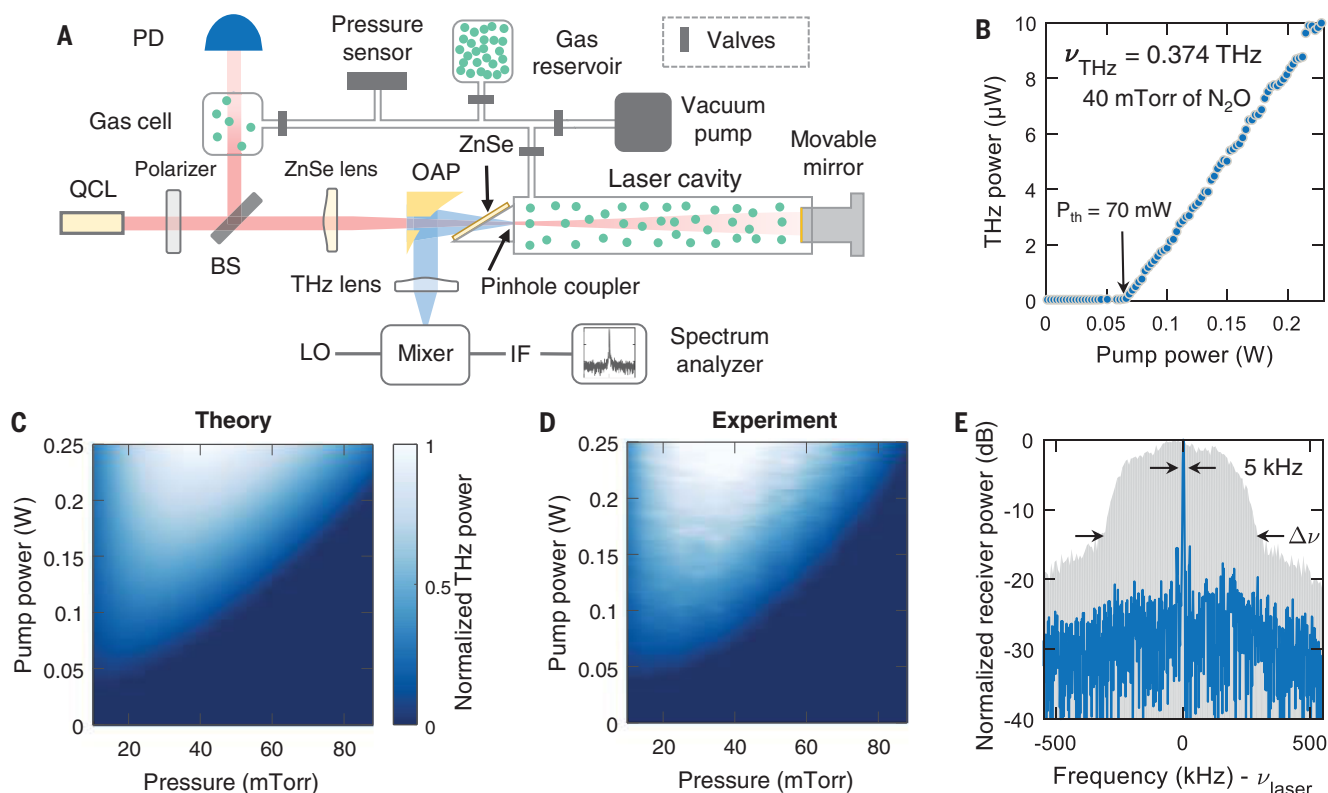


**Fig. 2. Experimental setup and results for the  $\text{N}_2\text{O}$  molecular laser.**

(A) Experimental setup: IR light from a widely tunable QCL is tuned to pump a ro-vibrational transition and create a rotational population inversion. Light from the QCL is deflected by a 90%–10% beam splitter (BS) and transmitted through a gas cell so that the QCL may be tuned into coincidence with the vibrational transition by minimizing the transmitted intensity measured using a photodiode (PD). Light is coupled into the laser cavity through a ZnSe window at Brewster's angle and through a pinhole coupler in the cavity. A vacuum pump, pressure sensor, and gas reservoir are used to set the pressure in both the laser cavity and gas cell. The radiation emitted from the pinhole of the QPML is collected with the off-axis parabolic mirror (OAP), focused through a Teflon lens, and measured by a power meter, a detector, or a receiver that uses a frequency-multiplied local oscillator (LO) mixed with the signal to produce the

intermediate frequency (IF) measured by a spectrum analyzer. The pump power from the QCL is varied using a wire grid polarizer on a calcium fluoride substrate. The laser cavity is tuned into resonance with the lasing frequency by moving a copper mirror on a translation stage. (B) The measured output power of the QPML is plotted as a function of the IR pump power from the QCL. The threshold is  $P_{\text{th}} = 70 \text{ mW}$ . After accounting for losses in the collection of the emitted terahertz radiation, the maximum power is  $\sim 0.04 \text{ mW}$ , and  $\eta \approx 0.2 \text{ mW/W}$  at 40 mTorr for the  $J_U = 15 \rightarrow 14$  transition at 0.374 THz. Predicted (C) and measured (D) QPML normalized laser power as a function of gas pressure and QCL pump power for the same direct transition. (E) Emission spectrum of the laser (blue line) showing a linewidth of  $\leq 5 \text{ kHz}$  at 0.374 THz, corresponding to the  $J_U = 15 \rightarrow 14$  transition. The full tuning range of the QPML (broad gray feature) is achieved by varying the cavity length.

on collision cross sections that may not be known. We have previously reported a comprehensive, multilevel model that thoroughly captures these behaviors, finding that the IR-to-terahertz photon conversion efficiency of an optimized  $\text{CH}_3\text{F}$  OPFIR laser may exceed 30% (23). This model has been adapted to predict the performance of QPMLs as a function of  $P_{\text{QCL}}$  and pressure (25).

To illustrate the performance and tunability of a compact QPML, we chose nitrous oxide ( $\text{N}_2\text{O}$ ), whose  $\nu_3$  vibrational mode falls within the 2119 to 2342  $\text{cm}^{-1}$  tuning range of our 320-mW QCL. The spacings of the  $\text{N}_2\text{O}$  lasing transitions are  $\sim 2B_{\text{N}_2\text{O}} = 25.1 \text{ GHz}$ , and the frequency span over which this QPML may be tuned is  $\sim 1.5 \text{ THz}$ . QCL frequency tuning was accomplished by monitoring the IR signal transmitted through a separate 15-cm gas cell

containing 50 mTorr of  $\text{N}_2\text{O}$  using a HgCdTe detector. The QCL frequency was tuned by precise temperature control until molecular absorption minimized the transmitted IR power (Fig. 2A). Here, we will refer to lasing transitions (both direct and refilling) by the quantum number  $J_L$  of the lower level drained by the IR pump.

We observed lasing for all 29 direct lasing transitions (Fig. 3A), as well as eight refilling transitions (Fig. 3B), between 0.251 and 0.955 THz (corresponding to  $9 \leq J_L \leq 37$ ) by exciting each R-branch  $\nu_3$  ro-vibrational transition over a QCL tuning range of 2231 to 2250  $\text{cm}^{-1}$ . Refilling transitions and direct transitions corresponding to the same  $J_L$  exhibit slightly different frequencies owing to different  $B$  rotational constants for the ground and excited vibrational states. Lasing below 0.251 THz could

not be observed because it occurred below the radiation-suppressing cutoff frequency of the pinhole output coupler. For most transitions, we measured the strength of the laser emission as a function of pressure for maximum QCL pumping power, and in some cases we also measured the laser emission as a function of QCL pumping power (see Fig. 2B for  $J_L = 14$ ). From these measurements, we were able to obtain the threshold power  $P_{\text{th}}$  and power efficiency  $\eta$  of many laser lines (25), providing critical information for ascertaining the molecular dipole-dipole and thermalizing gas kinetic collisional cross sections needed in the comprehensive model (22, 23, 28).

We also used heterodyne receivers operating between 0.300 and 0.775 THz to measure the spectrum of these laser transitions (see Fig. 2E for the recovered line at  $\nu_{\text{THz}} = 0.374 \text{ THz}$ ).



**Table 1. Predicted QPML power (Eq. 1) and QCL threshold pump power (Eq. 2) for the highest power lasing transition of nine candidate laser molecules at 20 mTorr.** Assumes a 0.25-W QCL pumping through a 1-mm-diameter pinhole output coupler into a 5-mm-diameter cylindrical laser cavity (loss = 0.06 m<sup>-1</sup>) containing the molecular gas with dipole moment  $\mu$ . With optimized pressure, even higher power is achievable (23).

Molecule	$J_L$ (peak)	$\nu_{\text{THz}}$ (THz)	$P_{\text{THz}}$ (mW)	$P_{\text{th}}$ (mW)	$\eta$ (mW/W)	$\mu$ (D)	$\nu_{\text{IR}}$ (cm <sup>-1</sup> )	$\alpha_{\text{IR}}$ (m <sup>-1</sup> )
CH <sub>3</sub> F	15	0.806	4.8	0.041	19.2	1.85	1072.774	4.59
NH <sub>3</sub>	3	1.073	16.7	0.056	66.6	1.46	967.346	10.8
OCS	31	0.389	5.2	0.069	20.5	0.72	2073.894	19.6
HCN	11	1.063	0.8	0.164	3.11	2.98	1447.962	0.76
H <sub>2</sub> CO	13	1.087	0.8	0.218	3.28	2.33	1776.861	0.96
CH <sub>3</sub> <sup>35</sup> Cl	20	0.558	0.04	2.42	0.14	1.90	1459.582	0.07
N <sub>2</sub> O	21	0.553	4.3	3.14	17.4	0.17	2240.439	12.7
CH <sub>3</sub> OH	15	2.523	0.2	4.88	0.92	1.41	1031.477	0.07
CO	9	1.153	3.2	27.2	14.5	0.12	2179.772	4.93

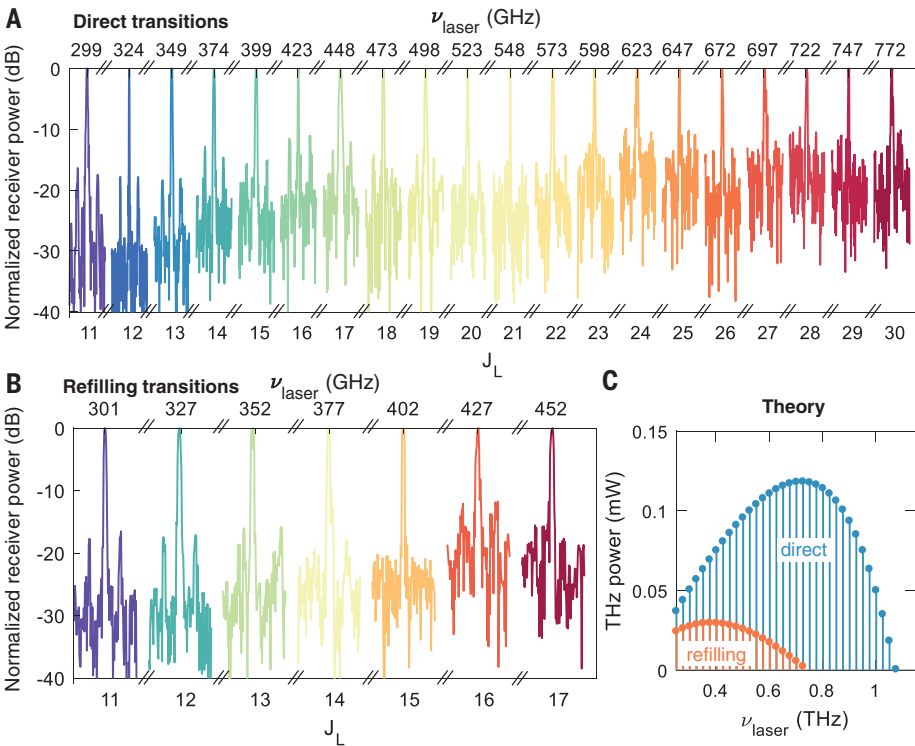


**Fig. 3. Tunability of the optically pumped N<sub>2</sub>O laser.** Emission spectra of the laser were measured as the QCL pump laser was tuned to different IR transitions of N<sub>2</sub>O. The x axes show the measured emission frequency and the associated quantum number  $J_L$  of the lower level of the pumped R-branch transition. The QCL power was maximal (up to 0.25 W coupled in the cavity), and the pressure was 40 mTorr for direct transitions and 20 mTorr for refilling transitions. (A) Measured spectra of direct transitions with  $J_L$  from 11 to 30. (B) Measured spectra of refilling transitions with  $J_L$  from 11 to 17. (C) The output power of the laser predicted by the comprehensive model (23) using the deduced collisional parameters of N<sub>2</sub>O and the estimated cavity losses, plotted as a function of frequency for the optimal pressure.

The instantaneous linewidths were <1 kHz, but because of frequency jitter the effective linewidths were typically 3 to 6 kHz. Other measured lines are shown in Fig. 3, A and B, over a 200-kHz span. We were able to dem-

onstrate frequency tuning of the laser across its full Doppler-broadened gain bandwidth by precisely adjusting the cavity length with a motorized micrometer. The broad feature (gray curve) in Fig. 2E envelopes the range

of individual frequencies over which the laser was tuned while keeping the pump laser at a constant power and frequency. Importantly, the QPML frequency was quite stable (routinely <10 kHz) while freely running and could be made even more stable through active frequency stabilization of the QCL (29) and the laser cavity (30).

Constrained by these experimental measurements of terahertz power as a function of pressure and pump power, our comprehensive theoretical model (23) was able to estimate the collisional cross sections and predict the optimal performance of the laser. The dipole-dipole collisional cross section was estimated to be 35 Å<sup>2</sup>, well within the expected range (25), while the cavity loss ( $\alpha = 0.3 \text{ m}^{-1}$  at 374 GHz) was estimated to be five times higher than the theoretical minimum (25). Figure 2, C and D, respectively, reveal the excellent agreement between the predicted and measured output terahertz power for  $J_L = 14$  as a function of N<sub>2</sub>O pressure and QCL pump power. The model predicts, and measurements confirm, that the optimal and maximum pressure for laser operation increases with increasing  $J_L$  (25), a consequence of the increasing Doppler width of the gain profile with increasing laser frequency.

The comprehensive model was used to predict the expected laser power for each transition at its optimal gas pressure, and Fig. 3C shows that the direct lasing transition with maximum power occurs not for  $J_L = 15$ , where  $n_{J_L}$  is largest, but for  $J_L = 28$  because of the Manley-Rowe effect. While the output power increased as a function of the frequency, the signal-to-noise ratio in the heterodyne measurement (Fig. 3, A and B) was limited by the decreasing efficiency of the electronic subterahertz source. An emitted power of 69  $\mu\text{W}$  was predicted for the  $J_L = 14$ ,  $\nu_{\text{THz}} = 0.374 \text{ THz}$  direct transition. Although we measured only 10  $\mu\text{W}$  (Fig. 2B), our power measurements underestimate the emitted power by at least a factor of four, for reasons including significant diffraction of the emitted terahertz beam beyond the collection optics, absorption and reflection by the ZnSe Brewster window and Teflon lens, and use of the power meter at the edge of its calibrated range.

Like traditional OPFIR lasers, QPMLs exhibit high brightness temperatures  $T_b = Ic^2 / (2k\nu_{\text{THz}}^2 \Delta\nu) > 10^{14} \text{ K}$  for laser radiance  $I = 1 \text{ mW} \cdot \text{cm}^{-2} \cdot \text{sr}^{-1}$  (where  $k$  is the Boltzmann constant,  $c$  is the speed of light, and  $\Delta\nu = 1 \text{ kHz}$  the linewidth). Because our theoretical models and experimental demonstrations with N<sub>2</sub>O confirm the universal concept of a terahertz molecular laser source broadly tunable across its entire rotational manifold when pumped by a continuously tunable QCL, the outlook for QPMLs is indeed very bright.

## REFERENCES AND NOTES

1. T. Nagatsuma, G. Ducournau, C. C. Renaud, *Nat. Photonics* **10**, 371–379 (2016).
2. R. A. Lewis, *J. Phys. D Appl. Phys.* **47**, 374001 (2014).
3. A. Maestrini *et al.*, *IEEE Trans. Microw. Theory Tech.* **58**, 1925–1932 (2010).
4. J. H. Booske *et al.*, *IEEE Trans. Terahertz Sci. Technol.* **1**, 54–75 (2011).
5. Y. Shen, P. Upadhyay, E. Linfield, H. Beere, A. Davies, *Appl. Phys. Lett.* **83**, 3117–3119 (2003).
6. K. McIntosh *et al.*, *Appl. Phys. Lett.* **67**, 3844–3846 (1995).
7. K. Evenson, D. Jennings, F. Petersen, *Appl. Phys. Lett.* **44**, 576–578 (1984).
8. M. Inguscio, P. D. Natale, L. Veseth, *Comments At. Mol. Phys.* **30**, 3 (1994).
9. R. Köhler *et al.*, *Nature* **417**, 156–159 (2002).
10. L. Bosco *et al.*, *Appl. Phys. Lett.* **115**, 010601 (2019).
11. C. A. Curwen, J. L. Reno, B. S. Williams, *Nat. Photonics* 10.1038/s41566-019-0518-z (2019).
12. T. Chang, T. Bridges, E. Burkhardt, *Appl. Phys. Lett.* **17**, 249–251 (1970).
13. J. Faist *et al.*, *Science* **264**, 553–556 (1994).
14. A. Pagies, G. Ducournau, J.-F. Lampin, *APL Photonics* **1**, 031302 (2016).
15. I. Gordon *et al.*, *J. Quant. Spectrosc. Radiat. Transf.* **203**, 3–69 (2017).
16. JPL Molecular Spectroscopy Database (2017); <https://spec.jpl.nasa.gov/>.
17. Splatalogue Database for Astronomical Spectroscopy (2007); [www.cv.nrao.edu/php/splat/](http://www.cv.nrao.edu/php/splat/).
18. C. Townes, A. L. Schawlow, *Microwave Spectroscopy* (Dover Publications, 1995).
19. W. Gordy, R. L. Cook, *Microwave Molecular Spectroscopy* (Wiley-Interscience, 1984).
20. H. O. Everitt, D. D. Skatrud, F. C. De Lucia, *Appl. Phys. Lett.* **49**, 995–997 (1986).
21. R. McCormick, H. Everitt, F. De Lucia, D. Skatrud, *IEEE J. Quantum Electron.* **23**, 2069–2077 (1987).
22. S.-L. Chua *et al.*, *Opt. Express* **19**, 7513–7529 (2011).
23. F. Wang *et al.*, *Proc. Natl. Acad. Sci. U.S.A.* **115**, 6614–6619 (2018).
24. K. Knabe *et al.*, *Opt. Express* **20**, 12432–12442 (2012).
25. See supplementary materials.
26. R. Bansal, *Fundamentals of Engineering Electromagnetics* (CRC Press, 2006).
27. J. Manley, H. Rowe, *Proceedings of the IRE* **44**, 904–913 (1956).
28. H. O. Everitt, F. C. De Lucia, *Adv. At. Mol. Opt. Phys.* **35**, 331–400 (1995).
29. R. M. Williams *et al.*, *Opt. Lett.* **24**, 1844–1846 (1999).
30. R. L. Crownover, H. O. Everitt, F. C. De Lucia, D. D. Skatrud, *Appl. Phys. Lett.* **57**, 2882–2884 (1990).

## ACKNOWLEDGMENTS

The authors acknowledge F. De Lucia (Ohio State Univ.), T. Goyette (U. Mass Lowell), and S. Paolini (Harvard CNS) for helpful advice.

**Funding:** This work was partially supported by the U.S. Army

Research Office (W911NF-19-2-0168 and W911NF-13-D-0001) and by the National Science Foundation (NSF; ECCS-1614631) and its Materials Research Science and Engineering Center Program (DMR-1419807). Some of this work was performed at the Harvard University Center for Nanoscale Systems (CNS), part of the NSF-supported National Nanotechnology Coordinated Infrastructure Network (ECCS-1541959). Any opinions, findings, conclusions, or recommendations expressed in this material are those of the authors and do not necessarily reflect the views of the Assistant Secretary of Defense for Research and Engineering or of the NSF. **Author contributions:** H.O.E. conceived of the QPML concept; developed the theory with F.W. and S.G.J.; and demonstrated its operation with P.C., A.A., M.P., and F.C. All authors contributed to the writing of the manuscript. **Competing interests:** A provisional patent application has been filed on the subject of this work. **Data and materials availability:** All data are available in the manuscript or the supplementary materials.

## SUPPLEMENTARY MATERIALS

[science.sciencemag.org/content/366/6467/856/suppl/DC1](http://science.sciencemag.org/content/366/6467/856/suppl/DC1)  
Materials and Methods  
Supplementary Text  
Figs. S1 to S8  
References (31–36)

15 August 2019; accepted 21 October 2019  
10.1126/science.aay8683



## OPTOELECTRONICS

# Nano-opto-electro-mechanical switches operated at CMOS-level voltages

Christian Haffner<sup>1,2,3\*</sup>, Andreas Joerg<sup>1</sup>, Michael Doderer<sup>1</sup>, Felix Mayor<sup>1†</sup>, Daniel Chelladurai<sup>1</sup>, Yuriy Fedoryshyn<sup>1</sup>, Cosmin Ioan Roman<sup>4</sup>, Mikael Mazur<sup>5</sup>, Maurizio Burla<sup>1</sup>, Henri J. Lezec<sup>3</sup>, Vladimir A. Aksyuk<sup>3</sup>, Juerg Leuthold<sup>1</sup>

Combining reprogrammable optical networks with complementary metal-oxide semiconductor (CMOS) electronics is expected to provide a platform for technological developments in on-chip integrated optoelectronics. We demonstrate how opto-electro-mechanical effects in micrometer-scale hybrid photonic-plasmonic structures enable light switching under CMOS voltages and low optical losses (0.1 decibel). Rapid (for example, tens of nanoseconds) switching is achieved by an electrostatic, nanometer-scale perturbation of a thin, and thus low-mass, gold membrane that forms an air-gap hybrid photonic-plasmonic waveguide. Confinement of the plasmonic portion of the light to the variable-height air gap yields a strong opto-electro-mechanical effect, while photonic confinement of the rest of the light minimizes optical losses. The demonstrated hybrid architecture provides a route to develop applications for CMOS-integrated, reprogrammable optical systems such as optical neural networks for deep learning.

Electrically reconfigurable photonic networks have the potential to enable technological advances in many fields such as optical neural networks used to process information with low power at the speed of light (1), optical metrology to feed multiple sensors with a single light source (2), all-optical routing to avoid the current bottleneck of optical-electrical-optical conversion (3), and integrated quantum optical circuits (4). However, to make such reconfigurable photonic networks practical, they need to be up-scaled into large circuits and co-integrated with complementary metal-oxide semiconductor (CMOS) electronics. To achieve this level of scaling and integration, the elementary electro-optical switch unit needs to feature compact footprints ( $\sim 1 \mu\text{m}^2$ ), CMOS driving voltages ( $\sim 1 \text{ V}$ ), short switching times ( $\sim 1 \text{ ns}$ ), low optical losses ( $\leq 0.1 \text{ dB}$ ), and low power consumption ( $< 1 \text{ mW}$ ) (5).

Electro-optical switches typically rely on interferometric waveguide configurations to divert light to different outputs by means of constructive or destructive interference. This is achieved by changing the refractive index ( $\Delta n$ ) of the waveguide material. State-of-the-art networks control  $\Delta n$  by the electro-thermo-optical effect (6); however, the milliwatt power con-

sumption per switch limits scalability of this approach (3). Furthermore, all-optical (7), phase-change (8, 9), and electro-optical (10–13) switching approaches show notable results (e.g., compact footprint or low loss) but struggle to excel in all requirements simultaneously. For instance, under a CMOS driving voltage of 1 V, electro-optical materials currently yield  $\Delta n < 10^{-2}$ , requiring device lengths of  $> 100 \mu\text{m}$  to achieve full switching (10, 13). Resonant approaches reduce the footprint by leveraging the high finesse of micrometer-sized cavities. Yet, the frequency tunability of lowest-loss resonators is  $\leq 50 \text{ GHz/V}$ , limiting the switches' optical bandwidth (13, 14). Moreover, power-hungry stabilization is required because similar resonance frequency shifts occur for single-kelvin temperature fluctuations (15).

Opto-electro-mechanical (OEM) switches provide an alternative way to control the flow of light by mechanically changing the waveguide geometry rather than modulating the material's intrinsic refractive index (16), with waveguide motions leading to local  $\Delta n$  on the order of unity. Because of the strong  $\Delta n$ , small actuations suffice to induce large effective refractive index changes ( $\Delta n_{\text{eff}}$ ). Importantly, OEM switches consume negligible amounts of energy in stand-by, because the mechanical geometry is controlled by electrostatic forces that are not accompanied by static currents. Photonic OEM devices have been switched by actuating hundreds of nanometer-scale gaps between two silicon waveguides, using a remote electro-mechanical driver (17, 18). The all-photonic approach yields low optical losses ( $< 0.1 \text{ dB}$ ), whereas the large gap size requires high driving voltages ( $> 10 \text{ V}$ ). By contrast, the subwavelength confinement of light (19) in all-plasmonic devices enables stronger OEM responses, which reduces the drive voltages (20). All-plasmonic switches

utilize two metal surfaces to form a tens-of-nanometers-wide gap, where light is confined and its phase is modulated by electro-mechanical actuation of the gap width (21). However, such confinement comes with considerable metal induced optical losses ( $\sim 1 \text{ dB}/\mu\text{m}$ ) (22), which have limited the realization of large-scale plasmonic switching networks.

Here, we introduce a hybrid photonic-plasmonic (HPP) OEM technology that benefits a strong plasmonic OEM-effect to fully switch light with a CMOS-level voltage ( $\sim 1.4 \text{ V}$ ), low optical losses (0.1 dB), and a compact footprint ( $\approx 10 \mu\text{m}^2$ ).

Figure 1A illustrates the dynamic routing of light by two nano-OEM (NOEM) switches, respectively biased to two different resonance states (wavelength  $\lambda_{\text{res}}$ ): drop state (foreground device, 0 V) and through state (background device, 1 V). Incident light (wavelength  $\lambda_0$ ) guided in the through port is transmitted ( $\lambda_{\text{res}} \neq \lambda_0$ ) or dropped ( $\lambda_{\text{res}} = \lambda_0$ ) depending on the individual, bias-dependent  $\lambda_{\text{res}}$  of the encountered resonant switches. The HPP resonator comprises a thin gold membrane partially suspended above a silicon disc forming an air gap ( $z_0$ ) (see Fig. 1B) (23). The air HPP waveguide combines low-loss propagation in the silicon waveguide with strong field enhancement at the metal surface in the gap (24, 25). Additionally, gold and silicon form an air capacitor able to actuate  $z_0$  by means of an electrostatic force generated by an applied voltage ( $V_{\text{drive}}$ ). The gold membrane bending ( $dz$ ) induces a resonance shift ( $\Delta\lambda_{\text{res}}$ ) by changing the mode index ( $\Delta n_{\text{eff}}$ ) (Fig. 1C).

Figure 1D indicates that the large tunability of the resonance wavelength and  $dz$  as small as 4 nm already provide  $\Delta\lambda_{\text{res}}$  larger than the resonance's loaded full-width half-maximum (FWHM). Low-loss coupling to the drop port requires that the waveguide-resonator coupling rates are larger than the resonator's plasmonic loss rate (e.g., intrinsic FWHM) (fig. S3) (25). Thus, the switching efficiency is limited by the ratio of  $\Delta\lambda_{\text{res}}$  to the intrinsic FWHM.  $\Delta\lambda_{\text{res}}$  exceeds the FWHM by more than an order of magnitude when reducing  $z_0$  (Fig. 1E). A tunability of  $> 1 \text{ THz/V}$  ( $> 10 \text{ nm/V}$ ) and a sub-nanometer FWHM is achieved for  $z_0 \approx 35 \text{ nm}$ , enabling a large extinction ratio (ER) and low-loss switching (25).

This strong tuning can be understood by separating the OEM effect into its two sub-processes. First, the opto-mechanical coupling ( $G_{\text{OM}} \propto d\lambda_{\text{res}}/dz$ ) increases for decreasing gaps because of the plasmonic confinement of light to the gap (fig. S2) (25). Thus, more light experiences the strong  $\Delta n$  between air and metals upon actuation (26). The gold's skin depth for infrared light is  $\approx 25 \text{ nm}$ ; thus, thin and low-mass membranes suffice as high reflectors to concentrate light in the gap. Second, the electro-mechanical coupling ( $G_{\text{EM}} = dz/dV$ )

<sup>1</sup>Institute of Electromagnetic Fields (IEF), ETH Zurich, 8092 Zurich, Switzerland. <sup>2</sup>Maryland NanoCenter, Institute for Research in Electronics and Applied Physics, University of Maryland, College Park, MD 20742, USA. <sup>3</sup>Physical Measurement Laboratory, National Institute of Standards and Technology, Gaithersburg, MD 20899, USA. <sup>4</sup>Micro- and Nanosystems, ETH Zurich, 8092 Zurich, Switzerland. <sup>5</sup>Photonics Laboratory, Department of Microtechnology and Nanoscience, Chalmers University of Technology, Gothenburg, Sweden.

\*Corresponding author. Email: christian.haffner@nist.gov

†Present address: Department of Applied Physics and Ginzton Laboratory, Stanford University, 348 Via Pueblo Mall, Stanford, CA 94305, USA.

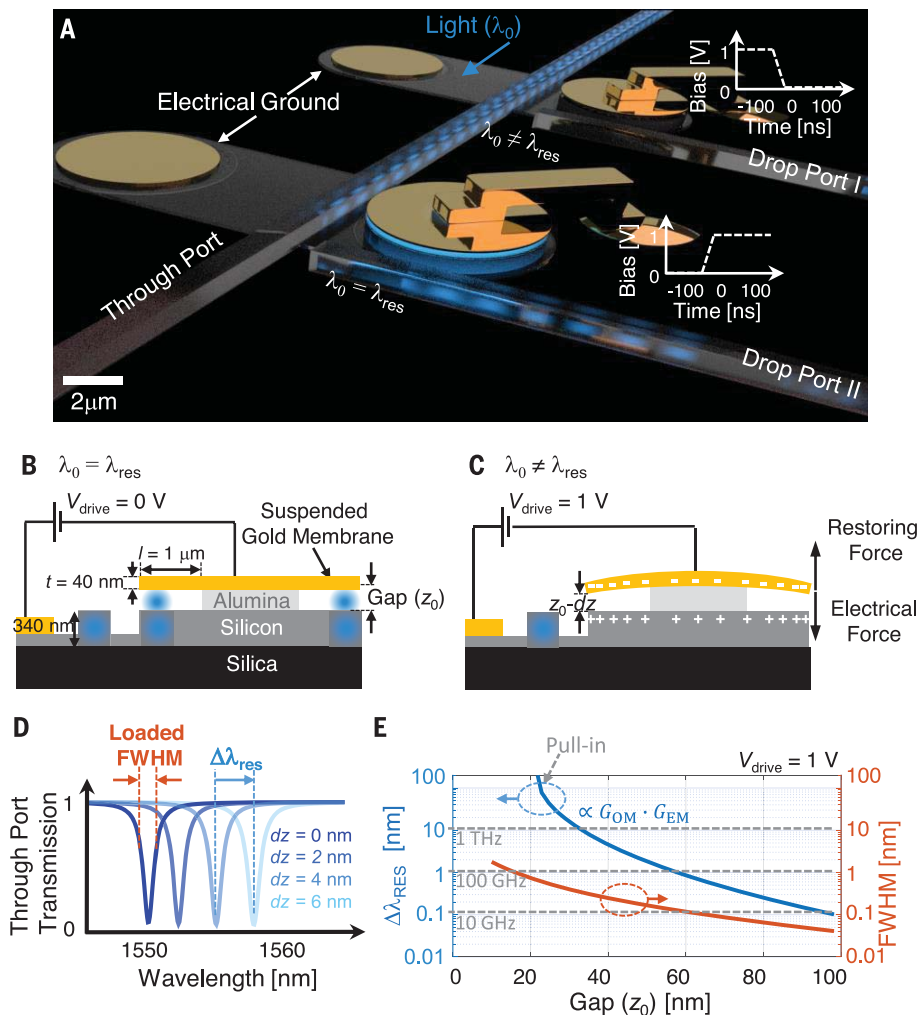


**Fig. 1. Operating principle of plasmonic NOEM networks.** (A) Incident light guided in the through port is switched to a drop port if its wavelength ( $\lambda_0$ ) matches the node's resonance wavelength ( $\lambda_{res}$ ), whereas off-resonance ( $\lambda_{res} \neq \lambda_0$ ) light continues along the waveguide and bypasses the plasmonic resonator, thereby avoiding ohmic losses (29). (B) HPP disc resonators (radius 2  $\mu\text{m}$ ) are formed by a thin gold membrane suspended above a silicon disc forming a gap ( $z_0$ ). (C) Doped silicon and gold bridges are used to apply a voltage across the gap, thus inducing an electrostatic force that bends the membrane and prevents light from coupling to the resonator. (D) Through-port spectra for various  $dz$ . (E) Calculations (25) show that  $\Delta\lambda_{res}$  increasingly exceeds the intrinsic FWHM when reducing  $z_0$ .

reaches large values because the voltage, which is applied over nanometer-scaled gaps, induces strong electrostatic forces ( $\propto 1/z_0^2$ ) (fig. S4) (25).

Furthermore, the dynamics of the NOEM switch are determined by its geometrical parameters similar to those of a ruler that extends beyond the edge of a table. Shorter suspensions (i.e., stiffer spring) and a lighter mass result in faster ruler oscillations ( $f_{res}$ ). Here, we make the overhang as short and thin as possible. The combination of small moving mass, large forces, and small mechanical quality ( $Q$ ) factors enables tens of nanosecond switching at CMOS driving voltages.

The fabricated resonators are shown in Fig. 2. The drop port was omitted to probe the resonator's intrinsic OEM properties. Vertical HPP waveguide geometries were uniformly created by depositing and selectively removing a sacrificial alumina layer, by wet-etching to a typical undercut value of  $\approx 1.1\text{ }\mu\text{m}$ . Here, atomic layer deposition provides  $z_0$  with atomic-level precision. The critical feature size is the lateral waveguide-disc separation ( $w > 120\text{ nm}$ ), which is achievable with low-cost photolithography.

The cavity's intrinsic  $Q$  factor ( $\propto 1/\text{FWHM}$ ) was measured by varying  $w$  (Fig. 2C). At critical coupling,  $Q_{intrinsic} = 2 \cdot Q_{loaded} \approx 7000$ , which translates to propagation lengths and losses of  $395 \pm 70\text{ }\mu\text{m}$  and  $0.01 \pm 0.002\text{ dB}/\mu\text{m}$ , respectively (fig. S6) (25). The reason for such low plasmonic losses is multifold. First, ohmic losses are proportional to the fraction of the optical-mode energy penetrating the metal. This fraction drops with decreasing permittivity of the gap dielectric; air or vacuum provides a low dielectric permittivity, minimizing loss (fig. S7) (25). Second, excess losses induced by typical adhesion layers for gold (27) are minimized as air exposure oxidizes the 2-nm titanium adhesion layer used here. Third, the interaction of the HPP mode with the gold membrane is mostly restricted to the smooth metal surface facing the gap, reducing scattering losses (28).

Characterization of the switching capability (see Fig. 2D) yields a  $\Delta\lambda_{res} > 6\text{ nm}$ , which equals five times the FWHM. The nonlinear red shift is expected from electro-mechanical effects as the growing proximity of the metal membrane increases  $\Delta n_{eff}$  (25). Furthermore, the nonlinear

dependence allows one to enhance the voltage sensitivity of the resonance shift ( $\Delta\lambda_{res}/V$ ) to  $\approx 10\text{ nm}/V$  (i.e.,  $\approx 1.25\text{ THz}/V$ ) by biasing the device with 1 V (25). The demonstrated tuning capability enables the compensation of thermally induced shifts in  $\lambda_{res}$ , which are typically hundreds of picometers per kelvin (14, 29). The large values of  $G_{OM}$ ,  $G_{EM}$ , and  $Q$  factors allow reduction of the required actuation distance to a few nanometers and, correspondingly, the switching time to tens of nanoseconds (see Fig. 3).

The suspended membrane features a  $f_{res}$  of  $\approx 12\text{ MHz}$ . The small mechanical  $Q$  factor and the roll-off in modulation at lower frequencies is attributed to squeeze-film damping and stiffening; for example, air compression increases the stiffness at higher frequencies and smaller gaps and thus reduces the actuation (25). This effect can be overcome by combining vacuum packaging and advanced driving signals (30). Figure 3B shows a two-step driving scheme, in which the applied drive voltages (I) and (III) exceeded the steady-state voltages (II) and (IV) at the start of the individual on- and off-switching pulses. This resulted in rise and fall times of 60 and 100 ns, respectively, where the



**Fig. 2. False-colored scanning electron microscopy images and measured device properties.** (A) Perspective view and transmission spectrum. The small cavity volume results in a free spectral range (FSR) of 45 nm. (B) Focused-ion beam cross section. Air gaps ( $z_0$ ) of 35 or 55 nm have been realized. Gap length, 600 nm. The inset shows a simulated optical field, which is strongest in the gap.  $E_{\text{norm}}$ , absolute value of the electric field; a.u., arbitrary units. (C) ER (blue triangles) and loaded  $Q$  factor (red circles) versus waveguide-disc separation ( $w$ ) for  $z_0 \approx 55$  nm. The ER peaks at  $\approx 200$  nm, indicating critical coupling. (D)  $\Delta\lambda_{\text{res}}$  (blue to green) and FWHM (red to yellow) as a function of voltage for  $z_0 \approx 35$  nm. The inset illustrates complete optical switching with a 200-mV difference. For (C) and (D), the 95% confidence intervals are approximately equal to the symbol size.

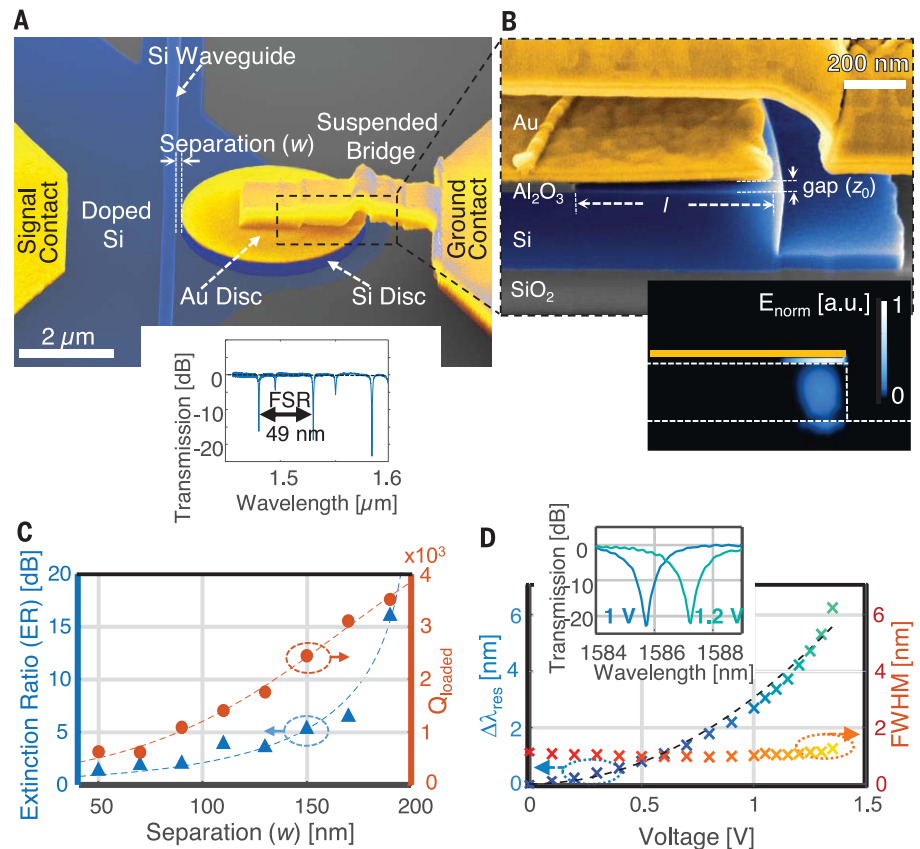
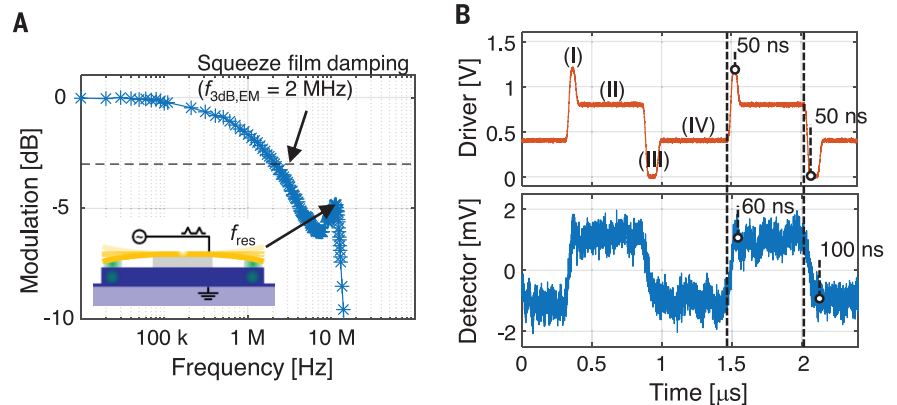


**Fig. 3. Time dynamics.** (A) Modulation response for a sinusoidal driving signal. The inset shows the mode shape of the fundamental mechanical eigenfrequency.  $k$ , thousand;  $M$ , million. (B) Utilizing more complex driving signals (red) enables optical (blue) rise and fall times on the order of tens of nanoseconds. The optical contrast between on and off state exceeds 90%.



difference is due to electrostatic actuation forces that are larger than the spring restoring forces. The devices were switched with megahertz frequencies over hours (billions of switching cycles) without degradation of the signal quality. The estimated electrical power consumption was  $\approx 600$  and  $12$  nW for a peak-to-peak driving voltage of  $1.4$  and  $0.2$  V, respectively (25). Further optimization could yield fall and rise times approaching  $\approx 10$  ns (fig. S5) (25).

Subsequently, we performed 1-by-2 switching experiments (see Fig. 4A). The through- and drop-port transmission spectra are plotted in Fig. 4B. Coupling the resonator to the drop

port broadens the FWHM (optical bandwidth) from  $\approx 1$  nm (125 GHz) to  $\approx 2.5$  nm (350 GHz) (see Fig. 4B). Still, a  $1.4$ -V driving voltage yielded a  $\Delta\lambda_{\text{res}}$  ( $\approx 6.2$  nm) that exceeded multiple FWHMs. This enabled light routing with a cross-talk below  $-15$  dB, drop-port insertion loss ( $IL_D$ ) of  $\approx 2$  dB, and through-port insertion loss ( $IL_T$ ) of  $\approx 0.1$  dB (fig. S10) (25). Optimization may further reduce  $IL_T$  to  $\approx 0.01$  dB and  $IL_D$  to  $\leq 0.5$  dB (fig. S9) (25). This loss asymmetry is ideal for applications in  $N$ -by- $N$  cross-switching grids, where  $N$  is any number, as envisioned in Fig. 4D. Because light experiences  $IL_D$  only once when propagating

through the network, accumulated losses (i.e., path of the red light beam) are dominated by through-port loss (i.e., overall loss  $\leq 2N \cdot IL_T + IL_D$ ). This would result in an average loss-to-port count ratio of  $0.12$  dB per port for an optimized  $15$ -by- $15$  network.

We present devices that challenge the common presumption that opto-electro-mechanics is a slow and bulky technology that requires high driving voltages. We demonstrate NOEM switches whose distinct compactness paves the way for high-density optical switch fabrics that are directly cointegrated with CMOS driving circuits. For instance,  $200$  switches and their

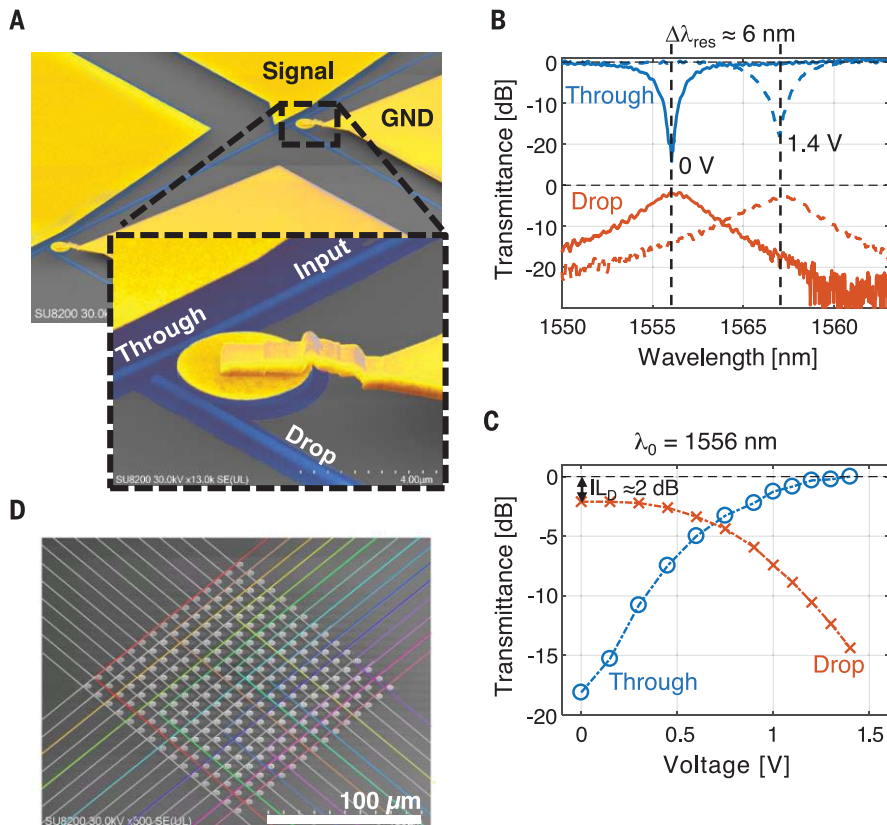


**Fig. 4. Performance of 1-by-2 NOEMS.** (A) Perspective false-colored scanning electron microscopy image of two fabricated NOEMS. GND, electrical ground. (B) Measured power spectrum of light coupled to the through port (blue) and the drop port (red) under 0 V (solid) and 1.4 V (dashed) bias. (C) Through-port (blue circles) and drop-port (red crosses) transmittance over voltage. (D) Low through-port losses are beneficial for switching architectures such as cross-grid networks envisioned here, where light (various rainbow colors) only needs to be switched once to a drop port while propagating through a 15-by-15 network. In (C), the 95% confidence interval is smaller than the symbol size.  $\lambda_0$ , probing wavelength.

electrical drivers could be integrated on an area as small as the cross section of a single human hair. Beyond that, the strong OEM interaction and low-loss could enable nonresonant functional units such as phase shifters and intensity modulators for purposes such as light detection and ranging (LIDAR) applications. The performance of phase shifters is typically evaluated by the voltage-length product  $V_\pi L$ , which states the minimal combination of  $\pi$  phase-shift voltage times device length. The HPP prototypes demonstrated here already feature a  $V_\pi L = 27 \pm 4$  V- $\mu$ m, which, in combination with low propagation losses ( $\alpha = 0.026 \pm 0.006$  dB/ $\mu$ m), represents a substantial improvement over the state-of-the-art electro-optical switches (fig. S1) (25). These switches could form the building blocks

of optical field-programmable gate arrays and trigger a technological revolution similar to the one enabled over the past few decades by electrical field-programmable gate arrays.

#### REFERENCES AND NOTES

1. X. Lin et al., *Science* **361**, 1004–1008 (2018).
2. M. C. Estevez, M. Alvarez, L. M. Lechuga, *Laser Photonics Rev.* **6**, 463–487 (2012).
3. Q. Cheng, S. Rumley, M. Bahadori, K. Bergman, *Opt. Express* **26**, 16022–16043 (2018).
4. J. Wang et al., *Science* **360**, 285–291 (2018).
5. D. A. B. Miller, *J. Lightwave Technol.* **35**, 346–396 (2017).
6. J. Sun, E. Timurdogan, A. Yaacobi, E. S. Hosseini, M. R. Watts, *Nature* **493**, 195–199 (2013).
7. V. R. Almeida, C. A. Barrios, R. R. Panepucci, M. Lipson, *Nature* **431**, 1081–1084 (2004).
8. M. Stegmaier, C. Rios, H. Bhaskaran, C. D. Wright, W. H. P. Pernice, *Adv. Opt. Mater.* **5**, 1600346 (2017).

9. A. Emboras et al., *Nano Lett.* **16**, 709–714 (2016).
10. M. Ayata et al., *Science* **358**, 630–632 (2017).
11. F. Bonaccorso, Z. Sun, T. Hasan, A. C. Ferrari, *Nat. Photonics* **4**, 611–622 (2010).
12. M. Z. Alam, I. De Leon, R. W. Boyd, *Science* **352**, 795–797 (2016).
13. C. Wang et al., *Nature* **562**, 101–104 (2018).
14. E. Timurdogan et al., *Nat. Commun.* **5**, 4008 (2014).
15. C. Sun et al., *Nature* **528**, 534–538 (2015).
16. L. Midolo, A. Schliesser, A. Fiore, *Nat. Nanotechnol.* **13**, 11–18 (2018).
17. T. J. Seok, N. Quack, S. Han, R. S. Muller, M. C. Wu, *Optica* **3**, 64 (2016).
18. S. Abe, K. Hane, *IEEE Photonics Technol. Lett.* **25**, 675–677 (2013).
19. M. L. Brongersma, V. M. Shalae, *Science* **328**, 440–441 (2010).
20. B. J. Roxworthy, V. A. Aksyuk, *Optica* **5**, 71 (2018).
21. B. S. Dennis et al., *Nat. Photonics* **9**, 267–273 (2015).
22. J. B. Khurgin, *Nat. Nanotechnol.* **10**, 2–6 (2015).
23. C. Haffner et al., in *Conference on Lasers and Electro-Optics, OSA Technical Digest (Paper STh3H.4*, Optical Society of America, Washington, DC, 2019).
24. R. F. Oulton, V. J. Sorger, D. A. Genov, D. F. P. Pile, X. Zhang, *Nat. Photonics* **2**, 496–500 (2008).
25. See supporting information in the supplementary materials.
26. X. Yang, Y. Liu, R. F. Oulton, X. Yin, X. Zhang, *Nano Lett.* **11**, 321–328 (2011).
27. M. Todeschini, A. Bastos da Silva Fanta, F. Jensen, J. B. Wagner, A. Han, *ACS Appl. Mater. Interfaces* **9**, 37374–37385 (2017).
28. P. Nagpal, N. C. Lindquist, S.-H. Oh, D. J. Norris, *Science* **325**, 594–597 (2009).
29. C. Haffner et al., *Nature* **556**, 483–486 (2018).
30. M. Imboden et al., *IEEE Control Syst. Mag.* **36**, 48–76 (2016).

#### ACKNOWLEDGMENTS

We thank C. Hierold, J. Strait, M. Davanco, J. A. Liddle, N. Zhitenev, and U. Drechsler for valuable discussions. **Funding:** ERC grant PLASILOR (640478). C.H. acknowledges support under a Cooperative Research Agreement between the University of Maryland and the National Institute of Standards and Technology Physical Measurement Laboratory, award 70NANB14H209, through the University of Maryland. C.H. acknowledges support by the Hans-Eggenberger Foundation. M.B. acknowledges funding from the SNSF Ambizione grant (173996). **Author contributions:** C.H. conceived the concept and supervised the project. C.H., A.J., F.M., and D.C. designed the switch and performed numerical optimization. C.H., A.J., and Y.F. fabricated the modulator and developed the required process technology. C.H., A.H., M.D., M.B., M.M., and V.A.A. designed and performed the experiments. All authors discussed and analyzed the data. C.H., A.J., M.M., H.J.L., V.A.A., and J.L. wrote the manuscript. **Competing interests:** J.L. is involved in activities toward commercializing high-speed plasmonic modulators at Polariton Technologies Ltd. Part of the work is subject to a patent application by C.H., V.A.A., H.J.L., D.C., J.L., M.M., and A.J. The remaining authors declare no competing interests. **Data and materials availability:** All data are available in the manuscript or the supplementary materials.

#### SUPPLEMENTARY MATERIALS

science.sciencemag.org/content/366/6467/860/suppl/DC1  
Materials and Methods  
Supplementary Text  
Figs. S1 to S10  
Table S1  
References (31–64)

5 August 2019; accepted 21 October 2019  
10.1126/science.aay8645



## GLASSES

# Highly ductile amorphous oxide at room temperature and high strain rate

Erkka J. Frankberg<sup>1,2,3\*</sup>, Janne Kalikka<sup>4</sup>, Francisco García Ferré<sup>3,†</sup>, Lucile Joly-Pottuz<sup>2\*</sup>,  
Turkka Salminen<sup>5</sup>, Jouko Hintikka<sup>1</sup>, Mikko Hokka<sup>1</sup>, Siddardha Koneti<sup>2</sup>, Thierry Douillard<sup>2</sup>,  
Bérangère Le Saint<sup>2</sup>, Patrice Kreiml<sup>6</sup>, Megan J. Cordill<sup>6</sup>, Thierry Epicier<sup>2</sup>, Douglas Stauffer<sup>7</sup>,  
Matteo Vanazzi<sup>3</sup>, Lucian Roiban<sup>2</sup>, Jaakko Akola<sup>4,8</sup>, Fabio Di Fonzo<sup>3</sup>,  
Erkki Levänen<sup>1</sup>, Karine Masenelli-Varlot<sup>2</sup>

Oxide glasses are an integral part of the modern world, but their usefulness can be limited by their characteristic brittleness at room temperature. We show that amorphous aluminum oxide can permanently deform without fracture at room temperature and high strain rate by a viscous creep mechanism. These thin-films can reach flow stress at room temperature and can flow plastically up to a total elongation of 100%, provided that the material is dense and free of geometrical flaws. Our study demonstrates a much higher ductility for an amorphous oxide at low temperature than previous observations. This discovery may facilitate the realization of damage-tolerant glass materials that contribute in new ways, with the potential to improve the mechanical resistance and reliability of applications such as electronic devices and batteries.

Inorganic oxide glasses show great promise for modern electronics, including potential uses in optoelectronics, flexible electronics, photovoltaics, single-electron transistors, and battery technologies (*1–6*). These glasses allow for a wide range of tailored, functional properties, from full dielectrics to tuned semiconductors coupled with visible light transparency, and good chemical and thermal stability. However, in practical terms inorganic oxide glasses are considered brittle, which has led to the current design paradigm of glass and ceramic materials.

In the thermodynamics of inorganic glasses, relaxation mechanisms, such as viscous flow and viscous creep, are thought to require high temperatures to activate. Viscous flow and viscous creep are separated by a notion that creep is always activated by external loading in addition to thermal activation. Above a certain critical temperature, the glass transition temperature ( $T_g$ ), bulk glass softens to a point where relaxation mechanisms activate and allow viscosity measurements. Viscosity is the proportionality factor of stress needed for a bulk glass to flow at a selected speed or strain rate. Below  $T_g$ , creep of an inorganic glass under its own gravity slows to the extent that it takes tens

of millions of years to detect any permanent deformation by viscous mechanisms (*7–10*). Therefore, in practice, we cannot make room temperature measurements of glass viscosity, and an oxide glass below  $T_g$  is effectively considered a solid. The evidence for this limitation is clear, but the current theory does not allow for the possibility of mechanical activation by an external stress field gradient, such as a gradient that occurs when a mobile device with a touch screen is dropped on a hard floor.

Moreover, oxide glasses are believed to be brittle at room temperature owing to their lack of active plastic deformation mechanisms. Under critical elastic load, stress concentrates on the most severe preexisting geometrical flaw, leading to a sudden, catastrophic failure (*11*). Nevertheless, the most profound evidence for plastic relaxation occurring in oxide glasses below  $T_g$  is the simple hardness test. Hardness of a bulk glass or any other material is measured from the dimensions of a permanent, residual indent made by a diamond indenter at room temperature. Permanent deformation is possible in glasses through diffusion-based mechanisms. Oxide glasses are known to permanently deform by densification (*12*) and shear flow (*13, 14*) under contact and hydrostatic loads. However, the plastic deformation mechanisms at room temperature are believed to be limited to geometrically confined loading modes, such as bulk indentation. It is also believed that brittleness always severely limits the use of glass structures under more-realistic, unconfined loading conditions, such as bending and pulling. Experimental observations of  $\text{Al}_2\text{O}_3$  at the nanoscale have been mixed: Some measurements show prerequisites for plastic deformation at room temperature (*15–18*), whereas others display fully brittle behavior (*19–21*).

We provide evidence that, under sufficient load, the viscosity of amorphous  $\text{Al}_2\text{O}_3$  ( $\alpha\text{-Al}_2\text{O}_3$ ) thin-films can be measured at room temperature. Furthermore, the viscous creep mechanism can induce large and fast permanent relaxation without substantial thermal activation. We consider the inorganic oxide glass to be in a supercooled liquid state, even if far below  $T_g$ . Under these conditions, the plastic relaxation requires a considerable external driving force, but we found that this behavior is possible, even within short time scales from seconds to nanoseconds.

We made micromechanical shear-compressive (Fig. 1A) and tensile (Fig. 1B) measurements and performed atomistic simulations to determine the viscosity of defect-free  $\alpha\text{-Al}_2\text{O}_3$ . The viscosity ( $\eta$ ) of  $\alpha\text{-Al}_2\text{O}_3$  follows a log-log linear power rule as a function of the strain rate ( $\dot{\epsilon}$ ) (Fig. 1C). The power rule indicates that as the strain rate approaches zero, the viscosity of the supercooled liquid approaches infinity, equivalent to a quasi-solid state as

$$\lim_{\dot{\epsilon} \rightarrow 0} \eta_{\alpha\text{-Al}_2\text{O}_3}(\dot{\epsilon}) = \infty$$

We detected no transition from solidlike to liquidlike behavior, and the viscosity must be a finite quantity for flow to occur in this supercooled liquid state. There is a strong decrease in viscosity as the strain rate increases, and notably-low simulated viscosity values were measured at simulated strain rates  $>10^8 \text{ s}^{-1}$ . Extrapolating the results to very high strain rates suggests a 1 Pa-s viscosity for  $\alpha\text{-Al}_2\text{O}_3$  at room temperature, comparable to glycerol at 300 K. This indicates that flow stress cannot substantially increase beyond the limit needed for atoms to diffuse through the glass network, which is reflected as a very low viscosity at very high strain rates.

We measured the viscosity during the plastic flow at flow stress, which is defined as the stress measured after the glass structure yields. No contrast changes were detected in the samples either during the plastic flow or by ex situ observations using transmission electron microscopy (TEM). We believe these observations, combined with no evidence for shear bands, indicate that the samples remained amorphous during the plastic deformation (supplementary text, section S2). The simulated plastic flow stress in tensile (Fig. 2A) and compressive (Fig. 2B) loading agrees closely with the respective experimental results, and, depending on the loading mode, a total strain of up to 100% can be measured in situ along the loading axis without fracture. We were able to visually record (Fig. 2, insets) the dynamic plastic deformation throughout each experiment in addition to comparing the deformation to numerical data (supplementary text, section S3).

We detected a fracture only in the experimental tensile test after 15% of total strain and

<sup>1</sup>Unit of Materials Science and Environmental Engineering, Tampere University, Tampere, Finland. <sup>2</sup>Université de Lyon, INSA-Lyon, UCBL, MATEIS, CNRS UMR 5510, Villeurbanne, France. <sup>3</sup>Center for Nano Science and Technology @Polimi, Istituto Italiano di Tecnologia, Milano, Italy. <sup>4</sup>Computational Physics Laboratory, Tampere University, Tampere, Finland. <sup>5</sup>Tampere Microscopy Center, Tampere University, Tampere, Finland. <sup>6</sup>Erich Schmid Institute of Materials Science, Austrian Academy of Sciences, Leoben, Austria. <sup>7</sup>Bruker Nano Surfaces, Bruker Inc., Eden Prairie, MN, USA. <sup>8</sup>Department of Physics, Norwegian University of Science and Technology, Trondheim, Norway.  
\*Corresponding author. Email: erkka.frankberg@tuni.fi (E.J.F.); lucile.joly-pottuz@insa-lyon.fr (L.J.-P.) †Present address: Corporate Research, ABB Switzerland Ltd., Baden-Dättwil, Switzerland.

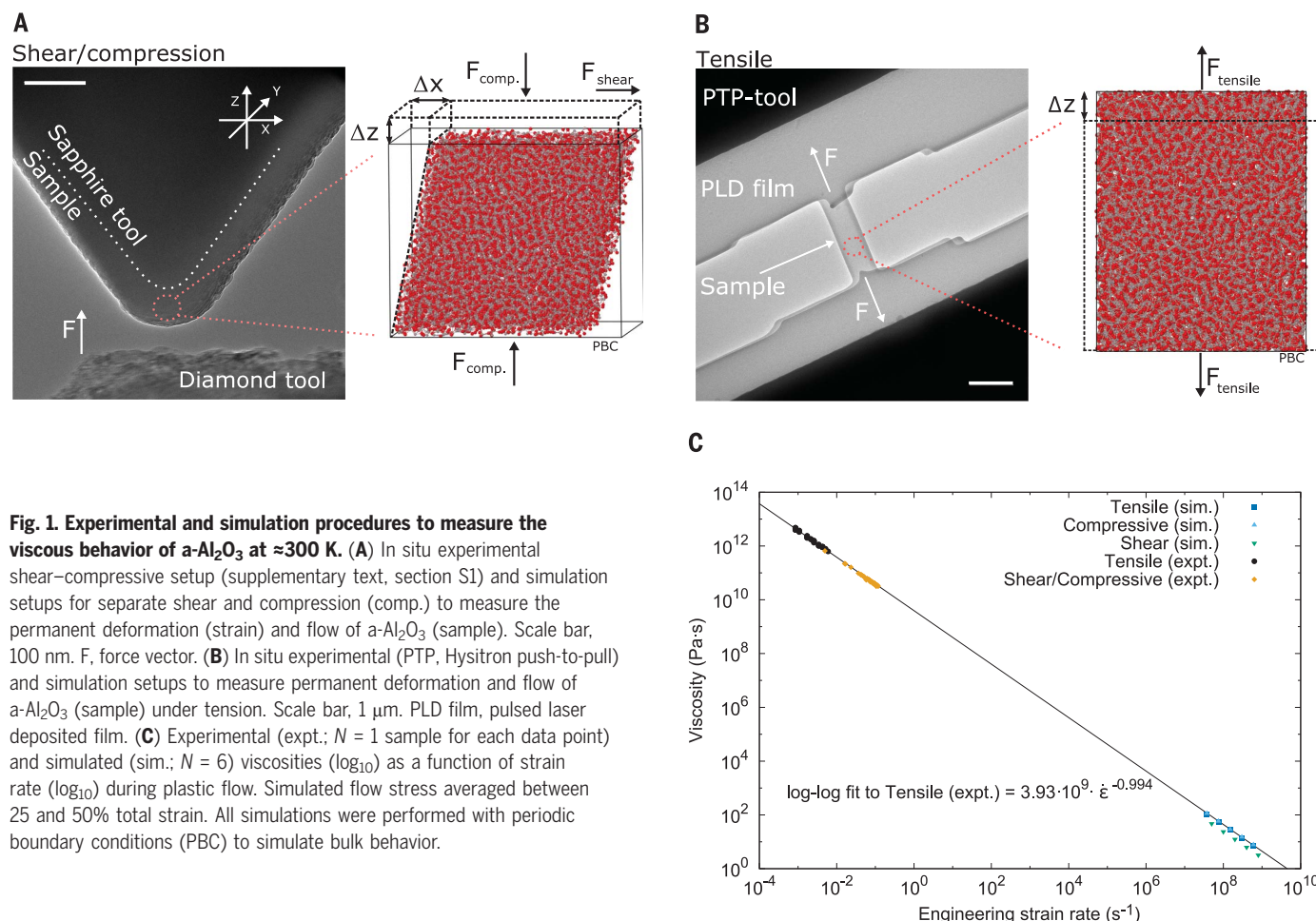


**Fig. 1. Experimental and simulation procedures to measure the viscous behavior of a-Al<sub>2</sub>O<sub>3</sub> at ~300 K.** (A) In situ experimental shear-compressive setup (supplementary text, section S1) and simulation setups for separate shear and compression (comp.) to measure the permanent deformation (strain) and flow of a-Al<sub>2</sub>O<sub>3</sub> (sample). Scale bar, 100 nm. *F*, force vector. (B) In situ experimental (PTP, Hysitron push-to-pull) and simulation setups to measure permanent deformation and flow of a-Al<sub>2</sub>O<sub>3</sub> (sample) under tension. Scale bar, 1 μm. PLD film, pulsed laser deposited film. (C) Experimental (expt.; *N* = 1 sample for each data point) and simulated (sim.; *N* = 6) viscosities (log<sub>10</sub>) as a function of strain rate (log<sub>10</sub>) during plastic flow. Simulated flow stress averaged between 25 and 50% total strain. All simulations were performed with periodic boundary conditions (PBC) to simulate bulk behavior.

5 to 8% of plastic strain, depending on the interpretation of the yield stress. We found that the fracture occurred in a localized region affected by ion damage, which is induced to the sample during sample preparation (supplementary text, sections S4 and S5). Ion damage leads to void nucleation, growth, and transformation into a sharp crack at the edge of the sample (fig. S6), which eventually induces the fracture.

The scatter of flow stress values at varying strain rates is evidence of the time-dependent nature of the plastic flow we observed. A strain rate-dependent flow stress is typically observed for viscoplastic materials (22) and would be an important piece of evidence for the viscous relaxation mechanisms active in a-Al<sub>2</sub>O<sub>3</sub>. The force variation we measured during flow stress was two to three orders of magnitude higher than the nominal noise floor of the force measurement of the experiment (Fig. 3A), which verifies the connection between stress and strain rate. When the strain rate was changed, the flow stress changed with the proportion given by the viscosity of the supercooled liquid, and similar behavior was observed in both repeated experiments and simulations (Fig. 3).

The lack of contrast change in our TEM observations suggests that the cumulative plastic deformation was likely driven by homogenous diffusion. We used our material model to determine plausible atomistic mechanisms that control the plastic deformation in a-Al<sub>2</sub>O<sub>3</sub> at room temperature. The first activated plasticity mechanism from our model is related to the change in the glass density in both tensile and compressive loading. The simulated density has a permanent reduction under tensile load when returning to 1 atm pressure (Fig. 4A). The permanent decrease was by 0.5 to 1.4%, which accounts for only 0.9 to 1.5% of the permanent elongation (or 0.006 to 0.021 in strain) of the model along the axis under tension. The density saturates at 20 to 25% of total tensile strain, and at higher strains the plastic deformation takes place solely by steady-state viscous creep (Fig. 4A). We found flow stress saturation at ~25% of tensile strain (fig. S5A), paralleling the density saturation.

Both plasticity phenomena occur by bond switching in our simulations, as shown by the evolution of nearest-neighbor bonding in both tension and compression as a function of strain (Fig. 4B). The interchange and rotation of

bonds, with the resulting atomic translocation, are fully accommodated without density changes, which allows for more versatile deformation in shear and tensile loading modes. This is supported by the unchanged coordination number, as bond changes during plastic flow are predominantly swaps. In other words, atoms retain the local environment while changing neighboring atoms (Fig. 4B and figs. S23 and S24).

The atomistic mechanisms of the plastic deformation we measured have both local and collective features (supplementary text, section S6). Our simulations [local plastic strain  $D^2_{\min}$  (see materials and methods for detailed definition), strain range  $\Delta\epsilon = 0.01$ ] show separate areas of high and low plastic tensile strain that correlate with flow stress data (Fig. 4C, panel a). The diffusion of atoms increases when the stress decreases, and vice versa (Fig. 4C, panel b, and fig. S10). Therefore, plasticity in a-Al<sub>2</sub>O<sub>3</sub> occurs when weaker local atomic groups are driven to yield by the accumulation of individual bond-switching events. An individual bond-switching event is shown to occur at the edge of a locally yielding atom group (Fig. 4C, panel c). In this event, the central



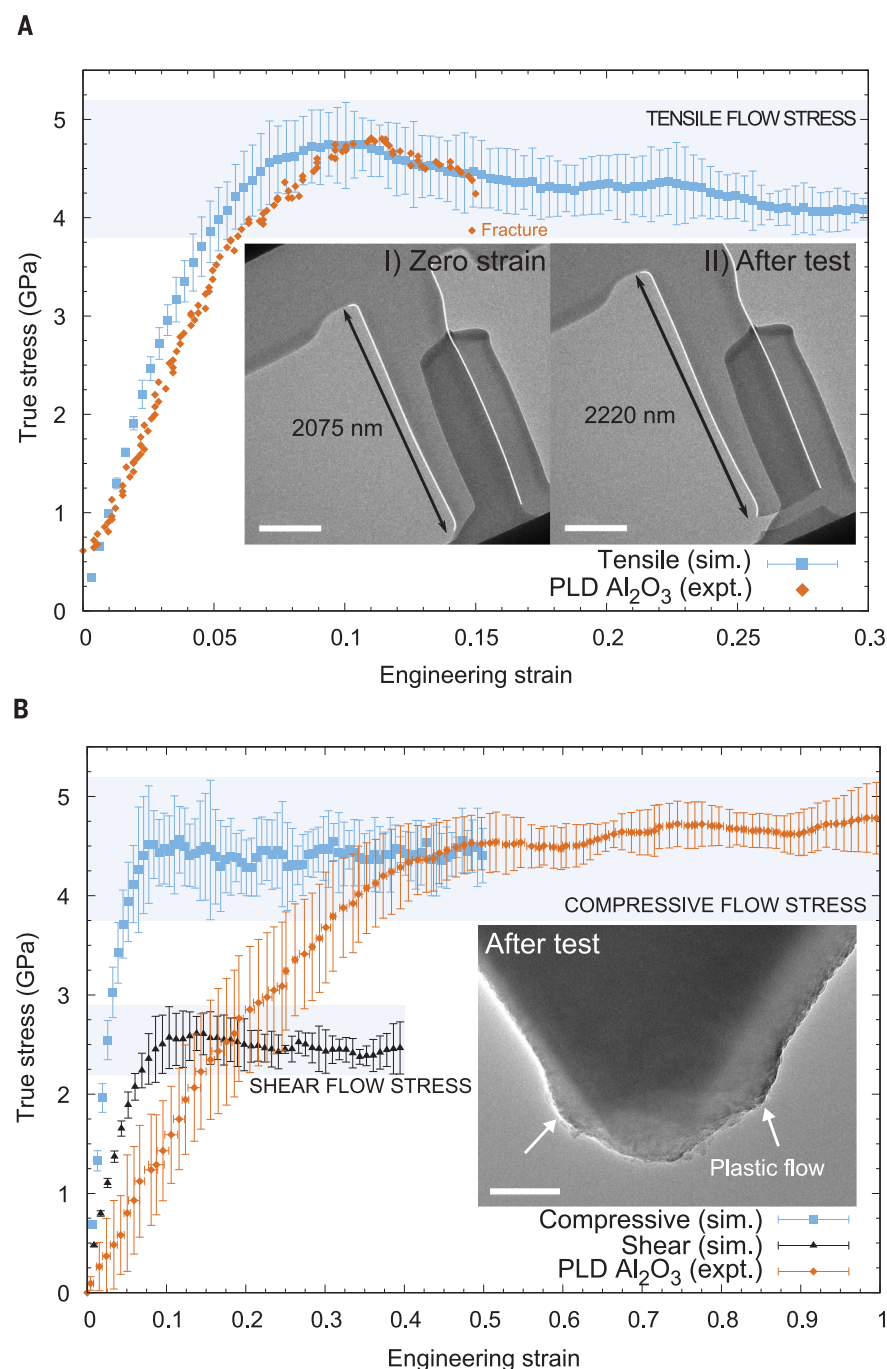


**Fig. 2. Mechanical response of a-Al<sub>2</sub>O<sub>3</sub> at room temperature: simulations and experimental data.**

(A) Average simulated ( $N = 30$ ) and experimental (electron beam on,  $N = 1$ ) tensile stress as a function of strain. Inset I shows the length of the free-standing tensile sample at the onset of elastic contact (strain 0.0), and inset II shows the length of the tensile sample after its fracture from the bottom part (scale bars, 500 nm). In the insets, the sample is highlighted with white borders, while another piece of the PLD film partially overlaps the sample in the image but does not interact with the sample during the test. (B) Average simulated ( $N = 30$ ) and average experimental (electron beam off,  $N = 7$ ) shear-compression stress as a function of strain, while the inset shows a deformed sample after the test (scale bar, 100 nm). Note that the experimental true stress is a compound of mixed shear and compression loading. Simulated error bars show the maximum variation (minimum to maximum) measured with different strain rates ( $37.5 \times 10^6$  to  $6.0 \times 10^8$  s<sup>-1</sup>), while experimental error bars show standard deviation between samples.

Al atom (gold) initially has four oxygen neighbors with open space next to it. The Al atom moves into the open space while replacing one oxygen bond with a new one. After this, it moves farther and gains two new oxygen neighbors that are kept for  $\sim 150$  ps. The Al atom stays bonded to five oxygen atoms until the end of loading. This type of bond switching is well known to occur in disordered materials (23, 24). Over a large cumulative strain, the localized plastic strain events vary randomly (movie S1) to accumulate an overall homogeneous plastic flow across the structure. The distribution of the cumulative plastic tensile strain ( $D^2_{\min}$ ,  $\Delta\epsilon = 0.5$ ) has intertwined areas of high and low  $D^2_{\min}$  with no large volumes of either (Fig. 4D; for compression, see fig. S11). This shows that the cumulative atomic movement related to plastic flow is homogeneous across the structure, with momentary large fluctuations. The fast relaxation we observed by atomic diffusion occurs far below the bulk  $T_g \approx 973$  K (25), which is not anticipated by the thermodynamic theory of inorganic glasses.

We considered several potential issues that could produce spurious results. Sample heating from the electron beam is limited to a maximum of 5 K (26), and plastic strain-induced adiabatic heating occurs only after yielding (supplementary text, sections S7 and S8). Adiabatic heating may contribute to our observed flow stress magnitude. Electron beam damage can decrease flow stress, as has been observed for amorphous SiO<sub>2</sub> (a-SiO<sub>2</sub>) (23, 27). We performed a dedicated mechanical test, in which the electron beam was switched off during the steady-state viscous creep of the a-Al<sub>2</sub>O<sub>3</sub> thin-film (supplementary text, section S9). The flow stress level did not change enough when the beam was off for us to interpret it as occurring outside the normal stress fluctuation caused by the dynamic strain rate. We performed multiple experiments in full beam-off conditions that verified this behavior. Together these experiments rule out the possibility that the electron beam had a substantial effect on the experimental test results. Moreover, it is possible to induce plasticity in amorphous oxides via a “size effect” by substantially increasing the ratio of surface atoms to bulk atoms (18, 24). However, our sample dimensions lead to bulk-like properties such as  $T_g$  and fracture toughness (supplementary text, section S10). The measured  $K_{Ic} = 3.1$  MPa $\sqrt{m}$  (where  $K_{Ic}$  is mode I fracture toughness) is similar to typical bulk Al<sub>2</sub>O<sub>3</sub>. However, because our initial flaw size was measured in situ to be sufficiently small or nonexistent, the stress field can reach a magnitude in which the material yields, even at room temperature. We also modified the molecular dynamic simulation setup (cell size and quenching method) for a-Al<sub>2</sub>O<sub>3</sub> to rule out artificial ductility, and we observed no fracture (supplementary text, sections S11 and S12).

Our results for  $\alpha\text{-Al}_2\text{O}_3$  differ from previous results obtained for  $\alpha\text{-SiO}_2$  (23, 24, 27). Bulk tensile plastic flow has not been observed in free-standing membranes or nanowires of  $\alpha\text{-SiO}_2$  at ambient conditions (24, 27). Densification accounts for 80 to 90% of the measured plastic deformation during indentation for  $\alpha\text{-SiO}_2$  (initiated between 9 and 13 GPa stress, at room temperature) that activates before viscous creep (13, 28). Tensile experiments with pristine  $\alpha\text{-SiO}_2$  samples under ambient conditions have reached only  $\sim 5$  GPa before fracture (24, 27), so finding zero plasticity at this stress level is not surprising. A tensile fracture is likely initiated by the intrinsic and interconnecting cavities (voids, free volume) found in the atomic structure of  $\alpha\text{-SiO}_2$  (29), which are far more abundant in  $\alpha\text{-SiO}_2$  [65.7 vol. % (30)] than in  $\alpha\text{-Al}_2\text{O}_3$  (8.7 vol. %) (supplementary text, section S13). The difference in cavity volumes is in line with the difference in atom densities, as  $\alpha\text{-SiO}_2$  has  $0.066 \text{ atoms}/\text{\AA}^3$  (31) whereas  $\alpha\text{-Al}_2\text{O}_3$  has approximately  $0.096 \text{ atoms}/\text{\AA}^3$ . The intrinsic cavities present in the  $\alpha\text{-SiO}_2$  structure were already proposed as the possible origin of fracture, in 2003 by Célarié *et al.* (32). Since then, mechanical properties of  $\alpha\text{-SiO}_2$  and the presence of cavities have been further studied with experiments and simulations (24, 27, 29, 30).

Bond switching is also one potential source for mechanical relaxation in  $\alpha\text{-SiO}_2$  (23, 24). However, our simulations show 8 to 25 times greater potential for bond switching in  $\alpha\text{-Al}_2\text{O}_3$  compared with  $\alpha\text{-SiO}_2$  (24), explaining the large plastic strain we observed in  $\alpha\text{-Al}_2\text{O}_3$  (supplementary text, section S11). Under tension, the preexisting cavities spatially inhibit bond switching from occurring in the  $\alpha\text{-SiO}_2$  structure, which likely results in further cavitation and fracture at low or zero plastic strain. Therefore, the preexisting cavities in the atomic structure of  $\alpha\text{-SiO}_2$ , coupled with the relatively high yield stress, present the most plausible hypothesis for the cause of tensile brittleness in  $\alpha\text{-SiO}_2$ .

We conclude that in parallel to flawlessness, the other main boundary condition for  $\alpha\text{-Al}_2\text{O}_3$  ductility at room temperature is the intrinsically-low effective activation energy, which is estimated to be  $Q_{\alpha\text{-Al}_2\text{O}_3} = 117.3 \pm 4.5 \text{ kJ/mol}$  (supplementary text, section S14), in accord with previous observations (33). This leads to plastic relaxation of  $\alpha\text{-Al}_2\text{O}_3$  by a stress gradient, because the stress concentrated on any pre-existing flaw (of intrinsic or manufacturing origin) remains below the critical value needed for fracture. Therefore, the flaw distribution coupled with the effective activation energy establish a criterion under which other inorganic oxide glasses may or may not achieve similar plasticity. This criterion provides a plausible path to find other oxide materials with similar ductile behavior and to explain

the origin of such behavior. In addition, a high Poisson's ratio measured for  $\alpha\text{-Al}_2\text{O}_3$  (16) could indicate potential plasticity in other oxides as well. Theoretically, there are no restrictions to apply the criterion to macroscopic bulk glasses. Instead, the challenge appears fully

technological, given that we lack processing technology that could produce such flaw-free amorphous materials at a macroscopic scale. For  $\text{Al}_2\text{O}_3$ , the challenge is also related to the low glass-forming capability. Conventional melt quench techniques typically fail

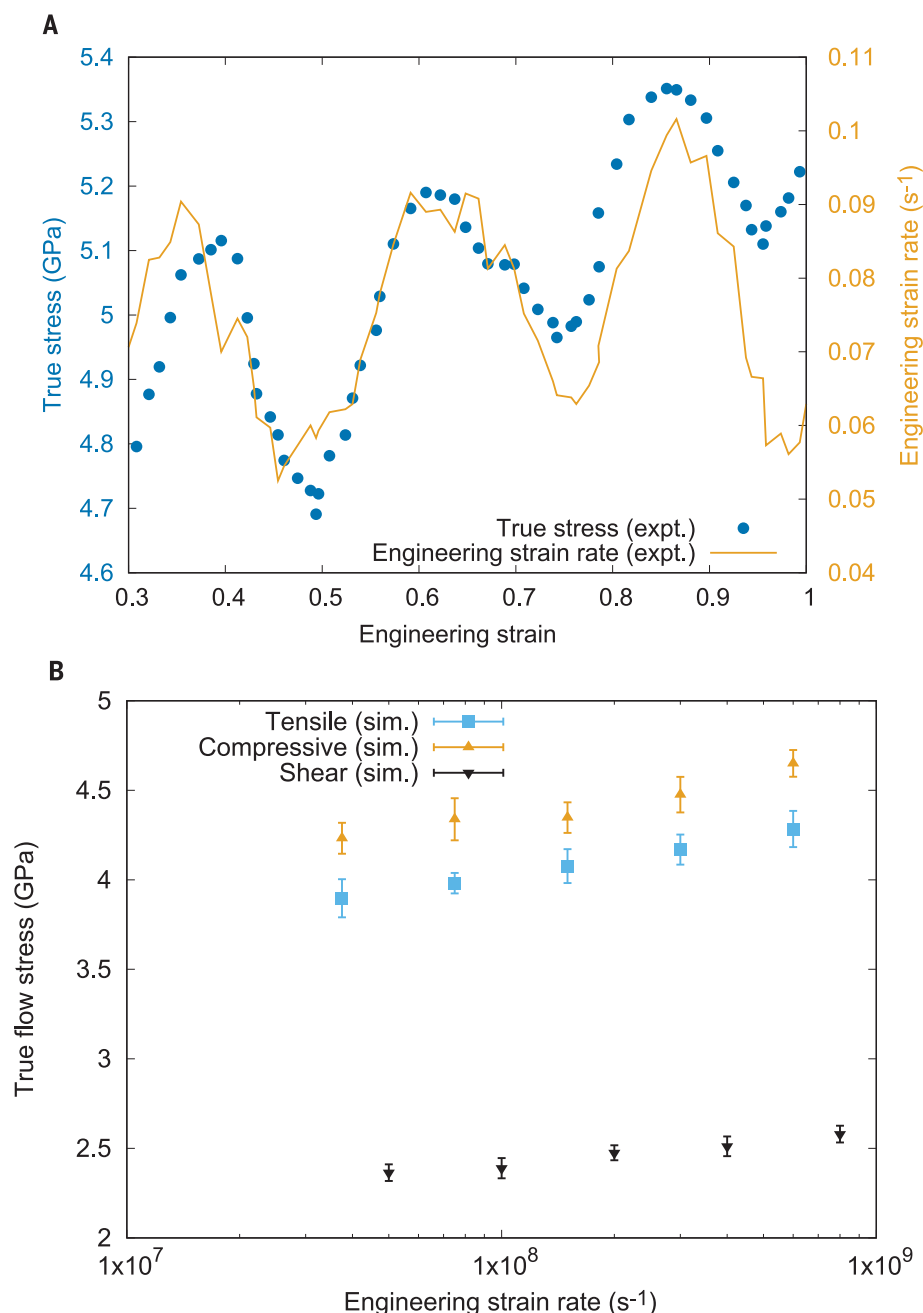


**Fig. 3. Time-dependent flow behavior of  $\alpha\text{-Al}_2\text{O}_3$  at room temperature: experimental and simulations.**

(A) Experimental flow stress and strain rate as a function of strain from a dedicated in situ TEM shear-compression test (electron beam on,  $N = 1$ ). The strain rate is measured using image correlation, and the data are filtered using the Savitzky-Golay method with 22 points of window and a fifth-order polynomial with the Origin software ([www.originlab.com/](http://www.originlab.com/)). Strain rate varies dynamically during the experimental measurement. True stress (GPa) is shown on the left scale, and engineering strain rate ( $\text{s}^{-1}$ ) is shown on the right scale. (B) Averaged simulated ( $N = 6$  for each data point) flow stress as a function of the strain rate measured and averaged between total strain of 25 and 50%. Error bars show standard deviation.



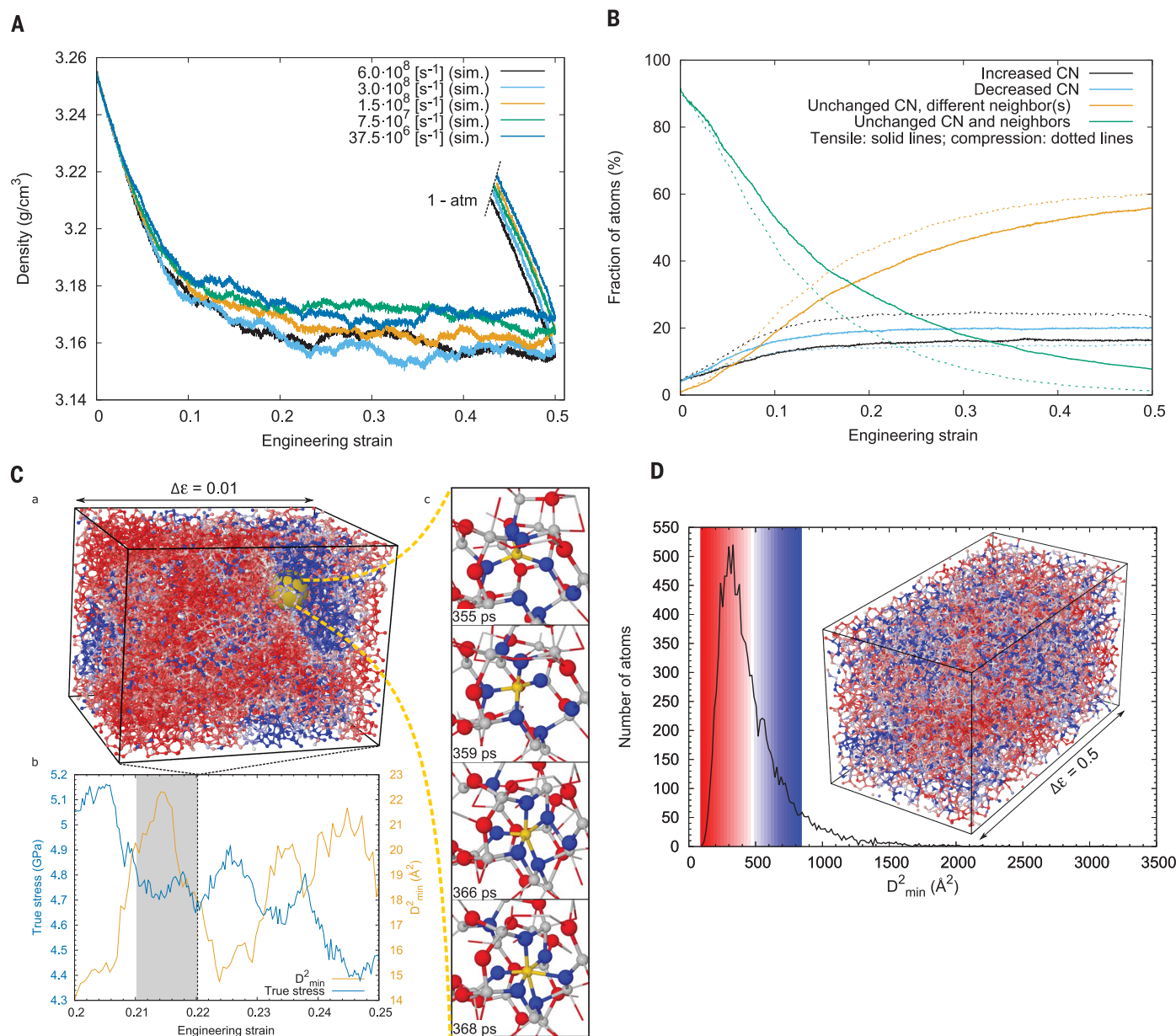


**Fig. 4. Plasticity mechanisms in  $\text{a-Al}_2\text{O}_3$ .** (A) Average simulated density ( $N = 6$ ) of  $\text{a-Al}_2\text{O}_3$  during tensile loading, starting from and ending at atmospheric pressure (1 atm). (B) Average changes ( $N = 3$ ) in bonding during tensile and compressive loading from 0.0 to 0.5 strain at  $37.5 \times 10^6 \text{ s}^{-1}$  strain rate (CN, coordination number). (C) Atomistic mechanism of room temperature plastic deformation in  $\text{a-Al}_2\text{O}_3$ . (a) Momentary distribution of the local plastic tensile strain at 0.22 strain, where  $D^2_{\min}$  is calculated from the preceding  $\Delta\epsilon = 0.01$  indicated by gray color in (b), which in addition shows the correlation between  $D^2_{\min}$  and flow stress data ( $N = 1$ ). (c) A single

bond-switching event occurring at the edge of a locally yielding atom group (central Al, gold; oxygen bound at least once to the central Al, blue; Al, gray; O, red). Strain rate of  $6.0 \times 10^8 \text{ s}^{-1}$  corresponds to  $\Delta\epsilon = 0.01$  in 16.67 ps. (D) Cumulative distribution of plastic tensile strain ( $D^2_{\min}$ ,  $\Delta\epsilon = 0.5$ ) in the  $\text{a-Al}_2\text{O}_3$  simulation cell between initial and final structure ( $7.5 \times 10^7 \text{ s}^{-1}$ ). Using a sliding color scale, atoms with below-average  $D^2_{\min}$  are shown in shades of red, average  $D^2_{\min}$  are white, and above-average  $D^2_{\min}$  are shades of blue. All atoms above the color scale are also in blue. Loading axes are shown by arrows.

to prevent crystallization of pure  $\text{Al}_2\text{O}_3$ ; success requires a processing method with an extreme quenching rate (e.g., pulsed laser deposition) or low temperature (e.g., atomic layer deposition) to retain the amorphous structure. Nevertheless, our results provide much-needed insight on the viscous relaxation behavior of inorganic glasses below  $T_g$  and present tools

to further study the thermodynamic theory of supercooled liquids. To improve the theory, we propose that, in addition to thermal activation, mechanical activation is equally and independently capable of inducing relaxation of a glass network.

In summary, we have shown that  $\text{a-Al}_2\text{O}_3$  is a substantially more ductile material than

previously believed. Our results indicate that plasticity by the viscous creep mechanism requires a dense and flaw-free glass network coupled with an effective activation energy that allows sufficient bond-switching activity. The plasticity could be directly applied in thin-film applications, such as electronics and batteries. In addition, the results indicate

that amorphous oxides have potential to be used as high-strength, damage-tolerant engineering materials. To realize this potential, we face a challenge to develop manufacturing and characterization technologies that allow us to control the material flaws in the atomic structure and at the nanoscopic scale.

## REFERENCES AND NOTES

1. X. Yu, T. J. Marks, A. Facchetti, *Nat. Mater.* **15**, 383–396 (2016).
2. K. Nomura *et al.*, *Nature* **432**, 488–492 (2004).
3. H. Hosono, J. Kim, Y. Toda, T. Kamiya, S. Watanabe, *Proc. Natl. Acad. Sci. U.S.A.* **114**, 233–238 (2017).
4. G. Karbasian *et al.*, *Appl. Sci.* **7**, 246 (2017).
5. J. Y. Kim *et al.*, *Adv. Mater.* **18**, 572–576 (2006).
6. Y. Idota *et al.*, *Science* **276**, 1395–1397 (1997).
7. E. D. Zanotto, *Am. J. Phys.* **66**, 392–395 (1998).
8. E. D. Zanotto, P. K. Gupta, *Am. J. Phys.* **67**, 260–262 (1999).
9. J. Zhao, S. L. Simon, G. B. McKenna, *Nat. Commun.* **4**, 1783 (2013).
10. Y. Yu *et al.*, *Phys. Rev. Lett.* **115**, 165901 (2015).
11. A. A. Griffith, *Philos. Trans. R. Soc. London Ser. A* **221**, 163–198 (1921).
12. F. M. Ernsberger, *J. Am. Ceram. Soc.* **51**, 545–547 (1968).
13. T. Rouxel, H. Ji, J. P. Guin, F. Augereau, B. Rufflé, *J. Appl. Phys.* **107**, 094903 (2010).
14. G. Kermouche, G. Guillonnet, J. Michler, J. Teisseire, E. Barthel, *Acta Mater.* **114**, 146–153 (2016).
15. E. Calvié *et al.*, *J. Eur. Ceram. Soc.* **32**, 2067–2071 (2012).
16. F. Garcia Ferré *et al.*, *Acta Mater.* **61**, 2662–2670 (2013).
17. A. S. Esmaily, S. Mills, J. M. D. Coey, *Nanoscale* **9**, 5205–5211 (2017).
18. Y. Yang, A. Kushima, W. Han, H. Xin, J. Li, *Nano Lett.* **18**, 2492–2497 (2018).
19. A. van der Rest *et al.*, *Acta Mater.* **125**, 27–37 (2017).
20. D. Mercier *et al.*, *Thin Solid Films* **638**, 34–47 (2017).
21. S.-H. Jen, J. A. Bertrand, S. M. George, *J. Appl. Phys.* **109**, 084305 (2011).
22. A. Malkin, V. Kulichikhin, S. Ilyin, *Rheol. Acta* **56**, 177–188 (2017).
23. K. Zheng *et al.*, *Nat. Commun.* **1**, 24 (2010).
24. J. Luo *et al.*, *Nano Lett.* **16**, 105–113 (2016).
25. S. K. Lee, C. W. Ahn, *Sci. Rep.* **4**, 4200 (2014).
26. R. Nakamura, M. Ishimaru, H. Yasuda, H. Nakajima, *J. Appl. Phys.* **113**, 064312 (2013).
27. M. Mačković *et al.*, *Front. Mater.* **4**, 10 (2017).
28. D. Wakabayashi, N. Funamori, T. Sato, T. Taniguchi, *Phys. Rev. B* **84**, 144103 (2011).
29. S. Kohara *et al.*, *Proc. Natl. Acad. Sci. U.S.A.* **108**, 14780–14785 (2011).
30. M. Murakami *et al.*, *Phys. Rev. B* **99**, 045153 (2019).
31. S. Kohara *et al.*, *Phys. Rev. B* **82**, 134209 (2010).
32. F. Célarie *et al.*, *Phys. Rev. Lett.* **90**, 075504 (2003).
33. R. Nakamura *et al.*, *J. Appl. Phys.* **116**, 033504 (2014).
34. E. J. Frankberg, thesis, Tampere University of Technology (2018). <http://urn.fi/URN:ISBN:978-952-15-4108-7>.

## ACKNOWLEDGMENTS

We thank A.T. Frankberg for making this study possible. In addition, we acknowledge E. Calvié, I. Issa, D. Krstic, J. Chevalier, J. Juuti, and R. Nowak for supporting the work. Simulation coordinates of a-SiO<sub>2</sub> structure are shown in fig. S18 by courtesy of M. Murakami *et al.* (30). **Funding:** We thank Tampere University graduate school, Tutkijat maailmalle mobility grant by Technology Industries of Finland Centennial Foundation, Tampere University of Technology strategic research funding, Consortium Lyon Saint-Etienne de Microscopie (CLYM), CNRS-CEA "METSA" French network (FR CNRS 3507) on the platform CLYM, CSC – IT Center for Science, Jenny and Antti Wihuri Foundation, Academy of Finland (grant no. 315451), Italian National Agency for New Technologies, Energy and Sustainable Economic Development, and Technoprobe SpA for providing the resources to perform the experimental and computational research. This project has received funding from the European Union's Horizon 2020 research and innovation program (grant agreement nos. 841527, 754586, 755269, and 740415). This work made use of Tampere Microscopy Center facilities at Tampere University. **Author contributions:** E.J.F. led the project and contributed to the experimental part, including design,

building, and implementation of the in situ experimental setup, and to the theoretical part, including designing the atomistic simulations. J.K. contributed to the theoretical part, including designing and performing the atomistic simulations. F.G.F. developed the PLD deposition method for a-Al<sub>2</sub>O<sub>3</sub> and prepared the thin-film samples. L.J.-P. contributed to the design and implementation of the in situ experimental setup. T.S. contributed to the design and building of the in situ experimental setup. J.H. performed the finite element method simulations. M.H. contributed to the image correlation measurements. S.K. performed the TEM tomography. T.D. contributed to the building of the in situ experimental setup. B.L.S. contributed to the building of the in situ experimental setup. P.K. and M.J.C. designed and performed the AFM measurements. T.E. and D.S. contributed to the design of the in situ experimental setup. M.V. contributed to the characterization of thin-film samples. L.R. contributed to the design of TEM characterizations. J.A. contributed to the design of the atomistic simulations. F.D.F. contributed to the design of the thin-film sample preparation. E.L. contributed to the design of the in situ experimental setup. K.M.-V. contributed to the design, building and implementation of the in situ experimental setup. All authors contributed to the writing of the article. **Competing interests:** The authors declare no competing interests. **Data and materials availability:** All data are available in the manuscript or the supplementary materials. This work is partly related to the open access content of a doctoral thesis by E.J.F. (34).

## SUPPLEMENTARY MATERIALS

science.sciencemag.org/content/366/6467/864/suppl/DC1  
Materials and Methods  
Supplementary Text  
Figs. S1 to S24  
Tables S1 to S3  
References (35–48)  
Movie S1

20 August 2018; resubmitted 3 July 2019  
Accepted 8 October 2019  
10.1126/science.aav1254



## 2D MATERIALS

# Electrical control of interlayer exciton dynamics in atomically thin heterostructures

Luis A. Jauregui<sup>1\*</sup>, Andrew Y. Joe<sup>1</sup>, Kateryna Pistunova<sup>1</sup>, Dominik S. Wild<sup>1</sup>, Alexander A. High<sup>1,2</sup>, You Zhou<sup>1,2</sup>, Giovanni Scuri<sup>1</sup>, Kristiaan De Greve<sup>1,2,†</sup>, Andrey Sushko<sup>1</sup>, Che-Hang Yu<sup>3,‡</sup>, Takashi Taniguchi<sup>4</sup>, Kenji Watanabe<sup>4</sup>, Daniel J. Needleman<sup>3,5,6</sup>, Mikhail D. Lukin<sup>1</sup>, Hongkun Park<sup>1,2</sup>, Philip Kim<sup>1,3,§</sup>

A van der Waals heterostructure built from atomically thin semiconducting transition metal dichalcogenides (TMDs) enables the formation of excitons from electrons and holes in distinct layers, producing interlayer excitons with large binding energy and a long lifetime. By employing heterostructures of monolayer TMDs, we realize optical and electrical generation of long-lived neutral and charged interlayer excitons. We demonstrate that neutral interlayer excitons can propagate across the entire sample and that their propagation can be controlled by excitation power and gate electrodes. We also use devices with ohmic contacts to facilitate the drift motion of charged interlayer excitons. The electrical generation and control of excitons provide a route for achieving quantum manipulation of bosonic composite particles with complete electrical tunability.

Long-lived excitons can be potentially used for the realization of coherent quantum many-body systems (1–3) or as quantum information carriers (4, 5). In conventional semiconductors, the exciton lifetime can be increased by constructing double-quantum well (DQW) heterostructures, in which spatially separated electrons and holes form interlayer excitons (IEs) across the quantum wells (6–12). Strongly bound IEs can also be formed by stacking two single atomic unit cells of transition metal dichalcogenides (TMDs) into a van der Waals (vdW) heterostructure. TMD heterostructures, such as MoSe<sub>2</sub>/WSe<sub>2</sub>, MoS<sub>2</sub>/WS<sub>2</sub>, and MoS<sub>2</sub>/WSe<sub>2</sub>, have shown ultrafast charge transfer (13), the formation of IEs with a large binding energy of ~150 meV (14), and diffusion over long distances (15). Moreover, the tight binding and small exciton Bohr radius potentially allow for quantum degeneracy of these composite bosons, which may lead to exciton condensation at substantially elevated temperatures compared to those of, e.g., conventional Bose-Einstein condensates of cold atoms (2).

In this work, we fabricate individually electrically contacted optoelectronic devices using hexagonal boron nitride (h-BN)-encapsulated

vdW heterostructures of MoSe<sub>2</sub> and WSe<sub>2</sub> (16, 17). Optically transparent electrical gates and ohmic electrical contacts realized for the individual atomic layers allow us to have complete control of the carrier densities in each TMD of the DQW while maintaining full optical access. The top and bottom insets of Fig. 1A show an optical image of a representative device with false-colored top gates and a schematic cross section, respectively [a detailed device scheme is illustrated in fig. S1 (18)]. The green and red false-colored gates depict the contact gates for doping the MoSe<sub>2</sub> and WSe<sub>2</sub> regions, respectively. These contact gates, together with the prefabricated Pt electrodes, provide ohmic contacts in the WSe<sub>2</sub> p-channel (19).

The presence of the top (optically transparent) and bottom electrical gates, in addition to the separately contacted TMD layers, allows us to control the carrier density in the individual TMD layers as well as the electric field across the TMD heterostructure,  $E_{\text{hs}}$ , using the voltage  $V_{\text{tg}}$  (or  $V_{\text{bg}}$ ) applied to the top (or bottom) gate. For intrinsic TMD layers (i.e., no free carriers and the chemical potential located within the semiconducting gap), where the heterostructure can be approximated by a thin dielectric slab,  $E_{\text{hs}}$  is controlled by a gate operation scheme in which we apply opposite gate polarity [supplementary text section 1 in (18)]. Figure 1A shows the photoluminescence (PL) spectrum measured at temperature  $T = 4$  K as a function of  $E_{\text{hs}}$ , keeping both TMD layers intrinsic. We observe a linear shift of PL peak energy with  $E_{\text{hs}}$ , suggesting a first-order Stark shift caused by the static electric dipole moment across the vdW heterostructure. By fitting the linear PL peak shift with the linear Stark shift formula  $-edE_{\text{hs}}$ , where  $ed$  is the dipole moment ( $e$ , electron charge;  $d$ , electron-hole separation), we estimate  $d \approx 0.6$  nm, in good agreement with the expected vdW separation between WSe<sub>2</sub>

and MoSe<sub>2</sub>. This analysis strongly suggests that the observed PL peak indeed corresponds to the IE emission of the WSe<sub>2</sub>/MoSe<sub>2</sub> heterostructure with out-of-plane-oriented electric dipoles. There is a ~10% nonlinearity in the energy shift dependence versus  $E_{\text{hs}}$ , which, combined with weak variations of the absorption intensity (as shown in Fig. 1B), might be attributed to the charging effect caused by uncompensated gating. Similar to a previous study (14), our findings indicate that the PL from the intralayer excitons is strongly suppressed compared with that of IEs in the WSe<sub>2</sub>/MoSe<sub>2</sub> heterostructure region [fig. S2 in (18)], suggesting a fast dissociation of intralayer excitons and an efficient conversion to IEs in this system. We further confirm from the constant normalized reflection  $\Delta R/R$  at the intralayer exciton resonances (20–22) that our gate operation scheme only varies  $E_{\text{hs}}$  while keeping the layers intrinsic (Fig. 1B).

The IEs in the vdW heterostructure can live longer than intralayer excitons, owing to the spatial separation of electrons and holes in the heterostructure. Figure 1C shows the IE lifetime  $\tau$  as a function of  $E_{\text{hs}}$ , measured by time-dependent PL after pulsed laser illumination. The lifetime  $\tau$  increases as  $E_{\text{hs}}$  increases, reaching ~600 ns for  $E_{\text{hs}} > 0.1$  V/nm, an order of magnitude larger than in previous studies (14, 23). The observed dependence of  $\tau$  on  $E_{\text{hs}}$  can be explained by changes in the overlap between the electron and hole wave functions [section 3 of (18)]. The recombination rate of an exciton is proportional to the probability that the electron and the hole occupy the same location. An electric field antiparallel to the IE dipole moment is therefore expected to reduce the recombination rate as it pulls the two carriers apart, consistent with our measurements. Considering the PL intensity modulation shown in Fig. 1A together with the measured  $\tau$ , we also demonstrate that the emission efficiency ( $\eta$ ) can be tuned with  $E_{\text{hs}}$ , reaching  $\eta \sim 80\%$  when  $E_{\text{hs}}$  is aligned against the IE dipole moment, promoting the recombination process [section 4 of (18)].

The electrostatic condition in our heterostructures is greatly modified if we change the gate operation scheme such that one of the TMD layers is doped electrostatically, introducing free charge carriers. Figure 1E shows the IE PL spectrum after the gating scheme depicted in Fig. 1D. In this scheme, as shown in the normalized reflection  $\Delta R/R$  at the intralayer exciton resonances (Fig. 1F), the carrier density of MoSe<sub>2</sub> (WSe<sub>2</sub>),  $n_{2D}$  ( $p_{2D}$ ), changes with positive  $V_{\text{tg}}$  (negative  $V_{\text{bg}}$ ) while the WSe<sub>2</sub> (MoSe<sub>2</sub>) layer remains intrinsic, keeping  $E_{\text{hs}}$  constant [section 5 of (18)]. We observe several pronounced changes in the IE emission spectrum as  $V_{\text{tg}}$  ( $V_{\text{bg}}$ ) increases (decreases) and  $n_{2D} > 0$  ( $p_{2D} > 0$ ). First, the IE PL peaks exhibit a sudden red shift for n-doping (p-doping) of MoSe<sub>2</sub>

<sup>1</sup>Department of Physics, Harvard University, Cambridge, MA, USA. <sup>2</sup>Department of Chemistry and Chemical Biology, Harvard University, Cambridge, MA, USA. <sup>3</sup>John A. Paulson School of Engineering and Applied Sciences, Harvard University, Cambridge, MA, USA. <sup>4</sup>National Institute for Materials Science, 1-1 Namiki, Tsukuba, Japan.

<sup>5</sup>Department of Molecular and Cellular Biology, Harvard University, Cambridge, MA, USA. <sup>6</sup>Faculty of Arts and Sciences Center for Systems Biology, Harvard University, Cambridge, MA, USA.

\*Present address: Department of Physics and Astronomy, University of California, Irvine, CA, USA. †Present address: Imec, Leuven, Belgium. ‡Present address: Department of Electrical and Computer Engineering, University of California, Santa Barbara, CA, USA.

§Corresponding author. Email: pkim@physics.harvard.edu

(WSe<sub>2</sub>). Second, the PL peaks continuously red-shift as doping increases for both n- and p-sides. In this regime,  $E_{\text{hs}}$  is fixed (as discussed above) and thus these shifts cannot be explained by the Stark effect. Lastly, the PL intensity diminishes rapidly as doping increases.

Our measurements in the doped regime can be explained by the formation of charged IEs (CIEs) (24). As shown in the normalized reflection measured with the same gating scheme, we can identify (i) intrinsic/p, (ii) intrinsic/intrinsic, and (iii) n/intrinsic regions by the disappearance of the absorption dips for intralayer excitons in MoSe<sub>2</sub> and WSe<sub>2</sub> (25), which are well aligned with the sudden red shift observed in IE PL (vertical dashed lines in Fig. 1, D to G). Thus, this jump in energy can be related to the CIEs. Note that charged excitons can be referred to as trions (i.e., three-body bound states) (26–29) or, alternatively, attractive polarons (i.e., excitonic states dressed by a polarized fermionic sea, similar to those in

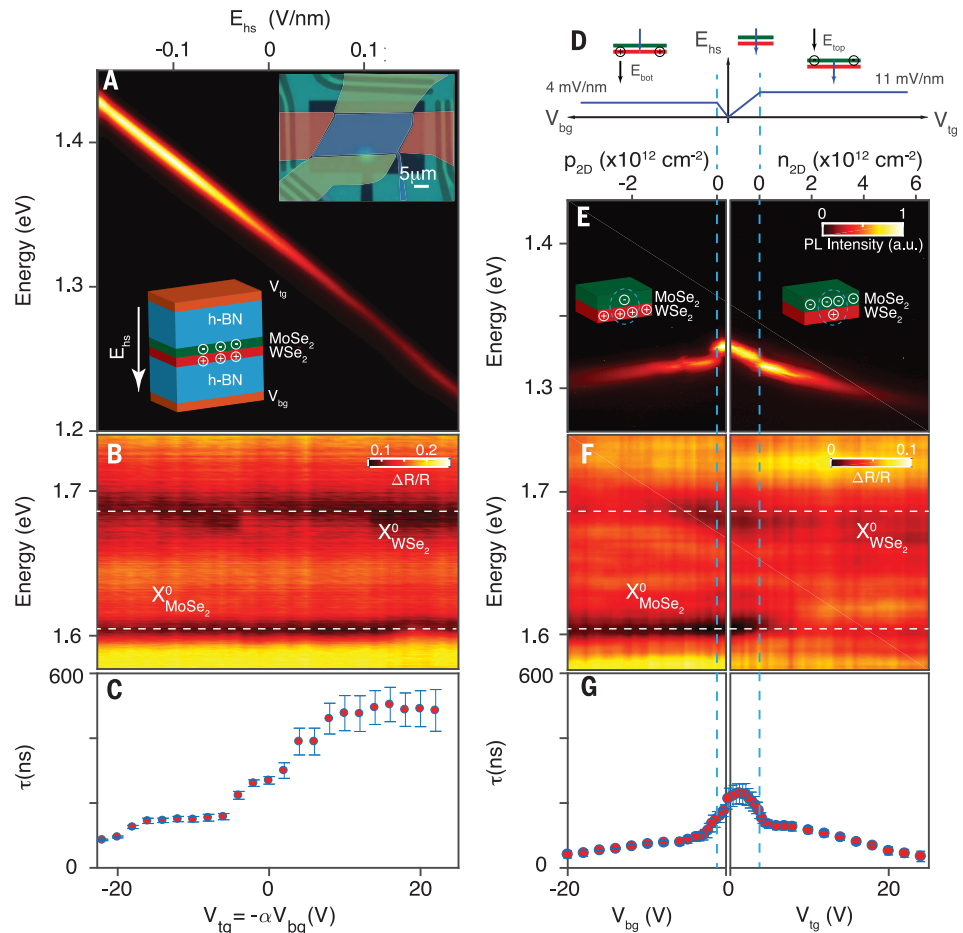
monolayer TMDs) (30, 31). The value of the observed jump  $\approx 10$  meV (15 meV) for positive (negative) CIEs is in good agreement with the calculated binding energy of CIEs (24). The lifetime of CIEs is  $\approx 100$  ns near the band edge but decreases with increased doping, presumably owing to additional decay channels enabled by scattering with free carriers (Fig. 1G).

We create high densities of IEs by increasing laser power. In particular, for neutral IEs, we observe that the PL emission is shifted to higher energy with increasing power (Fig. 2A), consistent with a mean-field shift stemming from the repulsive dipole-dipole interaction between oriented IEs. Following the analysis based on a parallel plate-capacitance model used for GaAs DQW IEs (32), we obtain a lower bound for the IE density of  $\sim 5 \times 10^{11} \text{ cm}^{-2}$  [section 6 of (18)]. The high density of long-lived IEs and the large  $\tau$  observed in our heterostructures can enable transport of IEs across the samples. Figure 2, B to D, shows the spatial map of the IE PL in-

tensity at different laser powers. The PL signal can be detected far away from the diffraction-limited focused laser spot ( $<1 \mu\text{m}$  in diameter). At the highest power, PL can be observed many micrometers away from the excitation spot, strongly suggesting transport of IEs across the sample. From these maps, we obtain the normalized, radially averaged PL intensity,  $I_{\text{PL}}^{\text{norm}}(r)$ , where  $r$  is measured from the center of the diffraction-limited steady-state laser spot. Here, the PL intensity is normalized by the value obtained at  $r = 0$ . As shown in Fig. 2E, away from the laser spot,  $I_{\text{PL}}^{\text{norm}}(r)$  decreases rapidly as  $r$  increases. Note, however, that at a given  $r$ ,  $I_{\text{PL}}^{\text{norm}}(r)$  increases with power ( $P$ ) even at a position far away from the laser spot. Similarly, an increase of  $I_{\text{PL}}^{\text{norm}}(r)$  is observed when adjusting  $E_{\text{hs}}$  to increase  $\tau$  at fixed  $P$ . The latter observation is consistent with exciton transport, as longer-lived IEs may travel farther [section 7 of (18)]. The characteristic length  $L_D$  for the decaying behavior of  $I_{\text{PL}}^{\text{norm}}(r)$  can

**Fig. 1. Electric field and carrier density control of interlayer excitons.**

(A) IE PL spectra versus electric field applied to the heterostructure [ $E_{\text{hs}} = (V_{\text{tg}} - V_{\text{bg}})/t_{\text{total}} * (\epsilon_{\text{h-BN}}/\epsilon_{\text{TMD}})$ ]. Here, the top ( $V_{\text{tg}}$ ) and bottom ( $V_{\text{bg}}$ ) gate voltages are swept together with a voltage ratio  $\alpha$  ( $\alpha = t_{\text{h-BN}}^{\text{top}}/t_{\text{h-BN}}^{\text{bottom}} = 0.614$ ;  $t_{\text{h-BN}}^{\text{top}} = 70\text{nm}$  and  $t_{\text{h-BN}}^{\text{bottom}} = 114\text{nm}$  are the top and bottom h-BN thicknesses, respectively),  $t_{\text{total}}$  is the total h-BN thickness, and  $\epsilon_{\text{h-BN}} = 3.9$  and  $\epsilon_{\text{TMD}} = 7.2$  are the h-BN and TMD permittivity, respectively. (Top inset) Optical image of a representative device with the top-gates shown in false color. (Bottom inset) Schematic of the heterostructure cross section, showing electrons (holes) accumulate on the MoSe<sub>2</sub> (WSe<sub>2</sub>) layers, forming IEs. The white arrow represents the positive direction of  $E_{\text{hs}}$ . (B) Normalized reflectance versus  $E_{\text{hs}}$ . (C) IE lifetime  $\tau$  versus  $E_{\text{hs}}$ . The lifetime is measured at low laser power (20 nW) to ensure a single exponential PL decay. Error bars are obtained by adjusting the fitting range. (D) Calculated  $E_{\text{hs}}$  versus  $V_{\text{tg}}$  and  $V_{\text{bg}}$ . The field  $E_{\text{hs}}$  remains constant once a given layer is doped. The top cartoons represent the heterostructure for different applied gate voltages. The fields  $E_{\text{hs}}$  and  $E_{\text{BN}}$  (electric fields on the top and bottom h-BN layers) are depicted as blue and black arrows, respectively. (E) Single-gate dependence ( $V_{\text{tg}}$  or  $V_{\text{bg}}$ ) of the PL shows formation of charged IEs with varying carrier density obtained from the gate operation scheme in (D). (Left inset) Cartoon of hole-doped IEs with  $V_{\text{bg}}$ . (Right inset) Cartoon of electron-doped IEs with  $V_{\text{tg}}$ . a.u., arbitrary units. (F) Normalized reflectance versus carrier density. The horizontal dashed lines in (B) and (F) represent the neutral excitons for WSe<sub>2</sub> ( $X_{\text{WSe}_2}^0$ ) and MoSe<sub>2</sub> ( $X_{\text{MoSe}_2}^0$ ). The normalized reflection spectrum from the top MoSe<sub>2</sub> layer is brighter than that from the bottom WSe<sub>2</sub> layer, owing to the dominant direct reflection of the top layer, which provides a simpler normalization scheme. (G) Neutral and charged IE lifetimes  $\tau$  versus carrier density. Error bars are obtained by adjusting the fitting range. The vertical light blue dashed lines in (D) to (G) mark the intrinsic region. Data in (E) to (G) were taken in different thermal cycles from (A) to (C). Thus, small shifts in the energy spectrum or lifetime occur, owing to different disorder configurations and measurement positions at low temperatures.





be obtained from fitting  $e^{-r/L_D}/\sqrt{r/L_D}$  to  $I_{PL}^{norm}(r)$  away from the laser excitation spot (dashed lines in Fig. 2E), following the two-dimensional diffusion model with a point source [section 8 in (18)]. As shown on the left axis of Fig. 2G, we find that  $L_D$  increases as  $P$  increases, suggesting increased diffusion at high IE density, possibly due to exciton-exciton interactions.

We also used a diffraction-limited focused pulsed laser to measure the temporal decay of the PL intensity. Figure 2F shows an estimate of the time-dependent exciton population (integrated PL signal along the heterostructure weighted by  $r^2$ ) after a laser pulse with peak

power  $P$ . The time-dependent PL initially exhibits a faster decay process with characteristic time scale  $\tau_1 \sim 10$  ns, followed by a slower decay process occurring on the time scale  $\tau_2 \sim 100$  ns, suggesting that there are two different mechanisms for the PL intensity decay. The value of  $L_D$  estimated above can be converted to a diffusion constant according to  $D = L_D^2/\tau$ . Two values  $D_1$  and  $D_2$  are obtained using the short ( $\tau_1$ ) and long ( $\tau_2$ ) decay times, respectively (Fig. 2H). Because our lifetime measurement uses a pulsed laser where the interaction-driven IE diffusion occurs just after the pulse is off when the IE density remains high,  $\tau_1$  could be more relevant than  $\tau_2$  for the IE diffusion.

However, the value of  $L_D$ , measured in steady state, would be dominated by  $\tau_2$ . Figure 2H shows that  $D_2$  is in the range of 0.01 to 0.1  $\text{cm}^2/\text{s}$ , whereas  $D_1$  changes from 0.1 to 1  $\text{cm}^2/\text{s}$ . Both  $D_1$  and  $D_2$  are increasing with increasing  $P$ , providing upper and lower bounds for nonlinear IE diffusion caused by dipolar repulsive interaction [section 8 in (18)], respectively.

We obtain further evidence for IE transport from time-dependent spatial PL maps with a pulsed laser illuminating the center of the sample. We measure the IE PL intensity  $I_{PL}(r, t)$  as a function of distance  $r$  (referenced to the laser illumination spot) and time  $t$  (referenced to the falling edge of the laser pulse). Figure 2, I

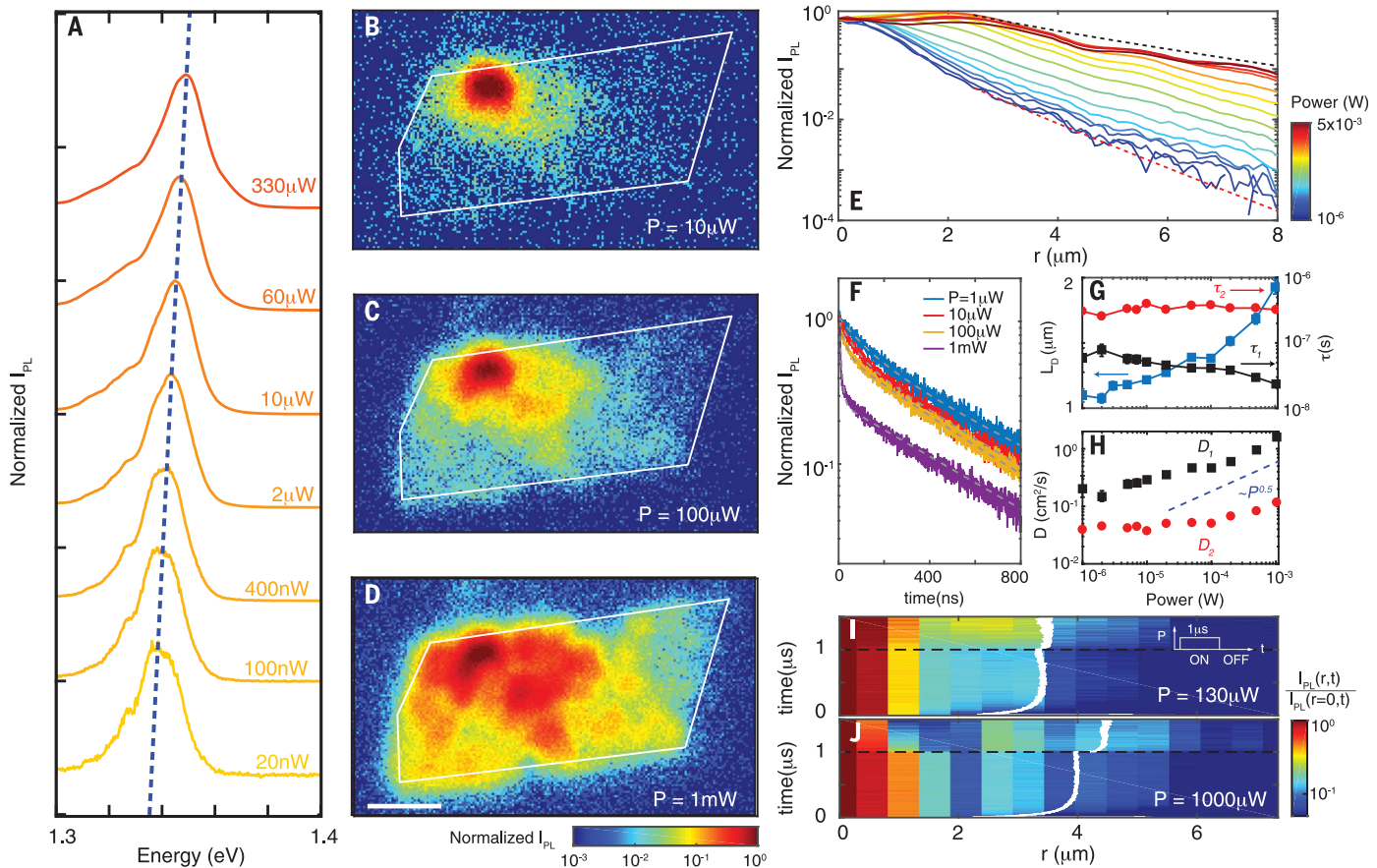


**Fig. 2. Spatial control of neutral interlayer excitons.** (A) Power ( $P$ ) dependence of the normalized PL spectra collected from the same spot as the excitation. The blue dashed line corresponds to the PL peak position versus power. (B to D) Spatial dependence of the intensity of the normalized PL for  $P = 10$ , 100, and 1000  $\mu\text{W}$ , respectively. The white outlines depict the heterostructure area. The continuous wave laser excitation ( $\lambda = 660$  nm) is fixed at the top left of the sample. Scale bar, 5  $\mu\text{m}$ . All measurements were performed at 4 K. Experiments performed at higher temperatures provide smaller spatial extension of PL around the excitation [see section 12 of (18) for details]. (E) Power dependence of normalized radially averaged  $I_{PL}$  (normalized  $I_{PL}$ ) versus  $r$  with the excitation fixed at the center of the sample. The red and black dashed lines represent  $e^{-r/L_D}/\sqrt{r/L_D}$  for  $L_D = 1.1$  and  $3.2$   $\mu\text{m}$ , respectively, where  $L_D$  is the diffusion length.  $P = 1, 2, 3, 5, 10, 20, 50, 100, 200, 500, 1000, 2000, 3000, 4000$ , and  $5000$   $\mu\text{W}$ . (F) Time-dependent PL normalized at  $t = 0$  for different “on” powers. For this measurement, we use a

pulsed 660-nm diode laser with a 100-kHz repetition rate and 1- $\mu\text{s}$  “on” time. The power we quoted is the “on” power or peak power. Dashed gray lines correspond to double exponential fits. (G) (Left axis)  $L_D$  versus  $P$  extracted from the data in (E). (Right axis) Lifetime ( $\tau$ ) versus  $P$  with two values of  $\tau$  extracted from the double exponential decay fit. (H) Diffusion constant ( $D = L_D^2/\tau$ ) versus  $P$  extracted from (G) using the two different values of  $\tau$ . The dashed line corresponds to  $D \sim P^{1/2}$ , as expected from the nonlinear diffusion model [section 8 of (18)]. (I and J) Normalized  $I_{PL}$  versus time and distance from the laser spot.  $I_{PL}(r, t)$  was estimated by averaging over a line cut through the laser spot. We normalize  $I_{PL}$  at each time by  $I_{PL}(r, t)/I_{PL}(r = 0, t)$ . Overlaid white lines represent  $\sqrt{\langle r^2 \rangle}$  obtained from the experimental PL map, assuming rotational symmetry of the sample. (Inset) The pulsed laser diode is turned on at  $t = 0$   $\mu\text{s}$  with powers of 130  $\mu\text{W}$  (I) and 1000  $\mu\text{W}$  (J) and turned off at  $t = 1$   $\mu\text{s}$  (also marked with dashed black lines).

and  $J$ , shows the normalized time-dependent  $PL I_{PL}^{norm}(r, t) = I_{PL}(r, t)/I_{PL}(r = 0, t)$  at different laser peak powers. The time-dependent root mean square radius,  $r_{rms}(t) = \sqrt{\langle r^2 \rangle}$ , computed from  $I_{PL}^{norm}(r, t)$  (white lines) increases rapidly when the laser is on, reaching a steady state within  $\sim 200$  ns. Notably,  $r_{rms}(t)$  increases again rapidly within 100 ns after the laser is turned off. Although the observed two decaying time scales and the dynamics of IEs can be explained by the diffusion of IEs driven by interaction and their recombination, an alternative scenario involving the diffusion of photoexcited free carriers (33) is also possible [see section 8 of (18)]. Future experimental studies with spatially resolved resonant excitation of IEs can be potentially used to distinguish these scenarios.

Unlike the neutral IEs discussed above, CIEs can be manipulated by an in-plane electric field. Figure 3A shows the spatial map of  $I_{PL}$  overlaid with the device image when CIEs are optically excited at the center of the sample. Similar to neutral IEs, CIEs generated at the laser-illuminated spot can diffuse across the entire sample. Both the  $WSe_2$  and  $MoSe_2$  layers in our device have multiple electrical contacts away from the heterostructure edge ( $\sim 10$   $\mu m$  away) that are used to control the lateral electric field while avoiding any local Schottky barrier effects. Figure 3B shows the spatial map of the PL intensity normalized as  $I_{PL}(V_{ds})/I_{PL}(V_{ds} = 0)$  when applying an interlayer bias voltage of  $V_{ds} = 3$  V across the  $WSe_2$  layer. We observe that the grounded edge of the sample becomes brighter with increasing  $V_{ds}$  (also see Fig. 3C for the normalized average emission intensity along the heterostructure channel). This increase in PL at the boundary between the heterostructure and the highly doped monolayer region can be explained by drift of CIEs under the applied bias voltage in the channel. The applied bias  $V_{ds}$  creates an electric field to tilt the band structure in the direction of the  $WSe_2$  channel, driving positive (+) CIEs along the same direction as shown in the schematic diagram in Fig. 3D. At the boundary of the heterostructure, however, the +CIE cannot be transported to the  $WSe_2$  p-channel because current across the boundary must be preserved. Therefore, the transported +CIEs recombine to turn into a hole in the  $WSe_2$  p-channel. In figs. S13 and S14, we further confirm this picture of CIE transport by changing the doping polarity and  $V_{ds}$  direction [see section 9 of (18) for details on gate configurations and alternative explanations]. We also note that, owing mainly to the limited resolution of our electrical setup, we do not observe any photocurrent  $>10$  pA.

Finally, we demonstrate the electrical generation of IEs by free-carrier injection using ohmic contacts in individual TMD layers. Because our heterostructure forms type II-

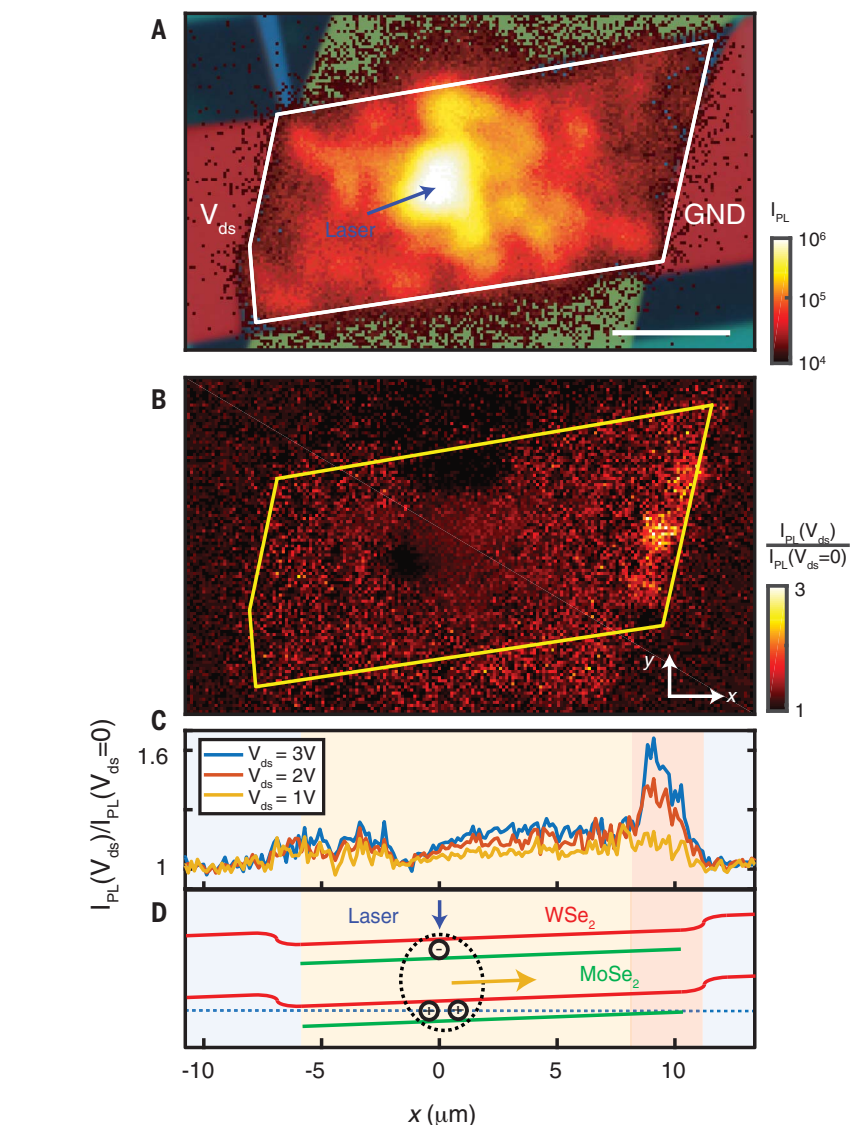


**Fig. 3. Spatial control of charged interlayer excitons.** (A) Spatial dependence of  $I_{PL}$  with the laser excitation fixed at the center of the heterostructure (blue arrow). An optical image of the device with false-colored top gates that cover the  $WSe_2$  and  $MoSe_2$  contacts is overlaid. An in-plane electric field is applied by a voltage ( $V_{ds}$ ) in one of the  $WSe_2$  contacts while the other contact remains grounded. GND corresponds to the grounded electrode. Scale bar, 5  $\mu m$ . (B) Spatial dependence of  $I_{PL}$  normalized according to  $I_{PL}(V_{ds})/I_{PL}(V_{ds} = 0)$  for  $V_{ds} = 3$  V. When  $V_{ds}$  increases, we observe a larger population of charged IEs near the right  $WSe_2$  electrode. (C) Normalized  $I_{PL}$  averaged over the  $y$  axis versus the heterostructure channel length  $x$  [depicted in (B)] for different  $V_{ds}$ . (D) Schematic of the heterostructure bands with applied  $V_{ds}$ . The red (green) bands correspond to  $WSe_2$  ( $MoSe_2$ ). A positive  $V_{ds}$  is applied while the chemical potential (blue dotted line) is kept inside the  $WSe_2$  valence band to form positively charged IEs. Under positive  $V_{ds}$ , the CIEs drift toward the grounded contact. The emission mainly occurs near the grounded contact, because the charged exciton cannot move beyond the heterostructure. The yellow arrow indicates the current direction.

aligned p- and n-layers, the charge transport across  $WSe_2$  to  $MoSe_2$  is expected to show diode-like rectifying behaviors (34, 35). Figure 4A shows interlayer current ( $I_{ds}$ ) versus interlayer bias ( $V_{ds}$ ) curves, whose characteristics can be modulated by  $V_{tg}$  and  $V_{bg}$ . Changing  $V_{tg}$  and  $V_{bg}$  adjusts the band offset in the type II heterojunction and the doping in each layer. The inset to Fig. 4A shows a map of the forward

bias current at a fixed bias voltage. One can identify the region in which both  $WSe_2$  and  $MoSe_2$  layers remain intrinsic, consistent with the absorption spectrum discussed in Fig. 1. Notably, we find that this p-n device generates detectable electroluminescence (EL) at sufficiently high bias. A particularly interesting EL condition occurs when both TMD layers are intrinsic, thus allowing electrons and holes to

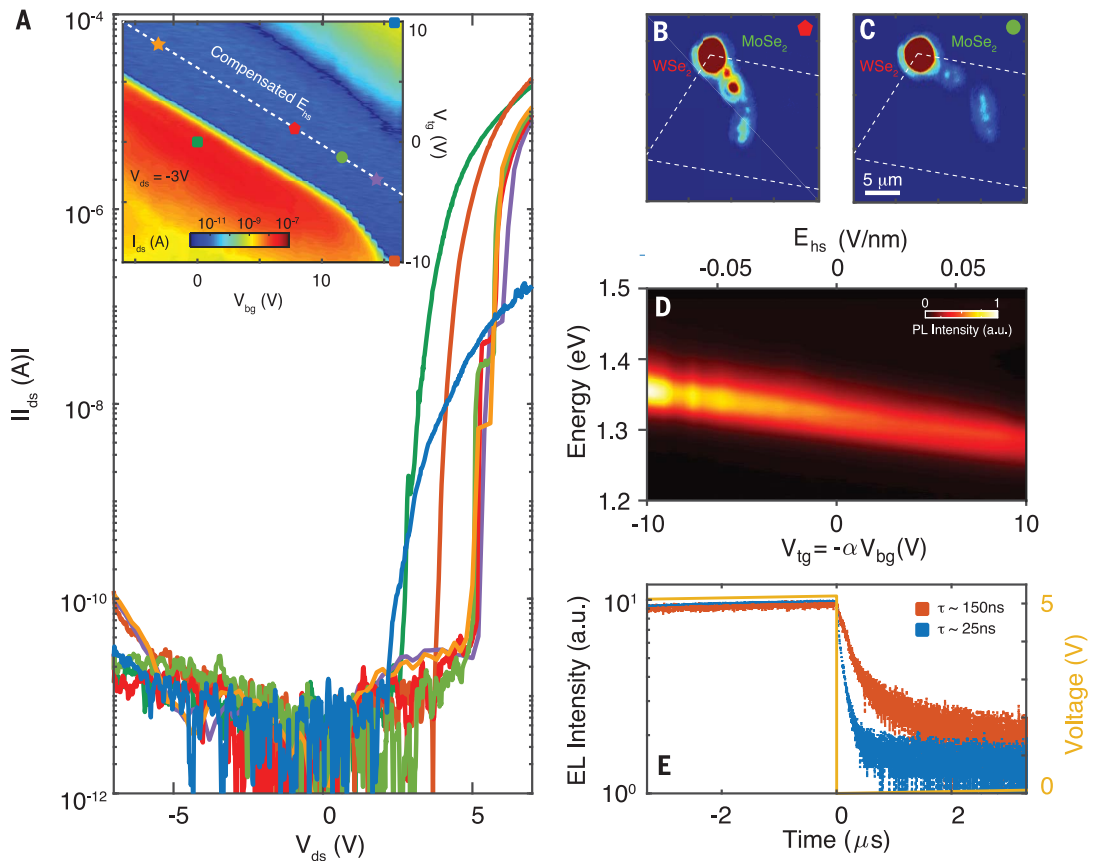


**Fig. 4. Electrical generation of interlayer excitons.**

(A)  $I$ - $V$  curves at various top ( $V_{tg}$ ) and bottom ( $V_{bg}$ ) gate configurations, with corresponding indicators in the inset. (Inset)  $I_{ds}$  versus  $V_{tg}$  and  $V_{bg}$  (with  $V_{ds} = -3$  V on  $\text{MoSe}_2$  and grounded  $\text{WSe}_2$ ).

The white dashed line represents the compensated electric field where  $V_{bg} = 10.37\text{V} - \alpha V_{tg}$ . The different symbols represent the gate voltages used in (A) to (C) and (E). (B and C) Spatially dependent EL maps for  $V_{tg} = -1$  V (1 V) and  $V_{bg} = 12$  V (8.75 V) at  $V_{ds} = 7$  V. The white dashed lines indicate the heterostructure area. (D) Electric field ( $E_{hs}$ ) dependence of the interlayer exciton EL. The electron-hole separation ( $d \approx 0.55$  nm) obtained from the slope agrees reasonably with the electron-hole separation extracted from PL.

(E) Time-dependent EL intensity for two different gate configurations: blue (orange) curve uses  $V_{tg} = 10$  V (−10 V) and  $V_{bg} = 16.28$  V. The yellow line represents the pulsed sawtooth voltage applied to  $V_{ds}$ . The measured EL lifetime is gate-tunable, as in the PL case, and of comparable magnitude to the PL lifetime.



recombine through the formation of IEs. Figure 4, B and C, shows the EL maps of the heterostructure region. The local EL intensity in the heterostructure depends on the local recombination current density, which can be controlled by  $V_{tg}$  and  $V_{bg}$  [section 10 of (18)]. We find that the EL spectrum resembles the PL spectrum in the same ( $V_{tg}$ ,  $V_{bg}$ ) configuration (34). Figure 4D shows EL versus  $E_{hs}$ . Similar to the PL shown in Fig. 1A, the EL spectrum shifts linearly with  $E_{hs}$ , which can be attributed to the IE Stark effect. More direct evidence that the EL process in our heterostructure is mediated through the IE formation by carrier injection is provided by the EL lifetime. Figure 4E shows the EL intensity as a function of time when we pulse  $V_{ds}$  at a fixed  $V_{tg}$  and  $V_{bg}$ . We measure the EL at the falling edge of the pulse. Long and short lifetimes of  $\sim 150$  and  $\sim 25$  ns are obtained for the gate voltages of  $V_{tg} = 10$  and  $-10$  V with  $V_{bg} = 16.3$  V, corresponding to the neutral IE and charged IE formation regime, respectively (Fig. 4A, inset).

The electrical generation of long-lived interlayer excitons provides an electrically driven near-infrared light source with an energy tunability that ranges over several hundreds of milli-electron volts and spatial control of the emission. Achieving high-density IEs without

optical excitation could pave a way to realize quantum condensates in solid-state devices. Large valley polarization (23, 36) strongly coupled to the spin may also lead to optoelectronic devices based on electrically driven CIEs. The spin degree of freedom in such devices could be potentially used for both classical and quantum information processing.

#### REFERENCES AND NOTES

1. L. V. Butov et al., *Phys. Rev. Lett.* **86**, 5608–5611 (2001).
2. M. M. Fogler, L. V. Butov, K. S. Novoselov, *Nat. Commun.* **5**, 4555 (2014).
3. M. Combescot, R. Combescot, F. Dubin, *Rep. Prog. Phys.* **80**, 066501 (2017).
4. I. Schwartz et al., *Science* **354**, 434–437 (2016).
5. E. Poem et al., *Nat. Phys.* **6**, 993–997 (2010).
6. A. A. High et al., *Nano Lett.* **12**, 2605–2609 (2012).
7. A. A. High et al., *Nature* **483**, 584–588 (2012).
8. A. A. High et al., *Phys. Rev. Lett.* **103**, 087403 (2009).
9. A. A. High et al., *Nano Lett.* **9**, 2094–2098 (2009).
10. A. T. Hammack et al., *Phys. Rev. Lett.* **96**, 227402 (2006).
11. L. V. Butov, C. W. Lai, A. L. Ivanov, A. C. Gossard, D. S. Chemla, *Nature* **417**, 47–52 (2002).
12. R. Rapaport et al., *Phys. Rev. Lett.* **92**, 117405 (2004).
13. X. Hong et al., *Nat. Nanotechnol.* **9**, 682–686 (2014).
14. P. Rivera et al., *Nat. Commun.* **6**, 6242 (2015).
15. D. Unuchek et al., *Nature* **560**, 340–344 (2018).
16. X. M. Liu, K. Watanabe, T. Taniguchi, B. I. Halperin, P. Kim, *Nat. Phys.* **13**, 746–750 (2017).
17. L. Wang et al., *Science* **342**, 614–617 (2013).
18. See supplementary materials.
19. B. Fallahzad et al., *Phys. Rev. Lett.* **116**, 086601 (2016).
20. G. Scuri et al., *Phys. Rev. Lett.* **120**, 037402 (2018).
21. Y. Zhou et al., *Nat. Nanotechnol.* **12**, 856–860 (2017).

22. Z. Wang, L. Zhao, K. F. Mak, J. Shan, *Nano Lett.* **17**, 740–746 (2017).
23. P. Rivera et al., *Science* **351**, 688–691 (2016).
24. I. V. Bondarev, M. R. Vladimirova, *Phys. Rev. B* **97**, 165419 (2018).
25. A. M. Jones et al., *Nat. Nanotechnol.* **8**, 634–638 (2013).
26. J. S. Ross et al., *Nat. Commun.* **4**, 1474 (2013).
27. G. Finkelstein, H. Shtrikman, I. Bar-Joseph, *Phys. Rev. B* **53**, R1709–R1712 (1996).
28. K. Kheng et al., *Phys. Rev. Lett.* **71**, 1752–1755 (1993).
29. M. A. Lampert, *Phys. Rev. Lett.* **1**, 450–453 (1958).
30. M. Sidler et al., *Nat. Phys.* **13**, 255–261 (2017).
31. R. Schmidt, T. Enss, V. Pietila, E. Demler, *Phys. Rev. A* **85**, 021602 (2012).
32. B. Laikhtman, R. Rapaport, *Phys. Rev. B* **80**, 195313 (2009).
33. L. V. Butov et al., *Phys. Rev. Lett.* **92**, 117404 (2004).
34. J. S. Ross et al., *Nano Lett.* **17**, 638–643 (2017).
35. C. H. Lee et al., *Nat. Nanotechnol.* **9**, 676–681 (2014).
36. X. D. Xu, W. Yao, D. Xiao, T. F. Heinz, *Nat. Phys.* **10**, 343–350 (2014).
37. L. Jauregui, Replication data for: Electrical control of interlayer exciton dynamics in atomically thin heterostructures. Harvard Dataverse (2019); <https://doi.org/10.7910/DVN/IZQAVH>.

#### ACKNOWLEDGMENTS

We thank E. Demler, S. Fang, and F. Pientka for discussions.

**Funding:** This work is supported by the DoD Vannevar Bush Faculty Fellowship (N00014-18-1-2877 for P.K., N00014-16-1-2825 for H.P.), AFOSR MURI (FA9550-17-1-0002), NSF and CUA (PHY-1506284 and PHY-1125846 for H.P. and M.D.L.), ARL (W911NF1520067 for H.P. and M.D.L.), the Gordon and Betty Moore Foundation (GBMF4543 for P.K.), and Samsung Electronics (for P.K. and H.P.). This work was performed in part at the Center for Nanoscale Systems (CNS), a member of the National Nanotechnology Coordinated Infrastructure (NNCI), which is supported by the National Science Foundation under NSF award 1541959. CNS is part of Harvard University. D.J.N. acknowledges

support from the NSF grant DBI-0959721. A.S. acknowledges support from the Fannie and John Hertz Foundation and the Paul & Daisy Soros Fellowships for New Americans. K.W. and T.T. acknowledge support from the Elemental Strategy Initiative conducted by the MEXT, Japan, and the CREST (JPMJCR15F3), JST. **Author contributions:** L.A.J., A.Y.J., and P.K. conceived the project. L.A.J., A.Y.J., K.P., A.A.H., Y.Z., G.S., K.D.G., and A.S. designed and performed the experiments. L.A.J., A.Y.J., and K.P. fabricated the devices and analyzed the data. L.A.J., A.Y.J., K.P.,

D.S.W., and P.K. wrote the manuscript with the help of all authors. D.S.W. developed the theoretical model. T.T. and K.W. grew the h-BN crystals. C.-H.Y. and D.J.N. developed the second harmonic generation setup, which was used to align the individual flakes. M.D.L., H.P., and P.K. supervised the project. **Competing interests:** The authors declare no competing interests. **Data and materials availability:** All data needed to evaluate the conclusions in the paper are present in the paper or the supplementary materials and have been deposited at the Harvard Dataverse (37).

#### SUPPLEMENTARY MATERIALS

[science.sciencemag.org/content/366/6467/870/suppl/DC1](https://science.sciencemag.org/content/366/6467/870/suppl/DC1)  
Materials and Methods  
Supplementary Text  
Figs. S1 to S18  
References (38–45)

19 December 2018; accepted 18 October 2019  
10.1126/science.aaw4194



## POLYMER CHEMISTRY

# A broadly applicable cross-linker for aliphatic polymers containing C–H bonds

Mathieu L. Lepage<sup>1\*</sup>, Chakravarthi Simhadri<sup>1\*</sup>, Chang Liu<sup>1</sup>, Mahdi Takaffoli<sup>2</sup>, Liting Bi<sup>1</sup>, Bryn Crawford<sup>2</sup>, Abbas S. Milani<sup>2</sup>, Jeremy E. Wulff<sup>1†</sup>

Addition of molecular cross-links to polymers increases mechanical strength and improves corrosion resistance. However, it remains challenging to install cross-links in low-functionality macromolecules in a well-controlled manner. Typically, high-energy processes are required to generate highly reactive radicals in situ, allowing only limited control over the degree and type of cross-link. We rationally designed a *bis*-diazirine molecule whose decomposition into carbenes under mild and controllable conditions enables the cross-linking of essentially any organic polymer through double C–H activation. The utility of this molecule as a cross-linker was demonstrated for several diverse polymer substrates (including polypropylene, a low-functionality polymer of long-standing challenge to the field) and in applications including adhesion of low-surface-energy materials and the strengthening of polyethylene fabric.

Addition of cross-links to polymeric materials confers several important advantages to the final product. By converting a thermoplastic into a thermoset, a polymer's impact resistance, tensile strength, and high-temperature performance are greatly enhanced, whereas material creep and unwanted thermal expansion are reduced (1). Cross-linked polymers also have increased resistance to solvents and electrical discharge as well as to chemical and biological effects. Although cross-linking can present challenges from the perspective of recyclability, it is advantageous in applications for which chemical, biological, or electrical degradation is a concern (2, 3). Cross-linked polyethylene, for example, is used for medical devices (4), insulation for electrical wires (5, 6), and containers for corrosive liquids (7). The principal disadvantage to cross-linking lies with an increase in brittleness, because the polymer chains are no longer free to slip across each other. Because these properties are highly correlated to the cross-link density, the control of the cross-linking process is key to the production of high-performance materials.

Cross-links can be established in polymers through various strategies. The most common method in the academic literature involves the use of copolymers wherein one of the monomer constituents incorporates a linkable fragment (1, 8). Alternatively, a monomer that has two functional groups may give rise to a linear prepolymer that can be thermally or photochemically cured (9). However, neither of the above strategies is appropriate when one needs to cross-link a polymer material that lacks func-

tionality within its chemical structure. This includes important commodity plastics like polyethylene and polypropylene. Similarly, biomass-derived polymers (e.g., polylactic acid) and important biodegradable polymers (e.g., polycaprolactone) often lack any cross-linkable functional groups, even though they contain some functionality within their linear chains.

For these reasons, high-energy radical processes involving peroxides or electron or  $\gamma$ -irradiation are used industrially to produce cross-linked polyethylene (2, 3). However, the conditions required to initiate cross-linking through hydrogen abstraction are a limitation, and such methods are ineffective for polypropylene (1). The need to break a strong C–H bond (390 to 400 kJ/mol) in the vicinity of comparatively weaker C–C bonds (~350 kJ/mol) sets the stage for competing fragmentation and branching processes that can compromise the integrity of the material (fig. S1). Moreover, these methods do not allow for control over the type of molecular cross-link established, meaning that one cannot easily tune the mechanical properties of the final material.

We hypothesized that a superior cross-linking strategy could emerge from the use of low-barrier C–H insertions. Singlet carbenes are known to add directly to C–H, O–H, and N–H bonds through a concerted process that does not involve the generation of any new high-energy species (10). Carbene-generating reagents have been used for decades in the field of chemical biology to link small molecules to their protein targets, with the 3-trifluoromethyl-3H-diazirine motif (Fig. 1A) established as a particularly effective carbene precursor (11). Although a few records of multivalent diazirines exist, their occasional application to polymer cross-linking has remained limited to substrates with weak C–H bonds such as polyethylene glycol and highly functionalized materials in organic electronics (12–15). The corresponding *bis*-azides (which function

through nitrene insertion) have been somewhat better developed (16), but nitrenes are generally less reactive toward C–H insertion than carbenes and are more prone to undesirable rearrangement reactions (17). We envisioned that an optimally designed *bis*-diazirine could permit the cross-linking of unfunctionalized alkane polymers under mild conditions and without unwanted branching or fragmentation (Fig. 1B).

We began our search for an effective *bis*-diazirine cross-linker by preparing the known compound **1** (12–15) and the pyridyl analog **2** (Fig. 2A). Both of these molecules were surprisingly volatile (fig. S2), and subsequent thermal analysis according to Yoshida's correlations (17, 18) (Fig. 2B and eqs. S2 and S3) suggested that each possessed a substantial explosion risk. Although preliminary cross-linking trials demonstrated their ability to cross-link model substrates, both the volatility and the explosion risk negated the utility of these molecules for practical applications.

Stimulated by these observations, we designed and synthesized improved cross-linker **3** (Fig. 2A). Design features for **3** included (i) an increased molecular weight relative to **1** and **2**, for reduced volatility and explosion risk; (ii) the absence of any labile C–O or C–N bonds (12–15), which would limit the robustness of cross-linked products; (iii) the use of an electron-deficient linker para to the diazirine motif, for improved handling under ambient conditions (19); and (iv) the absence of any aliphatic C–H bonds, to reduce the risk of self-reaction.

Cross-linker **3** was found to have many desirable properties. It showed good solubility in a wide range of solvents (facilitating its dispersal into polymer matrices) and had a melting point conveniently just above room

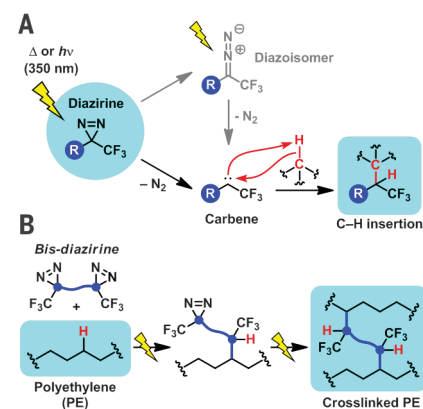


**Fig. 1. A *bis*-diazirine strategy for polymer cross-linking.** (A) Mechanism of carbene formation from the light- or heat-promoted decomposition of diazirines, followed by C–H insertion. *hν*, ultraviolet light. (B) Cross-linking of nonfunctionalized polymers through double C–H insertion of *bis*-diazirines.

<sup>1</sup>Department of Chemistry, University of Victoria, Victoria, BC V8W-3V6, Canada. <sup>2</sup>Materials and Manufacturing Research Institute, University of British Columbia, Kelowna, BC V1V-1V7, Canada.

\*These authors contributed equally to this work.

†Corresponding author. Email: wulff@uvic.ca

temperature (Fig. 2F), meaning that it could be handled either as a liquid or crystalline solid. Thermogravimetric analysis (TGA) revealed that it cleanly lost 2 equivalents of  $N_2$  upon gentle heating (Fig. 2C and eq. S1), whereas differential scanning calorimetry (DSC) and application of Yoshida's correlations confirmed that **3** was not a likely explosive (Fig. 2B and table S1). Subsequent mechanical tests (movies S1 and S2) revealed no propensity for explosion with **3**, at which point its synthesis was safely scaled up to afford multigram quantities (20).

Cross-linkers that are capable of inserting into the strong secondary ( $2^\circ$ ) C–H bonds of polyethylene should have equal or greater effectiveness against most other polymer substrates, because almost every other aliphatic polymer (aside from perhalogenated materials like Teflon) has C–H bonds of equal or lower strength (e.g., polypropylene or polystyrene) or contains O–H or N–H bonds that react more quickly with carbenes (e.g., polyalcohols or polyamides) (11). We therefore elected to first test **1** to **3** in models of polyethylene cross-linking, with the expectation that any successful cross-linkers identified in these trials would be broadly applicable to other systems. Seeking an initial substrate that would permit full spectroscopic characterization of cross-linked products, we first used cyclohexane as a molecular model for polyethylene, because it similarly contains only  $2^\circ$ -C–H bonds.

The cross-linking of cyclohexane with **1** to **3** was studied under both thermal and photochemical activation conditions (Fig. 2A). Both long-wave ultraviolet (UV) irradiation (350 nm) and heating ( $110^\circ$  or  $140^\circ\text{C}$ ) were effective in activating all three *bis*-diazirines. A difference in the rate of photochemical conversion was observed: Whereas **3** was consumed within 1 hour, **1** and **2** required ~2 hours and ~4 hours, respectively, for complete conversion. In all cases, a small amount of linear diazo isomer (resulting from the known rearrangement of the diazirine group) was detected under photochemical conditions (Fig. 2D and figs. S5 to S11). These isomeric species persisted two to three times longer but can also participate in cross-linking (21). Under thermal activation at  $140^\circ\text{C}$ , the reaction was much faster (<20 min), and no linear diazo intermediate was observed.

Successful cross-linking was confirmed by careful isolation and characterization of products **4** to **6** (Fig. 2F). For all three adducts,  $^1\text{H}$  nuclear magnetic resonance (NMR) spectra showed a doublet of quartets at ~3.1 parts per million (ppm), and  $^{19}\text{F}$  NMR revealed a proton-coupled resonance at ~63 ppm (coupling constant  $^3J_{\text{H-F}} = 10$  Hz), both indicating the presence of a hydrogen atom  $\alpha$  to a trifluoromethyl group and at the foot of a new C(H)–C(H) bond (Fig. 2E). The modest isolated yields for **4** to **6**, independent from the meth-

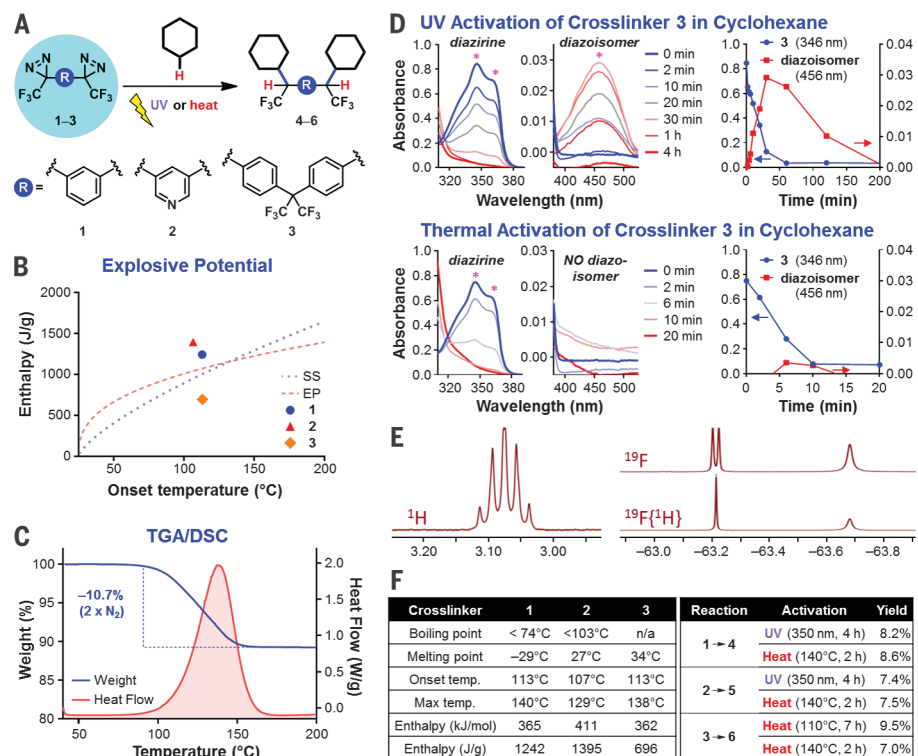


**Fig. 2. Survey of cross-linkers 1 to 3.** (A) Compound structures and illustration of cyclohexane cross-linking. (B) Yoshida correlations showing that **1** and **2**, but not **3**, are potential explosion hazards. EP, explosive propagation; SS, shock sensitivity. (C) TGA and DSC analysis of **3**, showing that the cross-linker is activated above  $100^\circ\text{C}$  and loses mass corresponding exactly to two equivalents of  $N_2$ . (D) UV spectra collected during the photochemical and thermal cross-linking of cyclohexane with **3**, showing that thermal initiation is faster and produces less diazo isomer. Asterisks indicate bands associated with each chromophore. (E)  $^1\text{H}$  and  $^{19}\text{F}$  NMR data for purified adduct **6**, produced from cross-linking of cyclohexane with **3**.  $^{19}\text{F}\{^1\text{H}\}$  indicates a proton-decoupled experiment. (F) Physical properties for **1** to **3** and yields for purified cyclohexane adducts. Max temp., maximum temperature.

od of activation, should not be taken as an absolute measure of cross-linking efficacy, because several alternative cross-link structures (e.g., those in which **1**, **2**, or **3** oligomerize before cross-linking) would not be included within these yields. Indeed, observations of the spectroscopic signatures described above within the crude NMR spectra indicate that the overall C–H insertion efficacy in each case is >50% (20). Although the pyridine unit within **2** was added in the hopes of increasing cross-linking efficiency (19), this compound did not offer any advantages relative to **1** or **3**.

With cross-linking of the molecular model substrate established, we turned our attention to cross-linking of relevant polymers, beginning with soluble, low-molecular-weight polyethylene (i.e., paraffin). Increasing amounts of *bis*-diazirine **3** [5 to 200 weight % (wt %)] (table S2) were readily dissolved in molten paraffin and activated at  $110^\circ\text{C}$  (figs. S15 and S16). Analysis by gel permeation chromatography (GPC) revealed a continuous increase in molecular weight with the amount of *bis*-diazirine added (Fig. 3A, blue arrow), providing evidence of cross-linking. Simultaneous

UV detection confirmed that the chromophore from **3** was predominantly associated with higher-weight fractions (red arrow)—again, consistent with successful cross-linking. At 200 wt % of **3**, cross-linking of paraffin afforded a tough gel with diminished solubility in tetrahydrofuran (THF) (fig. S16) (hence the decreased intensity in the GPC data), which supports the creation of a three-dimensional network. Subsequent studies also confirmed cross-linking in less-soluble, unbranched polyethylene (figs. S29 and S30).

Cross-linker **3** was then tested on other polymer substrates. Experiments with polydimethylsiloxane (PDMS) provided similar results to those for paraffin: Low-viscosity PDMS exhibited an increased molecular weight upon thermal cross-linking with 5 wt % **3** (Fig. 3B), whereas high-viscosity PDMS was transformed into a rubbery solid with negligible solubility in THF (fig. S17). Photochemical cross-linking with **3** (20) likewise converted the liquid PDMS substrate into a stable gel (movie S3). Similar observations were made when cross-linking polycaprolactone (figs. S19 and S20), polystyrene (figs. S31 to S33), and polyisoprene

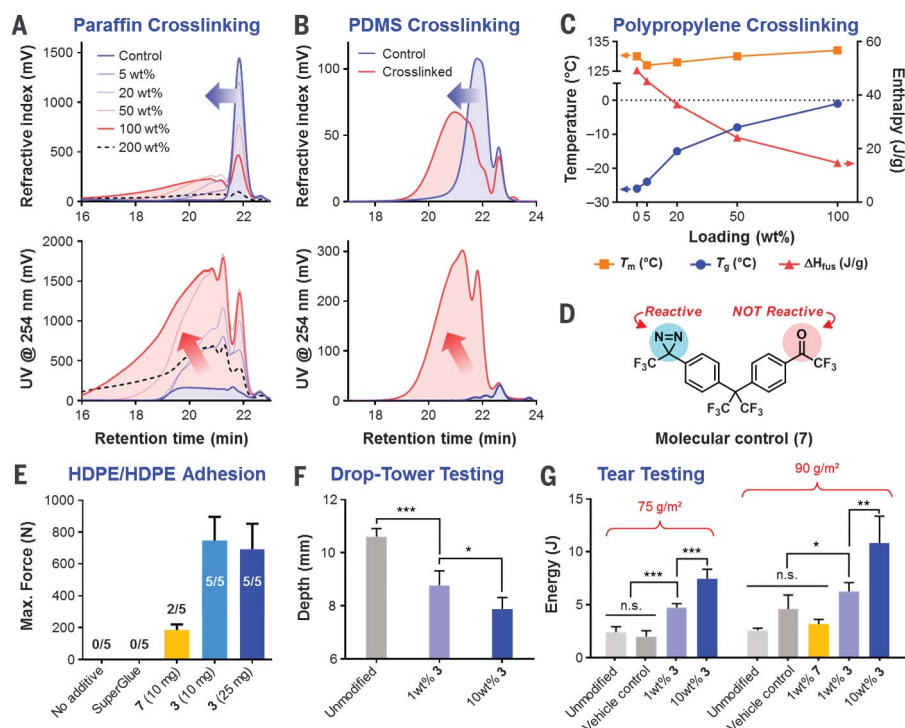


**Fig. 3. Cross-linking of soluble and insoluble polymers.** (A) Cross-linking of paraffin monitored by GPC. (B) Cross-linking of PDMS monitored by GPC. (C) Cross-linking of polypropylene increases the glass transition temperature ( $T_g$ ) and decreases the fusion enthalpy ( $\Delta H_{fus}$ ). (D) Structure of molecular control **7**, used to validate mechanism. (E) Lap-shear data confirming adhesion for HDPE samples treated with **3** but not those treated with **7**. Numbers indicate the total number of samples exhibiting sufficient adhesion for testing. (F) Drop-tower testing confirming reduced back-face signature and increased resistance to penetration upon cross-linking of UHMWPE fabric with **3**. (G) Tear-testing data confirming increased mechanical strength for UHMWPE samples treated with **3** but not those treated with **7**. Error bars correspond to standard deviations [ $N = 5$  for (E) and  $N = 4$  for (F); sample replicates for (G) are indicated in table S13]. \* $p < 0.05$ ; \*\* $p < 0.01$ ; \*\*\* $p < 0.001$ . n.s., not statistically significant.

(figs. S34 to S37). Polyvinyl alcohol cross-linked with increasing amounts of **3** progressively lost its aqueous solubility (figs. S24 and S25). The use of low concentrations of **3** for polyvinyl alcohol gave a product that floated atop the aqueous sample, whereas the use of higher concentrations gave a product that was heavier than water, demonstrating that cross-linker loading could control material density.

We next sought to demonstrate the efficacy of **3** for cross-linking commercial polypropylene samples. With increasing concentrations of cross-linker applied to low-molecular-weight polypropylene, we observed a monotonically increasing glass transition temperature ( $T_g$ ) and decreased solubility (Fig. 3C and fig. S26). We also observed a consistent decrease in the enthalpy associated with the melting transition, while the actual  $T_m$  temperature remained constant. This is consistent with a model of polymer cross-linking where cross-linked regions of the polymer structure will be nonmelting [leading to a reduction in fusion enthalpy ( $\Delta H_{fus}$ )], whereas residual non-cross-linked regions will have a  $T_m$  similar to

that of unmodified polypropylene. Even more profound effects were observed upon cross-linking of higher-molecular-weight polypropylene: The  $T_g$  was driven to a high of nearly room temperature, whereas the melting transition was almost completely lost at high-cross-linking density (fig. S27).

To demonstrate the utility of **3** for industrial processes, we were particularly interested to explore its effectiveness as an adhesive for high-density polyethylene (HDPE) and as a strengthening agent for polyethylene fabric. Adhesion of low-surface-energy materials like HDPE is an important problem in manufacturing (22). *bis*-Diazirine **3** can, in principle, connect two polymer surfaces through strong C–C bonds. We applied *bis*-diazirine **3** between bars of HDPE, cross-linked the assemblies at 110°C and then challenged them on a lap-shear experiment, along with appropriate controls (Fig. 3E). The cross-linked bars required far more load to be pulled apart than any of the controls, and analysis of separated samples by optical profilometry (figs. S40 and S41) indicated that residue derived from **3** was pre-

sent on both faces, consistent with a cohesive rather than adhesive failure mechanism (23). Control samples prepared with no additives or with an equivalent weight (10 mg) of commercial Super Glue could not be measured, because they did not adhere. A set of samples coated with an equivalent weight of molecular control **7** (Fig. 3D) only barely adhered, proving that most of the adhesive force was due to cross-linking rather than simple surface modification. The use of a larger amount of **3** (25 mg) did not increase bonding strength.

To explore the effect of cross-linking ultrahigh-molecular-weight polyethylene (UHMWPE) fabric, we dissolved **3** in pentane and applied this solution to two different deniers of fabric (75 or 90 g/m<sup>2</sup>) from two different suppliers. The pentane was evaporated, and impregnated samples (or vehicle controls, treated with pentane but not **3**) were cross-linked at 110°C. Samples treated with as low as 1 wt % **3** exhibited increased performance in both drop-tower and tear testing (Fig. 3, F and G). Increasing the cross-linker density to 10 wt % further improved material strength, but by a less marked increment. Surface sites on the UHMWPE fibers evidently become saturated, providing diminishing returns upon addition of more cross-linker. Fabric treated with molecular control **7** did not exhibit improved strength, once again confirming that the above results are due to authentic cross-linking and not surface modification. Cross-linking of aramid fabric likewise improved impact resistance, although the substantially increased rigidity in this case made the treated material easier to tear (figs. S43 to S46).

*bis*-Diazirine **3** is exceptionally stable (it can be recovered unchanged after dispersion in concentrated sulfuric acid at 70°C) but is readily activated by two complementary modes of activation: heating to >100°C or irradiation with ~350-nm light. Once activated, **3** is able to cross-link any aliphatic polymer containing C–H bonds, resulting in increased molecular weight, decreased solubility, increased  $T_g$ , and increased material strength: all well-known hallmarks of molecular cross-linking.

## REFERENCES AND NOTES

- W. Lin, Z. Shao, J.-y. Dong, T. C. M. Chung, *Macromolecules* **42**, 3750–3754 (2009).
- C. Meola, G. M. Carlomagno, G. Giorleo, "Cross-linked polyethylene" in *Encyclopedia of Chemical Processing*, S. Lee, Ed. (Taylor & Francis, ed. 1, 2006), pp. 577–588.
- K. S. Whiteley, T. G. Heggs, H. Koch, R. L. Mawer, W. Immel, "Polyolefins" in *Ullmann's Encyclopedia of Industrial Chemistry* (Wiley-VCH, 2000), pp. 1–103.
- P. Taddei, S. Affatato, C. Fagnano, A. Toni, *Biomacromolecules* **7**, 1912–1920 (2006).
- K. Ueno, I. Uda, S. Tada, *Int. J. Radiat. Appl. Instrum. Part C* **37**, 89–91 (1991).
- M. Sabet, A. Hassan, C. T. Ratnam, *Polym. Bull.* **69**, 1103–1114 (2012).
- PolyProcessing, High-density crosslinked polyethylene (XLPE); [www.polyprocessing.com/innovations/high-density-crosslinked-polyethylene/](http://www.polyprocessing.com/innovations/high-density-crosslinked-polyethylene/).
- S. Ahn, P. Deshmukh, M. Gopinadhan, C. O. Osuji, R. M. Kasi, *ACS Nano* **5**, 3085–3095 (2011).



9. T. J. Cuthbert, T. Li, A. W. H. Speed, J. E. Wulff, *Macromolecules* **51**, 2038–2047 (2018).
10. D. Bourissou, O. Guerret, F. P. Gabbaï, G. Bertrand, *Chem. Rev.* **100**, 39–92 (2000).
11. J. Brunner, H. Senn, F. M. Richards, *J. Biol. Chem.* **255**, 3313–3318 (1980).
12. A. Blencowe, C. Blencowe, K. Cosstick, W. Hayes, *React. Funct. Polym.* **68**, 868–875 (2008).
13. A. Welle, F. Billard, J. Marchand-Brynaert, *Synthesis* **44**, 2249–2254 (2012).
14. H. Burgoon, C. D. Cyrus, L. F. Rhodes, (Promerus, LLC, USA, 2016). Diazirine compounds, polymers, and photoimageable compositions derived therefrom. U.S. Patent WO2016049123 (2016).
15. L. F. Rhodes, H. Burgoon, I. Afonina, T. Backlund, A. Morley, (Promerus, LLC, USA; Merck Patent GmbH, 2017). Diazirine containing organic electronic compositions. U.S. Patent WO2017165478 (2017).
16. R.-Q. Png *et al.*, *Nat. Mater.* **9**, 152–158 (2010).
17. T. Yoshida, Y. Wada, N. Foster, “Experimental evaluation of fire and explosion hazards of reactive chemical substances” in *Safety of Reactive Chemicals and Pyrotechnics*, T. Yoshida, Y. Wada, N. Foster, Eds. (Elsevier, vol. 5, 1995), pp. 75–253.
18. J. B. Sperry *et al.*, *Org. Process Res. Dev.* **22**, 1262–1275 (2018).
19. A. B. Kumar, J. D. Tipton, R. Manetsch, *Chem. Commun.* **52**, 2729–2732 (2016).
20. See supplementary materials.
21. M. P. Doyle, R. Duffy, M. Ratnikov, L. Zhou, *Chem. Rev.* **110**, 704–724 (2010).
22. D. M. Brewis, D. Briggs, *Polymer (Guildf.)* **22**, 7–16 (1981).
23. S. Ebnesajjad, C. Ebnesajjad, “Theories of adhesion” in *Surface Treatment of Materials for Adhesive Bonding* (Elsevier, ed. 2, 2013), pp. 77–91.
24. C. Simhadri *et al.*, A broadly applicable cross-linker for aliphatic polymers containing C–H bonds: Raw NMR Data (2019); <https://doi.org/10.6084/m9.figshare.10110992>.

#### ACKNOWLEDGMENTS

We thank the research groups of I. Manners and M. Moffit for assistance with TGA, DSC, and GPC. In particular, M.L.L. thanks L. MacFarlane for helpful discussions. We also thank P. Berrang, R. Mandau, and G. DiLabio for their collaboration on ongoing projects related to the use of the cross-linkers described here and R. Spontak for the low-MW polypropylene used in these experiments. **Funding:** Operating funds were provided by Mitacs Canada (grant IT11982) and Epic Ventures, Inc. **Author contributions:** J.E.W. conceived the study. M.L.L., C.S., C.L., and L.B. synthesized the cross-linkers and

control compound. M.L.L., C.S., and L.B. carried out the cross-linking experiments. M.T. conducted the mechanical analyses with assistance from B.C. and supervision and infrastructure support from A.S.M. The manuscript was written by M.L.L. and J.E.W. with help from all authors. **Competing interests:** M.L.L., C.S., and J.E.W. are coauthors on U.S. Provisional Patent Application 62/839,062, which claims the use of cross-linkers described in this work. **Data and materials availability:** All data needed to reproduce the experiments described in the paper are available in the main text or the supplementary materials. Raw NMR data files for all synthesized compounds have been deposited with figshare (24).

#### SUPPLEMENTARY MATERIALS

[science.sciencemag.org/content/366/6467/875/suppl/DC1](https://science.sciencemag.org/content/366/6467/875/suppl/DC1)  
Materials and Methods  
NMR Spectra  
Supplementary Text  
Figs. S1 to S46  
Tables S1 to S13  
Movies S1 to S3

4 July 2019; accepted 9 October 2019  
10.1126/science.aay6230

## FRESHWATER ECOLOGY

# Catchment properties and the photosynthetic trait composition of freshwater plant communities

L. L. Iversen<sup>1,2\*</sup>, A. Winkel<sup>1\*</sup>, L. Baastrup-Spohr<sup>1\*</sup>, A. B. Hinke<sup>1</sup>, J. Alahuhta<sup>3,4</sup>, A. Baatrup-Pedersen<sup>5</sup>, S. Birk<sup>6</sup>, P. Brodersen<sup>1</sup>, P. A. Chambers<sup>7</sup>, F. Ecke<sup>8</sup>, T. Feldmann<sup>9</sup>, D. Gebler<sup>10</sup>, J. Heino<sup>4</sup>, T. S. Jespersen<sup>11</sup>, S. J. Moe<sup>12</sup>, T. Riis<sup>5</sup>, L. Sass<sup>13</sup>, O. Vestergaard<sup>14</sup>, S. C. Maberly<sup>15††</sup>, K. Sand-Jensen<sup>1††</sup>, O. Pedersen<sup>116††</sup>

Unlike in land plants, photosynthesis in many aquatic plants relies on bicarbonate in addition to carbon dioxide (CO<sub>2</sub>) to compensate for the low diffusivity and potential depletion of CO<sub>2</sub> in water. Concentrations of bicarbonate and CO<sub>2</sub> vary greatly with catchment geology. In this study, we investigate whether there is a link between these concentrations and the frequency of freshwater plants possessing the bicarbonate use trait. We show, globally, that the frequency of plant species with this trait increases with bicarbonate concentration. Regionally, however, the frequency of bicarbonate use is reduced at sites where the CO<sub>2</sub> concentration is substantially above the air equilibrium, consistent with this trait being an adaptation to carbon limitation. Future anthropogenic changes of bicarbonate and CO<sub>2</sub> concentrations may alter the species compositions of freshwater plant communities.

The biogeography of terrestrial plants is influenced by climatic factors—primarily air temperature and precipitation (1). Furthermore, the distribution of biochemical traits, such as the two terrestrial CO<sub>2</sub>-concentrating mechanisms, C<sub>4</sub> photosynthesis and crassulacean acid metabolism, are linked to temperature and water availability (2). Although freshwater angiosperms evolved from terrestrial ancestors (3), their growth is controlled by light, nutrients, and inorganic carbon (4) rather than water, and therefore the factors influencing their biogeography are likely to be different. Inorganic carbon potentially limits photosynthesis in aquatic systems, because the diffusion of CO<sub>2</sub> is 10<sup>4</sup>-fold lower in water than in air. Consequently, the CO<sub>2</sub> concentration needed to saturate photosynthesis is up to 12 times the air equilibrium concentration (5). Moreover, rapid photosynthesis can reduce CO<sub>2</sub> in water substantially below air saturation (4).

In response to carbon limitation, a few aquatic angiosperms evolved the same CO<sub>2</sub>-concentrating mechanisms found in their

terrestrial ancestors, but the most frequent mechanism, found in about half of studied submerged freshwater plants, is the exploitation of bicarbonate (HCO<sub>3</sub><sup>-</sup>) (4, 6), which is derived from mineral weathering of soils and rocks in the catchment. Bicarbonate is the dominant form of inorganic carbon in fresh waters when the pH is between ~6.3 and ~10.2, and its concentration often exceeds that of CO<sub>2</sub> by a factor of 10 to 100 (6). The ability to use bicarbonate is present in most taxonomic groups and appears to have evolved independently in cyanobacteria, eukaryotic algae, and vascular aquatic plants (7). This shows the fundamental importance of bicarbonate use to plant fitness (6); increase of photosynthesis, growth, and primary productivity at higher bicarbonate concentrations has been documented (8–10). However, bicarbonate use is not ubiquitous, because it involves costs as well as benefits. Costs include energy, as it is an active process (11) and rates of photosynthesis at limiting concentrations of inorganic carbon are greater in CO<sub>2</sub> users than in bicarbonate users (5, 12). Thus, where CO<sub>2</sub> concentrations are substantially above air saturation, as is often the case in streams, the benefit of bicarbonate use will be reduced (13). Furthermore, obligate CO<sub>2</sub> users can exploit alternative CO<sub>2</sub> sources in the air, lake sediment, or the water overlying the sediment (14), allowing continued photosynthesis without the need to invest in mechanisms required for bicarbonate use.

We hypothesized that because limitation of photosynthesis by inorganic carbon supply is widespread in freshwater plants, the relative concentrations of bicarbonate and CO<sub>2</sub> at a particular site should determine the proportion of plants that are obligate CO<sub>2</sub> users versus bicarbonate users. Because geochemical catchment characteristics determine bicarbonate concentration, there should be broad biogeographical patterns in the proportion of

freshwater plants able to use bicarbonate, whereas at a smaller scale both the CO<sub>2</sub> and bicarbonate concentrations in lakes and streams might structure the functional group composition.

To test these hypotheses, we generated a database of freshwater angiosperms and their ability to use bicarbonate as an inorganic carbon source, based on data found in the literature. These were complemented with new data we gathered on 35 species from mainly tropical regions where few prior data existed (table S1) (15). The resulting 131 species represent ~10% of known species with a submerged life stage (16), and of these, 58 (44%) can use bicarbonate. To quantify the distribution of bicarbonate users versus CO<sub>2</sub> users, we used: (i) ~1 million geo-referenced plant records, (ii) global plant ecoregion species lists, and (iii) 963 site-specific plant compositions from Northern Hemisphere lakes and streams (fig. S1). In each of the investigated 963 sites, plant composition was related to measured concentrations of CO<sub>2</sub> and bicarbonate. The geo-referenced plant records and ecoregion species lists were linked to local bicarbonate concentrations derived from a constructed global map of bicarbonate concentrations (fig. S2) (15).

In the analyzed lake and stream sites, concentrations of both bicarbonate and CO<sub>2</sub> affected the occurrence of obligate CO<sub>2</sub> users versus bicarbonate users, albeit differently within and between lakes and streams (Fig. 1 and fig. S3). The chance of observing a bicarbonate user in lakes and streams correlated directly with concentrations of bicarbonate and CO<sub>2</sub> [ $\Delta\text{Habitat} = 0.82 (-1.64, 0.01)$ ; mean (95% confidence interval);  $\Delta$  represents the difference between streams and lakes in parameter estimates on a log(odds) scale (fig. S3)] (Fig. 1A). However, with increasing bicarbonate concentrations, the likelihood of observing a bicarbonate user increased in lakes but not in streams [ $\Delta\beta_{\text{Bicarbonate}} = -0.82 (-1.10, -0.54)$ ] (Fig. 1B) [see (15) for an explanation of  $\beta$ ]. Moreover, with an increase in CO<sub>2</sub>, the chance of observing a bicarbonate user decreased in both habitat types [ $\Delta\beta_{\text{CO}_2} = -0.04 (-0.22, 0.13)$ ] (Fig. 1C). The present study shows that the concentration of bicarbonate has a different effect on the proportion of bicarbonate users in lakes versus streams. Unlike in lakes, no relationship between bicarbonate availability and bicarbonate users was found in streams. This upholds our hypothesis that where concentrations of CO<sub>2</sub> are high, the competitive advantage of using bicarbonate as a carbon source for photosynthesis will be reduced even if bicarbonate is available.

Across global plant regions (17), the shifting proportions of bicarbonate users versus obligate CO<sub>2</sub> users showed distinct spatial patterns (Fig. 2A). Compared to the overall mean, a higher proportion of bicarbonate users

<sup>1</sup>Department of Biology, University of Copenhagen, Copenhagen, Denmark. <sup>2</sup>School of Life Sciences, Arizona State University, Tempe, AZ, USA. <sup>3</sup>Geography Research Unit, University of Oulu, Oulu, Finland. <sup>4</sup>Finnish Environment Institute, Helsinki, Finland. <sup>5</sup>Department of Bioscience, Aarhus University, Aarhus, Denmark. <sup>6</sup>Aquatic Ecology, Universität Duisburg-Essen, Duisburg, Germany. <sup>7</sup>Environment and Climate Change Canada, Ottawa, ON, Canada. <sup>8</sup>Department of Wildlife, Swedish University of Agricultural Sciences, Uppsala, Sweden. <sup>9</sup>Institute of Agricultural and Environmental Sciences, Estonian University of Life Sciences, Tartu, Estonia. <sup>10</sup>Department of Ecology and Environment, Poznań University of Life Sciences, Poznań, Poland. <sup>11</sup>Niels Bohr Institute, University of Copenhagen, Copenhagen, Denmark. <sup>12</sup>Norwegian Institute for Water Research, Oslo, Norway. <sup>13</sup>Prairie Research Institute, University of Illinois, Champaign, IL, USA. <sup>14</sup>United Nations Environment Programme, Nairobi, Kenya. <sup>15</sup>Centre for Ecology & Hydrology, Bailrigg, Lancaster, UK. <sup>16</sup>School of Agriculture and Environment, The University of Western Australia, Perth, WA, Australia.

\*These authors contributed equally to this work. <sup>††</sup>These authors contributed equally to this work.

†Corresponding author. Email: scm@ceh.ac.uk (S.C.M.); ksandjensen@bio.ku.dk (K.S.-J.); opedersen@bio.ku.dk (O.P.)

†Corresponding author. Email: scm@ceh.ac.uk (S.C.M.); ksandjensen@bio.ku.dk (K.S.-J.); opedersen@bio.ku.dk (O.P.)

†Corresponding author. Email: scm@ceh.ac.uk (S.C.M.); ksandjensen@bio.ku.dk (K.S.-J.); opedersen@bio.ku.dk (O.P.)

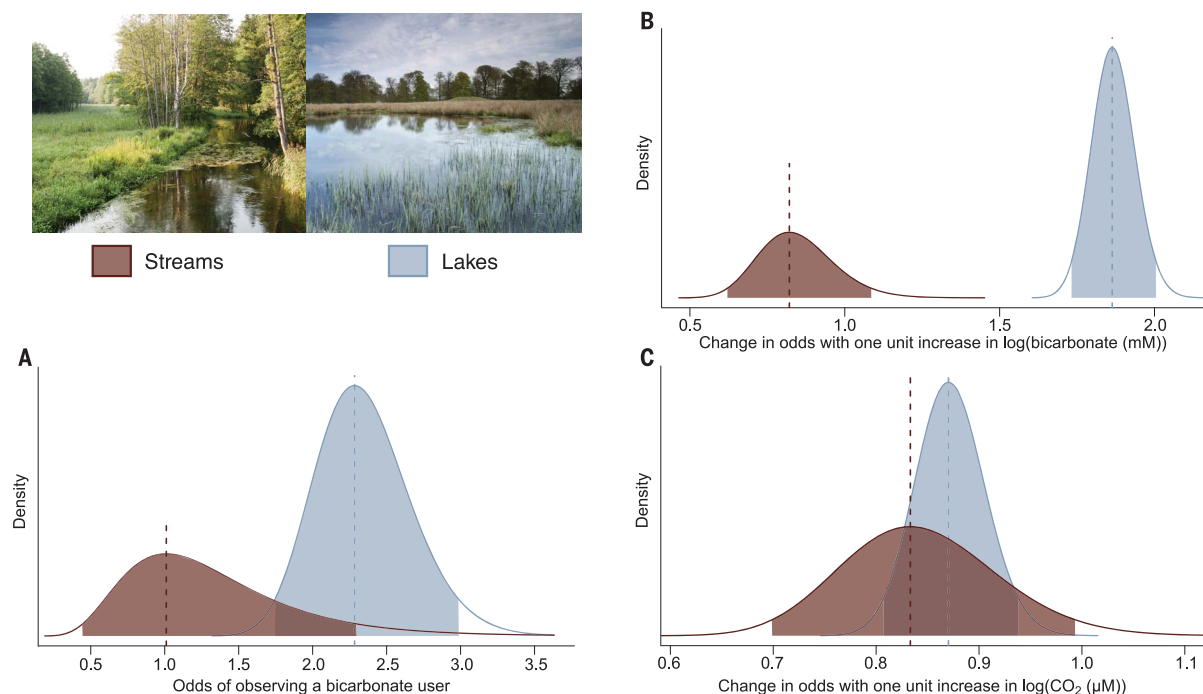


**Fig. 1. Bicarbonate use in submerged freshwater plant communities.**

(A) Likelihood of observing a bicarbonate user versus a CO<sub>2</sub> user in streams ( $n = 172$  samples; red) and lakes ( $n = 791$  samples; blue). (B and C) Modeled odds of observing a bicarbonate user versus a CO<sub>2</sub> user as a function of bicarbonate (B) or CO<sub>2</sub> (C)

concentration. Values  $>1$  indicate a higher likelihood (A) or increase in likelihood (B and C) of observing a bicarbonate user versus a CO<sub>2</sub> user with a one-unit increase in bicarbonate (B) or CO<sub>2</sub> (C) concentration. The dotted vertical lines show mean estimates, and shaded areas show the 95% confidence limits around the mean.

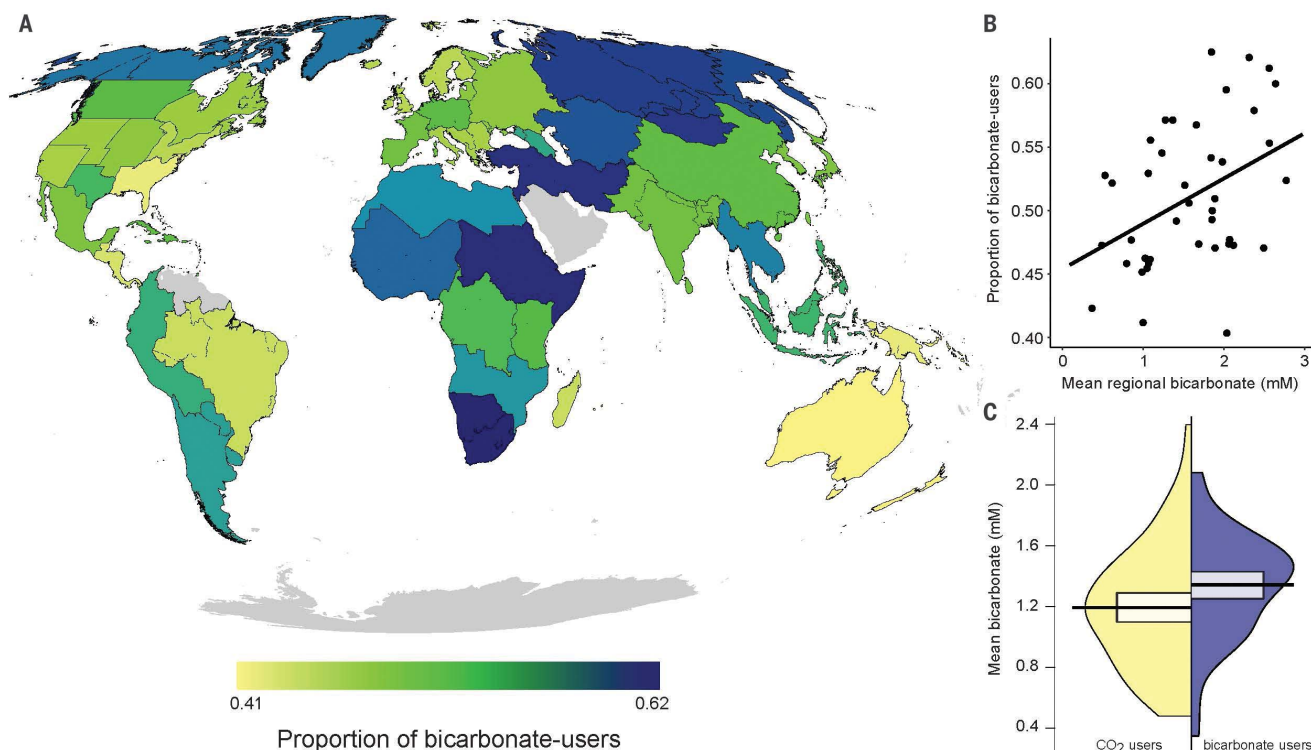


**Fig. 2. Global relationship between bicarbonate concentration and the proportion of bicarbonate users in freshwater plants.**

(A) Proportion of bicarbonate-using species across 52 plant ecoregions. Gray areas indicate regions where information on bicarbonate use in local plants is not available. (B) Relationship between mean bicarbonate concentration in plant regions and

frequency of bicarbonate users. The line represents the mean proportion of bicarbonate users. (C) Density plots of bicarbonate preferences for bicarbonate users ( $n = 57$ ) and obligate CO<sub>2</sub> users ( $n = 72$ ). The central horizontal black lines represent the means, and the boxes indicate the 95% confidence intervals around the means.



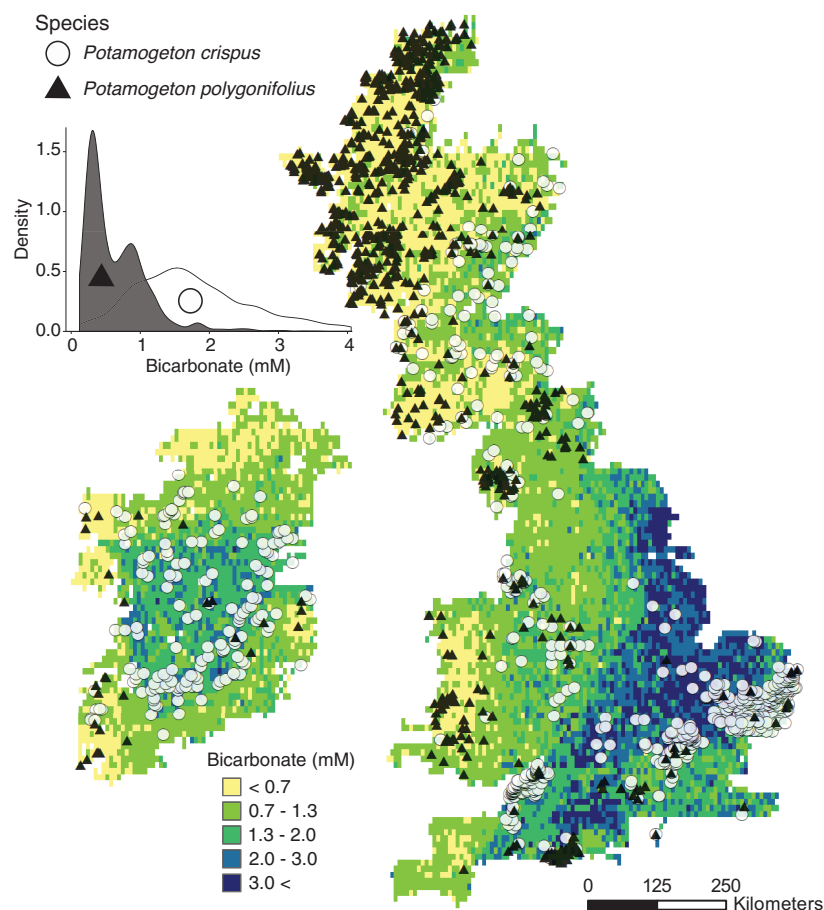


**Fig. 3. Steep gradients in bicarbonate concentrations and spatial separation in species distribution in the British Isles.** Distribution of two pondweed species with contrasting bicarbonate use in the British Isles. *Potamogeton polygonifolius* (obligate CO<sub>2</sub> user; black triangles) is found in areas with lower bicarbonate concentrations than are present where *Potamogeton crispus* (bicarbonate user; white circles) is found. The top left inset shows the density distribution of the two species across bicarbonate concentrations. Bicarbonate concentrations are from the global bicarbonate map (fig. S2), and species data were extracted from the geo-referenced plant occurrences (15).

was observed in Africa, temperate Asia, and the northern part of North America (Fig. 2A). Globally, species using bicarbonate were found in areas with higher bicarbonate concentrations [bicarbonate users – CO<sub>2</sub> users = 0.16 mM (0.02, 0.30)] (Fig. 2C; see Fig. 3 for a local example). The proportion of bicarbonate-using species increased with bicarbonate concentration within ecoregions [ $\beta = 0.14$  (0.05, 0.24)] (Fig. 2B). Because catchment geology and geological history shape the distributions of lakes and rivers, as well as the bicarbonate concentrations in freshwater ecosystems (18, 19), they are the chief determinants of plant distributions in fresh waters. CO<sub>2</sub> concentrations are largely regulated by local CO<sub>2</sub> supersaturated inflow (20) and ecosystem metabolism, making modeling difficult at large spatial scales (19, 21). Thus, future models of freshwater CO<sub>2</sub> concentrations may improve the prediction of plant distributions even further. Although global lake and river data exist to some extent as annual means (22), given the temporal varia-

bility in CO<sub>2</sub> concentration, the appropriate concentration would be that during the growing season at the specific site (20).

Anthropogenic changes as a consequence of deforestation, cultivation of land, application of nitrate fertilizers, and reduced atmospheric acid deposition (23) are causing large-scale increases in bicarbonate concentrations (24, 25). The observed increasing bicarbonate concentrations are expected to cause a severe impact on bicarbonate-poor lakes, because higher bicarbonate concentrations will markedly change species composition (26) by allowing tall, fast-growing bicarbonate users to colonize and suppress smaller species adapted to the use of CO<sub>2</sub> alone in or near the sediment (27). There is evidence for reestablishment of species that are able to use bicarbonate, after the bicarbonate has increased because of liming (28) or as a result of reduction in acid deposition (29). Moreover, systematic changes in species composition caused by changes in CO<sub>2</sub> concentration have also been demonstrated in a

river system where the proportion of CO<sub>2</sub> users declined as CO<sub>2</sub> decreased downstream (13). In contrast, increasing atmospheric CO<sub>2</sub> concentrations, even if they influence dissolved CO<sub>2</sub>, will have little effect on the abundance of bicarbonate users, because increases in CO<sub>2</sub> will be small relative to bicarbonate concentrations and will have little effect on plant photosynthesis rate (30).

Our study shows that bicarbonate use by aquatic angiosperms is widespread in fresh waters around the globe and that the proportion of obligate CO<sub>2</sub> users to bicarbonate users is significantly related to the bicarbonate concentration. Among terrestrial plants, the evolution of leaf traits and different photosynthetic pathways that enable rapid carbon assimilation and improved water economy (31) has resulted in global biogeographical patterns that are linked to variations in climate (32, 33). In contrast, for freshwater plants, we show that biogeographical patterns of bicarbonate use exist and that these are caused by catchment properties that determine the concentrations of bicarbonate and CO<sub>2</sub>. This insight will help evaluate the repercussions of future changes in concentrations of bicarbonate and CO<sub>2</sub> on the biodiversity and ecosystem functions for fresh waters.

## REFERENCES AND NOTES

1. M. C. Peel, B. L. Finlayson, T. A. McMahon, *Hydrol. Earth Syst. Sci. Discuss.* **4**, 439–473 (2007).
2. C. J. Still, J. A. Berry, G. J. Collatz, R. S. DeFries, *Global Biogeochem. Cycles* **17**, 1006 (2003).
3. D. H. Les, N. P. Tippery, *Early Events Monocot Evol.* **83**, 118–164 (2013).
4. T. V. Madsen, S. C. Maberly, *Freshw. Biol.* **26**, 175–187 (1991).
5. S. C. Maberly, T. V. Madsen, *Funct. Ecol.* **12**, 99–106 (1998).
6. S. C. Maberly, B. Gontero, *J. Exp. Bot.* **68**, 3797–3814 (2017).
7. M. Giordano, J. Beardall, J. A. Raven, *Annu. Rev. Plant Biol.* **56**, 99–131 (2005).
8. K. Sand-Jensen, H. Frost-Christensen, *Oecologia* **117**, 31–39 (1998).
9. M. R. Andersen, T. Kragh, K. Sand-Jensen, *Proc. R. Soc. B* **284**, 2017.1427 (2017).
10. T. V. Madsen, K. Sand-Jensen, *Oikos* **50**, 176–182 (1987).
11. J. A. Raven, J. Beardall, M. Giordano, *Photosynth. Res.* **121**, 111–124 (2014).
12. T. V. Madsen, S. C. Maberly, *Photosynth. Res.* **77**, 183–190 (2003).
13. S. C. Maberly, S. A. Berthelot, A. W. Stott, B. Gontero, *J. Plant Physiol.* **172**, 120–127 (2015).
14. T. V. Madsen, K. Sand-Jensen, *Aquat. Bot.* **41**, 5–40 (1991).
15. See supplementary materials.
16. K. Murphy et al., *Aquat. Bot.* **158**, 103127 (2019).
17. R. K. Brummitt, World geographical scheme for recording plant distributions, ed. 2. Biodiversity information standards (TDWG, 2001); [www.tdwg.org/standards/109](http://www.tdwg.org/standards/109).
18. R. Lauerwald, J. Hartmann, N. Moosdorf, S. Kempe, P. A. Raymond, *Chem. Geol.* **337–338**, 114–127 (2013).
19. R. Marcé et al., *Nat. Geosci.* **8**, 107–111 (2015).
20. S. C. Maberly, P. A. Barker, A. W. Stott, M. M. De Ville, *Nat. Clim. Change* **3**, 391–394 (2013).
21. L. J. Tranvik et al., *Limnol. Oceanogr.* **54**, 2298–2314 (2009).
22. P. A. Raymond et al., *Nature* **503**, 355–359 (2013).
23. P. A. Raymond, S. K. Hamilton, *Limnol. Oceanogr. Lett.* **3**, 143–155 (2018).
24. P. A. Raymond, N.-H. Oh, R. E. Turner, W. Broussard, *Nature* **451**, 449–452 (2008).
25. J. L. Stoddard et al., *Nature* **401**, 575–578 (1999).
26. O. Vestergaard, K. Sand-Jensen, *Aquat. Bot.* **67**, 85–107 (2000).

27. K. Sand-Jensen, M. Søndergaard, *Int. Rev. Gesamten Hydrobiol.* **66**, 529–552 (1981).
28. T. E. Brandrud, *Aquat. Bot.* **73**, 395–404 (2002).
29. D. T. Monteith *et al.*, *Environ. Pollut.* **137**, 83–101 (2005).
30. G. Bowes, *Annu. Rev. Plant Biol.* **44**, 309–332 (1993).
31. I. J. Wright *et al.*, *Nature* **428**, 821–827 (2004).
32. H. Lambers, F. S. Chapin III, T. L. Pons, *Plant Physiological Ecology* (Springer, 2008).
33. I. J. Wright *et al.*, *Science* **357**, 917–921 (2017).
34. L. L. Iversen, Iversen *et al* 2019 Catchment properties and the photosynthetic trait composition of freshwater plant communities, *Dryad* (2019); <https://doi.org/10.5061/dryad.18931zcrv>.

#### ACKNOWLEDGMENTS

We thank L. Adamec for providing data on *Oenanthe aquatica*, Tropica Aquarium Plants for the generous supply of tropical aquatic plants, and K. Murphy for sharing the species list of plants with a submerged life form. We acknowledge constructive suggestions by C. M. Duarte, H. Lambers, and H. H. Bruun.

**Funding:** L.L.I. was funded by the Carlsberg Foundation (CF17-0155 and CF18-0062). L.B.-S. was funded by the Aage V. Jensen Foundation. D.G. was funded by the Polish National Agency for Academic Exchange (PPN/BEK/2018/1/00401), J.A. was funded by The Academy of Finland (332652), and K.S.-J. was funded by the Carlsberg Foundation (grant CF14-0136). **Author contributions:** L.L.I., A.W., L.B.-S., S.C.M., K.S.-J., and O.P. designed the study, framed the research questions, and wrote the manuscript, with input from the working group (A.B.H., J.A., A.B.-P., P.B., P.A.C., F.E., T.F., J.H., T.S.J., S.J.M., T.R., L.S., and O.V.). L.L.I. analyzed the data and prepared the figures. A.B.H. and O.P. performed the pH drift experiments and together with A.W. searched the literature on bicarbonate uptake in aquatic plants. A.W., L.L.I., and L.B.-S. assembled the data for the global analysis. F.E., L.B.-S., L.S., S.C.M., S.J.M., J.A., and T.F. assembled the site-specific lake data; A.B.-P., P.B., P.A.C., D.G., K.S.-J., T.R., and T.S.J. assembled the site-specific stream data; O.V., A.W., L.L.I., and L.B.-S. prepared the site-specific data for further analysis. **Competing interests:** O.V. is a staff member

of the United Nations Environment Programme. The authors alone are responsible for the views expressed in the publication, and they do not necessarily represent opinions, decisions, or policies of the United Nations Environment Programme. The authors declare no other competing interests. **Data and materials availability:** All R scripts and cleaned datasets used for this analysis are available at the Dryad Digital Repository (34).

#### SUPPLEMENTARY MATERIALS

[science.sciencemag.org/content/366/6467/878/suppl/DC1](https://science.sciencemag.org/content/366/6467/878/suppl/DC1)  
Materials and Methods  
Figs. S1 to S7  
Table S1  
References (35–91)

[View/request a protocol for this paper from Bio-protocol.](#)

2 July 2019; accepted 15 October 2019  
10.1126/science.aay5945

## IMMUNOLOGY

# Microbiota-derived peptide mimics drive lethal inflammatory cardiomyopathy

Cristina Gil-Cruz<sup>1</sup>, Christian Perez-Shibayama<sup>1</sup>, Angelina De Martin<sup>1</sup>, Francesca Ronchi<sup>2</sup>, Katrien van der Borgh<sup>3</sup>, Rebekka Niederer<sup>1</sup>, Lucas Onder<sup>1</sup>, Mechthild Lütge<sup>1</sup>, Mario Novkovic<sup>1</sup>, Veronika Nindl<sup>1</sup>, Gustavo Ramos<sup>4,5</sup>, Markus Arnoldini<sup>6</sup>, Emma M.C. Slack<sup>6</sup>, Valérie Boivin-Jahns<sup>5,7</sup>, Roland Jahns<sup>5,8</sup>, Madeleine Wyss<sup>9</sup>, Catherine Mosser<sup>2</sup>, Bart N. Lambrecht<sup>3</sup>, Micha T. Maeder<sup>10</sup>, Hans Rickli<sup>10</sup>, Lukas Flatz<sup>1</sup>, Urs Eriksson<sup>11,12</sup>, Markus B. Geuking<sup>13</sup>, Kathy D. McCoy<sup>9</sup>, Burkhard Ludewig<sup>1\*</sup>

Myocarditis can develop into inflammatory cardiomyopathy through chronic stimulation of myosin heavy chain 6-specific T helper (T<sub>H</sub>1) and T<sub>H</sub>17 cells. However, mechanisms governing the cardiotoxicity programming of heart-specific T cells have remained elusive. Using a mouse model of spontaneous autoimmune myocarditis, we show that progression of myocarditis to lethal heart disease depends on cardiac myosin-specific T<sub>H</sub>17 cells imprinted in the intestine by a commensal *Bacteroides* species peptide mimic. Both the successful prevention of lethal disease in mice by antibiotic therapy and the significantly elevated *Bacteroides*-specific CD4<sup>+</sup> T cell and B cell responses observed in human myocarditis patients suggest that mimic peptides from commensal bacteria can promote inflammatory cardiomyopathy in genetically susceptible individuals. The ability to restrain cardiotoxic T cells through manipulation of the microbiome thereby transforms inflammatory cardiomyopathy into a targetable disease.

**M**yocarditis is an inflammatory heart disease that can develop into lethal cardiomyopathy (1–3). Acute immune activation during myocarditis is associated with the generation of autoimmune responses against myosin heavy chain 6 (MYH6) (4–7). Subsequent chronic stimulation of MYH6-specific T helper (T<sub>H</sub>1) and T<sub>H</sub>17 cells precipitates inflammatory cardiomyopathy (8–11). The progressive nature of autoimmune and chronic inflammatory diseases is determined by genetic susceptibility and distinct environmental conditions (12, 13). Susceptibility to inflammatory cardiomyopathy can be associated with HLA-DQB1\* polymorphisms (14, 15), whereas infection with pathogens predisposes patients, due to the death of cardiomyocytes and excessive presentation of self-antigens, to major histocompatibility complex (MHC) class II-restricted T cells (16). Alternatively, the antigenic mimicry of microbial components may drive these diseases (16–19).

To assess whether heart-specific T cells cross-react with microbial components, we used transgenic mice expressing a MYH6-specific T cell receptor on more than 95% of their CD4<sup>+</sup> T cells (TCRM) (10). All TCRM mice developed spontaneous autoimmune myocarditis, and ~50% of the animals progressed to lethal cardiomyopathy under specific pathogen-free (SPF) housing conditions (Fig. 1, A to D). In contrast, the lack of a commensal micro-

biome under germ-free (GF) conditions blunted the lethal disease outcome (Fig. 1A), abrogated cardiac dilatation (Fig. 1B), substantially reduced cardiac fibrosis (Fig. 1C), and significantly reduced disease severity (Fig. 1D). Echocardiographic analysis revealed that the hearts of GF TCRM mice functioned normally despite low-level cardiac inflammation (Fig. 1, E to G). Recolonization of GF TCRM mice with the SPF microbiome (fig. S1A) precipitated progression to lethal disease in ex-GF mice within 6 to 12 weeks (Fig. 1H), significantly exacerbated cardiac inflammation (Fig. 1I), and impaired cardiac function (fig. S1, B to D). Moreover, microbial colonization of GF TCRM mice exacerbated cardiac immune cell infiltration (Fig. 1J), including transgenic MYH6-specific CD4<sup>+</sup> T cells (Fig. 1K). The activity of heart-infiltrating TCRM T<sub>H</sub>17 cells (Fig. 1L), but not T<sub>H</sub>1 cells (Fig. 1M), depended on the microbial status of the mouse. Cohousing increased the fraction of both T<sub>H</sub>1 (Fig. 1M) and T<sub>H</sub>17 heart-specific CD4<sup>+</sup> T cells (Fig. 1L) and promoted the accumulation of inflammatory myeloid cells in the heart tissue (Fig. 1, N to Q, and fig. S1, E to H), including inflammatory monocytes (Fig. 1O), activated macrophages (Fig. 1P), and resident macrophages (Fig. 1Q). Thus, the presence of the microbiota fosters the imprinting of a T<sub>H</sub>17 phenotype in heart-specific CD4<sup>+</sup> T cells and favors the accumulation of myeloid cells in the myocardia of TCRM mice.

Heart-infiltrating CD4<sup>+</sup> TCRM cells showed significantly elevated expression of gut-homing receptors under SPF compared with GF conditions (Fig. 2A), and they homed to the T cell zones of colonic patches (Fig. 2B), colonic lymph nodes, and mesenteric lymph nodes in an adoptive transfer-model (fig. S2, A to C). Transferred TCRM T cells proliferated initially in the lamina propria, the colonic lymph node, and the mediastinal lymph node, and they subsequently migrated to the heart tissue (Fig. 2C and fig. S2D). Th cell responses in the hearts of TCRM mice were dominated by T<sub>H</sub>1 cells (fig. S2E), whereas the colonic lamina propria environment fostered the differentiation of T<sub>H</sub>17 cells (fig. S2, E and F). Next-generation sequencing of fecal 16S ribosomal RNA (rRNA) genes revealed that cohoused transgene-negative (Tg<sup>-</sup>) and TCRM mice possessed disparate microbiomes (fig. S2G). Cohousing with GF TCRM mice (fig. S2H) showed that the microbiome of ex-GF TCRM mice was more similar to the SPF TCRM microbiome than the SPF wild-type microbiome (Fig. 2D) and suggested that GF TCRM mice acquired the microbiome of SPF TCRM mice (Fig. 2E and fig. S2I). An in silico search revealed two potentially cross-reactive β-galactosidase (β-gal) mimic peptides in *Bacteroides thetaiotaomicron* (*B. theta*) and *B. faecis* with high similarity to MYH6 (table S1). CD4<sup>+</sup> TCRM T cells exhibited a functional avidity of  $6.3 \times 10^{-6}$  M for the *B. theta* peptide (fig. S3A), facilitating the efficient activation of TCRM T cells in vitro and in vivo (Fig. 2, F to H). Monocolonization of GF TCRM mice with *B. theta* or *Escherichia coli* (*E. coli*), or with our SPF microbiota (fig. S3C), showed that *B. theta* monocolonization fostered mainly the induction of T<sub>H</sub>17 cells (fig. S3D). Monocolonization of GF TCRM mice with a *B. theta* mutant lacking the β-gal *BT1626* gene encoding for the MYH6 peptide mimic (*B. theta* Δβgal) (fig. S3, E and F) or the parental strain resulted in the efficient seeding of the gut with both strains (fig. S3G). However, recolonization of TCRM mice with *B. theta* Δβgal reduced the accumulation of immune cells in the myocardium (Fig. 2I) and significantly diminished the activity of myosin-specific T<sub>H</sub>17 cells in the heart and colon (Fig. 2J). Moreover, the presence of TCRM cells substantially increased the production of immunoglobulin A (IgA) against commensal microbiota under SPF conditions (fig. S3, H and I), whereas the absence of the cross-reactive epitope in *B. theta* Δβgal led to a significantly reduced IgA response in

<sup>1</sup>Institute of Immunobiology, Kantonsspital St. Gallen, St. Gallen, Switzerland. <sup>2</sup>Maurice Müller Laboratories, Department of Biomedical Research, Universitätsklinik für Viszerale Chirurgie und Medizin Inselspital, University of Berne, Berne, Switzerland. <sup>3</sup>VIB Center for Inflammation Research, Department of Internal Medicine and Pediatrics, Ghent University, Ghent, Belgium. <sup>4</sup>Department of Internal Medicine I, University Hospital Würzburg, Würzburg, Germany. <sup>5</sup>Comprehensive Heart Failure Center, University Hospital of Würzburg, Würzburg, Germany. <sup>6</sup>Institute of Food, Nutrition and Health, ETH, Zurich, Switzerland. <sup>7</sup>Institute of Pharmacology and Toxicology, University of Würzburg, Würzburg, Germany. <sup>8</sup>Interdisciplinary Bank of Biomaterials and Data Würzburg (IBDW), University Hospital of Würzburg, Würzburg, Germany. <sup>9</sup>Department of Physiology and Pharmacology, Snyder Institute for Chronic Diseases, Cumming School of Medicine, University of Calgary, Calgary, AB, Canada. <sup>10</sup>Cardiology Division, Kantonsspital St. Gallen, St. Gallen, Switzerland. <sup>11</sup>Center for Molecular Cardiology University of Zurich, Zurich, Switzerland. <sup>12</sup>Department of Medicine, GZO Regional Health Center, Wetzikon, Switzerland. <sup>13</sup>Department of Microbiology, Immunology and Infectious Diseases, Snyder Institute for Chronic Diseases, Cumming School of Medicine, University of Calgary, Calgary, AB, Canada. \*Corresponding author. Email: burkhard.ludewig@kssg.ch



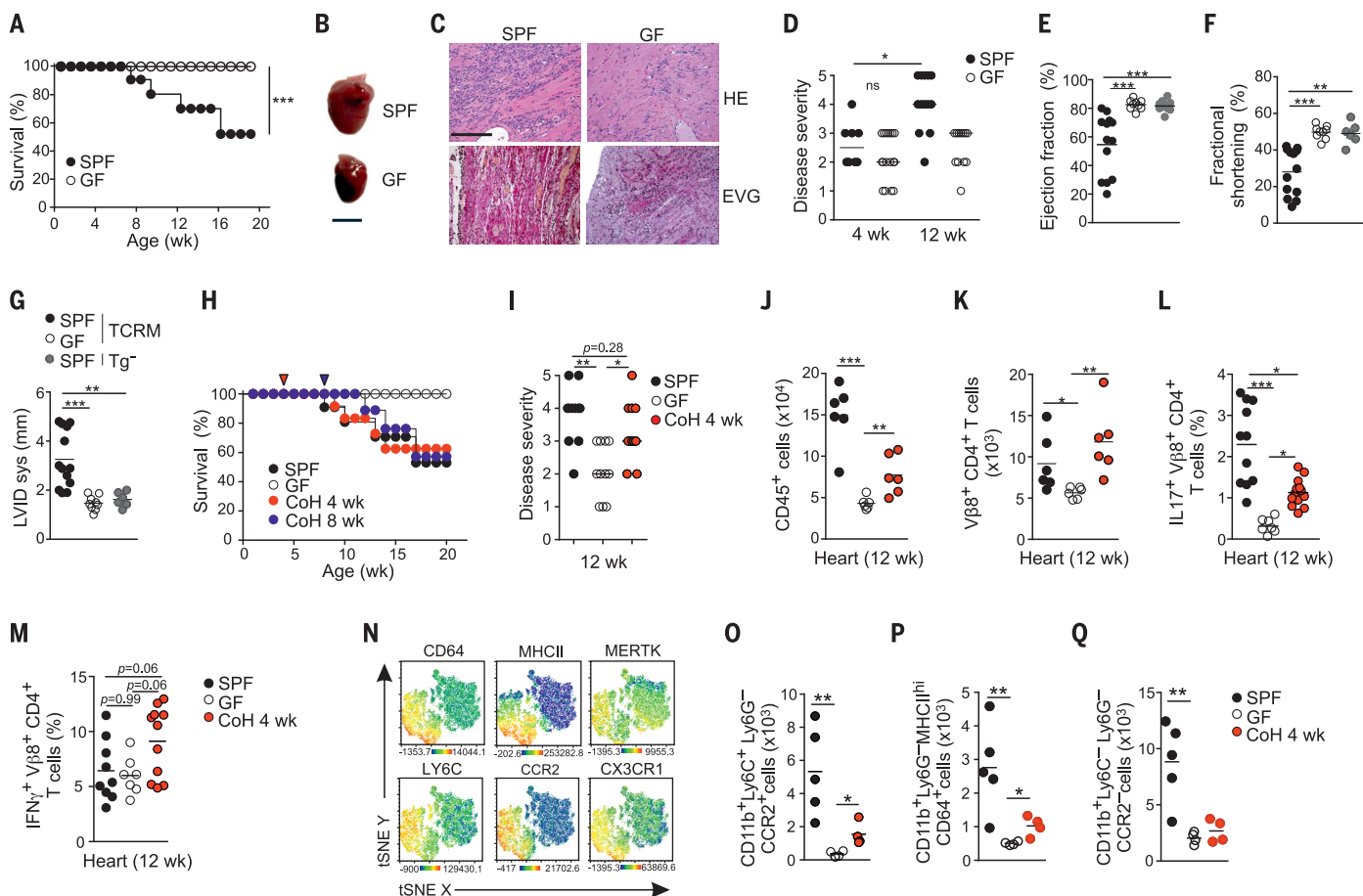


**Fig. 1. Microbiome-dependent transition of autoimmune myocarditis to dilated cardiomyopathy.** (A) Survival of TCRM mice under SPF or GF conditions. wk, weeks. (B) Gross pathology of hearts from 12-week-old SPF TCRM and age-matched GF TCRM mice. Scale bar, 4 mm. (C) Histological analysis of hearts of 12-week-old TCRM mice kept under SPF or GF conditions, using hematoxylin-eosin (HE) and Elastica-van Gieson (EVG) staining. Scale bar, 100  $\mu$ m. (D) Histopathological disease severity in TCRM mice under SPF and GF conditions, determined at the indicated ages. Dots represent values of individual mice and lines indicate median values. ns, not significant. (E to G) Echocardiographic parameters in SPF or GF TCRM mice and in transgene-negative littermates of controls ( $Tg^-$ ) with (E) ejection fraction, (F) fractional shortening, and (G) systolic left ventricular internal diameter (LVID sys) determined in individual mice. (H to Q) GF TCRM mice were transferred to SPF conditions and cohoused with SPF TCRM mice from 4 (CoH 4 wk) or 8 (CoH 8 wk) weeks of age until analysis. For comparison, TCRM mice under GF or SPF conditions were used. (H) Prospective survival analysis. Arrowheads indicate the age of transfer to SPF conditions. (I) Histopathological disease

progression. Dots represent individual mice and lines indicate median values. Enumeration of heart-infiltrating cells: (J)  $CD45^+$  cells and (K) myosin-specific  $CD4^+$  T cells ( $V\beta 8^+CD4^+$ ); (L) IL-17 $^-$  (interleukin-17 $^-$ ) and (M) IFN- $\gamma$ -producing heart-infiltrating MYH6-specific  $CD4^+$  T cells ( $V\beta 8^+CD4^+$ ). (N to Q) Heart-infiltrating myeloid cell subsets analyzed by flow cytometry. (N) Representative t-distributed stochastic neighbor embedding (t-SNE) plots of  $CD11b^+Ly6G^-$  cells in the hearts of SPF TCRM mice. Enumeration of (O) inflammatory monocytes, (P)  $MHCII^{hi}$  macrophages, and (Q)  $CD11b^+CCR2^-$  cardiac-resident macrophages. Dots represent individual mice and lines indicate mean values. Pooled data from two independent experiments with  $n = 4$  to 7 mice [(J), (K), (O) to (Q)] or three independent experiments with  $\geq 15$  mice [(A) and (H)],  $\geq 12$  mice [(B), (C), and (D)],  $\geq 6$  mice [(E) to (G)], or  $\geq 7$  mice [(L) and (M)] per group. Representative micrographs from one out of at least 12 mice [(B) and (C)]. Statistical analysis was performed using Mantel-Cox test (A) or Kruskal-Wallis  $H$  test [(D) and (I)] or one-way analysis of variance (ANOVA) with Dunnett's multiple comparison test [(E) to (G), (J) to (N), and (O) to (Q)] with \* $P < 0.05$ ; \*\* $P < 0.01$ ; \*\*\* $P < 0.001$ .

monocolonized TCRM mice (Fig. 2, K and L). Thus, heart-specific  $CD4^+$  T cells can shape the colonic microbiome, and distinct bacterial communities—in this case, *Bacteroides*—provide mimic peptides that can activate MYH6-specific  $CD4^+$  T cells.

Modification of the microbiome by antibiotic treatment (fig. S4A) prevented lethal cardiomyopathy (Fig. 3A) and reduced cardiac inflammation (Fig. 3B). Adoptive transfer of TCRM splenocytes into antibiotics-treated *Rag1* $^{-/-}$  mice

(fig. S4B) revealed that broad-spectrum antibiotics not only reduced *B. theta* levels in fecal samples (Fig. 3C) but significantly ameliorated cardiac disease at day 28 after adoptive transfer (Fig. 3D). There was a significantly reduced accumulation of  $CD45^+$  immune cells (Fig. 3E) and TCR-transgenic  $CD4^+$  T cells (Fig. 3F) in the hearts of *Rag1* $^{-/-}$  recipients treated with various antibiotics. Broad-spectrum antibiotic regimens primarily reduced immune cell accumulation in the colons (fig. S4, C and D), but

not in the spleens (fig. S4E), and had a pronounced impact on the cytokine production by heart-infiltrating and colonic  $T_H17$  cells.  $T_H1$  cell activity was also reduced, but to a lesser extent (Fig. 3G and fig. S4, F and G). Antibiotic treatment reduced *B. theta*-specific IgG antibody levels, but the treatment had variable effects on IgG antibody responses against *B. distasonis*, *B. vulgatus*, or *E. cloacae* (Fig. 3H). Moreover, the adoptive transfer of heart-specific TCRM cells to BALB/c mice

**Fig. 2. Interaction of MYH6-specific CD4<sup>+</sup> T cells with the intestinal microbiome.** (A) Flow cytometric analysis of  $\alpha 4\beta 7$ -integrin and CCR6 in heart-infiltrating MYH6-specific cells from SPF or GF TCRM mice. (B and C) Location and proliferation of carboxyfluorescein succinimidyl ester (CFSE)-labeled TCRM cells after adoptive transfer to *Rag1*<sup>-/-</sup> mice. (B) Confocal microscopy analysis of colonic patches at day 3 after adoptive transfer. Scale bar, 100  $\mu$ m. DAPI, 4',6-diamidino-2-phenylindole. (C) Proliferation of MYH6-specific cells. CFSE dilution in the indicated organs and at the indicated time points is quantified by flow cytometry. Bars indicate mean values. nd, not detectable; LN, lymph node; LP, lamina propria; MedLN, mediastinal lymph node. (D and E) Fecal bacterial composition of transgene-negative littermate controls (Tg<sup>-</sup>), SPF TCRM, and GF TCRM mice cohoused at 4 weeks of age under SPF conditions by 16S rRNA sequencing. (D) Principal component (PC) analysis. (E) Heat map of the relative abundance of the indicated bacterial classes and families. (F to H) MYH6-specific CD4<sup>+</sup> T cell cross-reactivity. (F) In vitro proliferation of CD4<sup>+</sup> T cells from TCRM mice after restimulation with MYH6,  $\beta$ -gal peptide from *Bacteroides*, or cysteine hydrolase-derived peptide from *E. cloacae* determined by CFSE-dilution assay. (G and H) Cytokine production of heart- and colon-infiltrating, V $\beta$ 8-expressing CD4<sup>+</sup> T cells from SPF TCRM mice after ex vivo restimulation with MYH6 or *Bacteroides*  $\beta$ -gal peptides. Dots represent values from individual mice, lines indicate mean values. (I to L) GF TCRM mice were mono-colonized with *B. theta* wild type (*B. theta* WT) or *B. theta* lacking the  $\beta$ -galactosidase *BT1626* gene (*B. theta*  $\Delta\beta$ -gal). (I and J) Flow cytometric analysis of (I) heart-infiltrating cells and (J) MYH6-specific cytokine producing cells in the heart and colon. Dots represent values from individual mice and lines indicate mean values. (K and L) IgA-bound fecal bacteria determined by bacterial flow cytometry (K) and pooled data from individual mice. Lines indicate mean values (L). SSC, side scatter; PE, phycoerythrin. Pooled data from *n* = 6 [(A) to (E)], (J) to (L)], *n* = 7 (G), and *n* = 5 (H) mice from at least two independent experiments. Representative plots showing percentage  $\pm$  SEM (A). Representative histograms from two independent experiments with duplicates (F). Representative plots and percentage values of IgA-bound bacteria are indicated (K). Statistical analysis was performed using Student's *t* test [(A), (G), (H), (I), (J), and (L)] or one-way ANOVA with Tukey's multiple comparison test (E) with \**P* < 0.05; \*\*\**P* < 0.001.

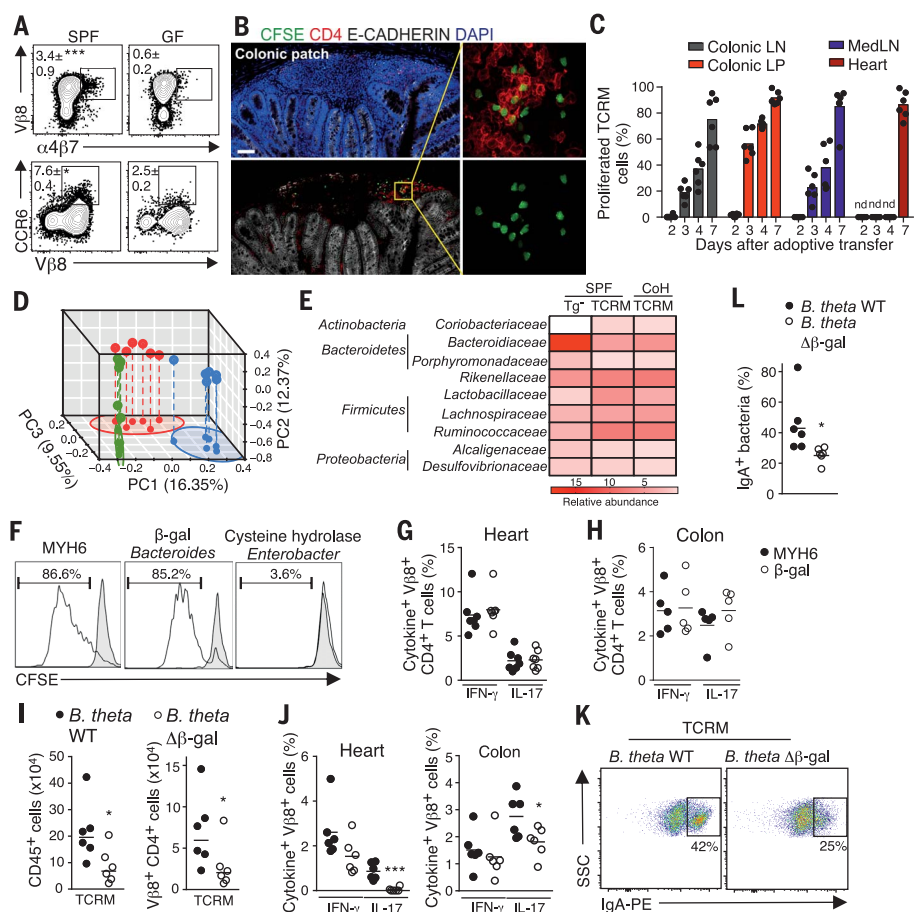


**Fig. 3. Impact of antibiotic treatment on lethal heart disease and immune reactivity in the TCRM model.** (A) Survival of and (B) disease severity in TCRM mice after postweaning treatment with a broad-spectrum antibiotics combination comprising sulphadoxine, trimethoprim, and metronidazole (S+T+M). Disease severity was determined in 20-week-old mice. Dots represent values of individual mice and bar indicates mean disease severity. Abx, S+T+M. (C to H) *Rag1*<sup>-/-</sup> mice were adoptively transferred with 10<sup>6</sup> TCRM splenocytes to induce fast progressing myocarditis; mice were treated or left untreated with the indicated oral antibiotics until analysis (day 28 after adoptive transfer). (C) *B. theta* quantification in feces by quantitative polymerase chain reaction. (D) Histopathological analysis of hearts. Dots represent values of individual mice and lines indicate median disease severities. (E and F) Quantification of heart-infiltrating CD45<sup>+</sup> cells (E) and V $\beta$ 8-expressing CD4<sup>+</sup> T cells (F). (G) Cytokine production of heart-infiltrating MYH6-specific V $\beta$ 8<sup>+</sup>CD4<sup>+</sup> T cells. (C and E to G) Box-and-whisker plots show mean values  $\pm$  the interquartile range; black dots indicate outliers. (H) Heat map of the specific IgG responses against *B. theta*, *B. distasonis*, *B. vulgatus*, and *E. cloacae* determined by enzyme-linked immunosorbent assay (ELISA). Pooled data from two to three independent experiments with *n* = 7 to 10 [(A) and (B)] and *n* = 5 to 13 [(C) to (H)]. Statistical analysis was performed using the Mann-Whitney *U* test (B); or one-way ANOVA with Dunnett's multiple comparison test [(C), (E) to (H)] or Kruskal-Wallis *H* test (D) with \**P* < 0.05; \*\**P* < 0.01; \*\*\**P* < 0.001.

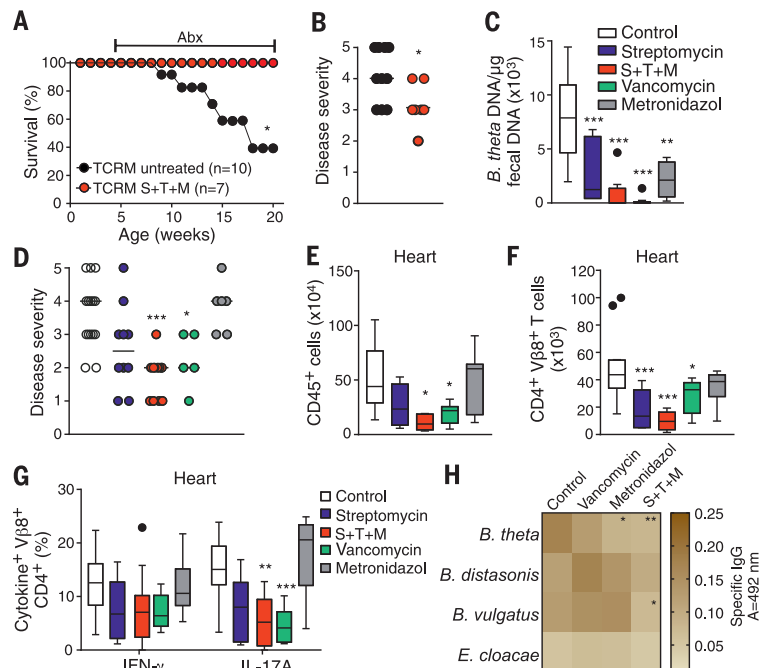
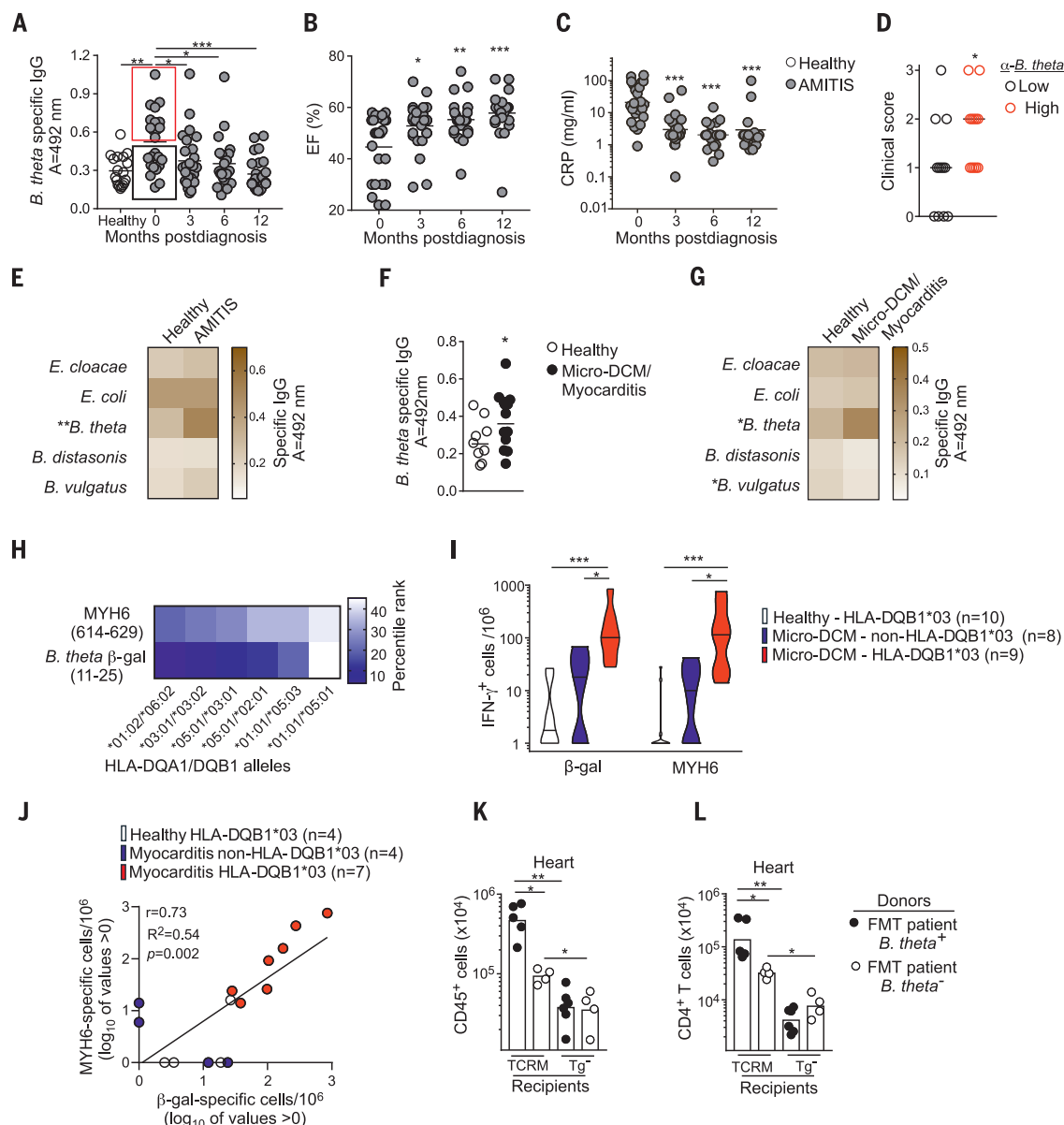


**Fig. 4. Immune reactivity against *Bacteroides* and cardiac myosin antigens in human myocarditis patients.**

**(A)** Analysis of *B. theta*-specific IgG antibodies in sera of myocarditis patients from the AMITIS cohort at admission and different time points post-diagnosis compared with sera from healthy individuals. Red and black boxes indicate patients with high or low anti-*B. theta* antibody levels, respectively. Dots represent individual antibody levels and lines indicate mean values. **(B)** Ejection fraction (EF) and **(C)** C-reactive protein (CRP) values in patients from the AMITIS cohort at the indicated time points. Dots represent individual values and lines indicate mean values. **(D)** Composite clinical scores of myocarditis patients from the AMITIS cohort with low versus high IgG antibodies against *B. theta* at their first visit [as indicated in (A)]. Dots represent individual clinical scores as the sum of positivity for anti-beta1-AR antibodies, CRP values  $\geq 16$  and EF  $\leq 40$ , and lines indicate median clinical scores. **(E)** Heat map of specific IgG response against *B. theta*, *B. distasonis*, *B. vulgatus*, and *E. cloacae* in the AMITIS cohort and healthy controls. **(F)** Serum *B. theta*-specific IgG levels in patients from the Micro-DCM cohort at admission. Dots represent individual patient values and lines indicate mean values. **(G)** Heat map of antibacterial IgG reactivity. **(H)** Heat map representing the in silico predicted binding of the MYH6<sub>614-629</sub> peptide or the *B. theta*  $\beta$ -gal<sub>11-25</sub> peptide to prevalent HLA-DQ alleles. **(I)** IFN- $\gamma$  enzyme-linked immunospot (ELISPOT) analysis of peripheral blood mononuclear cells of HLA-DQB1\*03 healthy volunteers ( $n = 10$ ) or Micro-DCM cohort patients (HLA-DQB1\*03  $n = 9$ ; other HLA  $n = 8$ ) after stimulation with the human MYH6<sub>614-629</sub> peptide or the *B. theta*  $\beta$ -gal<sub>11-25</sub> peptides. Violin plots show mean values  $\pm$  interquartile ranges. **(J)** Correlation between MYH6- or  $\beta$ -gal IFN- $\gamma$ -producing cells in myocarditis patients and healthy individuals with the indicated HLA-DQB1 alleles. Dots represent individual subjects.  $r$ , Pearson correlation coefficient;  $R^2$ , coefficient of determination. **(K)** and **(L)** Enumeration of heart-infiltrating CD45 $^{+}$  immune cells (K) and CD4 $^{+}$  T cells (L) in ex-GF recipient mice 4 weeks after fecal microbiome transplantation (FMT). Dots represent values of individual mice and bars indicate mean values. Statistical analysis was performed using one-way ANOVA with Dunnett's multiple comparison test [(A) to (C) and (I)] or Mann-Whitney  $U$  test (D) or Student's  $t$  test [(E) to (G)] and [(K) and (L)] or the Pearson correlation coefficient with two-tailed  $P$ -value calculation (J) with  $^{*}P < 0.05$ ;  $^{**}P < 0.01$ ;  $^{***}P < 0.001$ .



significantly enhanced anti-*B. theta* antibody responses (fig. S4H). Therefore, heart-specific CD4 $^{+}$  T cells specifically interact with microbial components in the intestine, thereby affecting systemic immune reactivity.

To establish translational relevance of these findings, we assessed serum anti-*Bacteroides* IgG responses from human patients with biopsy-confirmed acute myocarditis (table S2) (20).

These patients showed significantly elevated *B. theta*-specific IgG responses when compared with a healthy control group (Fig. 4A). Clinical improvement of these myocarditis patients (Fig. 4, B and C) was accompanied by a reduction in seroreactivity against *B. theta* (Fig. 4A). Patients with low anti-*B. theta* IgG reactivity (black box in Fig. 4A) showed a combined clinical score (fig. S5, A to C) that was signif-

icantly lower than that of the high-responder group (Fig. 4D). Although IgG antibodies against *B. theta* in myocarditis patients were diminished during subsequent visits (Fig. 4A), anti-*E. cloacae* antibodies (fig. S5D), anti-*E. coli* antibodies (fig. S5E), and total serum IgG levels (fig. S5F) did not change significantly. Moreover, IgG antibody reactivity against other *Bacteroides* species did not differ between



myocarditis patients and healthy controls (Fig. 4E). Likewise, myocarditis patients recruited in a prospective clinical study (table S3) showed significantly elevated anti-*B. theta* IgG antibodies (Fig. 4, F and G) when compared with healthy volunteers (table S4). Bioinformatics analysis of binding affinities of the *B. theta*  $\beta$ -gal<sub>11-25</sub> peptide mimic indicated several HLA-DQA1\*/B1\* combinations that are also predicted to bind human MYH6<sub>614-629</sub> (Fig. 4H). Peripheral blood T cells from patients exhibited significantly higher interferon- $\gamma$  (IFN- $\gamma$ ) reactivity against the MYH6 and  $\beta$ -gal peptides when compared with healthy controls (Fig. 4I). Moreover, there was a highly significant correlation between MYH6 and  $\beta$ -gal<sub>11-25</sub> peptide reactivity (Fig. 4J), indicating that heart-specific CD4<sup>+</sup> T cells cross-react with the bacterial peptide in human myocarditis patients. Finally, GF TCRM and Tg<sup>-</sup> mice (fig. S5, K and L) received fecal transplants from myocarditis patients positive or negative for *B. theta*. The accumulation of immune cells (Fig. 4, K and L) was significantly increased only in the hearts of TCRM mouse recipients given transplants from patients positive for *B. theta*. Thus, it is conceivable that inflammatory cardiomyopathy in humans is driven, at least in part, through the activation of heart-specific Th cells by bacterial peptide mimics derived from the intestinal microbiota.

Overall, in this scenario, cross-reactive CD4<sup>+</sup> T cells primed in the intestine can enter the myocardium and exacerbate the damage caused by infection by cardiotropic viruses or subclinical myocardial infarction (fig. S5M).

Likewise, the loss of control over self- and cross-reactive T cells during immune checkpoint inhibitor therapy may be a reason for potentially lethal cardiac inflammation in patients who share particular *HLADQA1\*/B1\** alleles (21–23). Thus, targeting the microbiome of genetically predisposed myocarditis patients or susceptible patients undergoing checkpoint inhibitor treatment through antibiotics may alleviate disease severity and may therefore help prevent the potentially lethal sequelae of inflammatory cardiomyopathy.

## REFERENCES AND NOTES

1. J. Buggey, C. A. ElAmm, *Curr. Opin. Cardiol.* **33**, 341–346 (2018).
2. R. G. Weintraub, C. Semsarian, P. Macdonald, *Lancet* **390**, 400–414 (2017).
3. L. T. Cooper Jr., A. Keren, K. Sliwa, A. Matsumori, G. A. Mensah, *Glob. Heart* **9**, 121–129 (2014).
4. N. R. Rose, *F1000Prime Rep.* **6**, 25 (2014).
5. B. H. Trachtenberg, J. M. Hare, *Circ. Res.* **121**, 803–818 (2017).
6. P. Krebs et al., *J. Autoimmun.* **28**, 224–233 (2007).
7. N. Neu et al., *J. Immunol.* **139**, 3630–3636 (1987).
8. M. Rangachari et al., *J. Exp. Med.* **203**, 2009–2019 (2006).
9. H. Lv et al., *J. Clin. Invest.* **121**, 1561–1573 (2011).
10. V. Nindl et al., *Eur. J. Immunol.* **42**, 2311–2321 (2012).
11. J. M. Myers et al., *JCI Insight* **1**, e85851 (2016).
12. E. Generali, A. Ceribelli, M. A. Stazi, C. Selmi, *J. Autoimmun.* **83**, 51–61 (2017).
13. A. Davidson, B. Diamond, *N. Engl. J. Med.* **345**, 340–350 (2001).
14. W. Liu, W. M. Li, N. L. Sun, *Ann. Hum. Genet.* **69**, 382–388 (2005).
15. I. Portig, A. Sandmoeller, S. Kreiling, B. Maisch, *Autoimmunity* **42**, 33–40 (2009).
16. S. Heymans, U. Eriksson, J. Lehtonen, L. T. Cooper Jr., *J. Am. Coll. Cardiol.* **68**, 2348–2364 (2016).
17. B. Maisch, P. Alter, *Herz* **43**, 423–430 (2018).
18. C. Massilamany, S. A. Huber, M. W. Cunningham, J. Reddy, *J. Cardiovasc. Transl. Res.* **7**, 165–171 (2014).
19. N. Tai et al., *J. Exp. Med.* **213**, 2129–2146 (2016).
20. N. Deubner et al., *Eur. J. Heart Fail.* **12**, 753–762 (2010).
21. D. B. Johnson et al., *N. Engl. J. Med.* **375**, 1749–1755 (2016).

22. L. Zhang et al., *Curr. Treat. Options Cardiovasc. Med.* **21**, 32 (2019).
23. Y. Yamami et al., *JAMA Oncol.* 10.1001/jamaoncol.2019.3113 (2019).
24. C. Gil-Cruz et al., Microbiota-derived peptide mimics drive lethal inflammatory cardiomyopathy. Figshare (2019); <https://figshare.com/s/229fc19d6d8db36ad1db>

## ACKNOWLEDGMENTS

We thank S. Caviezel-Firner, C. Engetschwiler, and R. De Guili for technical support. **Funding:** This study received financial support from the Swiss National Science Foundation (grants 130823 and 146133 to B.L.); the Interdisciplinary Centre for Clinical Research (IZKF Würzburg), Grant IZKF, project E-32; and the Bundesministerium für Bildung und Forschung (BMBF), grant “Molecular Diagnostics” FKZ 01ES0901 and FKZ 01ES0802 (to V.B.-J. and R.J.). G.R. received support from the Interdisciplinary Centre for Clinical Research (E-354). L.F. is supported by a Swiss National Science Foundation professorship (PP00P3\_157448). The funders had no role in study design, data collection and analysis, decision to publish, or preparation of the manuscript. **Author contributions:** B.L. designed the study, discussed data, and wrote the paper; C.G.-C. and C.P.-S. designed the study, performed experiments, and wrote the paper; A.D.M., K.v.d.B., V.N., F.R., R.N., L.O., M.L., M.N., M.A., M.W., and C.M. performed experiments and discussed data; G.R., E.M.C.S., V.B.-J., R.J., B.N.L., U.E., M.B.G., H.R., L.F., and K.D.M. discussed data and provided reagents; B.L. and M.T.M. designed the Micro-DCM cohort and account responsible for this study. **Competing interests:** The authors declare no competing interests. **Data and materials availability:** All sequence data are accessible at Figshare (24). All other data needed to evaluate the conclusions in the paper are available within the main text or supplementary materials. The TCRM mouse strain is available under a materials transfer agreement from the authors.

## SUPPLEMENTARY MATERIALS

science.sciencemag.org/content/366/6467/881/suppl/DC1  
Materials and Methods  
Figs. S1 to S5  
Tables S1 to S6  
References (25–36)

[View/request a protocol for this paper from Bio-protocol.](#)

7 September 2018; resubmitted 13 June 2019  
Accepted 9 October 2019  
10.1126/science.aav3487

## SOIL ECOLOGY

# The role of multiple global change factors in driving soil functions and microbial biodiversity

Matthias C. Rillig<sup>1,2\*</sup>†, Masahiro Ryo<sup>1,2\*</sup>, Anika Lehmann<sup>1,2</sup>, Carlos A. Aguilar-Trigueros<sup>1,2</sup>, Sabine Buchert<sup>1,2</sup>, Anja Wulf<sup>1,2</sup>, Aiko Iwasaki<sup>1,2</sup>, Julien Roy<sup>1,2</sup>, Gaowen Yang<sup>1,2</sup>

Soils underpin terrestrial ecosystem functions, but they face numerous anthropogenic pressures. Despite their crucial ecological role, we know little about how soils react to more than two environmental factors at a time. Here, we show experimentally that increasing the number of simultaneous global change factors (up to 10) caused increasing directional changes in soil properties, soil processes, and microbial communities, though there was greater uncertainty in predicting the magnitude of change. Our study provides a blueprint for addressing multifactor change with an efficient, broadly applicable experimental design for studying the impacts of global environmental change.

Global environmental change is a multifactorial phenomenon, and the concurrent action of multiple factors gives rise to large uncertainty in predicting effects [sensu (1)]. Soils are affected by multiple factors, but we do not know the effects of these factors when they act in concert. Understanding soils is important, because they provide a range of ecosystem functions, including carbon storage, and are central to agriculture and sustainable management. To address the impact of multiple drivers of global change, ecologists have used many tools, including

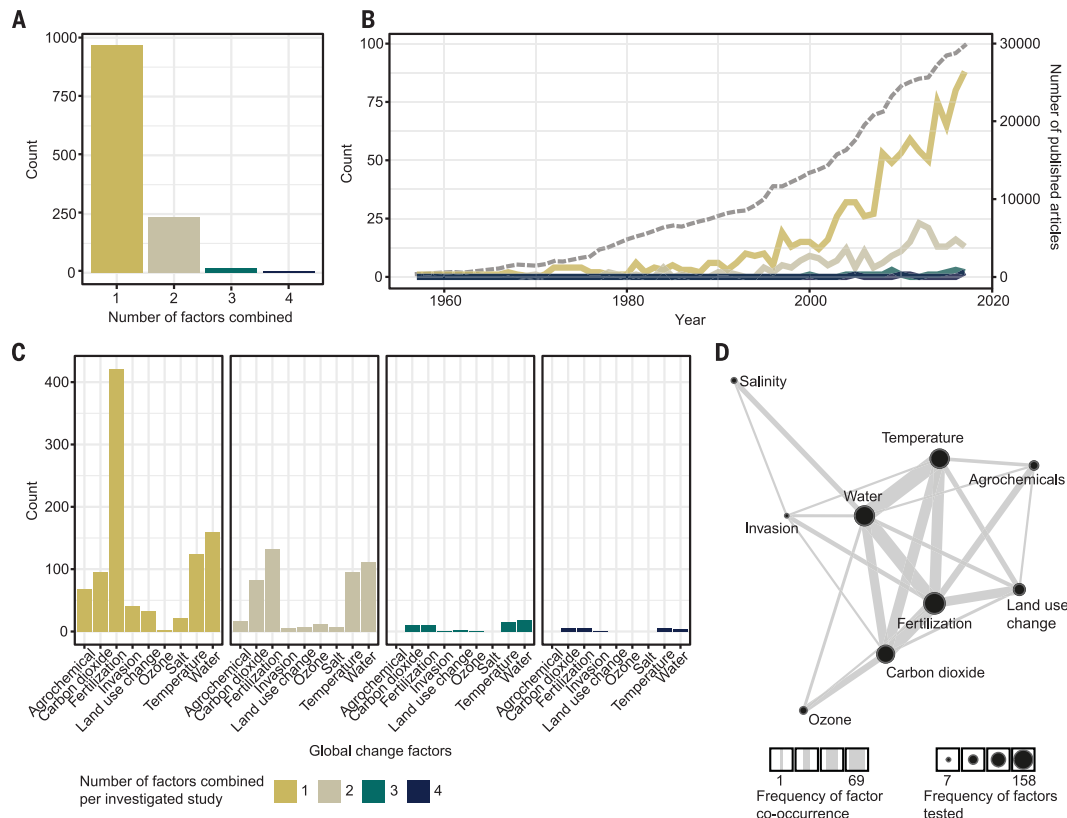
observational approaches such as studying complex environmental gradients (2), long-term time series (3), and modeling (4). However, in the canon of ecological approaches, experiments occupy a key role because they help establish causality between drivers and response (5).

Given the multiple pressures that soils experience, we first asked how ecologists have experimentally approached the study of global change in the context of soils. We conducted a systematic survey (Fig. 1), screening the literature on experimental studies of how global

change factors affect soil biota and processes. For each paper in our survey [1228 papers matched our inclusion criteria out of 4202 papers screened; (6)], we counted the number of global change factors included in the experiment. About 80% of studies examined only a single factor, 19% looked at the interaction of two factors, and only very few papers (<2%) tested the effects of three or more factors.

Thus, although global change involves many factors, soil ecologists typically have conducted experiments varying only one or two factors at a time (Fig. 1A), a pattern that shows no signs of change over time (Fig. 1B) and that is unlikely to be specific to the study of soils (7). These studies are dominated by certain factors (e.g., fertilization, likely owing to ease of application; Fig. 1C) and by certain factor combinations, to the exclusion of others (Fig. 1D). The reasons for these patterns, which shape our present knowledge of soil and ecosystem ecology, include logistical limitations and cost, but it is also clear that the main tool for addressing the interaction of multiple factors—the factorial experiment—starts to break down

**Fig. 1. Results from a literature survey on the number of global change factors included in soil ecology experiments, covering the years 1957 to 2017. (A)** Frequency distribution of the number of factors of global change included in experimental studies. For the 19 studies testing three-way interactions, we counted 38 investigated responses overall (across studies and variables), and in 21.05% of these, authors reported a significant interaction. We found five studies that included four-way interactions, and in none of these was the four-way interaction term significant. **(B)** Number of experimental studies that included a given number of factors over the past 50 years. For comparison, the dashed gray line (right y axis) represents the number of published articles per year for the Web of Knowledge category “Ecology.” **(C)** Number of papers that included a given global change factor for studies with one to four combined factors. **(D)** Network graph depicting the co-occurrence of global change factors in experimental studies, where circle size represents the frequency with which the driver was included in the studies and line thickness represents the frequency with which the drivers were tested as combinations.



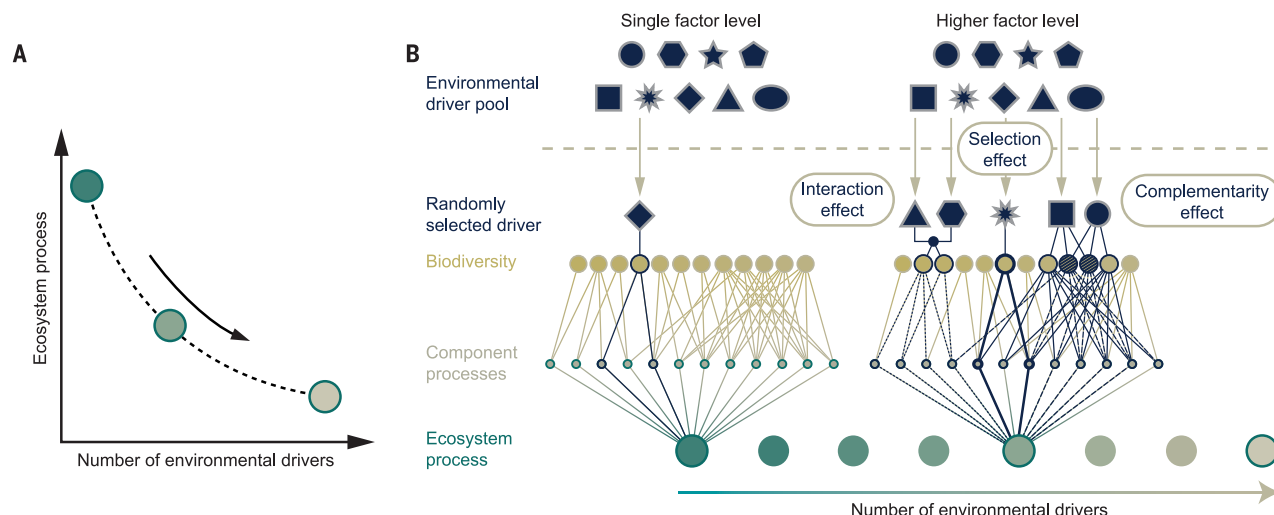


**Fig. 2. Diagrams expressing the idea that the number of global change factors alone might predict general trends in changes of biodiversity and ecosystem processes.** (A) Graphical representation of our hypothesis that biodiversity and ecosystem processes display a consistent directional change (this could be either an increase or decline, concave or convex; here, we only show a decline and only one possible curve shape) along the

number of environmental factors. (B) Graphical representation of the rationales behind this prediction, which are that with an increasing number of factors, there is an increased chance of including an influential factor (selection effect), that factors may increasingly affect different components (complementarity effect), and that factors may interact with each other, thus strengthening their effect (factor interaction effect).

because of the combinatorial explosion problem, that is, the rapid increase in possible combinations with the number of factors (8).

Although examining a particular factor combination may provide mechanistic insights, we propose that it is also useful to ask how soils might change when exposed to an increasing number of factors. Here, we experimentally show that an increasing number of global change factors causes directional change in soil properties, processes, and microbial communities but that predicting the magnitude of the changes remains challenging.

We examined the effects of an increasing number of these factors in combination using a design that takes inspiration from studies of biodiversity effects on ecosystem function (6, 9). In these designs, species are randomly selected from a pool along a gradient of species number (richness) in order to draw general conclusions about how changes in species number would affect ecosystem functions overall, regardless of species identity. Analogously, we here use a pool of 10 global change factors, from which we randomly selected a gradient of increasing factor number [see also (10)], namely the levels 2, 5, 8, and 10 factors, each replicated 10 times, thus testing if patterns of biodiversity and ecosystem processes show a consistent directional trend along the number of factors (Fig. 2). We tested abiotic factors (including temperature), resource availability (including chemical toxicants and compounds (inorganic and synthetic organic), and an agent of physical change (microplastics). A system would rarely encounter all 10 factors simultaneously, but it may encounter many of them, for example, in in-

tensive farming systems. Each replicate in these “factor richness” levels had a different, randomly determined combination of factors.

At the single-factor level, some factors had neutral, negative, or positive effects on a number of key responses, which included soil aggregation (a key component of soil structure), soil water repellency (water drop penetration time), decomposition, and soil respiration (Fig. 3, A, E, I, and M). Therefore, predictions that combine single-factor effects often had broad confidence intervals [Fig. 3, B, F, J, and N; see (6) for how effects were combined]. Soil aggregation and soil water repellency changed strongly with eight or more factors, and effects deviated from predictions, indicating synergistic interactions. Nonetheless, in agreement with our prediction (Fig. 2), the changes in all response variables showed a consistent directional change with the number of factors included [Fig. 3, C, G, K, and O; coefficient of determination ( $R^2$ ) = 13 to 52%, using random forest machine learning modeling]. Knowing factor identity increased the amount of variability explained compared with just knowing the number of factors, but not for water repellency (Fig. 3, D, H, L, and P; and fig. S1).

We also examined effects on soil biodiversity as measured by richness, community composition, and its dispersion. Here, we focus on soil fungi, which are strongly related to the processes we measured [e.g., (11)]. We assessed communities of soil fungi using high-throughput sequencing (Illumina MiSeq), identifying 346 amplicon sequence variants (ASVs). A detailed description and analysis of the dataset is available (6). As in the results

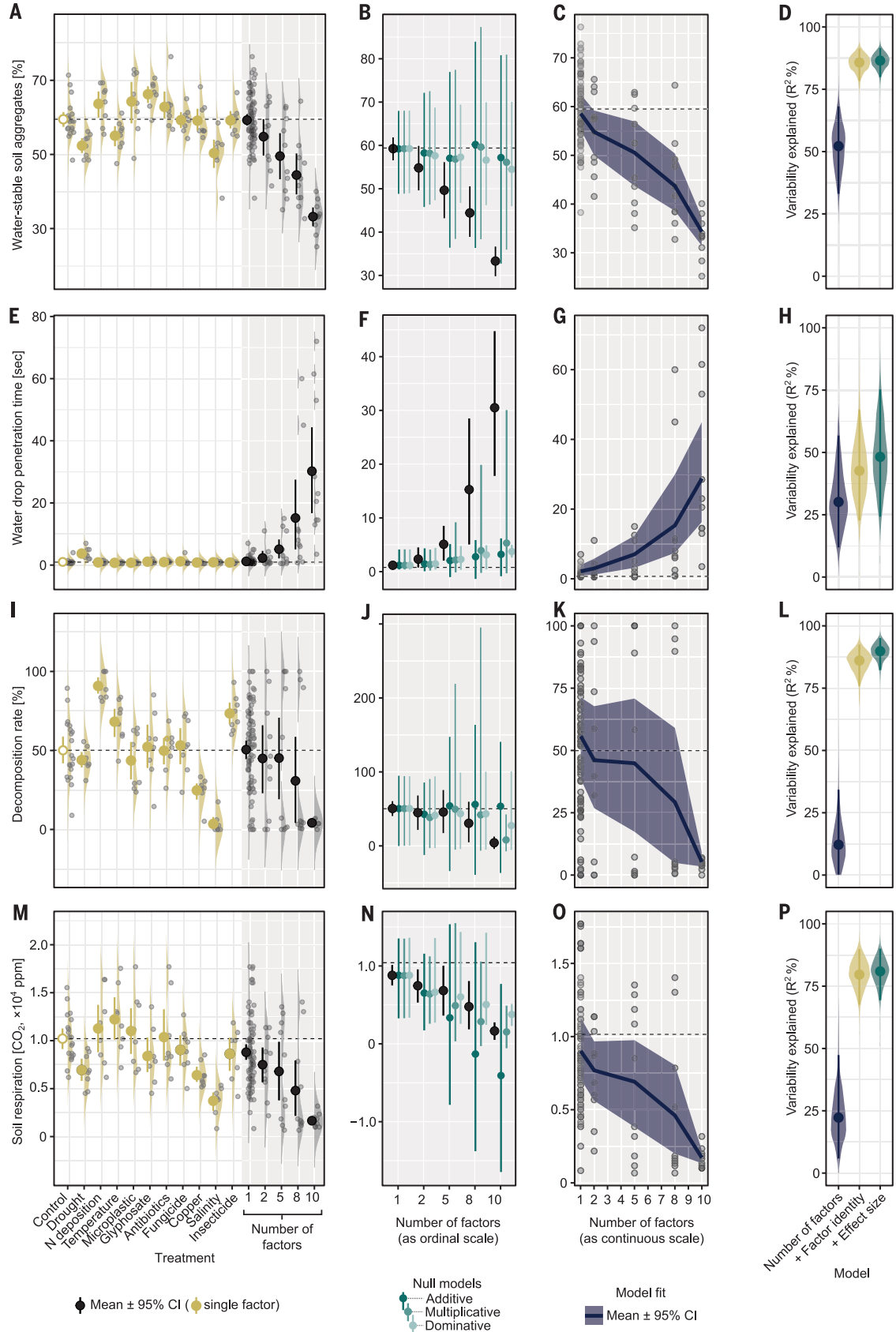
for soil properties, we found directional changes related to the number of factors, namely a reduction in ASV richness and a shift in community composition and dispersion (Fig. 4, D, H, and L; and figs. S2 and S3). For community dispersion, the magnitude of the changes was unpredictable from the single-factor effects (Fig. 4J). ASV-poor communities were a subset of ASV-rich communities [temperature = 7.3, standard effect size (SES) = -8.3,  $p$  = 0.001]. When exposed to more factors, communities became species poorer (being mostly composed of generalist stress-tolerant fungi and losing mainly Basidiomycota; figs. S2 and S3).

Our study expands understanding of the effects of multiple global change factors on soils and shows that an increasing number of global change factors cause directional changes in soil properties, processes, and microbial communities; however, predicting the magnitude of change was not always straightforward (fig. S1). We found that there were “ecological surprises” that only became apparent at higher levels (especially 8 and 10) of factor interaction. This was best illustrated by the soil property “water repellency,” which was barely affected at the single-factor level but was greatly affected at the multifactor level. Such phenomena clearly render predictions of effects of global change more challenging, but our results emphasize that simply projecting the direction of change and recognizing unpredictable impacts in the first place are important and a step toward achieving better predictions.

Factors of global change will not be equally strongly expressed in all situations, and, in



**Fig. 3. Effects on soil properties of different global change factors applied singly and using different numbers of factors (2, 5, 8, and 10 interacting factors).** (A to P) For each measured soil property [(A) to (D), (E) to (H), (I) to (L), and (M) to (P)], single-factor effects were estimated [(A), (E), (I), and (M)] and then used to predict multifactor effects based on three different assumptions on how to combine multiple effect sizes [(B), (F), (J), and (N)]. An ideal prediction should have a small bias (accuracy) and narrow confidence interval (CI) (precision), but for (A) to (D) and (E) to (H), predictions were neither accurate nor precise, regardless of the assumption used. The predictions are made difficult because the single-factor effects have large variability and/or because there are strong factor interactions. The direction of the treatment effects was consistent with an increasing number of factors for all properties [(C), (G), (K), and (O)]. These curves were estimated using random forest machine learning, and their predictability is shown in (D), (H), (L), and (P) (dark blue). Predictability was improved by adding factor identity information (O/1 for each factor; dark yellow) or effect size information (predicted values based on three assumptions; dark green) to the models as predictors [(D), (H), (L), and (P)], but predictability did not always improve [see (H)]. The measured soil properties were water-stable soil aggregates [(A) to (D)], soil water repellency measured as water drop penetration time [(E) to (H)], decomposition rate [(I) to (L)], and soil respiration [(M) to (P)]. Replicates are represented by dots with density ridgeline plots. Horizontal dashed lines represent mean values of the control.



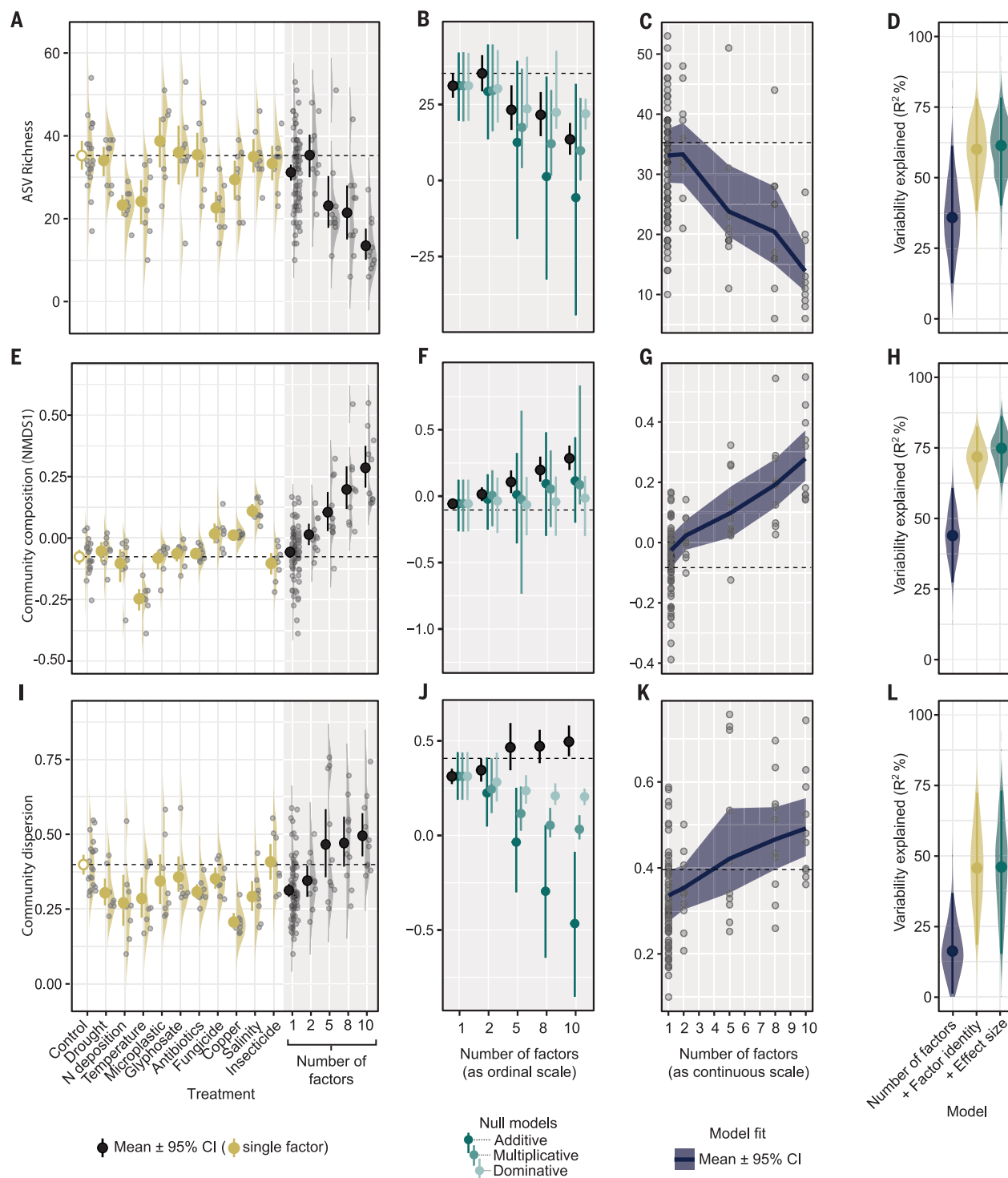


**Fig. 4. Effects on the soil fungal community of different global change factors applied singly and using different numbers of factors (2, 5, 8, and 10 interacting factors).** (A to L) For each biodiversity property [(A) to (D), (E) to (H), and (I) to (L)], single-factor effects were estimated [(A), (E), and (I)] and then used to predict multifactor effects based on certain assumptions [(B), (F), and (J)]. As with soil functions (Fig. 3), the effect directions were consistent along the number of factors for all properties as predicted using random forest machine learning [(C), (G), and (K)]. The

model predictability is shown in (D), (H), and (L) (dark blue). Adding factor identity (dark yellow) or single-factor effect size information (dark green) to the model improved predictability only for community composition, indicating that factor interactions exist [(D), (H), and (L)]. Fungal diversity is represented by ASV richness [(A) to (D)], community composition [(E) to (H)], and community dispersion [(I) to (L)]. Community composition is represented by the first axis of an unconstrained multivariate ordination (NMDS) of the Bray-Curtis sample pairwise dissimilarities.

reality, different combinations of factors may be at work. Nevertheless, our results offer general insights into system responses along such gradients of multiple global changes. As well as showing that factor number is important, data distributions also suggest that system responses (measured by combining data from all response variables after standardization at a given factor-combination level) tended to develop in a bimodal-like pattern (fig. S4) and that this contributes to the observed unpredictability of the interactions. Such a bimodal pattern has been used to infer the occurrence of regime shifts (12). Regime shifts may be triggered by increasing diversity of drivers, but most experimental work on regime shifts has focused on single factors and has therefore overlooked the possibly greater effects of multiple factors (13, 14). Responses converge again at the highest level (10 factors), but this is likely to be an artifact because factor level 10 is, by necessity, one particular factor combination. It remains to be established if intermediate levels of factor richness have less predictable effects and how this depends on the particular composition of factors.

Our experimental design was such that it could reveal trajectories for important aspects of ecosystem and biodiversity properties using a logistically feasible number of replicates (i.e., 140). Therefore, the approach is applicable to

more complex systems, including plants and soil fauna, and possibly even in the field (table S2). Our literature survey and experimental results suggest the need to rethink global change biology with a focus on the number of factors and their higher-order interactions, and such a shift in focus would also benefit many other fields in which concurrent multiple factors are common (10, 15–17).

## REFERENCES AND NOTES

1. J. Lehmann, M. Rillig, *Nat. Clim. Chang.* **4**, 153 (2014).
2. N. B. Grimm *et al.*, *Front. Ecol. Environ.* **6**, 264–272 (2008).
3. M. Fischer *et al.*, *Basic Appl. Ecol.* **11**, 473–485 (2010).
4. O. E. Sala *et al.*, *Science* **287**, 1770–1774 (2000).
5. P. W. Boyd *et al.*, *Glob. Chang. Biol.* **24**, 2239–2261 (2018).
6. See supplementary materials.
7. A. R. Gunderson, E. J. Armstrong, J. H. Stillman, *Ann. Rev. Mar. Sci.* **8**, 357–378 (2016).
8. I. Katzir, M. Cokol, B. B. Aldridge, U. Alon, *PLOS Comput. Biol.* **15**, e1006774 (2019).
9. D. Tilman, D. Wedin, J. Knops, *Nature* **379**, 718–720 (1996).
10. G. Brennan, S. Collins, *Nat. Clim. Chang.* **5**, 892–897 (2015).
11. A. Lehmann, W. Zheng, M. C. Rillig, *Nat. Ecol. Evol.* **1**, 1828–1835 (2017).
12. V. Dakos, S. R. Carpenter, E. H. van Nes, M. Scheffer, *Philos. Trans. R. Soc. London Ser. B Biol. Sci.* **370**, 20130263 (2015).
13. A. Conversi *et al.*, *Philos. Trans. R. Soc. London Ser. B Biol. Sci.* **370**, 20130279 (2015).
14. C. Moellmann, R. Diekmann, in *Global Change in Multispecies Systems Part 2*, vol. 47 of *Advances in Ecological Research*, G. Woodward, U. Jacob, E. J. Ogorman, Eds. (2012), pp. 303–347.
15. R. Altenburger, T. Backhaus, W. Boedeker, M. Faust, M. Scholze, *Environ. Toxicol. Chem.* **32**, 1685–1687 (2013).
16. M. C. Rillig, A. Lehmann, *New Phytol.* **223**, 517–519 (2019).
17. E. Tekin *et al.*, *Systems Biology and Applications* **4**, 31 (2018).

## ACKNOWLEDGMENTS

We thank the following individuals for help with the experiment: P. Yakubovskaya, M. Ballhausen, and G. Erzigkeit. Students in the Master of Science course Plant Ecology helped with conceptual design. We thank J. Antonovics for comments and Forschungsstation Linde (Zwillenberg-Tietz Foundation, M. Wicke) for providing the soil. **Funding:** M.C.R. acknowledges funding from an ERC Advanced Grant (Gradual\_Change) and from BMBF for the project “Bridging in Biodiversity Sciences (BIBS).” M.R. acknowledges funding from the Grant-in-Aid for JSPS Overseas Research Fellowships. **Author contributions:** M.C.R. designed the study and set up the experiment with the help of A.L., G.Y., S.B., and A.W. C.A.A.-T. contributed respiration measurements. A.L. measured soil aggregation and conducted the literature synthesis. A.I. helped with the literature synthesis. A.W. measured water repellency and decomposition. J.R. carried out molecular ecology analyses. M.R. visualized the concept and carried out statistical analyses. G.Y. designed the warming system. M.C.R. wrote the first draft, and all authors contributed to the writing of the paper. **Competing interests:** The authors confirm that there are no competing interests. **Data and materials availability:** Data for this paper have been deposited to <https://figshare.com/s/30b479473025f366013d>. Molecular data are available under ENA study accession number PRJEB34737. R code for effect size estimates is deposited at <https://github.com/masahiroryo/joint-ES-estimate>.

## SUPPLEMENTARY MATERIALS

[science.sciencemag.org/content/366/6467/886/suppl/DC1](https://science.sciencemag.org/content/366/6467/886/suppl/DC1)  
Materials and Methods  
Supplementary Text  
Figs. S1 to S6  
Tables S1 and S2  
References (18–68)  
Data S1

5 June 2019; resubmitted 28 August 2019  
Accepted 15 October 2019  
10.1126/science.aay2832



## SOLAR PHYSICS

# Generation of solar spicules and subsequent atmospheric heating

Tanmoy Samanta<sup>1</sup>, Hui Tian<sup>1\*</sup>, Vasyli Yurchyshyn<sup>2</sup>, Hardi Peter<sup>3</sup>, Wenda Cao<sup>2</sup>, Alphonse Sterling<sup>4</sup>, Robertus Erdélyi<sup>5,6</sup>, Kwangsu Ahn<sup>2</sup>, Song Feng<sup>7</sup>, Dominik Utz<sup>8</sup>, Dipankar Banerjee<sup>9</sup>, Yajie Chen<sup>1</sup>

Spicules are rapidly evolving fine-scale jets of magnetized plasma in the solar chromosphere. It remains unclear how these prevalent jets originate from the solar surface and what role they play in heating the solar atmosphere. Using the Goode Solar Telescope at the Big Bear Solar Observatory, we observed spicules emerging within minutes of the appearance of opposite-polarity magnetic flux around dominant-polarity magnetic field concentrations. Data from the Solar Dynamics Observatory showed subsequent heating of the adjacent corona. The dynamic interaction of magnetic fields (likely due to magnetic reconnection) in the partially ionized lower solar atmosphere appears to generate these spicules and heat the upper solar atmosphere.

**S**olar spicules are small-scale, jet-like plasma features observed ubiquitously in the solar chromosphere, the interface between the visible surface (photosphere) of the Sun and its hot outer atmosphere (corona) (1–4). Spicules may play a role in the supply of energy and material to the corona and solar wind (4, 5). They often have lifetimes ranging from 1 to 12 min and are characterized by rising and falling motions with speeds of 15 to 40 km s<sup>−1</sup> (1, 6). Some spicules may have apparent speeds of ~100 km s<sup>−1</sup> and

lifetimes less than 1 min (7). In on-disk observations of the chromosphere, these spicules often appear as elongated, short-lived dark structures (8). Some spicules are heated to ≥100,000 K (9, 10).

Theoretical models of spicules have included driving by shock waves (2, 3), Alfvén waves (11, 12), amplified magnetic tension (13), or magnetic reconnection (14). However, observations of their formation process are limited, owing to insufficient resolution and sensitivity. Two observations revealed a tendency for

the presence of opposite-polarity magnetic flux near magnetic field concentrations during the occurrence of some spicules (15, 16). However, further analysis did not yield an obvious association between spicules and magnetic field evolution (16).

We observed spicules (fig. S1) using the 1.6-m Goode Solar Telescope (GST) (17, 18) at the Big Bear Solar Observatory (BBSO). We performed H $\alpha$  wing observations and simultaneous magnetic flux measurements with GST's Near Infra-Red Imaging Spectropolarimeter (NIRIS) (19). NIRIS enables us to obtain information on photospheric magnetic fields by spectropolarimetric observations of the Fe I 1.56  $\mu$ m line (18) (figs. S2 and S3). Figure 1A shows a solar image at the blue wing (−0.8 Å from line core) of the H $\alpha$  line. It is dominated by numerous elongated dark jets, i.e., spicules. These spicules mostly originate from the magnetic network, indicated by the locations of magnetic field concentrations with positive polarity (Figs. 1 and S2).

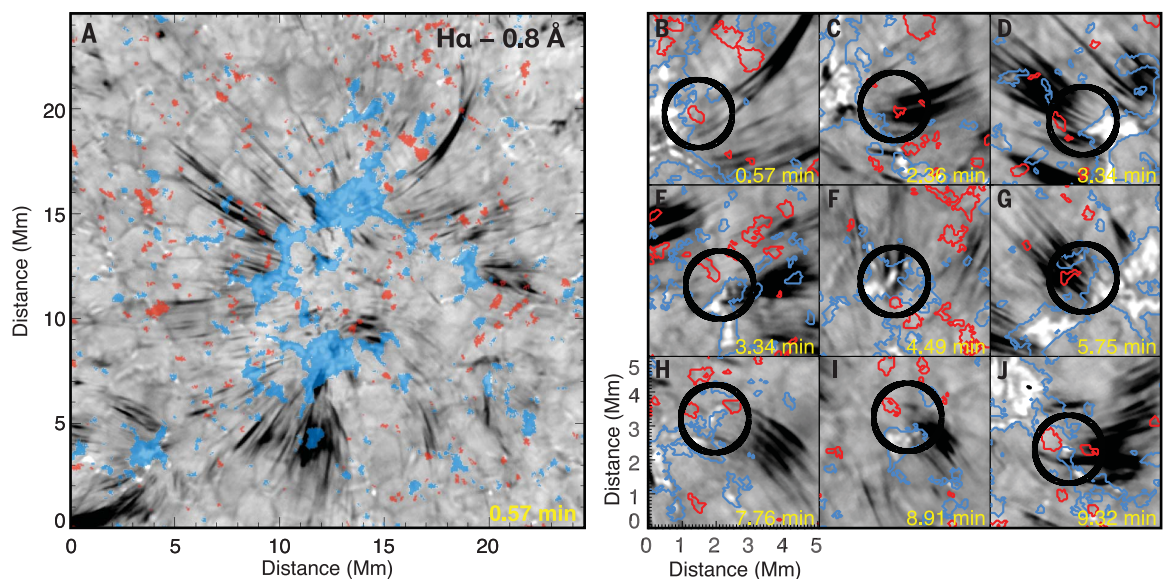
In addition to frequent individual spicules, occasionally several spicules originate simultaneously from a small region, appearing as enhanced spicular activity at a single location (movie S1). These enhanced spicular activities are accompanied by the presence of weak magnetic elements with a polarity opposite to the dominant polarity of the magnetic

<sup>1</sup>School of Earth and Space Sciences, Peking University, Beijing 100871, People's Republic of China. <sup>2</sup>Big Bear Solar Observatory, New Jersey Institute of Technology, 40386 North Shore Lane, Big Bear City, CA 92314-9672, USA. <sup>3</sup>Max Planck Institute for Solar System Research, Justus-von-Liebig-Weg 3, D-37077 Göttingen, Germany. <sup>4</sup>NASA Marshall Space Flight Center, Huntsville, AL 35812, USA. <sup>5</sup>Solar Physics and Space Plasma Research Centre, School of Mathematics and Statistics, University of Sheffield, Hounsfield Road, Sheffield S3 7RH, UK. <sup>6</sup>Department of Astronomy, Eötvös Loránd University, Budapest, H-1117 Budapest, Hungary. <sup>7</sup>Faculty of Information Engineering and Automation, Kunming University of Science and Technology, Kunming 650500, People's Republic of China. <sup>8</sup>Institute for Geophysics, Astrophysics and Meteorology—Institute of Physics, University of Graz, Universitätsplatz 5, 8010 Graz, Austria. <sup>9</sup>Indian Institute of Astrophysics, Koramangala, Bangalore 560034, India.

\*Corresponding author. Email: huitian@pku.edu.cn

**Fig. 1. Association of enhanced spicular activities with opposite-polarity magnetic fields.**

(A) H $\alpha$  blue wing image (gray-scale) overlain with a binary magnetic field map shown in blue and red, representing longitudinal flux densities of at least +10 Mx cm<sup>−2</sup> and −10 Mx cm<sup>−2</sup>, respectively (1 Mx = 10<sup>−8</sup> Wb; the unit of Mx cm<sup>−2</sup> is equivalent to Gauss). Movie S1 shows an animated version of this panel. Figure S1 shows the location of this region, and observational parameters are listed in table S1. (B to J) Examples of enhanced spicular activities. Blue and red contours outline regions of ±10 Mx cm<sup>−2</sup> for the longitudinal flux density. Axes are the same in different panels. The black circle (with a radius of 1 Mm) in each panel highlights a region around the footpoint of a region of enhanced spicular activity, where at least one small negative-polarity magnetic element is observed in each case.



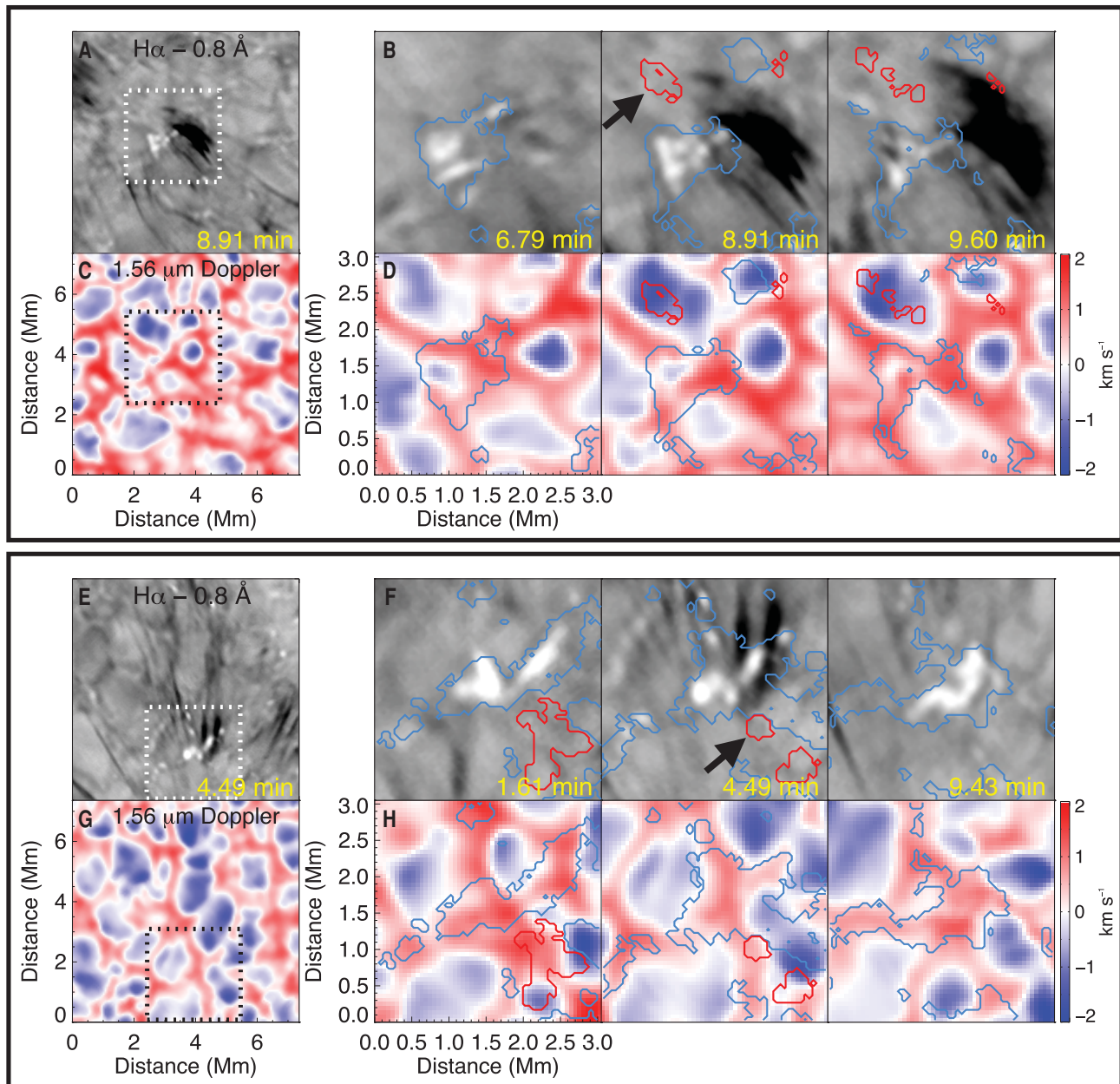


**Fig. 2. Enhanced spicular activity triggered by flux emergence (A to D) (movie S2) and flux cancellation (E to H) (movie S3).** (A) Enhanced spicular activity in a  $H\alpha$  blue wing image. (C) Photospheric Doppler shift pattern of the same region. (B and D) Temporal evolution around the spicule footprint region [dotted boxes in (A) and (C)]. Contour colors and levels are the same as in Fig. 1B. The arrow in (B) indicates the presence of an opposite-polarity flux. Panels (E) to (H) are the same as (A) to (D) but for a different region.

network around their footpoints (Fig. 1, B to J). When spicules occur, these weak elements are typically within several hundred kilometers from the edge of the strong network fields. By contrast, the strong and evolving unipolar fields (present for a much longer time in the network) generally do not produce enhanced spicular activities.

These enhanced spicular activities appear to be driven by the dynamical interaction of magnetic fields, often preceded by new flux emergence or appearance, and sometimes ac-

companied by apparent flux cancellation near the network edge. Figure 2, A to D, shows a patch of small-scale weak field with negative polarity that emerges near the strong positive-polarity network fields in the photosphere. Its coincidence with a patch of large blue shift of  $\text{Fe I}$  also indicates the emergence of the field (movie S2 and figs. S4 and S5). This flux emergence is followed within minutes by enhanced spicular activity, observed in the blue wing of  $H\alpha$ . Figure 2, E to H, shows a larger patch of weak negative-polarity field

that approaches the strong network fields; the subsequent flux cancellation leads to enhanced spicular activity (movie S3). The flux cancellation takes place at the boundary of a convection cell that is characterized by red shifts of the  $\text{Fe I}$  line.

Almost all the enhanced spicular activities that we observed are associated with emergence or appearance of negative-polarity fluxes and/or subsequent flux cancellation around the boundary of the positive-polarity magnetic network (Figs. 2 and S6 and movie S4). Furthermore,



**Fig. 3. Connection of individual spicules to opposite-polarity magnetic fluxes.**

(A) The same image as Fig. 1A, overlain with an inner white circle (a radius of 5.25 Mm) representing the approximate boundary of the network, and an outer white circle 3 Mm outside it. Black circles mark the footpoint regions of the same regions with enhanced spicular activity as shown in Fig. 1, B to J. Yellow circles have a radius of 0.75 Mm and indicate regions shown in (B) to (Q) and in fig. S7, which mostly lie within the outer white circle. Movie S4 shows an animated version of this panel. (B to Q) Sixteen examples showing the presence of an opposite-polarity flux near the spicule footpoint (indicated by the yellow circles). Contour colors and levels are the same as in Fig. 1B. The white arrow in each panel indicates the direction radially outward from the center of the white circles.

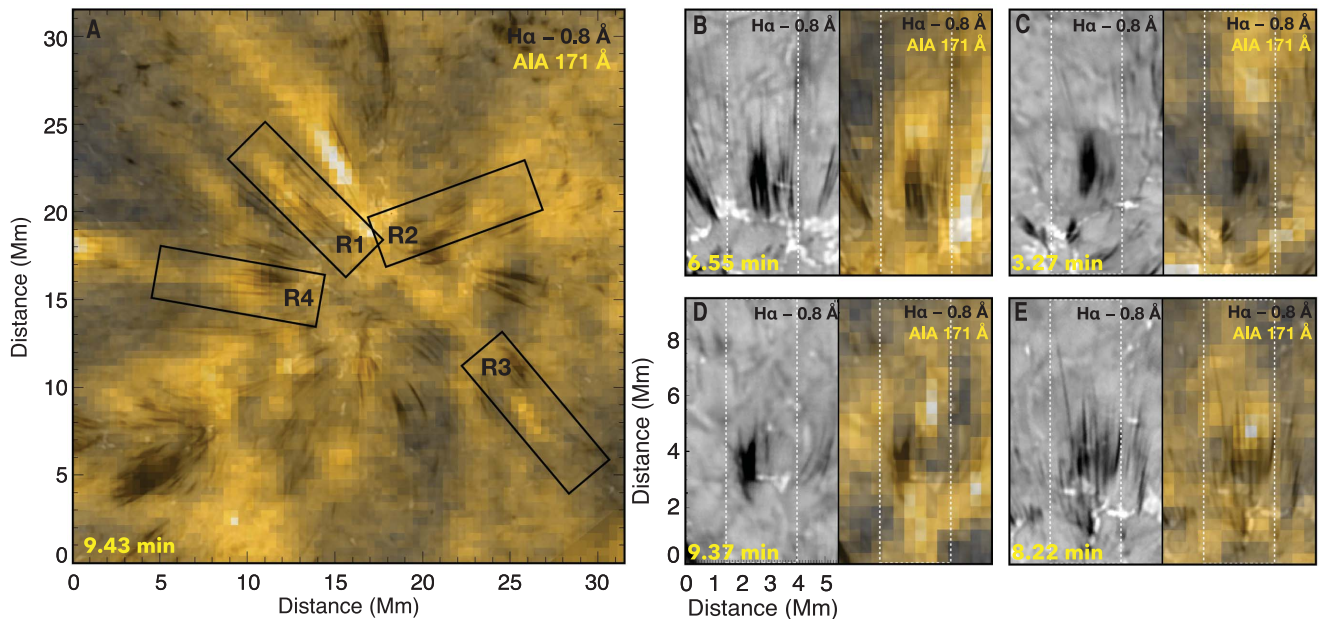
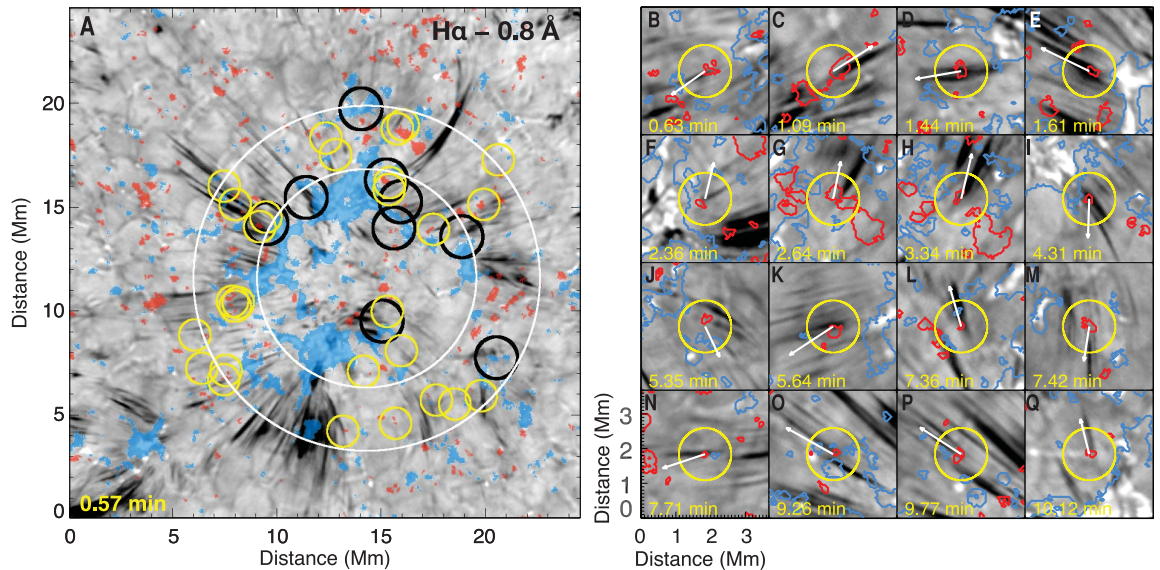


**Fig. 4. Coronal connection of enhanced spicular activities (movie S5).** (A)  $H\alpha$  blue wing image (grayscale) overlain with the simultaneously taken AIA 171 Å image (yellow). Boxes indicate regions shown in the other panels. (B to E) Four examples showing the enhancement of coronal emission above regions of enhanced spicular activity (more examples are in fig. S8). The  $H\alpha$  blue wing and the same image overlain with the simultaneous AIA 171 Å image are shown in each pair of panels. The white dotted boxes in (B) to (E) correspond to the black boxes (R1 to R4) in (A), respectively.

many individual spicules appear to originate, sometimes repeatedly, from small-scale negative-polarity magnetic features located near the strong network fields (Fig. 3 and fig. S7). Although small-scale flux emerges or appears ubiquitously in the quiet Sun, our observations indicate that only when it is close to the strong network fields (often  $<3$  Mm; Fig. 3 and movie S4) does

it generate spicules. For some small spicules, no opposite polarity is detected at their footpoints. Because the magnetograms have a spatial resolution ( $\sim 150$  km) about three times lower and a cadence (71 s) around 20 times slower than the  $H\alpha$  images, there may be smaller-scale or highly dynamic fields at the footpoints of these small spicules that we cannot detect.

Our results support the hypothesis that fast spicules originate from magnetic reconnection (14, 20, 21). It is possible that a subphotospheric local dynamo mechanism (22) or magnetoconvection process (13, 23) generates weak magnetic fields close to the large-scale network fields. These small-scale weak fields may occasionally emerge into the photosphere and



rise to the chromosphere, where they could reconnect with adjacent or overlying network fields to produce spicules. Alternatively, an opposite-polarity magnetic element could appear as a result of the coalescence and concentration of previously existing dispersed and unresolved fluxes (24), then reconnect with the network fields to generate spicules.

Spicules might supply hot plasma to the solar corona (4, 5, 9). We analyzed coronal observations of the same region with the Atmospheric Imaging Assembly (AIA) (25) on the Solar Dynamics Observatory (SDO) spacecraft (18). Most of the enhanced spicular activities are seen to channel hot plasma into the corona (Fig. 4, figs. S8 and S9, and movies S5 to S8). Coronal emission (visible in AIA images at 171 Å) generally appears at the top of the spicules. Our observations in a quiet-Sun region (fig. S1) complement previous observations (4, 26) that identified similar coronal signatures for some chromospheric upflow events observed above the solar limb or in on-disk active regions (regions around sunspots). Our observations reveal that magnetic reconnection events at network boundaries can drive spicules and produce hot plasma flows into the corona, providing a link between magnetic activities in the lower atmosphere and coronal heating. It remains unclear whether this process can provide sufficient heating to explain the high temperature of the corona (27, 28).

Heated material sometimes falls back from the corona (fig. S10 and movie S9), which could be responsible for the prevalent redshifts of emission lines formed in the chromosphere-corona transition region (29, 30). Our observa-

tions of the formation of spicules, the subsequent heating, and the return flows reveal a complete mass cycling process between the chromosphere and corona.

## REFERENCES AND NOTES

1. J. M. Beckers, *Annu. Rev. Astron. Astrophys.* **10**, 73–100 (1972).
2. A. C. Sterling, *Sol. Phys.* **196**, 79–111 (2000).
3. B. De Pontieu, R. Erdélyi, S. P. James, *Nature* **430**, 536–539 (2004).
4. B. De Pontieu et al., *Science* **331**, 55–58 (2011).
5. R. G. Athay, T. E. Holzer, *Astrophys. J.* **255**, 743 (1982).
6. G. Tsiropoulou et al., *Space Sci. Rev.* **169**, 181–244 (2012).
7. B. De Pontieu et al., *Publ. Astron. Soc. Jpn.* **59** (sp3), S655–S652 (2007).
8. L. Rouppe van der Voort, J. Leenaarts, B. de Pontieu, M. Carlsson, G. Vissers, *Astrophys. J.* **705**, 272–284 (2009).
9. H. Tian et al., *Science* **346**, 1255711 (2014).
10. T. M. D. Pereira et al., *Astrophys. J.* **792**, L15 (2014).
11. S. R. Cranmer, L. N. Woolsey, *Astrophys. J.* **812**, 71 (2015).
12. H. Iijima, T. Yokoyama, *Astrophys. J.* **848**, 38 (2017).
13. J. Martínez-Sykora et al., *Science* **356**, 1269–1272 (2017).
14. J. Y. Ding et al., *Astron. Astrophys.* **535**, A95 (2011).
15. V. Yurchyshyn, V. Abramenko, P. Goode, *Astrophys. J.* **767**, 17 (2013).
16. N. Deng et al., *Astrophys. J.* **799**, 219 (2015).
17. W. Cao et al., *Astron. Nachr.* **331**, 636–639 (2010).
18. Materials and methods are available as supplementary materials.
19. W. Cao et al., *Astron. Soc. Pac. Conf. Ser.* **463**, 291 (2012).
20. R. L. Moore, A. C. Sterling, J. W. Cirtain, D. A. Falconer, *Astrophys. J.* **731**, L18 (2011).
21. A. C. Sterling, R. L. Moore, *Astrophys. J.* **828**, L9 (2016).
22. T. Amari, J.-F. Luciani, J.-J. Aly, *Nature* **522**, 188–191 (2015).
23. F. Moreno-Inertis, J. Martínez-Sykora, V. H. Hansteen, D. Muñoz, *Astrophys. J.* **859**, L26 (2018).
24. D. A. Lamb, C. E. DeForest, H. J. Hagenaar, C. E. Parnell, B. T. Welsch, *Astrophys. J.* **674**, 520–529 (2008).
25. J. R. Lemen et al., *Sol. Phys.* **275**, 17–40 (2012).
26. H. Ji, W. Cao, P. R. Goode, *Astrophys. J.* **750**, L25 (2012).
27. J. A. Klimchuk, *J. Geophys. Res.* **117** (A12), A12102 (2012).
28. M. L. Goodman, *Astrophys. J.* **785**, 87 (2014).
29. H. Peter, P. G. Judge, *Astrophys. J.* **522**, 1148–1166 (1999).
30. S. W. McIntosh, H. Tian, M. Sechler, B. De Pontieu, *Astrophys. J.* **749**, 60 (2012).

## ACKNOWLEDGMENTS

BBSO operation is supported by NJIT and NSF. GST operation is partly supported by the Korea Astronomy and Space Science Institute (KASI); Seoul National University; the Strategic Priority Research Program of CAS (grant no. XDB09000000); and the Operation, Maintenance and Upgrading Fund for Astronomical Telescopes and Facility Instruments administrated by CAS. The AIA is an instrument on SDO, a mission of NASA's Living With a Star Program. We thank the GST and SDO teams for providing the data and S. K. Solanki and L. R. Bellot Rubio for helpful discussion. **Funding:** This work is supported by NSFC grants 11825301, 11790304(11790300), 41574166, 11729301, U1931107, and 11850410435; NSF grants AGS 1821294, 1620875, and AST-1614457; AFOSR grant FA9550-19-1-0040; NASA grants HGC 80NSSC17K0016 and HGI 17-HGISUN17-2-0047; Max Planck Partner Group program, Strategic Priority Research Program of CAS (grant XDA17040507), Key Applied Basic Research Program of Yunnan Province (FS: 2018FA035), FWF project N27800, CAS Presidents International Fellowship Initiative grant no. 2019VMA052, UK STFC grant ST/M000826/1, and the Royal Society. **Author contributions:** H.T. and T.S. conceived the study and wrote the manuscript. T.S. analyzed the data and generated the figures and movies under H.T.'s guidance. V.Y. generated the GST observations, processed the GST data, and advised on the data analysis. W.C. developed instruments on GST. K.A. processed the GST NIRIS data for scientific use. S.F. helped co-align the data. Y.C. performed the energy calculation and helped verify the results. H.P., A.S., R.E., D.U., and D.B. contributed to the interpretation of the observations. All authors discussed the results and commented on the manuscript. **Competing interests:** There are no competing interests. **Data and materials availability:** The GST dataset that we used is available at <http://ftp.bbsso.njit.edu/pub/20170619/>. The AIA data are available at the Joint Science Operations Center, [http://jsoc.stanford.edu/AIA/AIA\\_level1.html](http://jsoc.stanford.edu/AIA/AIA_level1.html); we used the 12 s 171 Å and 24 s 1700 Å observations in the time range 2017 June 19 18:45–18:57 UT.

## SUPPLEMENTARY MATERIALS

[science.sciencemag.org/content/366/6467/890/suppl/DC1](http://science.sciencemag.org/content/366/6467/890/suppl/DC1)  
Materials and Methods  
Supplementary Text  
Figs. S1 to S10  
Table S1  
References (31–88)  
Movies S1 to S9

4 December 2018; accepted 24 October 2019  
10.1126/science.aaw2796

## QUANTUM OPTICS

# Thermally condensing photons into a coherently split state of light

Christian Kurtscheid<sup>1\*</sup>, David Dung<sup>1</sup>, Erik Busley<sup>1</sup>, Frank Vewinger<sup>1</sup>, Achim Rosch<sup>2</sup>, Martin Weitz<sup>1\*</sup>

The quantum state of light plays a crucial role in a wide range of fields, from quantum information science to precision measurements. Whereas complex quantum states can be created for electrons in solid-state materials through mere cooling, optical manipulation and control builds on nonthermodynamic methods. Using an optical dye microcavity, we show that photon wave packets can be split through thermalization within a potential with two minima subject to tunnel coupling. At room temperature, photons condense into a quantum-coherent bifurcated ground state. Fringe signals upon recombination show the relative coherence between the two wells, demonstrating a working interferometer with the nonunitary thermodynamic beam splitter. Our energetically driven optical-state preparation method provides a route for exploring correlated and entangled optical many-body states.

Achieving order by populating the ground state of composite systems, such as in the formation of the low-energy bonding superposition state of the  $H_2^+$ -molecular ion or the singlet ground state of atomic helium, is the experimental basis of many quantum phenomena, including the emergence of strongly correlated electron physics upon the refrigeration of solids (1). The observation of phenomena such as superconductivity or the (fractional) quantum Hall effect also depends on this approach. Cooling to the ground state is the prime example for an irreversible temporal evolution that leads to a well-defined quantum state. For light, by contrast, reversible unitary processes (such as a beam splitter) are the standard manipulation tools, with irreversibility only possible when introducing photon loss (2). For classical physics phenomena, loss can be balanced with gain, and laser-like nonequilibrium processes efficiently achieve macroscopic population of excited-state modes (3–5). Entangled few-body states of light can be created through parametric down-conversion, which requires careful postselection when aiming at more than two entangled particles (6). Advances toward the ordering of complex optical quantum systems include the observation of exciton-polariton and photon Bose-Einstein condensates (BECs) (7, 8). Although not thermalizing into the ground state of the multimode problem, recent work has demonstrated periodic potentials for both polariton and photon microcavity systems (9–12) and reported simulations of the classical XY model (13, 14). The fast time scales, in the picosecond regime for both photons and polaritons, make it impractical to temporarily alternate between

cooling and trap manipulation phases for optical quantum gases. Although this technique is used in the study of cold atoms in lattices, the required adiabatic mapping of the condensate state into the lattice is a main bottleneck to reach ultralow entropy states in those systems (15).

We thermalized light in a potential with two minima. Through contact to an external reservoir—that is, by means of an irreversible process—the system reaches a coherently split state. To achieve this, a double-well superimposed with a shallow harmonic trapping potential is tailored by shaping mirror surfaces in an optical dye microcavity.

In our experiment (Fig. 1A), photons were trapped in a dye-filled microcavity. Two-dimensional photon gases in such dye microcavities show a thermodynamic phase transition to a macroscopically occupied ground state, the BEC (8, 16, 17). To engineer the desired potential, one of the two ultrahigh reflectivity cavity mirrors (cavity finesse near 100,000) has a microstructured surface profile, manufactured by use of a delamination technique (18). In brief, the profile is created by scanning an auxiliary laser beam transversally over the mirror plane, inducing heat from absorption in a 30-nm-thick silicon layer placed below the dielectric coating (12). The heating causes a controlled local delamination of the reflective surface, which for the cavity results in a shorter distance between mirrors at the corresponding transverse position. In the paraxial limit, this induces a repulsive potential for light, which intuitively means that shorter-wavelength (higher-energetic) photons are required to match the boundary conditions of the reflecting surfaces.

A spatial profile of the structured mirror profile used for this work is shown together with a cut and the calculated potential for photons within the microcavity in Fig. 1B. Near the mirror center, two indents spaced by 13  $\mu\text{m}$  cause a double-well potential sufficiently shallow

that only a single eigenfunction per site is trapped. Tunneling between the sites leads to a coupling of the localized wave functions, which hybridize to a symmetric  $\psi_s = \frac{1}{\sqrt{2}}(\psi_1 + \psi_2)$  and an antisymmetric wave function  $\psi_a = \frac{1}{\sqrt{2}}(\psi_1 - \psi_2)$ , where  $\psi_1$  and  $\psi_2$  denote the wave functions localized in the wells (Fig. 1C). The eigenenergies of the hybridized wave functions are split by  $\hbar\Delta$ , where  $\hbar$  is Planck's constant  $h$  divided by  $2\pi$  and  $\Delta \approx 2\pi \cdot 30$  GHz denotes the tunnel coupling, with the symmetric state  $\psi_s$ , which is akin to the bonding state in molecular physics, being energetically lower than  $\psi_a$  (the antibonding state). To allow for Bose-Einstein condensation in two dimensions, the double-well potential is superimposed with a weak harmonic trapping potential (18).

Thermalization of photons was achieved by following methods described previously (8, 19). The two cavity mirrors, because of their small spacing in the micrometer regime, impose an upper limit of the optical wavelength that fits inside the resonator, corresponding to a restriction of energies to a minimum cutoff of  $\hbar\omega_c \approx 2.1$  eV, which we identify here with the eigenenergy of the bonding state  $\psi_s$  of the double well. Moreover, the optical dispersion of cavity photons in the paraxial limit becomes quadratic, the same as it would for a massive particle. Given that interparticle interactions are weak, (number-conserving) thermalization of photons was achieved by means of repeated absorption re-emission processes on the dye molecules, which occurred to the rovibrational temperature of the dye, which is at room temperature. Because of the frequent collisions of solvent molecules with the dye (18, 19), photons emitted by the dye molecules were thermally equilibrated in an irreversible process. Because of the large mode spacing in the wavelength-spaced cavity, of order of the emission width of the dye, thermalization leaves the longitudinal mode unchanged, whereas the remaining transverse degrees of freedom make the photon gas two dimensional. It has been shown (19) that the system is formally equivalent to a two-dimensional system of trapped massive bosons with effective mass  $m_{\text{ph}} = \hbar\omega_c n^2/c^2$ , where  $n$  is the refractive index of the dye solution and  $c$  is the vacuum speed of light. To inject photons and compensate for losses, the dye is weakly pumped with a laser beam. Despite pumping and losses, the photon gas well follows an equilibrium Bose-Einstein distribution

$$n_B(u_i) = \frac{g(u_i)}{\exp\left(\frac{u_i - \mu}{k_B T}\right) - 1} \quad (1)$$

because photons thermalize faster than they are lost through, for example, mirror losses (20, 21).

Here,  $u_i$  is the excitation energy above the cut-off,  $g_i$  is the mode degeneracy,  $\mu$  is the

<sup>1</sup>Institut für Angewandte Physik, Universität Bonn, Wegelerstraße 8, 53115 Bonn, Germany. <sup>2</sup>Institut für Theoretische Physik, Universität zu Köln, Zùlpicher Straße 77, 50937 Cologne, Germany.

\*Corresponding author. Email: kurtscheid@iap.uni-bonn.de (C.K.); martin.weitz@uni-bonn.de (M.W.)

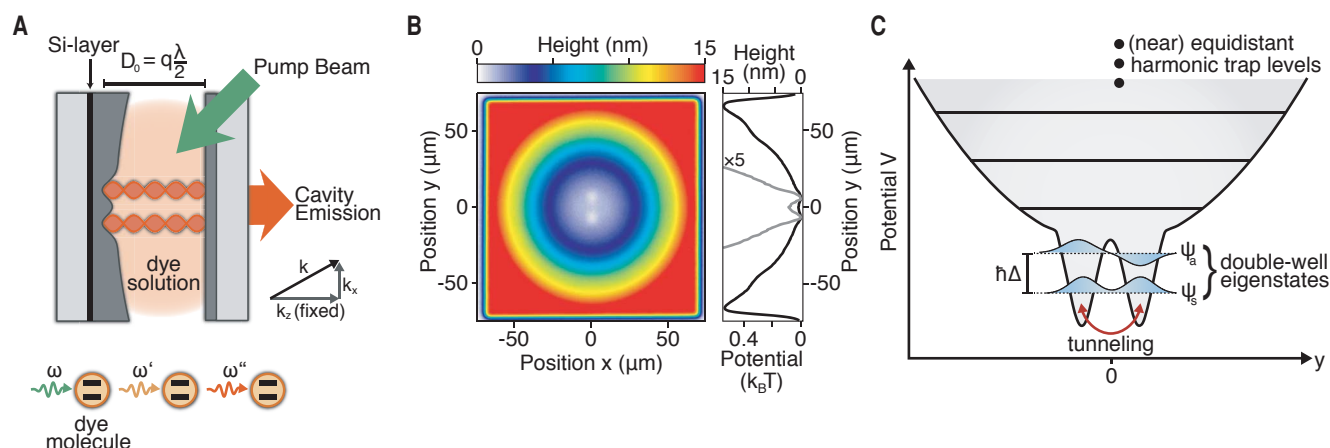


**Fig. 1. Experimental environment.** (A) Photons are trapped in a microresonator with a mirror spacing corresponding to an optical path of 5.5 wavelengths, where one mirror is laterally microstructured. The photons thermalize through radiative contact to the dye molecules (bottom schematics).  $D_0 = q\lambda/2$  describes the mirror spacing, where  $q$  is the longitudinal mode number and  $\lambda$  is the optical wavelength. (B) Height profile of the microstructured mirror surface (main plot) and profile of the corresponding expected trapping potential for cavity photons (right), realizing a double-well structure in the center superimposed with a harmonic trapping potential. (C) Schematic energy level structure, with the symmetric eigenstate of the double well as the lowest energetic eigenstate.

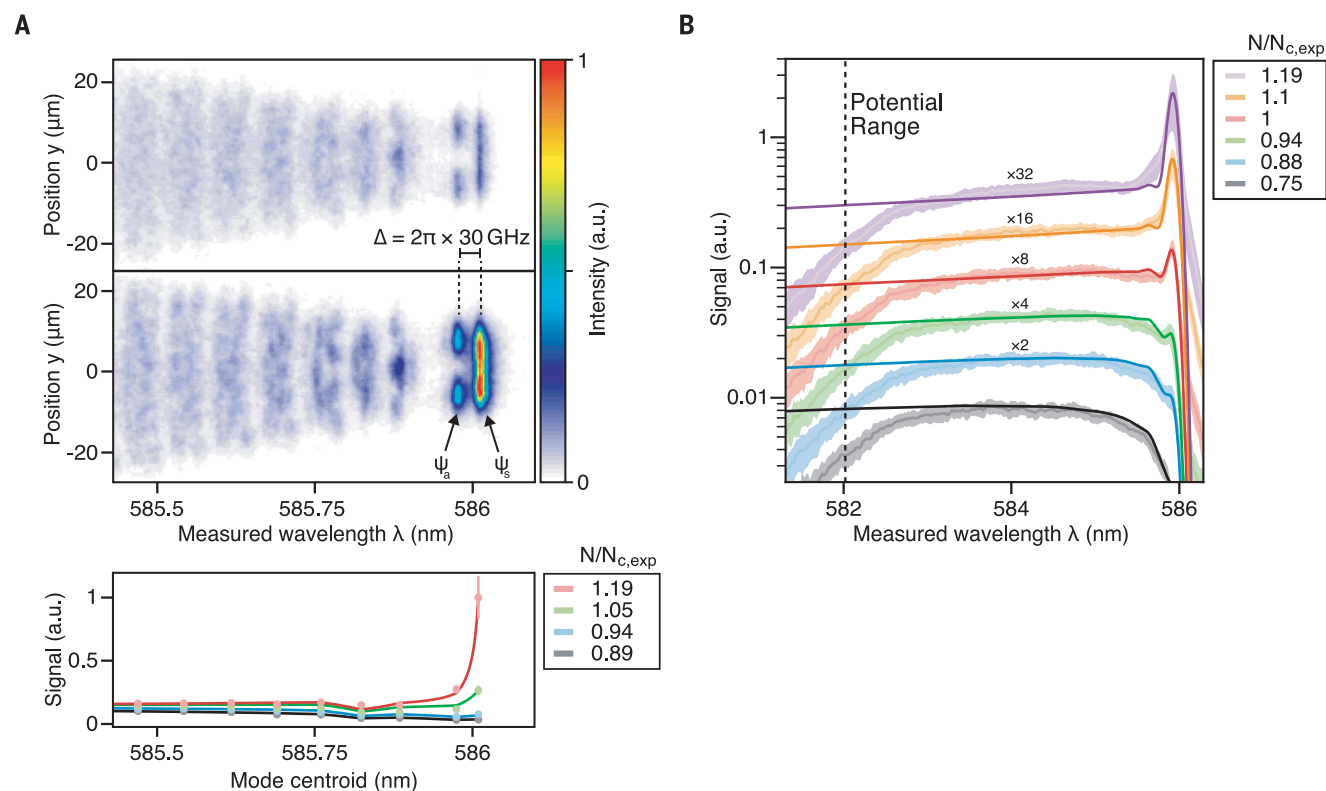


**Fig. 2. Spectrally resolved measurements.** (A) Measured wavelength versus transverse position along the axis of the double well both below (top,  $N/N_{c,\text{exp}} \approx 0.94$ ) and above (middle,  $N/N_{c,\text{exp}} \approx 1.05$ ) the threshold to Bose-Einstein condensation (18).  $N$ , measured total photon number;  $N_{c,\text{exp}}$ , measured critical photon number. The high-resolution spectra cover the range of the first nine lowest-energetic (highest-wavelength) modes. From right to left, the first two modes are the symmetric and antisymmetric modes of the double well, followed by modes not confined in the wells, which for the higher-order modes are well described by harmonic oscillator modes with a trap frequency of  $\Omega/2\pi \approx 63(2)$  GHz. The enhanced emission of the symmetric superposition observed in the latter image is attributed to Bose-Einstein condensation. a.u., arbitrary units. (Bottom) Spectra for different photon numbers. (B) Broadband, low-resolution spectra for different photon numbers (dots), along with theory for the dye microcavity temperature  $T = 300$  K. The observed width of the BEC peak is dominated by spectrometer resolution. The spectral position of the rim of the potential well is indicated with the dashed line. For all measurements, the critical photon number is  $N_{c,\text{exp}} \approx 8000$ .



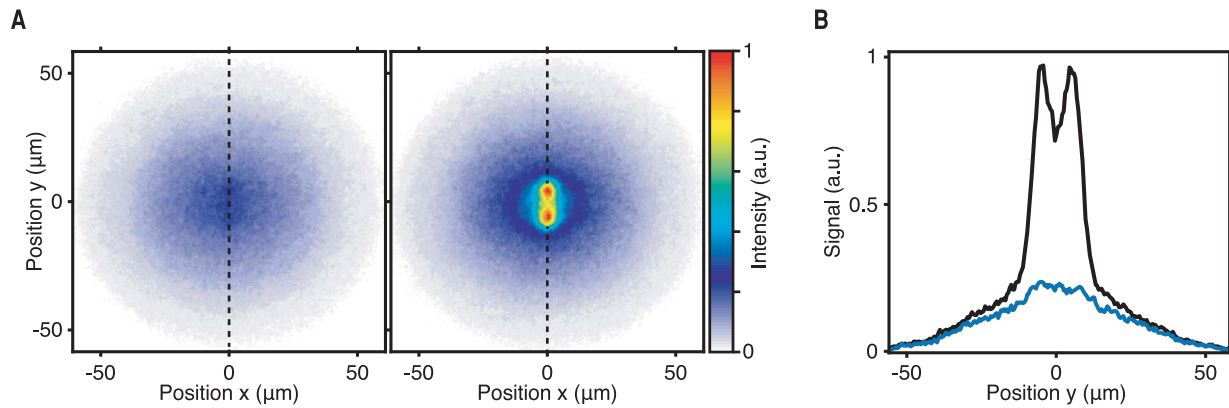


**Fig. 3. Imaging the emission pattern.** (A) Spatial images of the cavity emission, both below (left) and above (right) the critical photon number (for  $N/N_{c,exp} \approx 0.89$  and 1.19, respectively). The double peak in the latter image on top of the thermal cloud is an in situ image of the split condensate. (B) Cuts along the direction of the double well, indicated by the dotted lines in (A), for both the thermal cloud (blue) and the condensed phase (black) data.

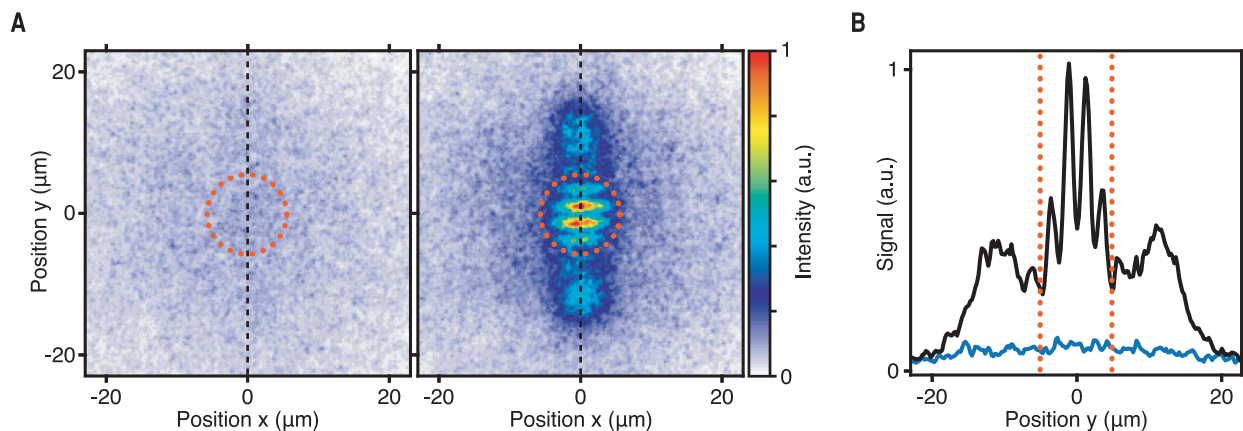


**Fig. 4. Relative phase of the microsites emission.** (A) The emission from the two individual microsites is overlapped (indicated with the marked central region in the camera images) with a small tilt. The resulting interference pattern is shown for total photon number below (left) and above (right) the critical photon number, where in the condensed phase a stable interference signal is observed. The data are the average of 50 image-intensified charge-coupled device images recorded in 1- $\mu$ s measurement time each, corresponding to the length of the pump beam pulses (18). (B) Corresponding cuts along the double-well axis above (black) and below (blue) criticality (for  $N/N_{c,exp} \approx 1.18$  and 0.88, respectively).

chemical potential,  $k_B$  is the Boltzmann constant, and  $T$  is the temperature. For the lowest two levels of our system, the bonding and antibonding states of the double well, we have  $u_s = 0$  and  $u_a = \hbar\Delta$ , with  $g_i = 2$  in both cases because of polarization degeneracy [details of our theoretical modeling are provided in (18)].

In the experimental data analyzing the microcavity emission, Fig. 2A, top and middle, gives color-coded high-resolution spectra spatially resolved along the direction of the double-well axis. Shown in Fig. 2A, top, are data recorded in the thermal regime with a photon number far below the Bose-Einstein condensation threshold. On the long-wavelength (low photon energy) side, we observed emission of the antisymmetric (slightly below 586 nm) and symmetric (slightly above 586 nm) double-well modes. In the former case, the emission in the center vanishes, indicating photons in the antisymmetric state, whereas the finite intensity in the center for the latter case corresponds to a

population of the symmetric wave function. To verify the thermal distribution of modes, we recorded broadband spectra for different total photon numbers; see Fig. 2B, along with theory curves (Fig. 2B, solid lines), for a Bose-Einstein distribution (Eq. 1). The bottom curves in Fig. 2B correspond to the thermal regime, whereas at high photon numbers, we observed a peak at the position of the cavity low-frequency cutoff near 586 nm, which we attribute to photon Bose-Einstein condensation. The experimental data are in good agreement with the equilibrium theory for 300 K down to a wavelength near 582 nm, at which we approach the finite rim of our imprinted potential (Fig. 1B) at  $\sim 0.54 \cdot k_B T$  above the cutoff energy, owing to present limits of our delamination technique. The thermal cloud saturates for photon numbers above the BEC threshold, verifying a central prediction of BEC theory.

Data above the condensation threshold are shown in Fig. 2A, middle, with the individual

cavity mode energies spectrally resolved (Fig. 2A, bottom, green data points). The visible strongly enhanced emission at the position of the cavity low-frequency cutoff is evidence for Bose-Einstein condensation of photons into the symmetric superposition  $\psi_s$  of the two microsites' eigenfunctions, where the condensate contains approximately 1200 photons (Fig. 2A, bottom, red data points). The energetic spacing to the first excited state ( $\psi_a$ ) is  $\hbar\Delta \approx k_B \cdot 1.4$  K, which is roughly a factor of 200 below the thermal energy of the room-temperature system. This comparison, in addition to the good agreement of our data with BEC theory, makes it clear that the observed population enhancement was a consequence of quantum, rather than classical, statistics.

The full spatial profile of the cavity emission is shown in Fig. 3A both below (Fig. 3A, left) and above (Fig. 3A, right) the critical photon number. Corresponding cuts along the direction of the double-well are shown in Fig. 3B for

both the data below (Fig. 3B, blue line) and above (Fig. 3B, black line) criticality, where in the latter case the split spatial profile of the condensate is clearly visible. To determine the relative phase of the emission originating from the individual microsites, we directed the cavity output through an optical interferometer. Camera images are shown in Fig. 4A of the resulting signal recorded in the thermal (Fig. 4A, left) and the condensed phase (Fig. 4A, right), respectively; the marked central areas in Fig. 4A, left and right, correspond to the region where the emission of the individual microsites spatially overlap. In this region, we observed a stable interference signal for the condensed phase (Fig. 4B), even though the shown data are the average of many subsequent experimental realizations (Fig. 4) (18). This verifies the fixed phase relation between the microsites, as expected for a delocalized, macroscopically occupied superposition state. In other words, the observation of a fringe pattern sets an upper limit on the indistinguishability (“which-path information”) left in the individual microsites upon thermalization. This can be understood from the tunneling time  $\pi/\Delta \approx 17$  ps being below the  $\approx 100$  ps dye reabsorption time during the absorption and emission cycles for the used experimental parameters (21).

Our observation of Bose-Einstein condensation of photons into the bonding low-energy superposition state of a double-well potential demonstrates the irreversible but coherent population of split states of light, in which the bifurcated single-photon state is massively occupied because of Bose-Einstein statistics.

Thermalization of light to cold reservoirs in tailored trapping geometries provides a possible route for the direct preparation of more

complex quantum states. Strong photon interactions are expected from using second-order nonlinear materials in a doubly resonant cavity setup, yielding a controllable effective Kerr interaction (22). When in a periodic lattice potential quantum many-body states then become the ground state; they then can be selectively populated through thermalization (18, 23–26), which is not yet achievable in present atomic physics experiments (15). For analysis, optical many-body state tomography can be performed with correlation measurements (6). Other perspectives of our work include the exploration of correlated quantum states in both double-well and periodic potential lattice systems coupled by means of effective particle exchange to the photoexcitable dye molecules (27, 28). Last, applications of the described delamination-based adaptive optics method can range from gain-dissipative simulations of the classical XY model in partial equilibrium condensate arrays (13, 14) to optical phase holography (3).

## REFERENCES AND NOTES

1. L. H. Greene, J. Thompson, J. Schmalian, *Rep. Prog. Phys.* **80**, 030401 (2017).
2. C. Gardiner, P. Zoller, *Quantum Noise: A Handbook of Markovian and Non-Markovian Quantum Stochastic Methods With Applications to Quantum Optics* (Springer, 2004).
3. P. W. Milonni, J. H. Eberly, *Lasers* (Wiley, 1988).
4. T. Schwartz, G. Bartal, S. Fishman, M. Segev, *Nature* **446**, 52–55 (2007).
5. I. Carusotto, C. Ciuti, *Rev. Mod. Phys.* **85**, 299–366 (2012).
6. X.-C. Yao et al., *Nat. Photonics* **6**, 225–228 (2012).
7. J. Kasprzak et al., *Nature* **443**, 409–414 (2006).
8. J. Klaers, J. Schmitt, F. Vewinger, M. Weitz, *Nature* **468**, 545–548 (2010).
9. M. Abbarchi et al., *Nat. Phys.* **9**, 275–279 (2013).
10. P. Cristofolini et al., *Phys. Rev. Lett.* **110**, 186403 (2013).
11. M. Milićević et al., *Phys. Rev. Lett.* **118**, 107403 (2017).
12. D. Dung et al., *Nat. Photonics* **11**, 565–569 (2017).
13. H. Ohadi et al., *Phys. Rev. X* **6**, 031032 (2016).
14. N. G. Berloff et al., *Nat. Mater.* **16**, 1120–1126 (2017).
15. A. Mazurenko et al., *Nature* **545**, 462–466 (2017).
16. J. Marelic, R. A. Nyman, *Phys. Rev. A* **91**, 033813 (2015).
17. S. Greveling, K. L. Perrier, D. van Oosten, *Phys. Rev. A* **98**, 013810 (2018).
18. Supplementary text is provided as supplementary materials.
19. J. Klaers, F. Vewinger, M. Weitz, *Nat. Phys.* **6**, 512–515 (2010).
20. P. Kirton, J. Keeling, *Phys. Rev. Lett.* **111**, 100404 (2013).
21. J. Schmitt et al., *Phys. Rev. A* **92**, 011602 (2015).
22. A. Majumdar, D. Gerace, *Phys. Rev. B* **87**, 235319 (2013).
23. M. J. Hartmann, F. G. Brandao, M. B. Plenio, *Nat. Phys.* **2**, 849–855 (2006).
24. A. D. Greentree, C. Tahan, J. H. Cole, L. C. L. Hollenberg, *Nat. Phys.* **2**, 856–861 (2006).
25. D. G. Angelakis, M. F. Santos, S. Bose, *Phys. Rev. A* **76**, 031805 (2007).
26. A. W. de Leeuw, O. Onishchenko, R. A. Duine, H. T. C. Stoof, *Phys. Rev. A* **91**, 033609 (2015).
27. J. Schmitt et al., *Phys. Rev. Lett.* **116**, 033604 (2016).
28. W. Verstraeten, M. Wouters, *Phys. Rev. A* **100**, 013804 (2019).
29. C. Kurtscheid, D. Dung, E. Busley, F. Vewinger, A. Rosch, M. Weitz, Thermally condensing photons into a split state of light. Zenodo (2019).

## ACKNOWLEDGMENTS

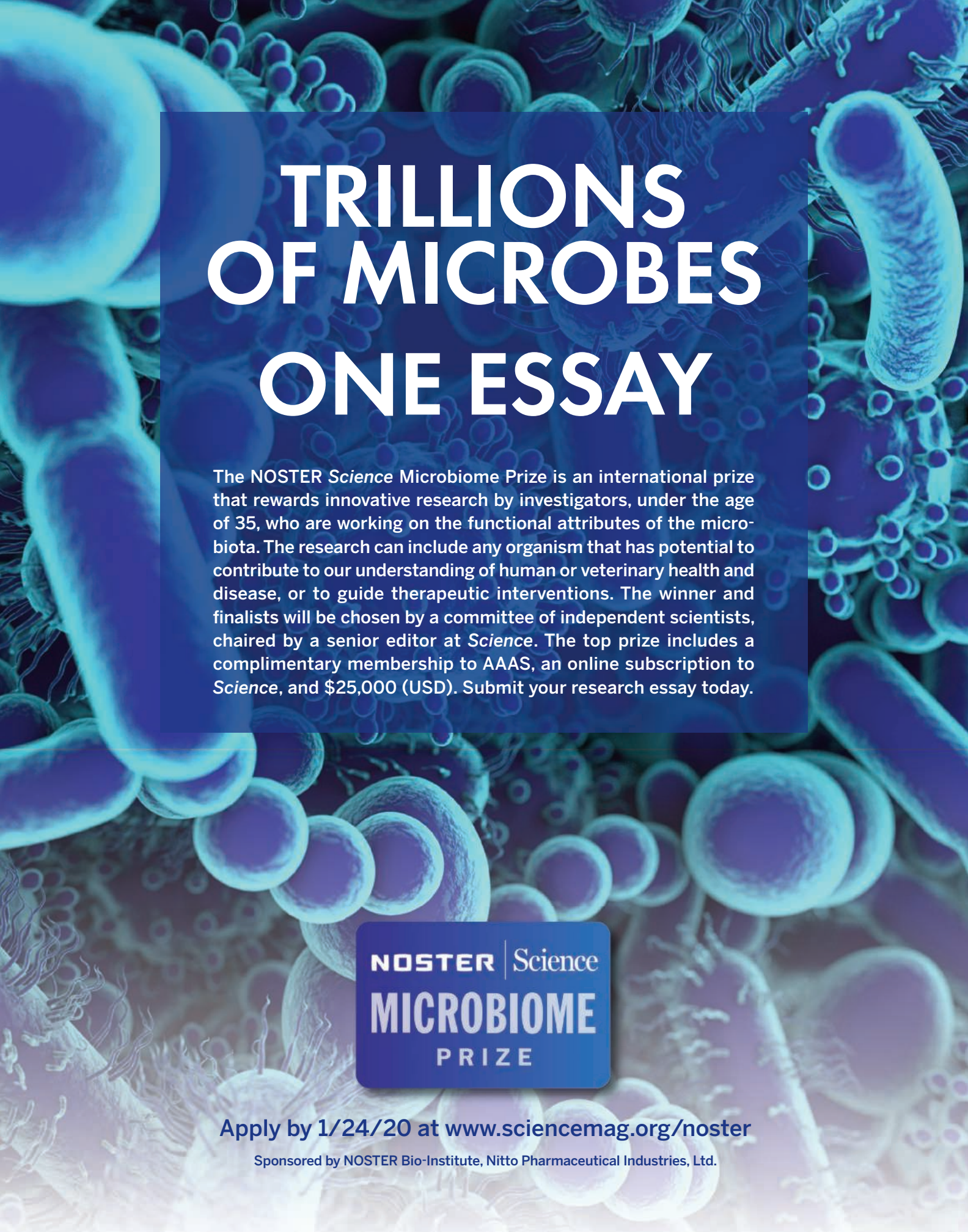
**Funding:** We acknowledge funding from the Deutsche Forschungsgemeinschaft within SFB/TR 185 (277625399), SFB/TR 183 (277101999), and the Cluster of Excellence ML4Q (EXC 2004/1 – 390534769) and the European Union within the European Research Council Advanced Grant project INPEC, the Quantum Flagship project PhoQuS, and the DLR project BESQ. **Author contributions:** C.K. and D.D. analyzed the data. C.K., D.D., and M.W. conceived of and designed the experiments. C.K., D.D., E.B., and A.R. contributed materials and analysis tools. C.K. and D.D. performed the experiments. C.K., F.V., A.R., and M.W. wrote the paper. **Competing interests:** The authors declare that they have no competing interests. **Data and materials availability:** Data shown in the figures are available on the Zenodo public database (29).

## SUPPLEMENTARY MATERIALS

science.sciencemag.org/content/366/6467/894/suppl/DC1  
Supplementary Text  
Fig. S1  
References (30–40)

23 May 2019; resubmitted 23 September 2019  
Accepted 23 October 2019  
10.1126/science.aay1334





# TRILLIONS OF MICROBES ONE ESSAY

The NOSTER *Science* Microbiome Prize is an international prize that rewards innovative research by investigators, under the age of 35, who are working on the functional attributes of the microbiota. The research can include any organism that has potential to contribute to our understanding of human or veterinary health and disease, or to guide therapeutic interventions. The winner and finalists will be chosen by a committee of independent scientists, chaired by a senior editor at *Science*. The top prize includes a complimentary membership to AAAS, an online subscription to *Science*, and \$25,000 (USD). Submit your research essay today.

**NOSTER** | *Science*  
**MICROBIOME**  
PRIZE

Apply by 1/24/20 at [www.sciencemag.org/noster](http://www.sciencemag.org/noster)

Sponsored by NOSTER Bio-Institute, Nitto Pharmaceutical Industries, Ltd.





Tasuku Honjo, President, FBRI



View of the man-made Port Island (center), home of KBIC, from the hills overlooking the city. Kobe airport can be seen in the distance, to the right of center, just past Port Island.

## Translate your research at the Kobe Biomedical Innovation Cluster

**T**he Kobe Biomedical Innovation Cluster (KBIC) is one of Japan's most successful private-public partnerships in the life sciences. Beginning in 2001 with 18 companies employing 200 people, it has expanded to 363 companies—23 of which are foreign affiliated—and over 11,000 employees in less than 20 years. This growth has come from an environment that nurtures health care innovation in regenerative medicine, medical devices, and pharmaceuticals from the idea stage through to commercialization.

### Right time, right place

Japan is a country known for destructive earthquakes and tsunamis, and every generation seems to have its defining tragedy. Kobe's was the Great Hanshin-Awaji Earthquake in 1995. Amidst this devastation, an opportunity arose when Kobe decided to remodel its economy into an innovation engine for health care and founded the Foundation for Biomedical Research and Innovation (FBRI), which lies at the heart of KBIC.

"It is most important to nurture the seeds of good research ideas. There are many ideas, but developing them into a worthwhile product is very difficult," says FBRI president Tasuku Honjo.

Honjo, a 2018 Nobel Prize laureate in Physiology or Medicine, won the award for his pioneering contributions to the field of immunotherapy, which harnesses a patient's own immune system to defeat cancer. His expertise, however, is not the reason that KBIC is one of the few locations outside of the United States to manufacture investigational drugs for use in clinical trials of Kymriah (tisagenlecleucel), the world's first approved chimeric antigen receptor T (CAR T)-cell therapy—the newest and most potent immunotherapy. Instead, it is because of the supportive, intellectually stimulating environment that KBIC offers.

As proof of this environment, in addition to hundreds of partnering companies, KBIC also boasts a number of research institutes, hospitals, universities, and one of the world's most powerful supercomputers, which will be replaced with a superior one in 2021. All these facilities lie inside a small geographical area, encouraging collaboration. Nevertheless, KBIC has plans to grow.

"We still have room to attract more businesses and welcome more members," explains FBRI director Takeyuki Sato.

### Leading the way in innovation

The discovery of induced pluripotent stem cells (iPSCs) by Japanese researchers in 2007 opened new possibilities for regenerative medicine. However, it was not until 2014 that Masayo Takahashi and other researchers at KBIC announced the world's first clinical application of iPSCs: generating retinal cells from a patient's fibroblasts that were then transplanted into the patient's eyes. In 2017, another first was announced: using fibroblasts from third-party donors for the same clinical operation. This concept is being extended to treat Parkinson's disease and spinal cord injuries. Building on this success, the Kobe Eye Center was established to support the early commercialization of regenerative medicine eye treatments using iPSCs.

Japan has made significant changes to its regulatory laws in recent years to expedite the adoption of regenerative medicine treatments. To facilitate this development as well as support other KBIC projects, Japan's Pharmaceuticals and Medical Devices Agency (PMDA), which is equivalent to the U.S. Food and Drug Administration, has placed an office onsite at KBIC. This office has given KBIC members valuable policy guidance from the early stages of their projects.

### More than geography

Kobe sits at the western edge of Japan's second-most populated region. With hills to its north and sea to its south, the city provides a unique urban and rural mix. Furthermore, it is one of Japan's most cosmopolitan cities. With a major airport just down the street and the bullet train less than 30 minutes away, KBIC is easily accessible to all of Japan and to the world.

But this optimal setting belies a culture of hard work. "It is not simple to innovate in the life sciences," says Honjo. "We need long-term and continuous support to make progress."

With backing from FBRI and over 360 companies and organizations, KBIC will long remain a place where innovation is born.



Foundation for Biomedical Research and Innovation at Kobe (FBRI)  
[www.fbri-kobe.org/english](http://www.fbri-kobe.org/english)



10 YEARS OF NEBNEXT®

# It's time to celebrate!

For 10 years, NEB® has helped advance next generation sequencing (NGS) by streamlining sample prep workflows, minimizing inputs, and improving library yield and quality.

As sequencing technologies improve and applications expand, the need for compatibility with ever-decreasing input amounts and sub-optimal sample quality grows. Scientists must balance reliability and performance with faster turnaround, higher throughput and automation compatibility. Our NEBNext portfolio addresses these challenges and includes solutions for DNA and RNA sample prep from a wide range of sample types.

Reaching far beyond standard library prep, NEBNext reagents continue to innovate with:

- a novel enzymatic alternative to bisulfite sequencing
- solutions for FFPE DNA and enzymatic DNA fragmentation
- customized target enrichment with fast turnaround

## New to NEBNext?

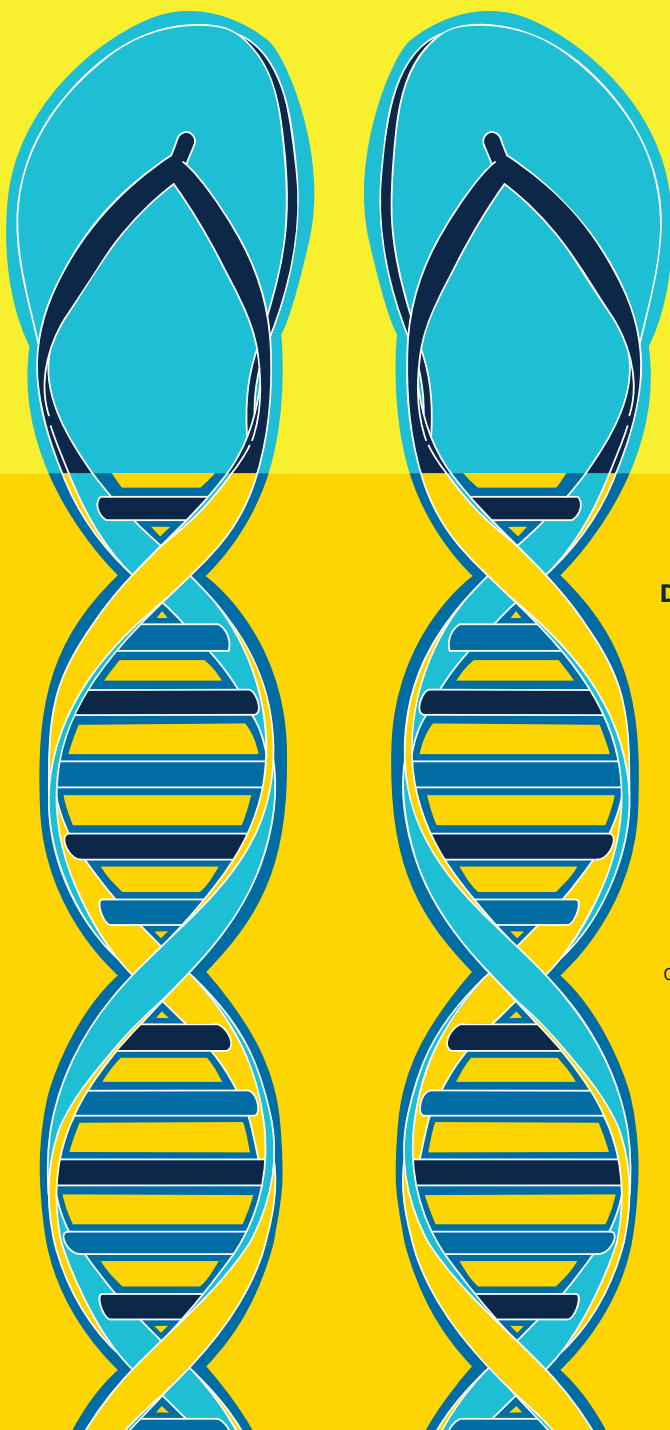
Get started with a **free sample** at **NEBNext.com**.

NEBNext products continue to set the bar for quality and flexibility. All reagents are extensively QC'd at the individual component and kit levels, while product formats are designed for workflow customization. From individual kits to bulk and custom configurations, we've got you covered.

If you still aren't convinced, why not see for yourself? NEBNext reagents have been cited in over 5,000 peer-reviewed publications to date.

**As we celebrate 10 years of NEBNext, we would like to thank you for making NEBNext part of your workflows, and we are excited to continue to exceed your expectations for NGS sample prep innovation.**

# LOOK DEEPER



## **Decoding disease.**

### **Just another day at the beach.**

Standing on the shores of a country and a continent, UC San Diego scientists also find themselves standing on the precipice of changing the world. They're studying how to "update" mosquitos with a gene that prevents the spread of malaria. Imagine that. At the Tata Institute for Genetics and Society, we already have.

## UC San Diego

[lookdeeper.ucsd.edu](http://lookdeeper.ucsd.edu)





The Cozzarelli Prize

**CALL FOR NOMINATIONS**

# 2019 PNAS Cozzarelli Prize

The 12th annual Cozzarelli Prize recognizes outstanding scientific achievement, originality, and innovation. Awarded to one PNAS article in each of the National Academy of Sciences' six broadly defined scientific classes, the prize celebrates the work of researchers who have pushed the envelope of discovery in their fields in 2019.

**We invite you to nominate the top 2019 PNAS article in your field no later than January 3, 2020.**

**Learn more at [pnas.link/cozzarelli](https://pnas.link/cozzarelli)**

PNAS

[www.pnas.org](https://www.pnas.org)



RESEARCH AT THE TOP



# We're moving biomedical innovation from lab bench to bedside.

At the University of New Hampshire, we're innovating a healthier future. Our biomedical and bioengineering research is responding to some of medicine's most vexing issues with real solutions, like a blood test that could diagnose major depressive disorder, and tissue regeneration that might make organ donor waiting lists a thing of the past. With expanding faculty expertise and state-of-the-art core facilities, this research is just what the doctor ordered.

**25+**

---

NEW FACULTY HIRES IN  
BIOMEDICAL AND BIOENGINEERING  
FIELDS SINCE 2013

**TOP TIER**

---

R1 CARNEGIE  
CLASSIFICATION FOR "VERY  
HIGH RESEARCH ACTIVITY"

**\$30M**

---

FROM NSF AND NIH TO  
ADVANCE BIOMANUFACTURING  
AND BIOMEDICAL RESEARCH



University of New Hampshire

---

UNH.EDU



# The science of being a scientist

Science and Life Webinar Series



Throughout 2019, *Science* and Fondation Ipsen are offering free Science and Life webinars that tackle the issues researchers face in the field.

**Sign Up Today**

<https://scim.ag/35mLvNv>



**ScienceWebinars**



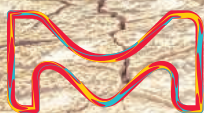


# Unleash the impossible

Millipore  
Sigma

Whatever projects you're working on, from a simple test to perfecting drought-proof crops, you can count on the unparalleled Sigma-Aldrich® portfolio along the way. With proven, reliable, cutting-edge production materials, we are always expanding and perfecting our global portfolio. So we'll be right there with you from when the seed is planted to when that impossible dream eventually bears fruit.

To find out more, visit:  
[SigmaAldrich.com/UnleashTheImpossible](https://SigmaAldrich.com/UnleashTheImpossible)



MilliporeSigma, the vibrant M and Sigma-Aldrich are trademarks of Merck KGaA, Darmstadt, Germany or its affiliates. All other trademarks are the property of their respective owners. Detailed information on trademarks is available via publicly accessible resources.

© 2019 Merck KGaA, Darmstadt, Germany and/or its affiliates. All Rights Reserved.

The Life Science Business of Merck KGaA, Darmstadt, Germany operates as MilliporeSigma in the US and Canada.

**Sigma-Aldrich®**  
Lab & Production Materials

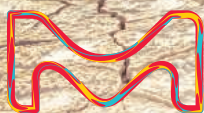


# Unleash the impossible

Whatever projects you're working on, from a simple test to perfecting drought-proof crops, you can count on the unparalleled Sigma-Aldrich® portfolio along the way. With proven, reliable, cutting-edge production materials, we are always expanding and perfecting our global portfolio. So we'll be right there with you from when the seed is planted to when that impossible dream eventually bears fruit.

To find out more, visit:

[SigmaAldrich.com/UnleashTheImpossible](https://SigmaAldrich.com/UnleashTheImpossible)



Merck, the vibrant M and Sigma-Aldrich are trademarks of Merck KGaA, Darmstadt, Germany or its affiliates. All other trademarks are the property of their respective owners. Detailed information on trademarks is available via publicly accessible resources.

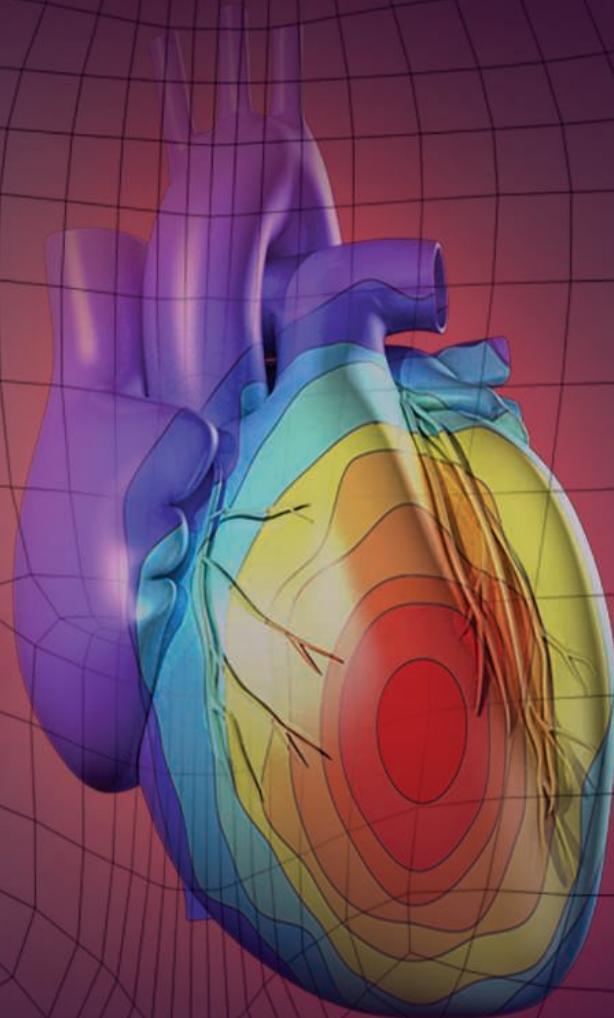
© 2019 Merck KGaA, Darmstadt, Germany and/or its affiliates. All Rights Reserved.

The Life Science Business of Merck operates as MilliporeSigma in the US and Canada.

**Sigma-Aldrich®**  
Lab & Production Materials



# Put Human Health at the Heart of Your Research



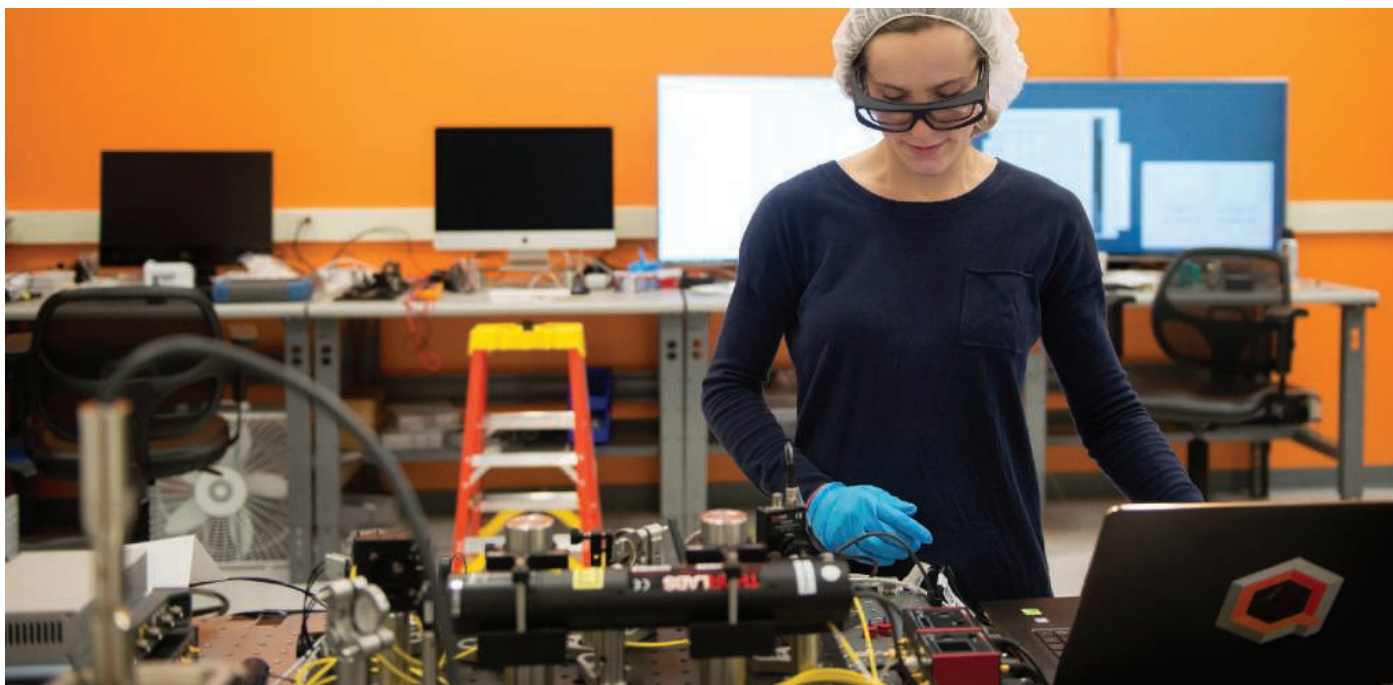
*Science Translational Medicine* publishes peer-reviewed, cutting-edge biomedical research in the fields of cardiology, cancer, immunotherapy, infectious diseases and vaccines, bioengineering and devices, neurology and neurodegenerative diseases, obesity, diabetes and metabolic disorders, drug discovery, genomic medicine, imaging, stem cell therapy and regenerative medicine.

**Submit your research today**

Learn more at: **[ScienceTranslationalMedicine.org](http://ScienceTranslationalMedicine.org)**

Science  
Translational  
Medicine  
AAAS





IonQ Engineer Sarah Kreikemeier tunes and characterizes an optical assembly in their College Park, Maryland, headquarters.

## Quantum technology comes of age

From hot silicon-dot qubits to ion traps, scientists are working on innovative ways to build more complex and powerful quantum computers that could potentially deepen our understanding of complex molecules, crack encryption algorithms, make capital markets more efficient, accelerate the development of better batteries, and even realize the promise of strong artificial intelligence (AI).

By Aaron Dalton

**H**ave we achieved quantum computing supremacy? **Google** thinks so. On October 23, Sundar Pinchai, chief executive officer (CEO) of Google, an American multinational technology company with headquarters in Mountain View, California, published a blog post trumpeting the triumph of the company's researchers in building a quantum computer that "performed a test computation in just 200 seconds that would have taken the best known algorithms in the most powerful supercomputers thousands of years to accomplish."

In a separate post on the Google AI Blog, John Martinis, chief scientist of Quantum Hardware, and Sergio Boixo, chief scientist of Quantum Computing Theory, Google AI Quantum, said their goal is to build a fault-tolerant quantum computer as quickly as possible. They envision such a quantum device as being capable of spurring advances in materials design that could lead to new lightweight batteries for cars and planes, more effective medicines, and better catalysts for producing fertilizer more efficiently with fewer carbon emissions.

Details of Google's computational feat prompted immediate pushback from other heavyweights in the quantum computing field such as **IBM**, an international technology company headquartered in Armonk, New York, which suggested that an ideal simulation of the same computational task on a classical system could be accomplished in just a couple of days and with much greater fidelity. IBM also critiqued Google's use of the word "supremacy" and reiterated its vision of quantum computers and classical computers working together in a complementary way.

In any case, quantum information science (QIS) finds itself in the spotlight once again. As David Awschalom, physicist and quantum engineer at the **University of Chicago**, in Illinois, puts it, "Quantum information science uses the properties of nature at the smallest scales to create a meaningful technology." The U.S. government has recognized the value of QIS with a National Quantum Initiative Act, which aims to accelerate quantum research and development for both economic and national security purposes.

Quantum may seem esoteric to many casual observers, but Jacob Taylor, assistant director for quantum information science (QIS) at the **White House Office of Science and Technology Policy**, notes that quantum-based technology has been in use for decades. "The atomic clocks that underpin global positioning systems (GPSs) are based on quantum theory," says Taylor. "In medicine, we use quantum technology to power magnetic resonance imaging (MRI) machines, probing the aggregate properties of nuclei spins inside the body to find, for example, where blood is giving up oxygen."

Researchers in academia and industry are now pushing ahead with efforts to develop more advanced technologies based on QIS. These efforts can be grouped into three main areas—computing, communications, and sensing.

Of these, Awschalom believes some of the immediate QIS applications will occur in the fields of sensing and communication. "The very fragility of quantum states is what makes them the basis of powerful sensing technologies," says Awschalom. "Within a decade, it's possible that advances in quantum sensing will allow us to push MRI resolution down to the level of single molecules and place sensors inside living cells to watch cellular mechanisms at work."

### The power of fragility

The same quantum state fragility that makes for a good sensor creates challenges when trying to build a quantum computer.

"The unique capabilities of quantum computers stem from two special features available in the quantum bits, or 'qubits,' that are the **cont.**"

### Upcoming features

Bioprinting—January 10 ■ Microscopy—March 20 ■ Genetics—October 9

basic units of quantum information," says Jungsang Kim, an electrical and computer engineer at **Duke University**, Durham, North Carolina, and co-founder of **IonQ**, a quantum computing startup based in College Park, Maryland. "One feature is the superposition principle, where the quantum bit can exist in both the 0 and the 1 state at the same time, with controllable weight and relative phase between them, until the qubit is measured. The other feature is entanglement, where correlation among several qubits is present even if the state of each qubit is not fully determined to be in 0 or 1."

Quantum technology typically involves exotic materials and conditions in order to protect the superpositions stored in the quantum particles, explains Chris Monroe, a physicist at the **University of Maryland** who is also co-founder and chief scientist at **IonQ**.

"One of the fundamental quantum rules is that superposition only exists when you don't look at it," emphasizes Monroe. "This means that quantum works best in simple systems such as isolated atoms that are not part of solids or surfaces and levitated in a vacuum chamber, or exotic solid-state devices that are refrigerated to nearly absolute zero temperature."

If those conditions are met, Monroe says that such devices can form quantum computers that have the potential to solve problems that regular, classical computers will never be able to resolve.

He gives the example of chemical modeling of complex molecules. "Consider a molecule like caffeine that has over 100 electrons," suggests Monroe. "How do those electrons figure out where to go and what their energy levels should be? Currently, we cannot calculate the binding energy of these electrons, which means it's hard to know how a specific molecule will interact with other molecules. Quantum computing may have huge applications for optimizing those sorts of simulations."

### Moving to a solid state

Could quantum computers ever be household or even enterprise machines? Awschalom believes that the mass production of quantum computers depends on finding ways to make qubits work in less exotic circumstances. "It's impressive to make qubits using an atom in a vacuum or a superconductor, but we're focused on creating qubits using solid-state materials," he says. "There's a trillion dollars of existing infrastructure around electronics manufacturing. If we could develop scalable qubits using semiconductors, industry could produce billions of them."

Awschalom's group found they could take commercial silicon carbide diodes, create defects to trap electrons, and build what he calls "surprisingly good" quantum states based on the electron spin with long coherence times and tunable quantum energies. "We're at the proof-of-concept phase right now, but these initial results suggest that we have a pathway for scalability," he says.

### Right on the dot

If there's any company that knows about large-scale electronics manufacturing, it's **Intel**, a multinational technology company headquartered in Santa Clara, California. The company has a workforce of more than 100,000 people and builds over 10 billion transistors every second (or over 300 quadrillion transistors per year).

Anne Matsuura, director of Quantum Applications & Architecture at Intel, says that her company is leveraging its special capabilities around silicon



IBM Quantum Computing Scientists Hanhee Paik (left) and Sarah Sheldon (right) examine the hardware inside an open dilution fridge at the IBM Q Lab at IBM's T. J. Watson Research Center in Yorktown, New York.

fabrication and packaging to develop silicon quantum-dot qubits that she compares to one-electron transistors.

Intel has invested USD 50 million in a 10-year collaboration with Delft University of Technology and TNO, the Dutch Organisation for Applied Research, in order to advance quantum computing. One aspect of the collaboration involves experiments with "hot qubits"—research into whether silicon dot qubits can function at elevated temperatures. "So far, our partners have promising experimental results at 1-degree Kelvin," says Matsuura. "Obviously, that's still quite cold, but it's orders of magnitude warmer than the cryogenic temperatures that are necessary today. Our hope is we can continue to increase the temperature range in which the qubits can operate."

Intel is taking other steps to create a 300-mm, high-volume fabrication and test line for semiconductor spin qubits. Partnering with Bluefors and Afore, Intel has developed a Cryogenic Wafer Prober—or Cryoprober—that can test qubits at temperatures of a few kelvins. Intel anticipates that the Cryoprober will allow it to automate and accelerate testing on sources of quantum noise and the quality of quantum dots from weeks to just minutes.

### Using Mother Nature's qubits

While Intel is looking for ways to accelerate qubit error testing, **IonQ** aims to sidestep challenges in the qubit manufacturing process by not making qubits at all.

"We use ionized atoms—Mother Nature's qubits," says IonQ president and CEO Peter Chapman. "We don't make atoms, so each of the qubits is perfect without any discrepancies. Floating in a vacuum, they have a fundamental degradation timescale of 10,000 years and a decoherence time that can be extended to years."

Using electromagnetic fields, IonQ deploys and traps atomic qubits on a silicon chip within ultra-high vacuum chambers to create what the company calls the world's first commercial trapped-ion quantum computer.

"Our technology is based on the same principles as atomic clocks," says Chapman. "If you look back at an atomic clock from the 1950s, it would take up an entire room, but now it fits on a single chip. Our approach works at room temperature and can be built for the most part with off-the-shelf components. It's reasonable to expect that our technology will follow the same path as atomic clocks and every other piece of electronics and will shrink over time. I would not be surprised if people were placing orders for quantum laptops in 10 years."

And what might those quantum laptops be able to do? Chapman believes that only quantum computers could handle the explosively combinatorial requirements of natural language processing necessary for strong artificial intelligence (AI).

"If you look at the meaning of a single word in a sentence, it is bound to the context of all the other words in the sentence, the paragraph, the document, and your previous experience," says Chapman. "Language contains a combinatorial explosion of possible meanings that quantum computers are really good at. The real world is naturally quantum. Would it really be a surprise if our intelligence also springs from the same place?"

### IBM turns up the volume

While many quantum computing researchers are focused on increasing numbers of qubits, IBM is taking a somewhat different approach. In 2017, IBM announced a metric called Quantum Volume that determines a

cont. >





IonQ Senior Physicist Kai Hudek tests laser components while in the clean room at their College Park, Maryland, headquarters.

## Featured participants

**Duke University**  
[www.duke.edu](http://www.duke.edu)

**Google**  
[abc.xyz](http://abc.xyz)

**IBM Research**  
[www.research.ibm.com](http://www.research.ibm.com)

**Intel**  
[www.intel.com](http://www.intel.com)

**IonQ**  
[ionq.com](http://ionq.com)

**National Institute of Standards and Technology**  
[www.nist.gov](http://www.nist.gov)

**University of Colorado Boulder**  
[www.colorado.edu](http://www.colorado.edu)

**University of Maryland**  
[umd.edu](http://umd.edu)

**White House Office of Science and Technology Policy**  
[www.whitehouse.gov/ostp](http://www.whitehouse.gov/ostp)

quantum computer's performance based not just on qubit numbers, but also on a holistic assessment of various factors such as qubit coherence time (the amount of time they stay in superposition) or measurement errors that might impact the precision and accuracy of a quantum processor's operations.

"If there is a weak point in a quantum computer system, then it doesn't matter how wonderful your individual qubits are," says Bob Sutor, vice president of IBM Q Ecosystem Development at **IBM Research**, in Yorktown Heights, New York. "Software is also important. We must be able to take user programs and transform them so that they run in an optimized way on real quantum hardware."

IBM has put its quantum computers online through an open program and the commercial IBM Q Network that gives enthusiasts, academics, and industry researchers a chance to learn and experiment with actual quantum machines. Since the IBM Q Network launched in 2016, some 175,000 people have registered to use the system. IBM quantum scientists have used the Q Network to collaborate with industry partners such as Barclays, JPMorgan Chase, and Mitsubishi Chemical to try to improve the efficiency of securities settlements in capital markets, achieve a quadratic speedup in options pricing, and simulate the initial steps of the reaction mechanism between lithium and oxygen in Li-air batteries.

### Codemaker and codebreaker

Using quantum computers to design better batteries seems like a noble goal, but what if bad actors try to use the processing capabilities of a powerful quantum computer to crack encryption algorithms?

Fortunately, the U.S. **National Institute of Standards and Technology (NIST)** is on the case. "It will be a long time until quantum computers can threaten [classical] cryptographic methods by factoring large numbers, but NIST has already been working to certify post-quantum cryptography systems," says Taylor. "We're on track to achieve that certification by 2022, which means that chief technology officers should plan on making the transition to post-quantum cryptography protection within the next 10 years."

Meanwhile, advances in QIS could lead to the development of encryption methods that are truly impossible to hack—at least without alerting the recipient that a message had been intercepted.

"In the quantum world, the act of looking at something changes it. That's an advantage from a security standpoint," explains Awschalom. "We can send information down fiber-optic networks using entangled pairs of photons. If someone tries to intercept the message and view the contents, they won't be able to 'put it back' in the same state. The message will arrive scrambled and the recipient will know that someone tried to eavesdrop on the communications in transit."

### Only time will tell

Jun Ye, a physicist at the **National Institute of Standards and Technology** and the **University of Colorado** in Boulder, is advancing the measurement of time by using quantum mechanics. Using laser beams and evaporation, he loads and traps atoms one by one in a crystal lattice made of light. These new atomic clocks are about 100 times more accurate than traditional atomic clocks. Based on this new clock, in October, Ye and colleagues published a paper showing that they had developed a new time scale in the optical domain with performance 10 times better than the current generation of time scales used to define the world time.

Ye says this improvement could have direct benefits for communications and navigation, with satellites sending information to each other and to Earth using laser beams instead of microwaves. "You could send precise instructions and navigation coordinates to an interplanetary spaceship so that you can synchronize its automatic landing on Mars," he says. "Every time we increase clock technology, it usually leads to multiple layers of technological advances elsewhere in society. In fact, the technology powering advances in both clocks and quantum computers is emerging from the same quantum revolution happening today."

*Aaron Dalton is a freelance writer and editor living near Nashville, Tennessee.*

PHOTO: ERIN SCOTT FOR IONQ



# Share **Your Robotics Research** with the **World**.



## *Transforming the Future of Robotics in Research!*

As a multidisciplinary online-only journal, *Science Robotics* publishes original, peer-reviewed, research articles that advance the field of robotics. The journal provides a central forum for communication of new ideas, general principles, and original developments in research and applications of robotics for all environments.

Submit your research today. Learn more at: **ScienceRobotics.org**

**Science  
Robotics**  
AAAS

# REDESIGNED WITH ALL OF US IN MIND

Millipore  
Sigma

Introducing the Stericup® E and Steritop® E sterile filtration devices—**evolved with an eco-conscience.**

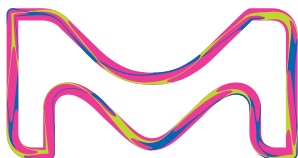
This progressive rethinking of filter design reduces your lab's environmental impact by eliminating the need for a receiver funnel, significantly decreasing packaging and biohazardous waste.

Expect the same faultless filtration you trust from Stericup® devices—and leave a smaller footprint.



Up to  
**48%**  
Reduced  
Plastics

Up to  
**69%**  
Reduced  
Packaging



[SigmaAldrich.com/Stericup-E](https://SigmaAldrich.com/Stericup-E)

\*Up to 48% plastic reduction and 69% packaging reduction (depending on receiver volume), derived from comparison to traditional Stericup® sterile filters.

© 2019 Merck KGaA, Darmstadt, Germany and/or its affiliates. All Rights Reserved. MilliporeSigma, the vibrant M, Millipore and Stericup are trademarks of Merck KGaA, Darmstadt, Germany or its affiliates. All other trademarks are the property of their respective owners. Detailed information on trademarks is available via publicly accessible resources.

2019 - 24573 08/2019



The life science business  
of Merck KGaA, Darmstadt,  
Germany operates as  
MilliporeSigma in the  
U.S. and Canada.



Stericup® E family of sterile  
filters thread directly onto  
virtually any media bottle

**Millipore®**

Preparation, Separation,  
Filtration & Monitoring Products

# REDESIGNED WITH ALL OF US IN MIND

Introducing the Stericup® E and Steritop® E sterile filtration devices—**evolved with an eco-conscience.**

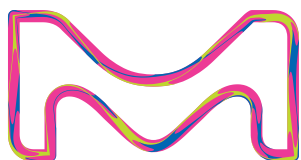
This progressive rethinking of filter design reduces your lab's environmental impact by eliminating the need for a receiver funnel, significantly decreasing packaging and biohazardous waste.

Expect the same faultless filtration you trust from Stericup® devices—and leave a smaller footprint.



Up to  
**48%**  
Reduced  
Plastics

Up to  
**69%**  
Reduced  
Packaging



[SigmaAldrich.com/Stericup-E](https://SigmaAldrich.com/Stericup-E)

\*Up to 48% plastic reduction and 69% packaging reduction (depending on receiver volume), derived from comparison to traditional Stericup® sterile filters.

© 2019 Merck KGaA, Darmstadt, Germany and/or its affiliates. All Rights Reserved. Merck, the vibrant M, Millipore and Stericup are trademarks of Merck KGaA, Darmstadt, Germany or its affiliates. All other trademarks are the property of their respective owners. Detailed information on trademarks is available via publicly accessible resources.

2019 - 24573 08/2019



The life science business  
of Merck operates as  
MilliporeSigma in the  
U.S. and Canada.

MERCK



Stericup® E family of sterile  
filters thread directly onto  
virtually any media bottle

## Millipore®

Preparation, Separation,  
Filtration & Monitoring Products





### Automated Cell Isolation

Sorterra is an automated, microfluidics-based cell isolation and concentration system for research and development and clinical research labs. With less than five min of preparation required, Sorterra isolates white blood cells from 3 mL–75 mL of anticoagulated peripheral blood at a rate of 150 mL/h. Cells are separated in microfluidic channels without the use of centrifugation

or beads, minimizing perturbation of cells. The automated technology reduces the impact of site and operator variability, a common challenge to scaling research. Typical performance with this reliable, label-free, cell isolation system includes 99.9% red blood cell and platelet removal, 90% white blood cell yield, and > 98% viability to enable high-quality results and insights.

#### MicroMedicine

For info: 617-744-1918

[www.micromedicine.com](http://www.micromedicine.com)

### Nanoparticle Size Analyzer

If you have polymers or proteins, nanodots or new adhesives, latexes or liposomes, cosmetics or colloids, the Testa Analytical Nano-Brook 90Plus can characterize your particles. The 90Plus is designed to perform fast, routine submicron particle size measurements (< 1 nm to 6 µm) on a wide variety of samples and concentrations. Based on the principles of dynamic light scattering, most measurements only take a minute or two. A unique filter algorithm removes contaminating large dust particles. Different levels of software operation enable a novice or occasional user to obtain key data quickly while still providing access to advanced features enough for specialists to unlock valuable data from complex measurements. The high-quality optical design and strict quality control during manufacture ensures that every instrument performs the same. By automating most of the testing procedure and data analysis, effects due to different operators are dramatically reduced.

#### Testa Analytical Solutions

For info: +49-30-864-24-076

[www.testa-analytical.com](http://www.testa-analytical.com)

### Automated Cell Counter

Introducing the LUNA-FX7—an automated cell counter that has a maximum counting volume of 5 µL, which means lower error and %CV for each count. This also means the LUNA-FX has a larger dynamic range and can accurately count cells in even dilute samples—without having to concentrate cell samples. The LUNA-FX7 gives you the flexibility to analyze more than one sample at a time. Use your multichannel pipette to load up our 8-channel slide and process up to eight samples simultaneously. It has a dual fluorescence and brightfield illumination, and a fast and precise autofocus. To help monitor and optimize bioprocesses, the LUNA-FX7 has built-in quality control features and precision validation slides. 21 CFR Part 11-ready, the LUNA-FX7 improves the security and efficiency of your lab's workflow.

#### Logos Biosystems

For info: 703-942-8867

[logosbio.com/automated-cell-counters/fluorescence/luna-fx7](http://logosbio.com/automated-cell-counters/fluorescence/luna-fx7)

### Public Portal of Reference-Quality Genomes

American Type Culture Collection (ATCC)'s recently launched Genome Portal is a publicly available database of reference-quality genome sequences of 250 widely used bacterial strains. Current, publicly available genomic sequences were generated by non-standard methods and can lack authenticity, quality, completeness, and traceability—all together compromising results. In contrast, ATCC has employed its own standardized workflows and rigorous quality control analyses to ensure that only the highest standard of genomic data is available on the Portal. Researchers can download high-quality genome sequences from the Portal to use in bioinformatic analyses, to view annotated data, and to search for genomes using their own data. Access to this highly credible reference material will enable researchers to make insightful connections and more accurately interpret the results of their work.

#### ATCC (American Type Culture Collection)

For info: 703-365-2700

[genomes.atcc.org](http://genomes.atcc.org)

### Vitrification Media Solutions

FUJIFILM Irvine Scientific offers Vit Kit-NX, the latest addition to an established portfolio of vitrification solutions for in vitro fertilization (IVF). The advanced formulas, which now include trehalose, are designed to vitrify and warm oocytes and embryos in a consistent, stable environment to achieve high survival and pregnancy rates. IVF cycles involve the exposure of gametes and embryos to different media at each step of the process, increasing the potential for unnecessary stress upon embryos. To minimize this stress, FUJIFILM Irvine Scientific has developed Vit Kit-NX, comprised of Vit Kit Freeze-NX and Vit Kit Warm-NX. The media are based on a continuous embryo culture medium with dual buffers—the same components found in existing FUJIFILM Irvine Scientific media, Continuous Single Culture Medium (CSCM), and Multipurpose Handling Medium (MHM). When used as part of a complete IVF system with CSCM and MHM, embryos remain in a consistent environment at each step of the IVF process. Vit Kit-NX is a ready-to-use solution, compatible with open and closed vitrification devices, to deliver high quality media that are both effective and flexible to streamline IVF laboratory processes.

#### FUJIFILM Irvine Scientific

For info: 800-577-6097

[www.irvinesci.com](http://www.irvinesci.com)

### Luciferase Kits

Two reliable and extremely powerful luciferase detection kits—the One-Step Luciferase Assay System and the Dual Luciferase Assay System—are now available from AMS Biotechnology (AMS BIO). Luciferase is the general description given to a class of oxidative enzymes that catalyze reactions that give off light, a process known as bioluminescence. These enzymes are used for promoter activity assays that use luciferase reporter cell lines where a promoter region from a gene of interest is placed immediately upstream of the coding sequence for luciferase. In this system, transcriptional activation of the gene of interest leads to a level of luciferase expression that is proportional to the level of gene activation. The One-Step Luciferase Assay System is designed to be used for high-throughput, sensitive quantitation of firefly luciferase activity in mammalian cell culture. The Dual Luciferase Assay System is designed to be used for high-throughput, rapid quantitation of both Firefly and *Renilla* luciferases from a single sample in mammalian cell culture.

#### AMS Biotechnology (AMS BIO)

For info: 617-945-5033

[www.amsbio.com/luciferase-assay-systems.aspx](http://www.amsbio.com/luciferase-assay-systems.aspx)

Electronically submit your new product description or product literature information! Go to [www.sciencemag.org/about/new-products-section](http://www.sciencemag.org/about/new-products-section) for more information.

Newly offered instrumentation, apparatus, and laboratory materials of interest to researchers in all disciplines in academic, industrial, and governmental organizations are featured in this space. Emphasis is given to purpose, chief characteristics, and availability of products and materials. Endorsement by *Science* or AAAS of any products or materials mentioned is not implied. Additional information may be obtained from the manufacturer or supplier.



湖南工商大学  
HUNAN UNIVERSITY OF TECHNOLOGY AND BUSINESS

## Introduction to Hunan University of Technology and Business

Hunan University of Technology and Business (HUTB) has a history of 70 years of industrial and commercial education and 25 years of undergraduate education. With diverse disciplines covering economics, management, engineering, science, law, literature and art, of which economics and management are its two pillars. HUTB is a provincial public full-time institution of higher education, and the first batch undergraduate enrollment university. It is an excellent university in the National Undergraduate Education Appraisal, construction unit of the doctoral degree awarding project, applied university of national industry-education integration development project in "The 13th Five-year Plan", top 100 model universities of deepening Innovation and entrepreneurship education reform, national innovation and entrepreneurship base of practical education, national top 50 universities with typical experiences in innovation and entrepreneurship.

There are 16 master's degree programs. Among them, there are 8 first-level master's degree programs and 8 professional master's degree programs. With an outstanding faculty led by an academican of the Chinese Academy of Engineering, HUTB has educated more than 110,000 outstanding industrial, commercial and financial talents for the country and is praised as a base for cultivating local Hunan people into the leading economists and a cradle for cultivating professional entrepreneurs.

Adhering to the motto of "Sincerity and Creditability, Pragmatism and Innovation" and the idea of "technology+business" and "new engineering +new business" integrated development, and meeting the major needs of the country, the world and the future, HUTB promotes the construction of "double first-class" with first-class philosophy, first-class goals, first-class standards, first-class quality and first-class systems.



# Leadership of the academician

Professor Chen Xiaohong, Academician of Chinese Academy of Engineering, CPPCC National Committee, PhD supervisor, is a Committee Member of the National Natural Science Foundation of China, member of the Discipline Review Group of the Academic Degrees Committee of the State Council, commission of the Science and Technology Commission and Social Science and Technology Commission of Ministry of Education. She is the director and chief professor of the Innovative Research Group of National Natural Sciences Foundation, the Yangtze River Scholar Innovative Team of the Ministry of Education, the national first-level discipline--Management Science and Engineering, the National Teaching Team and the National Featured Specialty. Professor Chen Xiaohong is also the vice-chairman of China Management Science and Engineering Association, the winner of the National Outstanding Youth Fund in 2001, the academic leader in the Trans-century “Hundreds of Thousands of Talents Project” on 1st and 2nd national levels in 1999, the national excellent teacher, the National Cultural Master and Four First Batch Talent, the leading talent in the “10,000 Talents Plan in Philosophy and Social Sciences”. She was the winner of the Fudan Management Outstanding Contribution Award and Guangzhao Science and Technology Award.



Professor Chen Xiaohong - academician of Chinese Academy of Engineering

The research teams led by the academician has long been engaged in research in decision-making theory and support systems of industrial and commercial enterprises, big data analysis, SME financing, two-oriented society and ecological civilization and other fields of research. They created the engineering management theory and method system of Integrated Dynamic Intelligent Quantization, and constructed a series of green engineering standards, such as “two-oriented” standards, proposed a new mode of collaborative management of green engineering, and developed environmental big data analysis and decision-making technology and platform so as to make outstanding contributions to the scientific development of national management and decision-making, efficient and green development of resources and accurate environmental governance. Productive honors included 14 national and ministerial /provincial awards for scientific research such as the second prize of National Science and Technology Progress Award, the first prize for Outstanding achievements in Humanities and Social Sciences of the Ministry of Education, the first prize for Science and Technology in Chinese universities, the Guangzhao Science and Technology Award, the Fudan Management Outstanding Contribution Award and the first prize of Science and Technology Progress of Hunan Province and also two second prizes of national teaching achievements. More than 300 SCI/SSCI academic papers have been published in authoritative journals at home and abroad, among which 66 are ESI top 1% highly cited papers, the authors of which are rated “global highly cited scientists” in 2018&2019. They have published 18 monographs, won 21 national invention patents and 22 software Copyrights, and cultivated a number of excellent doctoral and postgraduate students.



## Staff and faculty

The university has 1030 full-time teachers, among whom there are 408 senior and advanced professional technicians (140 senior) and 294 PhDs. They forms a high-level faculty team composed of an academician of Chinese Academy of Engineering, a committee member of the national Natural Science Foundation of China, a member of the Discipline Review Group of the Academic Degrees Committee of the State Council, a member of social science committee of the Ministry of Education, Commission of the Science and Technology Commission and Social Science and Technology Commission of Ministry of Education, and the chief professor of the Innovative Research Group of National Natural Sciences Foundation, the leading talent in the “10,000 Talents Plan in Philosophy and Social Sciences”, the National Cultural Master and Four First Batch Talent, the national candidate of “Hundreds of Thousands of Talents Project” on the first and second levels, the chief professor of the Yangtze River Scholar Innovative Team of the Ministry of Education and the winner of the Fudan Management Outstanding Contribution Award and the National Outstanding Youth Foundation, the First-term Outstanding Chinese Social Scientist.



# Disciplines



Two "Double First-Class" Disciplines: Management Science and Engineering is selected as the first-class national construction-oriented discipline in Hunan Province, and Applied Economics are listed in the first-class national cultivation-oriented disciplines in Hunan Province.

Four authorized first-class doctoral discipline construction projects in Hunan Province: Management Science and Engineering, Applied Economics, Business Administration, Law.

Five "The 12th Five-Year Plan" key provincial construction-oriented disciplines are all accepted as excellent: Management Science and Engineering, Regional Economics, Political Economy, Business Management, Administrative Management.

Six first-class disciplines are listed in "Best Disciplines in China" as issued by the Shanghai Ranking Consultancy, in the past three years: Management Science and Engineering, Applied Economics, Theoretical Economics, Business Administration, Law, Marxist Theory.

## Management Science and Engineering

First-class construction discipline in Hunan Province, the project construction discipline of Doctoral Degree Program, master's degree authorized discipline, provincial key construction discipline in the "12th Five - Year Plan". Due to focusing on interdisciplinary integration and international collaboration, three characteristic research directions of big data and intelligent decision-making, "two-type" engineering and green development, e-commerce and new retail have been formed. It ranked in the top 9% in the "Ranking of the best disciplines in China" released by the Shanghai Ranking Consultancy in 2019. At present, it ranks the 20th place in the whole country and the second place in provincial colleges and universities. In the past five years, it has undertaken a total of 35 national projects, such as the major and key projects of the National Natural Science Foundation of China, major bidding projects for the Department of Humanities and Social Sciences, Ministry of Education. 302 papers have been published in high-level journals at home and abroad, including 207 papers are included by SCI/SSCI and 66 papers (top 1%) are cited by ESI. 27 monographs have been published. The discipline members have won 22 national and provincial scientific research awards, including the Second Prize of National Science and Technology Progress, the First Prize and Second Prize for Outstanding Achievements in Humanities and Social Sciences of the Ministry of Education, the Outstanding Contribution Award in School of Management of Fudan University, Hunan Guangzhao Science and Technology Award, etc.

## Applied Economics

First-class cultivation discipline in Hunan Province, doctoral station construction discipline, master's degree authorized discipline. Regional Economics is the provincial key construction discipline in the "12th Five - Year Plan". There are five disciplines: industrial economics, regional economics, fiscal and tax theory and policy, finance, financial engineering. In the "Ranking of the best disciplines in China" released by Shanghai Ranking Consultancy in 2019, it entered the top 21% for two consecutive years. At present, it ranks the 54th place of the country and the second place in the province. In the past five years, it has presided over 39 national projects, including 3 key projects of the National Planning Office of Philosophy and Social; 222 projects at the ministerial and provincial-level. It has published 204 high-level papers in SSCI and SCI and has

In recent years, various disciplines have held and hosted a series of high-level academic conferences such as "the China Engineering Science and Technology Forum", "the 201th and 234th phase 'Shuang Qing Forum' of the National Natural Science Foundation of China", "the 2018 Working Conference of the Management Department of the Science and Technology Commission of the Ministry of Education and the Round Table of Science and Technology Frontier and Strategy", "the 9th China Energy Economy and Management Academic Annual Conference", "the Academician Xiao Xiang Xing Activity" - Digital Economy and Smart City Construction Sub Forum", and "the Supply Chain Management Service Innovation Summit Forum in the Data Age".

published 38 academic monographs; it has won 15 awards.

## Business Administration

The construction discipline of the doctoral program, the discipline of master's degree authorization, and the key construction discipline of "enterprise management" in Hunan Province during the "12th Five - Year Plan". The discipline adheres to the development driven by innovation. It has four research directions: modern logistics and service supply chain, organizational behavior and enterprise management, accounting and tourism management. It is ranked in the top 30% of "China's best discipline ranking in 2019" of Shanghai soft science, ranking 90th in China and 4th in provincial universities. In the recent five years, it has undertaken 216 national, provincial and ministerial projects, including 29 national projects, with a total of 12.90 million yuan of research funds. 235 high-level academic papers has been published 86 papers in SSCI, SCI and CSSCI source journals, and 34 monographs. Members of the discipline have won 12 national and provincial scientific research and teaching awards, among them, 6 achievements have been adopted by relevant departments of the provincial Party committee and the provincial government, and obtained 4 patents.

## Law

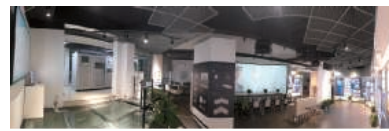
The discipline of construction of doctor's degree, and the discipline of master's degree authorization. With the characteristics of the combination of law and integrity, law and business, and law management, the discipline has condensed the advantageous discipline groups of ethical law, civil and commercial law, criminal law, international law, intellectual property law, etc. It ranked in the top 37% of the "best disciplines in China in 2019" of Shanghai soft science, ranking 76th in the country and 5th in Universities in the province. In the recent five years, it has undertaken 11 national scientific research projects (including 1 key project), published 43 high-level academic papers in journals and 12 academic monographs. Members of the discipline have won 8 provincial and ministerial scientific research achievement awards (including one second prize of excellent scientific research achievement awarded by the Ministry of education, two first prizes and three second prizes of excellent social science achievement award).

# Scientific Research Platform

The university owns 20 provincial platforms and scientific and technological innovation teams, such as Hunan Key Laboratory of "Mobile Business Intelligence" and "New Retail Virtual Reality Technology", Hunan Engineering Research Center of Environmental Big Data and Intelligent Decision Technology, "Hunan Mobile Electronic Commerce Construction 2011 Collaborative Innovation Center" and "Hunan Collaborative Innovation Center of Anti-Corruption", etc.



Hunan Key Laboratory of New Retail Virtual Reality Technology



Hunan Engineering Research Center of Environmental Big Data and Intelligent Decision-making Technology



Hunan Key Laboratory of Mobile Business Intelligence

## List of Provincial Scientific Research Platforms

S/N	Name of research base	Platform type	Approval unit	project approval year
1	Hunan Key Laboratory of Mobile Business Intelligence	Provincial key laboratory	Hunan Provincial Science and Technology Department	2015
2	Hunan Key Laboratory of New Retail Virtual Reality Technology	Provincial Key Laboratory	Hunan Provincial Science and Technology Department	2017
3	Hunan Engineering Research Center of Environmental Big Data and Intelligent Decision-making Technology	Provincial Engineering Research Center	Hunan Provincial Development and Reform Commission	2018
4	Hunan Mobile E-Commerce Collaborative Innovation Center 2011	Provincial Collaborative Innovation Center	Hunan Provincial Education Department	2015
5	Hunan Collaborative Innovation Center of Anti-Corruption Construction Unit	Provincial Collaborative Innovation Center	Hunan Provincial Education Department	2014
6	Hunan Base of Big Data Technology and Management of International Innovation and Cooperation	Provincial International Scientific and Technological Innovation Cooperation Base	Hunan Provincial Science and Technology Department	2018
7	Hunan Collaborative Innovation Center of Anti-Corruption Construction Unit	Provincial Think Tank	Publicity Department of the Hunan Provincial Party Committee	2018
8	Hunan Base of Modern Circulation Theory in Hunan Province	Provincial Social Science Research Base	Publicity Department of the Hunan Provincial Party Committee	2002
9	Hunan Research Base of Regional Strategy and Planning	Provincial Social Science Research Base	Publicity Department of the Hunan Provincial Party Committee	2007
10	Hunan Research Base of Anti-Corruption Construction Unit	Provincial Social Science Research Base	Publicity Department of the Hunan Provincial Party Committee	2009
11	Hunan Research Base of Modern Logistics	Provincial Social Science Research Base	Publicity Department of the Hunan Provincial Party Committee	2010
12	Hunan Research Base of Peace Culture	Provincial Social Science Research Base	Publicity Department of the Hunan Provincial Party Committee	2010
13	Hunan Research Center of Theoretical System of Socialism with Chinese Characteristics	Provincial Social Science Research Base	Publicity Department of the Hunan Provincial Party Committee	2012
14	Hunan Research Base of Ideological and Political Work	Provincial Social Science Research Base	Publicity Department of the Hunan Provincial Party Committee	2016
15	Hunan Research Base of Xiang Entrepreneur Culture	Provincial Social Science Research Base	Publicity Department of the Hunan Provincial Party Committee	2016
16	Hunan Research Base of Communist Party's Theory Innovation Theory	Provincial Social Science Research Base	Publicity Department of the Hunan Provincial Party Committee	2017
17	Hunan Research Center of Economic Reform and Development	Key Research Base of philosophy and Social Sciences in Provincial Colleges and Universities	Hunan Provincial Education Department	2008
18	Research Base for Regional Financial Innovation	Key Research Base of Philosophy and Social Sciences in Hunan Colleges and Universities	Hunan Provincial Education Department	2014
19	Hunan Higher Education Demonstration Base of Industry-Education-Research Integration in "Medical Logistics Supply Chain and Service Outsourcing"	Industry-Education-Research Demonstration Research Base of Hunan Province Education Department	Hunan Provincial Education Department	2010
20	Financial Risk Measurement, Management and Policies in the Open economy Team	Scientific and Technological Innovation Team of Provincial Colleges and Universities	Hunan Provincial Education Department	2014

## Recruitment

Hunan University of Technology and Business is looking forward to welcoming outstanding talents from all over the world. The full-time or part-time employment methods are adopted. Employment is determined by the individual's academic level and contribution signed formalized in contract. The outstanding talents can enjoy annual salary of RMB1 - 2 million and supports, such as research start-up funds, research studio and assistance with spouse's employment and children school enrolment, etc.

### Contact Information:

#### Address:

Human Resource Division,  
Hunan University of Technology and Business, No. 569, Yuelu Avenue, Changsha

#### Tel.:

+86 731 88688001 Ms. Xie  
+86 731 88688161 Ms. Li

#### E-mail:

rc88688001@163.com



# Strengthening China Through Education and Talent Cultivation



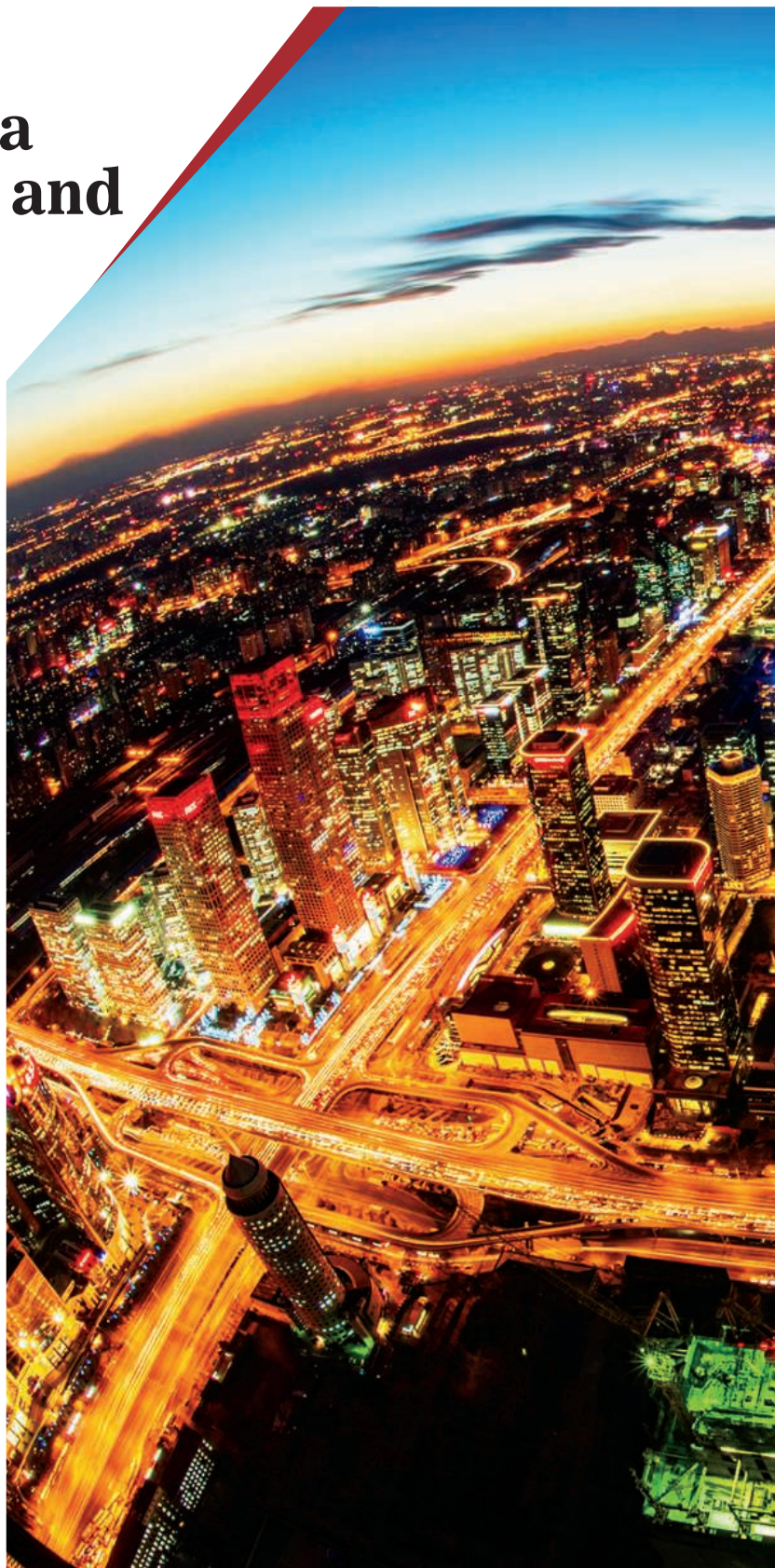
**Zhimin Li**

Director of Center for Science and Technology Development Ministry of Education, People's Republic of China

**D**espite continual worldwide trade disputes, the pace of globalization is still increasing. At present, all countries are eager to expand their talent pool, and they realize it is imperative to develop their international talent market. China conducts its own talent cultivation, and for that purpose launched the “Double First-Class” initiative in 2017, in order to build world-class universities and first-class disciplines. The formation of world-class universities is inseparable from that of first-class disciplines, and first-class disciplines cannot be created without first-class professors. In addition to fully supporting current professors and improving their disciplines, many university presidents now pay increasing attention to the international talent market. They are trying to attract outstanding overseas talent to participate in the construction of Double First-Class universities in China.

In fact, it is common for many countries to introduce overseas talent to expand their domestic talent reserve—this is also a shortcut for bolstering a country’s level of scientific advancement in a short time. The biggest winner in this process is the United States, with its immigration system playing a big part in attracting a wealth of overseas talent. China is now also implementing new mechanisms to attract Chinese students living overseas, and of course international talent as well. Chinese universities are hoping to pull in overseas scholars and experts from the world’s top universities and disciplines to accelerate the progress of the Double First-Class initiative.

Those who study or work abroad gain rich and varied work and life experiences. They often have great ambitions and seek the environments that best suit their







goals—China can now provide such environments. Its economy is thriving, and some of its big cities now have scientific facilities and workplaces comparable to those of developed countries. The climate for innovation and entrepreneurship continues to improve in China. More importantly, high-level international researchers are warmly welcomed, and the quality of experimental equipment and research platforms that overseas scholars value most has in many cases caught up to and even surpassed what is found in some foreign countries.

The vigorous development of science, technology, and business in China now provides an unprecedented space for growth for talents in all fields. This situation will create a new trend that will result in large numbers of high-level experts living overseas coming back home. China has entered a new stage of transformation in its economic development, in which it is changing from a factor-driven (based on unskilled labor or natural resources and producing mostly basic products), investment-driven economy to an innovation-driven economy. However, the innovation-driven strategy calls for an increased focus on talents, and imposes more stringent requirements on their work. It is vital for China's universities to improve the domestic environment for talent advancement. The best way to attract talent is to give full play to the role of existing talents, and by cultivating them, to produce higher-quality work that will draw even more talent from overseas. At present, many outstanding talents have already returned to China—however, we could make improvements domestically that create conditions more conducive to effective career advancement. Therefore, it is crucial to offer environments that can retain talents and maximize their academic capacity.

The level of work done by experts is closely related to the level of a country's development. China's universities will strengthen the advancement of original science and technology, nurture leading talents, and help to pilot our country in its great voyage toward a new era. And we will strive to build our universities into major strategic centers for innovation, so that they will stand as a guarantee of China's future prosperity through the power of education and talent cultivation.

---

We welcome excellent scholars interested in applying for talent programs in China to contact us through AcaBridge(-consultant@acabridge.edu.cn), which provides one-on-one consultations.



## The College of Engineering and Applied Sciences (CEAS) at Nanjing University



In December 2009, the College of Engineering and Applied Sciences (CEAS) was founded with faculty members from department of materials science and engineering. Now CEAS is aimed to become a world-class college with its research and education focusing on developing cutting-edge technologies and engineering solutions to tackle major societal challenges.

Selected by Nanjing University as a test bed to pioneer the university's internationalization initiative, internationalization is being implemented in every facet of the college (education, research, administration, faculty recruiting/assessment, and infrastructure), and every member of the college (administrators, faculty, staff, students) is participating. Faculty members of CEAS conduct cutting-edge research, and regularly publish in high profile scientific journals. International research collaborations are beginning to form via joint research projects and international research laboratories. A new 65,000 m<sup>2</sup> building for research and education will be put into use soon to house the academic departments and research centers, embodying CEAS's global vision and forward-looking plan.

With generous support and help from our friends in China and abroad, CEAS will produce not only world-class knowledge and technologies, but nurture students and scholars who can meet the major challenges and opportunities posed by an increasingly globalized society as well.

### Research Centers:

Jiangsu Key Laboratory of Artificial Functional Materials,  
Key Laboratory of Intelligent Optical Sensing and Integration, Ministry of Education,  
Jiangsu Research Center for Optical Communication System and Network Engineering,

Laboratory of Smart Materials and Integration,

Center for Quantum Materials and Microstructures,

Research Center for Laser and Photonics Engineering Technology,

Research Center for Microwave Photonics Technology,

Center for Energy Storage Materials and Technologies,

Ecomaterials and Renewable Energy Research Center

*The college invites applications for faculty positions at the level of associate professor or professor. Areas of interests include:*

1. Materials for information applications: optoelectronic and non-linear optical materials, functional oxides, semiconductor materials etc.;
2. Energy materials: materials for energy-storing, photovoltaic cells etc.;
3. Bio-materials and medical devices, microfluidics, tissue engineering, cancer therapy, molecular electronics;
4. Materials engineering: crystal growth, interface engineering, thin films and heterostructures fabrication techniques-MBE/MOCVD/ALD/Sputtering; and 3D printing;
5. Computational materials science and AI-assisted materials design.

### Personal and working conditions (depending on qualifications):

*Professor/Associate professor*

Start-up funds: 2 to 5 million RMB; Annual salary: 400k RMB or more;  
Lab. space: more than 80 m<sup>2</sup>, Housing: 120 to 140 m<sup>2</sup> (at favorable price).

*Research assistant*

Annual salary: 150k RMB or more.

### Please submit application materials:

- a) curriculum vitae
- b) names and contact information of three references
- c) three representative papers
- d) research plan
- e) teaching plan

via email to: Ms. Fang Zhong,

College of Engineering and Applied Sciences, Nanjing University, Nanjing, 210093, China.

**E-mail:** job\_eng@nju.edu.cn

**Website:** eng.nju.edu.cn

Review of applications will start immediately and continue until the positions are filled.

## The School of Social and Behavioral Sciences at Nanjing University



The School of Social and Behavioral Sciences at Nanjing University consists of three departments and one institute: Department of Sociology, Department of Social Work and Social Policy, Department of Psychology, and the Institute of Social Anthropology. According to the evaluation conducted by the Ministry of Educa-

tion of China in 2017, its sociology major ranks third in China. The school has 52 full-time faculty members, including 23 professors, 23 associate professors, 3 assistant professors and 3 lecturers. The school has an international faculty, including 18 members graduating from the universities outside the mainland China, such as University of Chicago, Northwestern Univer-

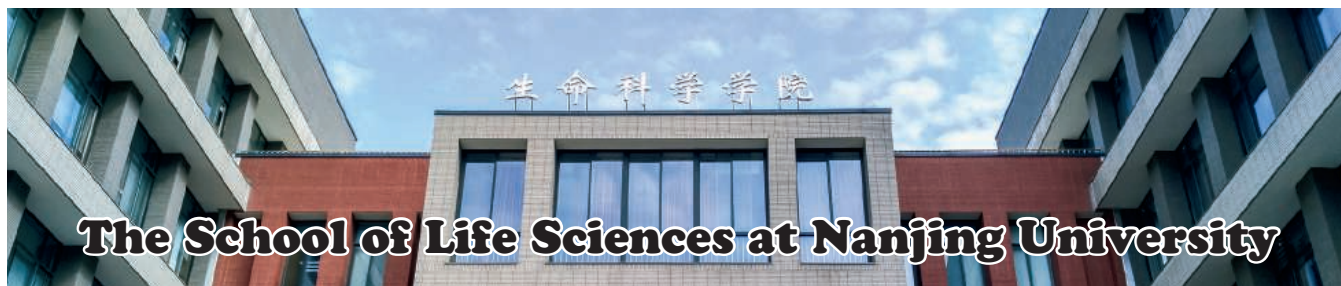
sity, University of Oxford, Free University of Berlin, University of Tokyo, etc.

The school specializes in sociological studies on many areas such as social theory, education, stratification and mobility in Chinese society, family, gender and population, urban studies, emotion, and also specializes in anthropology of religion. Its faculty members employ a

variety of research methods.

The school is eager to recruit established scholars or recent graduates focusing on the study of the societies outside China or visual sociology and anthropology. It is also devoted to expanding its academic network of China studies around the world.

If you are interested, please visit its **website:** sociology.nju.edu.cn



## The School of Life Sciences at Nanjing University

### School Introduction

Founded in 1902, Nanjing University is one of the oldest and most prestigious institutions of higher learning in China. The School of Life Sciences, originated from Department of Biology established in 1920, has three major disciplines – Biology, Pharmacy, and Ecology. The Biology subject is one of China's seven key national biology programs; Pharmacy and Ecology are both national First-Level disciplines. The School has clear and interdisciplinary research focus on biology and biochemistry, botany and zool-

ogy, environment and ecology, pharmacology and toxicology, neuroscience and behavioral science, molecular biology and genetics, agriculture, all among the Top 1% in ESI international rankings. Through the decades, the School has always been upholding the spirit of seeking truth from facts, pursuing research excellence and nurturing talents for the society.

### Recruitment Information

1. The Recruitment Program of Global Experts
2. Young Overseas High-Level Talents Introduction Plan

3. Deng Feng Scholars Program A of Nanjing University
4. Deng Feng Scholars Program B of Nanjing University
5. Professors, associate professors, young talented scientists and post-doctoral researchers

### Salary and benefits

Salary is commensurate with qualifications and experiences. Successful applicants will be offered decent benefits including scientific research start-up grant, settling-in allowance, assistance in establishing research group and scientific platform, adequate laboratory space.

### Qualification Requirement

1. A comprehensive CV
2. Abstract of academic achievement and future research plan
3. Five selected publications in PDF format
4. Contact information of three referees including E-mail & Telephone number

### Contact Information

Ms. Jingjie Liu

**E-mail:** jingjie@nju.edu.cn

**Tel:** +86-25-89684720

For more information, please visit our website: [life.nju.edu.cn](http://life.nju.edu.cn)

Welcome to join School of Life Sciences, Nanjing University!



## Medical School at Nanjing University

Nanjing University Medical School (NJUMS), a premier institution for medical education originally founded in 1935 as part of the National Central University and re-opened in 1987, was the first medical school in a comprehensive research university in China since 1980's. The school, located in two campuses, Gulou and Xianlin, has maintained an elite program in educating physician-scientists and top-notched leaders in basic and clinical medicine. NJUMS offers three majors with doctoral degrees in Basic Medicine, Clinical Medicine, and

Stomatology Medicine and is among the first medical universities eligible for the National Excellent Doctor Education Program with an Eight-year M.D. program in Clinical Medicine. Top-ranked affiliated teaching hospitals include prestigious Gulou Drum Tower Hospital, Jinling Hospital, and Nanjing Stomatological Hospital (NSH), all at the Grade-III Class-A level. Gulou and Jinling Hospitals are equipped with state-of-the-art facilities with 2,500 and 2,400 beds, more than 3 million and 2.4 million outpatients, and 86,000 and 79,000 inpatients each year, respectively. Currently about

150 distinguished Full Professors are employed, who teach medical and graduate students and perform scientific research and/or clinical practice. The school professors work on competitive grants from national funding agencies including NSFC and MOST and in 2019 obtained ~110 grants, which account for a quarter of the total grants awarded university-wide.

Nanjing University has prioritized medicine to be one of a few disciplines for strategic expansion and rapid development, which benefits NJUMS enormously in preferential policies and resources. NJUMS expects to

expand its programs both in basic and clinical medicine and recruit faculty in multiple disciplines including Basic Medicine, Clinical Medicine, Stomatological & Dental Medicine, Public Health and Preventive Medicine, and Advanced Medical Materials. Candidates are expected to excel and be innovative in ideas and methodology in their respective fields with distinguished accomplishments and great potential and meet the criteria for the existing national, provincial, or university-wide Talents programs, and. **Three categories of scholars are recruited:**

**I. Distinguished Full Professors:** Candidates have established academically with extramural grants or sustained financial support for accomplished research program(s). The candidates have already played a leading role in a selected research field. Currently possessing an academic rank at associate professor (or equivalent) is needed and establishing an internationally renowned program at NJUMS is expected with leading roles in obtaining major grants from various resources.

**II. Distinguished Young Scholars:** Candidates have completed PhD/MD with a few years of postdoctoral training and have demonstrated potential of being an academic or technological leader in their disciplinary field. Preference will be given to the applicants who have freshly started an independent research program or met the criteria with significant accomplishments for the national talents programs.

**III. University Dengfeng Scholars (登峰学者):** Candidates are expected to have completed their PhD/MD and at the stage of their postdoctoral training. Preferential consideration is given to those who distinguish themselves from their peers with high-impact and innovative accomplishments in the earlier stage of their career.

Perspective applicants please send Peng Yiling the application package including resume, names of three references, and the statement of research at Email: [ylpeng@nju.edu.cn](mailto:ylpeng@nju.edu.cn) and Phone: 86-025-83686451. More information: <http://med.nju.edu.cn>.





**S**hanghaiTech University is a young and dynamic higher education institution committed to carrying out China's national development strategy and nurturing the next generation of innovative scientists, inventors and entrepreneurs. With the backing and support of the Shanghai Municipal Government and China Academy of Science, ShanghaiTech's five schools, three research institutes and General Education Center seek cutting-edge solutions to address the challenges that China and the world is facing in the fields of energy, material, environment, human health, and artificial intelligence. As an integral part of the Zhangjiang Comprehensive National Science Center, ShanghaiTech is now leading several frontier research projects and large-scale facilities.

For more information, please visit: [www.shanghaitech.edu.cn](http://www.shanghaitech.edu.cn).

**ShanghaiTech is now seeking talents in the following fields:**

**School of Physical Science and Technology:** energy, system materials, photon and condensed state, material biology, environmental science and engineering

**School of Life Science and Technology:** molecular and cell biology, structural biology, neuroscience, immunology, stem cells and regenerative medicine, system biology and biological data, molecular imaging, biomedical engineering

**School of Information Science and Technology:** computer science, electrical engineering, information engineering, artificial intelligence, network and communication, virtual reality, statistics, big data and data mining

**School of Entrepreneurship and Management:** economics, finance, accounting, management, marketing, strategy and entrepreneurship

**School of Creativity and Art:** innovative design, filmmaking, game design, tech-driven art, big data visualization, creativity, design thinking

**Shanghai Institute for Advanced Immunological Studies:** antibody therapy, Immunotherapy, cell therapy, regeneration medicine

**iHuman Institute:** bio-imaging, biology, chemistry, computational biology, AI/ML

**Institute of Mathematical Sciences:** pure mathematics, theory of computing, applied mathematics

**Institute of Humanities:** Chinese philosophy, Western philosophy, logic, science philosophy, aesthetics, Ancient literature, modern literature, literary theory, comparative literature and world literature, Chinese writing, Chinese history, world history, historical theory, British and American language and literature, French language and literature, German language and literature, Japanese language and literature.

**Following positions are opening:**

**1.Tenured and Tenure-track positions:** assistant professor, associate professor and full professor.

Successful applicants will have a doctoral degree, and are expected to establish a record for independent, internationally recognized research, supervise students and teach high-quality courses.

**2.Research positions:** post-doctoral research fellow, research assistant professor, research associate professor and research professor. Successful applicants will have a doctoral degree, a good research record and great passion for research.

**3.Assistant positions:** teaching assistant, research assistant, and administrative officer. Successful applicants will have a Master's degree and relevant working experience.

**ShanghaiTech will offer attractive compensation packages, including:**

**Initial research support package:** reasonable start-up funds, research associates and post-doctoral fellows, laboratory space to meet research needs.

**Compensation and benefits:** highly competitive salary commensurate with experience and academic accomplishments, a comprehensive benefit package.

**Subsidized housing:** on-campus 80/100/120 m2 faculty apartments available at low rent for tenured and tenure-track faculty, on-campus postdoctoral dormitories, off-campus postdoctoral apartments and municipal apartments subsidized by Shanghai government.

**Relocation & travel allowance:** reimbursement of expenses for household relocation and family's one-way travel.

**Family assistance:** support with children's education; affiliated kindergarten, primary and middle schools.

**To apply:** using this format, please submit a cover letter (Firstname\_Lastname\_Cover\_Letter.pdf), a research plan (Firstname\_Lastname\_Research\_Plan.pdf), and a CV (Firstname\_Lastname\_CV.pdf) to [shanghaitechuniversity@gmail.com](mailto:shanghaitechuniversity@gmail.com)



廣州中醫藥大學

# Guangzhou University of Chinese Medicine

## Inviting Global Talents

**G**uangzhou University of Chinese Medicine (GUCM), one of the first four oldest institutions of Chinese Medicine, is currently supported by the National “Double First-rate” plan and the Program of High-level University of Guangdong Province. GUCM is located at the economically developed South China, it offers great opportunities for the researchers who are working in medicine and pharmacy.

**H**igh-level talents in the fields of basic or clinical medicine and pharmacy including traditional Chinese medicine, integrative Chinese and Western medicine, acupuncture and rehabilitation medicine, the fields of pharmacology, life sciences, medicinal chemistry and other related research areas are warmly welcome.

Tel: +86(020)39358219

Email: [rcb@gzucm.edu.cn](mailto:rcb@gzucm.edu.cn)

Scan and find  
more information



廣州中醫藥大學

Guangzhou University of Chinese Medicine





太原理工大学  
TAIYUAN UNIVERSITY OF TECHNOLOGY



**Dear young talents from around the world,**

*Greetings from HUANG Qingxue, the President of Taiyuan University of Technology!*

*As an institution of higher learning with a history of 117 years, TYUT is a "Double World-Class" key construction university in China, with a focus on engineering, a combination of science and technology, and a coordinated development of multiple disciplines.*

*Putting students at the center and with the world-class disciplines taking the lead, TYUT has been, over the recent years, vigorously implementing the five university-driven strategic projects with the strategy of reinvigorating TYUT through human resource development at its core.*

*With the broad vision of "openness and inclusiveness", TYUT welcomes young talents from around the globe. I am confident that with our joint efforts, TYUT will soon build itself into a university featuring high standards, internationalization, and innovation.*

#### Faculty Recruitment for Taiyuan University of Technology

TYUT is a "Double World-Class" key construction university, as well as a national "211 Project" key construction university. It is among the first batch of the Ministry of Education(MOE)'s experimental program of "Education Program of Excellent Engineers" and the national program of "Experiment Program of College Student Innovation".

At present, TYUT has 3 academicians of the Chinese Academy of Engineering, 15 academicians of dual employment, 51 doctoral research centers (15 for first-class disciplines), 15 post-doctoral mobile stations, 3 national key disciplines, 4 national experimental teaching demonstration centers, 5 national distinctive branch construction sites, 7 national "engineering practice education centers", 1 national key laboratory cultivation base jointly constructed by Shanxi province and the MOE, 4 MOE's key laboratories, 1 MOST (Ministry of Science and Technology)'s innovation team in key areas, and 2 MOE's Yangtze River scholars' innovation teams. TYUT's three disciplines, i.e. engineering, materials and chemistry, are among ESI's global top 1%.

TYUT is looking for high-level talents from across the world around the clock. We will provide you with a good research environment, a huge development space and highly competitive remunerations. We sincerely invite talents worldwide to join us!

#### Requirements & Remunerations

Positions	Requirements	Salaries & Benefits
Chief Scientists	Academician of the CAS, CAE, CASS, and famous overseas academic institutions	Case-by-case negotiation
Leading Scholars	Chief experts of national key disciplines and key laboratories, National 1000 or 10000 talents, Yangtze River Scholar professors, Winners of national outstanding youth fund or professors of top overseas universities	Annual salary: ¥800,000-1,200,000 for full-timers; mutually-agreed salary for short-termers; Family allowance: ¥1,000,000; Scientific research start-up funds: ¥2,000,000-5,000,000
Academic Leaders	Directors of MOE's key laboratories, Sanjin Scholars, Provincial 100 Talents, Yangtze River youth scholars, Winners of national outstanding youth fund, Associate professors of overseas high-level universities, Professors of 985 project universities or leaders the NNSF of China	Annual salary: ¥400,000-800,000 for full-timers, mutually-agreed salary for short-termers; Family allowance: ¥700,000; Scientific research start-up funds: ¥1,000,000-3,000,000
Academic Backbones-Fourth level	Associate professors of 985 project university, Professors of 211 project university, Winners of national 100 excellent doctoral dissertations, Sanjin youth scholars, Youth 100 talents of Shanxi, Doctoral supervisors	Annual salary: ¥200,000-400,000 for full-time, mutually-agreed salary for short-term; Family allowance: ¥500,000; Scientific research start-up funds: ¥500,000-1,500,000
Academic Backbones-Fifth level	Postdoctoral fellows or Ph. D. graduates of top overseas universities or institutions (THE top 200 universities, or ESI top 1% disciplines) who have published papers at the SCI(JCR Q1), SSCI, A&HCI journals or highly cited papers	Monthly salary: ±¥8500; Family allowance: ¥400,000; Scientific research start-up funds: ¥200,000-500,000
Teaching and Research Staff	Ph. D. graduate students of famous overseas universities (THE top 400 universities)	Monthly salary: ±¥7000; Family allowance: ¥150,000-400,000; Scientific research start-up funds: ¥50,000-120,000
Postdoctorals (as Backup Teachers)	47.92.163.91:8088/newszpw/show-1136.aspx	Annual salary: ¥200,000

#### How to apply

Applicants are requested to submit their CVs, along with other corresponding materials, at <http://47.92.163.91:8088/indexzpw.aspx>.

Contact information: High-level Talent Recruitment Office, Personnel Division, Taiyuan University of Technology  
Yanhua Wang(Mr) Guofang Meng(Mrs) Email: tyutrcyj@tyut.edu.cn Tel: 0351-6018078, 0351-6010382  
Address: Address: Room 535 or 529, Administration Building, Taiyuan University of Technology, 79 West Yingze Street, Taiyuan, Shanxi province, China 030024



# HIGH-LEVEL GLOBAL TALENTS RECRUITMENT



**Welcome back to hometown.**

**Thousands of academic job vacancies are in fast-developing China.**

## **On-the-spot Recruitment in UK**

Dec. 10, 2019 Imperial College London

Dec. 11, 2019 Queen Mary University of London

## **On-the-spot Recruitment in France**

Dec. 14, 2019 Pierre and Marie Curie University

Dec. 15, 2019 Université Paris-Sud

## **Participating Universities**

Jiangsu Normal University

Xuzhou Medical University

Shanghai Institute of Technology

The First Affiliated Hospital of Jinan University

Notheastern University

Shanghai University of Electric Power



Scan the QR code to apply  
for UK&France Job Fair

## **Online Job Fair**

Dec. 21, 2019(GTM+8) [www.edu.cn/cv](http://www.edu.cn/cv)

## **Participating Universities**

Shanghai University of Political Science and Law

Shanghai International Studies University

Nanchang University, Xi'an Technological University

Inner Mongolia University of Technology

Inner Mongolia University of Finance and Economics

Hunan University of Technology and Business



Scan the QR code to  
apply for Online Job Fair

## **Qualification for Applicants**

Overseas scholars, Doctor and Post-doctor

## **Participating Approach**

Please send your CV to [consultant@acabridge.edu.cn](mailto:consultant@acabridge.edu.cn) for  
on-the-spot Recruitment in UK and France and Online Job Fair.

**Job Vacancies in China's Universities and Institutes**

Please visit <https://www.acabridge.edu.cn/>

Contact [consultant@acabridge.edu.cn](mailto:consultant@acabridge.edu.cn)



乡愁，  
是那一汪大海，  
我在这头，  
家人在那头。

千万个  
不回的理由，  
难抵  
一个归根的念头。

Nostalgia,  
is like an ocean,  
I am here,  
the family is over there.

Thousands of reasons  
to stay abroad,  
but one decision to  
return to the roots.

**Overseas Chinese Scholars'**  
**Visit to Top Chinese Universities**  
Check the Details from [www.edu.cn/zgx](http://www.edu.cn/zgx)

- **10,000+ academic job vacancies in China**
- **Free one-to-one consultation service**

Send your CV to [consultant@acabridge.edu.cn](mailto:consultant@acabridge.edu.cn)



**上海外国语大学**  
SHANGHAI INTERNATIONAL STUDIES UNIVERSITY



**贵州医科大学**  
GUIZHOU MEDICAL UNIVERSITY



**南京工业大学**  
NANJING TECH  
UNIVERSITY



**江西理工大学**  
Jiangxi University of Science and Technology



**天津师范大学**  
Tianjin Normal University



**山东第一医科大学 (山东省医学科学院)**  
Shandong First Medical University & Shandong Academy of Medical Sciences



## Ohio State's Pelotonia Institute for Immuno-Oncology Seeks Multiple Tenure-Track Faculty Positions

The Ohio State University Comprehensive Cancer Center – Arthur G. James Cancer Hospital and Richard J. Solove Research Institute (OSUCCC – James) is seeking experienced tenure-track faculty (basic as well as clinical researchers) to work in the recently announced **Pelotonia Institute for Immuno-Oncology (PIIO)** in the following research areas:

- T-cell biology
- Innate immunity and inflammation
- Immune regulation and tolerance
- Cell therapy, synthetic immunology, immunogenomics and cancer vaccines
- Translational and clinical immuno-oncology (IO)
- Immune monitoring and discovery

Led by founding director and renowned immunologist **Zihai Li, MD, PhD**, the PIIO ([cancer.osu.edu/PIIO](http://cancer.osu.edu/PIIO)) is a comprehensive bench-to-bedside research initiative and represents Ohio State's commitment to grow the exciting area of immuno-oncology.

The **OSUCCC – James** ([cancer.osu.edu](http://cancer.osu.edu)) is a National Cancer Institute (NCI)-designated comprehensive cancer center and is rated "Exceptional," the highest rating given to cancer centers by

the NCI; is one of only a few centers funded by the NCI to conduct phase I and II clinical trials on novel anticancer drugs; and includes the third-largest freestanding cancer hospital in the country.

Candidates will have access to state-of-the-art laboratory spaces, cutting-edge core research facilities, a competitive salary and start-up funding. Applicants must hold advanced degrees, such as an MD, DVM, PharmD, PhD or MD/PhD. The successful candidate is expected to maintain an extramurally funded research program, perform collaborative research, participate in graduate and medical education, be board-certified and meet medical licensure requirements in Ohio if also pursuing a clinical position. Located in Columbus, Ohio ([go.osu.edu/whycolumbus](http://go.osu.edu/whycolumbus)), The Ohio State University is an EOE/AA/M/F/D/V employer.

**Send cover letter, CV, 2-3 page description of current and future research interests and contact information for three references via email to Tamra Brooks at [tamra.brooks@osumc.edu](mailto:tamra.brooks@osumc.edu).**

Applications will be accepted until the positions are filled.

### The James



**THE OHIO STATE UNIVERSITY**  
COMPREHENSIVE CANCER CENTER

## LSU Health NEW ORLEANS

### School of Medicine

#### FACULTY POSITION

#### Department of Microbiology, Immunology and Parasitology

The Department of Microbiology, Immunology and Parasitology in the School of Medicine at LSU Health Sciences Center in New Orleans, LA invites applications for a full-time, tenure-track position in Bacteriology or Virology at the academic rank of Assistant or Associate Professor. Applicants should hold a Ph.D., M.D. or equivalent degree. Special consideration will be given to candidates with outstanding records of research accomplishment in bacterial or viral genomics, host: pathogen interactions, vaccine development, or microbiomes, who complement existing research strengths in Chlamydia/STI's, mycobacteria and HIV infection. The Department has a highly interactive faculty in the disciplines of bacteriology, virology, mycology, parasitology, and immunology. Information on the department can be viewed at: <http://www.medschool.lsuhsu.edu/microbiology/>. The appointee will be expected to maintain an active, extramurally funded research program, engage in collaborative research efforts, serve on institutional and peer-review committees, mentor PhD and MD/PhD graduate students and postdoctoral fellows, and participate in graduate and undergraduate teaching programs. Collaborative opportunities are available for interaction with researchers in basic science and clinical departments, and in Centers of Excellence at the University, who engage in microbiology, immunology and genome research. This position is supported by state-of-the-art infrastructure, including core laboratories in genomics, proteomics, bioinformatics, imaging, flow cytometry, and a BSL-3 facility. The successful candidate will have significant laboratory space, a competitive salary, and an excellent start-up package commensurate with qualifications and experience. LSUHSC encourages women and minority candidates to submit applications for this position.

Applicants should submit their curriculum vitae that includes previous and current research support, teaching experience, a statement of research plans, e-prints of three representative publications, and the complete contact information of three professional references via the LSUHSC career portal at <http://lsuhsc.peopleadmin.com/postings/6501>.

*LSU Health is an Equal Opportunity Employer for females, minorities, individuals with disabilities and protected veterans.*

# UConn HEALTH

## RESEARCH SCIENTIST DEPARTMENT OF ORTHOPAEDIC SURGERY

The Department of Orthopaedic Surgery within the UConn Musculoskeletal Institute invites applications for a tenure track position at the Assistant or Associate Professor level as a research scientist. Outstanding individuals working in skeletal cell biology and wanting to make a difference in the field of musculoskeletal research are encouraged to apply. A Ph.D. or an M.D. degree is required. Candidates' research should be aimed at addressing fundamental questions related to cellular, molecular or physiological mechanisms of the skeletal system. We are particularly interested in individuals currently funded by the National Institutes of Health. The University of Connecticut School of Medicine has a highly interactive research environment in musculoskeletal biology with interdisciplinary graduate and medical science training programs. The Musculoskeletal Institute offers a collegial environment and houses investigators working in various aspects of skeletal cell biology and biomechanics of bone. Appropriate laboratory space and a start-up package will be offered.

Applicants should submit a letter, curriculum vitae and research plan as well as the names (with addresses and email addresses) of at least three references. Information should be submitted via this website [https://jobs.uconn.edu/CSS\\_External/CSSPage\\_Welcome.asp](https://jobs.uconn.edu/CSS_External/CSSPage_Welcome.asp). Search number 2017-1229.

*UConn Health is an affirmative action employer, in addition to an EEO and M/F/V/PWD/PV employer.*



## Northeastern University College of Engineering

With **185** tenured/tenure-track faculty (over **90** hired since 2012), and **17** multidisciplinary research centers and institutes, with funding by eight federal agencies, Northeastern's College of Engineering is in a period of dynamic growth. Our emphasis on interdisciplinary, transformative and innovative research—tied to Northeastern's unique history of industry collaboration through the university's signature cooperative education program—enables partnerships with academic institutions, medical research centers, and companies near our centrally located Boston campus and around the globe.

### The college seeks outstanding faculty candidates across engineering disciplines.

Consideration will be given to candidates at the assistant, associate, and full professor levels; successful applicants will lead internationally recognized research programs aligned with one or more of the college's strategic research initiatives.

### Learn more and apply at [coe.northeastern.edu/faculty-hiring](http://coe.northeastern.edu/faculty-hiring)

Northeastern University is an equal opportunity employer, seeking to recruit and support a broadly diverse community of faculty and staff. Northeastern values and celebrates diversity in all its forms and strives to foster an inclusive culture built on respect that affirms inter-group relations and builds cohesion.

All qualified applicants are encouraged to apply and will receive consideration for employment without regard to race, religion, color, national origin, age, sex, sexual orientation, disability status, or any other characteristic protected by applicable law.

To learn more about Northeastern University's commitment and support of diversity and inclusion, please see [northeastern.edu/diversity](http://northeastern.edu/diversity).



The University of Georgia

### Postdoctoral Associate in Trypanosome Biology and Drug Discovery

A position in molecular cell biology (protein kinases or endocytosis or kinetoplast biogenesis), molecular pharmacology, and drug discovery in *Trypanosoma brucei* is available in the laboratory of Kojo Mensa-Wilmot at the University of Georgia. A PhD in molecular or cell biology is required.

Applicants should submit a *curriculum vitae*, and research/career goals (less than 4 pages) at:

<https://www.ugajobsearch.com/postings/126286>

Two confidential letters of recommendation are required, and applicants should list contact information of referees in their application.

**myIDP:**  
A career plan customized  
for you, by you.



For your career in science, there's only one **Science**

### Features in myIDP include:

- Exercises to help you examine your skills, interests, and values.
- A list of 20 scientific career paths with a prediction of which ones best fit your skills and interests.
- A tool for setting strategic goals for the coming year, with optional reminders to keep you on track.
- Articles and resources to guide you through the process.
- Options to save materials online and print them for further review and discussion.
- Ability to select which portion of your IDP you wish to share with advisors, mentors, or others.
- A certificate of completion for users that finish myIDP.



Visit the website and start planning today!  
[myIDP.sciencecareers.org](http://myIDP.sciencecareers.org)

**Science Careers**

MAAS

In partnership with:



# HUNGARY WELCOMES LEADING RESEARCHERS

The National Research, Development and Innovation Office of Hungary is committed to support science and innovation.

With our latest call for proposals called **"FRONTLINE RESEARCH EXCELLENCE PROGRAMME"** we invite excellent researchers of any nationality to conduct their projects at a Hungarian host institution.

- Up to EUR 910,000 funding per project for the next five years, in any field of science
- Selection criteria is based on high international standards
- Submission deadline: December 17, 2019

For further details and conditions, please visit:  
<https://nkfih.gov.hu/frontline>



NATIONAL  
RESEARCH, DEVELOPMENT  
AND INNOVATION OFFICE

## Who's the Top Employer for 2019?

Science Careers' annual survey reveals the top companies in biotech & pharma voted on by Science readers.

Read the article and employer profiles and listen to podcasts at [sciencecareers.org/topemployers](http://sciencecareers.org/topemployers)



ÖAW

AUSTRIAN  
ACADEMY OF  
SCIENCES

IWF - SPACE RESEARCH INSTITUTE

The Austrian Academy of Sciences (OeAW), Austria's central non-university research and science institution, seeks to appoint a new

### DIRECTOR (F\*M) at the Space Research Institute.

The statutory mission of the Austrian Academy of Sciences (OeAW) is to "promote science in every aspect" by operating a total number of 28 research institutes, which are engaged in innovative research of international standing in a variety of disciplines.

The Space Research Institute (Institut für Weltraumforschung, IWF; [www.iwf.oeaw.ac.at](http://www.iwf.oeaw.ac.at)) in Graz is one of the largest research institutes of the OeAW. The long-lasting basic research focus of the IWF concentrates on the physics of space plasmas, planetary atmospheres and (exo-)planets. With its about 100 qualified and experienced scientists and engineers from 20 different nations, the IWF develops and builds space-qualified instruments and analyzes and interprets the data returned by them. Its core engineering expertise is in building magnetometers and on-board computers, as well as in satellite laser ranging. In terms of science, the institute focuses on dynamical processes in space plasma physics and on the upper atmospheres of planets and exoplanets.

The institute is involved in numerous international space missions led by the European Space Agency (ESA), NASA, or national space agencies in Japan, Russia, China, and South Korea. The missions cover fleets of satellites in near-Earth space, the observation of the Sun, and the exploration of planets such as Mercury, Jupiter, and extrasolar planets. From building the instruments to analyzing their data, these projects last 10-30 years.

The IWF has a basic funding by the OeAW, and additional national and international third-party funding for designated research projects. The institute offers a world-class scientific and collaborative research environment for space science and is supported by skilled in-house administrative and technical staff.

The OeAW now seeks to appoint a strong and ambitious personality with an outstanding scientific track record in at least one of the relevant research fields. The ideal candidate is expected to have strong scientific leadership and management qualities and to be well connected within the international scientific community. The success of the candidate's research should also be reflected in peer-reviewed third-party funding. The OeAW is confident to appoint a future director who wants to continue his/her cutting edge research strategy and activities at the IWF.

We offer an attractive recruitment package that includes an internationally competitive salary and a substantial annual research budget (personnel, consumables, investments).

The term of appointment is initially limited to 5 years with a possible extension, depending on external review. The OeAW strives for gender equity and strongly encourages applications from women.

Qualified candidates are encouraged to apply and submit a detailed application to Anton Zeilinger, President of the Austrian Academy of Sciences, at [IWF.search.director@oeaw.ac.at](mailto:IWF.search.director@oeaw.ac.at), containing:

- Curriculum vitae
- Publication list with copies of the five most important publications
- Overview of recent research and funding activities
- Concept for the strategic development of IWF

Closing date for applications: December 31, 2019

[WWW.IWF.OEAW.AC.AT](http://WWW.IWF.OEAW.AC.AT)

SCHWIEDLSTRASSE 9 | 8042 GRAZ, AUSTRIA  
T: +43 316 4120-400 | F: +43 316 4120-410  
IBAN: AT5110000026359590 | BIC: BKAUATWW | VAT: ATU37116303





By Jeff Clark

# An escape into fiction

I arrived home from work, my mind racing. I was scheduled to perform an experiment using a pricey piece of equipment—one that I'd be unlikely to gain much access to again during my Ph.D.—and I needed it to go flawlessly. "Will the x-rays transmit correctly?" I wondered. "What's my backup plan if things go wrong?" I had spent the whole day fretting about the experiment, and I wanted to shut off my anxious thoughts. So after dinner, I made a cup of hot chocolate, curled up on my sofa, and cracked open a novel I'd been reading. Almost immediately, my mind left behind the details of experimental design and parachuted into a land of dæmons, magic dust, and armored bears. It was exactly what I needed.

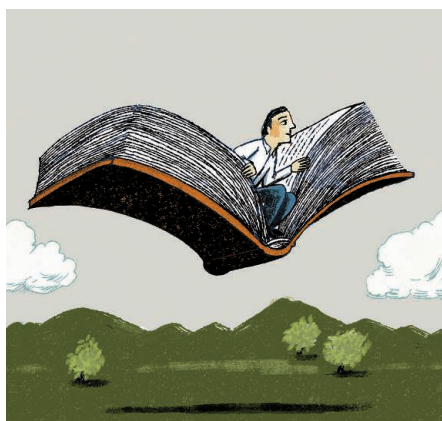
Growing up, I was a voracious reader but never a big fan of novels. My classmates would rave about the latest Harry Potter book, while my copy sat collecting dust on a shelf. I saw those kinds of books as a waste of time. "Why read a made-up story when I could read a book that actually teaches me something?" I reasoned.

As an undergraduate, keen to learn something at every opportunity, I would reject typical holiday reads in favor of educational books. On a trip to Portugal, my friends took turns reading a Dan Brown mystery novel. Meanwhile, I couldn't put down a Malcolm Gladwell book that took a deep dive into social science research.

After I started graduate school, though, that approach to extra-curricular reading didn't work for me anymore. I spent my time on campus digesting research papers and textbooks—trying to become an expert in my field—and my mind couldn't handle processing fact-filled nonfiction books at home, too. I knew that I needed to find a way to enjoy reading again.

My partner had a bookcase full of novels, so I figured, "Why not try fiction?" To help me stick with it, I made a New Year's resolution: I would read two fiction books per month for the entire year. The result was an almost instantaneous appreciation of fiction, along with many unintended consequences—including ones that have benefited my work.

What surprised me the most was how much I learned. Some of the best books I read were historical fiction—fictional stories that take place in a realistic historical setting. I learned about life in Afghanistan and Ghana, as well as struggles people there faced during difficult periods



**"When I'm engrossed in a good book, I can temporarily switch off and explore a different world."**

in those countries' histories. The books have helped me build empathy and understanding, with an unexpected side benefit: I've started to think more deeply about inclusion and diversity issues in the scientific community.

My foray into fiction also introduced me to new writing styles. The no-frills prose that's typical of journal articles doesn't always make for compelling reading. Scientific authors, it seems, often assume that interest in the science will be enough to hold the reader's attention. Fiction authors don't have that luxury, so they work hard to build intrigue and draw out a compelling story arc—concepts that I've begun to implement when presenting my science in written form and in talks. I now aim to

keep my readers and audience members engaged by laying out a dynamic story, taking care to clearly describe the context of my research and to eliminate potentially confusing details.

Beyond those benefits, I've discovered that reading fiction is good for my mental health. Life as a grad student is taxing, and it's often difficult to distance yourself from work, with the day's worries stealthily following you home. But when I'm engrossed in a good book, I can temporarily switch off and explore a different world. It's an excellent way to gain distance from stress so that I can rejuvenate myself and regain energy for my work.

So, if you haven't done so already, give fiction a try. You'll be surprised how much it brings to your life. ■

Jeff Clark is a Ph.D. candidate at Imperial College London. Do you have an interesting career story to share? Send it to [SciCareerEditor@aaas.org](mailto:SciCareerEditor@aaas.org).